CLEAVAGE FRACTURE

GEORGE R. IRWIN SYMPOSIUM

19990107 036

DTIC QUALITY INSPECTED 3

REPORT DOCUMENTATION PAGE

Form Approved
OMB No. 0704-0188

Public reporting burden for this collection of information is estimated to average 1 hour per response, including the time for reviewing instructions, searching existing data sources, gathering and maintaining the data needed, and completing and reviewing the collection of information. Send comments regarding this burden estimate or any other aspect of this collection of information, including suggestions for reducing this burden to Washington Headquarters Services, Directorate for Information Operations and Reports, 1215 Jefferson Davis Highway, Suite 1204, Arlington, VA 22202-4302, and to the Office of Management and Budget, Paperwork Reduction Project (0704-0188), Washington, DC 20503.

1. AGENCY USE ONLY *(Leave blank)*	2. REPORT DATE	3. REPORT TYPE AND DATES COVERED
	Dec. 29, 1998	Final

4. TITLE AND SUBTITLE
George Irwin Symposium on Cleavage Fracture

5. FUNDING NUMBERS
N00014-97-1-0850

6. AUTHOR(S)
Kwai S. Chan, Editor

7. PERFORMING ORGANIZATION NAMES(S) AND ADDRESS(ES)
The Minerals, Metals & Materials Society, Inc.
420 Commonwealth DR
Warrendale, PA 15086

8. PERFORMING ORGANIZATION REPORT NUMBER

9. SPONSORING / MONITORING AGENCY NAMES(S) AND ADDRESS(ES)
Office of Naval Research
Regional Office Chicago
536 S. Clark St., Room 208
Chicago, IL 60605-1588

10. SPONSORING / MONITORING AGENCY REPORT NUMBER

11. SUPPLEMENTARY NOTES
Compilation of presentations at the Symposium included in the proceedings.

a. DISTRIBUTION / AVAILABILITY STATEMENT
Approved for Public RElease

12. DISTRIBUTION CODE

13. ABSTRACT ***(Maximum 200 words)***

14. SUBJECT TERMS

15. NUMBER OF PAGES

16. PRICE CODE

17. SECURITY CLASSIFICATION OF REPORT	18. SECURITY CLASSIFICATION OF THIS PAGE	19. SECURITY CLASSIFICATION OF ABSTRACT	20. LIMITATION OF ABSTRACT

CLEAVAGE FRACTURE

GEORGE R. IRWIN SYMPOSIUM

Proceedings of a symposium held at the 1997 TMS Fall Meeting
Indianapolis, Indiana
September 15-17, 1997

Edited by
Kwai S. Chan

A Publication of
TMS
Minerals • Metals • Materials

A Publication of The Minerals, Metals & Materials Society
420 Commonwealth Drive
Warrendale, Pennsylvania 15086
(412) 776-9000

The Minerals, Metals & Materials Society is not responsible for statements or opinions and is absolved of liability due to misuse of information contained in this publication.

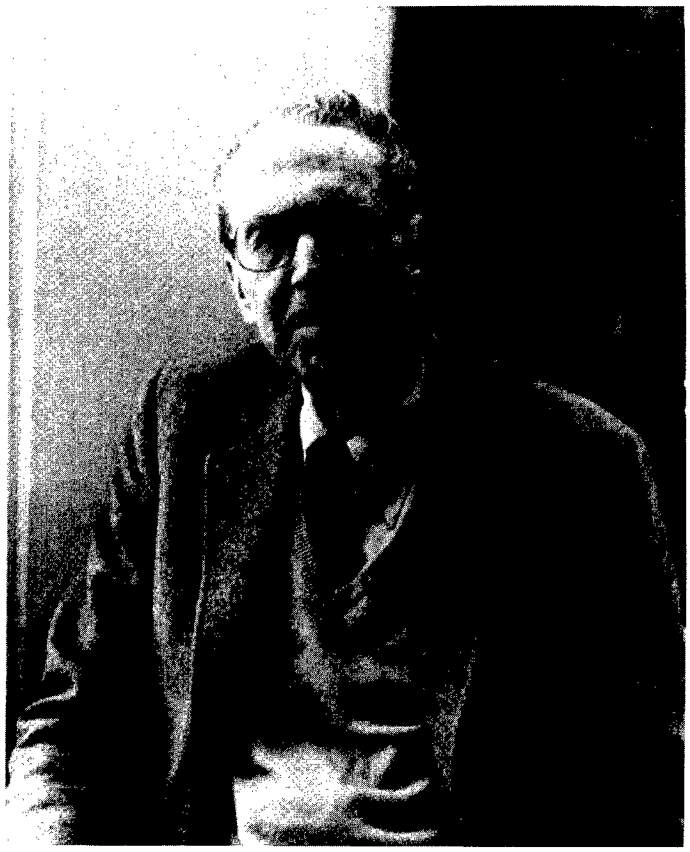
Printed in the United States of America
Library of Congress Catalog Number 97-73309
ISBN Number 0-87339-381-3

Authorization to photocopy items for internal or personal use, or the internal or personal use of specific clients, is granted by The Minerals, Metals & Materials Society for users registered with the Copyright Clearance Center (CCC) Transactional Reporting Service, provided that the base fee of $3.00 per copy is paid directly to Copyright Clearance Center, 27 Congress Street, Salem, Massachusetts 01970. For those organizations that have been granted a photocopy license by Copyright Clearance Center, a separate system of payment has been arranged.

TMS
Minerals • Metals • Materials

© 1996

If you are interested in purchasing a copy of this book, or if you would like to receive the latest TMS publications catalog, please telephone 1-800-759-4867 (U.S. only) or 412-776-9000, Ext. 270.



This symposium is dedicated to Dr. George R. Irwin, Professor Emeritus of University of Maryland, for physics, mechanics, and metallurgical contributions that have provided a foundation for the engineering discipline of Fracture Mechanics.

PREFACE

This symposium was originally proposed to TMS under the title of "Cleavage Fracture: Theory, Experimentation, and Modeling." The goal of the symposium was to be an in-depth coverage of the recent work on the phenomena of cleavage fracture in the presence of plastic flow. After the initial call-for-papers went out, subsequent discussion with Professor Ronald W. Armstrong, University of Maryland, led to the dedication of this symposium to Professor George R. Irwin for his landmark contributions to the field of fracture mechanics and its applications to cleavage fracture. The George R. Irwin Symposium on Cleavage Fracture is a companion symposium to the Frank A. McClintock Symposium on ductile fracture, which was held earlier in February 1997 at the TMS Annual Meeting in Orlando, Florida.

The initial response to the Irwin Symposium was overwhelming with more than sixty tentative titles submitted. Unfortunately, some authors had to withdraw later for various reasons. The final program consists of thirty-nine papers organized into five sessions, with one on the biography of Professor Irwin to be presented at the symposium banquet by Professor H. P. Rossmanith, Institute of Mechanics, Vienna University of Technology. The symposium proceedings is a collection of twenty nine papers and ten abstracts on the subjects of fracture mechanics, dislocation theory of fracture, atomistic fracture, micromechanical and microstructural modeling of cleavage, cleavage mechanisms, fractographic characterization, experimental techniques, and cleavage studies in metals, welds, intermetallics, ceramics, and minerals. The diverse topics reflect the wide range of disciplines that Professor Irwin has impacted through his pioneer work on fracture mechanics.

As organizer of the symposium and editor of the proceedings, I would like to acknowledge the sponsorship of the TMS-SMD Mechanical Metallurgy Committee, ASM-MSD Flow and Fracture Committee, and the ASM-MSD Computer Simulation Committee. The financial supports provided by Office of Naval Research, Dr. George R. Yoder, Program Monitor, and the TMS Structural Materials Division are also acknowledged. I thank all the participants and the TMS staff for making the symposium a success. I am grateful to Drs. John D. Landes, David L. Davidson, Vaclav Vitek, William W. Gerberich, Robert O. Ritchie, Anthony A. Thompson, Alan R. Rosenfield, Donald A. Koss, and Dennis M. Dimiduk for serving as the session chairs. My thanks also go to Professor Ronald W. Armstrong for providing suggestions to the organization of the conference and for furnishing personal information and a photograph of Professor Irwin. The clerical and administrative assistance provided by Ms. Patty A. Soriano, Southwest Research Institute, is very much appreciated.

Kwai S. Chan
Southwest Research Institute
San Antonio, Texas

May 12, 1997

INTRODUCTION

George Rankin Irwin

With that middle name, no wonder George Irwin moved from English and Physics to at least the mechanics part of Mechanical Engineering. The English and Physics was at Knox College, in Galesburg, Illinois. The Physics was developed at the University of Illinois, Urbana, with a Masters Degree in 1935 and the doctorate in 1937, including a joint paper on a mass ratio of the lithium isotropes. Someone has said that a Doctor's Degree should be a professional license to do anything. George Irwin put that challenge to work when he joined the Naval Research Laboratory and became head of the Ballistics Branch, a position he held until 1953.

During World War II Irwin worked on projectile penetration, combat damage to aircraft, and the development of new armor materials. He worked out and applied a direct, but demanding, technique for measuring the force as a projectile enters the target, which was presented after the war to the Sixth International Congress for Applied Mechanics. Later, it was used by others in the Ballistics Branch to develop non-metallic armor for personnel. This was widely used in the Korean and Vietnam wars.

Irwin's interest in brittle fracture was kindled by seeing armor-plate which cracked in full-scale testing, although being ductile in small Charpy V-notch tests. Even though he had now become Superintendent of the Mechanics Division, a post he held from 1950 to 1967, this started him on his best-known work. First some background. In the 1920's Griffith had shown that the instability of tensile cracks in brittle materials depended on the strain energy release per unit crack advance G. In a classic paper presented at the Ninth International Congress of Applied Mechanics in 1956, Irwin showed a simple relation between G and a new quantity, the stress intensity factor K, which was the constant of proportionality in equations he gave for the local elastic stress and strain field around the crack tip. If the structure was elastic enough for this field to exist, a critical value K_c supplied the boundary condition at fracture for materials even with plasticity within the K-region. He gave data for a variety of such alloys. He also gave an experimental method to measure K. Thus in seven small, widely-spaced pages he founded the field of fracture mechanics. The field has now been generalized to predict that a crack in a structure will grow when the value of a parameter or a function calculated by ordinary mechanics from the geometry and loading reaches a critical material-dependent value found from laboratory test specimens. The idea was so original that I heard an esteemed colleague say it could not be mechanics because it had dimensions never seen in mechanics!

While Irwin had been approaching the problem of fracture in structures through elastic fracture mechanics, I had come at the problem through plasticity. Each naturally had his own set of implied assumptions, and we did not always see eye to eye. In the early 1960's, some of the fracture community thought we should get our acts together and write a joint paper on elastic-plastic fracture. We met at both his house and mine, and discovered we had much in common. We both had modest, comfortable homes, supportive wives, and like to mix cold cereals for breakfast. Where

there was solid ground, we found that we could both reach it, and we could understand when it was not solid. George's mild manner and tolerance with a young upstart was essential to the success of the enterprise.

Irwin's interests included the practically important fields of dynamic fracture and crack arrest, as expressed in about twenty papers and reports over a nearly 40-year period starting in 1947. This work stimulated that of many others. His elastic fracture mechanics was extended to non-linear elasticity, and extensively applied to elastic-plastic crack initiation and early growth by Rice, Hutchinson, and Shih, for example, and in turn, to creep by Landes, Sadananda, Riedel, and others. Paris took the crucial step of extending Irwin's ideas to the growth of cracks in fatigue.

In 1967 Irwin became University Professor at Lehigh, working on the development of senior and graduate level courses in fracture mechanics. His research was primarily on structural steels, as applied to pipe-lines, bridges, and pressure vessels.

1972 he became part time professor at the University of Maryland, where he continued his academic interests. With his colleagues there, his research was now extended to include polymers, photoelasticity, and fractography. This last topic, turning to the micron-scale phenomena underlying the values of the material-dependent critical stress intensity factor K_C, is remarkable for someone who has spent his career making such great contributions at the scale of continuum mechanics.

In addition to the above work, Irwin has been active with the famous ASTM Committee E-24 on Fracture Testing, as well as with the ASCE, ASM, NAE, and SEM. He has consulted for industrial, non-profit, and government laboratories such as Boeing, Allis Chalmers, Battelle, Southern Research Institute, Material Research Laboratory, NRC, NBS (now NIST), and ORNL.

He is a member of many technical societies including the Washington Philosophical Society, Sigma Xi, AAUP, and the National Academy of Engineering. He is a fellow of the SEM, AAAS, Washington Academy of Sciences, and the ASTM (of which he is also an Honorary Member). He has received some twenty major awards and medals, including an honorary Doctor of Engineering from Lehigh University.

George, we salute you!

Frank A. McClintock
Massachusetts Institute of Technology
Cambridge, Massachusetts
With the help of others of Dr. Irwin's colleagues

May 12, 1997

TABLE OF CONTENTS

HISTORICAL REVIEWS

George Rankin Irwin—The Father of Fracture Mechanics 3
H.P. Rossmanith

The Influence of a Great American Scientist and Engineer in Germany 39
E. Sommer

Brittle Cleavage Fracture: An Overview of Some Historical Aspects (abstract only) 47
P.C. Paris

FRACTURE MECHANICS

Microstructural Mechanics Description of Cleavage Fracturing in Polycrystals 51
R.W. Armstrong, G.R. Irwin, and X.J. Zhang

Interpretation of River Line Steps Associated With the Growth of Cracks 59
D. Hull

SEM Stereo-Section Fractography (SSF) Observations 69
X.J. Zhang, R.L. Tregoning, R.W. Armstrong, and G.R. Irwin

A Three-Dimensional Model for Polycrystalline Cleavage and Problems in Cleavage After Extended Plastic Flow or Cracking 81
F.A. McClintock

The Role of Plastic Deformation in Cleavage Crack Propagation and Arrest in Ferritic Steels 95
E. Smith

An Instability and Energy Rate Model for Cleavage Fracture 107
C.E. Turner

DISLOCATION AND ATOMISTIC THEORIES

Kinetics of the Crack-Tip-Governed Brittle to Ductile Transitions in Intrinsically Brittle Solids 125
A.S. Argon, G. Xu, and M. Ortiz

Modelling Crack Tip Plastic Zones and Brittle-Ductile Transitions 137
P.B. Hirsch and S.G. Roberts

Inside the Crack Tip 147
M. Marder

A New Model of the Brittle-to-Ductile Transition Based on a Collective Dislocation Generation Instability 157
R.H. Folk II, S.M. Labovitz, and D.P. Pope

Atomistic Simulations of Fracture (abstract only) 163
D. Farkas

Atomistic Study of Three-Dimensional Fracture and Deformation (abstract only) 165
S.J. Zhou, D.M. Beazley, P.S. Lomdahl, B.L. Holian, and D. Preston

Effect of Impurities on Cleavage Fracture: H, C, B, and S in Ni_3Al (abstract only) 167
N. Kioussis, G. Lu, M. Ciftan, and A. Gonis

MICROMECHANICAL AND MICROSTRUCTURAL MODELING

Recent Advances in the Micro-Modelling of Cleavage Fracture in Steel 171
J.F. Knott

An Application of the J-Q Model for Estimating Cleavage Stress in the Brittle to Ductile Transition 183
J.D. Landes and C.A.J. Miranda

Modeling a Cleavage-Characteristic Stress (S_{co}) of Ferritic Steels 193
D.M. Li and M. Yao

Shear-Induced Cleavage Fracture 207
K.S. Chan

Cleavage-Quasi Cleavage in Ferritic and Martensitic Steels (abstract only) 221
G.R. Odette, K.V. Edsinger, and G.E. Lucas

Statistical and Constraint Factors in Cleavage Initiation (abstract only) 223
G.R. Odette, K.V. Edsinger, and G.E. Lucas

The Fractography-Modeling Link in Cleavage Fracture (abstract only) 225
A.W. Thompson

FRACTURE MECHANISMS

Micromechanisms of Cleavage Fracture 229
A.R. Rosenfield

An Investigation Into the Mechanism of Cleavage Fracture in a Dual Phase Steel 237
W.-D. Cao

Brittle Fracture in High-Strengthening Single Crystals of Austenitic Stainless Steels 247
Y.I. Chumlyakov, I.V. Kireeva, E.I. Litvinova, V.I. Kirillov, and N.S. Surikova

Influence of TiN Particles and Microstructure on Cleavage Fracture in Simulated HAZ 263
L.P. Zhang, C.L. Davis, and M. Strangwood

A New Tool for Crystallographic and Topographic Analysis of Cleavage Fracture Surfaces 271
C.O.A. Semprimoschnig, O. Kolednik, and R. Pippan

A Fractographic Study of the Low Temperature Fracture of a High Mn, High N Austenitic Stainless Steel 277
J.I. Dickson, J.-B. Vogt, A.H. Messai, and J. Foct

Oxide Film Effects on Cleavage (abstract only) 285
W.W. Gerberich, N.R. Moody, and M.D. Kriese

Surface Film Softening as a Problem of Cleavage Fracture (abstract only) 287
R. Gibala

Cleavage Mechanism in Vanadium Alloys (abstract only) 289
G.R. Odette, E. Donahue, and G.E. Lucas

CLEAVAGE FRACTURE IN ALUMINIDES AND CERAMICS

Fracture and Fracture Toughness of Directionally Solidified TiAl-Based Two-Phase Alloys 293
N. Akiyama, S. Yokoshima, D.R. Johnson, K. Kishida, H. Inui, and M. Yamaguchi

Deformation and Fracture Behavior in TiAl Alloys Under Monotonic and Cyclic Loading Conditions 305
Y.-W. Kim and D.M. Dimiduk

An Investigation of Cleavage Fracture in Mn-Containing Gamma-Based Titanium Aluminides 319
W.O. Soboyejo, C. Mercer, and K. Lou

Brittle Fracture in B2 Compounds 329
P.R. Munroe and I. Baker

Mixed-Mode Cleavage Fracture of an Iron Aluminide Under Monotonic Loading 347
F.R. Frasier and J.P. Hirth

Cleavage of Ceramic and Mineral Single Crystals 355
R.C. Bradt

Static and Cyclic Fatigue Failure at High Temperature in Ceramics Containing Grain Boundary Phase: Experiments 367
K.J. Hsia, N. Dey, and D.F. Socie

Subject Index 377

Author Index 383

HISTORICAL REVIEWS

George Rankin Irwin - The Father of Fracture Mechanics

H.P.Rossmanith

Institute of Mechanics
Vienna University of Technology
Vienna, Austria

Abstract

This contribution gives a short overview of the history of fracture research and highlights G.R. Irwin's struggle for recognition of fracture mechanics to become a universally accepted discipline in science and engineering. Many aspects presented in this paper derive from discussions with Professor G.R. Irwin during numerous professional and private visits of the author to the Irwin family and a careful study of the private archive of Dr Irwin during the past two decades.

1. Introduction

Fracture mechanics has been actively used since neolithic times when man invented and produced simple and later more sophisticated stone tools. The development of the flint knapping technique for the production of blades, adzes and other stone tools required at least some knowledge of how stones would break and chip [1]. However, it is doubtful that these early ancestors of modern man did understand the mechanism of fracturing.

2. Early documented fracture tests

In China, to the kings of the late Shang dynasty (800 B.C.) divination was a matter of supreme importance. By employing so-called oracle bones, they often sought the advice and guidance of the gods and royal ancestors on a wide variety of topics. The court temple priest would cut and polish the divination tablets typically prepared from bones of cattle or the flat underside of turtle shells, drill a hemispherical cap and then chisel a semi-deep notch tangent to the indent. Applying a heated bronze rod to the bone would induce large localized thermal stresses which could produce a *divinatory* crack on the back side of the bone which were then carefully interpreted by the priests. Knowledge gained from these fracture patterns formed the expert data base for all political and private decisions made by the emperors. The remains of the „bone" library of some several hundred thousand bones collected and utilized by the Shang dynasty priests was found and, as the priests annotated the (positive) outcome of their divinating power, it is available for further scientific study. Unfortunately, many of the missing bone tablets have been retrieved by local farmers who ground them into powder and used the cracked bone tablets in an aphrodisiac fashion. The outcome of these experiments is not recorded.

Several fracture related incidences which occurred in 12th and 13th century Europe are documented in the literature. In the 14th century early quality control and testing of cannon bronze was by charging an up-side-down placed cannon and let the gun barrel be thrown into the air. If, upon fall of the tube there was no crack or complete fracture the material was considered tough enough and the

George R. Irwin Symposium on Cleavage Fracture
Edited by Kwai S. Chan
The Minerals, Metals & Materials Society, 1997

cannon could safely be put to service. Otherwise, this dynamic fracture test resulted in a broken cannon tube and the military device was in need of a re-cast.

In the Western countries the first historically recorded study of fracture strength is due to Leonardo da Vinci [2,3] who studied the strength of iron wires. The testing apparatus depicted in da Vinci's notebook in the Codex Atlanticus and discussed in the paper by Irwin and Wells [4] employed a basket that received a flow of fine sand from a hopper through an orifice. The flow of sand into the basket stopped abruptly when the wire broke as a spring was actuated to close the orifice. Da Vinci's comments have the appearance of instructions for testing and reveal his findings that wires of shorter length carry comparatively larger loads. Iron wires available in the 15th century were not of very high quality and clearly da Vinci's experiments illustrated the effect of flaws on strength. However, by using the pre-tested specimen fractions the quality of the wire at large could not be tested and Leonardo's particular way of shortening and reusing the already tested specimen fractions did not allow him to detect any true size effect. Several centuries later, around 1830, Lloyd noted that, on average, the strength of short bars tended to exceed that of longer bars and independent tests on iron wires by LeBlanc in 1839 demonstrated that long wires were weaker than short wires of the same diameter. The observed size effects were small and were interpreted as and ascribed to 'inhomogeneities'.

Whereas Leonardo was concentrating on wires of different lengths but of the same thickness, Galileo Galilei [5] studied the strength of wires of constant length and various thicknesses. In addition, he also studied fracture of marble columns in bending as well as loaded in axial tension. Galileo's quasi-analytical approach led to ideas concerning dimensional similitude which, particularly in the 19th century, dominated in the development of subsequent engineering design criteria.

Around 1650, Louis XIV of France, had an opulent palace built at Versailles. The magnificent gardens contained fountains which required containment of substantial amounts of pressurized water. The court engineer in charge, E. Mariotte [6], conducted tests by measuring the deformation and burst pressure of cylindrical pressure vessels and observed a direct proportionality between pressure and circumferential stretch [7]. He also noted that the vessels burst when the circumferential elongation increased by a certain fraction. This led to the practice of using maximum strain (or maximum stress) as a criterion for predicting fracture strength.

Ch.A. Coulomb, when in charge of the French fortifications in the West Indies and working on soil mechanics problems associated with slope stability, noted that the strength in compression would be enhanced due to sliding friction along the shear planes.

3. The Industrial Revolution and the emergence of professional material testing

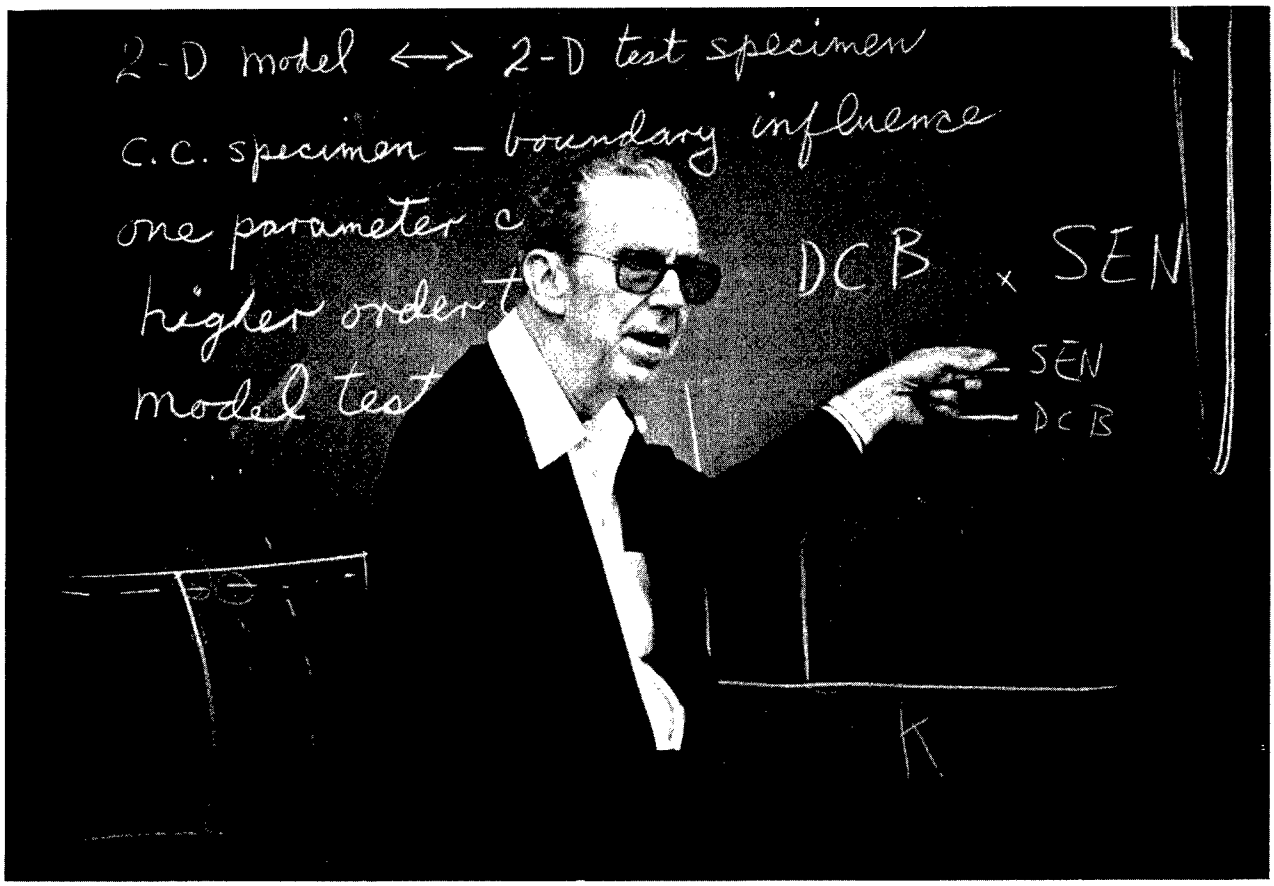
The demand for iron and steel was greatly enhanced in the course of the Industrial Revolution of the 19th century. This large and fierce expansion of the engineering world was accompanied by a rather large rate of failure of engineering structures. In fact, fracture of railway axles and track was so common that in the 1870's the British magazine *Engineering* printed weekly statistics about railway accidents. This situation led to an increased public concern and awareness about safety of railway transport and bridges. As a result the designers were forced to become more concerned with a suitable steel for a particular application and required accurate determination of relevant material properties. The Krupp composition alloy steel, introduced around 1870 in Germany, often became embrittled upon slow cooling from the tempering temperature. The development of impact testing and the use of notched bar impact methods to determine the fracture quality of steels enabled the detection of this undesirable condition of embrittlement. To address the concerns of design engineering a large number of material testing laboratories were established in Europe. One of the first and most notable material testing laboratories was built in 1865 by David Kirkaldy in London where by using equipment of his own design he tested specimens subjected to tensile and fatigue loadings. The conclusion drawn by Kirkaldy were that the appearance of fractured iron and steel could be changed from 'wholly fibrous to wholly crystalline in three different ways. Public pressure on high quality tested material was so strong that a proof sign was invented and the test mark of Kirkaldy's Testing & Experimenting Works became the first quality mark and was highly respected. In fact, the Krupp company had their cannon steel tested in Kirkaldy's laboratory in London before the Germans built their own testing laboratories.

3.1. Notched bar testing and size effects

Kirkaldy's results, along with those of his colleagues in other countries, marked the beginning of notched bar testing of steel. Notched bar impact testing of iron and steel was widely used by the end of the 19th century because these tests indicated the ductile-to-brittle temperature transition in steels and hence assisted control of heat treatment. Methods of adjusting design loadings for impact and fracture were based crudely on fracture failures in service.

G.R.Irwin

The Father of Fracture Mechanics - during lecturing at the University of Maryland in 1978



George Rankin Irwin, born February 26, 1907 in El Paso, Texas; Springfield High School, West Adams St. (1921-1925) in Springfield, Illinois; A.B. degree in English from Knox College in Galesburg in 1930; bicycle tour in Europe in 1929; change of interest from writing to physics and mathematics; extra year at Knox College; marriage to Georgia Shearer; half-time teaching job as a Graduate Assistant at the Physics Department at the University of Illinois; M.A. degree in Physics in 1933; repaired Knox College Observatory; PhD Degree in Physics also from the University of Illinois (in Urbana, 1933-1937) in 1937; in July of 1937 joined the US Naval Research Laboratory, Washington D.C., as Head of the Ballistics Branch of the Mechanics Division 1937-1953; promoted to Associate Superintendent of the Mechanics Division in 1948 and Superintendent from 1950-1967; laboratory studies of penetration ballistics, combat damage to aircraft, and the development of new armor materials; planning and directing the effective administration of the Mechanics Division; development of *fracture mechanics*; understanding of fracture behaviors, fracture testing, and fracture control plans; applications of modern fracture mechanics; retirement from NRL in 1967; September 1967-1972 full time employment at Lehigh University, Bethlehem, Pennsylvania as Boeing University Professor of Mechanics; intensive study of fundamental and applied aspects of fracture mechanics relative to integration of this subject into the teaching of engineering science at universities; cooperation with Paul C. Paris; establishment of the Annual National Symposium on Fracture Mechanics; founding of the Journal of Engineering Fracture Mechanics; in 1972 retirement from Lehigh University; Adjunct Research Professor and consultant at the University of Maryland from 1972-to date; development of a Crack Arrest Toughness Characterization Standard in the USA; prime consultant to the nuclear power industry involving Oak Ridge National Laboratories and Battelle in Columbus, Ohio; papers on metal fractography and cleavage-ductile transitional behavior of steels; numerous awards including the 'Grande Medaille' of the Metallurgical Society of France in 1976, the Nadai Award of ASME in 1977, the Timoshenko Medal of ASME in 1986, the Gold Medal of ASM 1987; Honorary Member of numerous learned societies including American Society for Testing & Materials (ASTM), National Academy of Engineering, Foreign Member of the Royal Society of London; published more than 300 papers, reports and numerous lecture notes and brief summaries of almost every aspect of fracture research including the history of fracture mechanics.

In 1909, P. Ludwik [8] put forward a theory that helped to explain the relatively abrupt increase of notched bar fracture work with increase of test temperature, i.e. the transition behavior by assuming that steel had a plastic flow (yield) strength which decreased with temperature and an independent cohesive (fracture) strength which was nearly independent of temperature. When elevating the test temperature to the point where the yield strength is less than the fracture strength, extensive plastic deformation occurs prior to fracture whereas at sufficiently low temperatures, the yield strength exceeds the fracture strength and brittle fracture is observed. Ludwik's simplistic theory, although relatively simple and capable of qualitatively explaining many of the features observed, lost favor because at least some plastic strain was observed during cleavage crack initiation and propagation in structural steels, regardless of the degree of brittleness.

The Ludwik theory was formulated in terms of stress and strain, so that one could infer that the laws of dimensional similitude should apply. Experiments conducted on notched bars of structural steel, however, soon demonstrated that the similitude argument was invalid. The first tests showing size effects in fracture were reported by Stanton and Batson from the National Physical Laboratory in Teddington [9] when they conducted impact tests on notched bar bend specimens of structural steel and found that a substantial decrease in the fracture work per unit volume occurred, as the specimen dimensions were increased. In fact, the temperature of brittle-ductile transition could be increased by increasing the test bar size and the fracture work decreased with scaled increase of bar dimensions. The serious implications of this finding as regards the general applicability of notched bar testing, and upon structural strength estimates based on the usual scaling laws as well, were not overlooked in published discussions of the Stanton-Batson paper. Contributed discussions brought out that, apparently, the fracturing energy consisted of two parts: the bending of the bar as a whole which would be proportional to the volume of the test piece, and the work expended in progressive extension of the crack after its start whereas the second part might be nearly proportional to the severed area, and would be responsible for the observed fracture size effect.

P. Ludwik's work had its Eastern counterpart in the work by Davidenkov and his school [10]. Using notched specimens in bending, low temperature influence and impact-induced rate effects on metals were systematically studied by N.N. Davidenkov and his group in order to improve the understanding and evaluate the susceptibility of metals to brittle fracture. They attempted to characterize the material's resistance to brittle fracture by means of a critical temperature.

The existence of a large fracture size became again evident in static notched bar bend tests conducted by Docherty [11-12] in the 1930's to eliminate dynamic uncertainties inherent in the tests by Stanton and Batson. After witnessing one of Professor Docherty's spectacular size effect demonstrations, an editor of the journal *Engineering* wrote a description of the test in which he commented that the principles of mechanical similitude appeared to be overthrown when cracking occurs. He also noted that similar size effects had been demonstrated in fatigue testing of notched bars, however, the Stanton-Batson and Docherty test results had no perceptible influence on design practices of that era.

As the concept of toughness is associated with the breaking of materials - the tougher a material, the harder it is to break - the original measure of toughness was the amount of work done in breaking a bar and, in 1975, toughness was still defined by ASTM as the ability of a metal to absorb energy and deform plastically before breaking. It is usually taken to be the measured energy loss in a notched-bar impact test and corresponds to the area under the stress strain curve in tensile testing. Consequently, a brittle behaving material is one that absorbs little energy, while tough behaving materials would require a large expenditure of energy in the fracture process.

It was very soon realized that fracture and fatigue are greatly influenced by notches and one can tacitly say that the story of failure is a tale of notches, nicks, keyways, oil holes, screw threads, scratches, rough surfaces, quenching cracks, grinding cracks, sharp changes in section, thin outstanding fins, poor fillets, tool marks, inclusions in the metal, corrosion pits, and the like, i.e. some localized nucleus from which failure started. The fact that only a tiny spot need to be stressed above the critical limit in order for the entire piece to fail by a crack developing from that spot deserves emphasis.

In the 1930's G. Sachs [13] and his coworkers, in establishing the effects of notch depth and notch root radius on the nominal notch strength values, introduced the sharply notched cylindrical specimen as a means for investigating the so-called notch sensitivity of high strength steels. Their investigations show that the effect of notch root radius was dependent on the tensile strength level of the alloy and at high strength levels, the notch strength decreased rapidly with decreasing root radius. Sachs concluded that bodies undergoing plastic strain without fracture obey dimensional similitude laws, but that similitude is violated when fracture takes place. At this time, it was well known that the safety factors customarily used in design depended considerably upon judgment estimates of the possibilities of fracture, however, no

attempts were made to replace the notch by a natural crack and measure the sensitivity of the steels to the presence of crack-like defects. In fact, at that time, in the 1940's, there was still inadequate recognition that cracks or crack-like defects were significant factors in reducing the load carrying capacity of structures made from high strength steels. The early work on notch sensitivity was rarely criticized because the notches were not sharp enough but rather they were thought to be too sharp to represent any practical situation of high stress concentration that might be encountered in service.

There was an awakening of interest toward improvement of design details stimulated by Neuber's work, particularly his book on notch stress analysis [14].

In addition, prior to 1950 it was not customary for a fracture failure report to cite a fabrication-induced crack as responsible for the failure. All specifications stated that fabrication cracks (of any size) were not acceptable and there appeared to be a reluctance to recognize that fabricated structures so perfect as to contain no crack-like flaws are highly improbable. When the size of the initial crack was ignored, it was rarely possible to decide how the cause of failure should be distributed between stress level, toughness and prior crack size, the three quantities in Griffith formula and in the Irwin analysis.

3.2. Testing of ductile materials

In France in 1866, A. Dupre [15] stated that the *macroscopic work* W required to rupture a liquid or a solid was equal to the free surface energy of the two rupture surfaces, 2A, $W = 2 \gamma A$, where γ is the specific interfacial energy of the material. When Dupre's thesis is applied to fracture of liquids and solids, where upon elongation of a droplet (tensile specimen) a neck is formed and separation into two droplets (parts) occurs, the above equation fails as the surface area decreases rather than increases during the process of fracture. If this is compared to a purely brittle fracture case then one recognizes that most of the energy available is expended in deformation (plastic work) leading to fracture.

When testing stretched copper-aluminum single crystal specimens it was found that distributed imperfections assist in spreading of slip over the entire atomic planes, a mechanism which was first described by L. Prandtl [16,17], who received his education at the Munich Polytechnical Institute and later became A. Föppl's assistant in the materials testing laboratory. Working at the Hannover Polytechnic Institute in 1903, Prandtl [18] published his famous membrane analogy of the torsion problem where he shows that by using a soap film all the information on stress distribution in torsion can be obtained experimentally. T. von Karman, one of Prandtl's first and finest students, Prandtl, Bauschinger, Bach, Lüders, Nadai and others contributed a great deal to the understanding of plastic behavior of materials shortly after the turn of the century.

Timoshenko in his book on the *History of Strength of Materials* [19] remarks that the practical importance of Prandtl's soap film analogy was recognized by A.A. Griffith and G.I. Taylor [20]. While employed at the Royal Aircraft Establishment at Farnborough with the assistance of G.I. Taylor, A.A. Griffith measured the stress elevation at notches, notably longitudinal grooves in aircraft components such as propeller shafts. They used this technique for the determination of torsional rigidities of rods of various cross-sections and remarked that greatest use of the technique had been made in aeronautics with air-screws and propellers. However, despite of mentioning that „...a few isolated experiments had been made in this country and **in Germany**..." they failed to acknowledge the work by Prandtl which had been well known 14 years already.

In studying the phenomena of fracture, Prandtl (1907) [16] proposed the existence of two types of fracture failures: a) cohesive or brittle fracture and b) shear fracture. When tensile testing cylindrical steel specimens he as well as Ludwik observed that in the cup-and-cone formation the crack would start and extend in the flat brittle center section and continue to stretch plastically at the conical rim.

4. Early contributions to the mechanics of fracture

Despite enormous technological progress over thousands of years, one can safely say that, during the early history of fracture, the conditions of failure were only poorly understood. The viewpoints on strength of materials at the start of the 20th century are presented well by Love in his *Treatise on the Mathematical Theory of Elasticity* [21], however, the sections of dealing with applicability of linear-elastic concepts show no influence of fracture studies in the period 1900-1926. Love notes that the „safety factors" commonly used reduce the working stress into a range where linear-elastic analysis should be quite accurate and examples of safety factors are given as: 6 for boilers, 10 for pillars, 6-10 for railway bridges, 12 for screw propeller shafts and for parts of machines subjected to sudden reversal.

With regard to fracture, Love, as late as in the fourth edition of 1926 of his book concludes *„that the properties of rupture are but vaguely understood"*. However, in his discussion of the loss of strength due to repeated loading (fatigue), Love describes this as a „gradual deterioration" of

the material and with this respect he was closer to what is now called continuum damage mechanics.

Following 1900, with the advent of automobiles followed by airplanes, the provision of adequate safety factors became increasingly more difficult and the need for better understanding of „rupture" more apparent. However, the response was directed mainly toward better materials, improved fabrication and inspection. With these aids, the practice of fracture control consisting mainly of failure experience, safety factors and proof testing endured through the 1900-1950 period. As a guard against costs of (large) fracture failures, insurance was an available option. However, during this period several fracture investigations occurred which assisted the introduction of fracture mechanics.

4.1. Wieghardt's pioneering work

The first analytical investigation in fracture mechanics and application to a practical engineering problem (mixed-mode fracture of a roller bearing case) is due to K. Wieghardt [22] in 1907, a student of A. Sommerfeld, where a special ansatz by Sommerfeld is employed to derive the complete stress field around a static crack in a mixed-mode loading environment. Wieghardt applied his theory to Bach's problem of mixed-mode fracture of a roller bearing case for which he derived the first mixed-mode fracture criterion. He also correctly gave the structure of the decomposition of the stress field, $\sigma = r^m G(\theta)$, for any wedge-type notch - including the crack as a special case - by developing an alternating technique. He investigates crack initiation using a maximum tensile stress criterion and a maximum shear stress criterion depending on the behavior of the material and correctly states that

„...knowledge of the theoretical stress distribution does not allow to evaluate crack initiation upon exceedance of the loading with certainty; and it is not at all possible to determine the path of further cracking."

Unfortunately, Wieghardt's paper was published in German in an obscure German journal which later ceased publication and, therefore, it was forgotten and did not exert any long-living impact in fracture mechanics.

4.2. Inglis' work on stress concentrations

Professor Inglis [23] is usually credited with having published in 1913 the first significant and fundamental paper on elliptical openings subjected to stresses from which the special case of a crack could be derived. Inglis developed and provided a function theory solution for the stress field near an elliptical opening of arbitrary eccentricity in a plate loaded by remote tension. In his opening comments, Inglis makes it clear that the purpose of his analysis was to assist the understanding of crack extension, particularly by load fluctuations as in fatigue tests of structural metals as encountered in ship building. The results could be used, in the limiting case, to model a crack as a slender elliptical cavity, for which the exact 2-D stress field could be derived. In fact, Inglis points out that, when the shape of the ellipse becomes crack-like the regions close to the tip of the major axis will experience large reversals of plastic strain even for load fluctuations of relatively small size. With regard to a plate of less ductile material which contains a crack-like opening, Inglis writes as follows:

„..a small pull applied to the plate across the crack would set up a tension at the ends sufficient to start a tear in the material. The increase in length due to the tear exaggerates the stress yet further and the crack continues to spread in the manner characteristic of cracks."

Subsequent parts of the Inglis' paper dealt with the use of his results to assist estimates of stress elevations in a plate near notches. Inglis points out that any narrow groove with a well defined root radius will have the same stresses at the tip region as if the shape was elliptical. From considerations of the stress near the tip of the ellipse, he developed equations for calculating the stress concentrations due to cavities of other shapes, such as square holes, star-shaped holes, and surface notches and provided a simple expression for maximum stress at the tip of a notch which is still useful. He shows the maximum stress equation has the form $\sigma_{max} = R\,[1 + 2\sqrt{(a/\rho)}]$ where 'a' is the half- length of the equivalent notch and ρ is the notch root radius.

The description of fatigue growth given by Inglis is quite modern but his paper has been usually referenced with regard to stress elevation at notches for which his work received practical use widely, e.g. in Peterson's book [24] on notch stress concentrations in 1940 and his study formed the basis of Neuber's book [14] on notch stress analysis of 1937.

4.3. Griffith's approach to fracture mechanics

Following 1913, England was at war and airplanes were receiving the first usage in armed combat. The equations provided by the Inglis paper were used to verify certain aspects of the experimental results. The understanding of surface tension and familiarity with the Inglis paper proved to be very useful relative his famous 1920 paper.

In 1920, A.A. Griffith [25] published a technical paper on

fracture strength of glass which was of continuing interest and value. The paper was essentially Griffith's PhD thesis in the Engineering Department at Cambridge University under the guidance of his prinicipal advisor G.I. Taylor. Griffith assumed that the surface of the soda-lime glass tube and bulb specimens contained numerous small, crack-like flaws and that a crack in a brittle material such as glass, would have a crack-tip radius which was essentially zero. He assumed that under tensile loading crack extension and fracture would occur when the loss of stress field energy per increment of crack extension became greater than the gain of surface energy. Equations for the rate of loss of stress field energy with crack extension were obtained using the equations of Inglis adjusted for zero root radius. The calculation of the energy loss rate was not an easy task and was completed nearly without error. The paper describes Griffith's supportive experiments and presents measurements of solid glass surface energy in detail. Experimental results for the comparison to stress field energy loss Griffith needed only the remote tension required to initiate fracture of glass containing a small crack of known size. For that purpose Griffith used thin-walled spheres and cylinders which were pre-cracked and subjected to increase of internal pressure. The fracture stress values obtained in this way supplied estimates of the stress field energy loss rate for comparison to twice the value of the surface energy. The result was an energy loss rate of only 20 percent, too low for exact agreement, an exciting confirmation of a novel idea.

Griffith noted that crack-like flaws in glass should be of unimportant size in freshly drawn glass fibres and provided confirming measurements. The use of hot-work orientation of flaws parallel to the direction of the tension expected in service and the concept of stress field energy loss rate as an important factor relative to crack extension were the features of lasting value in Griffith's 1920 paper. The attention given to surface energy as the resistance to crack extension was distractive.

Griffith's 1920 paper was reviewed by G.I. Taylor and accepted for publication prior to the discovery of an oversight error in Griffith's equation for the relationship between tension normal to the crack and the loss rate of stress field energy. The corrected calculation indicated an energy loss rate larger than twice the surface energy by a factor of three. A brief footnote was added to the paper stating that no correction of the text was needed since only *order of magnitude* agreement was of importance. Actually an accurate measurement of energy loss rate was not possible using thin-walled test vessels with internal pressure due to outward bulging of the crack walls. This effect of outward bending of the shell flanges adjacent to the pre-crack and also the effect of moisture assisted slow-stable crack extension in glass were not taken into account. Following introduction of fracture mechanics methods, tests using flat plates of similar glass and low humidity indicated a rate of loss of stress field energy larger than twice surface energy by a factor of about 13!

The contribution most often derived from the Griffith paper has been the equation relating the fracture stress to crack size, $\sigma_f\sqrt{(\pi a)} = \sqrt{(2\gamma E)}$ where σ_f is the fracture stress and E is Young's modulus. The surface energy term, 2γ, (later termed G_C) is the strain-field energy loss per increment, 'da', of crack extension, and 'a' is the half length of a central crack, normal to the tension applied, in a large plate. To derive this equation, Griffith used the Inglis' stress equation for an elliptical opening in a large plate subjected to tension. It was necessary to revise these equations, so as to represent a straight crack in a plate, and then to calculate the rate of loss of strain-field energy with increase of crack size assuming fixed boundaries. This was a formidable task with the analysis tools then available.

After 1920, when low-stress slow-stable cracking was observed in a solid exposed to an aggressive environment, the behavior was sometimes explained in terms of a lowering of the surface energy of the solid due to attack from the environment. However, the most useful result of Griffith's 1920 paper is the proportionality of fracture stress to the inverse square-root of crack size, a relation which is still important in fracture failure analysis and assists judgments related to fracture control. Griffith noted that the theory was only applicable to glass and other brittle materials, thereby excluding most structural metals.

The agreement between theoretical prediction and experimental results claimed appears now to have been coincidental.

The degree of understanding of fracture testing prior to 1960 did not provide a clear understanding of Griffith's 1920 paper. As a result it was generally assumed that Griffith had shown a close relationship between solid state surface energy and fracture strength of glass. Subsequent investigations of the effect of environment (moisture, etc.) on fracture strength of ceramic materials frequently referenced Griffith's paper. The proportionality between fracture stress and inverse square root of mirror size, for plate glass fractures, was noted and often used to assist fracture failure analysis for plate glass.

In this manner, interest in Griffith's 1920 paper continued into the post WW II period when Irwin [26] and Orowan [27] introduced their 'modified Griffith' ideas. However, the substantial interest in Griffith's 1920 paper during the following years was not shared by Griffith and he published

only one additional paper related to fracture in 1924 for the First IUTAM Conference in Delft. But this paper does not use the stress field energy loss idea and reflects no significant interest in the energy balance idea.

4.4. Developments in Eastern Europe

Fracture and strength related problems were of particular interest to academia and industry in the former Soviet Union during the period 1920-1940. The mathematical schools of elasticity and plasticity headed by G.V. Kolosov, N.I. Muskhelishvili, A.Yu. Ishlinsky, G.N. Savin, S.G. Lekhnitsky, L.A. Galin and others intrinsically contributed to the mathematical solution of important strength and fracture problems.

Brittle fracture studies related to the physics of fracture of crystals have been pioneered in the 1930's by A.F. Joffe [28], I.V. Obreimoff [29] and A.V. Stepanov in Eastern Europe contemporaneously with the developments by E. Orowan, A. Nadai, N.J. Petch, A. Smekal, G.I. Taylor, R. Thomson and others in the Western countries. Problems associated with wedge opened cleavage cracks in mica were investigated by P.A. Rehbinder, Ya.I. Fraenkel and by I.V. Obreimoff. At the same time, A.P. Aleksandrov and S.N. Zhurkov [30] were studying scale effects as well as environmental effects in connection with strength and fracture of glass fibers.

Investigations by A.F. Joffe and his coworkers in 1924 on the phenomena of plastic flow and tensile strength induced fracture of single crystal rock salt specimens contributed to the understanding of the large discrepancies between the theoretical strength of single crystals and the strength of a macro-volume of a polycrystalline solid. Tests conducted under various environmental conditions (air, water) demonstrated that the smoothing effect of the surface has a large effect on the tensile strength. Joffe wrote:

„Rupture never occurs along the whole section but begins from a small crack which after deepening divides a crystal in two. At each moment the entire load is acting on a small area near the front of the crack, and this load is large enough to deepen the crack."

4.5. The engineering point of view

Because of the wide usage of notched bar impact tests, for engineers, the paper on fracture of most importance must have been the one by Stanton and Batson on notched bar impact tests. In the 1930-1935 period, Docherty conducted similar fracture size effect studies at the Royal Naval College in Greenwich, using slow loading. The steel test bars were similar to those used by Stanton and Batson and the test results were also similar. Some of the larger specimens broke completely and so suddenly, that the severed ends were thrown apart by the energy release with nearly enough force to penetrate wooden barriers fixed to contain their impact. Visitors were sometimes invited to witness these large specimen tests, and an editorial writer from the journal *Engineering*, when writing an account of his visit, stated that Docherty's tests demonstrated a *restriction to the laws of mechanical similitude enunciated over 50 years ago by Professor James Thomson of Glasgow and long used as the scientific basis of model testing*. The *vague* understanding of rupture indicated by Love was not visibly helped by these demonstrations of fracture size effects.

A novel idea, the statistical theory of strength which draws from a Griffith type fracture theory, introduced by W. Weibull [31] in 1939, attracted interest and seemed of value towards an understanding of fracture size effect. Weibull predicted strength variations with respect to test volume and specimen shape that qualitatively corresponded to observed fracture behavior. This new viewpoint became known as the *Weibull worst flaw theory*. In 1946, Davidenkov presented test results for the fracture of round bars of a relatively brittle steel which illustrated close correspondence to Weibull's idea. The high strength of glass fibers reported by Griffith in his 1920 paper could be regarded in a similar way.

5. The role of dislocations and plasticity in the formation of fracture mechanics

In the 1920-40 period, while the understanding of fracture remained vague, dislocation and plasticity mechanics were introduced and made significant progress. The development of crystalline dislocation mechanics in the 1930's and following decades furnished important ideas which were directly transferable to fracture. The alignments of lattice faults termed dislocations provided an answer to plastic flow weakness of metal single crystals. In structural metals, interference to easy glide of dislocations occurs due to the internal complexities such as grain boundaries and minute inclusions. Although the resistance of metals to plastic deformation is generally understood, the details are quite complex and the yield strength was normally determined by measurement rather than by computation.

Similar considerations are directly applicable to fracturing. Historically, structural fractures which were *vaguely understood* were those which occurred when the stress applied was substantially less than the yield strength of the structural material. If we assume that separation occurs simultaneously everywhere on the plane of separation, then the applied stress necessary for separation cannot be less

than the ultimate tensile strength and is probably larger. However, given the presence of an initial crack, the natural stress concentration influence of the crack produces very large stresses near the leading edge or front of the crack. If these local stresses are large enough to cause progressive fracturing, then complete separation may occur at an applied stress much less than the yield strength of the structural material.

In dislocation mechanics, it can be shown that the stress field force driving a dislocation is computed as the derivative of the (system isolated) stress field energy per increment of forward motion of the dislocation line. Knowing the deformation details within the core of the dislocation is not required. Assuming that inelastic strains along the crack front are well enclosed by an elastic stress field, the same generalized force concept can be applied to the leading edge of a crack. If the force is computed per unit of length along the zone of disturbance, i.e. the crack front, in a manner similar to the dislocation line force, the result has the same dimension, i.e. force/length. In fact, one obtains the Griffith crack theory if the crack extension force is equated to twice the solid state surface energy of the material. However, the deformation details which provide resistance to crack extension are even more complex than those which provide resistance to plastic straining. Thus, critical values of crack extension force necessary for various kinds of actual crack extension must be determined by experimental measurements. Although the Griffith crack theory had suggestive value, the influence of dislocation mechanics upon the development of modern fracture mechanics was direct and more persuasive.

5.1. The Westergaard paper of 1939

A 1939 paper by Westergaard [32], for many years considered to be of major importance in the development of analytical fracture mechanics, provided a relatively simple stress function method for determining stresses near a straight, 2-D crack in an infinite solid. As the Westergaard method is but a special case of the more general complex function theory of 2D elasticity as developed by Kolosov around the turn of the 20th century and extensively generalized in the early 1930's by N.I. Muskhelishvili [33] and his school, it must be used with care as the Westergaard type stress functions, in general, do not represent the complete stress field around a crack tip but contain only that part which contributes to the stress intensity factor! A fact, which has led to numerous mistakes in the development of stress intensity factor determination procedures. Although the Westergaard method in the period 1954 - today enjoys widespread use in linear-elastic fracture mechanics primarily in the USA, its value was not recognized until 1954 when D. Post used it to explain photoelastic fringe patterns near a crack.

6. The Liberty Ship failures

Following 1936, during the rebuilding of the US Naval fleet brittle behavior of heavy armor plates for battleships was soon encountered. In retrospect, the Liberty ship brittle failures enormously popularized fracture mechanics by pushing this young discipline from being a scientific curiosity to a useful engineering discipline [34].

Helping to fight the German Navy, under the Lend-Lease Act, the USA was supplying ships and planes to the UK. The famous US construction engineer Kaiser headed and guided a revolutionary and speedy technique for fabricating ships which was developed in a hurry. Of the roughly 2700 all-welded hull ships built during the war years with this novel technique approximately every seventh ship sustained fractures with 90 boats in serious conditions, 20 totally fractured and about 10 broken in two. Failure investigation revealed that the Liberty ship failures were caused by the orchestrated action of three causes:

- welds produced by largely unskilled work force;
- fractures initiated at deck square hatch corners where there was a stress concentration;
- the ship steel had fairly poor Charpy impact tested fracture toughness, so that some of the ships broke apart even before they were shipped for service into the cooler waters of the combat zone.

The ship steel fracture toughness was perfectly adequate for riveted ships where any fracture would have been arrested at the rivet, however, in a welded ship a crack does not encounter any crack arresting barrier and is able to traverse the entire hull. As soon as the reasons for the failures were identified, remedies could be designed which consisted in reinforcing the hatch corners and riveting high toughness steel arrester plates to the deck at endangered positions. These actions prevented further serious failures of the ships. The long term impact of the Liberty ship failures was the development of structural steel with improved fracture toughness and of weld quality control standards. Many of these developments were stimulated and initiated at the Naval Research Laboratory in Washington D.C.

7. G.R.Irwin *The Father of Fracture Mechanics*

This section will briefly highlight the family background, education and interests of George R. Irwin (GRI).

7.1. Family Background

George Rankin Irwin was born on February 26, 1907 in El Paso, Texas. GRI's mother, Mary Susan Ross, was a member of the sizable Ross family which originated in Scotland but in 1749 came to the American colonies and settled in the Western Shennandoah valley to escape religious persecution in the Old World in the days of Oliver Cromwell. The ancestors of his father came from England. When the West opened up the Ross family fraction, GRI is related to, moved up to the surroundings of Springfield, Illinois. Mary Susan, GRI's mother attended a business school where she studied short-hand and writing.

Stories of troubles with Indians are reported with members of two generations of the Ross family with several persons burned to death at stake and others being able to flee.

GRI's father's family, the Irwins, can be traced back to the Revolutionary war, though the name Irwin and its many variants Erwin, Everwine, Irwine, Irwing and Urwin is of patronymic origin and is recorded in English documents as early as 1124. GRI's father, William Rankin Irwin, was born November 25, 1877 in Monmoth, Illinois. GRI had an elder brother by name William Ross Irwin, and a sister, Constance Elisabeth.

The connection between the Irwins and the Rankins is of importance for the name-giving of GRI. Nathaniel Alexander Rankin, a great admirer of Abraham Lincoln, living in Springfield, Illinois, entertained Lincoln for dinner when Lincoln stopped in Monmoth when running for Congress. When, in the 1890's, Theodore Roosevelt was visiting Springfield he made an acquaintance with George Rankin, a son of Nathaniel, who owned riding horses. Being a horse riding enthusiast, Roosevelt was glad to be able to ride Mr Rankin's horses around Springfield. Later on, when Mr Roosevelt became president he invited his friend George Rankin to come to Washington D.C. and gave him a secure job in the Treasury Department. It is President Roosevelt's riding companion after whom George Rankin Irwin, the Father of Fracture Mechanics, was named.

7.2. George Rankin Irwin

Prior to the birth of GRI, his father, for health reasons, moved to the South of the US, where he worked for the railroad holding various positions in New Mexico and Texas. However, on December 13, 1907, GRI's father suddenly passed away leaving back a young wife and three children (GRI of age 10 months only) with no income.

GRI's mother went back to Illinois to join her family, and eventually found a job as a managing secretary in the Springfield Boiler Company.

GRI spent his youth period in Illinois where he went to school at age 5. He attended Springfield High School, West Adams St. (1921-1925), where he graduated in the class of 1924. During his boyhood days GRI was active with various jobs including selling ice-cream, distributing news-papers and doing garden and house work for other families and the money saved helped his family to survive.

7.3. Primary Education

In High School, the only classes GRI really enjoyed were those in physics. History was fascinating and exciting, just like learning by stories, Hammurabi and his codex of laws etc., but physics with lenses and optics was much more interesting.

In chemistry everything was a complete mystery to GRI: *„You took substance A and substance B - which was acid or so -, mixed it and you got some liquid which was colored; the textbook was ok, but what was not in the textbook was left completely unclear."* Halfway through his first semester of chemistry GRI managed to drop that subject and get out of the class, and as he never liked the subject, he never got back to chemistry. Mathematics was straight forward for GRI.

And then there was English and Latin, the latter of which was mastered through 2 semesters with a passing grade.

GRI's grades, in general, were fairly high though he certainly didn't work a lot. He had a few friends who were not remarkable for good behavior and eventually led him astray. Quickly he got into difficulties with the principal of the school when cutting classes. George finished with highest grade average in a class of about 50.

During the summer months GRI worked on the farm of his grandfather, picking potatoes with an occasional payment of money and driving an old buggy to the fields that was loaded up with jugs of water for distribution to the farm hands. One day he accepted an offer from a farmer as a day laborer, but the monotonous work of lifting large burden of hey with the fork and throwing it up into a hay-bailer pretty much led to complete worn out, and by the time of the evening meal, where he could hardly keep his eyes open, the farmer's wife concluded that he wasn't strong enough for this kind of work.

7.4. College Years

GRI pursued his secondary education at Knox College in Galesburg (September 1926- June 1931) and received an A.B. degree in English in 1930. One of the advanced courses GRI enrolled in College was on Middle English and it seemed strange to have a course like this, but the subject sounded interesting.

With respect to professional preference and development GRI's judgement was based on his boyhood work with a newspaper, the *Illinois State Journal*, the largest daily newspaper in Central Illinois, and he wanted to start a career as a journalist. As recording of crimes and sports events seemed to be more interesting writing about, he developed a certain facility for „hunt and type", a typing technique which he mastered rapidly (he never learned to type systematically). The atmosphere of the working place with the newspaper seemed adventuresome to him.

7. 5. The 1929 Europe Bicycle Tour - A Change of Interest

In 1929, GRI and his friend Baird Hellfrith decided to tour Europe for a semester. In order to be able to still graduate with their class they enrolled in additional courses so that, upon return, they could catch up with their colleagues. GRI and Brian went across the Atlantic working on a freighter and toured Europe starting in Glasgow, went into Sweden and Germany. A visit to the Deutsches Technisches Museum in Munich changed a whole career in GRI's life. He was so fascinated by the scale models and artifacts on exhibit and the explanations offered, that he decided to study science and engineering. The journey took them to Austria, Italy and France and into Paris where they visited quite a number of churches and (as GRI confesses in a letter addressed to his mother around Christmas 1929) a large number of cafes - probably more cafes than churches! GRI characterizes Paris as a 'big bad city', but as the friends are seasoned enough now by travel, he assures his mother not to worry about their getting into troubles. Via the UK they steamed back to the United States, again working their way as machinists on a boat. During this trip, GRI had to crawl into a fuel container and find a leak - his first encounter with fracture failure!

Upon return from Europe, GRI found himself in a kind of a debate in personal things what to do. Advanced studies of English language didn't sound too attractive and his teacher's comments on doctoral degree studies with frequently unattractive tasks (counting the feminine endings of Shakespearian writing) to pursue was not pretty encouraging.

Due to this shift of interest from journalism and writing to science, GRI, with his A.B. degree in English, felt rather inappropriately equipped for studying the natural sciences and engineering. Being pretty good in mathematics and physics, he decided to go for an extra year at Knox College enrolling in integral calculus skipping differential calculus which he learned from a textbook during the summer break.

At Knox College he received some financial support for working part-time as an instructor while staying there as a post graduate student taking the courses he needed. With a 'fair' in reading French and German at Knox in addition to 'excellent' in maths and physics during that extra year GRI was able to graduate (for a second time) 1931 in Physics.

7.6. At the University of Illinois

During College time GRI developed his relationship with his school friend Georgia Shearer whom he married in 1933.

In 1931, a letter arrived from the head of physics of the University of Illinois which indicated they would offer GRI a half-time teaching job as a graduate assistant in the physics laboratory. After two years GRI had enough credit to sign off in 1933 with a Master's degree in Physics.

More income was needed when the Irwin family increased and, therefore, during the period September 1935-June 1936, GRI took the position of an Associate Professor offered at Knox College. There he operated a one man Physics Department, taught elementary physics, heat, light, advanced mechanics and advanced measurements. The teaching experience gained as an instructor was interesting. He also had to put the Knox College Observatory in order, which had been neglected for many years, and urgently needed repair.

In order not to lose GRI's active help at the University of Illinois (GRI was getting excellent grades and reputation), he was promoted chief laboratory assistant with Professor Almy in the Optics Laboratory of the Physics Department and the special circumstances allowed GRI to complete his PhD in Physics (in Urbana, Ill., 1933-1937) and graduate in June 1937. In his PhD thesis he addressed the topic of mass ratio of the lithium isotopes from the band spectrum of Li_2.

GRI's favorite reading was always on the technical side of literature with very little 'idle time' for reading thick novels and so. His 'bestsellers' were the books by Sir James Jeans on the atmosphere and by Sir Arthur Eddington, astronomer royal of England on the stars in their courses.

8. The Naval Research Laboratory

The need for the installation of a Naval Research Laboratory (NRL) in Washington D.C. was initiated by an interview in July 1915 in the *New York Times Magazine* when Thomas A. Edison proposed that the Navy should have its own scientific laboratory and staff to exploit the ideas of inventive people to suit the peculiar needs of the Fleet. The Naval Experimental and Research Laboratory was founded on July 2, 1923 on the northern shore of the Potomac river in Washinton D.C. with Theodore Roosevelt, Jr. as the principal speaker of the festive event. The key to success in Naval research lay in the choice of original staff, particularly civilian scientists which often were recruited directly from the alumni of the universities.

8.1. George R.Irwin at NRL

In July of 1937, Dr Irwin was hired by Ross Gunn to join NRL as Head of the Ballistics Branch of the Mechanics Division. He served in this capacity between 1937-1953 when he was promoted to Associate Superintendent of the Mechanics Division in 1948, and Superintendent in 1950, a position which he held until August 1967. The portion of this employment closely related to World War II was devoted to laboratory studies of penetration ballistics, combat damage to aircraft, and the development of new armor materials.

Acting as Superintendent of the Division of Mechanics at NRL, GRI was responsible for planning and directing the effective administration of the Mechanics Division which contained about 85 persons distributed in the following branches: Administration, Ballistics, Dynamics, Structures, Shock and Vibration, and Engineering Research.

Although today overshadowed by his identification with the development of fracture mechanics, GRI's earlier work on penetration ballistics led to substantial improvement in armor and gunfire damage resistant structures for the U.S.Navy and Army during World War II. The NRL group under his leadership played a central role in the development of a number of new non-metallic cloth-laminated armor for flak curtains and body armors extensively used in the Korean and Vietnam conflicts.

Following World War II, GRI's major personal research efforts and technical contributions have been directed toward organization and understanding of fracture behaviors, fracture testing, and fracture control plans. GRI's major technical contributions have been in the areas of mechanics where he introduced basic concepts, test procedures, and methods of analysis which are fundamental both to practical and to research applications of modern fracture mechanics. His papers on the mechanics of fracturing led to the establishment of an entire new discipline, termed *fracture mechanics.*

The methods of testing and analysis resulting from his work were used in the development of understanding and remedies for the pressurized jet aircraft fuselage fractures experienced by deHavilland Comets (1953-54); the fracture of heavy rotating components of large steam turbine electric generators (1955-56), and fractures of ultra-high strength steel chambers of solid-propellant rockets (1957-1960). In 1960, the first report of a special committee on fracture testing of the American Society for Testing and Materials stated that the methods of fracture mechanics were well enough understood to serve as a basic tool for the development and use of standardization methods of fracture testing. Extensive revisions and improvements have resulted from use of fracture mechanics in fracture toughness evaluations, fatigue cracking, corrosion cracking, and fracture control plans. Engineering methods founded on his work are widely used for fracture control particularly in the aerospace industry.

However, most of the leading engineers during this time of development of fracture mechanics did not believe in the applicability of GRI's approach to fracture, as there was no precise definition of fracture toughness and on occasion fractures without obvious reasons did occur. Although GRI was looked at as the preacher in the desert, due to his high qualification he managed to get the message across and convince others, less by persuasive power or indoctrinative missionary behavior in fracture mechanics but by the exchange of ideas and precise answers.

8.2. Work on armor penetration and protection

Studies of armor materials were begun at the U.S. Naval Research Laboratory in 1935 in a small Mechanics Division group. In 1937, G.R. Irwin began his NRL employment serving as the head of this group, which soon became the Ballistics Branch of a new Mechanics Division. The Ballistics Branch had two research objectives:

- a better understanding and solution of brittle fracture problems in heavy armor, and
- exploring the feasibility and development of suitable light armor for aircraft.

These tasks were performed mainly by direct observation of armor penetration events and by studies of terminal ballistics literature. The NRL terminal ballistics studies included small-scale model tests of heavy armor material which had shown an unusual degree of brittleness in the full-scale ballistic test. The ductile behavior observed in

ballistic tests of small specimens showed convincingly that the heavy armor brittleness problem was enhanced substantially by the same fracture strength size effect as was demonstrated in papers by Stanton and Batson. The problem of size effects in metal fracture was attacked for the third time here. A theory similar to the Griffith crack theory, in which the resistance in crack extension was proportional to increase of fracture surface, would clearly assist understanding of the fracture size effect. However, the Griffith concept was regarded as applicable only to glass and brittle ceramics. This heavy armor temper brittleness problem was resolved by steel company metallurgists employing techniques of improved heat treatment practice.

8.3. Size effects reconsidered

The critical influence of fracture strength upon armor quality, the evidence of fracture size effects, and the obvious lack of understanding of fracture required additional study. Fracture toughness was an important factor in resistance of armor of any thickness, and a satisfactory understanding of this property was an attractive research goal.

This interest resulted in a research contract for studies of fracture at the University of North Carolina (Chapel Hill) across the time period 1941 through 1948 with funding from the NRL Ballistics Branch budget. To clarify fracture size effect behaviors in armor steels and a high strength aluminum alloy a large testing machine was available, and a group of the physics faculty headed by A.E. Ruark was instrumental in doing the tests.

The reports published from this project dealt mainly with fracture size including an extensive survey of previous fracture investigations with special attention to Weibull's *worst flaw* theory, notch stress analysis, and Griffith's 1920 paper.

At the outset, it was clear that the new viewpoint would provide at lest a partial explanation for fracture size effects. The notched bar fracture size effect observations indicated that the energy associated with fracture varied with specimen size in a manner intermediate between proportionality to specimen volume and proportionality to area severed. In addition, continued study of dislocation mechanics viewpoints provided strong support for the new fracture research plan. The viewpoints basic to linear-elastic fracture mechanics were suggested by Irwin in 1948 and were presented more firmly in unrefined but useful form in 1952-54.

Although the fracture size effect studies at Chapel Hill did not provide an explanation of fracture size effects, come fracture behavior aspects could be clarified and it seemed clear enough that a testing method which related toughness directly to crack extension was required. The studies also furnished a thorough review of fracture research literature. Following the end of the war in 1945, a Fracture Section was established within the NRL Ballistics Branch to investigate possibilities of that kind.

8.4. The Irwin-Orowan extension of Griffith's work

To be of interest to the US Navy, the NRL fracture research needed to be applicable to steels. Orowan's 1945 results from an X-ray scattering study of the depth of plastic straining from cleavage facets in a low strength structural steel (low carbon steel) were of special interest to the new fracture program at NRL [35]. Irwin noted that a rough estimate of the energy loss due to plastic straining per unit of cleavage area could be made on the basis of Orowan's results. The out-come indicated that even for brittle cleavage fracture, the stress field energy loss to gain of surface energy was trivial in comparison to the loss rate due to plastic strains. In fact, these results corresponded to a strain-field energy loss rate many times larger than the surface energy, and it was concluded that the Griffith concept might be helpful and retained value at least for relatively brittle fracture behavior, if, in place of Griffith's surface energy, one substituted energy loss in work due to plastic strains occurring close to the crack tip. Following the 1946 Conference on Applied Mechanics in Paris, Irwin visited Orowan in Cambridge and discussed his plans with Orowan.

This novel idea was presented by Irwin at the ASM Symposium in 1947 [26] and Orowan [27] presented the same idea in 1949 but regarded it as unlikely to be useful for structural materials. Thus, Orowan's 1945 paper [35] encouraged selection of a modified Griffith concept as a promising starting point for a new fracture research program. The development and implementation of this new research program at NRL begins a new era in the development of fracture mechanics.

8.5. Fracture mechanics studies at NRL

At the end of World War II, scientists at the Naval Research Laboratory (NRL) were encouraged to select and pursue research areas which promised significant rewards. The modification of the Griffith theory as proposed and worked out by Irwin to predict the onset of fracture by crack initiation in engineering materials served as a guide for a new study of fracture.

The editor of the proceedings of the ASM organized Symposium 'Fracturing of Metals' in 1948, W.P. Roop,

insisted on using the term 'fracturing' rather than 'fracture' in the book title. Indeed, there was a general feeling at that time that fracture of structural materials should be regarded as a 'process' rather than an 'event'. Fracture mechanics developed when fracturing was viewed as a progressive crack extension process: the start, spreading and arrest furnishing measurable features of interest. New concepts usually have forerunners: e.g. in his 1913 paper Inglis writes:

„...the ellipse in this case would appear as a fine straight crack and a small pull across the crack would set up a tension at the ends sufficient to start a tear in the material. The increase in the length, due to the tear, exaggerates the stress yet further and the crack continues to spread in the manner characteristic of cracks."

The modified Griffith viewpoint, which is based upon the idea of progressive crack extension, expands the original Griffith concept by including the plastic-strain work rate for crack extension in addition to the rate of increase of surface energy from crack extension. The onset of unstable crack extension occurs when the strain energy release rate, driving crack extension, exceeds the inelastic dissipation rate. By the inclusion of the work done in plastic deformation, the modified Griffith theory seemed potentially useful for analyzing fracture in engineering materials exhibiting ductility. Both Irwin and Orowan recognized that for metals, the work required for plastic deformation greatly exceeded the work needed to create new surfaces, and they reasoned that the surface energy term was negligible [36]. As the 1945 Orowan paper proved very helpful reference to the modified Griffith concept as the Irwin-Orowan theory seems appropriate.

8.6. Joseph A. Kies at the NRL

The employment of Joseph A. Kies in 1948 as Head of the Fracture Section of the Ballistics Branch at NRL considerably re-enforced the strength of the fracture group. After leaving the University of Illinois, from 1936-1945 Kies worked at the Bureau of Standards, where he was assigned to study fracturing of aluminum alloys for airplanes before he moved on to the NRL. Tests discussed in a 1949 technical paper from that group provided photographic evidence that crack extension in metals and polymeric solids occurred progressively by formation and joining of advance separations. Although the accurate calculation of the energy loss rate for various plate materials, including mild steel at temperatures low enough for cleavage fracturing, was a problem, it was, however, clear that the basic idea of a 'modified Griffith' approach could be used for toughness evaluations and for fracture control in service applications. How to use fracture mechanics for fracture control was first explained and reflected in papers by Irwin and Kies in 1952 [37] and 1954 [38].

8.7. The role of photomechanics in the development of fracture mechanics

By 1953, the value of focusing attention upon the initiation and control of crack extension was clear. Optical fractography showed that the opening and joining of separations in regions ahead of the crack tip was a common crack extension mechanism as fracture marking produced in this way revealed local regions of low toughness and indicated direction of crack extension [39].

Significant help came from photoelastic studies of stress distributions near a crack tip. Experiments showed that isochromatic patterns near the crack tip were similar both for stationary and rapidly moving cracks. On the other hand, in their search for a suitable stress analysis for these observations, Post [40], Wells and Post [41] and Irwin [42] found that Westergaard's method of 1939, when applied to the region near the crack tip, provided both an explanation of the crack-tip isochromatic fringes and, in addition, assisted design of fracture test specimens for which energy loss rates could be estimated with acceptable accuracy. The important result of this work was the clear visualization of the stress singularity at a crack tip.

8.8. The crack extension force concept

In 1956, Irwin [43] developed a new approach which deviated from the modified Griffith concept. This approach assumed that the energy needed for creating new surfaces during crack extension comes from strain energy loss from the entire elastic solid. Irwin defined this strain energy release rate as G (in honor of Griffith) and then showed that this single parameter G, the crack extension force, was a measure for the intensity of the crack tip stress field (as long as plastic deformation is limited to a small region near the crack tip) and it could be determined from the stress and displacement fields in the local region near the crack tip.

Consideration of the Peierls-Nabarro 'force' to move a dislocation line showed that the same basic 'generalized force' concept could be applied to a nearly ideal crack. The result led to the term 'crack extension force' for the strain energy release rate, G. Shifting major emphasis away from G as a 'force' concept seemed, for some purpose, undesirable.

Irwin established the critical fracture toughness (G_c) criterion, which specifies that crack propagation occurs

when G attains a value equal to G_c. He also discussed the effects of thickness (constraint) and strain rate on G_c. Relevant publications included data for G_c from many practical materials, such as ship steels, aluminum alloys, polymeric glazing materials, and glass. Although the data presented were impressive, Irwin noted that further experimental results were necessary before the concept could receive widespread application. These ideas formed the basis for linear-elastic fracture mechanics (LEFM).

There were three fundamental ideas:

- Progressive forward motion of the crack front (leading edge or crack tip);
- The crack extension force, G, was the rate of loss of stress field energy at the crack front per increment of crack extension;
- The resistance to crack extension was the rate of energy dissipation into non-elastic strains close to the crack front.

Initial trials conducted using metallic sheet materials, plastics, and glass provided entirely favorable results. The prospects for practical applications to brittle fracturing were enhanced by recognition that energy loss per increment of severed area depended only on the stress-strain field surrounding the limited zone of non-linear strains at the crack tip. Thus, knowledge from prior measurements of the critical value of G for crack propagation, termed G_c, furnished a one-parameter criterion which could be used to predict the critical load for propagation of a prior crack of given size and location in a service component. The Irwin-Kies paper provided an experimental method for determination of G which is usually termed compliance calibration.

8.9. The K-concept

Studying the papers by Sack [44], Green and Sneddon [45], particularly Sneddon's paper [46] on the stress field around a flat elliptical crack, Irwin noted that the structure of the leading term in the asymptotic expansion of the stress field around the crack tip would be the same for all crack fronts and an intensity factor, K, the stress intensity factor, could be singled out. This property of the crack edge stress field was obviously overlooked by Sneddon.

In the 1957 papers [47,48] Irwin used Westergaard's semi-inverse method to relate G to the stress field at the crack tip. The complex analysis as employed by Westergaard in his 1939 paper [32] was a kind of eye-opener to the fracture group at NRL. To the great enjoyment of Irwin, Ericksen (then with R. Rivlin working at the Applied Mathematics Section of the Division headed by Irwin) generated the stress function for the „pair of splitting forces" loading arrangement of a crack, a solution which enabled Irwin to work out the relationship between the energy release rate and the stress intensity factor: $K^2 = G\,E'$ [47], where E' is Young's modulus specified for plane stress or plane strain.

Although Irwin suggested that strain gages be employed to experimentally measure G-values, the method was not used in practice for 30 years until uncertainties concerning gradient effects and the size of the K-dominated region were resolved. An alternative method to measure G by a compliance technique was developed. In 1958 Irwin [49] published a comprehensive summary of the state-of-the-art of fracture mechanics which includes convenient expressions for stresses and displacements near the crack tip under the three basic modes of loading (opening mode, in-plane and out-of-plane shear modes) and a discussion of theoretical and experimental aspects of fracture mechanics, which was employed for some time as a textbook for courses in fracture mechanics.

9. The first successful application of fracture mechanics

The new fracture mechanics was - in the period 1953-56 for the first time - successfully applied to a practical problem associated with the development of stretch-toughened Plexiglas. This material, initially of interest to the military, is now routinely used in windows of pressurized airplanes. A major contributor to the project was Joseph A. Kies, who was a highly respected frequent visitor to the West Coast airplane manufacturers. Experiments by Irvin Wollock at the National Bureau of Standards (NBS) showed that craze cracking of PMMA (by alcohol and tension) could be eliminated by hot stretching, a result which led Kies to the idea that hot stretching would add to the toughness of PMMA windows. Kies [50] solved this problem by pointing out that the critical stress for a given crack size depended only on the product G_cE, which could be directly computed from the applied stress and crack size for the test. The response to this suggestion, by West Coast airplane engineers, was to express their fracture test results in terms of values of $\sqrt{(G_cE)}$, which they termed K_c (K for Kies).

Physically, the marriage between K and G was accomplished by Irwin's relation, $K = \sqrt{(GE/\pi)}$ which showed the equality between a global (G-based) and a local (K-based) description of the fracture problem. The acceptance by the engineers of the transition from G to K corresponding to a shift in the emphasis from the energy-rate parameter G to a crack-tip stress-field parameter had been discussed within the NRL group. In retrospect, this shift of emphasis may seem to have been 'obviously' desirable, however, most of the NRL group experts had

their basic training in *'physics' mechanics* rather than *engineering mechanics.*

10. Analytical fracture mechanics

With the establishment of G and K as important crack-tip parameters, it became necessary to relate the stresses, strains, and displacements at the crack tip to these parameters. Closed form solutions had been obtained for simple 3D geometries (1945-1952) including stress distributions for 3-D cracks in infinite bodies subjected to various loading conditions, e.g. penny-shaped and elliptical crack. Although the complex function technique had extensively been used, numerous more complicated crack problems could not be solved with the mathematical tools available at the time. It is interesting to note that fracture mechanics has been extraordinarily stimulating to mathematicians and particularly in the field of integral equations and numerical modeling enormous advances have in the development of new techniques have been made. The practical significance of the solutions was realized mainly after the introduction of the G and K parameters. Many of the solution techniques for crack problems can be found in a book by Sneddon some of which he prepared as part of his involvement in fracture research with the North Carolina State College in Rayleigh [51].

In 1957, when Irwin [47] employed the Westergaard's semi-inverse method to relate G to the stress field at the tip of a single crack in an infinite plate under mode-I loading, a series expansion solution of the stress field around a crack tip was presented by Williams [52,53]. His analysis treated the crack tip stress field as the special case of the stress field at a re-entrant corner and, as the analysis centered on the local behavior at the tip of a single-ended crack it was independent of specimen geometry. Williams [53] presented a series solution for the stress field surrounding the crack tip, which contained both singular and higher order terms. The series, when separated into symmetric and asymmetric parts, gave results for mode-I and II loading which could be related to the stress intensity factors K_I and K_{II}. The solutions apply to planar problems and have been used extensively, even though the completeness of the series is still debated. Specifically, this form has proven to be useful for boundary collocation and finite element analyses. It should be noted that the Williams' approach is almost identical with the analysis of Wieghardt [22,54] of 1907!

11. The struggle for recognition of fracture mechanics

Fracture mechanics has proved a powerful tool and the development of stretch toughened glazing materials for aircraft in the period 1953-1956, the fractures of the welded Liberty ships during the war years, bursts of several large petroleum storage tanks, as well as the pressurized cabin fractures of the deHavilland Comet jet airplanes all seemed understandable in terms of this new fracture strength viewpoint and could be explained in terms of G_c which was estimated from laboratory tests of pre-cracked specimens. A substantial collection of critical values of the energy loss rate, G_c, were made at NRL during the 1950-1956 period. In all failure cases the comparison showed that the toughness had not been large enough to prevent crack propagation. Crack producing defects can be introduced into a structure in various ways during design, fabrication, assemblage of structures, service, maintenance, even during repair and demolition.

Today it is understood and expected that structures such as bridges and pressure vessels provided many years of faithful service despite the presence of such defects. However, this was not an accepted viewpoint during the early development period of fracture mechanics when most engineers preferred to take the 'no cracks' clause usually included in specifications. On the other hand the possibilities for planning calculable fracture safety in a sure way required recognition that overlooked defects of finite size may be unavoidable.

As with many new ideas and technologies, the reaction to fracture mechanics during the 1950's by the engineering community was often one of sceptical disinterest and it was necessary to overcome a substantial amount of unsympathetic reaction. Not only did the analytical and testing techniques need improvement but, obviously, endorsements from engineers without NRL affiliation were needed both for credibility and for assistance with the research needed to advance and improve fracture mechanics technology. The interest in fracture mechanics of A.A. Wells, a British scientist, provided an opportunity of that kind.

11.1. The Wells' approach to fracture mechanics

In 1953, a joint paper by Irwin and Kies [37] attracted the attention of Wells, who had finished his PhD in Engineering Science at Cambridge University and was employed at the nearby laboratory of the British Welding Research Association (BWRA) [55]. Wells recognized that the exchange of stress field energy into heat would represent most of the energy transfer involved in crack extension. During the 1954-55 period when Wells spent some time as a guest worker with the NRL Mechanics Division, Wells and Post used an improved Cranz-Schardin high speed camera to furnish four views of the photoelastic fringes near the tip of a running crack in a plate of CR-39 resin. The result, published in a 1958 paper [41] with a

famous comment contributed by Irwin [42], have been referenced as an early experimental illustration of dynamic fracture mechanics. The fracture mechanics research established by Wells at the BWRA laboratory (now termed, The Welding Institute) - the UK connection with NRL - played a leading role in the growth of fracture mechanics research in the UK and attracted the attention of other European countries as well.

11.2. Fracture mechanics in Germany

German research in Irwin style fracture mechanics started in March 1961 when G.R. Irwin, on the occasion of a Symposium organized by the Deutscher Verband für Materialprüfung, DVM (German Association for Materials Research and Testing), gave his first lecture introducing the tools of fracture mechanics. The interaction with many German scientists and engineers, notably Dr Kerkhof from Karlsruhe, stimulated numerous research projects and convinced some younger engineers to concentrate their research efforts to the new discipline of fracture mechanics. Many a visit of the leading German fracture experts of the younger generation to the USA and the establishing of close contacts over several years, culminating in the one month stay of Irwin in Freiburg in 1965 and the teaching of a fracture mechanics short-course in Stuttgart together with P.C. Paris, H.T. Corten, J.R. Rice and others, strengthened the prospering group of fracture mechanics experts in Germany and helped to overcome strong scepticism against fracture mechanics. A DVM Working Group on Fracture Processes was established in 1969 and, in 1989, Irwin and Wells jointly were awarded honorary membership to DVM.

11. 3. Historical failure cases

By 1960 fracture mechanics had matured to a stage so as to guarantee acceptance and continued growth of fracture mechanics technology. Several major serious fracture failure problems that occurred during the 1950's and the successful application of fracture mechanics principles to these serious failures enormously contributed to the acceptance of fracture mechanics by the engineering community.

These events were:

- the high-altitude bursts of deHavilland Comet jet aircraft in 1953-55,
- the fractures of 3600 rpm heavy section rotating components of large steam turbine electric generators in 1955-56,
- the failures of Polaris and Minuteman solid propellant rocket motor cases in 1957, and
- the failure of gas transmission pipe lines.

Most of these failures were related to the introduction of newly developed high-yield strength metals in high performance structures. These cases provide examples for failures where insurance coverage turned out to be too costly. More importantly, the penalties for failure to solve each of these problems in a timely way were unacceptable. The new methods of analysis afforded by fracture mechanics formed an important element in the solution of each of these problems. In return, each of these fracture investigations led to significant contributions in terms of new advances regarding fracture behavior, analysis methods, and testing techniques.

11.3.1. The Comet Airliner story

The high altitude destruction of the deHavilland Comet passenger jet airplanes in 1953-55 provided the first service fracture trial for fracture mechanics. The study of the wreckage of one Comet airframe (the famous G-ALYP which inaugurated scheduled jet service), which on 10 January 1954 after takeoff from Rome fell into the Mediterranean, showed that rapid extension of a corner crack at one of the windows had caused the failure. Previously, G_c values had been measured at NRL for aluminum alloy skin material similar to that of the Comets. In addition, trials with stress measurements near a small slot cut from one corner of an opening, which modeled an airplane window, verified that a window corner crack needed only a small extension before the G value became comparable to that of a crack nearly as large as the window. A similar explanation for the fast fractures causing crashes of the Comets was given by Wells [56].

In 1956, Kies and Irwin visited a number of US West Coast airplane companies to discuss fracture mechanics and its application to fracture-safe design [57,58]. The significance of these visits was demonstrated by the incorporation of crack-arrest features and materials with higher fracture toughness in subsequent aircraft designs.

11.3.2. Heavy rotating machinery failures

A second major engineering problem occurred in 1955-1956 when three heavy rotors of new electric generators fabricated by GE and Westinghouse failed as a result of a design change from 4-pole generators rotating at 1800 rpm to 2-pole generators rotating at 3600 rpm. Reduction of the rotor diameter from 66 inches to 44 inches did not compensate for the doubling of the number of rpm. The result was an increase of stress, which was accommodated by using a steel alloy of higher strength. The broken parts from these fractures wee available for examination.

B.M. Wundt [59] from General Electric (GE), entrusted

with the investigation of this problem was impressed by the work done by Irwin at NRL, and his team used Irwin's critical strain energy release rate parameter G_c to analyze the rotors. Fracture tests conducted on large disks fabricated from the failed rotors and post-fracture examinations showed flaw sizes from which progressive fracture occurred. The results of the investigation led to the use of an improved steel for rotor forgings with lower impurities and with higher fracture toughness. The closing sentence of Wundt's Memorandum [60] on the subject of catastrophic crack propagation reads:

„I therefore, appeal to other engineers and metallurgists to collaborate in this approach to achieve better criteria for a safe design of large rotors suspected of containing weak areas or actual cracks."

11.3.3. Rocket chamber failures

During the last months of 1957, scheduled progress of the military rocket program was threatened due to failures of the rocket chambers for the Polaris and Minuteman systems during hydro-tests. The NRL fracture mechanics group, led by Joe A. Kies [61], was asked to provide assistance. To increase the size of this group, arrangements were made to obtain assistance from scientists at the Naval Gun Factory, the University of Illinois (Department of Theoretical and Applied Mechanics), and Frankfort Arsenal. Examination and analysis of each hydro-test fracture, as soon as possible after occurrence, was of critical importance. The steel used for fabrication of the rocket chambers was difficult to weld without introducing defects. In addition, the water used in testing acted as an aggressive environment, and small defects grew into cracks of significant size as the pressure was applied in hydro-tests. From the post-fracture examinations, the expected relationships between crack size, stress, and fracture toughness were always confirmed. The use of automated welding processes eliminated defects of significant size. The practical value of the fracture mechanics approach was such that it clearly revealed the nature of the fracture problem.

11.3.4. Fracture mechanics of pipelines

Improved techniques for proof testing of gas transmission pipe lines called for new techniques and, as the gasline companies needed fracture mechanics help, Irwin entered into this exciting new field. Gas transmission pipelines were typically in the order from 15 to 30 km in length, entrenched and covered by soil before proof testing the entire length of the pipe. In case of a burst, it turned out to be very expensive to section and take out the sections lost. A few companies promoted proof-testing at high pressures of typically up to 80% of the yield strength of the metal with one company even going up to 99,5% of yielding in their proof-testing, suggesting and adopting this a requirement in order to reduce the number of rupture failures during construction. These failures could be extremely expensive as, with pipelines carrying natural gas, soil and rocks thrown during a burst could hit the wall of the pipe and sparks could ignite the gas to produce enormous heat with fumes and flames endangering populated environments.

Irwin with the expert assistance of H.T. Corten visited several gasline companies and collected information about failures in testing and in service. On-site inspections of the way joining and the welding was being done revealed that during the loading and transport of the stacked 15m pipe sections on railway cars, fatigue cracks were introduced during transport. At the construction site these 15m long pipes were dipped, automatic-welded into 45m sections and the final welding was done manually by two highly skilled and qualified welders when the 45m sections were lifted up, welded together and together moved back into the trench. This pretty tricky operation had to be done fairly close to the trench in order to avoid excessively large bending of the pipe. The pipe was then high pressure proof tested in sections.

At the time of the Irwin-Corten cooperation, Battelle in Columbus, Ohio, with ample funding from the American Gas Association, did independent research in the important field of gas transmission line failure.

The conclusion of the very well accepted Irwin-Corten Report [62] was that the workers must understand the chance of getting a loss, good workmanship practice must be improved in order to have the pipe carefully welded and safely put back into the trench. The high pressure test was accepted as a good proof test against bursts.

12. Research in fracture mechanics in Eastern Europe

In the post-war period considerable interest arose in the work of Griffith and the energy balance method and possible generalizations. Notable are the works of V.I. Mossakovsky concerning an inclined Griffith central crack in a stress field, the work by L.I. Sedov associated with a generalization of Griffith's method to include physical fields other than mechanical, and the work by G.I. Barenblatt.

Based on earlier work by Yu.P. Zheltov and S.A. Khristianovich [63], G.I. Barenblatt [64] developed the concept of limiting equilibrium state for cracks where interatomic forces would act in the crack tip zone. Ya.B.

Fridman and E.M. Morozov [65] derived a variational principle for the limiting equilibrium state. Despite the Cold War period there has been active exchange of ideas across the political borderline as correspondence between G.R. Irwin and G.I. Barenblatt attests, particularly Barenblatt's request of December 1973 addressed to Irwin for a photograph of the „Father of Fracture Mechanics".

Important contributions to the energetic concept of fracture mechanics are due to G.P. Cherepanov [66] who derived an integral expression for the limit equilibrium of a crack which is identical to the Rice-integral in the West. Similar to Irwin, who showed the equivalence of the energy balance (Griffith) approach and the fracture toughness approach, Cherepanov showed the equivalence of his integral expression with Irwin's K-approach. Based on adhesion forces in the crack tip vicinity, Barenblatt [64] derived a criterion similar to Irwin's K-criterion in 1959. Stress based fracture initiation criteria have been proposed for the first time by Wieghardt [22] and then, later, contemporaneously in the West by F. Erdogan and G.C. Sih [67] and in the East by G.P. Cherepanov [68] and V.V. Panasyuk [69] and L.T. Berezhnitsky. Dynamic fracture problems were attacked by G.I. Barenblatt and G.P. Cherepanov as well as V.Z. Parton and V.G. Boriskovsky. However, the failure cases motivating and driving research in fracture mechanics were not made public, even to date.

An account of the most important developments in fracture research in Eastern Europe including the famous controversy concerning the difference between the Griffith-Irwin fracture model and the Khristianovich-Barenblatt model of fracture stability and the fierce debate on this issue is discussed in some detail in a Foreign Science Bulletin of ONR London by V. Klein [70].

13. Fracture mechanics and standardization

The failure of the missile and rocket chambers also prompted the Office of the US Secretary of Defense to seek assistance from the American Society for Testing and Materials (ASTM). In response to that request, ASTM formed a Special Technical Committee (STC) in 1959 to study the application of the new fracture mechanics viewpoint to high strength materials in detail and to develop test methods for determining the brittle-fracture resistance of these high-strength metals. The committee chairman, J.R. Low, and its members (about 15) were well respected for their experience and understanding of fracture. The work of this committee provided the impetus for rapid technological developments in fracture mechanics, in which the ASTM STC and its sequel, ASTM Committee E-24, assumed a leadership role.

The First Report by the ASTM STC of ASTM in January of 1960 [71] states that

„...the principles of fracture mechanics were well enough understood to permit their use both in fracture testing and in interpretation of the results of fracture tests."

The methods of fracture mechanics were recognized and in some way officially acknowledged as a guide in the design of fracture tests and to assist the applications of fracture tests to service fracture problems. This constituted a change of paradigm as, prior to 1955, design allowances for the chance of structural fractures were based upon fracture failure experience. However, during the post-war period of rapid technological advancement, fracture failure experience became too expensive and no insurance company would be willing to jump in.

In the ASTM STC Report [71], fracture behavior was based upon a crack-tip stress field parameter K rather than directly in the energy parameter G from the modified Griffith theory. The report gave specific directions for conducting fracture toughness tests with sharply notched sheet tension specimens, explored the effects of temperature on fracture toughness and fracture mode transition, and described the effects of specimen dimensions, including the radius of the notch tip on fracture behavior. The necessity for developing two types of tests, one for quantitatively measuring fracture toughness to provide data useful for structural design, and a simple screening test for qualitatively ranking the fracture toughness of different materials was recognized by the members of the committee.

This first report on fracture testing of metals also addressed and confirmed the applicability and transferability of the result of fracture tests to more complex structure existing in service.

Four additional reports [72-75] were completed by the ASTM Committee during the period 1961-1964. The second, third, and fourth provided clarifications and concepts that had been developed further than those presented in the first report. The fifth report described modifications to the test methods, including a recommendation to extend the machined notch by fatigue and to test high-strength materials at slow loading rates. While the committee emphasized the effects of loading rate on the fracture toughness of materials sensitive to strain-rate, no technical basis was available for a testing recommendation.

These reports reflected the main research activities and rapid technical developments that had occurred in the early 1960's and, therefore, the publication of these reports

significantly contributed to the acceptance of fracture mechanics and aided in its subsequent widespread use in the USA. The ASTM endorsement, together with prior successful applications of fracture mechanics, given by the report was important because the 'sceptical disinterest' response, noted previously, still handicapped the progress of fracture mechanics in the early 1960's, and assured continued progress of fracture mechanics following 1960. Although, by this time, the US Naval Research Laboratory program on fracture mechanics was only a moderate portion of a national effort, with regard to practical applications, leadership of this effort through the activities of ASTM Committee E-24 has been consistent, helpful and of special value.

Currently it may seem obvious that a structural fracture cannot occur unless progressive crack extension moves a crack front through or nearly through a component. Thus the focus of attention in fracture testing should be upon characterization and prediction of conditions which control progressive crack extension. It may well have been recognized by some, prior to 1945, that analysis and characterization of that kind was desirable. However, structural fractures were abrupt events. The initial emphasis was on repair of damage. Considerations of the reasons for the event began at a later time and parts needed for failure analysis were sometimes not available. Whether to put the blame on stress too high, material too brittle, or some overlooked prior flaw was hard to determine. Specifications routinely stated that prior cracks were not acceptable. However, equipment for detection of prior cracks was of limited accuracy and careful inspections were expensive. Using fracture mechanics, one could avoid these difficulties by assuming a credible size for overlooked defects and calculating a 'safe' load relative to crack extension. With respect to application of fracture mechanics in forensic engineering, for contractual or legal purposes, in general, it would be easier to assess the danger of a single flaw or a group of flaws by using available fracture mechanics than to prove that using a non-fracture mechanics based technique for that purpose was adequate.

The quantitative determination of fracture and materials resistance characterizing parameters was clearly recognized in the Socialist countries too. The development of testing methods, reliable estimation of fracture toughness parameters and their usage in the choice of materials and in design generally, for the determination of admissible conditions to structures in service etc. has been a primary goal in Eastern industry as well. In the Soviet Union studies of this aspect began relatively late, almost a decade after the ASTM pioneering work. Many scientific research units and industrial production divisions started a series of thorough investigations pertaining to materials testing for crack resistance determination. The Scientific-Methodical Commission of Standardization of Methods for Material Crack Resistance, organized in 1977 on the basis of the Scientific Technical Council of Gosstandart of the former USSR and headed by the first chairman Yu.N. Rabotnov (famous for his investigations in creep fatigue) has been instrumental in the preparation of recommendations for the determination of structural materials crack resistance. A successful synthesis of domestic research and testing and foreign expertise led to a series of new recommendations which are similar in character to the ASTM recommendations. The first Soviet standard on fracture toughness testing was adopted in 1982. In 1992 the Physico-Mechanical Institute of the National Academy of Sciences of Ukraine compiled instructions for fatigue testing of materials.

Since about 1970 definition uncertainties pertaining to a variety of concepts such as start of crack extension, crack arrest etc. have resulted in unnecessary confusion and has been detrimental to the general acceptance of fracture mechanics concepts in industry and for inclusion into recommendations and codes. Obviously the development and common approval of definitions covering the concepts essential to current, well established portions of fracture mechanics is desirable. Although the task of formulating a set of useful definitions is a very formidable one and the quality of the definitions and degree of perfection varies in accordance with variations of personal judgment, the nomenclature task has been of great concern to ASTM E-24 and, after many years of considerable effort the Committee for Nomenclature headed by G.R. Irwin succeeded with the first terminology list published in the Annual Book of Standards.

14. The Lehigh Years

Irwin's interest in spending more time for research and academic activities (writing, teaching and research) made him take retirement from NRL and, in September 1967, he began full time employment at Lehigh University, Bethlehem, Pennsylvania, where he occupied the position of a Boeing University Professor of Mechanics. The Lehigh University employment was undertaken primarily for intensive study of fundamental and applied aspects of fracture mechanics relative to integration of this subject into the teaching of engineering science at universities.

During this 1967-1972 period, Irwin worked with faculty associates, particularly with P.C. Paris, in the development of senior level and graduate level courses on fracture mechanics. He assisted in the development of the introductory course, establishment of the Annual National Symposium on Fracture Mechanics, and the founding of the

Journal of Engineering Fracture Mechanics. Irwin's personal research and advisory work at Lehigh was mainly directed to fracture problems involving the widely used structural steels, particularly fracture problems of gas transmission pipe-lines, steel bridges, and pressure vessels.

Irwin's brilliant work of converting the theory of fracture from a branch of fairly pure physics into something of great importance to the design engineer was internationally acknowledged.

15. Extensions of linear-elastic fracture mechanics

LEFM fracture mechanics concepts allowed the treatment of a large number of brittle and to some extent also quasi-brittle fracture problems. Very soon, however, extensions of the linear-elastic fracture mechanics (LEFM) concepts began to appear in the literature during the period 1960-1965 with several most notable extensions related to:

(1) fatigue crack growth,
(2) stress-corrosion cracking,
(3) plasticity effects at the crack tip,
(4) dynamic fracture mechanics,
(5) creep and visco-elastic fracture.
(6) numerical modeling of fracture.

These topics will be briefly addressed in the following sections.

15.1. Fracture mechanics based approach to fatigue

Possibilities for applying fracture mechanics to fatigue cracking were recognized early at NRL, but this topic was considered less important than the characterization of conditions governing abrupt crack initiation. W.E. Anderson of the engineering staff at Boeing-Seattle, and P.C. Paris, a part-time affiliate to the Boeing Company, recognized the possibility to apply fracture mechanics to the fractures of the crashed British Comet aircrafts and were familiar with the papers by Irwin and Williams describing the stresses at crack tips. Moreover, they understood that fatigue-initiated cracks in airplanes dictated structural integrity.

The first publication relating the growth of a fatigue crack to K was published by Paris, Gomez and Anderson [76] in 1961. The authors recognized that the stresses and strains near a crack tip were specified by K_{max} and the ratio K_{max}/K_{min} and theorized that the amount of crack extension per cycle was also governed by the same variables. Subsequent work showed that $\Delta K = K_{max} - K_{min}$ was the primary parameter determining the rate of crack growth per cycle of loading.

Initially, the resistance to this approach from the engineering community was such that Paris and his colleagues were unable to find a peer-reviewed journal which would publish their paper. Having failed to find a receptive audience for their ideas by having been turned down by three leading peer-reviewed international scientific and engineering journals, the paper [76] ultimately appeared in *The Trend in Engineering*, a periodical published by the University of Washington in St.Louis. Most of the pioneering development of this new application of fracture mechanics occurred during the 1960's, with Paris playing a leading role.

Concurrent developments occured in Eastern Europe with Cherepanov as the driving force, where much attention has also been paid to crack growth by fatigue and related problems and where many scientists were concerned with the construction of appropriate analytical expressions of the functional relationship between cyclic crack growth and stress intensity. In 1962, G.P. Cherepanov [68] worked out a fracture mechanics based theory of fatigue macro-crack propagation presenting a formula which already contains the essential ingredients of the equation later worked out by Forman. Ultimately the work of a large number of researchers led to methodical instructions of the USSR: the RD50-345 recommendations.

15.2. Environmental assisted cracking

During the 1930's, when experimenting with single crystals and mica, Obreimoff [29] and others noted that moisture assisted slow crack extension in glass and that moisture greatly reduced the force necessary for splitting of mica. These effects were explained as due to the action of the water molecule in reducing cohesive type attractive forces between atomic size components of the solid. Thus, there was a close relationship of these explanations to the Griffith crack theory. In the Soviet Union, Rehbinder and his associates studied and developed liquids which assisted the drilling and crushing of rock. The „Rehbinder effect" was interpreted in a similar manner and attributed to the influence of water on fracture of glass. But this work was not very well known outside the Soviet Union until after World War II.

The post WW II work which led to the development of modern fracture mechanics began with a modification of the Griffith theory idea in which the resistance to crack extension was assumed to be plastic deformation at the leading edge of the crack rather than solid state surface energy. This corresponds to a shift from solid state physics to engineering mechanics. It is of interest that Dr Arthur Ruark, one of the principal advisors of G.R. Irwin advocated re-programming of the existing NRL fracture

studies toward use of the Griffith theory in conjunction with the Rehbinder effect. Irwin's rejection (at that time) of this advice was based on the fact that, at that time, it was not clear that recognition of the dominating importance of plastic strain at the leading edge of a crack was compatible with the surface energy concepts of Rehbinder.

Prior to 1957, fracture control techniques for stress corrosion cracking were developed entirely without reference to the synergistic effect of fabrication flaws acting like initial cracks. Ships moored in sea water and underground steel piping are usually protected by the system termed anodic protection which is based upon electrochemical effects. In other cases, surface coatings which are inert to corrosion may be applied by plating or oxidation. In the case of bridges, ship super-structures, and other outdoor metal structures, painting is regarded as furnishing adequate protection of the metal surface from chemical attack. The attractiveness for the use of austenitic 'stainless' steels rests mainly on the well known inertness of these metal alloys to chemical attack. Normally they do not require protection from corrosion.

In the case of rotor coil support rings for turbine generator rotors the use of austenitic steel, primarily for its non-magnetic characteristics, appeared to provide additional benefits against stress corrosion cracking. Under normal conditions this material does not show any evidence of chemical attack in the form of rusting or pitting, however, rings fabricated without cold expansion were shown to be susceptible to stress corrosion cracking in moist conditions due to chlorides and nitrides. The idea that stress corrosion cracking was a relative thing and would occur in a non-susceptible material due to a large enough starting crack was unknown prior to 1960 and did not become widely known until about 1965.

While, starting in about 1958, Paul C. Paris and coworkers at the Transport Division of the Boeing Company pioneered work on stable crack growth due to fatigue loading, intensive studies were also made of fracture failures occurring mainly during hydro-testing of ultra-high-strength steel solid propellant rocket chambers. It was not realized at first, that many of these fracture were due to very small prior cracks which grew to critical size for propagation during the slow application of the hydro-test pressure or during the pressure hold time period.

The time dependent nature of these fracture processes was ascribed to action of hydrogen introduced into the steel in high stress regions from the water.

In 1965, at NRL, Brown and Beachem [77] extended fracture mechanics concepts to treat stress-corrosion cracking problems discussing a standard testing practice for rating the stress corrosion cracking susceptibility of a metal containing a prior crack. They showed that a stress-corrosion cracking threshold, K_{Iscc}, exists, below which crack extension does not occur for a given material-environment system. The authors demonstrated that the K_{Iscc} data determined from cantilever beam specimens were identical to K_{Iscc} data obtained from surface-flawed tension specimens and this success prompted subsequent investigators to use the cantilever beam specimen to study K_{Iscc} characteristics of steels and alloys during the late 1960's and 1970's.

The novelty and great potential value of these new procedures for the study of stress corrosion cracking were responsible for the establishment of an ARPA financed project, jointly conducted by NRL, the Boeing Company, Lehigh University, Carnegie-Mellon Institute, and Georgia Institute of Technology in 1966, the results of which made it clear that the enhancement of the danger of stress corrosion cracking by a prior crack must be given increased attention and ultimately led to intensive research in this field.

In Europe, the effect of corrosive media on crack growth behavior was studied by M.O. Speidel [78] and others. Work performed by researchers in the countries of the former USSR is also published in the journal *Physico-Khimicheskaya Mechanica Materialov* since 1965 (English translation in the USA under the title: *Soviet Materials Science*).

15.3. Plastic crack tip behavior

It is a modeling artifact in LEFM that, when the crack tip is approached, the stresses become infinite. Real materials, however, respond by forming a plastic zone as the stresses are limited by the flow stress.

15.3.1. Small scale yielding at the crack tip and strip yield models

Elasticity theory based first attempts to characterize the size of this region of plastic behavior are due to Irwin and his coworkers. In 1958 papers [49,61] they describe test methods for measuring G_c using laboratory specimens to simulate both plane-strain and plane-stress conditions. Adopting a strip yield zone analysis, by simply equating the stress ahead of the crack equal to the yield stress, σ_Y, Irwin [79] was able to estimate the size of the plastic zone at the crack tip as $r_Y = 1/2\pi\,(K/\sigma_Y)^2$, where r_Y is the plastic zone size and K is the stress intensity factor. An improved second estimate for the plastic zone size, $2r_Y$ as compared to r_Y, can be obtained if the redistribution of the stresses in

the crack tip zone is taken into account.

While these simplified strip zone analyses gave an estimate for the extent of the plastic zone in the crack plane, no prediction was made for the real shape of the plastic zone as a limit elasticity analysis chosen by Irwin, without any reference to plasticity. Irwin initially assumed a circular plastic zone of radius r_Y associated with mode-I loading, however, a truly plasticity based analysis contributed by Hult and McClintock [80] in 1957 showed that the plastic region at the tip of a mode-III (transverse shear) loaded crack was circular. McClintock and Irwin [81,82] became first acquainted at the IUTAM Conference in Brussels in 1954 where Muskhelishvili, one of the main features of the conference, was the chairman of the session where Irwin presented his ideas.

Plasticity at the crack tip was also addressed in the First Report of the ASTM Special Committee in 1960 [71]. The report states that the presence of plasticity at the crack tip causes K to be underestimated if no correction is employed. For engineering purpose and for contained plasticity at the crack tip (quasi-brittle material behavior) the effect of a plastic zone in an elastic-plastic material can be taken into account by extending the length of the crack slightly in a perfectly elastic material as $a_{eff} = a + r_Y$, where 'a' is the true crack length in the elastic-plastic material, a_{eff} is the effective crack length in the perfectly elastic material, and r_Y is the 'radius'of the plastic zone strip.

During the period 1959-1963 alternate concepts for modeling the plastic zone at crack tips were introduced in the UK by Dugdale (1960) [83] and in the Soviet Union by Panasayuk and his coworkers (1959) [84,85]. For a thin sheet loaded in tension, Dugdale as well as Panasyuk and his coworkers stated that yielding was confined to a narrow band along the crack line. This case is equivalent, mathematically, to placing internal stresses equal in magnitude to σ_Y at the end of the crack, which tend to close the crack and remove the stress singularity at the crack tip. Dugdale derived a formula for the length of the plastic zone 'd' at each side of the crack as $d = \pi/8\ (K/\sigma_Y)^2$.

Experiments with steel sheets having both internal and edge slits showed good agreement with the predictions and the size estimate of 'd' compared favorably with the size estimate of $2r_Y$ due to Irwin.

Despite the apparent success of the predictions, Dugdale's approach was not immediately accepted because no photographic evidence of yielding was presented in the paper. This lack of proof was remedied by an etching technique introduced in 1965 by Hahn and Rosenfield [86] who showed the size and shape of local yielding at the crack tip of steel specimens containing edge cracks. The results indicated that the Dugdale model is useful for approximating the size and shape of the plastic zone under plane stress conditions. The papers by Panasyuk and his coworkers, appearing somewhat academic in nature and not showing any experimental results, remained largely unperceived in the West. This regrettable negligence must also partly be attributed to the fact that, in the Soviet Union, there existed several schools of fracture research bitterly fighting each other for supremacy.

Other variations of the strip yield model appeared in the period 1962-65 when Barenblatt published an extensive article concerning the equilibrium of cracks in brittle fracture [87]. He introduced the idea of molecular cohesive forces acting over a small distance at the end of the crack, which also tended to remove the stress singularity and keep the crack closed. While this approach, from a mathematical point of view, was similar to Dugdale's model, the physical basis was on molecular cohesion rather than macroscopic plasticity.

Finally, in 1963, dislocation mechanics yielded a further strip yield model, based on linear arrays of dislocations, which was presented by Bilby, Cottrell, and Swinden [88]. The BCS model represents the distribution of elastic-plastic strain in the yielded region by an inverted pile-up of dislocations. Subsequent development by Bilby and Swinden [89] produced a model in which plastic relaxation occurs by dislocation pile-ups on slip planes inclined symmetrically to the slip plane. This modification is called the Bilby-Swinden or inclined strip yield model.

15.3.2. Crack opening displacement concepts

In 1963, Wells [90,91] in the UK introduced an alternate concept. The idea was based on a critical displacement at the crack tip, the crack opening displacement (COD), which could be used to characterize crack extension. Wells evaluated the COD by employing Irwin's r_Y estimate and displacement equations for a center crack in an infinite elastic body to find the relationship $COD = (4/\pi)\ K^2/E\sigma_Y$, where E is Young's modulus. Wells believed that the COD criterion, consistent with LEFM, would be applicable even beyond general yielding, although this latter point was not proven.

A later paper [92] by Wells of 1965, also based on the COD concept, demonstrated the correlation between fractures of large (wide-plate) and small (Charpy V-notch) test specimens, either of which could be related to service failures. The significance of this example was not to develop the precise form of the correlation between specimen and service behavior, but rather to demonstrate

that such correlations were both possible and accurate. Wells's criterion is now known as the crack-tip opening displacement (CTOD) criterion and is widely used to characterize elastic-plastic and plastic fracture behavior.

As far as spreading of fracture mechanics in Europe is concerned, A.A. Wells and C.E. Turner have been extremely active with Wells having the backing of the International Welding Society. In contrast to the US where fracture research in the late 1960's and early 1970's was primarily driven by the nuclear power industry, fracture research in the UK was stimulated and motivated by the exploration of the oil reserves in the North Sea.

Based on previous work by Wells on the CTOD, in the period 1966-71, Burdekin and coworkers [93,94] from the Welding Institute developed the CTOD design curve which is a semi-empirical fracture mechanics methodology for welded steel structures. It is interesting to note, that the British nuclear industry developed their own fracture design analysis (1980) which is based on the strip zone plastic model developed by Dugdale and Barenblatt.

15.3.3. Elasto-plastic fracture mechanics

In the 1950's and early 1960's plasticity mechanics was employed in the design of structures to find critical loads for buckling. Irwin, finding that plasticity ideas could be quite helpful in fracture mechanics, wrote to Prager (an authority in plasticity at the time) for advice and the response letter by Prager contained the message that Irwin's ideas were nice but too complicated and it was about 10 years before the technology he had could be applied to fracture. This was in 1958. However, with Prager at Brown University, the U.S. Navy got interested in plasticity and considerably financially supported research in plasticity at Brown University, for it was a real big thing at that time.

Correspondence from the early 1960's indicates that, while still at Brown University, Jim Rice received strong encouragement and help from G.R. Irwin, who wanted Rice to develop some better model of the plastic zone which would help to improve the meaning of a fracture toughness test. Rice was aware of the developments and, although Irwin was not directly interested in mode-III other than using it in the fracture mechanics short courses, Rice carried further and succeeded in introducing work hardening.

By idealizing plastic deformation within the deformation theory of plasticity as nonlinear elastic material, Rice was able to generalize the energy release rate concept to nonlinear materials and to show that this energy release rate was equivalent to an integral expression which he called J-integral. In fact, modeling with mode-III, suggested to him the idea of path independent integral as a method of calculating a quantity which is now called J-integral (J for Jim Rice).

The results of this investigation Rice published in his famous 1968 paper [95] for which he received an award from ASTM. At the time of publication it became known to him that Eshelby, a dislocation expert in England who was not directly working in fracture mechanics, has previously (in 1951) derived so-called conservation integrals [96,97] of which the Rice-Integral was a special case. Although Rice should have referenced the work, he, however, did not need Eshelby's work when he applied his integral to represent the plasticity effects within the crack tip region. P. Paris, a promoter of J. Rice, conceived of the idea that the J-integral could also be used very close to the zone of yielding. In 1973, they took a notched bent specimen assuming that the stress across the ligament was proportional to the area under the curve and gave it a value for J. Tests were performed at Westinghouse.

The J-integral was a special feature of the National Symposium on Fracture Mechanics held in 1970 at the University of Illinois, and it received a big boost when ASTM Committee E-24 indicated that it could be used as a further measure of characterizing toughness.

In two very interesting papers, Hutchinson [98] and Rice and Rosengren [99] independently showed that J controlled crack tip conditions and related the J-integral to the crack tip stress fields in non-linear elastic materials. A new multi-axial small strain theory based singularity, named after the three authors HRR-singularity, contains the same apparent anomaly as the LEFM counterpart. It was found, that the J-integral defines the amplitude of the HRR singularity in the same way as the stress intensity factor K characterizes the amplitude of the crack tip singularity in linear elastic materials. The HRR theory does not consider the effect of crack tip blunting nor does it take into account the large strains which develop in the immediate crack tip vicinity. These effects were taken into account in a numerical finite element analysis by McMeeking and Parks [100] in 1979.

The importance of this non-linear extension of J as a stress field characterizing parameter was first fully conceived by the experts concerned about safe operation of nuclear power plants. Political and public awareness regarding safety of nuclear power plants together with the active research efforts of the nuclear power industry in the USA in the early 1970's to integrate the state-of-the-art technology in reactor design, construction and maintenance, brought fracture mechanics into the field of nuclear engineering. Fracture mechanics as developed by 1971 could not easily be applied

to nuclear pressure vessel grade steels as the enormous toughness of this material did allow a rational description in terms of LEFM and acceptable testing would require large equipment.

In 1971, Begley and Landes [101], two research engineers at Westinghouse, recognized the importance of Rice's 1968 paper and decided to apply the J-integral to characterize fracture toughness of these reactor steels. Despite high level scepticism offered by their colleagues, Begley and Landes succeeded with their experiments and a decade later a standard procedure for J-testing was issued by ASTM (1981) [102].

However, a general relationship between toughness, flaw size and stress loading for elasto-plastic material behavior, similar to the Griffith equation well established in LEFM, was still missing. A fracture mechanics based design methodology became available in 1976 with the theoretical framework worked out by Shih and Hutchinson [103] which, a few years later, in 1981, formed the basis of a fracture design handbook [104] published by the Electric Power Research Institute (EPRI) in California. The Shih analysis of 1981 [105] which uses the HRR solution to evaluate displacements shows that there is a unique relationship between J and the CTOD for a given material, hence, fracture toughness can be quantified in terms of a critical value of either J or CTOD.

Many materials characterized by high ductility (or toughness) do not fail in a sudden manner (often misleadingly termed catastrophical). These materials exhibit a rising R-curve where J as well as CTOD both increase with crack extension.

Whereas initiation toughness characterizes and provides information about the onset of stable cracking of ductile materials, J-controlled continuing stable crack growth stretches this concept to its limits when excessive plasticity or significant crack growth occur [106,107]. The conditions for application of J as a fracture characterizing parameter beyond ductile initiation include the requirement that the HRR based stress and strain relationships be valid in the process zone surrounding the crack front, where the microscopic physical processes that lead to fracture occur.

Stability of ductile crack growth is determined by essentially the same conditions as in the linear-elastic case with load control being less stable than displacement control. Stability of real structures is determined by conditions varying between load and displacement control and the R-curve slope can be characterized by the tearing modulus concept developed by Paris and coworkers [108] in 1979.

For elastic materials all relevant state variables and derived quantities are independent of the loading history. In fracturing of real materials (elasto-plastic, visco-plastic etc.), the energy absorbed during crack growth exhibits a history dependence (incremental theory of plasticity). In addition, the J-R curve becomes geometry dependent when crack growth occurs. In an effort to repair this deficiency, Ernst, in 1983 [109] proposed a modification of the deformation theory of plasticity. At present, the effect of specimen dimensions and loading on J-R curves in ductile materials has not been quantified for ready engineering application and work is in progress.

15.4. Dynamic fracture mechanics

The response of materials and structures to time-varying loading is different from statics [110]. When, in fracture processes, inertia effects become important, one is led to the field of dynamic fracture mechanics. Dynamic fracture is intrinsically more complicated than static fracture mechanics because of three effects:

- Inertia effects must be taken into account when either the load changes abruptly or the crack movement occurs in a jump-like fashion;
- Rate dependent material behavior may play an important role;
- Reflected stress waves interfere with the rapidly propagating crack.

15.4.1. Analytic and numerical work

Early work on dynamic fracture mechanics is summarized in the review papers by Erdogan et al (1968) [111] and Irwin and Wells (1965) [4]. The classical (though somewhat pathological) problem of the constant-speed moving Griffith crack considered by E. Yoffe [112] gave the first hint for the possibility of crack branching for running cracks. Non-stationary crack problems were considered by Broberg [113], Baker [114] and others.

A break-through in dynamic fracture analysis was achieved by L.B. Freund in his pioneering four part paper [115-118] in the *International Journal of the Mechanics and Physics of Solids* (1972-1976) where the fundamental solution for static and variable speed running cracks subjected to dynamic loading is derived. Essential contributions to dynamic fracture were done in the field of numerical simulations and development of contour integrals.

15.4.2. Experimental work

From a material characterization point of view, it was recognized that the toughness of the material would change

at higher crack propagation speeds. Dynamic crack propagation toughness could be measured as a function of crack speed by means of photomechanics techniques, primarily photoelasticity and the method of caustics in conjunction with high speed photography. The Fracture Mechanics Group at the University of Maryland advised by Prof. Irwin [119] and a string of other laboratories all over the world employed dynamic photoelasticity in dynamic fracture mechanics in an effort to characterize the dynamic relationship between the crack speed and the stress intensity factor during rapid crack propagation. Most of these studies were motivated and partially supported by the nuclear industry (in the USA the Nuclear Regulatory Commission) and electricity generating companies (in the USA the Electric Power Research Institute) pressed by growing concerns about crack arrest in pressure vessels and piping.

15.4.3. Crack arrest

In the 1970's it was noted that a static K_{Ic} measurement for a structural steel may sometimes yield smaller values for the toughness than the value at crack arrest, K_{Ia}. This effect was attributed to crack front roughening with increasing crack speed and explained as an R-curve effect. Methods of rapid loading K_{Ic} testing and K_{Ia} evaluation can be regarded as measurements of the minimum resistance of structural steel to crack extension. During the period 1970-90 several research groups in the US [120], in Europe [121] and elsewhere were heavily involved in characterizing crack arrest and developing appropriate design codes and standards primarily for the nuclear industry where the problem was addressed first. Irwin's cooperation and guidance has been instrumental in the development of crack arrest methodologies and suitable standards and recommendations for the nuclear industry.

15. 5. Creep and visco-elastic fracture

Structural components that operate at high temperatures may fail by slow stable deformation, so-called creep. Classical creep assumes uniform conditions for creep to occur, whereas in fracture mechanics creep is localized in the immediate vicinity of a crack where several hierarchical creep controlled deformation regimes form. The crack tip is embedded or even replaced by a tertiary process zone, contained in the steady state creep zone which in turn is embedded in the primary creep zone, which is engulfed by elastic material. As the material fails locally the tertiary process zone is the controlling zone on a microscopic level.

After the J-integral was accepted as a fracture characterizing parameter, various researchers proposed a creep version of the J-integral for crack growth in material undergoing steady state creep which became known as the C*-integral which characterizes the crack tip fields in a viscous material for which the time-dependent growth rate depends only on the C*-integral. Experimental studies by Landes and Begley [122] in 1976 and Riedel [123-124] in 1989 compare well with the theoretical predictions provided steady state creep is the dominant deformation mechanism and crack growth occurs at speeds slow enough that the creep zone can spread throughout the structure before fracture follows. If crack growth becomes larger and eventually overtakes creep growth, then a C* characterization becomes invalid and the classical K-approach is adequate. The transition zone from short time elastic to long time viscous behavior was analyzed by Riedel and Rice (1980) [125] by utilizing a simplified stress-strain law and neglecting primary creep.

As much of the fracture mechanics as was developed for steel and other metals cannot directly be applied to polymers, visco-elastic fracture mechanics requires the incorporation of visco-elastic material response. Familiar with the concepts of fracture mechanics as well as with the molecular structure of polymeric materials, S.N. Zhurkov contributed to the elucidation of the physical phenomena which take place at a crack tip in a stressed polymer by pointing out that the breakage of macro-molecule chain bonds plays a fundamental role in the fracture of polymers. Fundamental to the development of visco-elastic fracture mechanics is the work by Schapery [126-128], who assumed a nonlinear visco-elastic constitutive equation in the form of a hereditary integral and, by means of the well known correspondence principle, developed a generalized J-integral. Major contributions to the field of visco-elastic fracture mechanics may be found in the 1984 book by J.G. Williams [129].

16. The general acceptance of fracture mechanics

Two events occurred in the year 1965 which had a profound influence on the continued development of fracture mechanics. The first was the formation of ASTM Committee E-24 on Fracture Testing of Metals from the Special Technical Committee. The E-24 Committee has contributed significantly to the development of standardized fracture test methods and to the understanding of fatigue and fracture behavior in materials and structures. Also, the committee promotes the knowledge and further developments of fracture mechanics by sponsoring conferences, workshops, and symposia. every year, including an annual National Symposium on Fracture Mechanics.

Beginning in June 1967, and at the suggestion of Paul C. Paris, a series of annual National Symposia on Fracture Mechanics have been held with the intention to be

primarily national (as opposed to international) and include appropriate recognition of applied science aspects of fracture mechanics. Most of the papers presented at these meetings appear in ASTM Special Technical Publications (STP's). University campus facilities were utilized for these meetings and a shift of location for each year was enforced. The undesirable and unnecessary risks involved with the entrustment of publication of the symposium proceedings to an international, commercially operated journal publisher could be avoided by utilizing the backing of a permanent national organization such as ASTM through Committee E-24 as proposed by John Srawley.

The second important event was the publication of ASTM STP 381 entitled *Fracture Toughness Testing and Its Applications* [130]. This volume, later reprinted, contains informative papers concerning different aspects of fracture mechanics technology including a critical review of fracture mechanics principles, the first handbook of stress intensity factors [131], a critical review and evaluation of test methods employed for measuring fracture toughness, the use of electron microscope for studying fracture surfaces and the first comprehensive example of the application of fracture mechanics to the design and analysis of a pressure vessel.

Also included was the transcript from a panel discussion, during which leading experts debated and clarified different aspects of fracture mechanics.

The significance of this publication is evident because many of these papers continue to be referenced in current literature. Extensions of the concepts contained in ASTM STP 381 [e.g. 131-132] are numerous and on-going and form the basis of a worldwide spread of fracture mechanics activities periodically reviewed in the various national and international conferences.

17. The University of Maryland Years

After Irwin's retirement, in 1972, from Lehigh University, a natural choice for a good location for continuation of his research work was the University of Maryland, close to both, his first employer, the NRL, and his home in College Park. Because of research activities at Lehigh University which used his advisory assistance, GRI's shift of residence close to the University of Maryland in September 1972 did not imply severance from fracture studies at Lehigh University, where he continued to serve as an Adjunct Research Professor and consultant for many more years.

Irwin's activity at the University of Maryland was as diverse as his interest has always been. He has been extremely active in the development of a Crack Arrest Toughness Characterization Standard in the USA and has been prime consultant to a research gremium concerning crack arrest methodologies for the nuclear power industry involving Oak Ridge National Laboratories and Battelle in Columbus, Ohio.

18. Teching and Education in Fracture Mechanics

Currently, one of the most important tasks in fracture mechanics is educational. Although not all aspects of fracture failures are fully understood, the information now available is basic, widely applicable, and should be integrated into courses of instruction in strength of materials. Numerous short courses on engineering fracture mechanics as well as advanced fracture mechanics have been taught by Irwin and his coworkers during the period of formation of fracture mechanics. Lecture notes have been prepared and continually updated according to the target group and/or state of the art of fracture research. Copies and translations into several languages of Irwin's famous Lecture Notes [133,134] are in use in the USA and abroad. The special value of a volume on „Teaching and Education in Fracture and Fatigue" by Rossmanith (1996) [135] is the emphasis on practical transfer of knowledge in fracture mechanics and the use of the available information - by presenting the basic concepts in a direct and simple manner - in mastering fracture failure problems in engineering. Obviously, a body of correct definitions of the terms used in fracture mechanics forms the basis of successful education [136]. Important for teaching as well as for industry are stress intensity factor handbooks where the basic solutions for K factors can be found from which, by superposition, solutions for more complex problems can be derived and composed. The first collection of stress intensity factors is due to Paris and Sih [132] in the famous ASTM STP 381. This collection was continually expanded to become the Tada-Paris-Irwin Handbook [137] the most recent update to be published by ASTM in 1997. A recent 3-volume handbook of stress intensity factors has been edited by Murakami [138].

The adage *„Experience is the best teacher"* directly refers to history and gaining experience is a life-long learning process essentially coupled to it. As every new finding has its roots in the past, reflection on the development of a subject will unveil many a truth and bring things into the right perspective.

19. Irwin and the History of Fracture

Historical aspects of fracture mechanics have always been of greatest interest to Irwin and were first reviewed by Irwin and Wells [4] in 1965 for the time prior to 1963. A Special Volume [139] honoring G.R. Irwin and featuring papers on

the historical development and applications of linear elastic fracture mechanics was published by Sih, Wei and Erdogan 1975.

An ASTM Publication, edited in 1989 by Barsom [140], provides a collection of 'Early Classic Papers' for the period 1913-1965. From these it is apparent that complexities associated with fracture occurrence, fracture behaviors, and fracture testing delayed the introduction of fracture mechanics for a substantial time period. The concepts basic to linear elastic fracture mechanics involved less analytical and conceptual complexities than those associated with the mechanics of plasticity and dislocations. However, plasticity and dislocation mechanics were well developed topics before the introduction of fracture mechanics during the 1947-1960 time period [141].

In fact, a longer delay might have occurred if technological enterprise could have continued with the safety factor business and taking insurance against failure. Lack of understanding of the influence upon fracture failure of the size effects, fabrication flaws, cleavage in structural steels along with fatigue and stress-corrosion cracking made fracture failures seem largely unpredictable and interfered with the development of suitable and appropriate analysis models. The complexities were large and the incentives were not high.

In 1981, Paris and Hermann compiled a review on main questions related to fatigue [142] and, more recently, Paris in summarizing the state of the art of fracture research to date, particularly addressed the role of ASTM in the development of fracture research [143].

Owing to Irwin's pioneering work in fracture mechanics, on innumerable occasions he has been asked to contribute and lecture on the history of fracture mechanics. While working through Irwin's extensive archive the author counted a large number of manuscripts and pamphlets dedicated to the historical development and background of fracture research. It is most lamentable that, except for the joint 1965 paper [4] with Wells and an unfinished draft of a history of fracture mechanics [144], Irwin never carried any of the numerous historical essays beyond the stage of a draft or introductory lectures.

During the last decade research in fracture has proliferated enormously and the number of studies has exponentially grown. Hence, a selection of important topics becomes a serious problem. Concomitant with the present development is a strong thrust towards interdisciplinary character in order to understand failures due to fracturing. These expanded horizons must not let us lose sight of the basic objectives and goals in fracture research, which is to:

Understand fracture
and put fracture mechanics to work.

Exploring and reflecting on the history of fracture is essential for understanding of the development of future research in fracture. A call for papers on the social and developmental history of fracture research was favorably responded to by more than 35 acknowledged fracture research experts. These contributions - some of them were presented in a Special Session at the recent ICF-9 Congress in Sydney - will be published in a Special Anniversary Volume [145] honoring the 90th birthday of George R. Irwin.

20. Epilog

Although now already retired for the third time, George R. Irwin still keeps an office at the University of Maryland where he shows up almost every day, at least to answer the mail and stay in contact with international research work. In addition, he also keeps an apartment in Bethlehem, PA for his occasional visits to Lehigh University. He has just finished his most recent paper on metal fractography which he values very highly. In fact, he told visitors that he now has returned to that point in his career where he started to be interested in cleavage-ductile transitional behavior of steels.

George Rankin Irwin and his charming wife, Georgia Shearer Irwin are happily married for 66 (!) years and enjoy the company of their large family and many a good friend. Both enjoy good health and love their hobbies, and an occasional glass of Taylor Dry Sherry. In earlier years, George R. Irwin was an excellent tennis player, and he still likes good sea-food. Georgia likes reading historic novels and solving cross-word puzzles. During many of the author's visits and stays at their lovely home, long evenings were spent together searching for unknown rivers and mountains in far distant regions of the world in order to assist Georgia to complete the cross-word puzzle.

21. Acknowledgment

The author would like to thank the Austrian Science Foundation for financially supporting this work under contract # P 10326 GEO. He would also like to express his deep appreciation to Professor Dr G.R. Irwin and his charming family for the numerous stimulating technical discussions and their kind hospitality and cooperation in the course of this work. The author would also acknowledge the advice and help of Professors Dr Brian Cotterell and

Paul C. Paris, as well as many other fracture mechanics colleagues. Special appreciation for careful proof-reading is expressed to Dr Natalia Kouzniak.

22. References

1. Cotterell, B. and Kaminga, J. (1990) *Mechanics of Pre-industrial Technology*. Cambridge Univ. Press.

2. da Vinci, L. (date unknown) *Codice Atlantico*, folio 82 recto-b.

3. Uccelli, A. (1956) *Leonardo da Vinci*. NY: Reynal & Co.

4. Irwin, G.R., Wells, A.A. (1965) A continuous mechanics view of crack propagation. *Metallurgical Rev.* 10(38): 223-270.

5. Galilei, G. (1638) *Discorsi e Dimostrazioni Matematiche Sopra due Nuove Scienze* (ed. Elsevini, Leiden).

6. Mariotte, E. (1686) *Traite de Mouvement des Eaux*. Paris.

7. Hooke, R. (1678, 1686) *De Potentia Restitutiva*. London: Printed for John Martyn Printer to the Royal Society.

8. Ludwik, P. (1909) *Elemente der Technologischen Mechanik*. Berlin: Springer-Verlag.

9. Stanton, T.E. and Batson, R.G.C. (1921) On the characteristics of notched-bar impact tests. *Minutes of Proc. Inst. Civil Eng.* 211: 67-100.

10. Davidenkov, N.N., Shevandin, E. and Wittmann, F. (1947) Influence of size on the brittle strength of steels. *Amer. Soc. Mech. Eng.* 69: A63.

11. Docherty, J.G. (1932) Bending tests on geometrically similar notched bar specimens. *Engineering.* 133: 645-647.

12. Docherty, J.G. (1935) Slow bending tests on large notched bars. *Engineering.* 139: 211-213.

13. Sachs, G. (1941) Some fundamentals of the flow and rupture of metals. *Trans. Amer. Inst. Mining and Metallurgical Eng.* 143: 13-29.

14. Neuber, H. (1937) *Kerbspannungslehre (Theory of Notch Stresses)*. Berlin: Springer-Verlag.

15. Dupre, A. (1866) Ann. Chim. et Phys. Vol.4(7): 245.

16. Prandtl, L. (1907) *Verhandlungen deutscher Naturforscher und Ärzte*. Dresden.

17. Todhunter, I. and Pearson, K. (1886) *History of the Theory of Elasticity and of the Strength of Materials.* Cambridge University Press, UK.

18. Prandtl, L. (1903) *Zeitschrift für Physik.* Vol.4.

19. Timoshenko, S.P. (1953) *History of Strength of Materials.* NY: McGraw-Hill Inc.

20. Griffith, A.A. and Taylor, G.I. (1917) The use of soap films in solving torsion problems. *Proc. Inst. Mech. Eng.*: 755-809.

21. Love, A.E.H. (1926) *A Treatise on the Mathematical Theory of Elasticity.* NY: Dover Publications.

22. Wieghardt, K. (1907) Über das Spalten und Zerreissen elastischer Körper. *Z. Mathematik und Physik.* 55(1-2): 60-103. (English translation by H.P.Rossmanith: Wieghardt, K. (1995) On splitting and cracking of elastic bodies. *Fatigue and Fract. Eng. Mater. Struct.* 12(12): 1371-1405).

23. Inglis, C.E. (1913) Stresses in a plate due to the presence of cracks and sharp corners. *Proc. Inst. Naval Arch.* 55: 219-241.

24. Peterson, R.E. (1940, 1974) *Stress Concentration Factors.* NY: J. Wiley & Sons.

25. Griffith, A.A. (1920) The phenomena of rupture and flow in solids. *Phil. Trans. Roy. Soc. London.* A, 221: 163-198.

26. Irwin, G.R. (1948) Fracture dynamics. *Fracturing of Metals*: 147-166. Cleveland, OH: ASM.

27. Orowan, E. (1949) Fracture and strength of solids. *Reports on Progress in Physics.* 12: 185-232.

28. Joffe, A.F. (1929) *Physics of Crystals*. M.: Gostekhizdat.

29. Obreimoff, I.V. (1930) The splitting strength of mica. *Proc. Roy. Soc.* A127: 290-297.

30. Aleksandrov, A.P. and Zhurkov, S.N. (1933) *Brittle Fracture Phenomena*. M.: Gostekhizdat.

31. Weibull, W. (1939) A statistical theory of strength of metals. *Proc. Roy. Swedish Inst. Eng. Res.* No.151.

32. Westergaard, H.M. (1939) Bearing pressures and cracks. *J. Appl. Mech. Trans. ASME.* 6: A49-A53.

33. Muskhelishvili, N.I. (1953) *Some Basic Problems in the Theory of Elasticity.* Noordhoff, Ltd., Netherlands.

34. Tipper, C.F. (1962) *The Brittle Fracture Story.* Cambridge Univ. Press.

35. Orowan, E. (1945) Notch brittleness and the strength of metals. *Transactions, Institution of Engineers and Shipbuilders in Scotland.* 89: 165-215.

36. Orowan, E. (1955) Energy criteria of fracture. *Welding Journal. Res. Sup.* 34(3): 157s-160s.

37. Irwin, G.R. and Kies, J.A. (1952) Fracturing and fracture dynamics. *Welding Journal. Res. Sup.* 31(2): 95s-100s.

38. Irwin, G.R. and Kies, J.A. (1954) Critical energy rate analysis of fracture strength. *Welding Journal. Res. Sup.* 33(4): 193s-198s.

39. Kies, J.A., Sullivan, A.M. and Irwin, G.R. (1950) Interpretation of fracture markings. *J. Appl. Phys.* 21: 716-720.

40. Post, D. (1954) Photoelastic stress analysis for an edge crack in a tensile field. *Proc. Soc. Exp. Stress Anal.* 12(1): 99-116.

41. Wells, A.A. and Post, D. (1958) The dynamic stress distribution surrounding a running crack - A photoelastic analysis. *Proc. Soc. Exper. Stress Analysis.* 16(1): 69-96.

42. Irwin, G.R. (1958b) Comment to a paper by Wells and Post (1958). *Proc. Soc. Exper. Stress Analysis.* 16(1): 97-100.

43. Irwin, G.R. (1956) Onset of fast crack propagation in high strength steel and aluminum alloys. *Proc. 2nd Sagamore Conf. Ordnance Materials.* Vol. II: 289-30. Syracuse, NY: Syracuse University Press, and *NRL Report No. 4763 (U),* May, PB121224.

44. Sack, R.A. (1946) Extension of Griffith's theory of rupture to three dimensions. *Proc. Phys. Soc. London.* 58: 729-736.

45. Green, A.E. and Sneddon, I.N. (1950) The distribution of stress in the neighborhood of a flat elliptical crack in an elastic solid. *Proc. Cambridge Philosophical Soc.* 46: 159-163.

46. Sneddon, I.N. (1946) The distribution of stress in the neighborhood of a crack in an elastic solid. *Proc. Roy. Soc. London.* A, 187: 229-260.

47. Irwin, G.R. (1957a) Relation of stresses near a crack to the crack extension force. *Proc. 9th Int. Congr. Appl. Mech.* Vol VIII: 245-251. University of Brussels.

48. Irwin, G.R. (1957b) Analysis of stresses and strains near the end of a crack traversing a plate. *J. Appl. Mech. Trans. ASME.* 24: 361-364.

49. Irwin, G.R. (1958a) Fracture. In: S.Flügge (ed). *Encyclopedia of Physics. Vol. VI - Elasticity and Plasticity:* 551-590. Berlin: Springer-Verlag.

50. Kies, J.A. and Smith, H.L. (1955) Toughness testing of hot-stretched acrylics. *Proc. Aircraft Industries Association and Air Research & Development Command Joint Conference.* Dayton, OH, March 1955.

51. Sneddon, I.N. (1961) Crack problems in the mathematical theory of elasticity. *Report No ERD-126/1 of the North Carolina State College,* May 15.

52. Williams, M.L. (1952) Stress singularities resulting from various boundary conditions in angular corners of plates in extension. *J. Appl. Mech.* 74: 526-528.

53. Williams, M.L. (1957) On the stress distribution at the base of a stationary crack. *J. Appl. Mech. Trans. ASME.* 24: 109-114.

54. Rossmanith, H.P. (1995) An introduction to K.Wieghardt's historical paper „On splitting and cracking of elastic bodies". *Fatigue and Fract. Engng. Mater. Struct.* 12(12): 1367-1369.

55. Wells, A.A. (1953) The mechanics of notch brittle fracture. *Welding Research Journal.* Vol. 7.

56. Wells, A.A. (1955) The condition of fast fracture in aluminum alloys with particular reference to Comet failures. *British Welding Research Association Report, NRB 129.* April 1955.

57. Irwin, G.R. (1963) Fracture of Pressure Vessels. In: E. Parker (ed). *Materials for Missiles and Spacecraft,* Chapter 7. McGraw-Hill.

58. Tiffany, C.F. and Masters, J.N. (1965) Applied fracture mechanics. *Fracture Toughness Testing and Its Applications, ASTM STP 381*: 249-278. Philadelphia: ASTM.

59. Winnie, D.H.J. and Wundt, B.M. (1958) Application of the Griffith-Irwin theory of crack propagation to the bursting behavior of disks, including analytical and experimental studies. *Trans. ASME.* 80: 1643-1658.

60. Wundt, B.M. (1956) *Catastrophic Crack Propagation.* Memorandum, Structural Engineering Unit, Small Steam Turbine Department, Fitchburg Works, October.

61. Irwin, G.R., Kies, J.A. and Smith, H.L. (1958) Fracture strengths relative to onset and arrest of crack propagation. *Proc. ASTM.* 58: 640-657.

62. Irwin, G.R. and Corten, H.T. (1968) *Evaluation the Feasibility of Basing Pipeline Operating Pressure on In-Place Hydrostatic Test Pressure.* Report to Northern Natural Gas Company and El Paso Natural Gas Company.

63. Zheltov, Yu.P. and Khristianovich, S.A. (1955) *Izv. AN SSSR,* ONTI 5:3-41.

64. Barenblatt, G.I. (1959) On the equilibrium cracks due to brittle fracture. *Doklady AN SSSR.* 127: 47-50.

65. Fridman, Ya.B. and Morozov, E.N. (1962) On the variational principles of mechanical fracture. *Izv. vuzov. Mashinostroyenie.* 4: 56-71.

66. Cherepanov, G.P. (1967) On crack propagation in continuum. *Prikl. Math. Mekh.* 31(3): 476-493.

67. Erdogan, F. and Sih, G.C. (1965) Stress analysis of cracks. *ASTM STP 381*:30-83.

68. Cherepanov, G.P. (1974) *Brittle Fracture Mechanics.* M: Nauka.

69. Panasyuk, V.V. and Berezhnitsky, L.T. (1964) Determination of limiting force under the tension of a plate containing arc-type

crack In: *Voprosy Mekhaniki Tverdogo Tela*. 3: 3–19. Kiev: Naukova Dumka.

70. Klein, V. (1969) Debate on approaches used in Soviet studies of crack propagation. *Foreign Science Bulletin ONR London.*

71. ASTM (1960) Fracture Testing of High-Strength Sheet Materials - First Report of a Special ASTM Committee. *ASTM Bulletin*. N 243, January 1960: 29-40, and N 244, February 1960: 18-28.

72. ASTM (1961a) The slow growth and rapid propagation of cracks - Second Report of a Special ASTM Committee. *Materials Research and Standards*. 1(5): 389-393.

73. ASTM (1961b) Fracture testing of high-strength sheet materials - Third Report of a Special ASTM Committee. *Materials Research and Standards*. 11(11): 877-885.

74. ASTM (1962) Screening tests for high-strength alloys using sharply notched cylindrical specimens - Fourth Report of a Special ASTM Committee. *Materials Research and Standards.* 2(3): 196-203.

75. ASTM (1964) Progress in measuring fracture toughness and using fracture mechanics - Fifth Report of a Special ASTM Committee. *Materials Research and Standards*. 4(3): 107-119.

76. Paris, P.C., Gomez, R.E., and Anderson, W.E. (1961) A rational analytic theory of fatigue. *The Trend in Engineering.* 13(1): 9-14. University of Washington.

77. Brown, B.F. and Beachem, C.D. (1965) A study of the stress factor in corrosion cracking by use of the pre-cracked cantilever beam specimen. *Corrosion Science.* 5: 745-750.

78. Speidel, M.O. (1971) Theory of stress corrosion cracking in alloys. In: J.C. Scully (ed). NATO Scientific Affair Division. Brussels, 345-354.

79. Irwin, G.R. (1960) Plastic zone near a crack and fracture toughness. *Proc. 7th Sagamore Research Conf. on Mechanics & Metals Behavior of Sheet Material.* Vol. 4: 463-478. Racquette Lake, NY, August 1960. Proc. published by Syracuse University.

80. Hult, J.A.H. and McClintock, F.A. (1957) Elastic-plastic stress and strain distribution around sharp notches under repeated shear. *Proc. 9th Int. Congr. Appl. Mech.* Vol. VIII: 51-58. University of Brussels.

81. McClintock, F.A. (1971) Plasticity aspects of fracture. In: *Fracture: An Advanced Treatise*. Vol.3: 47-225. Academic Press, New York;.

82. McClintock, F.A. and Irwin, G.R. (1965) Plasticity aspects of fracture mechanics. *Fracture Toughness Testing and Its Applications, ASTM STP 381*: 84-113. Philadelphia: ASTM.

83. Dugdale, D.S. (1960) Yielding of steel sheets containing slits. *J. Mech. Phys. Solids*. 8: 100-104.

84. Leonov, M.Ya. and V.V.Panasyuk (1959) The development of the smallest cracks in solids. *Prykladna Mekhanika.* 5(4): 391-401.

85. Panasyuk, V.V. (1960) On the theory of crack propagation during brittle body deformation. *Dop. AN Ukr.RSR.* 9: 1185.

86. Hahn, G.T. and Rosenfield, A.R. (1965) Local yielding and extension of a crack under plane stress. *Acta Metallurgica.* 13: 293-306.

87. Barenblatt, G.I. (1962) The mathematical theory of equilibrium cracks in brittle fracture. Advances in applied mechanics. Vol 7: 55-129. In: H.L. Dryden and T. von Karman (eds). NY: Academic Press.

88. Bilby, B.A., Cottrell, A.H. and Swinden, K.H. (1963) The spread of plastic yield from a notch. *Proc. Roy. Soc. London*. A, 272: 304-314.

89. Bilby, B.A. and Swinden, K.H. (1965) Representation of plasticity at notches by linear dislocation arrays. *Proc. Roy. Soc. London*. A, 285.

90. Wells, A.A. (1961) Unstable crack propagation in metals: cleavage and fast fracture. *Proc. Crack Propagation Symp.* Vol.1, Paper 84. Cranfield, UK.

91. Wells, A.A. (1963) Application of fracture mechanics at and beyond general yielding. *British Welding Journal.* 11: 563-570.

92. Wells, A.A. (1965) Notched bar tests, fracture mechanics and the brittle strengths of welded structures. *The Welding Institute Journal.* 12(1): 2-13.

93. Burdekin, F.M. and Stone, D.F.W. (1966) The crack opening displacement approach to fracture mechanics in yielding materials. *J. Strain Analysis.* 1: 145-153.

94. Burdekin, F.M. and Daws, M.G. (1971) Practical use of linear elastic and yielding fracture mechanics with particular reference to pressure vessels. In: *Proc. Inst. Mech. Eng. Conf.* London: 28.

95. Rice, J.R. (1968) A path independent integral and the approximate analysis of strain concentration by notches and cracks. *J. Appl. Mech.* 35: 379-386.

96. Eshelby, J.D. (1951) On the force on an elastic singularity. *Proc. Roy. Soc.* 244A: 87-112.

97. Eshelby, J.D., Frank, F.C. and Nabarro, F.R.N. (1951) The equilibrium of linear arrays of dislocations. *Phil. Mag.* 42: 351.

98. Hutchinson, J.W. (1968) Singular behavior at the end of a tensile crack tip in a hardening material. *J. Mech. Phys. Solids.*

16: 13-31.

99. Rice, J.R. and Rosengren, G.F. (1968) Plain strain deformation near a crack tip in a power law hardening material. *J. Mech. Phys. Solids.* 16: 1-12.

100. McMeeking, R.M. and Parks, D.M. (1979) On criteria for J-dominance of crack tip fields in large-scale yielding. *ASTM STP 668*: 175-194. Philadelphia: ASTM.

101. Begley, J.A. and Landes, J.D. (1972) The J-Integral as a fracture criterion. In: *ASTM STP 514*, 1-20. Philadelphia, ASTM.

102. ASTM (1981) Standard test method for J_{Ic}, a measure of fracture toughness. *ASTM E813-81.* Philadelphia: ASTM.

103. Shih, C.F. and Hutchinson, J.W. (1976) Fully plastic solutions and large-scale yielding estimates for plane stress crack problems. *J. Eng. Mat. Techn.* 98: 289-295.

104. EPRI (1981) Methodology for Plastic Fracture. *EPRI NP-1735, RP 601-2.* March, 1981.

105. Shih, C.F. (1981) Relationship between the J-Integral and the crack opening displacement for stationary and extending cracks. *J. Mech. Phys. Solids.* 29: 305-326.

106. Shih, C.F. and German, M.D. (1981) Requirement for a one-parameter characterization of crack tip fields by the HRR singularity. *Int. J. Fract.* 17: 27-43.

107. Hutchinson, J.W. and Paris, P.C. (1979) Stability analysis of J-controlled crack growth. *ASTM STP 668*: 37-64. Philadelphia: ASTM.

108. Paris, P.C. (1979) CSNI specialists meeting on plastic tearing instability. *Proc. US NRC NUREG/CP-0010.* CSNI Report No 39.

109. Ernst, H.A. (1983) Material resistance and instability: Beyond J-controlled crack growth. ASTM-STP 803; I-191-213, American Society for Testing and Materials, Philadelphia.

110. Krafft, J.M. and Irwin, G.R. (1965) Crack-velocity considerations. *Fracture Toughness Testing and Its Applications, ASTM STP 381*: 114-129. Philadelphia, PA: ASTM.

111. Erdogan, F. (1968) Crack propagation theories. In: H. Liebowitz (ed). *Fracture.* Vol. II: 497-590. NY: Academic.

112. Yoffe, E. (1951) The moving Griffith crack. *Philosophical Magazine.* 42: 739-750.

113. Broberg, K.B. (1960) The propagation of a brittle crack. *Arkiv för Fysik.* 18: 159-192.

114. Baker, B.R. (1962) Dynamic stresses created by a moving crack. *J. Appl. Mech.* 29: 449-458.

115. Freund, L.B. (1972) Crack propagation in an elastic solid subjected to general loading- I. Constant rate of extension. *J. Mech. Phys. Solids.* 20: 129-149; II Non-uniform rate of extension. 20: 141-152.

116. Freund, L.B. (1973) Crack propagation in an elastic solid subjected to general loading. - III Stress wave loading. *J. Mech. Phys. Solids.* 21: 47-61.

117. Freund, L.B. (1974) Crack propagation in an elastic solid subjected to general loading. - IV Obliquely incident stress pulse. *J. Mech. Phys. Solids.* 22: 137-146.

118. Freund, L.B. (1976) Dynamic crack propagation. In: *The Mechanics of Fracture,* pp.105-134. New York: ASME.

119. Irwin, G.R. et al (1976) A photoelastic characterization of dynamic fracture. *U.S. NRC Report NUREG-0072.*

120. Kumar,V., Gmerna, M.D. and Shih, C.F. (1981) An engineering approach for elastic-plastic fracture analysis. *EPRI Report NP-1931.* Palo Alto, CA, USA: Electric Power Research Institute.

121. Kalthoff, J.F., Beinert, J., Winkler, S., and Klemm, W. (1980) Experimental analysis of dynamic effects in different crack arrest test specimens. *ATM STP 711*: 109-127. Philadelphia: ASTM.

122. Landes, J.D. and Begley, J.A. (1976) A fracture mechanics approach to creep crack growth. *ASTM STP 590*: 128-148. Philadelphia: ASTM.

123. Riedel, H. (1981) Creep deformation at crack tips in elastic-viscoplastic solids. *J. Mech. Phys. Solids.* 29: 35-49.

124. Riedel, H. (1989) Creep crack growth. *ASTM STP 1020*: 101-126. Philadelphia: ASTM.

125. Riedel, H. and Rice, J.R. (1980) Tensile cracks in creeping solids. *ASTM SPT 700*: 112-130. Philadelphia: ASTM.

126. Schapery, R.A. (1975) A theory of crack initiation and growth in viscoelastic media - I. Theoretical development. *Int. J. Fract.* 11: 141-159; II- Approximate methods of analysis. 11: 369-388; III- Analysis of continuous growth. 11: 549-562.

127. Schapery, R.A. (1984) Correspondence principles and a generalized J Integral for large deformation and fracture analysis of viscoelastic media. *Int. J. Fract.* 25: 195-223.

128. Schapery, R.A. (1990) On some path independent integrals and their use in fracture of nonlinear viscoelastic media. *Int. J. Fract.* 42: 189-207.

129. Williams, J.G. (1984) *Fracture Mechanics of Polymers.* Chichester, UK: Ellis Horwood Ltd.

130. ASTM (1965) Fracture toughness and its applications. *ASTM STP 381*. Philadelphia: ASTM.

131. Paris, P.C. and Sih, G.C. (1965) Stress analysis of cracks. *Fracture Toughness Testing and Its Applications, ASTM STP 381*: 30-83. Philadelphia: ASTM.

132. Srawley, J.E. and Brown, W.F. (1965) Fracture toughness testing methods. *Fracture Toughness Testing and Its Applications, ASTM STP 381*: 133-198. Philadelphia: ASTM.

133. Irwin, G.R. (1979) *Lectures Notes on Engineering Fracture Mechanics*. University of Maryland, September 10, 1979.

134. Irwin, G.R. Mechanics of Progressive Fracturing - 10 lectures (ed. H.P. Rossmanith, in preparation, 1997).

135. Rossmanith, H.P. (1996) (ed.) *Teaching and Education in Fracture and Fatigue*. E&FN SPON (an imprint of Chapman & Hall), London.

136. Irwin, G.R. and de Wit, R. (1978) Survey of fracture toughness testing and data with reference to meaning and application. *Report to ASTM,* Mag. Card. No 120, March.

137. Tada, H., Paris, P.C. and Irwin, G.R. (1973, 1997) *The Stress Analysis of Cracks Handbook*. Hellertown, PA: Del Research Corporation.

138. Murakami, Y. (1987) *Stress Intensity Factors Handbook*. NY: Pergamon Press.

139. Sih, G.C., Wei, R.P. and Erdogan, F. (1975) *Linear Fracture Mechanics. Historical Developments and Applications of Linear Fracture Mechanics Today*. Envo Publishing Company, Inc.

140. Barsom, J.M. and Rolfe, S.T. (1987) *Fracture and Fatigue Control in Structures*. Englewood Cliffs, NJ: Prentice-Hall, Inc.

141. Barsom, J.M. (1987)(Ed) Fracture Mechanics Retrospective. Philadelphia: ASTM.

142. Paris, P.C. and Hermann, L. (1981) Twenty years of reflection on questions involving fatigue crack growth. Part I: Historical observations and perspectives; Part II (with L. Hermann) Some observations of crack closure. In: *Proc. Int. Conf. on Fatigue Thresholds: Fundamentals and Engineering Applications*. Vol.1: 3-32. EMAS.

143. Paris, P.C. (1995) Reflections on progress in fracture mechanics research. *ASTM STP 1207*: 5-17.

144. Irwin, G.R., Dally, J.W. and Bonnenberger, R.W. (1992) Draft of a history of fracture mechanics (unpublished).

145. Rossmanith, H.P. (1997) (ed) *Fracture Research in Retrospect*. G.R. Irwin Anniversary Volume. Rotterdam: Balkema.

Appendix -A

Selected Technical Publications of George R. Irwin

Irwin, G.R. and Almy, G.M. (1935) Mass Ratio of the Lithium Isotopes. Physical Review, 48, p.104 (Doctoral Thesis)

Irwin, G.R. (1948) Fracture Dynamics. In Fracturing of Metals, 1947 ASM Symposium, (Trans. ASM 40A), Cleveland, 147-166.

Irwin, G.R. (1949) Penetration resistance measurements at ballistic speeds. Presented at 6th Int. Congress of Applied Mechanics , September 1946 (Reference was from Masket's article in Journal of Applied Physics, 20, 132-140, 1949.

Kies, J.A., Sullivan, A.M. and Irwin, G.R. (1950) Interpretation of Fracture Markings. J. Applied Physics, 21:716-720.

Irwin, G.R. (1952) High speed strain measurements. Modern Research Techniques in Physical Metallurgy, Americ. Soc. for Metals, 205-224; NRL Reprint No 31-53.

Irwin, G.R: and Kies, J.A. (1952) Fracturing and Fracture Dynamics. Welding Journal Res. Sup. 31: 95-100, February.

Irwin, G.R. (1953) Angle and strain relations in flat plate Lüders'-bands. Journal of Applied Mechanics, Vol.20: 449.

Irwin, G.R. and Kies, J.A. (1954) Critical energy rate analysis of fracture. The Welding Journal Research Supplement 33;193-198.

Irwin, G.R. (1954) The effect of size upon fracturing. **ASTM; STP** 158:176-194.

Irwin, G.R. (1957) Analysis of stresses and strains near the end of a crack traversing a plate. Jnl of Appl. Mechanics, Vol.24(3);361-364.

Irwin, G.R. (1957) Discussion to a paper by Wells, A.A. and Post, D.. Experimental Mechanics.

Irwin, G.R. (1958) Fracture. Encyclopedia of Physics, IV, pp. 551-590, Springer-Verlag..

Irwin, G.R. (1960) Effects of size and shape on fracture of solids. SPT 283;118-128.

Irwin, G.R. (1963) Fracturing and fracture mechanics. T&AM Report No 202, Department of Theoretical and Applied Mechanics, University of Illinois, October 1961 (First of three series of lectures).

Irwin, G.R. and Srawley, J.E. (1962) Progress in the development of crack toughness fracture tests. Material-prüfung 4, No 1, January 1962.

Irwin, G.R. (1962) Analytical aspects of crack stress field problems. T&AM Report No 213, Department of Theoretical and Applied Mechanics, University of Illinois, March 1962 (Second of three series of lectures).

Irwin, G.R. (1962) Relation of crack toughness measurements to practical applications. Welding Journal Res. Sup. 41(11): 1-10.

Irwin, G.R. (1962) Crack-extension force for a part-through crack in a plate. J. of Applied Mechanics, Vol. 29(4): 651-654.

Irwin, G.R. (1963) Relatively unexplored aspects of fracture mechanics. T&AM Report No 240, Department of Theoretical and

Applied Mechanics, University of Illinois, February 1963 (Third of three series of lectures).

McClintock, F.A. and Irwin, G.R. (1965) Plasticity aspects of fracture mechanics. ASTM-STP 381, pp. 84-113.

Krafft, J.M. and Irwin, G.R. (1965) Crack velocity considerations. ASTM-STP 381, 114-129.

Irwin, G.R. and Wells, A.A. (1965) A continuum-mechanics view of crack propagation. Metallurgical Reviews, 10, pp. 223-270, No 38, 1965.

Sih, G.C., Paris, P.C. and Irwin, G.R. (1965) On cracks in rectilinearly anisotropic bodies. Int. J. Fracture Mechanics, Vol.1(3);189-203.

Clark, A.B.J. and Irwin, G.R. (1965) Crack propagation behaviors. Experimental Mechanics, SESA, Vol. 6(6):321-330, June.

Irwin,G.R. (1966) Moisture assisted slow crack extension in glass plates. NRL Memorandum Report 1678, 28 January.

Irwin,G.R. (1967) Fracture mechanics applied to adhesive systems. In: Treatises on Adhesives and Adhesion. 233-267, Ed.: Robert Patrick, Dekker, New York.

Irwin, G.R. (1968) Linear fracture mechanics, fracture transition, and fracture control. Journal of Engineering Fracture. 1(2): 241-257.

Irwin, G.R. and Corten, H.T. (1968) Evaluating the feasibility of basic pipeline operating pressure on in-place hydrostatic test pressure. Report to Northern Gas Company and El Paso Natural Gas Company. November.

Irwin, G.R. (1969) On the future of fracture mechanics. ASM Materials Engineering Congress, 11-16 Oct.

Irwin, G.R. (1969) Basic concepts for dynamic fracture testing. ASME J. of Basic Engineering, Vol. 91:519-524.

Sih, G.C. and Irwin, G.R. (1969) Dynamic analysis for two-dimensional multiple crack division. Journal of Engineering Fracture Mechanics, Vol.1, No.4, pp.603-614.

Irwin, G.R. and Paris, P.C. (1969) Fundamental Aspects of Crack Growth and Fracture. In H. Liebowitz (ed). Fracture. Vol. 3: 1-46. Academic Press.

Irwin, G.R. (1970) Basic concepts for dynamic fracture testing. ASME, Journal of Basic Engineering, Vol. 91.

Irwin, G.R. (1970) Trends in fracture mechanics. ASM Conference on Fracture Control, 1970.

Madison, R.B. and Irwin, G.R. (1971) Fracture analysis of King's Bridge Melbourne. ASCE Journal of Structural Division, pp 2229- September.

Irwin, G.R. (1972) Characterization of part-through cracks in tension. In: The Surface Crack. ASME Publication (J.L. Swedlow, Ed.) ASME, pp. 1-10.

Tada, H., Paris, P.C. and Irwin, G.R. (1973) Stress analysis of cracks Handbook. Del Research Corporation, Hellertown, PA, 1973.

Madison, R.B. and Irwin, G.R. (1972) Dynamic K_c-testing of structural steel. Journal of Structural Division, ASCE, pp1331-1349, July 1974.

Irwin, G.R. et al (1975) A photoelastic study of the dynamic fracture behavior of Homalite 100. U.S.NRC Report NUREG-75-107, University of Maryland.

Erdogan, F., Irwin, G.R. and Ratwani, M. (1976) Ductile fracture of cylindrical vessels containing a large flaw. ASTM STP 601:191-208.

Rossmanith, H.P. and Irwin, G.R. (1979) Analysis of dynamic isochromatic crack-tip stress patterns. University of Maryland Report, 443pp, July .

Fisher, J.W., Pense, A.W., Hausammann, H., and Irwin, G.R. (1980) Quinnipiac River Bridge Cracking. J. of the Structural Division, ASCE, pp. 773-789.

Irwin, G.R. (1981) Advancements in fracture mechanics. Honorary Lecture for International Congress of Fracture, ICF-5, (Ed. D. Francois) Cannes, France.

Ogawa, K., Zhang, X.J., Kobayashi, T., Armstrong, R.W., and Irwin,G.R. (1982) Microstructural aspects of the fracture toughness cleavage-fibrous transition for reactor grade steel. 15th National Symposium on Fracture Mechanics, July 1982, ASTM-STP.

Chona, R., Irwin, G.R. and Shukla, A. (1982) Two and three-parameter representation of crack-tip stress fields. Journal of Strain Analysis, Vol 17, No 2, pp79-86.

Friedland, I.M., Albrecht, P. and Irwin, G.R. (1982) Fatigue of two-year weathered A588 stiffeners and attachment. Journal of Structural Division. ASCE, pp125-144.

Irwin, G.R. (1982) Crack arrest in structural steels: An overview. Report, University of Maryland, September.

Irwin,G.R. and DeWit,R. (1983) A summary of fracture mechanics concepts. Journal of Testing and Evaluation, ASTM, Vol.11(1):56-65.

Chona, R., Irwin, G.R. and Sanford, R.J. (1983) Influence of specimen size and shape on the singularity dominated zone. **ASTM STP 791** Vol.1, pp. 3-23 (Eds: J.C. Lewis and G. Sines).

Irwin, G.R. (1984) Fracture Mechanics. In: Metals Handbook, 9th Edition, Vol.8;439-458.

Irwin, G.R. (1985) Concepts in Fracture Mechanics (A 10hour Video Course featuring J.R .Rice, J.W. Hutchinson, P.C. Paris and G.R. Irwin), Paris Productions nc., St.Louis.

Dally, J.W., Fourney, W.L. and Irwin, G.R. (1985) On the uniqueness of the stress intensity factor - crack velocity relationship. Int. J .Fracture 27:159-168.

Zhang, X.J., Armstrong, R.W. and Irwin, G.R. (1989). Cleavage fracturing stages at micrometre-size inclusions in pressure vessel steel weld metal. J. Mat Science Letters 5: 961.

Irwin, G.R. (1987) Brittle-ductile transition behaviors in reactor vessel steels. Proc. of the 14th WRSI Meeting, NUREG/COP 0082, Vol.2; 251-272.

Zhang, X.J., Armstrong, R.W. and Irwin, G.R. (1989) Fractography of isolated cleavage regions in nuclear vessel steels. Metall.Trans.20A, 2862-2868.

Zhang, X.J., Kumar, A., Armstrong, R.W. and Irwin, G.R. (1990) Fractographic study of isolated cleavage regions in nuclear vessel steels and weld metals. ASTM STP 1086;89-101.

Irwin, G.R. (1990) Fracture mechanics in applications. Forensic

Engineering, Vol.2, No1/2:81-84.

Irwin, G.R., Dally, J.W., Zhang, X.J. and Bonnenberger, J.R (1992) Lower-bound initiation toughness of A533B reactor-grade steel. In Rapid Load Fracture Testing, ASTM STP 1130 (Eds: R. Chona and W. Corwin); 9-23, ASTM Philadelphia.

Irwin, G.R. (1993) Brittle Fracturing. Keynote Address of Live Satellite Broadcast Univ.of Maryland Course on *Microstructural Apects of Fracture Mechanics*. Friday, 20 August.

Irwin, G.R. and Zhang, X.J. (1994) Cleavage behavior in structural steels. Int. J. Solids Struct. .32: 2447-2456.

Appendix -B

Selected Memberships of George R. Irwin (1937-1997)

Society	Country	Year
American Physical Society	USA	1937-
Sigma Xi	USA	1937-
Washington Philosophical Society	USA	1945-
Fellow of Washington Academy of Sciences	USA	1946-
American Society for Testing & Materials ASTM	USA	1959-
ASTM Committee E-24	USA	1965-
American Assoc. Univ. Professors	USA	1969-
Honorary Membership ASTM	USA	1973
Member of Nat. Acad. of Engineering NAE	USA	1977
Foreign Member of the Royal Society of London	UK	1987-
German Society for Testing Materials, Honorary Member, DVM	Germany	1988
American Ceramic Society, Honorary Member	USA	1988
ISTLI Honorary Member ISTLI	Austria	1993-

Appendix -C

Selected Activities of George R. Irwin (1937-1997)

1936-37 Prediction accuracy of Li^7/Li^6 mass ratio from shift of Li^7/Li^7 bands relative to Li^6/Li^7 bands (PhD Thesis).
1939 Plate testing type ballistic pendulum (blast shield)
1940-44 Force curves for projectile penetration
1943 Cloth laminate body armor
1945 3 1/2 months in Western Pacific, late March to early June of 1945, as fracture mechanics consultant, U.S.Marine Corps.
1947-54 Modified Griffith theory for fracture of metals
1948 Pendulum type measurement of projectile momentum loss
1952-54 Irwin-Kies papers 1952-54; examples of Comet bursts 1956, examples of rotor bursts 1958.
1957 Values of K^2 from photoelasticity
1955-57 Relation of G vs K^2 ; fracture of pure liquids; Encyclopedia of Physics article.
1957-59 r_Y plasticity adjustment factor; Plane stress and plane strain fracture transition
1958-62 Polaris fracture team
1959-60 Leak before burst criterion
1959-60 Fracture mechanics accepted by ASTM "over-the-hill" point
September 1959-January 1960.
1960 June 1960: First view of crack opening stretch concept
First trial of nuclear reactor safety study
1961 K-values for flat-elliptical crack and for part-through surface cracks
1961-63 Rate sensitive steels: minimum or crack arrest toughness, K_{Ia} from DW-NDTT testing
1960- Fracture mechanics of adhesive joints
1961 Crack at a free surface boundary edge crack subjected to thermal or shrinkage stress
1963 Irwin-Wells review paper - History of Fracture Mechanics
1964 McClintock-Irwin "plasticity aspects of fracture mechanics"
1965 Close relation of COD to r_Y corrected *G*, 1965 (good calculation by Tada in 1970-1972)
1965 H_2O assisted slow cracking of glass, velocity versus K, plateau and threshold (work done at Freiburg, Germany)
1966 Fracture safety of nuclear reactor vessels (review study)
1967-68 Dynamic problems - equally spaced running cracks ending on a circular locus; semi-infinite running crack with wedge forces
1968 Study of pipe-line fracture with H. Corten
1968-70 Dynamic K_{Id} measurements and study of King's Bridge fracture
1969-71 Long part-through cracks with plastic net ligament, θ and δ characterization (with Krishna)
1969-72 Solution using alternative stress removal with Tada
1970 First Conference on Fracture Control Plans - ASM
1972-74 Long part-through cracks in cylinders (axial) with strip plastic zones and plastic net ligaments (with Ratwani and Erdogan)
1973-74 Experimental K calibrations; aluminum vessels, precise crack opening measurements using diffractometry
1975-76 Start of ASTM E-24 Nomenclature Sub-Committee; Resolution of "conflict" on crack arrest toughness
1977-85 Studies on crack branching and higher order parameter methods
1977-96 Studies in highway bridge failure prevention and other specific problems.

Appendix -D

Selected Awards of George R. Irwin (1937-1997)

Type	year
Distinguished Civilian Navy Service Award	1947
Alumni Achievement Award Knox College	1948
C.B. Dudley Medal ASTM	1960
Applied Science Award of the Scientific Research Society of America Sigma Xi Award	1960
Ford Foundation Lecturer	1961
R.H. Thurston Lecture ASME	1966
Award of Merit ASTM	1967
Capt R.D. Conrad Award Navy Department	1969
Alumni Award for Distinguished Service in Engineering University of Illinois	1969
Murray Lecture SESA	1973
Sauveur Award ASM	1974
Academic Leadership Award Lehigh University	1974
Grande Medaille Metallurgical Society of France	1976
Commendation Letter, Office of Nuclear Regulatory Research	1976
Nadai Award ASME	1977
Lazan Award SESA	1977
Doctor of Engineering (h.c.) Lehigh University	1977
Irwin Medal ASTM E-24	1978
Clamer Award Franklin Institute	1979
Honory Lecture ICF-5 Cannes	1981
Governor's Citation Maryland	1982
Tetmajer Award Univ. of Techn Vienna, Austria	1985
Society for Exp. Mech. Fellow Award SEM, USA	1985
Timoshenko Medal ASME, USA	1986
Gold Medal ASM, USA	1987
Engineering Innovator Award Univ. of Maryland,	1993
ISTLI Award Austria	1993

The Influence of a Great American Scientist and Engineer in Germany

Erwin Sommer
Fraunhofer-Institut für Werkstoffmechanik
Wöhlerstr. 11, D-79108 Freiburg

G.R. Irwin's historical traces in Germany

In March 1961 the German Society for Material Testing - the DVM - organized the conference *DVM-Tag 1961* in Würzburg. One of the invited papers - presented by Dr. George R. Irwin and coauthored by John E. Srawley - was entitled: *Progress in the development of crack toughness fracture tests (Fig. 1).*
The authors discussed in their contribution the basic principles of fracture mechanics. The article was published almost one year later in the journal *Materialprüfung* [1].
The meeting itself was a historical event: 550 participants from 15 European countries and the United States were present. It was the first big conference of international character the DVM organized after its refoundation in 1954.
According to the general topic of the conference *Fracture Phenomena and Fracture Testing of Materials* G.R. Irwin's presentation was in the center of interest, but most of the participants were faced with a new engineering approach to cope with fracture processes. Irwin's basic ideas were already published in the *Journal of Applied Mechanics* [2] under the famous title *Analysis of Stresses and Strains Near the End of a Crack Traversing a Plate*. The leading thought in this early publication was that *a substantial fraction of the mysteries associated with crack extension might be eliminated if the description of fracture experiments could include some reasonable estimate of the stress conditions near the leading edge of a crack particularly at points of onset of rapid fracture and at points of fracture arrest.* As a consequence, the stress intensity factor K, which turned out to be the most useful parameter for solving problems by means of linear elastic fracture mechanics, has been introduced and related to the strain energy release rate G.

At this time only a few scientists - mainly physicists and not engineers - were acquainted with the name George Irwin through the literature. The reason for that was twofold:
Physicists - more used to think in terms of theoretical abstractions and to model the reality by concentrating on dominating parameters - had studied G.R. Irwin's article on the fundamentals of fracture in the *Handbook of Physics* [3].
Most of the material scientists and engineers, however, during that time did not believe in the applicability of such simplified approaches. According to their experience the idealized description of the behavior of large cracks in specimens had nothing to do with real failure processes in components. Rather, they recommended to improve the material properties, in particular the toughness of materials in order to achieve a high reserve of plastic deformation before final failure. However, they also had to overcome severe difficulties: a precise definition of
the property *toughness* was lacking, one had to rely on Charpy test results, and furthermore on occasion fracture processes were observed without preceeding extensive plastic deformation although the Charpy energy seemed to be acceptable.
But, as it always happens, there were a few exemptions and they should be mentioned in this context. At the same conference two other speakers presented their recent investigations. One of them was working in the field of basic material science and correspondingly investigated the mechanisms of brittle and ductile fracture of metals [4] (Fig. 2).
The other author Hans Rumpf [5] was convinced that the principles of fracture physics would be helpful for the understanding of the problems of comminution (Fig. 3).

Progress in the development of crack toughness fracture tests



By **G. R. Irwin** and **J. E. Srawley**, Washington

UDC 539.375.5 : 620.172.24
Materialprüf. 4 (1962) Nr. 1 p. 1/11 (24 Fig. 8 Ref.)
Received April 27, 1961

Progrès dans le développement des essais de rupture pour détermination de la ténacité à la fissuration

Fortschritt in der Gestaltung von Bruchversuchen zur Bestimmung der Rißzähigkeit

Figure 1: Publication G.R. Irwin and J.E. Srawley

George R. Irwin Symposium on Cleavage Fracture
Edited by Kwai S. Chan
The Minerals, Metals & Materials Society, 1997

Neuere Vorstellungen über den Mechanismus des spröden und des zähen Bruchs von Metallen



Von Prof. Dr. rer. techn. habil. **Albert Kochendörfer,** Düsseldorf

DK 539.375.5 : 539.55 : 539.56 : 669.017

Materialprüf. **3** (1961) Nr. 7 S. 266 74 (9 Fig. 61 Ref.)

Manuskript-Eing. 18. Mai 1961

Current ideas on the mechanism of brittle and ductile fracture of metals

Des idées récentes sur le mécanisme de la rupture fragile et ductile des métaux

Mitteilung aus dem Max-Planck-Institut für Eisenforschung, Düsseldorf
Vorgetragen auf dem DVM-Tag 1961 des Deutschen Verbandes für Materialprüfung in Würzburg am 16. März 1961

Figure 2: Publication A. Kochendörfer

G.R. Irwin's first scientific visit to Germany in 1961 would not have left the same traces if a personal contact to another speaker of the conference would not have been established: Frank Kerkhof, vicedirector of the Ernst-Mach-Institut in Freiburg. He presented a paper entitled *Untersuchungen von Bruchvorgängen mit Hilfe von Ultraschall* [6] (Fig. 4). His investigations of fracture processes in glasses had proven that - due to their extreme brittleness - glasses were ideal materials for applying the methods of fracture mechanics without too many correction terms.

The first stimulating contact between Frank Kerkhof and George Irwin led to a second scientific visit of Dr. Irwin to Germany. In 1965 he stayed for a period of three months in Freiburg and used this short time effectively:

- he carried out research in the field of stress corrosion cracking and summarized the results of his investigations in a report entitled *Moisture Assisted Slow Crack Extension in Glass Plates* [7];
- he visited leading institutes in Germany concerned with failure processes;
- he spent many hours for stimulating discussions with coworkers of the host institute; furthermore, he encouraged the young fellows of the institute to extend their studies in the United States - in those years a country very attractive for German scientists.

The author of this article happened to be the first of those young scientists who had the chance to work as a postdoctoral fellow with Professor Paul C. Paris at Lehigh University, Bethlehem Pa. in 1967/68. This was the time when Dr. Irwin changed from the Naval Research Laboratory in Washington, D.C. to a teaching position as a professor at Lehigh University.

Following up George Irwin's visit to Germany a regular exchange of ideas based on personal contacts was established between American material and fracture research groups and German scientists.

In 1968 the first *National Symposium on Fracture Mechanics* was organized at Lehigh University. One of the key persons at this conference was Professor George Irwin; one of the invited speakers Professor Frank Kerkhof.

From then on numerous visits back and forth took place and have led to very stimulating and fruitful discussions. Especially for the fracture group in Freiburg, which later on became the Fraunhofer-Institut für Werkstoffmechanik, Professor Irwin was the well accepted teacher and personal friend. No wonder that his visits - often accompanied by his wife Georgia - were not just formal technical events, but covered historical, cultural and sightseeing activities and became part of the private life of many of the institute's members. Probably the Fraunhofer-Institut für Werkstoffmechanik would not exist if this one highly respected personality did not have such a tremendous influence on this group of scientists.

Problemstellungen und neuere Ergebnisse der Bruchtheorie



Von Prof. Dr.-Ing. **Hans Rumpf,** Karlsruhe

DK 539.375.001 : 539.422

Materialprüf. **3** (1961) Nr. 7 S. 253 65 (17 Fig. 28 Ref.)

Manuskript-Eing. 4. Mai 1961

Theory of fracture, its problems and recent results

La théorie de la rupture, ses problèmes et ses nouveaux résultats

Mitteilung aus dem Institut für Mechanische Verfahrenstechnik der TH Karlsruhe
Vorgetragen auf dem DVM-Tag 1961 des Deutschen Verbandes für Materialprüfung in Würzburg am 16. März 1961

Figure 3: Publication H. Rumpf

Untersuchungen von Bruchvorgängen mit Hilfe von Ultraschall

Von Dr. phil. (nat.) **Frank Kerkhof,** Freiburg i. Br.

DK 539.375.5 : 534.321.9 : 620.179.16

Materialprüf. **3** (1961) Nr. 10 S. 376/82 (13 Fig. 9 Ref.)

Manuskript-Eing. 27. Juni 1961



Studies on fracture phenomena by means of ultrasonics

Etudes sur des phénomènes de rupture effectuées à l'aide d'ultrasons

Mitteilung aus dem Ernst-Mach-Institut der Fraunhofer-Gesellschaft
Vorgetragen auf dem DVM-Tag 1961 des Deutschen Verbandes für Materialprüfung in Würzburg am 16. März 1961

Figure 4: Publication F. Kerkhof

Meanwhile, the name George R. Irwin stands for the whole field *Fracture Mechanics*. The list of important papers he has published is very impressive. Even his early publications concentrated on topics which are still of interest. Accordingly, many of the solutions he offered years ago are still extremely useful. For this reason Professor Irwin has received numerous awards, medals and honorary degrees. In 1989 he became an honorary member of the DVM.

G.R. Irwin's scientific traces in Germany

When George Irwin visited Freiburg in 1965 the fracture group working with Frank Kerkhof [8] had mainly investigated dynamic fracture problems. In order to analyze the onset and propagation of fast moving cracks optical methods and short time photography had been applied, special ultrasonic techniques for modulating fracture surfaces with time markings had been developed and the effect of time dependent thermally induced stress fields on the propagation i.e. velocity and direction of cracks had been investigated. Especially from the fractographic studies it had been realized that glasses were ideal materials for testing the principles of fracture mechanics.

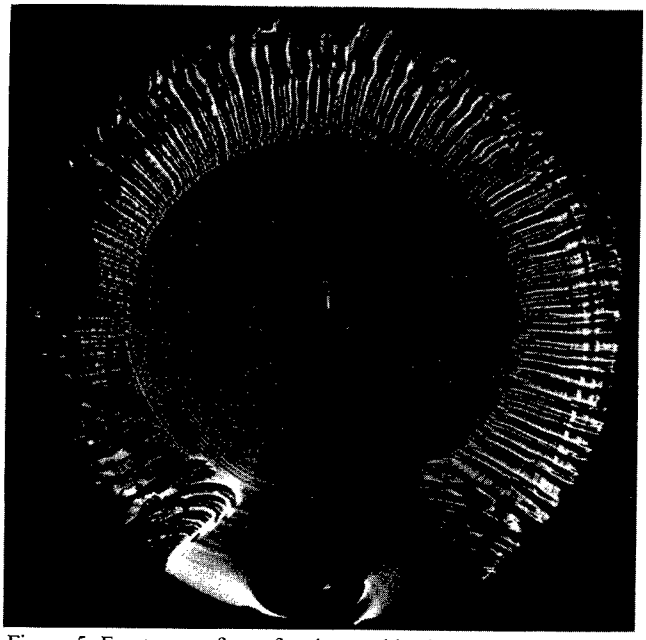


Figure 5: Fracture surface of a glass rod broken under tension and torsion [9]

The interaction of this experimental experience and theoretical knowledge on fracture processes turned out to be a fertile soil for further stimulating investigations and applications. A few examples of these traces will be selected and shortly discussed.

Safety and availabilty of components

Acquainted with the engineering demands of the nuclear technology dynamically developing in that time Dr. Irwin strongly supported the idea to model the critical situation of a loss of coolant accident (LOCA) in an irradiation embrittled pressure vessel in glass experiments. Experiments of this kind were started in 1972 heating up precracked glass cylinders and applying a thermal shock at the inner surface by cold water. The resulting crack arrest phenomena could be explained by the decreasing thermal stress field [10] and were in accordance with the predictions based on the methods of the linear elastic fracture mechanics. However, reality is more complex than these simplified experiments: reactor vessels have an austenitic inner cladding which avoids the influence of the cooling liquid on the fracture process; the total loading results from a superposition of internal pressure, residual stresses, and thermal stresses which are induced by postulated transients and vary over the inner circumference because the cold water safety injection is performed by one or more inlet nozzles depending on the safety case studied.

Figure 6 describes the result of a recent LOCA-analysis: a strip cooling situation in the pressure vessel of a German 600 MEW pressurized water reactor resulting from an assumed leak on the hot

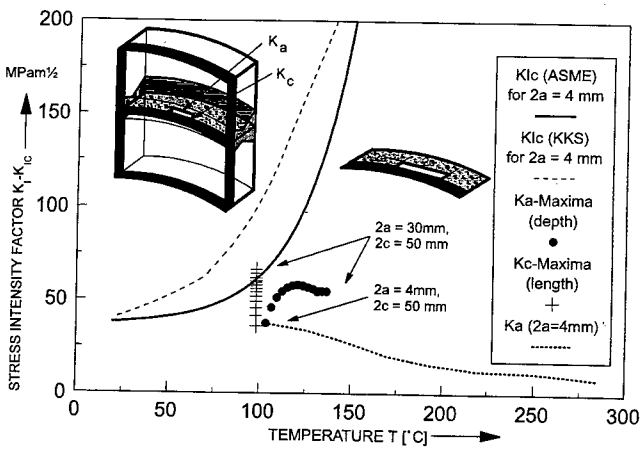


Figure 6: Postulated cracks in the core weld of a reactor pressure vessel loaded by a LOCA transient at end of life material conditions

side has been calculated using a 3D finite element model to evaluate temperatures and elastic-plastic stresses based on plant and case specific thermohydrolic input data [11].

Extension of part-through cracks

According to the principles of fracture mechanics it is expected that at any given position of a crack front fracture should initiate and extend when the locally released energy exceeds the fracture resistance of the material. In many practical cases - for instance when a component contains surface cracks - both the distribution of the loading parameters K or G for elastic material behavior (or the J-integral in the elastic-plastic regime) may show a pronounced variation along the crack contour [12] as well as the distribution of the local fracture resistance. Assessment procedures can usually be based on simplifying assumptions choosing a maximal value of the loading parameter or a constant value of the resistance. However, when more precise predictions of the crack growth characteristics are needed - as for instance for a leak before break assessment - more sophisticated methods have to be available. The fracture surface in figure 7 shows the typical features of such a situation: although the maximum value of the loading parameter along the contour of the semielliptical surface crack located in a plate of the reactor steel 22 NiMoCr 37 and supposed to a tensile load normal to the fracture surface is expected to be found near the vertex at $\phi = 0°$ the maximum of stable crack growth is found at smaller angles - an indication that the fracture resistance curves vary along the crack front [13].

Since direct methods for measuring fracture resistance curves locally along a crack contour are lacking an indirect determination of the varying resistance behavior is necessary. From 2D investigations it is well known that the slope of J-resistance curves is highly influenced by constraint effects [14, 15]. The constraint is considered to be the restraint of plastic deformation due to the specimen geometry and the type of loading. A definition in a general manner is difficult to provide. However, the local constraint at the crack tip can be quantitatively related to a parameter σ_m/σ_v which defines the state of triaxiality; σ_m is the mean stress, σ_v the equivalent stress [16]. Unfortunately, the ratio σ_m/σ_v is not only varying along the crack contour, but is also a function of the local crack tip coordinates forming a maximum close to the crack tip. This maximum value as well as the corresponding value of the J-integral can be calculated by 3D-FEM analysis for a certain position of the contour and has been successfully related to the amount of stable crack extension experimentally determined at the same place [17]. As a result obtained for an outer surface crack with the depth to length ratio a/c = 0,22 located in axial direction in a pressure

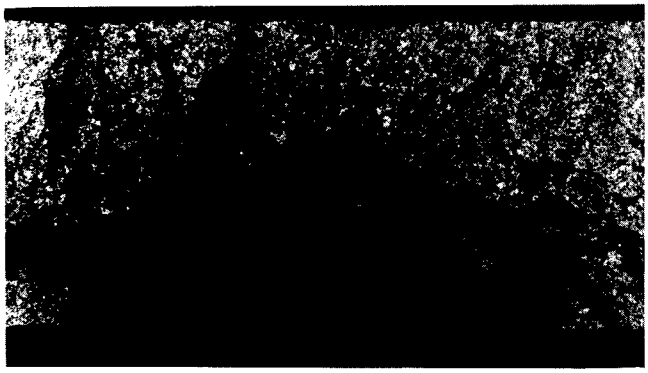


Figure 7: 1. zone: semielliptical fatigue crack in a plate of the reactor steel 22 NiMoCr 37; 2. dark zone: stable crack growth by interrupted uniaxial tensile load at room temperature; 3. zone: final fracture by bending at low hydrogen temperature.

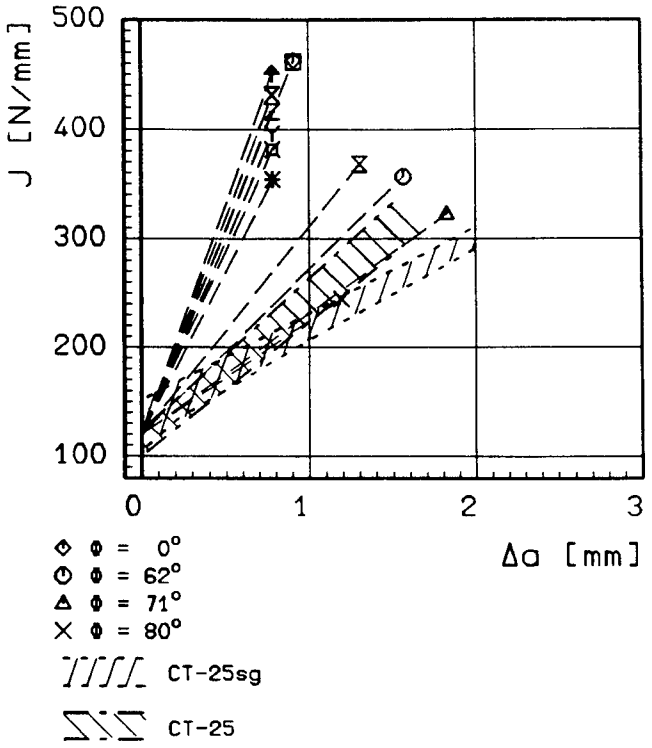


Figure 8: Local crack resistance curves determined at several points along the contour of an outer surface crack in a pressure vessel [17]

vessel of the reactor steel 20 MnMoNi 55 under pressure the J-resistance curves have been constructed and compared with corresponding curves obtained with normal and side-grooved compact tension specimens. As can be seen from figure 8. the slope of the local resistance curves is lowest in a range $60° < \phi < 80°$ where the maximum crack growth occurs and corresponds to that of the CT-specimens. The maximum slope of the resistance curve as well as the maximum value of the J-distribution along the contour is found in the center part $\phi = 0°$.

Whereas the preceeding investigations were mainly related to the assessment of the safety and availability of components the basic knowledge on fracture processes turned out to be extremely helpfull for other branches of application as well.

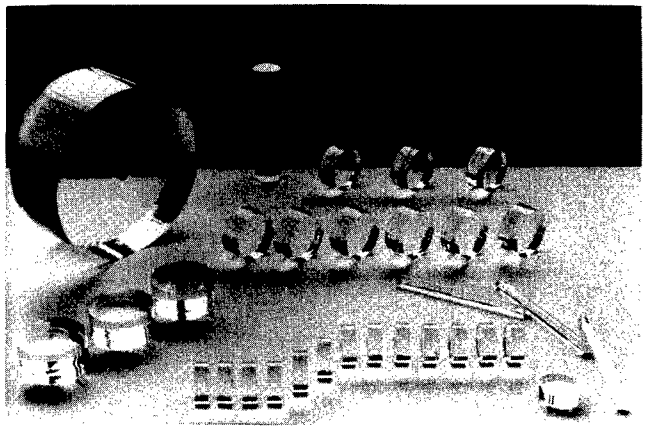


Figure 9: A variety of specimens of different dimensions with high quality fracture surfaces severed by thermally induced stresses



Figure 10: TiAlN-coated forming tools and moulded optical lenses of inorganic glasses [22]

Severing of glass - Forming of precision lenses

As mentioned before fracture processes caused by thermally induced stresses had been studied intensively by the group of Frank Kerkhof in Freiburg [8, 18]. In order to transfer this knowledge of a basic kind to practical application severing processes of glass specimens of different geometry have been investigated [19]. In close cooperation with German firms of the glass and the optical industry several techniques have been developed. These intentions were pursued under different aspects as for instance:

- the automatization of simple glass cutting procedures help to save costs;
- the improvement of the edge cut which leads to a higher strength of the product than conventional cutting procedures can guarantee a sufficient quality without costly additional grinding;
- the production of clean undisturbed glass surfaces by fracture allows to shorten certain steps of manufacturing by replacing sawing, grinding and polishing processes [20, 21]; an example of this kind has been a step in the production of eye lenses.

A variety of such specimens with high quality fracture surfaces is shown in figure 9.

The ability to produce clean undisturbed glass surfaces leads necessarily to the next higher research demand: how to supply the surface with precise spheric or aspheric contour without grinding and polishing procedures. For this purpose the tools of fracture mechanics are only of indirect use. The problem has been solved by developing forming tools which were coated by physical vapor deposition with TiAlN in order to warrant the high standards of optical requirements and to withstand the aggressive attack of the glass to be moulded at a temperature of about 600°C. Some examples of tools and formed precision lenses are shown in figure 10 [22].

Machining of brittle materials

The knowledge of fracture mechanics has been proven extremely useful for optimizing machining processes of materials as glasses, silicon or ceramics. Its main contribution in this case is to provide criteria which allow to assess how surface and subsurface damage may develop during machining and can be avoided or minimized by altering the parameters of the process. In general guidelines for optimizing machining processes are dictated by technical and economical demands, i.e. best results in shortest time at lowest costs.

Two examples enlighten that the local reaction of materials known for their brittle behavior at room temperature to the action of the machining tool can be brittle or ductile.

To a great extent the prize of products manufactured of structural ceramics is determined by the processing costs of the final finishing. Therefore, the Fraunhofer IWM in cooperation with other German institutes and firms pursued two directions of research: to improve grinding and lapping processes and to optimize the forming of products by numerically simulating dry press and sintering processes.

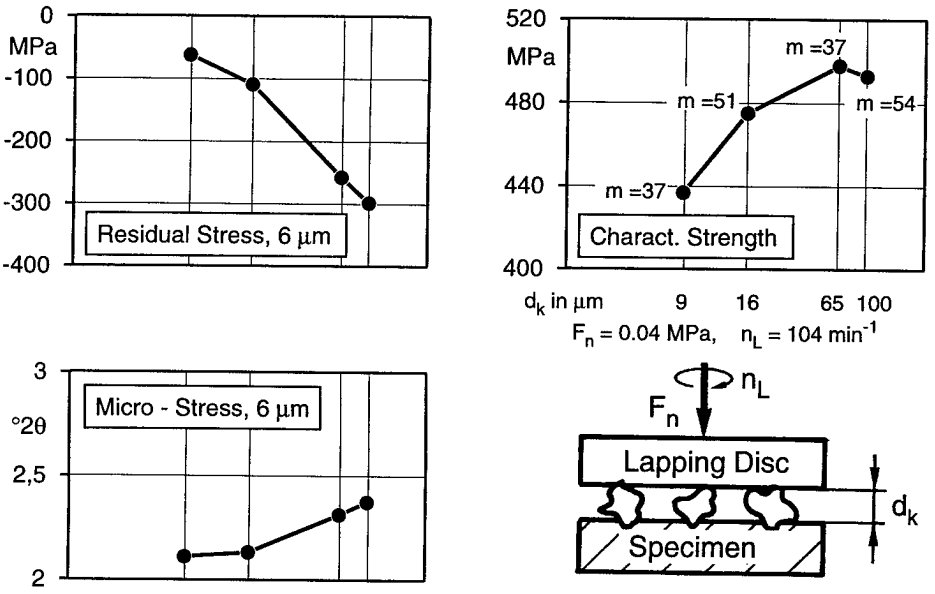


Figure 11: Lapping of partially stabilized zirconia, using large grain sizes, leads to transformation-induced high compressive residual stresses which increase the strength [23]

Grinding or lapping of structural ceramics Processes as grinding or lapping of structural ceramics strongly influence the service behavior of manufactured products since they cause macro and micro surface and subsurface damage accompanied by residual stresses. Therefore, the complex correlation between machining parameters and strength controlling damage and residual stresses of alumina, silicon nitride and zirconia has been investigated using advanced x-ray diffraction techniques, strength tests and fracture mechanics methods [23, 24]. The bending strength has been measured using the concentric ring test which provides a symmetry of the applied stresses. The x-ray diffraction techniques allow to determine the decay in depth direction of the residual stresses acting parallel to the surface as well as the micro strains due to machining induced dislocations. The amount of this machining induced damage can be substituted by a hypothetical flaw size model. This *effective* flaw size does not describe the real situation, but may be taken as a parameter characterizing the damage. Accordingly an *effective* stress intensity factor K_e can be calculated when assuming that the external bending and internal residual stress field is acting on this hypothetical crack. Surprisingly the simple balance between the fracture resistance K_{Ic} - determined independently by other means - and the effective stress intensity factor K_e provides a helpful method for assessing the optimization procedure. As a result figure 11 demonstrates that the characteristic strength may increase although a larger grain sized_k has been chosen for the lapping process. Since the compressive residual stresses dominate the micro damage developing with increasing grain size these findings can be explained quantitatively.

Numerical simulation of dry press and sintering processes. Theoretical and experimental investigations have been carried out in order to optimize forming processes by numerical simulation. For this purpose constitutive material laws have been developed and implemented in FEM codes [25]. Since the details of this work are too far from the scope of this paper the reference shall only be cited.

Turning of glasses and silicon Whereas the foregoing example shows that the machining processes as grinding or lapping of structural ceramics are dominated by brittle material behavior the following example shall demonstrate that under defined circumstances turning processes of glasses and silicon can be realized when the local depth of cut can be reduced to a few tenth of a micrometer [26]. From careful investigations result that the essential effects which control the quality of the diamond turned surfaces are: thermally induced local changes of the physical properties, residual stresses and microcrack systems of different origin. The changes of quality achieved by turning a glass surface with a diamond tool can be interpreted from the microinterferographs in figure 12. The depth of cut lies between 0.11 µm < D < 1.1 µm per revolution.

Characterisation of surface layers by indentation processes

The properties of surface layers are of great significance for the reliability and for the life time of products. For practical application the characterization of the surface quality achieved is very often restricted to the use of purpose-oriented testing methods as the indentation test or the scratch test or even simpler methods which provide some properties easily to be measured, but hardly to be correlated to the properties of practical interest, i.e. for instance whether the surface layer is sustainable against wear or corrosion . The reason for that is obvious: the situation of technical relevance is usually determined by a variation of a whole bunch of interacting parameters whereas the test situation describes a simplified state nevertheless also caused by a complicated field of parameters. In

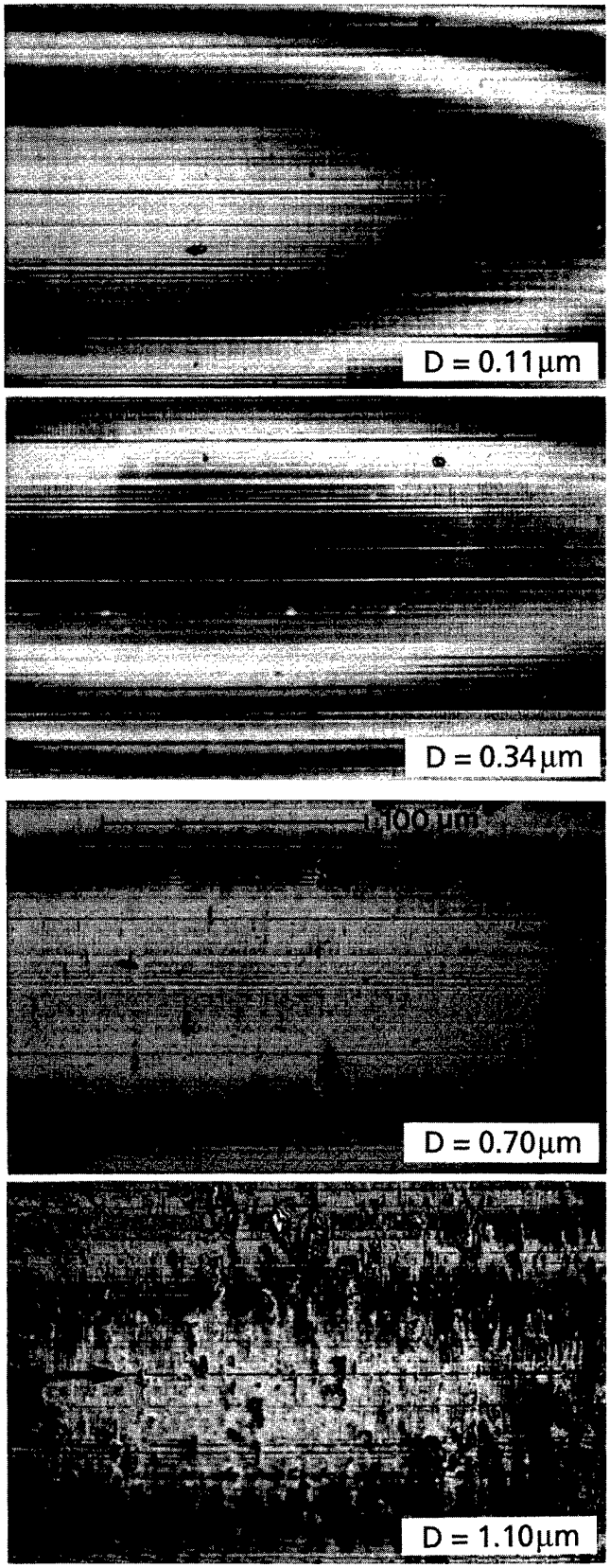


Figure 12: Microinterferographs ($\lambda/2$ = 270 nm) of radial plunge cuts produced under dry conditions at a cutting speed of 10 m/s with different depth of cut D in the glass 900403 [26]

addition some features of these contact problems have a similarity to certain basic principles of machining processes. As a consequence there seems to be a need for a better understanding of these parameter interactions. Therefore, a simplified system as the indentation of a sphere under normal and shear forces has been numerically analyzed and compared with experimental findings [27, 28]. Only one example selected from these results shall demonstrate the effectiveness of this numerical simulation procedure: a sphere (radius = 15 µm) under normal force contacts a surface layer with linear elastic behavior (TiAlN of 1 µm thickness) on a steel substrate simulated by a bilinear material law and is displaced by a tangential force in a quasistatic manner in order to suppress time- and temperature-dependence. In figure 13 the resulting distribution of the maximum principle stresses in the surface layer is plotted. Whereas the contact area (dotted) remains the same the influence of the friction parameter μ_r causes pronounced differences in the stress distribution. When the friction coefficient $\mu_r = 0.2$ the maximum of the stress distribution is shifted from the position in front of the sphere to the side. Sensitivity studies of this kind are not only helpful for the interpretation of accompanying experimental investigations, but also provide information on the dominance of the acting parameters.

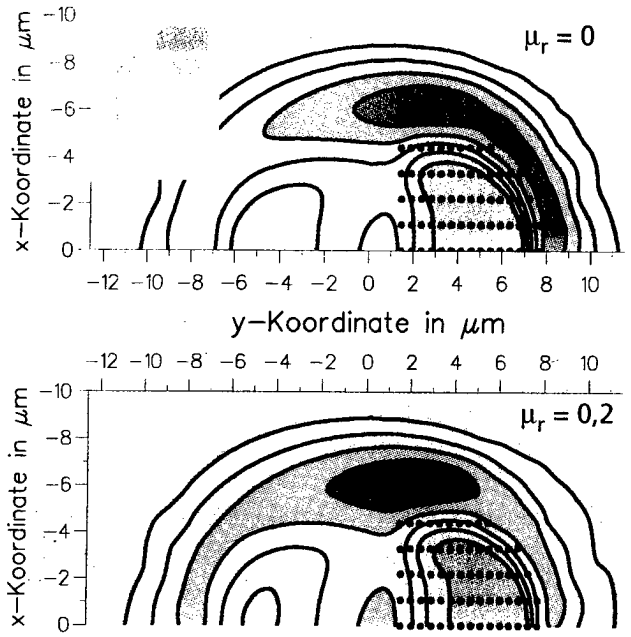


Figure 13: Comparison of the distribution of the maximum principle stresses resulting in a surface layer from the contact of a sphere under superimposed normal and tangential forces without and with friction (lower figure: $\mu_r = 0.2$)

Concluding remarks

The aim of this publication is to visualize the enormous impact of G.R. Irwin's basic investigations to the field of applied technical science, to thank this great scientist for many fruitful and stimulating discussions and to congratulate him to his ninetieth birthday.

Literature

1. G.R. Irwin, J.E. Srawley, "Progress in the development of crack toughness fracture tests", Materialprüfung, 4 (1962), 1-11.

2. G.R. Irwin, "Analysis of Stresses and Strains Near the End of a Crack Traversing a Plate" Journal of Applied Mechanics, 24 (1957), 531-590.

3. J.R. Irwin, "Fracture", in Encyclopedia of Physics, S. Flügge, ed., vol. VI, (Springer-Verlag, 1958), 551.

4. A. Kochendörfer, "Current ideas on the mechanism of brittle and ductile fracture metals", Materialprüfung, 3 (1961), 266-274.

5. H. Rumpf, "Theory of fracture, its problems and recent results", Materialprüfung, 3 (1961), 253-265.

6. F. Kerkhof, "Untersuchungen von Bruchvorgängen mit Hilfe von Ultraschall", Materialprüfung, 3 (1961), 376-382.

7. G.R. Irwin, "Moisture, Assisted Slow Crack Extension in Glass Plates", NRL Memorandum Report, 1965, 1678.

8. Frank Kerkhof, Bruchvorgänge in Gläsern (Deutsche Glastechnische Gesellschaft, 1970), 1-250.

9. E. Sommer, "Formation of Fracture *Lances* in Glass", Engng. Fracture Mech., 1 (1969), 539-546.

10. J.G. Blauel, J.F. Kalthoff, D. Stahn, "Model Experiments for Thermal Shock Fracture Behavior", J. Engineering Materials and Technology, ASME Ser. H 96 (4) (1974), 299-308.

11. J.G. Blauel et al., "Effect of Cladding on the Initiation Behavior of Finite Length Cracks in a RPV", to be published in Nucl. Eng. & Design (1997).

12. G.R. Irwin, "Crack Extension Force of a Part-Through Crack in a Plate", J. Applied Mechanics, Trans. ASME Series E, 29 (1962), 651-654.

13. Erwin Sommer, Bruchmechanische Bewertung von Oberflächenrissen (Berlin-Heidelberg-New York: Springer-Verlag, 1984).

14. H. Kordisch, E. Sommer, and W. Schmitt, "The Influence of Triaxiality on Stable Crack Growth", Proc. of 13th MPA-Seminar, Stuttgart, (1987), 7.1-7.17.

15. E. Sommer, D. Aurich, "On the Effect of Constraint on Ductile Fracture", Proc. Europ. Symposium on Elastic-Plastic Fracture Mechanics: Elements of Defect Assessment, Freiburg, Germany, 1989.

16. H. Clausmeyer, "Über die Beanspruchung von Stahl bei mehrachsigen Spannungszuständen", Konstruktion 20 (1968), 395-401.

17. W. Brocks et al., "Experimental and numerical investigations of stable crack growth of axial surface flaws in a pressure vessel", Pressure Vessel Technology, Proc. 6th Int. Conf. (Liu Chengidan & R.W. Nichols, eds.), Vol. 2, Oxford/New York/Beijing/Frankfurt/ Sao Paulo/Sydney/Tokyo/Toronto: Pergamon Press, (1988), 807-817.

18. J. G. Blauel, "Thermisch induzierte elastische Spannungen und ihr Einfluß auf Auslösung und Ausbreitung von Brüchen" (Dissertation, Universität Karlsruhe, Fakultät für Chemieingenieurwesen, 1970).

19. D. Stahn, "Zur Nutzung des Bruchvorganges beim Trennen von Glas", 13. Sitzung des AK Bruchvorgänge, (DVM, Hannover, 1981), 125-133.

20. M. Schinker, J. Brormann, D. Stahn, W. Döll, G. Kleer, P. Manns, "Molds for Manufacturing Molded Glass-Articles for Precision-optical Purposes", US-Patent: 5,028,251, Date of Patent: July 2, 1991.

21. D. Stahn, M. Jüngling, W. Döll, "Verfahren zum Zerteilen von quaderförmigen Blöcken aus Glas", Deutsches Patent: 28 12 304, Date of Patent: May 21st 1981.

22. G. Kleer, et al., "Entwicklung von keramischen Multilayerschichten für Werkzeuge zum Heißformen optischer Gläser", BMFT Verbund Projekt 03 M 3039, 1994.

23. W. Pfeiffer, "Influence of Machining-Induced Residual Stresses on the Strength of Ceramics", Proc. of 9th Int. Conf. Exper. Mechanics, Copenhagen, (1990), 1237-1245.

24. W. Pfeiffer, Th. Hollstein, E. Sommer, "Strength Properties of Surface-Machined Components of Structural Ceramics", ASTM STP 1220, Fracture Mechanics: Vol.25 (F. Erdogan, ed.), 1995.

25. H. Zipse and H. Riedel, "The Mechanical Behavior of Sintering Powder Compacts", in: Ceramic Tansactions, Vol. 51, Processing and Technoloy, (H. Hausner, G.L. Messing and S.-I. Hirano, eds.,) American Ceramic Society, Westervill, OH, 1995, 489-493.

26. M. Schinker, "Subsurface Damage Mechanisms at High-Speed Ductile Machining of Optical Glasse", Precision Eng. 3, (3) (1991), 208-218.

27 M. Schulze "Untersuchungen zur Charakterisierung mechanischer Eigenschaften von Schichten" (Dissertation, Universität Freiburg, 1996).

28 E. Sommer, "Modellierung und Simulation von Kontaktbeanspruchungen", Reibung und Verschleiß, (Paper presented at DGM-Symposium Bad Nauheim, 21.-23.03.1996).

BRITTLE CLEAVAGE FRACTURE: AN OVERVIEW OF SOME HISTORICAL ASPECTS

Paul C. Paris

Washington University
Department of Mechanical Engineering
St. Louis, MO 63130

Abstract

Many aspects of cleavage fracture were not well understood by the mid-1950s when George R. Irwin coined the term "Fracture Mechanics." This discussion will attempt to relate some of the common concepts and misconceptions of that period. The leadership of Dr. Irwin in developing new concepts and methods for clarifying the understanding of "brittle fracture" will be emphasized here. An essential part of the progress made was to bring together the Engineering Mechanics, Metallurgy, and Physics of the subject into a reasoned balance in trying to further understand the nature of the phenomena. This is illustrated by recalling some of the "personalities" of that time period and their concepts and claims and how they interacted to make progress toward today's state of knowledge. Indeed today's closer ties between fields such as mechanics and metallurgy were in part caused by these requirements of analysis of "BRITTLE CLEAVAGE FRACTURE." We should all be thankful that Irwin was around to bring us together!

George R. Irwin Symposium on Cleavage Fracture
Edited by Kwai S. Chan
The Minerals, Metals & Materials Society, 1997

FRACTURE MECHANICS

MICROSTRUCTURAL MECHANICS DESCRIPTION OF CLEAVAGE FRACTURING IN POLYCRYSTALS

R.W. Armstrong, G.R. Irwin and X.J. Zhang

Department of Mechanical Engineering
University of Maryland
College Park, MD 20742-3035

Abstract

Grain size and particle size/distribution influences are considered in relation to the ductile-brittle transition and cleavage fracture toughness properties of steel materials. Stereosection fractographic observations have revealed the spread of cleavage from single particle fractures and, more recently, from local hole-joining failures at particle clumps where rapid load transfer is reasoned to produce the necessary stress elevations for transition from ductile fracturing to cleavage.

The ductile-brittle transition

An early method of analysis for accounting for the ductile-brittle transition temperature measured in Charpy v-notch (CVN) impact tests was based on the equation:

$$\alpha\ \sigma_y \left\{ T,\ \dot{\epsilon} \right\} = \sigma_c \qquad (1)$$

where α is a numerical factor to account for the triaxial stress state in the notch, σ_y is the yield stress at the temperature and strain rate appropriate to the Charpy test, and σ_c is the essentially athermal cleavage fracture stress for ferrite (1).

The analysis was initially used to describe the increase in transition temperature produced by an increase in polycrystal grain size or increase in neutron irradiation embrittlement (2).

Figure 1 shows later application of the analysis (3) to experimental yield stress, cleavage stress and CVN ductile-brittle transition temperature measurements reported for a 0.15 carbon mild steel at two grain sizes (4). In this case, very complete measurements had been made of all the quantities needed to verify the applicability of equation (1). In the figure, the cleavage stress and CVN measurements are connected by a computed band of temperature and strain rate dependent yield stress values obtained from a dislocation mechanics based constitutive equation description (5) applied to reference laboratory test measurements. The prediction of the higher CVN transition temperature for the larger grain size material, specified near to the "foot" of the rise in CVN energy absorption values, is reasonably close to the experimental measurement. The significantly lower transition temperature predicted for the smaller grain size material falls below the experimental measurement. The problem was traced to a role for carbide cracking in determining the cleavage fracture stress.

Two features of Figure 1 provide evidence for enhanced cracking of carbides to be involved in determining a somewhat raised transition temperature for the smaller grain

George R. Irwin Symposium on Cleavage Fracture
Edited by Kwai S. Chan
The Minerals, Metals & Materials Society, 1997

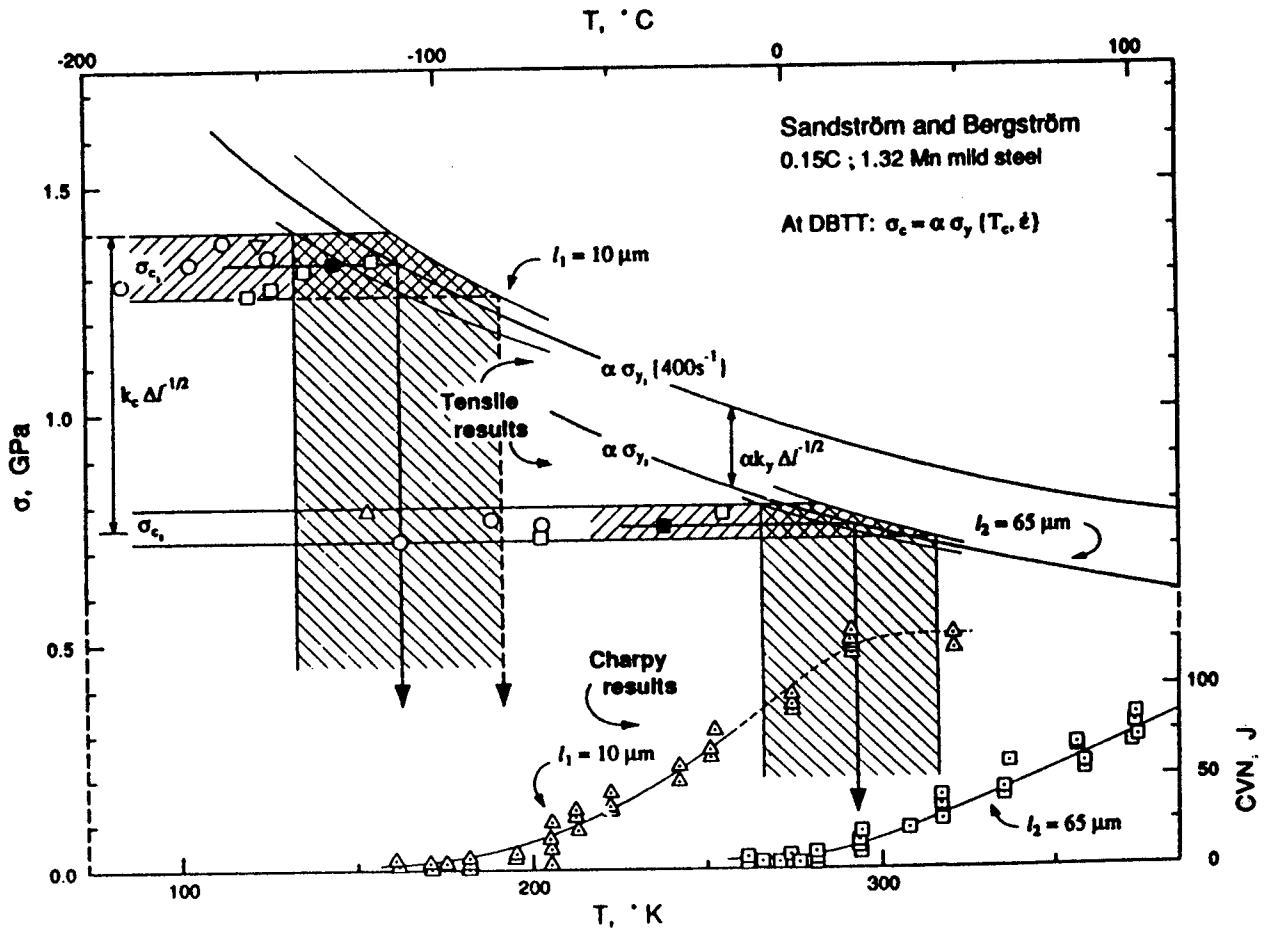


Figure 1 - Description of grain size dependent connections between reported yield stress, cleavage stress and Charpy v-notch ductile-brittle transition measurements.

size material. First, a wider band of cleavage stress measurements is shown to occur for the smaller grain size material in contradiction to the expectation of more sharply defined ferrite cleavage to occur on a temperature dependence of yield stress basis. Secondly, the mean value of the cleavage stress at small grain size falls below the Hall-Petch prediction of a linear increase in cleavage stress with increase in reciprocal square root of average grain diameter. To demonstrate the influence of carbide assisted cleavage fracturing of ferrite, a combined analysis of grain diameter, ℓ, and grain boundary carbide thickness, t, influences on the ductile-brittle transition temperature (6) was employed to derive a carbide-affected microscopic cleavage fracture stress in the form (7):

$$\sigma_c = k_c \, t^{-1/2} \left\{ f \, [k_y \, , \, k_c \, , \, \ell, \, t] \right\} \qquad (2)$$

where

$$k_c = [\, 8 \; G \; \gamma_p \; / \; (1-\nu)]^{1/2} \qquad (3)$$

and, k_c is the stress intensity for carbide cracking, k_y is the microstructural stress intensity for yielding of ferrite, G is the shear modulus, γ_p is the effective surface energy for carbide cracking and ν is Poisson's ratio. Figure 2 shows combined results for the t and ℓ dependencies of the modified cleavage fracture stress obtained by employing γ_p values consistent with a range of experimental measurements (7).

Figure 3 shows a modern application of the ductile-brittle transition analysis, based on equation (1), for conventional yield stress, cleavage stress and CVN measurements reported for HY 130 steel weld metal (8). The innocuous temperature

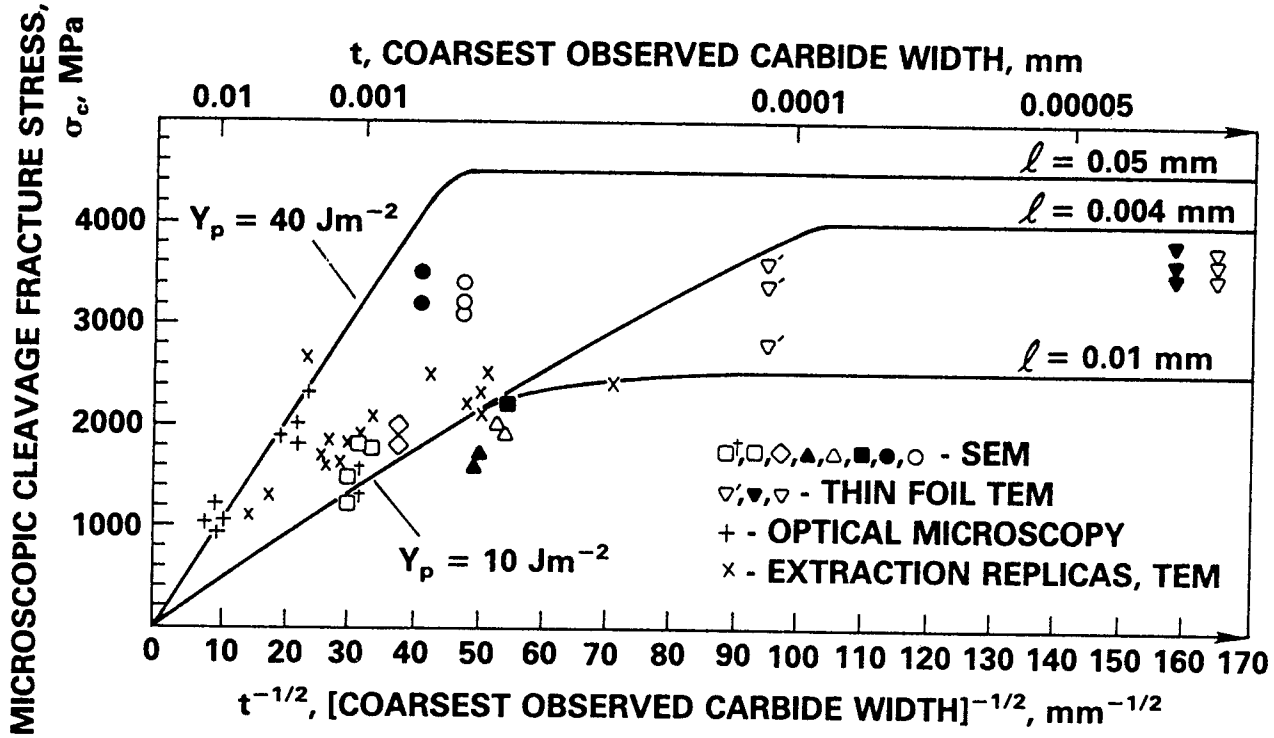


Figure 2 - Microscopic cleavage fracture stress dependence on reciprocal square root of carbide plate thickness or width, adapted from measurements for a variety of steel microstructures and compared with computed dependencies for different grain diameters.

dependence of the conventional yield stress measurements was transformed for the Charpy test representation by employing the same triaxiality factor and strain rate consideration used in Figure 1. In this case, the low temperature cleavage stress measurements were determined by bend testing at low strain rate, hence, the increase in cleavage stress at the higher temperatures was attributed to pre-cleavage plastic flow that eventually prevented cleavage from occurring at even higher temperatures.

The transition to cleavage from ductile fracturing

An approach to the ductile-brittle transition from ductile fracturing at higher temperatures applies at the upper shelf energy of CVN measurements and is associated with the earliest occurrence of isolated cleavage regions (ICRs) amid surrounding areas of ductile fracturing by hole-joining mechanisms. Figure 4 shows an ICR initiated by brittle fracturing of a single inclusion particle within a pressure vessel weld metal material (9). Cleavage was initiated in the ferrite adjacent to the broken particle and encircled the particle to produce the final prominent tear lip left by the progressive growth of cleavage, then, past the particle. The significant undercutting at such tear lips was taken to be indicative of appreciable local plastic work being associated with breakaway from the particle of the cleavage crack that nevertheless was stopped by difficulties of forward cleavage growth in making grain to grain transitions.

A similar frequency of ICRs were associated with debonded silicate particle clumps in the pressure vessel steel weld metal. For A508 and A533B Cl.1 heavy section nuclear vessel steels, no individual particle fractures but rather separated carbide particle clumps were observed to produce ICRs (10). Figure 5 shows one example of many observations made with the method of stereosection fractography (11) to pinpoint the particle clump origins of ICRs. Such observations led to the consideration that local strain rate enhancement was produced at such debonding events sufficient to force a rigid cleavage response in the adjacent ferrite matrix.

Figure 6 illustrates the model considerations derived from the ICR observations and leading to a sequence of events to explain the "rare event" nature of the ductile fracturing to cleavage transition (12). There are appearance features of first initiations at locally separated particle clumps, then lateral spreading of such initiations, followed by forward growth of cleavage. Local stress elevation, assisted by

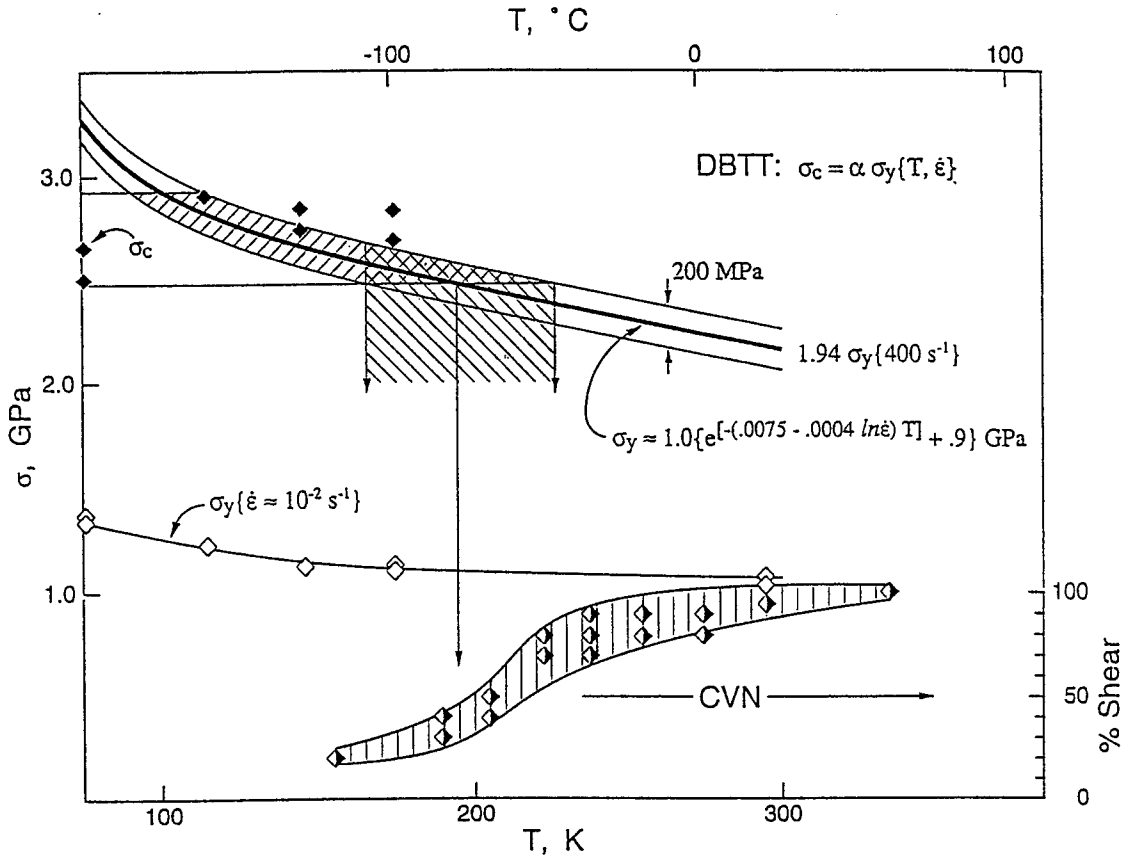


Figure 3 - Ductile-brittle transition analysis for HY-130 steel weld metal, involving [filled diamond point] cleavage stress measurements obtained in bend tests, [open diamond point] yield stress measurements employed to calculate the indicated temperature dependence of yield stress in the Charpy v-notch (CVN) test for which the [half-filled diamond points] show the ductile brittle transition on a percentage of shear basis.

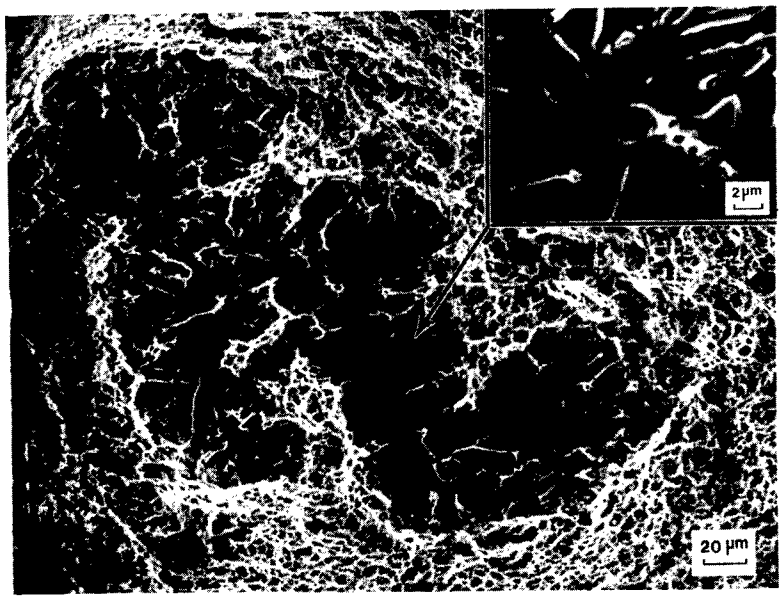


Figure 4 - An isolated cleavage region (ICR) initiated at a fractured inclusion particle and surrounded by hole-joining fracture within a nuclear pressure vessel steel weld metal.

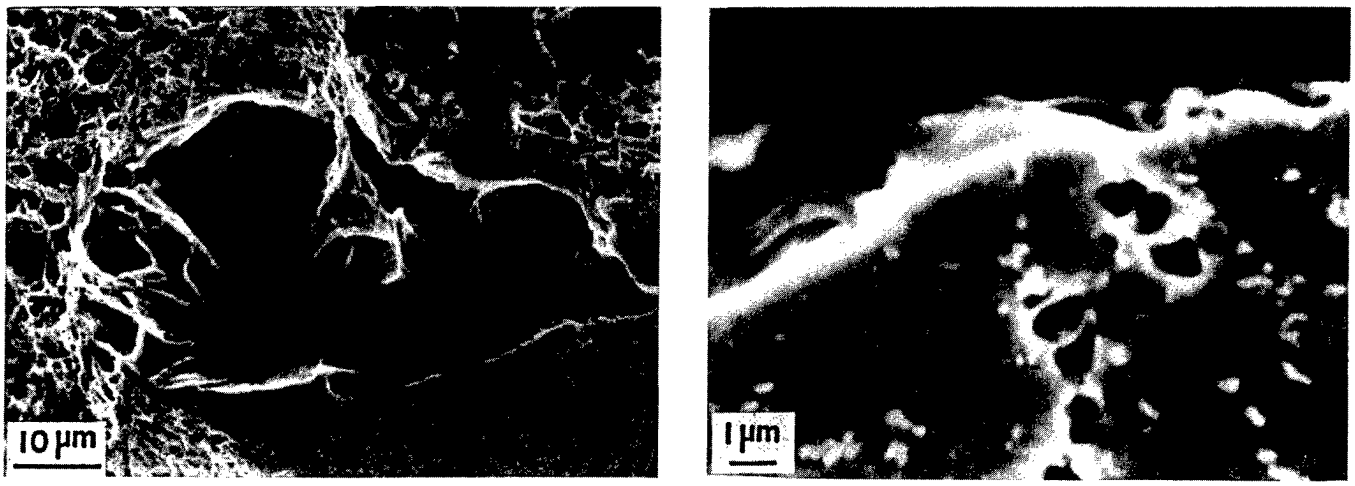


Figure 5 - Stereo (scanning electron microscopy) section fractography of an isolated cleavage region (ICR), also shown at higher magnification of the indicated region to have been initiated adjacent to a zone of local separations centered on a clump of small particles.

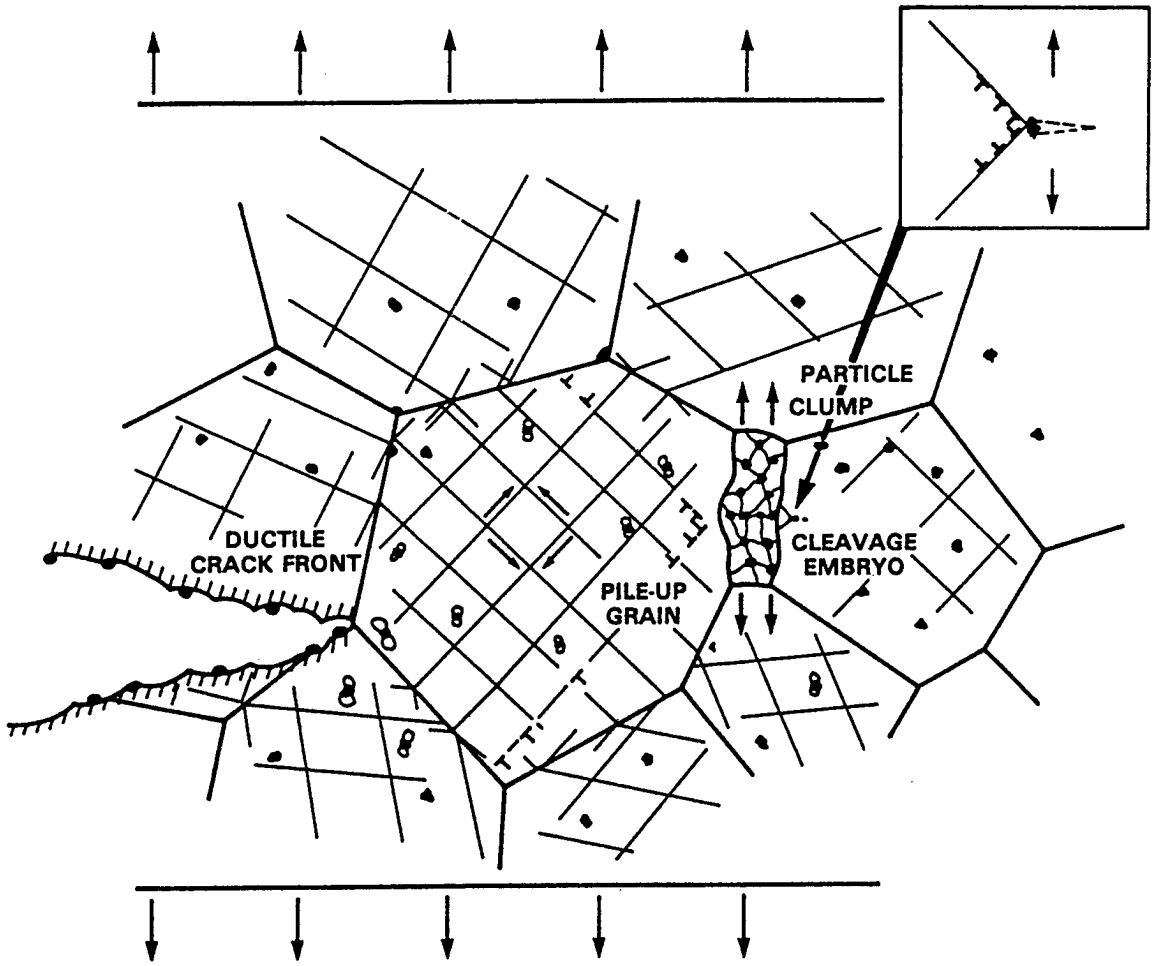


Figure 6 - Dislocation mechanics model for cleavage initiation at a ductile fracturing crack front involving rapid load transfer from local hole- joining failures localized at a particle clump.

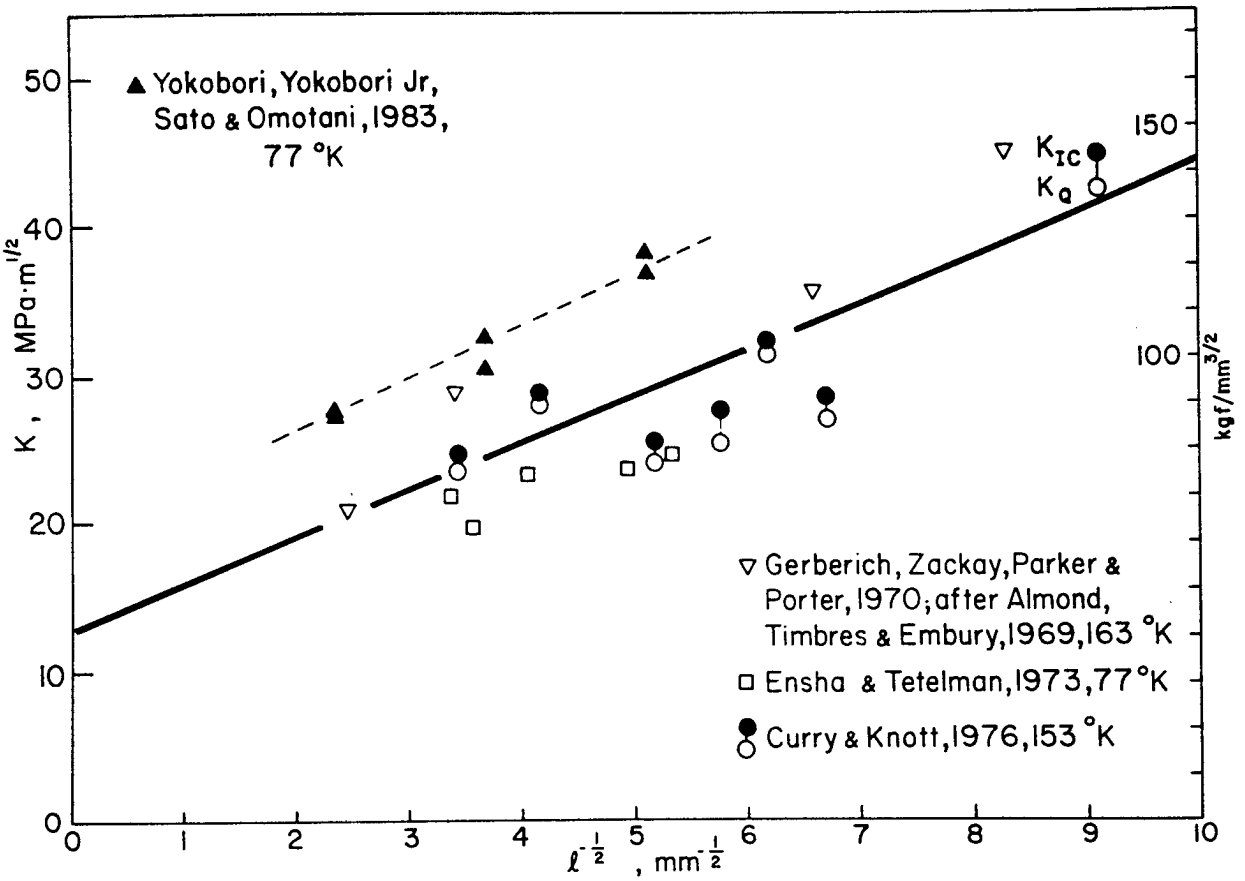


Figure 7 - Description of experimental results on a proposed Hall-Petch basis for the grain size dependence of the cleavage fracture stress intensity.

dislocation pile-ups, occurs at the particle clumps that themselves are not rare. When external loading is not rapid, local region stress elevation occurring at the unstable growth of particle separations is relatively more important in leading to initiation of cleavage. The particle clumps are associated with cleavage at higher external loading rates, as well, but then the scatter of fracture toughness measurements is reduced.

The dislocation pile-up role in causing particle fracturing produces an inverse fourth root of particle size dependence in accordance with the equations:

$$\sigma = \sigma_o + m\,[\pi\, G\, b\, /\, (2\, a\, \ell)]^{1/2}\, \sigma^{*1/2} \qquad (4)$$

where, now

$$\sigma^* = [8\, G\, \gamma_p\, /\, (1-\nu)\, t]^{1/2}\,, \qquad (5)$$

relating to equations (2) and (3), and σ_o is the Hall-Petch friction stress, m is an orientation factor, and a is 1.0 or (1-ν) for the dislocation character. There appears to be evidence for this type of particle dependence in weld metal fracturing results.

Microstructural aspects of toughness measurements

Both for the lower temperature entrance to the ductile-brittle transition and the higher temperature for transition of ductile fracturing to cleavage, an increase in yield stress of the material might be thought normally to promote cleavage --- but this is not the case on a variation of grain size basis! Grain size refinement, as shown in Figure 1, increases the yield strength of steel materials and lowers their ductile-brittle transition. The same influence is demonstrated in Figure 7 from the compilation of reported measurements for the fracture mechanics stress intensity in steels of various grain sizes (13). An explanation was given for the observation on the basis of the stress intensity, K, being expressed as

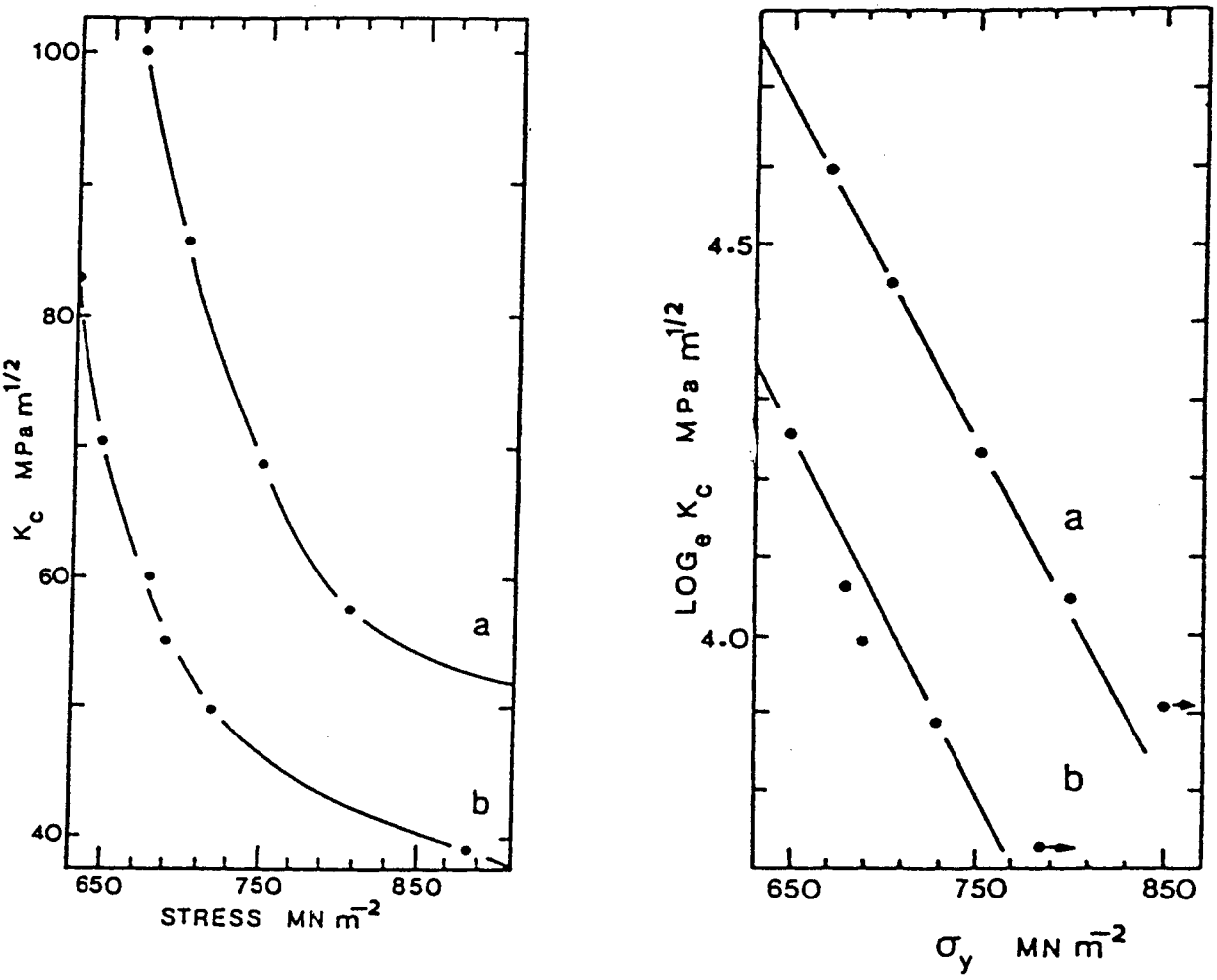


Figure 8 - A logarithmic dependence of cleavage stress intensity on yield stress for measurements obtained over a range of temperatures: (a) quenched and tempered alloy steel; and, (b) spheroidized steel.

$$K = C\, s^{1/2}[\sigma_o + k\, \ell^{-1/2}] \qquad (6)$$

where C is a numerical constant, s is a measure of the plastic zone size, and the terms in brackets are from the Hall-Petch relation for cleavage fracturing. Refinement of grain size raises the fracture stress even more than the yield stress and so the fracture toughness is increased. The result appears to carry over to the interpretation of ductile fracture toughness measurements (14).

Other methods of raising the yield stress than refining the grain size produce an opposite reduction in the material fracture toughness (15). The result can be understood from considering that in a fracture mechanics test, yielding starts at the crack tip and the material then strain hardens in the plastic zone until unstable cleavage is initiated. Consequently, increases in yield stress that leave the fracture stress unaltered, for example, as is the first order influence of neutron irradiation damage (1,2) produce a decrease in fracture toughness. A decrease in temperature or increase in strain rate accomplishes a similar response of decreasing the fracture toughness. An analysis of these other influences leads to a decrease of the logarithm of the fracture mechanics stress intensity with increase in yield stress, that is

$$\ln K = \ln K_o - \sigma_y / (2\, n\, A) \qquad (7)$$

where the product of n and A, from a power law expression for the material stress-strain relation, provides a simple

measure of the material strain hardening behavior that is essentially athermal for a wide range of steel microstructures. Figure 8 illustrates application of the analysis to matching K and σ_y results reported at different temperatures for (a) a quenched and tempered steel and (b) a spheroidized steel (15). In each case, the decrease in K (at lower temperature) is largely accounted for by an increase in the σ_o component of σ_y.

Acknowledgments

Support for this research was provided by the U.S. Office of Naval Research, Materials Science and Technology Division, and by the U.S. Nuclear Regulatory Commission, Heavy Section Steel Technology Program. Ms. Thelma Miller is thanked for assistance with this work.

References

1. R.W. Armstrong, "On Determining the Ductile-Brittle Transition Temperature", Philosophical Magazine, 9 (1964), 1063-1067; "Stress-Grain Size Analysis of the Brittle Fracture Transition of Steel," Brown University Report, ARPA E38 (February 1967).

2. R.W. Armstrong, "The Influence of Polycrystal Grain Size on Several Mechanical Properties of Materials," Metallurgical Transactions, 1 (1970), 1169-1176.

3. R.W. Armstrong, V. Ramachandran and F.J. Zerilli, "Dislocation Mechanics Description of Dynamic Plasticity and Fracturing Properties," Advances in Materials and Their Applications, ed. P. Rama Rao (New Delhi, India: Wiley Eastern, 1993), 201-229.

4. R. Sandström and Y. Bergström, "Relationship Between Charpy V Transition Temperature in Mild Steel and Various Material Parameters," Metal Science, 18 (1984) 177-185.

5. F.J. Zerilli and R.W. Armstrong, "Dislocation Mechanics Based Constitutive Relations for Material Dynamics Calculations," Journal of Applied Physics, 61 (1987) 1816-1825.

6. N.J. Petch, "The Influence of Grain Boundary Carbide and Grain Size on the Cleavage Strength and Impact Transition Temperature of Steel," Acta Metallurgica, 34 (1986) 1387-1394.

7. R.W. Armstrong, L. Roberson Link and G.R. Speich, "Analysis of Ductile-Brittle Transition Temperatures for Controlled-Rolled, Microalloyed, C-Mn Based Steels," Processing, Microstructure and Properties of HSLA Steels, ed. A.J. DeArdo (Warrendale, PA: The Metallurgical Society, 1988) 305-315.

8. R.W. Armstrong, F.J. Zerilli, W.H. Holt, and W. Mock, Jr., "Dislocation Mechanics Based Constitutive Relations for Plastic Flow and Strength of HY Steels," High Pressure Science and Technology - 1993, ed. S.C Schmidt, J.W. Shaner, G.A. Samara and M. Ross (New York: American Institute of Physics, 1993) AIP Conference Proceedings 309, Part 2, 1001-1004.

9. X.J. Zhang, R.W. Armstrong and G.R. Irwin, "Cleavage Fracturing Stages at Micrometer-Size Inclusions in Pressure Vessel Steel Weld Metal," Journal of Materials Science Letters, 5 (1986), 961-964.

10. G.R. Irwin, X.J. Zhang and R.W. Armstrong, "Isolated Cleavage Regions in the Ductile Fracturing Transition of Nuclear Vessel Steels and their Weld Metals," Journal of Materials Science Letters, 8 (1989), 844-848.

11. X.J. Zhang, R.W. Armstrong and G.R. Irwin, "Stereo (Scanning Electron Microscope) Section Fractography of Isolated Cleavage Regions in Nuclear Vessel Steels," Metallurgical Transactions, 20A (1989), 2862-2866.

12. J.P. Gudas, G.R. Irwin, R.W. Armstrong and X.J. Zhang, "A Model for Transition Fracture of Low Carbon Steel from Observations of Isolated Cleavage Regions," Defect Assessment in Components - Fundamentals and Applications, ed. J.G. Blauel and K.-H. Schwalbe (London: Mechanical Engineering Publishers, 1991) ESIS/EGF Publication 9, 549-568.

13. R.W. Armstrong, "The (Cleavage) Strength of Pre-Cracked Polycrystals," Engineering Fracture Mechanics, 28 (1987) 529-538.

14. M. Srinivas, G. Malakondaiah, R.W. Armstrong and P. Rama Rao, "Ductile Fracture Toughness of Polycrystalline Armco Iron of Varying Grain Size," Acta Metallurgica et Materialia, 39 (1991), 807-816.

15. N.J. Petch and R.W. Armstrong, "Work Hardening in Cleavage Fracture Toughness," Acta Metallurgica, 37 (1989) 2279-2285.

INTERPRETATION OF RIVER LINE STEPS ASSOCIATED WITH THE GROWTH OF CRACKS

Derek Hull*

Department of Materials Science and Engineering
University of Liverpool
Liverpool, U.K.

Abstract

The development of river line steps on fracture surfaces is common to cleavage in crystalline solids and to the fracture of amorphous and semi-crystalline solids. A brief review is given of the development of ideas about river lines, with particular reference to work on crystalline cleavage and the interpretation of river line patterns in terms of the intersection of cracks with arrays of screw dislocations. Topographical studies on fracture surfaces are described which provide a more general understanding of the origin and development of river line steps. It is shown, following Sommer [Eng. Fract. Mech., 1 (1969), 539-546], that river line patterns are a consequence of local mixed mode I/III conditions and the geometrical constraints associated with the 'no twist' condition [Hull, Int. J. Fract., 62 (1993), 119-138]. These ideas are extended to the interpretation of crack propagation under dynamic conditions and, in particular, to the influence of dynamic stress intensity and crack velocity on fracture surface topography.

1. Introduction

River patterns, or river line patterns, are the most characteristic feature of the fracture surfaces of brittle materials. Similar patterns occur on the fracture surfaces of semi-brittle materials. The river pattern shown in Fig. 1 was produced by a crack, growing in the direction of the arrow. Initially, it grew in mode I with a very small mode III component. At the boundary marked by X-Y the mode III component increased. There is an abundance of topographical detail in this image which provides information on the way that the crack propagated. Some of these details are considered in this paper.

River patterns are characterised by three main features which are illustrated in schematic form in Fig. 2. First, they consist of a series of steps on the fracture surface aligned in the general direction of crack propagation. Second, all the steps are of the same sign. Third, they form or nucleate as a series of closely-spaced steps which merge progressively to form larger steps.

The appearance of the steps is strongly dependent on material characteristics but the underlying pattern, as illustrated, applies to all materials. The shape of the steps and the surfaces between the steps in Fig. 2 illustrate only the difference in height of adjacent surfaces and not the detailed geometry. The scale of the patterns is also strongly dependent on the material. When the microstructural dimensions approach the spacing of the river line steps the pattern is no longer evident. In materials such as brittle, homogeneous, organic and inorganic glasses and single crystals, and individual grains in polycrystalline aggregates, the spacing of the steps may be less than $1\mu m$, with step heights approaching atomic dimensions. In materials with a coarse microstructure, such as rocks, the river line patterns only become evident on large scale fracture surfaces and the steps are widely spaced.

Since river lines are apparent on the fracture surfaces of both amorphous and crystalline solids and on complex aggregates it follows that the underlying origins derive from similar mechanisms even though there are many factors which distinguish river lines in different solids.

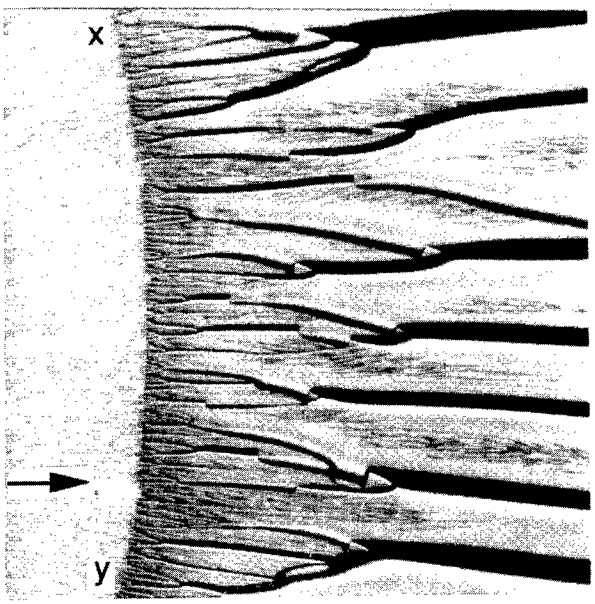


Figure 1: River patterns on the fracture surface of an epoxy resin tested in mixed mode I/III loading illustrating the nucleation, growth and coalescence of steps (river lines) parallel to the general direction of crack propagation. Photograph taken with transmitted light microscopy.

The term 'river pattern' was first used by Mrs C.F.Tipper[1] in 1948, in relation to the fracture surfaces of brittle steels, and then by Kies, Sullivan and Irwin[2] in 1950, who examined the fracture surfaces of a wide variety of materials and used the descriptive phrase 'level difference lines'. However, these characteristic patterns were undoubtedly observed on rock fractures thousands of years ago and they can be seen readily on almost every piece of fine-grained fractured rock. The expression is now accepted widely. It accurately represents the pattern associated with the confluence of streams into larger streams into rivers.

George R. Irwin Symposium on Cleavage Fracture
Edited by Kwai S. Chan
The Minerals, Metals & Materials Society, 1997

Branched patterns are observed in a wide range of natural phenomena such as in veins and arteries, trees and plants, static electrical discharges in lichtenberg figures, and crack patterns in explosive fractures. They provide a rich source of examples for fractal enthusiasts[3,4]. In natural rivers the water flows in the direction I (Fig. 2) as does the flow of blood in veins. In contrast, the flow of water in river deltas, the flow of blood flow in veins, the static discharge of electricity and the high speed expansion of bifurcating cracks produces patterns in direction II (Fig. 2). For river line steps on fracture surfaces the direction of crack growth is in direction I. It is this feature of river patterns which provides a simple method of determining the direction of crack growth, and hence the site of crack nucleation, from fractographic examinations.

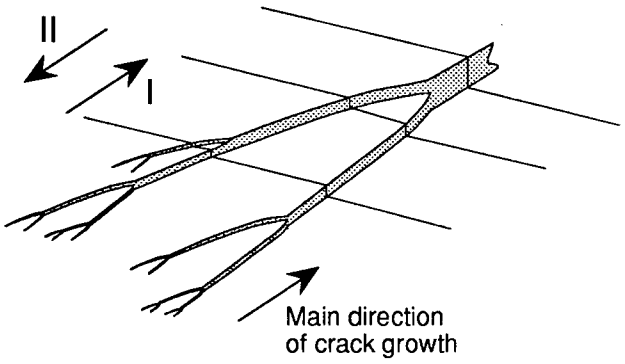


Figure 2: Schematic of river pattern showing sequence of steps, all of the same sign, merging to form larger steps.

Some of the early explanations of river patterns were based on observations of fracture surfaces of crystalline materials. This inevitable introduces microstructural factors but it provides a convenient starting point for explaining some of the basic features of the geometry of river lines. In the next section we review briefly the dislocation-based models. The importance of mixed mode I/III stress fields in generating river lines is best developed from Sommer's work on amorphous inorganic glass which is described in section 3 along with a consideration of the concept of nucleating river line steps. This leads to a consideration of the interaction of overlapping cracks and the influence of microstructure on the geometry of overlapping cracks which is treated in section 4.

The progressive development of river line patterns, when the mode III/I ratio is increasing, leads to progressive roughening of the fracture surface. It is important to distinguish between this type of roughening, which is associated with the inability of the crack to twist, and roughening arising from an increase in the stress intensity at the crack tip. We discuss the second type of roughening at the end of the paper. There are many features which are similar, particularly in relation to the effects of microstructure.

2. Dislocation models for river line formation in crystallographic cleavage

Tolansky[5], using multiple beam interferometry, demonstrated that atomically smooth surfaces, up to 1mm square, perfect to within 3nm, can be obtained by careful cleavage of mica. Such smoothness is not expected in most crystalline solids because they contain very high densities of dislocations. Gilman's[6] experimental observations of the formation of river line patterns in crystals of LiF, particularly when a cleavage crack crossed a low angle boundary with a twist component, demonstrated that river line steps are generated when cracks cross screw dislocations. This arises directly from the geometry of crystallographic (cleavage) planes around a screw dislocation as illustrated in Fig. 3. The orientation of the 'step difference line' is parallel to the local direction of crack growth and the height of the step is equal to the screw component of the Burgers vector of the dislocation normal to the cleavage plane.

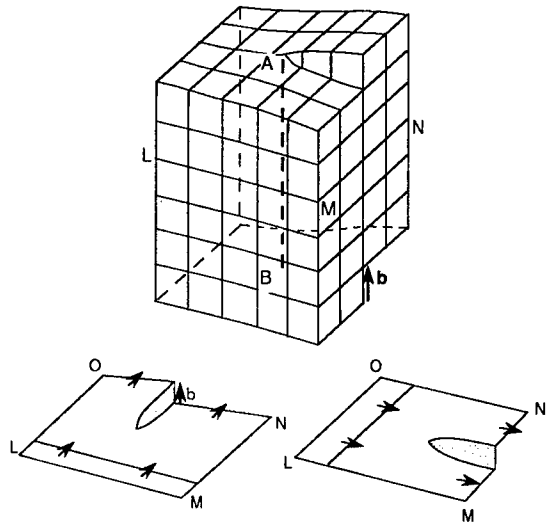


Figure 3: Formation of river line steps when a crystallographic cleavage crack crosses a screw dislocation. The direction of the step is parallel to the direction of crack propagation. For a crack growing from LM to NO the step is parallel to MN. Similarly, for a crack growing from LO to MN.

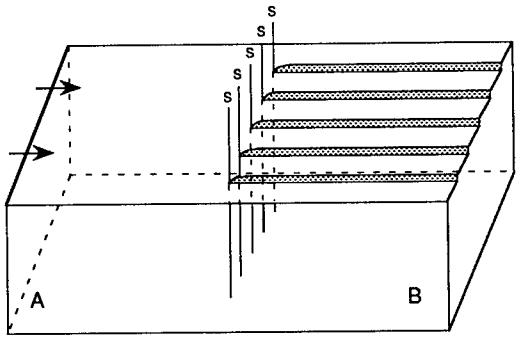


Figure 4: Schematic representation of the steps formed on a cleavage facet after it has crossed a low angle twist boundary, represented by a single array of parallel screw dislocations.

An array of parallel screw dislocations, of the same sign, in a low angle boundary produces a set of parallel steps (Fig. 4) and there is effectively a 'twist' of the cleavage plane as it crosses the boundary. The steps merge to form larger steps. A theoretical treatment of the movement of the crack front after intersection with an array of screw dislocations, leading to the formation of a river line pattern was given by Friedel[7]. Although the analysis is based on dislocation theory the general principles, which are described in this section, are applicable to the development of river line patterns in all solids, providing account is taken of scaling and microstructural issues.

Friedel modelled a crack as a piled-up group of climbing edge dislocations to demonstrate that the crack tip effectively possessing a line tension T. When a growing cleavage crack meets an array of screw dislocations it bows out between the dislocations. The critical condition for continued growth (for a crack growing slowly), is that T is balanced by the line tension generated by the step (Fig 5). Assuming that fracture at the steps involves only the formation of two new surfaces, and that the step has the simple geometry illustrated in Fig. 2, the dragging force of the step is $2\gamma h$, where γ is the energy per unit area of surface formed at the step and h is the height of the step. The crack fronts bow out to a radius R given by $F = 2T/R$, where F is the force driving the crack. The line tension T, of the crack front, acts parallel to the tip of the crack. For equally-spaced steps the crack bows out symmetrically about the steps and $\theta' = \theta''$ (see Fig. 5) and the condition for the whole of the crack front to move forward is

$$2\gamma h = 2T \sin \theta \qquad (1)$$

As the main crack front moves forward the individual segments of the crack front continue to bow out and the steps trail behind normal to the orientation of the main front to minimise the energy used in crack propagation (Fig. 5).

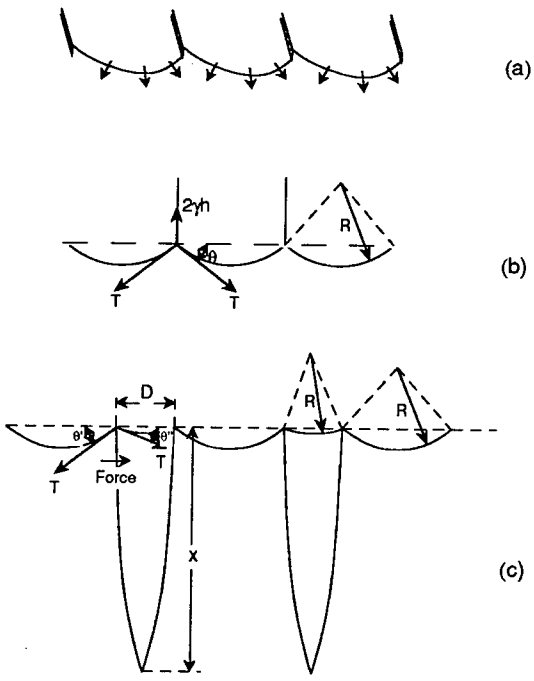


Figure 5: Illustration of Friedel's ideas for the formation of a river pattern. (a) Crack fronts bowing out between steps generated by a cleavage crack cutting screw dislocations. (b) Balanced forces acting at equally-spaced steps. (c) Steps merging to form the first stage of a river pattern as the crack expands between non-uniformly spaced cracks.

When the steps are not equally spaced (Fig 5c), or when any small perturbation in the spacing occurs, non-symmetric forces act at the step, $\theta' \neq \theta''$, so $T \sin \theta' \neq T \sin \theta''$. The non-symmetric forces cause the more closely-spaced steps to move towards each other as the crack propagates. The steps eventually merge to form a new step. If the height of the primary steps is 1b, and the steps are of the same sign, the new step height is 2b. Alternatively, if the primary steps are of opposite sign, merging of the steps results in their removal. As the steps grow, and move towards each other, the ratio θ'/θ'' increases so that the curvature of the steps towards each other increases; this determines the shape of the merging river lines[8]. The process then repeats itself and the result is a river pattern of steps. According to Friedel's model, the ratio $x/D = 5$ (Fig. 5c). A similar analysis can be used for the merging of multiple steps and on this basis one expects $x_1/D_1 = x_2/D_2 = x_3/D_3$ ..... as illustrated in Fig. 6. This geometry has the characteristics of a true fractal: a Cantor set.

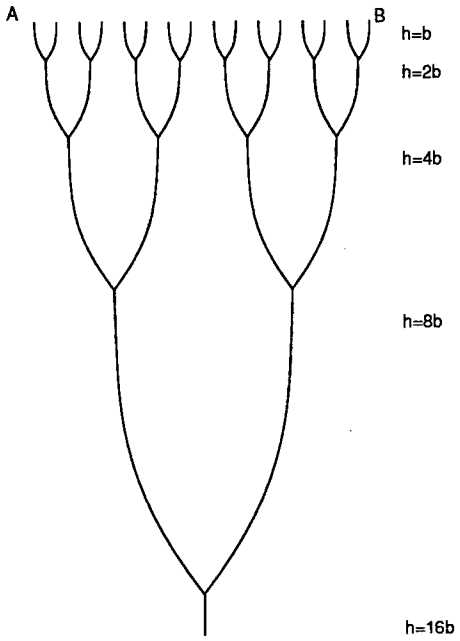


Figure 6: Ideal' river pattern formed by the progressive merging of an array of small steps all of the same sign.

Small steps (the smallest steps are about 0.2nm high) are not detected by light microscopy or SEM and so the earliest stages of coalescence of steps leave something for conjecture. The close similarity between the predicted patterns and experimental observations is clear evidence that this process occurs throughout a wide range of scales. For a low angle boundary in LiF, with a twist misorientation of 1°, the spacing of the primary steps produced by dislocations in the boundary is about 20nm. If we assume that the pattern repeats itself down to atomic dimensions, and that x/D is independent of scale, about seven coalescence sequences must have occurred before the steps are visible in light microscopy. For $x/D = 5$ these sequences occur over a distance of about 6μm which means that the position of the low angle boundary is 6μm from the position of the first visible river line steps.

River lines are observed on crystallographic cleavage fracture surfaces in the absence of low angle twist boundaries, see, for example, Fig. 7. These cannot be attributed to the crack intersecting grown-in dislocations or dislocations introduced by plastic deformation because, to a first approximation, there are equal numbers of left- and right-handed screw dislocations; the steps cancel each other and the surface remains very smooth.

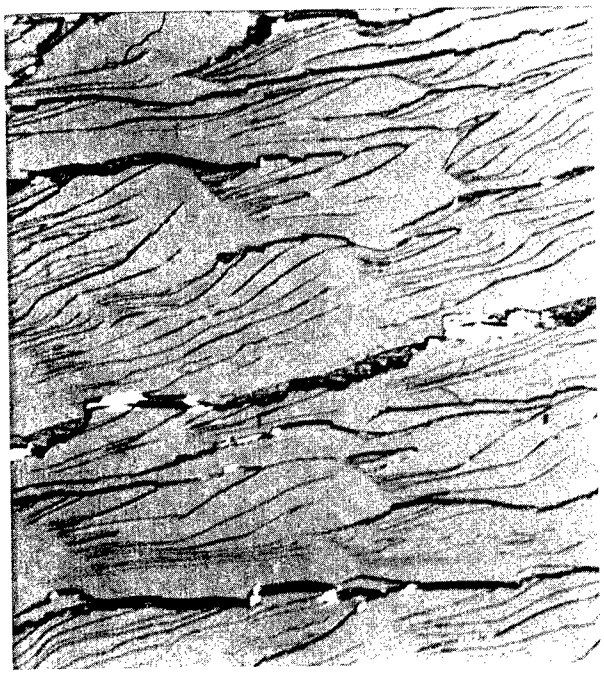


Figure 7: River line patterns on the fracture surface of cleaved calcite. Light microscope photograph.

Confirmation of this can be found from experiments on tungsten crystals[9]. When [001] crystals were fractured at 77K, after the introduction of a sharp crack by the spark discharge method[10], large parts of the surface were completely free from river line steps. Similar tests on crystals which had been deformed 10% at 473K, prior to low temperature testing, fractured in a similar way with large areas of the fracture surface free from river line steps.

The explanation for river lines rests with the effect of local mixed I/III loading conditions and the inability of the crack to twist[11] (see section 3) because of the geometrical constraint. For crystalline materials the details must be based on the influence of crack tip stresses on dislocation nucleation and movement. For a crack driven by a mode I/III loading condition the crack experiences a force tending to twist it into the plane of the maximum principal tensile stress. The stresses at the crack tip result in the nucleation of new dislocations at the tip and the activation of dislocation sources ahead of the tip. We suppose that a higher density of screw dislocations of one sign are produced by the biased I/III field and so, when the crack propagates through these newly generated dislocations, steps of one sign predominate. The average plane of crack growth is effectively twisted. In reality the crack does not twist but the plane of the crack has rotated in a manner closely analogous to the geometry produced when the crack crosses a low angle boundary (Fig. 4).

As cleavage steps of the same sign merge, and the step height (h) increases, the drag ($2\gamma h$) on the bowed out crack fronts increases[11]. Assuming that the crack front can be treated as having a line tension T, the shape of the crack front changes progressively as the river pattern develops. When θ reaches 90° (R = D/2) the two sections of adjacent crack fronts at the step are parallel to each other but the crack tips are moving in opposite directions (Fig. 8b). The interaction between these two fronts is identical to the geometry illustrated in Fig. 8d and the elastic interaction is the same. Subsequent movement of the crack fronts then depends on the local stress fields and the continuing requirement that cracks cannot twist. For crystals with strong cleavage anisotropy, and, in particular, for crystals like mica which have only one dominant cleavage plane, the cracks can bow out past each other[12] (Fig. 8c).

The interaction between cracks on parallel planes depends of the spacing between them. For complete separation of a solid the material between the two cracks, which bridges the two surfaces of the crack, has to fracture also. The mechanisms involved are strongly dependent on microstructure and other material variables. Some insights into these sensitivities are described in section 4 which deals with river lines in a variety of materials and the separation mechanisms in more detail.

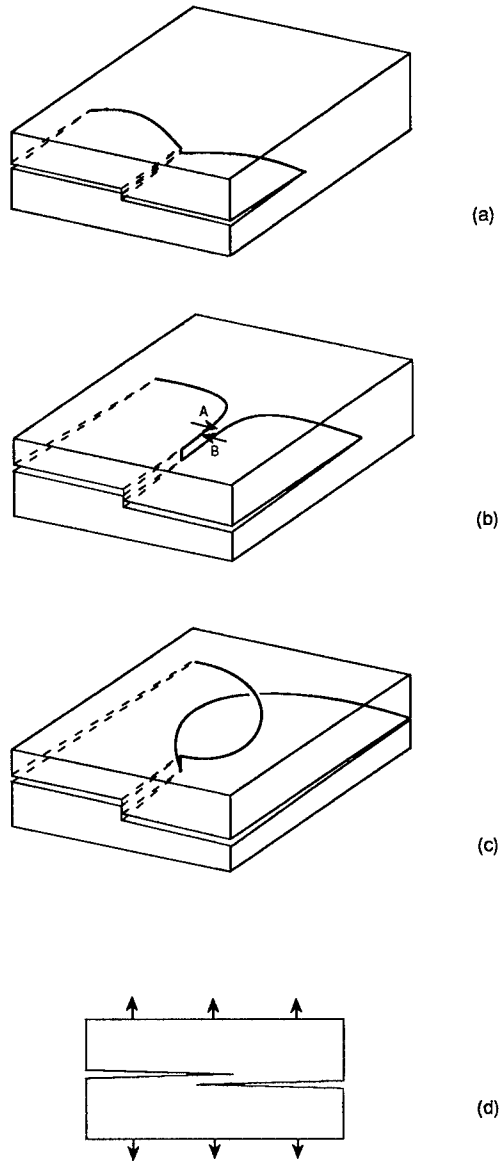


Figure 8: Bowing out of crack fronts at cleavage steps. (a) Small step produces only a small resistance to crack propagation, R is large. (b) Intermediate step, with R = D/2, close to the step the crack fronts at A and B are parallel to each other and moving in opposite directions; the mechanism of separation at the step is not shown. (c) Large step with cracks bowing out past each other. (d) Section through overlapping cracks showing bridging material.

3. River patterns in amorphous brittle solids

The low angle boundary model for the generation of river line steps is somewhat unique and derives purely from the geometry of the crystal planes and the presence of screw dislocations. The formation of steps by the asymmetric generation of screw dislocations in mode I/III conditions is now be extended to the more general case where discrete mechanisms associated with screw dislocations are inappropriate. The influence of mode I/III conditions dominates.

The most general picture is obtained by considering the formation of a river pattern in homogeneous, amorphous, brittle solids such as inorganic and organic glasses. For simplicity we assume that the process zone at the crack tip is very small. In these materials there is usually evidence for river patterns on almost all fracture surfaces even when the externally applied loads are pure mode I or mixed mode I/II. This is because it is almost impossible to avoid some local mixed mode I/III loads. These arise from a variety of secondary effects including reflected stress waves, local heterogeneities, and the movement of curved crack fronts. The occurrence of river patterns can be used as a diagnostic tool to identify the presence of mode I/III conditions during crack growth. It is very difficult to do experiments involving the propagation of cracks in controlled and changing mixed mode I/III fields. The experiment of Sommer[13], described below, is almost unique.

Two distinct crack growth conditions have to be considered. First, a pre-crack formed in mode I, is loaded in mode I/III. Second, a crack, growing in mode I, continues to propagate but the loading changes progressively to mode I/III with an increasing mode III component. The first case is readily demonstrated using a simple bend test. A pre-crack is introduced into the specimen which is aligned in the bend test so that the plane of the pre-crack is at an angle to the maximum tensile stress. The crack tends to propagate on a plane normal to the maximum principal tensile stress. Because the crack cannot twist, fracture occurs either by the nucleation of a new crack, or by the formation of a series of parallel cracks, at the tip of the pre-crack. The photograph is Fig. 1 shows the type of effect observed; in this case the boundary X-Y locates the position where the mode I/III ratio changed. The second case is much more difficult to demonstrate experimentally. Sommer's experiment is the only clear-cut experimental method.

Sommer's experiment

Using an ingenious experimental arrangement Sommer examined the propagation of a crack which was loaded initially in mode I and grew into a stress field which had a continuously increasing mode III component. The geometrical arrangement is shown in Fig. 9.

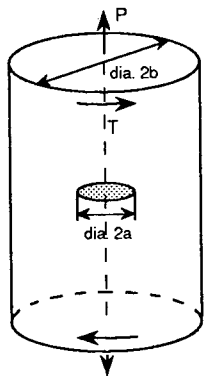


Figure 9: Mixed I/III loading of a penny-shaped crack, (after Sommer[13]).

A 10mm diameter glass rod (AR-glass, Ruhrglas), containing a central penny-shaped crack, was subjected to a combined tensile stress normal to the plane of the crack and a torsion stress parallel to the plane of the crack. The rod was held in sliding seals and subjected to an external pressure and a small torque. The ends of the rod were free from pressure other than frictional resistance of the pressure seals. The pressurised fluid entered surface flaws in the rod and a crack formed almost normal to the axis of the rod and tunnelled into the centre of the rod before expanding.

For the purposes of analysis Sommer treated the test configuration as a central penny-shaped crack normal to the axis of the rod subjected to axial tension and torsion. Under these test conditions the crack experiences mixed mode I/III. As the crack expands, the principal stress at the crack tip is turned through an angle ϕ with respect to the axis of the cylinder (see Fig. 10). At $a = 0$, $\phi = 0^\circ$ and ϕ increases as the crack diameter (2a) increases. Thus, at small crack diameters the loading conditions are almost pure mode I. The effect of an increasing mode III component of the stress field can be determined by direct observation of the fracture surface.

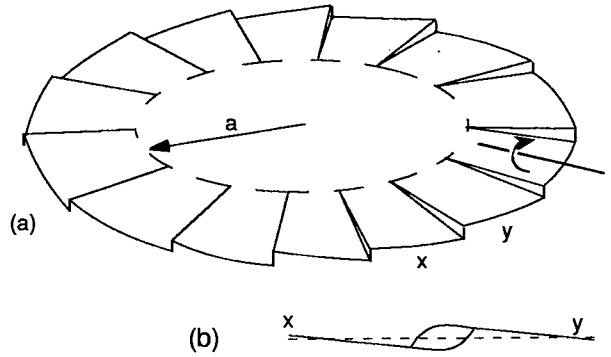


Figure 10: Schematic representation of the shape of fracture surface produced by the Sommer test. (a) Overview showing central flat region surrounded by radial steps. The surfaces of the inter-step regions have a helicoid shape and the overall fracture surface remains co-planar with the central flat region. (b) Detail of (a) illustrating the overlapping of cracks at the steps.

Hull[14] carried out a similar experiment on an epoxy resin (Ciba Geigy Araldite LY 1927 epoxy resin with hardener Araldite HY 1927 in proportions 100:36 by weight). In this case a central tensile crack was formed by impacting a cylindrical steel rod in the centre of the rod specimen which was simultaneously subjected to a torque. A flat, cone-shaped crack, formed at the end of the steel rod and expanded as a penny-shaped crack under the combined effect of a mode I tensile load and the torque. Details of the stress fields and fracture mechanics are given in Sommer's and Hull's papers.

We are concerned primarily with the geometry of crack growth under these smoothly changing mode I/III conditions. The description which follows is based on Sommer's results with an inorganic glass and Hull's results with a brittle epoxy resin, an organic glass. There are some differences in detail. Sommer's now famous photograph of the fracture surface of a glass rod has featured on the front cover of all issues of the journal *Engineering Fracture Mechanics* since 1969. The crack formed in the central region, which was mirror smooth and the stress field was predominantly mode I. At a critical radius, corresponding to a critical value of the I/III ratio, or, alternatively, to a critical value of $\phi = \phi_c$, river line steps were nucleated at the crack tip and grew radially with the expanding crack normal to the direction of crack growth. The steps were approximately evenly spaced.

A detail of the step nucleation region for an epoxy resin test is shown in Fig. 11. Similar features occurred on inorganic glass but there were some significant differences of detail. In particular, the spacing of the primary river lines in epoxy resin was about 4 μm. This is much less than in the inorganic glass where the spacing was about 40 μm. This is probably related to the ease of nucleation of the steps. Sommer found that nucleation occurred at a critical value of $\phi_c = 5.7 \times 10^{-2}$ radians or about 3.3°. It is probably significantly smaller in epoxy resin.

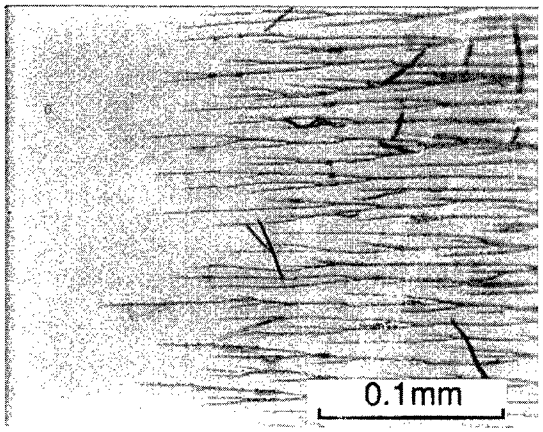


Figure 11: Nucleation of river line steps in a brittle epoxy resin. Steps form in a narrow band and are about 4mm apart. They merge to form large steps as illustrated in Fig. 2. Splinters or filaments of material have separated at the steps and lie at random angles on the surface. Light microscope photograph taken in transmitted monochromatic green light.

The topography of the fracture surface can be determined by light microscopy using either multiple beam interferometry or differential focusing. Fig. 10 is a schematic of the overall topography of the fracture showing the steps; the merging of steps to form river line patterns has not been included. In the central region, before nucleation of the steps, the surface is smooth and planar. After the steps formed the surfaces between the steps developed a helicoid shape, as shown in more detail in Fig. 10b. In this way the average fracture surface remains normal to the axis of the rod but is covered with radial steps which increase in height and number as the crack expands. The formation of the helicoid surface may be interpreted as the crack 'twisting'. The geometrical requirement that cracks cannot twist, which is discussed below, means that some further elucidation of the topography is required.

At the steps the cracks overlap and then bend towards each other to produce final separation. The process is closely analogous to the description of steps in crystalline solids. A photograph of the inter-step region for an epoxy resin specimen is shown in Fig. 12. The fine surface striations can be used to map out the growth of the crack between the steps, as illustrated in Fig. 12b. To interpret these features we need to consider the geometrical constraints to crack growth.

Tilting cracks

A full account of the development of the 'no-twist' condition is given elsewhere[15]. We consider the crack as a smoothly curving surface (Fig. 13). Suppose that on this surface there is a family of curves (unbroken lines) which correspond to consecutive positions of the crack front. Take also the family of orthogonal trajectories of these curves (broken lines), cutting the curves of the first family at right angles, which map out the directions of crack growth. The requirement for zero twist of the moving crack is that the change in the normal to the surface at any point P, as P moves along one of the normal trajectories, is along one of the trajectories. Under these circumstances the dotted lines are *lines of curvature* on the surface, and the original set of unbroken lines of the first family are then also lines of curvature. Every surface is covered by an orthogonal net of such lines.

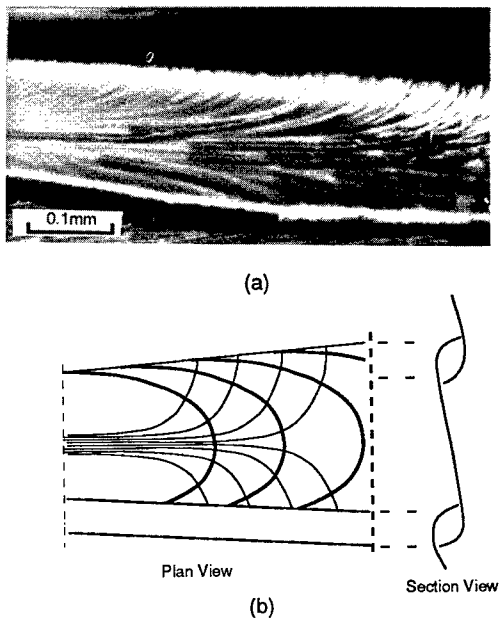


Figure 12: (a) Light micrograph of fine surface markings between level difference lines (river lines) on an epoxy resin showing expansion of crack front. (b) Schematic representation of (a); fine lines are directions of surface markings and broad lines are predicted positions of expanding crack front, (after Hull[14]).

Using this approach, the orientation of every point on the crack surface and the position of the crack tip at the point can be described by a principal frame field of three orthogonal vectors, $\mathbf{f}_1$, $\mathbf{f}_2$, $\mathbf{f}_3$, with $\mathbf{f}_1$ normal to the plane of the crack, $\mathbf{f}_2$ parallel to the direction of crack propagation, and $\mathbf{f}_3$ tangential to the crack tip, as illustrated in Fig. 14. Tilt is growth of a crack on a smooth surface involving rotation of the crack surface about $\mathbf{f}_3$. Twist, if it could occur, would be growth of the crack in such a way that the plane of the crack rotates about $\mathbf{f}_2$.

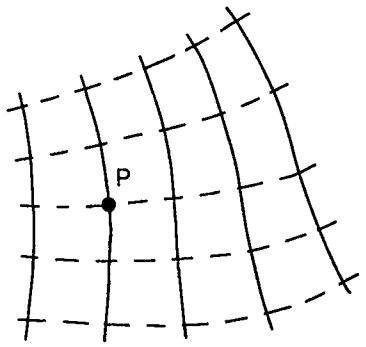


Figure 13: Lines of curvature on a smoothly curving surface.

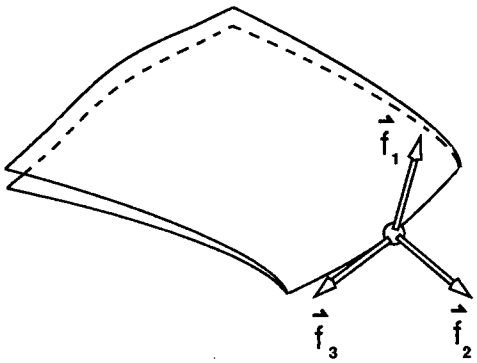


Figure 14: Principal frame field at the tip of a propagating crack.

The no-twist condition places a geometrical constraint on the shape of the crack and limits the way that cracks can grow on smoothly curving surfaces. It over-rides the fracture mechanics rules, such as the maximum principal tensile stress condition. The progressive splitting of the crack as evidenced by the generation of river lines is the practical outcome of this incompatibility.

Helicoid fracture surfaces

We return to the observations illustrated in Fig. 12. The fine striations map out successive and continuous position of the crack front. In other words, they map the positions of f_1, f_2, and f_3 as the crack expands. Hull[15] demonstrated that these crack positions, and the corresponding crack growth directions, follow the 'lines of curvature' on a helicoid surface and so allow the crack to produce the helicoid topography by tilting. Thus, although the crack appears to have twisted, the surface has been produced entirely by tilting.

The diagram in Fig. 5 shows that the crack front bows out between the steps. The extent of bowing and the subsequent movement of the separated cracks depends on the height of the steps. A graphic example of the bowing out of cracks between river lines is shown in Fig. 15. A crack which was growing under mixed mode I/III stopped inside the material, which was a transparent. The sample was viewed in reflected light . The overlapping of bowed-out cracks and river lines steps trailing behind a series of crack fronts is clearly visible. The fringe pattern results from the crack opening which causes interference between light scattered from the two faces of the crack.

Sommer used the term 'lances', first introduced by Smekal[16], to describe the appearance of the river line steps observed on the fracture surfaces of inorganic glasses, as observed in the light microscope, because they resemble the lances used in medieval battles. As the crack propagates the step height increases. The overlapping cracks produce filaments which bridge the crack and eventually fracture by bending leaving fragments on both fracture surfaces. As the step height increases the filaments become more prominent and the cross-sectional area increases. Fine river lines produce fine debris, coarse river lines produce coarse debris.

The crack movements associated with the coalescence of river lines can also be determined from the appearance of striations on the fracture surfaces. The shapes of two opposite fracture surfaces are shown in Fig. 16. Before coalescence three cracks are growing at different levels and after coalescence the cracks propagate at two levels. The two prismatic-shaped filaments, which formed in the overlap regions, coalesced to form a single coarser filament and at the junction a fork-shaped volume is formed. The filaments may or may not separate completely from the main fracture surface. Large filaments are readily removed from fracture surfaces.

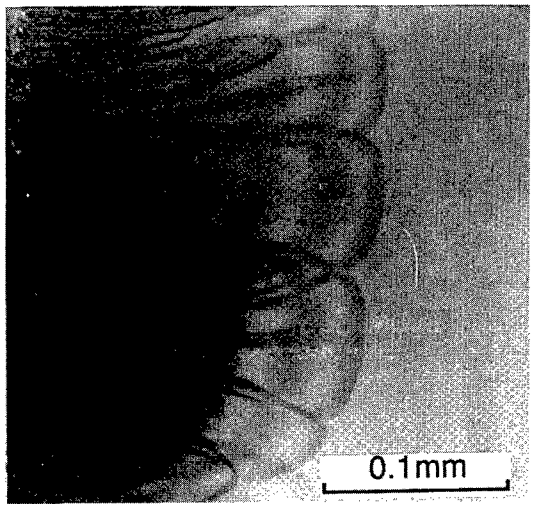


Figure 15: Transmission light microscope photograph of bowed out crack fronts and trailing river line steps on a mixed mode I/III crack which has stopped inside a transparent epoxy resin.

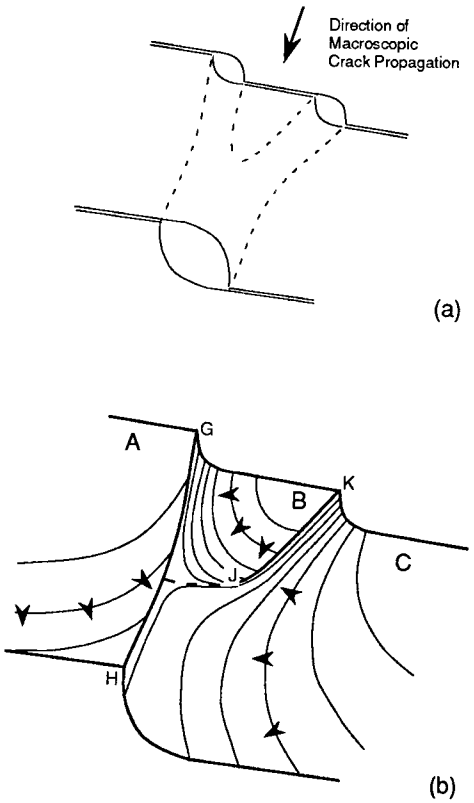


Figure 16: Evolution of crack fronts associated with coalescence of river line steps.

4. Other related topics

Nucleation of steps

Sommer demonstrated that visible river line steps nucleated at a critical value of ϕ. Occasionally, steps nucleated at small defects in the glass, at a lower value of ϕ. Otherwise, the origin of the nucleation is not know. The fact that the steps are approximately equally spaced, see Fig. 1 of Sommer's paper, suggests that the distribution of potential nuclei is greater than necessary to accommodate the twisting forces. Once a step has formed the local stresses are relaxed so that the uniform spacing is consistent with a stress relaxation model. As ϕ increases the steps merge and new steps are nucleated between existing steps.

A similar set of observations (see Fig. 11) was made on brittle epoxy resin although the ϕ_c was probably smaller than in glass, indicating that it is easier to nucleate steps in epoxy resin. Again, details of the nucleation sites are unknown. They are probably associated with local heterogeneities in the cross-linked molecular structure. For epoxy resin there is strong evidence that the nucleation of steps is preceded by the development of a wavy crack front associated with some form of crack instability.

Separation at the river line steps.

The formation of an echelon array of separate cracks as a result of mixed I/III loading leads to the individual cracks bowing out between the steps. Complete separation of the crack faces does not occur until the material at the steps fractures. The fracture process at the steps depends on the spacing of the cracks, h, and the scaling relationships between the spacing and the microstructural dimensions. The unfractured region at the step forms a bridge which spans the opening crack.

Fracture of the bridge must occur by micro-deformation and fracture processes, initially at the scale of nanometers, in crystalline cleavage, increasing to a scale of metres in rock formations. One can anticipate a multitude of mechanisms depending on the value of h and the microstructural l features. Some examples are illustrated in Fig. 17. More than one of these mechanisms may occur in the same river line system as h changes. Thus, for example, for crystalline cleavage monatomic steps formed in the initial development of the river line steps may separate, as Friedel supposed, by single cleavage (Fig. 17a). When h is large crack, overlapping and double cleavage can occur.

A feature of mechanisms illustrated in Fig. 17c to 17e is that a filament of material is produced parallel to the step which may separate from the surface. In crystalline cleavage these filaments have been likened to whiskers[17]. Similar prismatic-shaped filaments are produced on the fracture surface of amorphous materials.

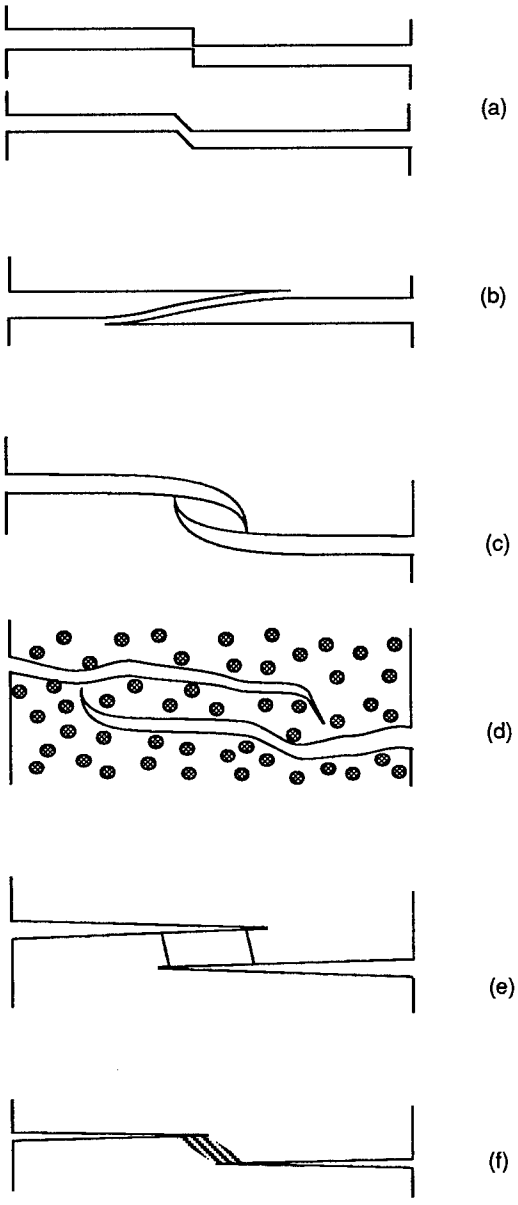


Figure 17: Micromechanisms of deformation and fracture at overlapping cracks along river line steps. (a) simple cleavage. (b) delamination-type fractures characteristic of layer structures. (c) crack tilting in amorphous glasses. (d) crack tilting in multiphase materials. (e) double cleavage. (f) shear failure.

5. Discussions and Conclusions

We have shown that the ideas about river patterns developed from crystallographic cleavage, such as the generation of river line steps at the intersection of a crack with an array of dislocations, can be applied to the brittle fracture of all materials. The geometry of the river line patterns is closely similar and independent of the material although the detail of separation of the fracture surfaces is strongly dependent on microstructural parameters.

Particular emphasis has been given to the influence of mixed I/III conditions. Because a crack cannot twist local mixed-mode loading results in the nucleation of steps and the growth of a series of cracks in echelon formation. The nucleation mechanism in crystalline cleavage involves dislocations which must be generated at the tip of the propagating cracks. Evidence from studies, not reported here, indicates that crack instabilities, yet to be modelled theoretically, can lead to step formation in amorphous solids.

The roughening, generated by increasing the mode III component, is fundamentally different from fracture surface roughening resulting from increasing crack velocity or dynamic stress intensity, K_d. However, the mechanisms of roughening have close similarities as described in detail elsewhere[18,19]. K_d effects generate 'river line' steps, or level difference lines, which are identical to mode I/III river line steps. Approximately equal numbers of steps of opposite sign are produced which tend to cancel each other out. As K_d increases the height of the steps increases and leads to micro-bifurcation and eventually macro-bifurcation. As with mode I/III river line steps, dynamic surface roughening appears to involve crack instabilities at velocities $v_c = 0.1\ v_t$ where v_t is the shear wave velocity. These effects have yet to be explained.

References

1. C. F. Tipper, "Admiralty Ship Welding Committee" (Report No.R.3, H.M.S.O. London, 1948).

2. J. A. Kies, A. M. Sullivan and G. R. Irwin, "Interpretation of fracture markings", J. Appl. Phys., 21 (1950), 716-720.

3. Z. V. Djordjevic, X. Feng Li, W. S. Shin, S. L. Wunder and G. R. Baran, "Fractal and topological characterization of branching patterns on the fracture surface of cross-linked dimethacrylate resins", J. Mat. Sci., 30 (1995), 2968-2980.

4. D. Hull, "Interpretation of river line patterns on indentation generated fracture surfaces with comments on the fractal characteristics described by Djordjevic et al. (J. Mat. Sci. 30, (1995) 2968-2980)", J. Mat. Sci. Letters, 15 (1996), 651-653.

5. S. Tolansky, Multiple Beam Interferometry, (Oxford, Clarendon Press, 1949).

6. J.J. Gilman, "Creation of cleavage steps by dislocations", Trans. A.I.M.E., 212 (1958), 310-315.

7. J. Friedel, Dislocations, (Oxford, Pergamon Press, 1964).

8. J. Chevrier, "Experimental analysis of river patterns in silicon brittle fractures", J. Phys. I France, 5 (1995), 675-683.

9. D. Hull, P. Beardmore and A. P. Valentine, "Crack propagation in single crystals of tungsten", Phil. Mag., 12 (1965), 1021-1041.

10. P. Beardmore and D. Hull, "Nucleation of cleavage cracks in tungsten and molybdenum by spark machining", J. Inst. Metals, 94 (1966), 14-18.

11. F. F. Lange and K. A. D. Lambe, "Interaction between a crack front and cleavage steps", Phil. Mag.,18 (1968), 129-136.

12. R. B. Leonesio, "An observation made on the fracture properties of mica", Eng. Fract. Mech., 1 (1968), 237-238.

13. E. Sommer, "Formation of fracture'lances' in glass", Eng. Fract. Mech.,1 (1969), 539-546.

14. D. Hull, "The effect of mixed mode I/III on crack evolution in brittle solids", Int. J. Fract., 70 (1995), 59-79.

15. D. Hull, "Tilting cracks: the evolution of fracture surface topography in brittle solids", Int. J. Fract., 62 (1993), 119-138.

16. E. Smekal, Osterreichische Ingenieur Arch.,7 (1953), 49-70.

17. J. D. Venables, "Cleavage whiskers", J. Appl. Phys., 31 (1960), 1503-1504.

18. D. Hull, "Influence of stress intensity and crack speed on fracture surface topography: mirror to mist transition", J. Mat. Sci., 31 (1996), 1829-1841.

19. D. Hull, "Influence of stress intensity and crack speed on fracture surface topography: Mirror to mist to macroscopic bifurcation", J. Mat. Sci.,31 (1996), 4483-4492.

SEM STEREO-SECTION FRACTOGRAPHY (SSF) OBSERVATIONS

X. J. Zhang*, R.L. Tregoning*, R.W. Armstrong**, and G.R.Irwin**

*Naval Surface Warfare Center, Carderock, West Bethesda, MD20817
**Dept. of Mechanical Engineering, University of Maryland, College Park, MD 20742

Abstract

Cleavage initiation in engineering materials is governed by local microstructural inhomogeneities. These features are often the principal reason for the large scatter evident in fracture toughness measurements which, in extreme cases, can mask the fundamental relationship between cracking resistance and global material properties. The SEM stereo-section fractography (SSF)[1] technique can be used to carefully evaluate these local inhomogeneities through simultaneous observation of both the fracture surface and the underlying microstructure. By sectioning the fracture surface close to the cleavage initiation site (within 10 μm), and perpendicular to both the fracture surface and the precrack front, a direct correspondence between initiation and the local microstructure can be established. Information obtained from this technique can provide quantitative input about important, local microstructural features which can then be used to calibrate or create realistic micromechanical models. A compendium of SSF results is presented herein for cleavage cracking in disparate materials (A533B steel plates, MIL-70S multi-pass weldments, and Ti6Al4V forgings), under various testing conditions. In each case, the SSF technique was able to unambiguously identify the dominant, local features which triggered cleavage initiation.

Introduction

When studying the cleavage fracture behavior of structural alloys, it is of utmost importance to not only identify the cleavage initiation site(s), but also the underlying microstructure. This information can then be used with knowledge of the testing conditions to determine reasons for scatter within the ductile-to-brittle transition regime. More importantly, once the microstructure has been identified, possible changes can be explored in an effort to improve the material's cracking resistance. However, relating initiation to local microstructural features is practically challenging due to both the small size-scale of typical cleavage sites --- 10 μm or less --- and the difficulty in viewing the microstructure and fracture surface in tandem. Good edge retention must be maintained and the microstructure must be closely juxtaposed to the initiation site to ensure it's authenticity. The SEM stereo-section fractography (SSF) technique[1] has been developed to overcome these obstacles and allow the fracture surface and the surrounding microstructure to be observed simultaneously.

Figure 1 illustrates the basic objective of this technique which is to prepare a transverse section which is adjacent to the main cleavage initiation site (MCIS). A transverse section is first cut and polished near the MCIS while the fracture surface is protected with an acetone-soluble polymeric coating[1]. The coating is then dissolved and the proximity of the transverse section to the cleavage site is ascertained. The fracture surface is coated again and the transverse surface is ground and polished to move the section closer to the MCIS. The protective coating is again removed for examination and the process is carefully repeated. In this manner, the final section can be located within a few microns of the MCIS. A final light polish and etch is then applied to reveal the microstructure and the fracture surface features and transverse-section microstructure are then ready to be examined simultaneously.

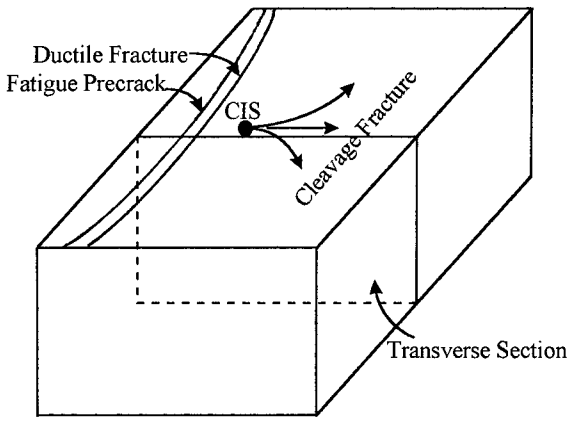
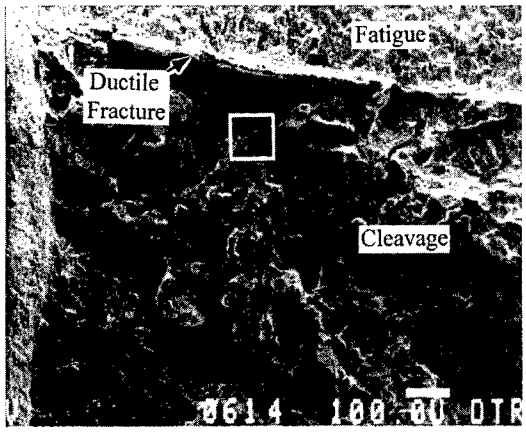


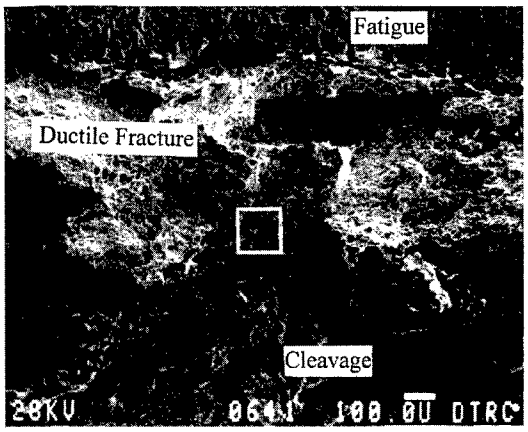
Figure 1: Typical transverse section created by the SSF technique.

In this report, SSF results are presented for three different materials (a A533B steel plate, a MIL-70S multi-pass weldment, and a Ti6Al4V forging) which were tested under different loading conditions (quasi-static bend, biaxial tension, and cyclic loading). The results demonstrate that this technique was useful for establishing a direct correspondance between the fracture surface morphology and the underlying microstructure. In all these alloys, microstructural inhomogeneities and texture were found to consistently trigger cleavage initiation. These local features also provided a clear explanation of the inherent scatter within bulk

George R. Irwin Symposium on Cleavage Fracture
Edited by Kwai S. Chan
The Minerals, Metals & Materials Society, 1997

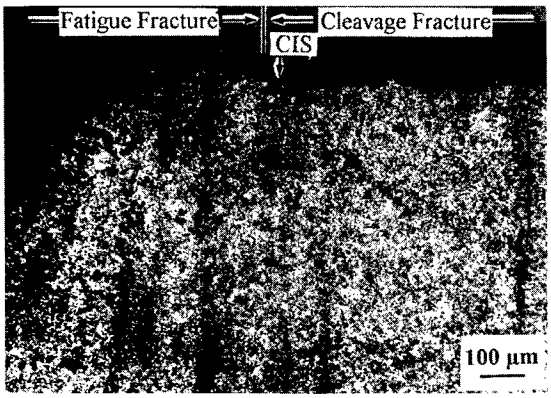


(a) C21U2

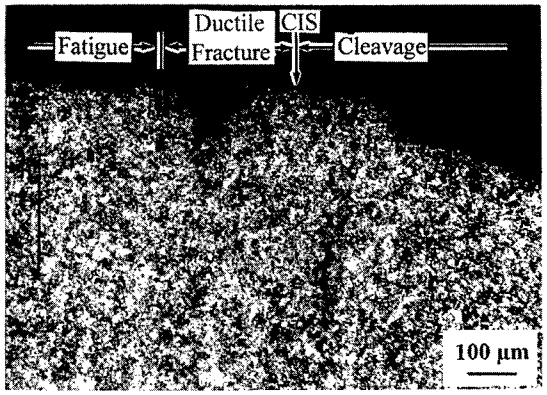


(b) C21B5

Figure 2: SEM fractographs showing a substantial difference in ductile fracture extension between specimens (a) C21U2 and (b) C21B5.



(a) C21U2



(b) C21B5

Figure 3: Optical micrographs of transverse sections showing the locations of the MCIR and the fatigue precrack tip for specimens (a) C21U2 and (b) C21B5.

fracture toughness measurements for these alloys. Although, the feature which triggered cleavage varied among the materials, a single dominant embrittled region was consistently apparent for a given material.

Cleavage Initiation in A533B steel: Effect of Carbide Banding

Carbide banding is one prevalent microstructural non-uniformity in heavy section plates of quenched and tempered A533B steel. The banding is relatively coarse (on the order of tens of microns) and is due to segregation during the solidification process. Significant carbon content and hardness differences between the high and low carbon bands have been found[2,3]. These differences imply that the high carbon bands are stronger and more brittle and also that the local mechanical properties are not uniform. Therefore, it should be expected that the location of fatigue precrack tip with respect to the banding substructure will be crucial to the overall fracture performance. Previously, Irwin, Armstrong , Zhang and et al. have shown that cleavage initiation in this type of steel is associated with high density carbide particle clusters within the carbide-rich band. It has also been demonstrated that this non-uniform structure is one of the primary sources of scatter within the fracture toughness measurements[1,3,4,5].

A group of nine ½T SENB specimens (B= 25.4 mm) of A533B steel were tested at -6.7°C and the J-integral values at cleavage (J_c) exhibited wide scatter[6]. The lowest J_c was 61 m-kN/m^2 (348 in-lbs/in^2) for specimen C21U2 while the highest J_c was 306 m-kN/m^2 (1750 in-lbs/in^2) for specimen C21B5. Low magnification SEM fractographs of the two specimens (Figures 2a-2b) illustrate a significant difference in ductile fracture width between the two specimens which reflects these J_c differences. The inlayed boxes in each figure identify the main cleavage initiation region (MCIR). A transverse section (as in Figure 1) was created a few microns away from the cleavage initiation site (CIS) in each specimen. The section was then etched and imaged optically (Figures 3a- 3b) to reveal the adjacent microstructure. The fatigue precrack tip, ductile zone width, and cleavage initiation site are indicated for each specimen in these figures. Their precise locations have been maintained here by tilting the specimen to reveal both the fracture surface and microstructure, identifying distinguishing features on each surface, and then slowing rotating the specimen until the

transverse section is normal to the imaging beam. It is then clearly evident that the narrower ductile fracture zone and subsequent rapid onset of cleavage observed in specimen C21U2 is associated with the relatively brittle, dark carbide band. Conversely, the wider ductile fracture zone and higher toughness of specimen C21B5 is associated with a relatively ductile, lower carbon region. The underlying microstructure explains the substantial spread of J_c in these specimens, but it even more clearly demonstrates Irwin's conjecture that cleavage initiation is a local event which is sensitive to microstructural variation within the material[7].

Cleavage Initiation in A533B Steel Biaxial Testing: Effect of Microstructural Variability

It is well known that low crack-tip constraint contributes to both an increase in scatter and in median J_c measurements by reducing the hydrostatic stress component ahead of the crack tip[8,9]. Traditional uniaxial testing methodology has evolved to ensure high crack-tip constraint, so that both a lower-bound material toughness is measured and the scatter is reduced. A new cruciform specimen, biaxial testing methodology has been developed[10] by extending this rationale to determine if increased out-of-plane constraint in structurally relevant, shallow flawed specimens leads to cleavage initiation toughness values which are lower than measured in uniaxial testing. The testing apparatus allows the normal to transverse stress ratio within the test section to be varied from 1:0 to 1:1 to simulate from uniaxial to maximum out-of-plane constraint.

Early results, however, exhibited substantial scatter in K_{JC} measurements even in the 1:1 biaxial tests. The K_{JC} was 113 MPa$\sqrt{m}$ (103 ksi$\sqrt{in}$) for specimen BB10, while the K_{JC} was 219 MPa$\sqrt{m}$ (199 ksi$\sqrt{in}$) for specimen BB07[10]. Such discrepancy was not expected due to the high crack-tip constraint, and microstructural reasons for the scatter were sought using the SSF technique.

Specimen BB10

Metallurgical analysis revealed that specimen BB10 had a pronounced banding structure. Further, substantial microhardness variations were found between the banded regions within the material. This banded microstructure is evident in a low-magnitude SEM micrograph (Figure 4a) of the transverse surface which is approximately 5 μm from the main cleavage initiation site (MCIS). This structure is similar to the different heat of this steel discussed earlier (Figure 3a, b).

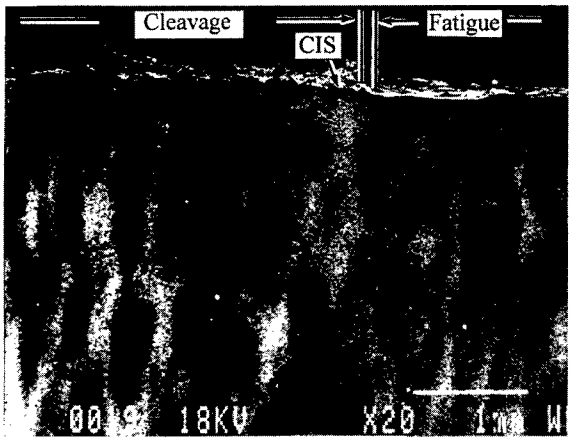


Figure 4a: An SEM micrograph of the banding structure in specimen BB10.

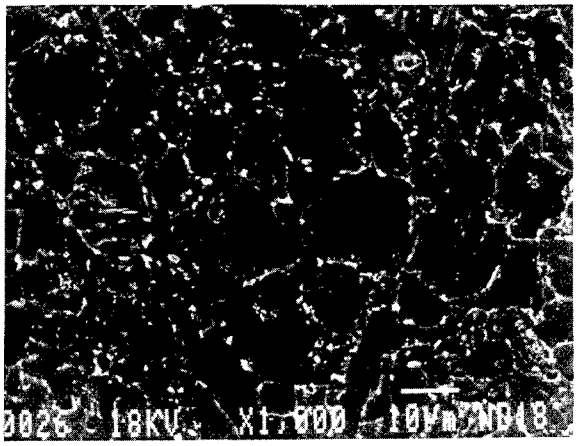


Figure 4b: An SEM micrograph of equiaxed ferrite grain structure of the dark band in Figure 4a.

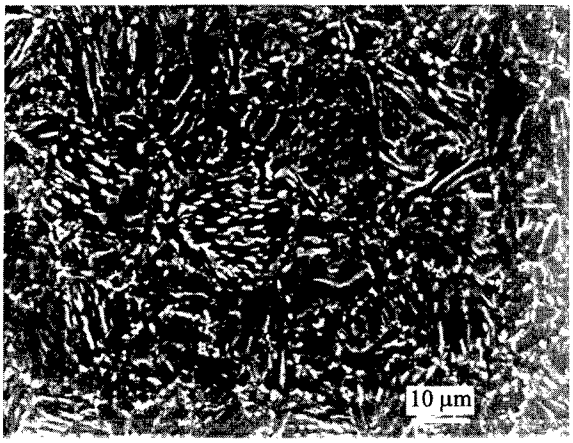


Figure 4c: An SEM micrograph of tempered martensitic or/and tempered bainitic structure of the light band in Figure 4a.

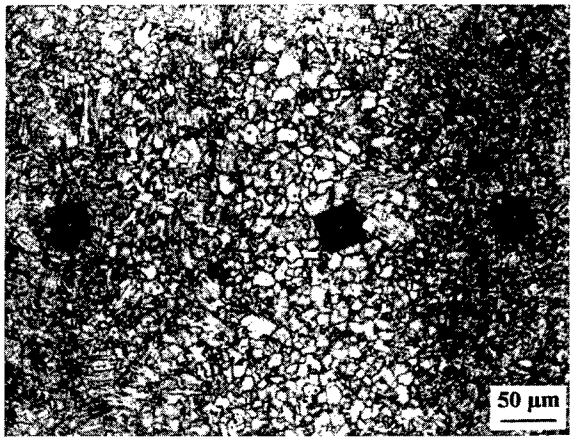


Figure 4d: An optical micrograph showing a significant difference in Vickers indentation size between the two microstructures.

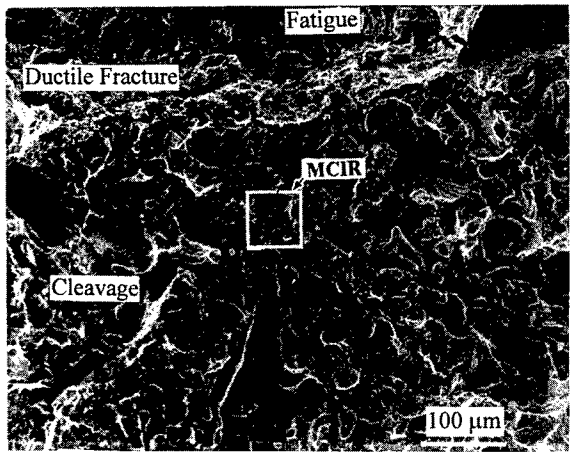


Figure 5a: A conventional SEM fractograph of specimen BB10 showing the location of the MCIR.

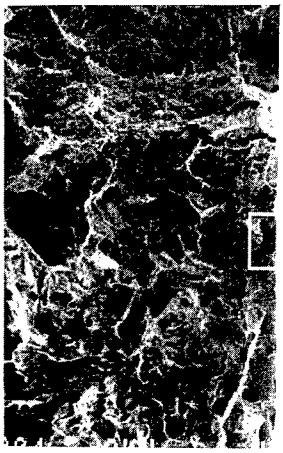


Figure 5b: A conventional SEM fractograph of specimen BB10 after sectioning.

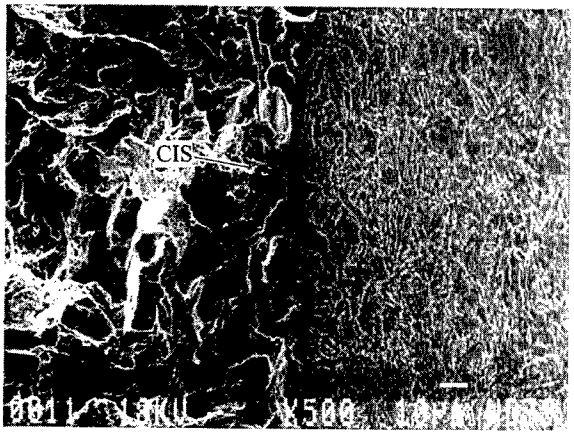


Figure 5c: An SSF micrograph: fracture surface and microstructure of the transverse section around the CIS illustrated simultaneously.

Higher magnification SEM micrographs (Figures 4b,c) illustrate the microstructure typical of these bands. The dark bands in Figure 4a consist of equiaxed ferrite grains (Figure 4b) which have no carbide precipitates within the grains and relatively few carbide particles scattered along the grain boundaries. The light bands in Figure 4a contain tempered martensite and/or tempered bainite and is characterized by dense carbide particles aligned along preferred orientations within the grains (Figure 4c). An optical image of adjacent bands is illustrated in Figure 4d. Imaging differences between the SEM and light microscope cause the equiaxed ferritic bands to appear darker than the transformed bands in the SEM and lighter optically. Hardness measurements within each region reveal that the equiaxed ferritic band --- the lighter region in Figure 4d --- has lower hardness (164 VHN) while the transformed band is 30% harder (210 VHN). It should therefore be expected that the transformed banding structure is more brittle than the equiaxed ferritic bands and should act as preferential sites for cleavage initiation.

The location of the fatigue precrack tip and cleavage initiation sites with respect to the banding structure for this specimen was determined using the SSF technique in the usual manner. A low-magnification SEM fractographic view (Figure 5a) was first used to identify the main cleavage initiation region (MCIR) of specimen BB10, and then the transverse section was prepared. The left-hand portion of the fracture surface after sectioning (Figure 5b) illustrates that the section plane is within 5 µm from the MCIS. After etching and tilting the specimen by 30° (Figure 5c), the banded microstructure at the MCIS is clearly visible. Slowly rotating the specimen while identifying visual cues allows the transverse section to be fully viewed at lower magnification (Figure 4a) while maintaining the position of critical fracture surface features. Here the extent of the banded region and it's juxtaposition to the fatigue precrack tip is obvious and unequivocally shows that the brittle, transformed microstructure triggered cleavage and the low measured toughness (113 MPa$\sqrt{m}$) results from the fatigue precrack's proximity to this brittle banded region.

Specimen BB07

The microstructure of this specimen is relatively uniform. Carbide particles are randomly distributed within the ferrite grains and

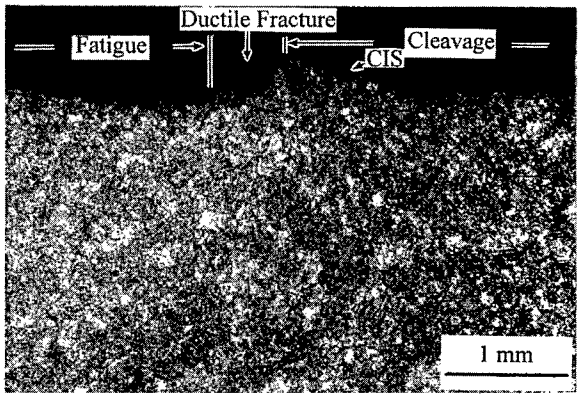


Figure 6: An optical micrograph of the transverse section of specimen BB07.

there are slight variations in grain size, shape, and carbide particle density within the matrix (Figures 6). However, no banding is

apparent here and the microstructure is substantially different than in specimen BB10 (Figure 5a). Microhardness measurements for this specimen exhibited a negligible variation as a function of location, and the average value was 183 VHN which is substantially lower than the brittle, transformed bands present in BB10. This easily explains why the ductile tearing region was so large in this specimen and consequently why the measured toughness was so much higher than for BB10.

These microstructural observations indicate that specimens from different locations within the same heavy-section steel plate can have dramatically different microstructures due to the solidification process and heat treatment history. Further, this variation governs the fracture performance and once again illustrates the fundamental interrelationship between cleavage initiation and the local microstructural features. The inhomogeneities within the local microstructure therefore invariably lead to scatter in fracture toughness measurements which cannot be eliminated, regardless of the severity of the local, crack-tip constraint. It should be possible to use these differences to provide a more rigorous, quantitative index of the material's toughness in much the same way that global chemistry and microstructural effects have historically been used. Further, these results indicate that the influence of the local microstructure and microstructural non-uniformity on cleavage should be rigorously incorporated into any cleavage-initiation models of steels.

Cleavage Initiation in MIL-70S Multi-pass Weldments

Extensive fractographic observations were performed on mismatched 1T SE(B) weldment specimens. The specimens were constructed from HY-80 baseplate and MIL-70S weld wire using an unsymmetric double-V joint. The crack tip was located within the center of weld[11]. Five specimens were examined using the SSF technique to evaluate the effect of welding zone microstructure on cleavage initiation. This technique was especially helpful in this study due to the extent of the local, small-scale variability inherent in multi-pass weld microstructure. Once again, it was determined that cleavage initiation could be traced to a single region; in this case the region was a narrow band of material surrounding the fusion line.

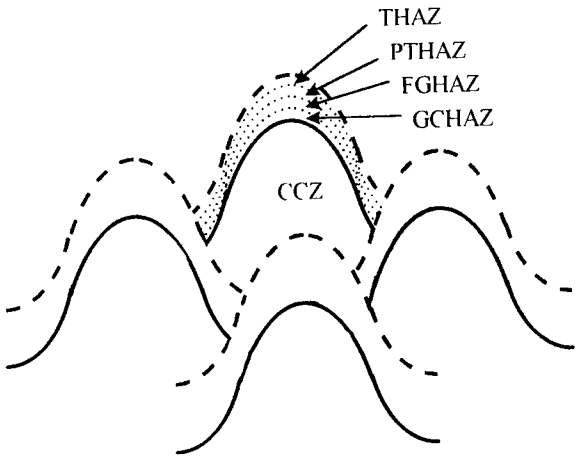


Figure 7: A simplified sketch of the microstructural zones present in a multipath weldment.

Microstructure Characterization

A simplified sketch of the microstructural zones present in a multi-pass weldment (Figure 7) illustrates the inhomogeneity associated with a single weld bead pass. Each welding pass produces: (a) a coarse columnar zone (CCZ) bounded by a visible fusion line (solid line in Figure 7) which exhibits the structural characteristics of a casting; (b) a fully transformed heat-affected zone (HAZ) in the base metal or previous weld beads, which can be further divided into a coarse grain (CGHAZ) and a fine grain (FGHAZ) region; (c) a partially transformed heat-affected zone (PTHAZ) next to the FGHAZ, which is heated to temperatures between A_{c1} and A_{c3} ; and (d) a tempered HAZ zone (THAZ) where the temperature has remained lower than A_{c1}. The microconstituents formed in each zone is a function of the weld filler chemistry and the welding parameters. Furthermore, in a multi-pass weld, a portion of the previous coarse columnar zone is reheated by the HAZ of subsequent passes (dashed line in Figure 7). These portions of the prior bead's coarse columinar region then essentially become form part of the HAZ of the succeeding bead. The central portion of the bead retains its original, untempered structure (region I in Figure 7).

Figure 8a illustrates the weld bead microstructure of specimen GXK 62. The microstructure surrounding the fusion line of one bead (A-A in Figure 8a) has been magnified in Figure 8b. In this picture, the FGHAZ, CGHAZ, fusion line, and the edge of the CCZ are evident. It is important to note the similarity between the CGHAZ and the edge of the CCZ adjacent to the fusion line: both contain attotriomorphic ferrite along the prior austenite grain boundaries, Widmanstatten side plates, acicular ferrite, and carbide particle clusters. The features of these bands compared to the remainder of the weld bead microstructure suggests that this narrow region surrounding the fusion zone are the most brittle. Therefore, the CGHAZ and edge of the CCZ should serve as the preferential cleavage initiation region for this group of weldments.

In single-pass weldments, the CGHAZ in the base metal is typically the most brittle weld zone region due to the formation of large prior austenite grains and fast cooling transformation products (such as attotriomorphic ferrite, Widmanstatten side



Figure 8a: The weld bead structure of specimen GXK 62.

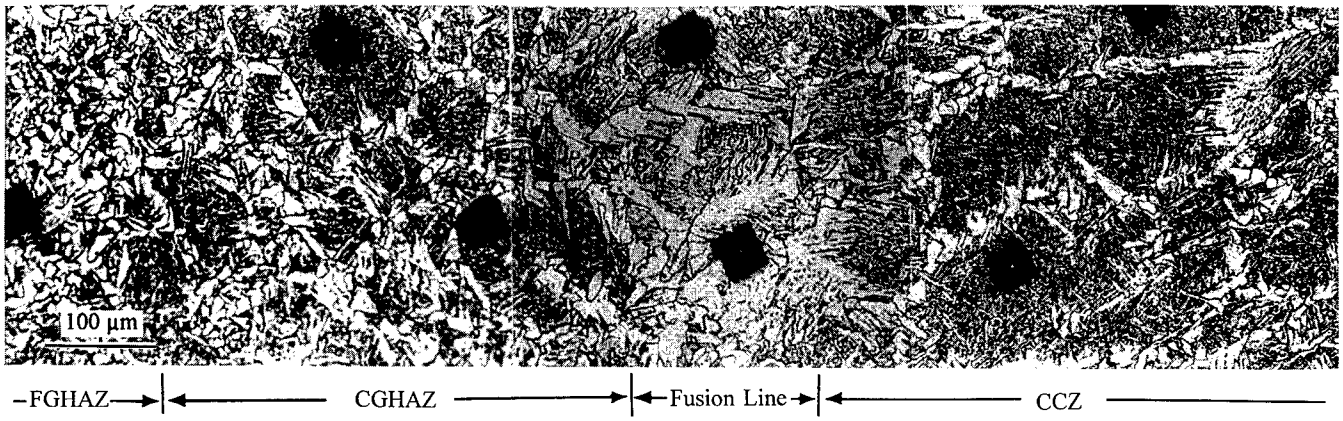


Figure 8b: The microstructure surrounding the fusion line of one weld bead; line A-A in Figure 8a.

plates, acicular ferrite, martensite, and bainite). The finding that both the edge of the CCZ and CGHAZ have similarly embrittled characteristics in this multi-pass weldment is due to the increased cooling rate possible near the fusion line from previously deposited weld beads. In addition, the edge of the CCZ retains the inherently weak as-deposited microstructure and may be even further embrittled due to segregation. It is therefore likely that the edge of the CCZ may be even more embrittled than even the reaustenitized CGHAZ.

SSF Results

The SSF results indicated that the MCIS in four of the five sectioned GXK specimens was located at the edge of the CCZ, adjacent to the fusion line. Specimen GXK 62 is typical of these specimens. The unsectioned fracture surface of this specimen (Figure 9a) clearly indicates the dominant CIS. The focal point of the site (within the white box in Figure 9a) is enlarged in Figure 9b and the cleavage initiation site has been identified by the black arrow. A transverse section was then prepared approximately 10 µm from the cleavage initiation site. Figure 9c shows the fracture surface and transverse section simultaneously after tilting the specimen 45° about the sectioning axis. In the figure, the small triangular cleavage facet near the cleavage initiation site (indicated by black arrow) was used to identify the location of the MCIS as the section is rotated to view solely the transverse microstructure surrounding the CIS and fatigue precrack (Figure 10). It is evident in Figures 9c and 10 that cleavage initiation was associated with long ferrite plates at the edge of the CCZ, adjacent to the fusion line. Further, it is evident that (1) the tip of the fatigue pre-crack was located in the middle of the CCZ; (2) ductile crack growth proceeded through the CCZ for approximately 1 mm without

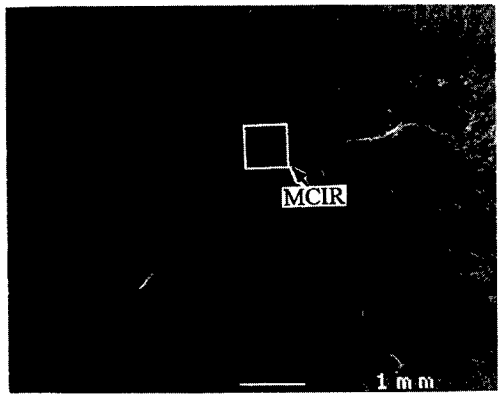


Figure 9a: A low magnification conventional SEM fractograph of specimen GXK 62.

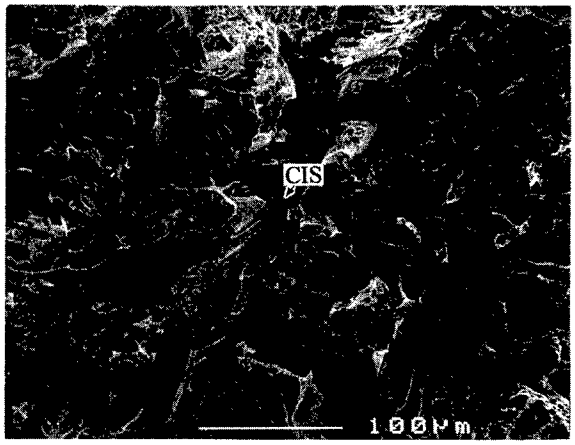


Figure 9b: An enlargement of the MCIR in Figure 9a.

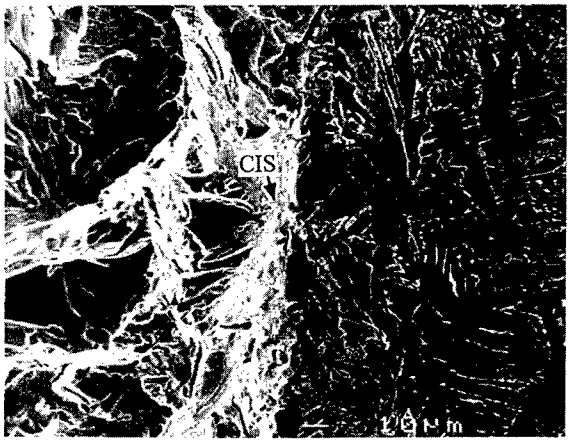


Figure 9c: Fracture surface and microstructure of the CIR region: tilted 45° about the section axis.

triggering cleavage cracking; and (3) cleavage was triggered only when the edge of the CC microstructure was sampled by the crack tip. As mentioned earlier, four of the five GXK specimens examined also exhibited cleavage initiation only within the CCZ, near the edge of the fusion line.

The only specimen analyzed that did not cleave within this region was GXK 59. The cleavage site was identified, and the transverse section was prepared as before. Once again, the transverse section was located within 10 μm from the CIS. The final etched section is shown in Figure 11. The fatigue crack tip in this specimen was located within the FGHAZ of this weld pass. The crack initiated as a stable, ductile crack and propagated through the FGHAZ, toward the fusion line. Only when the crack reached the CGHAZ, did cleavage initiation occur. Therefore, although the edge of the CCZ was not the triggering site in this specimen, the other susceptible microstructural site was responsible.

The SSF results of this MIL-70S weldment system establish that the microstructure surrounding the narrow fusion line governs cleavage initiation. Therefore, the distance between the fatigue crack tip and the fusion line region in the direction of crack propagation determines the amount of ductile tearing. The measured toughness results reinforce this observation: The lowest J_c value from this subset of specimens was 36.75 m-kN/m^2 (210 in-lbs/in^2) and corresponded to a specimen where the fatigue precrack was within 75 μm from the fusion line. Conversely, the highest J_c measured was 382 m-kN/m^2 (2180 in-lbs/in^2) and represents the specimen where the fatigue precrack tip was furthest from the fusion line.

It appears that it is possible to eliminate virtually all the measured scatter in J_c in this (and similar) weldment system with knowledge of the material's J-R curve and the distance from the fatigue precrack tip to the fusion line. It is also clear that any improvement in the fracture toughness of this weld can only be possible if the toughness of the fusion line microstructure is increased, such as by reaustenization of the underlying beads. Some initial efforts in this area have been made by Albery and Jones[12], and Reed[13].

Cleavage Initiation in Ti 6Al4V Environmental Fatigue Testing: Effect of Texture

The SSF technique was also applied to study the cracking behavior of a Ti 6Al-4V forging. This material was tested in 3.5% NaCl at room temperature under constant amplitude, R=0.1 loading. The fatigue crack growth rate (FCGR) behavior was highly nonuniform and exhibited sporadic crack growth acceleration and deceleration, especially between 10 MPa$\sqrt{m}$ < ΔK < 20 MPa$\sqrt{m}$ (Figure 12). Fractographic observation revealed three distinct features on the fatigue surface which contribute to this behavior (Figure 13a): (I) coplanar faceted regions; (II) brittle, randomly-oriented faceted regions; and (III) peculiar transverse regions featuring crystallographic facets and out-of-plane steps or jogs. An enlargement of one of these areas (Figure 13b) illustrates one of the peculiar surface feature III regions.

The SSF technique was again utilized to examine the usual transverse section (Figure 1) through a feature III region. These sections are revealed in Figures 14a,b and the acuity of these ledges becomes apparent; each is on the order of 100 - 200 μm out of the fracture plane. Closer examination of one of the troughs reveals extensive out-of-plane cracking that follows elongated α

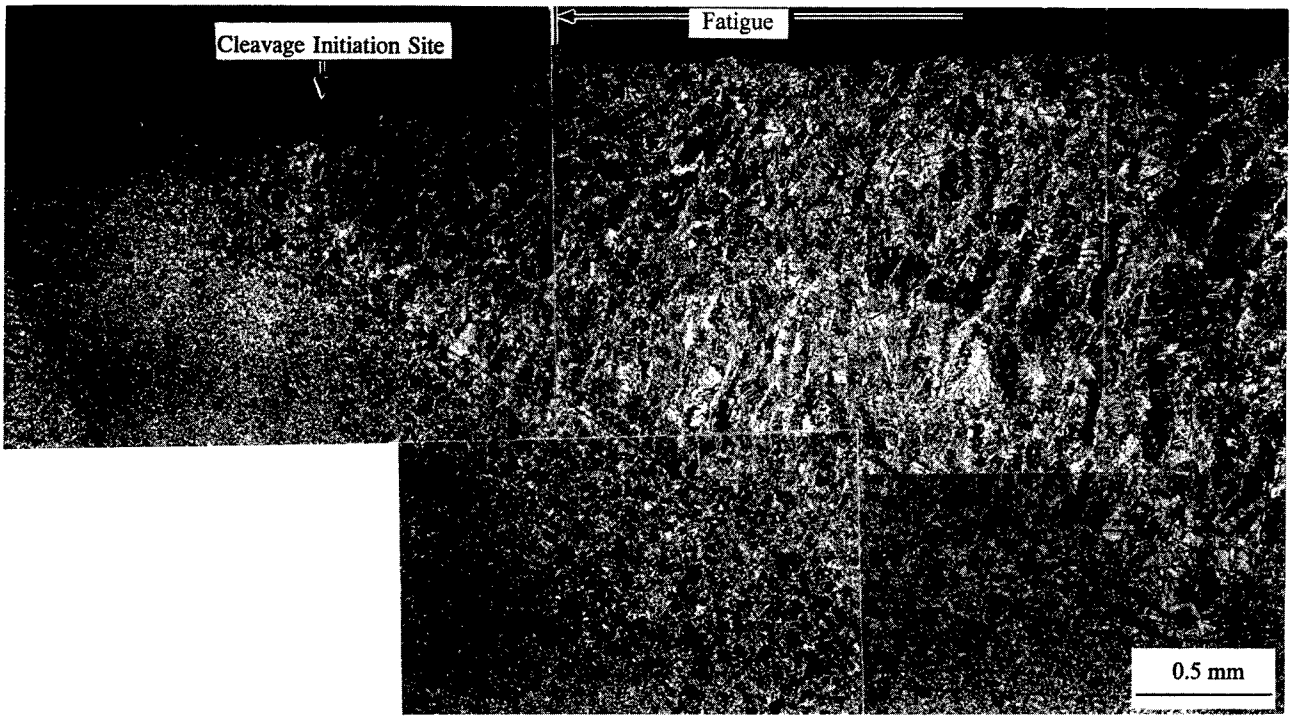


Figure 10: An optical micrograph of specimen GXK 62 showing the location of the fatigue precrack tip and the CIS with respect to the welding bead structure.

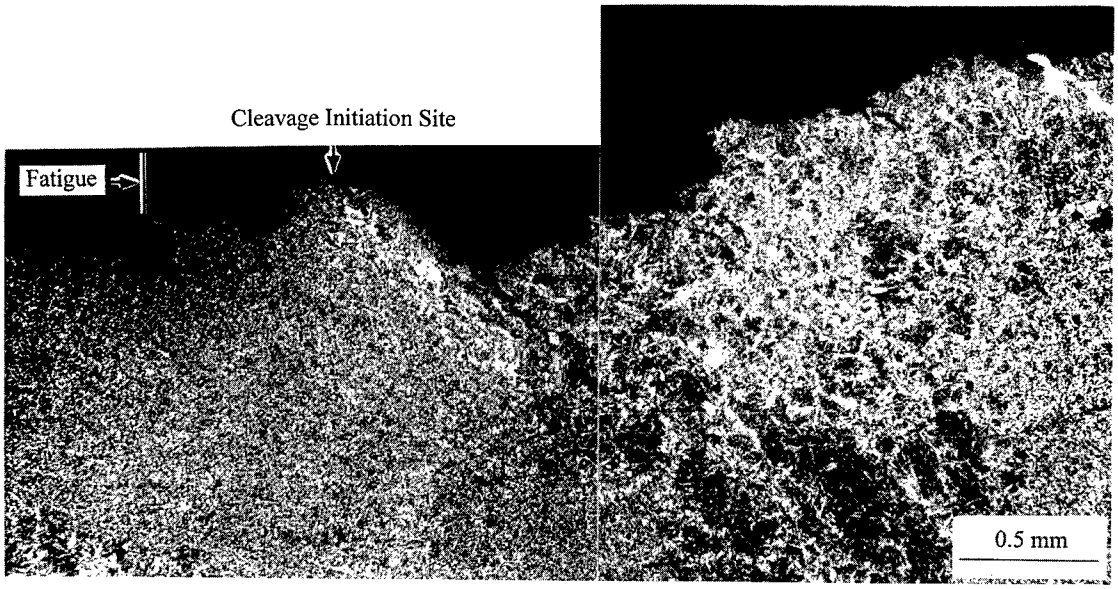


Figure 11: An optical micrograph of specimen GXK 59 showing the location of the fatigue precrack tip and the CIS with respect to the welding bead structure.

grains. A second SSF section was made perpendicular to the section in Figure 14b (section A-A) near the trough illustrated in this figure. The transverse cracking morphology is now clearly shown to propagate along elongated, preferably oriented α grains (Figure 15a). An enlargement of the trough (boxed area in Figure 15a) illustrates the coplanar nature of this cracking. The top-most plane is evident in the bottom portion of Figure 15b and is actually the polished and etched microstructure of section A-A (Figure 14b). The layers below this plane are the fracture surfaces of the secondary cracks that appear to the left of section A-A (Figure

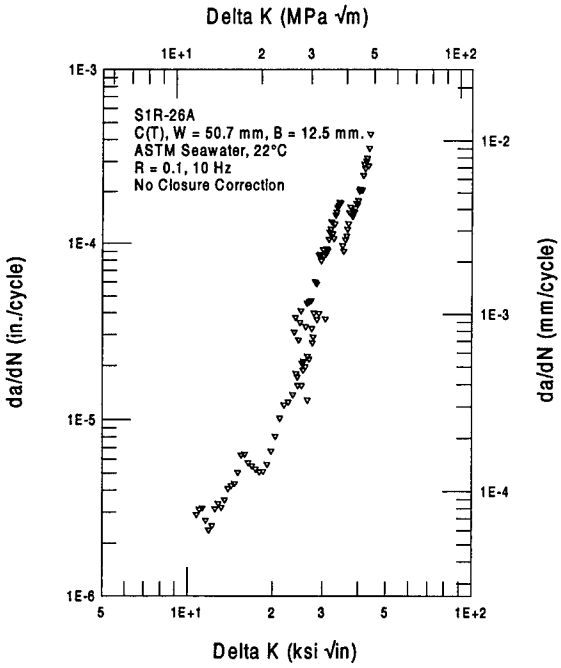


Figure 12: Fatigue crack growth rate behavior of Ti6Al4V forging: specimen SIR-26A.



Figure 13a: A conventional SEM fractograph of specimen SIP-26A showing three distinguishable features.

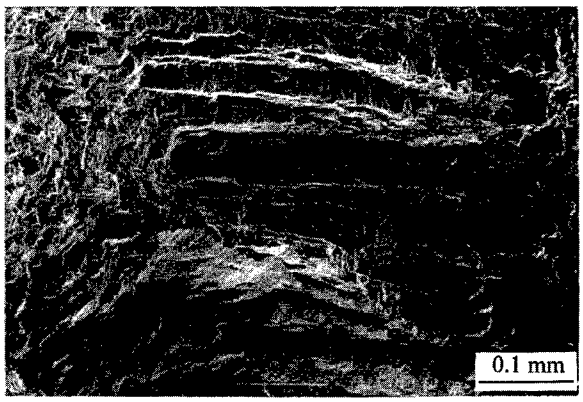


Figure 13b: An enlargement of the boxed area in Figure 13a.

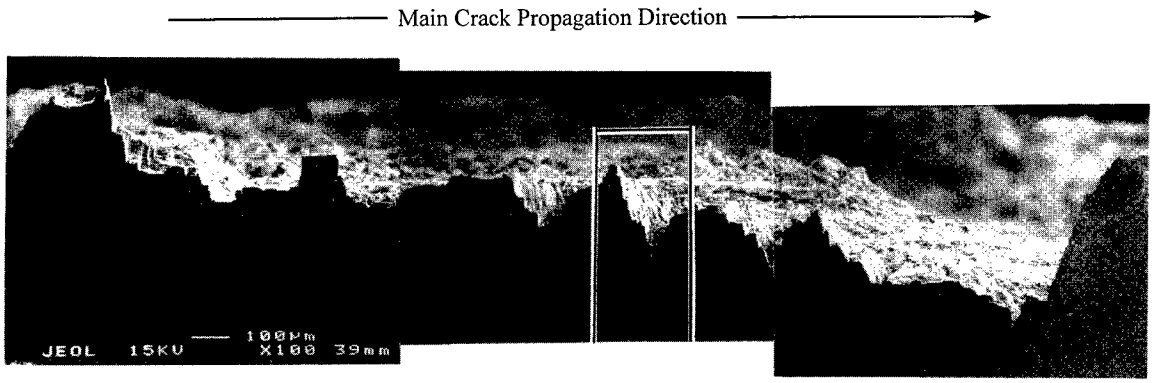


Figure 14a: An optical micrograph of the transverse section through the feature III region shown in Figure 13a



Figure 14b: An enlargement of the boxed area in Figure 14a showing the long vertical secondary crack.

14b). The correspondence between the crack surfaces and the microstructure is striking and indicates the crystallographic nature of this cracking, the relative weakness of this orientation, and the strong texture within this region.

These pictures elucidate the correspondence between the secondary cracking path and the preferably oriented α grains. The α grain orientation texture is produced during the solidification process and is not eliminated by subsequent heat treatment. The crystallographic appearance of this cracking implies that a cleavage-type mechanism may govern this phenomenon. This out-of-plane cracking is not desirable because of both its brittle nature and the fact that it implies this microstructural orientation in much weaker than in the normal plane within these regions. The texture can be eliminated through proper solution heat treatments to form either randomly oriented, equiaxed α grains mixed with (α + β) constituents, or a fully transformed structure. A more homogeneous, isotropic, and stronger fracture performance should then be achievable.

Summary

In this paper, the SSF results obtained from three different materials (a A533B plate, a MIL-70S multi-pass weldment, and a Ti 6Al4V forging) and three different types of tests (SE(B), biaxial tension, and fatigue) reinforce three primary points:

1. The stereo-section fractography technique can be used to reveal the microstructure located directly adjacent to the fracture surface feature of interest. This information is vital for establishing a direct relationship between the principal fracturing mechanism and the precipitating microstructural features.
2. Microstructural inhomogeneities governed the onset of cleavage in the materials studied herein. High carbon banded regions were identified as the triggering microstructure for the A533B plates while the microstructure surrounding the fusion line was the initiation site in MIL-70S multi-pass weldments. Ti 6Al-4V exhibited secondary, cleavage-like cracking along preferably oriented α grains within a 3.5% NaCl environment. While the specific constituency of the microstructurally brittle phase varied in all these materials, one dominant region was always found to be the underlying cause of cleavage initiation.
3. The distance between the sharp advancing crack front and the initiating microstructure is an underlying reason behind the

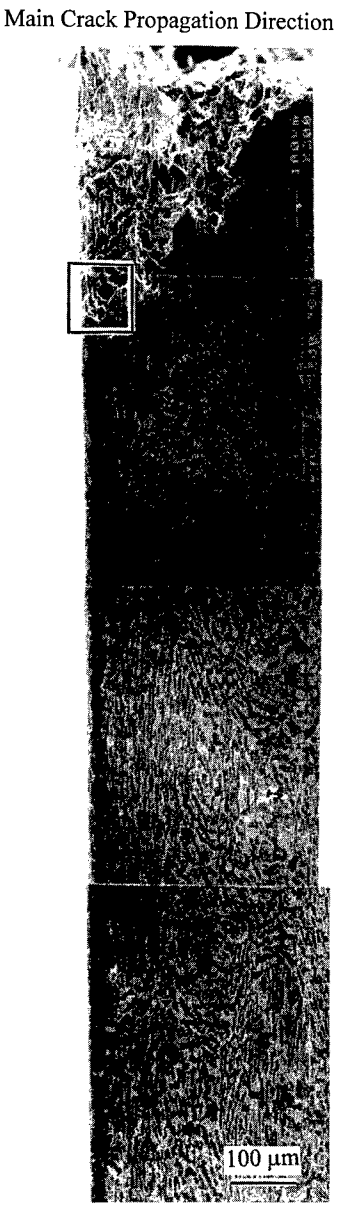


Figure 15a: An SEM micrograph of the second SSF section along line A-A in Figure 14b.

inherent scatter in fracture toughness measurements within the ductile-to-brittle transition regime. While scatter can be minimized by increasing crack-tip constraint, the remaining measured variability is indicative of the local material inhomogeneities which exist along the cracking plane.

Acknowledgments

Support for this research was provided by the Office of Naval Research, Code 332 (Dr. G. Yoder) under program element 62234N, task area 03460; and by the U.S. Nuclear Regulatory Commission, Heavy Section Technology Program (Tech. Manager: Dr. S. N. Malik), under job codes J6036 and B0119.



Figure 15b: Enlargement of the boxed area in Figure 15a: a good correlation between etched microstructure and secondary cracking fracture planes is apparent.

References

1. X. J. Zhang, R. W. Armstrong, and G. R. Irwin, "Stereo (SEM) Section Fractography of Isolated Cleavage Regions in Nuclear Vessel Steels," Metall. Trans. 20A (1989) pp.2862-2868.

2. K. Ogawa, X. J. Zhang, T. Kobayashi, R. W. Armstrong, and G. R. Irwin, "Microstructural Aspects of the Fracture Toughness Cleavage-Fibrous Transition for Reactor-Grade Steel, "Fracture Mechanics: Fifteenth Symposium, ASTM STP 833, R. J. Sanford, Ed., American Society for Testing and Materials, Philadelphia, 1984, pp. 393-411.

3. X. J. Zhang., "Cleavage-Fibrous Transition Behaviors of Structural Steels," Ph. D. Thesis, University of Maryland, College Park, ND, 1985.

4. G. R. Irwin, X. J. Zhang, and R. W. Armstrong, "Isolated Cleavage Regions in the Ductile Fracturing Transition of Nuclear Vessel Steels and Their Weld Metals", J. Mater. Lett.8 (1989), pp. 844-848.

5. J. P. Gudas, G. R. Irwin, X. J. Zhang, and R. W. Armstrong, "A Model for Transition Fracture of Structural Steels from Observations of Isolated Cleavage Regions," in Defect Assessment in Components - Fundamentals and Application, ESIS/EGF9, J.G.Blauel and K.H.Schwalbe, Eds., Mechanical Engineering Publications, London, 549-568, 1991.

6. R. .E. Link and J.A. Joyce, "Experimental Investigation of Fracture Toughness Scaling Models," Constraint Effects in Fracture Theory and Applications: Second Volume, ASTM STP 1244, Mark Kirk and Ad Bakker, Eds., American Society for Testing and Materials, Philadelphia, 1995.

7. G. R. Irwin and X.J. Zhang, .Private communication , March, 1996.

8. J. D. G. Sumpter and A.T. Forbes, "Constraint Based Analysis of Shallow Cracks in Mild Steel," Proceedings fo TWI/EWI/IS International Conference on Shallow Crack Fracture Mechanics Testing and Applications, Cambridge, UK, 1992.

9. C.F. Shih, N.P. O'Dowd, and M.T. Kirk, "A Framework for Quantifying Crack Tip Constraint," Constraint Effects in Fracture, ASTM STP 1171, American Society for Testing and Materials, Philadelphia, 1993.

10. W. E. Pennell, B. B. Bass, J. W. Bryson, T. L. Dickson, and J. G. Merkle, Martin Marietta Energy System Inc., Oak Ridge National Laboratory, "Preliminary Assessment of the Effects of Biaxial Loading on Reactor Pressure Vessel Structure-Integrity-Assessment Technology," ORNL/LTR/95-3, Oct. 1995.

11. R.L. Tregoning, "Experimental Investigation of Mismatched Weld Joint Performance," Fatigue and Fracture Mechanics: 27th Volume, ASTM STP 1296, R.S. Piascik, J.C. Newman, and N.E. Dowling, Eds., American Society for Testing and Materials, 1996.

12. P. J. Alberry and W. K. C. Jones, "Computer Model for Prediction of Heat-Affected Zone Microstructure in Multipass Weldmens," Met. Technol., 9, 419, 1982.

13. R. C. Reed, "The Characterisation and Modeling of Multipath Steel Weld Heat-Affected Zones," Ph.D. thesis, University of Cambridge, Cambridge, U. K., 1990,chap. 3.

A THREE-DIMENSIONAL MODEL FOR POLYCRYSTALLINE CLEAVAGE AND PROBLEMS IN CLEAVAGE AFTER EXTENDED PLASTIC FLOW OR CRACKING

Frank A. McClintock

Department of Mechanical Engineering, Massachusetts Institute of Technology
Room 1-304, 77 Massachusetts Avenue
Cambridge MA 02139-4307

Abstract

Fractures in the Northridge and Kobe earthquakes, as well as in new laboratory configurations, show the need to predict cleavage after extended plastic cracking. Fitness-for-service rather than traditional design and maintenance necessitate quantitative predictions. Those from micromechanisms revealed by microfractography provide insight, but are limited and require so much microstructural data as to be impractical. (An addition to this armamentarium is a model presented here for the reduction, with decreasing grain size, in the lower shelf work due to height differences and twisting between adjacent cleavage facets and for the increase in lower shelf work due to increasing roughness during crack growth.)

Without a detailed micromechanics model for the alloy at hand, quantitative prediction requires fracture mechanics to predict cleavage in large structures from tests on small specimens. Outstanding problems include the effects of strain reversals and aging. Another is fracture after extended plastic crack growth, or delayed cleavage. A statistical model is developed in terms of the probability of cleavage of an individual grain and the number of contiguous grains required for macrocleavage. This latter parameter appears to require a micromechanics analysis for the very low probabilities of macrocleavage that may be of practical interest.

Introduction

The Problems

Traditional design and maintenance, based on marginally related tests, on experience, and on factors of safety, may not apply to new situations. Fitness-for-service design and maintenance requires more accurate predictions. These can be made in either of two ways or a combination of them: from a knowledge of the microstructure and micromechanisms, or from fracture mechanics, pioneered by Irwin. Fracture mechanics is based on the idea that often the stress and strain fields in an annular region around the crack tip in both a structure and a small specimen can be characterized by a single number or function. In linear elastic fracture mechanics, the number is the strain energy release rate G or the stress intensity factor K. If this characterization is complete, initial crack growth within the K-controlled annular region of a large structure occurs when K in the structure reaches the critical value K_c at which crack growth begins in the small laboratory specimen. Contributions to both the micromechanism and fracture mechanics ways of predicting cleavage cracking are given here.

Lower-shelf grain boundary ligament tearing work. At sufficiently low temperatures, cleavage (normal separation across a (100) crystallographic plane in a BCC structure) predominates over yielding followed by cracking from hole nucleation, growth, and linkage. G_c reaches a "lower shelf" at which it no longer decreases with decreasing temperature. The work to cleave grains themselves is very small, so most of the work of macrocrack growth arises from plastic tearing of the ligaments left by microcleavage cracks that are offset or twisted across the grain boundary between them. An approximate model is used to find the average work per unit crack area due to this mechanism. Whereas the strength of steel increases with decreasing grain size, this lower shelf work decreases. It is compared with observed values.

Fracture after extended plastic crack growth. In a number of cases in the Northridge and Kobe earthquakes cracks initiated at welds and grew part way across the flanges of I-beams by ductile micromechanisms as slant fractures, before cleavage cracking intervened unexpectedly (1). Similar delayed transitions had already been observed, e. g. in tension of through-cracks in A710 steel plates by Reuter (see (2)).

Other unexpected cleavage fractures. Other kinds of unexpected transitions to cleavage should be mentioned, even though they cannot be treated here. Strain followed by aging can cause unexpectedly high transition temperatures (3), (4). Even strain reversals alone can cause a transition to cleavage, as has been known for a long time. See also (5).

Background

Tipper (6), (7) showed not only the contrasting limiting micromechanisms of fracture by cleavage and by hole growth, but also that cleavage required subsequent plastic deformation. The importance of plastic blunting and triaxial stress in initiating cleavage on overloading a fatigued pre-crack was

George R. Irwin Symposium on Cleavage Fracture
Edited by Kwai S. Chan
The Minerals, Metals & Materials Society, 1997

recognized by Ritchie, Knott, and Rice (8). Troshchenko et al. (9) showed that for various pressure vessel steels tested at low temperature, the critical stress intensity factor for cleavage was reduced by a factor of 1 to 1.5 if the crack was actively growing in fatigue.

The variety of microcrack initiation and growth mechanisms, as revealed by electron microscopy of sections and fracture surfaces, has led to a large number of analytical models which provide insight. But analysis may not be sufficiently detailed. Numerical methods must be used with care to avoid mesh size effects. They allow more accurate predictions than analysis, but can require so much microstructural data and computation as to be impractical for most large structures. Statistics may be required. As a few examples from these active fields, see Tvergaard and Needleman (10), Xia and Shih (11), and Besson and Pineau (12).

Lower Shelf Grain Boundary Ligament Tearing Work

For an estimate, idealize the grains in the path of a macrocrack as an array of square cylinders, normal to the macrocrack. Assume each grain cleaves in a single facet. Assume these facets have various orientations so that after neighboring grains cleave there remain grain boundary ligaments perpendicular to the plane of the macrocrack. Assume these ligaments separate by shear deformation and cracking normal to the plane of the macrocrack. Choose the ligament height in either of two ways: as a constant fraction of the grain size (the quasi-planar model), and as determined by statistically meandering, out-of-plane crack growth (the growing roughness model).

A Quasi-Planar Model for Tearing Work

Geometry. Assume that associated with each grain are one twist ligament and one ligament of constant height, as shown in Fig. 1.

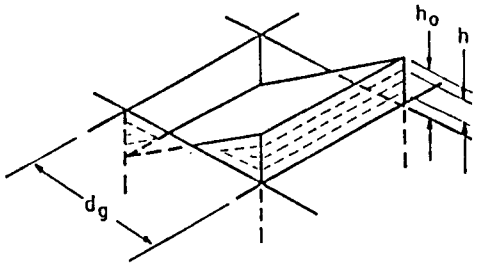


Figure 1: Decreasing ligament heights h left by crack opening displacements.

Ligament Limit Load. The mechanics is much simplified by assuming plane strain of a non-hardening, rigid-plastic metal of shear strength k, where $k = TS/\sqrt{3}$. Assuming pure shear along a ligament of initial height h_0 and length d_g along one grain gives an upper bound to its limit load: kh_0d_g. Some idea of the accuracy of this limit load can be obtained by considering two cases for which the slip line fields are known. First, for a singly face-grooved plate under through-thickness shear, the deformation field consists of a central fan and rigid region, and two arcs each leading to constant-state regions. The limit load is $0.978\ kh_0d_g$, nearly that for opposing grooves giving a single slip plane (13). Second, for a ligament left by cleavage cracks that have grown past each other by a total of 1.42 times their height, the resulting short beam still has a limit load of $0.62\ kh_0d_g$ (14).

Ligament Crack Growth. The above analyses, and experience with shear cracks in punching operations, show that the mode of deformation will be much more sensitive than the limit load to whether cleavage cracks at different heights have grown just past or just short of each other. Furthermore in Mode II shear, cracks tend to grow toward the tensile side of the direction of maximum shear strain. This is the reason clearance is needed between the punch and the die in punching operations. With no clearance, or if the cleavage cracks have already grown past each other, the shear cracks will not meet but will form a compressive ligament that markedly increases the ductility. In spite of these complications, for simplicity assume that the deformation across the ligaments is in pure shear as the ligament shrinks by a combination of shear deformation and coplanar microcrack growth, as shown by a cross-section in Fig. 2. Denote the growth of the compression side of a shear crack, a_c, per unit shear displacement w by $a_{c,w}$. Then a shear displacement w reduces the ligament from h_0 to

$$h = h_0 - w\left(1 + 2a_{c,w}\right) \quad . \tag{1}$$

Values of $a_{c,w} = 3.6$ correspond to punching operations (15). With transverse shear of singly face-cracked plates, an average value of 10 was found using 3 mm ligaments, but that average was taken from a plot showing sharply accelerating crack growth as might be expected in Mode II with a plastic zone giving a progressively flatter strain gradient ahead of the crack (13). Furthermore the ductility is likely to be much higher at a 20 micron scale, which is comparable to the size and spacing of the holes and second phase particles that determine macroscopic ductility. Pending more detailed studies, values of $a_{c,w} = 0$ to 3.6 seem plausible.

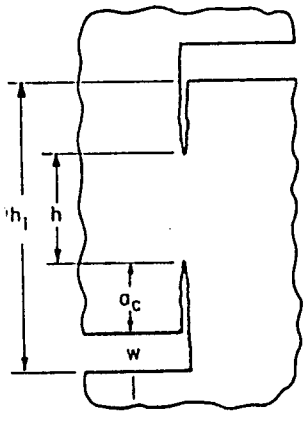


Figure 2: Cross-section with ligament height h for shear displacement w and compression-side crack growth a_c.

Analysis for Bridging Forces and Tearing Work. For the constant height ligament, find the force F_h in terms of the displacement w by using Eq. 1:

$$F_h = kd_g h = kd_g h_0 \left[1 - \left(\frac{w}{h_0}\right)\left(1 + 2a_{c,w}\right)\right] . \qquad (2)$$

Integration with respect to the displacement gives the work:

$$W_h = \int F_h dw = kd_g h_0 \int \left[1 - \left(\frac{w}{h_0}\right)\left(1 + 2a_{c,w}\right)\right] dw$$

$$= \frac{kd_g h_0^2}{2\left(1 + 2a_{c,w}\right)} . \qquad (3)$$

For the twist ligament the force falls off due to reductions in both the height and the width of the ligament. Assume that h_0/d_g is small enough so that the Mode III component is negligible compared to the Mode II:

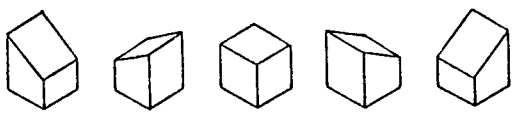
$$F_T = \frac{1}{2} kd_g h_0 \left[1 - \left(\frac{w}{h_0}\right)\left(1 + 2a_{c,w}\right)\right]^2 . \qquad (4)$$

Integration again gives the work:

$$W_T = \int F_T dw = \frac{kd_g h_0}{2} \int \left[1 - \left(\frac{w}{h_0}\right)\left(1 + 2a_{c,w}\right)\right]^2 dw$$

$$= \frac{kd_g h_0^2}{6\left(1 + 2a_{c,w}\right)} . \qquad (5)$$

The total work per facet is the sum of those from Eqs. 3 and 5, giving a numerical coefficient of 2/3. From it the critical stress intensity factor K_{Ic} and in turn the plastic zone size r_{Ic} can be found to see if the assumption of localized ligament plasticity is reasonable, as follows. For the discrete facet angles of Fig. 3, choose the ratio h_0/d_g by noting that the maximum angle before transition to another (100) cleavage plane is 45°. Assigning equal spherical angles to the five facets gives an average angle from the normal for the outer four facets of about 33°, or $h_0/d_g = 0.32$.



1 2 3 4 5

Orientation number in Table I.

Figure 3: Discrete crystallographic orientations of grains.

As discussed above, take $a_{c,w} = 0$ to 3.6 . Take TS/E = 0.005 at 77 K, and a grain diameter rather arbitrarily of d_g = 20 μm . Then for plane strain,

$$K_{Ic} = \sqrt{\frac{EG_c}{1 - \nu^2}} = \sqrt{\frac{2}{3} \frac{Ekh_0^2 / d_g}{\left(1 + 2a_{c,w}\right)\left(1 - \nu^2\right)}}$$

$$= \sqrt{\frac{2}{3} \frac{E\left(TS/\sqrt{3}\right) d_g (0.32)^2}{\left[\left(1 + 2 \times (0 \text{ to } 3.6)\right)\right]\left(1 - 0.3^2\right)}} = E\sqrt{\frac{(TS/E) d_g}{13 \text{ to } 109}} ;$$

$$K_{Ic} =$$

$$207{,}000\sqrt{\frac{0.005\left(20 \times 10^{-6}\right)}{13 \text{ to } 109}} = (6.3 \text{ to } 18)\ MPa\ m^{1/2} . \qquad (6)$$

This is low by a factor of 2 to 5 compared to the values of K_{Ic} = 25 to 42 MPa $m^{1/2}$ for ABS-C and ASTM 302B and 533B1 steels reported at 77 K (16). As mentioned in the introduction from (9), part of this factor may be due to a factor of up to 1.5 between the resistance to cleavage with blunting at a fatigued pre-crack, for which K_{Ic} is found, and that with quasi-steady growth of a macrocrack, analyzed here.

To complete the analysis before turning to a better estimate of the roughness of the crack, find the plastic zone size:

$$r_{Ic} = \frac{1}{2\pi}\left(\frac{K_{Ic}}{TS}\right)^2 = \frac{1}{3\pi\left(1 - \nu^2\right)} \frac{E}{\sqrt{3}TS} \frac{h_0^2 / d_g}{\left(1 + 2a_{c,w}\right)}$$

$$= \frac{(0.32)^2}{3\pi\sqrt{3}\left(1 - 0.3^2\right)\left[1 + 2 \times (0 \text{ to } 3.6)\right]} \frac{E}{TS} d_g$$

$$= \frac{1}{145 \text{ to } 1190} \frac{d_g}{0.005} = (0.17 \text{ to } 1.4) d_g . \qquad (7)$$

By itself, this plastic zone size would only marginally justify the assumption that plastic flow does not spread out of the ligaments.

A Growing Roughness Model for Tearing Work

Geometry. In contrast to the previous section, assume that the ligament heights are not a fixed fraction of the grain diameters, but are determined by statistically meandering out-of-plane crack growth. As discussed above, use the five discrete grain orientations shown in Fig. 3, with four having angles of 33° to the normal. Assigning the orientation numbers to an array of squares in front of an initial crack using a random number generator gave the orientations of Table I.

The Kinematics of Bursts of Microcracks. At Applied Stress 1 and as shown in Table Ia, Bursts 1-5 are triggered simultaneously by the forming of flat facets that are extensions of the macrocrack (the long edge to the left in Table Ia). Simultaneous bursts are arbitrarily numbered from top to bot-

Table Ia Randomly Chosen Orientations of Fig. 3, and Facet Corner Heights through Burst 5, in units of h_0. Starts of bursts denoted by ⊢; ends by →.

Col.	Burst	Row: 1	2	3	4	5	6
1		4	3	1	2	2	2
2	1	0 0 / ⊢3 / 0 0	5	1	4	1	3
3		1	4	1	5	4	2
4	2	0 0 / ⊢3 / 0 0 / 0 0	1	3	5	2	5
5		3 / 0 0	2	2	5	1	2
6		5	1	5	5	3	3
7		4	1	4	4	3	3
8		4	2	5	1	4	2
9		5	2	4	1	1	3
10		2	3	4	3	5	3
11	3	0 0 / ⊢→3 / 0 0	1	2	2	2	1
12		4	2	5	4	3	3
13	4	0 0 / ⊢→3 / 0 0	4	2	4	1	2
14		4	3	3	1	2	4
15	5	0 0 / ⊢→3 / 0 0	4	4	5	2	3
16		5	2	3	2	2	5
17		1	5	5	3	4	5
18		4	3	2	1	3	3
19		1	4	3	2	4	1
1		4	3	1	2	2	2

Table Ib Randomly Chosen Orientations of Fig. 3, and Facet Corner Heights through Burst 23, in units of h_0. Paths shown for Bursts 6 through 23.

Col.	Burst	Row: 1	2	3	4	5	6
1	8, 20	0 -2 -2 -2 / ⊢→4 ⊢→3 / 0 -2 -2 -2	1	2	2	2	
2	19	0 0 | 0 2 / 3 ⊢→5 / 0 0 | 0 2 / 2 2	1	4	1	3	
3	14	1 / 0 ↥ 0	4	1	5	4	2
4		0 0 / 3 / 0 0 / 0 0	1	3	5	2	5
5		3 / 0 0 / 0 2	2	2	5	1	2
6	9	⊢→5 / 0 2	1	5	5	3	3
7	11	0 -2 / ⊢4 / 0 -2 / 0 -2	1	4	4	3	3
8		4 / 0 -2	2	5	1	4	2
9	12	0 2 / ⊢→5 / 0 2 / -2 -2	2	4	1	1	3
10	15	2 / 0 ↥ 0	3	4	3	5	3
11		0 0 / 3 / 0 0 / 0 -2	1	2	2	2	1
12	6	⊢→4 / 0 -2	2	5	4	3	3
13	16	0 0 | 0 -2 -4 -4 / 3 ⊢→4 2 / 0 0 | 0 -2 -2 ↑ -2	4	1	2		
14	7, 18	0 -2 -2 -2 -2 -2 / ⊢→4 ⊢→3 3 / 0 -2 -2 -2 -2	1	2	4		
15	17	0 0 | 0 -2 -2 -4 / 3 ⊢→4 → 4 / 0 0 | 0 -2 -2 -4 / 0 2	5	2	3		
16	10	⊢→5 / 0 2	2	3	2	2	5
17	23	1 1 / ⊢→1 / -1 -1	5	5	3	4	5
18	13, 21	0 -2 -2 -2 / ⊢→4 ⊢→3 / 0 -2 -2 -2	2	1	3	3	
19	22	1 1 / ⊢→1 / -1 -1	4	3	2	4	1
1	8, 20	0 -2 -2 -2 / ⊢→4 ⊢→3	1	2	2	2	

Table Ic Randomly Chosen Orientations of Fig. 3 and Facet Corner Heights through Burst 24, in units of h_0. Path shown for Burst 24.

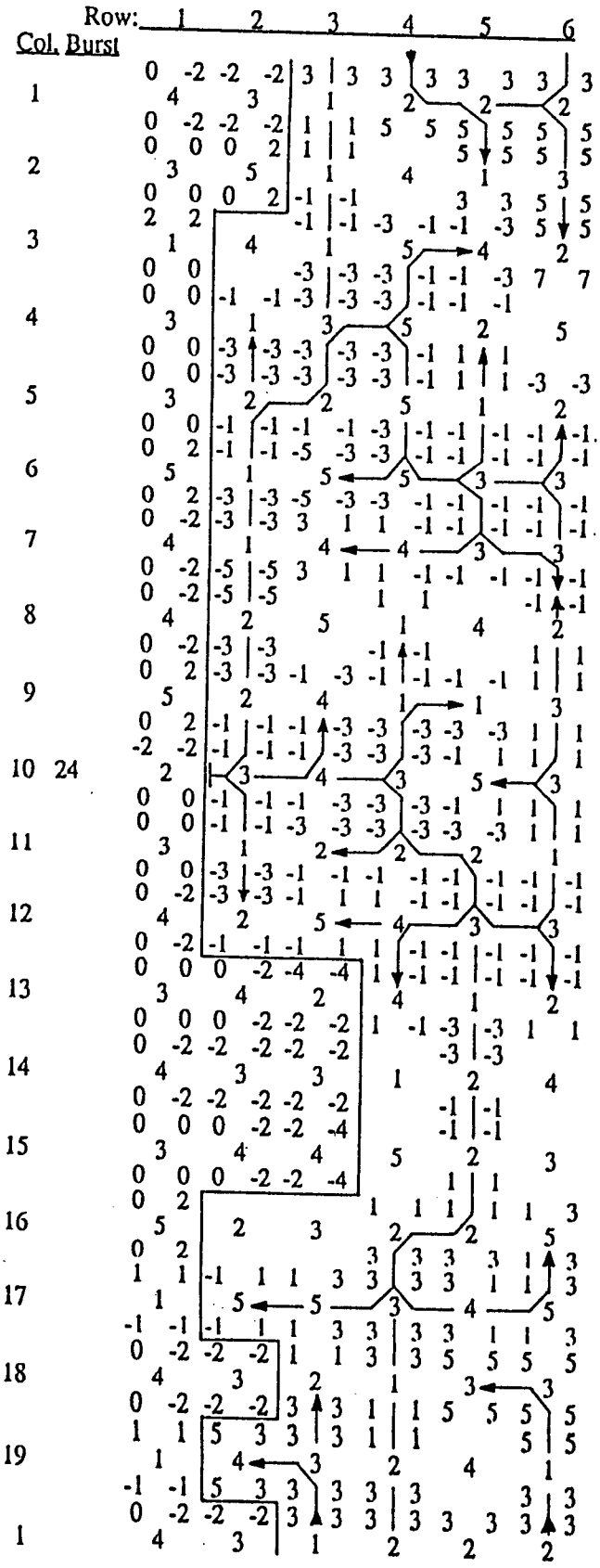
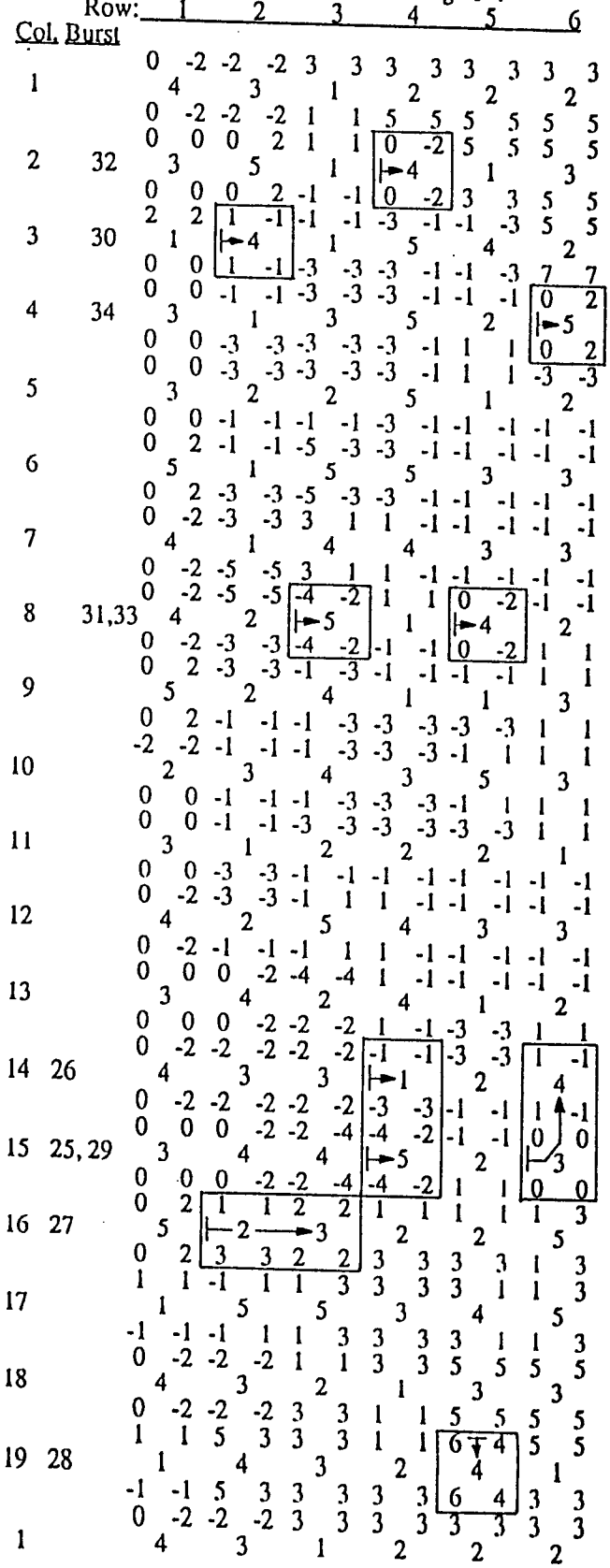


Table Id Randomly Chosen Orientations of Fig. 3, and All Post-cracking Facet Corner Heights, in units of h_0. Paths shown for Bursts 25 through 34.



tom. Burst 1 forms only a single facet. Whichever of Grains 1,4 and 1,5 cracked first in Burst 2, the other would follow unstably in the same burst due to the increased local stress concentration. Bursts 3-5 are all single-facet bursts. The elevations of each corner of the facets, here all zero, are given in units of $h_0 = 0.32\ d_g$ (see Fig. 1). An isometric view of the facets after final fracture is given in Fig. 4. The heights are scaled down by a factor of two to reduce the hiding of low facets by high ones. Also given for each column of the advancing crack front are the numbers of the bursts that began there. Thus, for example, the origin of Burst 2 can be located and its path followed.

For insight at higher applied stresses, choose facet formation intuitively, based on a few general principles:

a) Grains crack from a neighboring facet, not by initiation due to average stress.

b) Facets form with increasing difficulty from neighbors with orientations that are i) parallel, ii) that differ only by a pitch misorientation (i. e. by a tilt of the growth

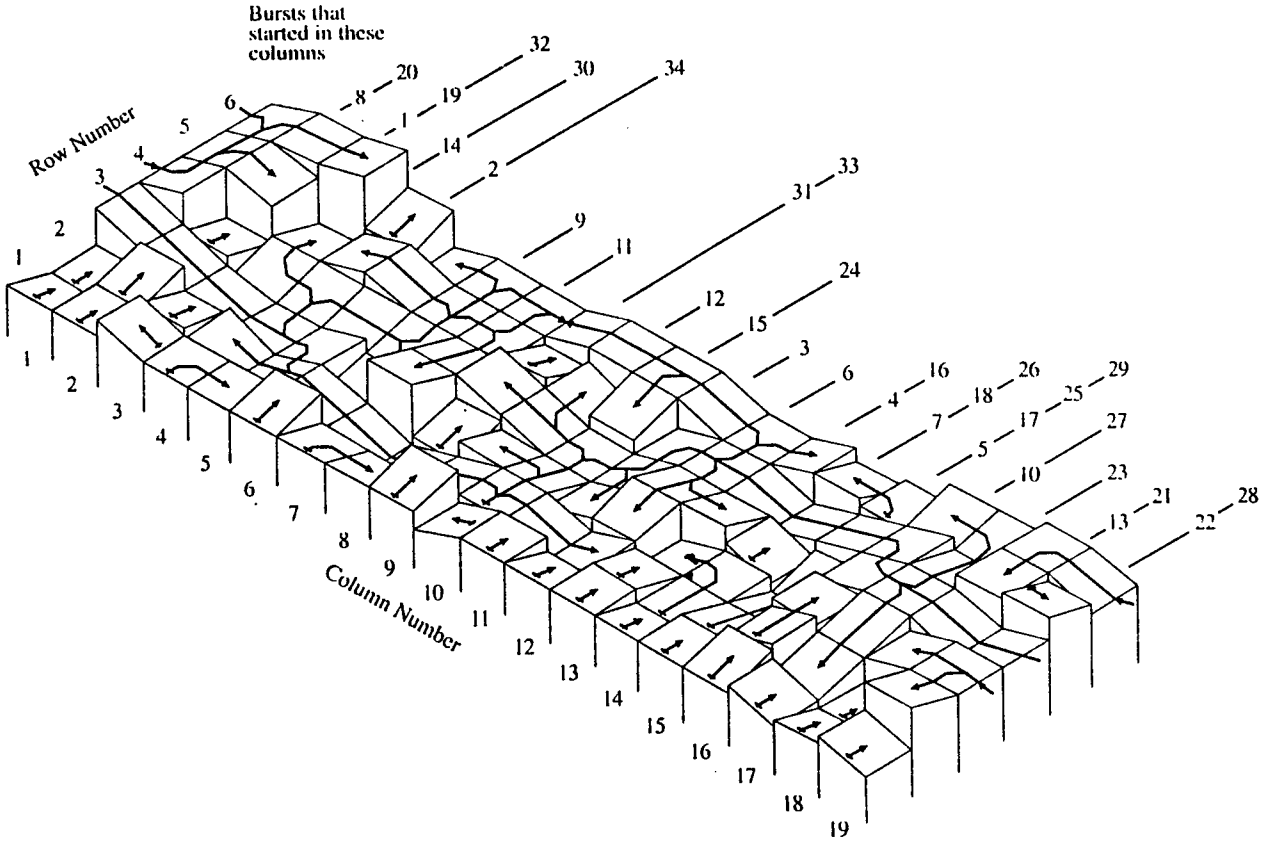


Figure 4: Isometric view of cracked facets, showing burst paths. Vertical distances reduced by a factor of two to reduce hiding.

axis), or iii) that differ by a twist misorientation (i.e. by a tilt about the growth axis).

c) Facets form more easily at re-entrant corners of the macrocrack and less easily along tunnels, especially at the ends of tunnels.

d) Cracking is less likely near a shear ligament left between neighboring facets at differing heights, where the ligament must be sheared or torn off to complete macrocrack growth.

Further choices are discussed as they arise in bursts at progressively higher applied stresses. Later, these choices could be quantified, as in numerical analyses for initiation and later instability of coplanar cracks (17), (18). For stresses, a three-dimensional boundary integral method (19) might be used.

The remaining bursts are shown in Tables Ib-d. The step-by-step description in the Appendix is essential for showing the variety of decisions that must be made in choosing the next facet to crack. These decisions determine the heights of ligaments between facets and the path of each burst. Such decisions would have to be built in to any computer model. The reader who is willing to take the facet heights and paths of Tables Ib-d as given can proceed here with their interpretation. Table 1b shows the bursts that would have occurred on reaching an intermediate level of applied stress. The bursts are short, and only a few lateral crack paths occur. The last facets to form, at Columns 19 and 17 of Row 1, were the first ones that required crossing a twist boundary. The next facet to form, starting Burst 24, must cross a combined pitch and twist boundary, and requires a higher applied stress.

Burst 24, shown in Table Id, forms most of the facets. It tends to branch both from flat facets and from strings of grains with identical orientations. It finds strings of up to nine facets joined by only pitch boundaries, and follows them for long distances, especially laterally. Neighboring facets formed by different long branches may have large ligament heights between them. The largest, at 9 times the height change h_0 across a half-ligament, occurs in Column 3 between Rows 5 and 6.

The remaining bursts, shown in Table 1d, would probably occur below the applied stress of Burst 24 because the facets are relatively isolated. The bursts might be more dependent on the ligament structure than was taken into account here.

Analysis for Bridging Forces and Tearing Work. The initial height differences $\Delta h_1/h_0$ for the ligaments left by the crack configuration of Table Id are summarized in Table II, along with the twists (differences in twist height, $T \equiv \Delta h_T/h_0$ defined in Fig. 5). The bridging forces and also the shearing work can be found by geometry from the results for the separate constant height and twist ligaments of Fig. 1, using the shapes of the progressively shrinking ligaments shown by the dashed lines in Fig. 5. The resulting coefficients for ligament force and work are normalized and multiplied by factors of 2 and 6, respectively, so that most of them are integers:

$$C_F \equiv \frac{F_1}{kd_g h_0/2} \; ; \; C_W \equiv \frac{W}{\dfrac{kd_g h_0^2}{6(1+2a_{c,w})}} \; . \qquad (8)$$

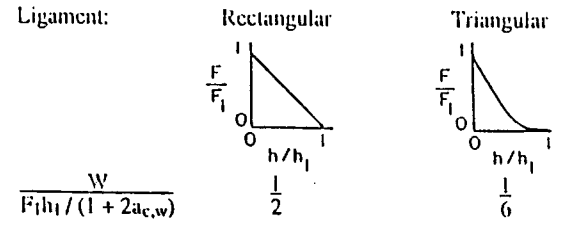
These coefficients are given in Table III in terms of the initial heights and twists of ligaments. For $|h_1/h_0| = 2$ and above, $C_F = 2|h_1/h_0|$, independent of twist. For all height differences, $C_W = 3|h_1/h_0|^2 + |T|^2$, as found empirically from Table III.

For insight into the maximum height of a ligament that will yield before it pulls out the matrix to which it is attached, compare, to the hardness of the matrix, the average stress tha the ligament exerts over the area of the grain it subtends. The

Table II Ligaments, from Facet Heights of Table Id

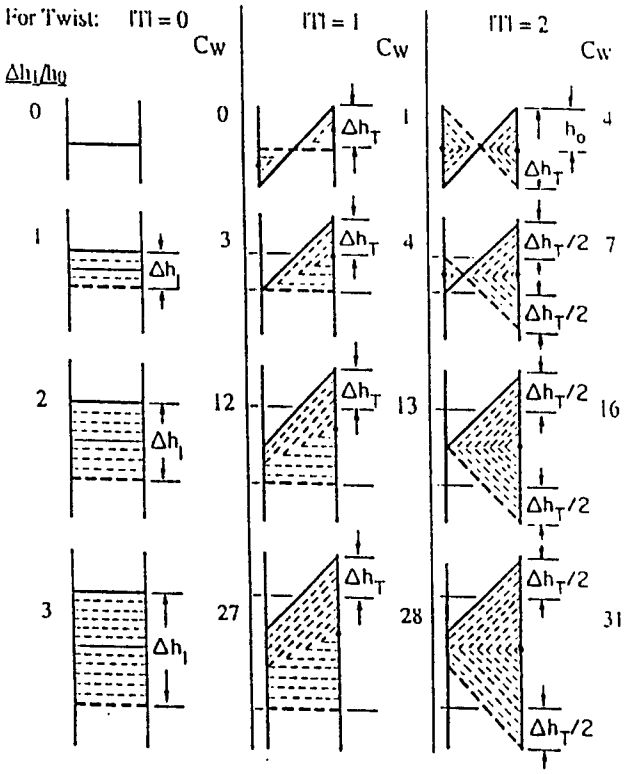
Initial height differences across ligaments, $\Delta h_1/h_0$, positive if upward with increasing row or column number, and twists across ligaments, $T = \Delta(\delta h_T/h_0)$, positive if ccw in the same directions.

Col. along-	Row from- leading edge of crack 1	2	3	4	5	6
	0, 1	-6,-1	0, 0	0, 0	-2,-1	0, 0
1	0, 0	0, 0	4,-1	2, 2	0, 0	0, 0
	1,-1	3,-1	0, 0	-6, 1	0, 0	0, 0
2	0, 0	0, 0	-2,-1	0, 1	6,-1	1, 1
	2, 0	-1, 2	0, 0	-1,-2	-5, 1	0, 0
3	1,-1	0, 1	-1,-1	-1, 1	0, 0	9, 1
	0, 0	-1,-1	0, 0	0, 0	1,-1	-6,-1
4	0, 0	-2,-1	-1, 1	0, 0	1, 1	0,-1
	0, 0	0, 0	0, 0	0, 0	0, 0	-4, 1
5	0, 0	-2, 1	0, 0	-1,-1	1,-1	-2, 2
	1,-1	0, 0	-3,-1	0, 0	0, 0	0, 0
6	0, 0	-4,-1	-3, 1	0, 0	0, 0	0, 0
	-2, 2	0, 0	6, 2	2, 2	0, 0	0, 0
7	0, 0	-2,-1	7, 1	0, 0	0, 0	0, 0
	0, 0	0, 0	-5,-2	1,-1	0, 1	0, 0
8	0, 0	-2, 1	0,-1	2,-1	0, 1	2, 1
	2,-2	0, 0	1, 2	0, 0	0,-1	0, 0
9	0, 0	-4, 1	1,-1	1,-1	0, 0	3, 1
	-3, 1	0, 0	0, 0	0, 0	3,-1	0, 0
10	-1, 1	0,-1	0, 0	0, 0	2, 0	0, 0
	0, 0	0, 0	-1,-1	0, 0	-3, 1	0, 0
11	0, 0	-2,-1	0, 2	0, 0	0, 0	2,-2
	-1, 1	0, 0	1,-1	1, 1	0, 0	0, 0
12	0, 0	0, 1	1,-1	0, 0	0, 0	0, 0
	1,-1	0, 1	-4, 1	0, 0	0, 0	0, 0
13	0, 0	0, 0	-1, 1	4,-1	-1,-1	2, 2
	-1, 1	-1,-1	0, 0	-1,-1	0, 0	-1, 1
14	0, 0	0, 0	0, 0	0,-1	0, 2	3,-1
	1,-1	1, 1	-1, 1	0,-1	0, 0	0,-1
15	0, 0	0, 0	0, 0	0, 0	2, 1	0,-1
	1,-1	2,-1	5,-1	4, 1	0, 0	2,-1
16	0, 0	0, 1	0,-1	0, 1	0, 0	-1,-1
	0, 1	-3,-1	0,-1	0, 0	-1. 1	0, 0
17	0,-1	-1, 1	0, 0	0, 0	0, 0	0, 0
	0, 1	-2, 1	-1, 1	0, 0	3,-1	3, 1
18	0, 0	0, 0	4, 1	0,-2	3, 1	0, 0
	2,-1	6, 1	0, 0	0, 0	0, 1	0, 0
19	0,-1	5, 1	0, 0	-1, 1	4,-1	0,-1
	0, 1	-6,-1	0, 0	0, 0	-2,-1	0, 0
(same as before Column 1)						



a) Force reduction with ligament height.

Define: $T \equiv \frac{\Delta h_T}{h_0}$ and $C_W \equiv \frac{W}{kd_g h_0^2 / [6(1 + 2a_{c,w})]}$



b) Shapes of decreading ligaments; worksof separation, C_W.

Figure 5: Calculating the work of separation.

indentation hardness is about three times the tensile strength, or $3\sqrt{3}$ times the shear strength k . Each ligament subtends one-quarter of the area of the two neighboring grains, or $d_g^2/2$. The maximum height for ligament yield is found by equating the limit loads:

$$khd_g = 3\sqrt{3}kd_g^2/2 \;\; ; \;\; h \approx 2.6d_g \quad . \qquad (9)$$

Taking $h_0/d_g = 0.32$ from the discussion following Eq. 5 gives $h_{mx}/h_0 = 7.8$. Only one ligament in Table II, that in

Table III Bridging Force Coefficients C_F , and Tearing Work Coefficients C_W , as Functions of Initial Height Differences $|\Delta h_1/h_0|$ and Twists $|T| \equiv |\Delta h_T/h_0|$ (see Fig. 3).

$$C_F \equiv \frac{F_1}{kd_g h_0/2} \;\; ; \;\; C_W \equiv \frac{W}{\frac{kd_g h_0^2}{6(1+2a_{c,w})}} \quad . \qquad (8)$$

|T|:	0		1		2	
	C_F	C_W	C_F	C_W	C_F	C_W
$\|\Delta h_1/h_0\|$						
0	0	0	1	1	2	4
1	2	3	2	4	2.5	7
2	4	12	4	13	4	16
3	6	27	6	28	6	31
4	8	48	8	49	8	52

$C_F = 2|\Delta h_1/h_0|$ for $|\Delta h_1/h_0| \geq 2$; $C_W = 3|\Delta h_1/h_0|^2 + |T|^2$.

Table IV Initial Bridging Forces per Ligament, $F_1/(kh_0d_g/2)$, from Table II using Table III, and Row-Average of those Forces per Ligament.

Col. along-		Row from- leading edge of crack 1		2		3		4		5		6
		1		12		0		0		4		0
1	0		0		8		4		0		0	
		2		6		0		12		0		0
2	0		0		4		1		12		2	
		4		2.5		0		2.5		10		0
3	2		1		2		2		0		18	
		0		2		0		0		2		12
4	0		4		2		0		2		1	
		0		0		0		0		0		8
5	0		4		0		2		2		4	
		1		0		6		0		0		0
6	0		8		6		0		0		0	
		4		0		12		4		0		0
7	0		4		14		0		0		0	
		0		0		10		2		1		0
8	0		4		1		4		1		4	
		4		0		2.5		0		1		0
9	0		8		2		2		0		6	
		6		0		0		0		6		0
10	2		1		0		0		4		0	
		0		0		2		0		6		0
11	0		4		2		0		0		4	
		2		0		2		2		0		0
12	0		1		2		0		0		0	
		2		1		8		0		0		0
13	0		0		2		8		2		4	
		2		2		0		2		0		2
14	0		0		0		1		2		6	
		2		2		2		1		0		1
15	0		0		0		0		4		1	
		2		4		10		8		0		4
16	0		1		1		1		0		2	
		1		6		1		0		2		0
17	1		2		0		0		0		0	
		1		4		2		0		6		6
18	0		0		8		2		6		0	
		4		12		0		0		1		0
19	1		10		0		2		8		1	
		1		12		0		0		4		0
(same as before Column 1)												
Row-averaged normalized initial ligament forces			2.0		2.8		3.0		1.8		2.1	1.7
	0.3		2.7		2.5		1.5		2.3		2.8	

Col. 3 between Rows 5 and 6, exceeds this value. Thus in general, the assumption of an elastic matrix seems justified. The resulting normalized bridging forces were given above in Table IV.

The tearing work per ligament is found similarly by applying the coefficients of Table III to the ligaments of Table II. The results are presented in Table V, including the average work per ligament for each half-row.

Table V Tearing Work per Ligament,

$$C_W \equiv W \Big/ \frac{kd_g h_0^2}{6\left(1+2a_{c,w}\right)} ,$$

and Row-Averaged Tearing Work per Ligament.

Col. along-	Row from- leading edge of crack 1	2	3	4	5	6
	1	109	0	0	13	0
1 0	0	49	16	0	0	0
	4	28	0	109	0	0
2 0	0	13	1	109	4	
	12	7	0	7	76	0
3 4	1	4	4	0	244	
	0	4	0	0	4	109
4 0	13	4	0	4	1	
	0	0	0	0	0	49
5 0	13	0	4	4	16	
	4	0	28	0	0	0
6 0	49	28	0	0	0	
	16	0	112	16	0	0
7 0	13	148	0	0	0	
	0	0	79	4	1	0
8 0	13	1	1	4	13	
	16	0	7	0	1	0
9 0	49	4	4	1	28	
	28	0	0	0	28	0
10 4	4	0	0	12	0	
	0	0	4	0	28	0
11 0	13	4	0	0	16	
	4	0	4	4	0	0
12 0	1	4	0	0	0	
	4	1	49	0	0	0
13 0	0	4	49	4	16	
	4	4	0	4	0	4
14 0	0	0	1	4	28	
	4	4	4	1	0	1
15 0	0	0	0	13	1	
	4	13	76	49	0	13
16 0	1	1	1	0	4	
	1	28	1	0	4	0
17 1	4	0	0	0	0	
	1	13	4	0	28	28
18 0	0	49	4	28	0	
	13	109	0	0	1	0
19 1	76	0	4	49	1	
	1	109	0	0	13	0
(same as before Column 1)						
Row-averaged work per ligament	6.1	16.8	19.4	10.2	9.7	10.7
	0.5	13.2	16.5	5.3	12.1	19.6

Aside from an increase in the work per unit area from that in the first row, the results are too variable to draw any conclusions about roughness increasing with crack growth. As a first approximation, however, take the normalized work per ligament to be 15. Then the critical stress intensity factor can be estimated following Eq. 6:

$$K_{Ic} = \sqrt{\frac{EG_c}{1-\nu^2}} = \sqrt{\frac{E}{\left(1-\nu^2\right)} \frac{15kd_g h_0^2 / \left(d_g^2/2\right)}{6\left(1+2a_{c,w}\right)}}$$

$$= E\sqrt{\frac{5}{\sqrt{3}} \frac{(TS/E)(0.32)^2 d_g}{\left(1-0.3^2\right)\left[1+2\times(0\text{ to }3.6)\right]}} = E\sqrt{\frac{(TS/E)d_g}{3.1\text{ to }25.2}}$$

$$= 207{,}000\sqrt{\frac{0.005\left(20\times10^{-6}\right)}{3.1\text{ to }25.2}} = (13\text{ to }37)\text{ MPa m}^{1/2}. \quad (10)$$

Find the plastic zone size as with Eq. 7:

$$r_{Ic} = \frac{1}{2\pi}\left(\frac{K_{Ic}}{TS}\right)^2 = \frac{1}{2\pi\left(1-\nu^2\right)} \frac{5}{\sqrt{3}} \frac{E}{TS} \frac{h_0^2/d_g}{\left(1+2a_{c,w}\right)}$$

$$= \frac{5(0.32)^2}{2\pi\sqrt{3}\left(1-0.3^2\right)\left[1+2\times(0\text{ to }3.6)\right]} \frac{E}{TS} d_g$$

$$= \frac{1}{19.3\text{ to }159} \frac{d_g}{0.005} = (1.3\text{ to }10.3)d_g \ . \quad (11)$$

While this plastic zone size might seem too large for the assumption of a rigid matrix to be valid, bear in mind that this size is based on an abrupt crack front. Here most of the work is done in tearing ligaments that are behind the cleavage cracking, so there is a large process (Barenblatt-Dugdale) zone which decreases the strain concentration at the tip of the macrocrack.

Discussion of Ligament Tearing Model

This model of cleavage cracking illustrates a number of factors that must be taken into account in making predictions from micromechanisms. Item 4 also applies to making predictions with fracture mechanics.

1. Pitch misorientations have little blocking effect on cleavage cracking across grain boundaries. Twist misorientations have much stronger blocking effects, so microcracks tend to go around grains with twist boundaries.
2. Strings of pitch boundaries tend to conduct microcleavage over several grains in any direction.
3. Branching occurs most often from facets parallel to the macrocrack, but also from strings of similarly tilted facets.
4. The above mechanisms make macrocrack advance by microcracking essentially a three-dimensional process, not one of plane strain. Lateral microcracking means that in extrapolating small specimen data to large structures, the lateral and forward units of size must be treated differently. A similar necessity probably also applies in conventional K_{Ic} data for cleavage macrocracking that initiates in the blunted region formed ahead of a fatigue-sharpened pre-crack.
5. All of the tension in, and most of the work done on, ligaments left behind the microcracks is due to height differences between facets, not twist differences.

6. For the six rows ahead of the crack that were studied, only one ligament appeared strong enough to cause fully plastic flow in the adjoining matrix. Therefore a decohering zone as in the Barenblatt-Dugdale model, seems more realistic han a sharp crack tip as in typical fracture mechanics.
7. After a low value in the first row, the ligament work per unit area was more or less constant, and gave a stress intensity factor for crack growth of 13 to 37 MPa $m^{1/2}$. This is comparable to the K_{Ic} = 25 to 42 MPa $m^{1/2}$ mentioned after Eq. 6 for medium structural steels at 77 K (16). The agreement might be better yet if account were taken, as mentioned in the Inrtoduction, of the factor of 1 to 1.5 of K_{Ic} for initiation with blunting from fatigue-sharped precracks, over that for cleavage from actively growing fatigue cracks (9). These results tend to support the approximate model presented here. .
8. Equation. 6 shows that if grain size did not affect the hardness, the critical stress intensity should decrease as the square root of the grain size. The increase in hardness with decreasing grain size would somewhat reduce this effect.
9. Deeper crack growth and more attention to the delay of crack growth by bridging effects would be required to study the growth of roughness, its fractal dimension, and its effect on increasing the crack growth resistance. At the same time, the crack front would have to be lengthened so that the roughness would have the space to spread laterally. Chevron markings, e. g. (7), (20), would require modeling the increased tearing resistance at the surface of a plate with a tunneling through-crack. Increased roughness would probably require more attention to the forces by and work on the ligaments, and to the matrix plasticity near them. This would seriously complicate the model.
10. Longer crack fronts would increase the probability of macrocrack initiation, but apparently would not affect the resistance to growth.
11. Relatively minor improvements in the model include hexagonal grains, more pitch and twist misorientations, river markings that form steps, and quantitative criteria for microcrack nucleation at twist boundaries and internal and external corners.

Statistics for Cleavage Cracking after Extended Plastic Crack Growth

The Problem

As discussed in the Introduction, a number of cases have been observed, both in practice and in the laboratory, in which macrocracking of plates or flanges of I-beams at first occurred by quasi-steady hole growth, and then while still stable after growing 20 to 200 mm, abruptly changed to cleavage fracture with subsequent instability. Several phenomena may contribute to such transitions, as follows. a) Microcracks reinitiate from grain boundary crossing points when they encounter grain boundaries with twist misorientations, e.g. (21). b) There is a distribution of grain sizes, with the larger cleaving at lower stress. c) The stress and strain distributions ahead of the crack are not steady, but evolve with time in several ways. Finite elements solutions have suggested an increasing ratio of normal to flow stress (11). d) As a grain sweeps past the tip of a growing crack, it encounters an increasing and then a falling tendency to cleavage, limiting the chance for a neighbor crack to form until the peak in tendency to cleavage becomes less acute. e) The strain gradients ahead of the crack may flatten out, giving a larger volume for cleavage nucleation and easier microcleavage growth. A rough model of this possibility by superimposed quasi-static HRR fields for power-law hardening metals gave logarithmically decreasing strain gradients in front of a crack (22). Decreasing strain gradients were also observed and modeled in thin sheets (23). (Even without cleavage intervening, this process leads to increasing crack growth rates per unit far-field applied displacement. In a large enough structure, the elastic compliance of the surroundings eventually gives instability, after which rate effects promote cleavage.)

A Model

We consider here yet a different mechanism of cleavage intervention during stable, hole growth cracking, as follows. When such a crack grows in quasi-steady state through a field where the propensity for cleavage is locally constant, with a small fraction p_g of the grains cracking, there is an increasing chance that the stable macrocrack will have encountered a large enough patch of such pre-cracked grains that macrocleavage ensued. The engineer may need to limit the probability of that event, P_{clv} , to the order of parts per million as the stable crack sweeps through an area A of the structure. That is, the probability of survival without macrocleavage, $P_{srv} = 1 - P_{clv}$, should be less than unity by only a few parts per million. A precise statistical analysis of this problem is a daunting task, so consider a rough approximation for insight. Assume all grains have the same cross-sectional area A_g and the same probability p_g of microcleaving under the given quasi-steady conditions near the crack tip.

Analysis

The probability of finding a critical patch of area A_p of grains each of area A_g all with the critical microcleavage orientation is $p_g^{A_p/A_g}$, if the probabilities for the grains are independent of each other. As an area A is swept out by a crack growing in quasi-steady state, it will encounter A/A_g different patches. The probabilities that these patches will all have critical orientations will not be independent of each other, because if one patch is entirely of critical grains, its neighbor one grain away will consist of many of the same grains and be more likely to be critical than a random patch. On the other hand, a neighbor patch with no grains in common is likely to be uncorrelated, except possibly for metallurgical reasons. Thus take the number of independent patches encountered in an area A to be between A/A_g and $A/A_p = (A/A_g)/(A_p/A_g)$. The probability P_{srv} of survival to area A is the engineering objective. It is the probability of no critical cleavage patch in the area A :

$$P_{srv} = \left(1 - p_g^{A_p/A_g}\right)^{\left(A/A_g\right)\left(A_g/A_p \text{ to } 1\right)}$$

$$= e^{\left(A/A_g\right)\left(A_g/A_p \text{ to } 1\right)\ln\left(1-p_g^{A_p/A_g}\right)} . \qquad (12)$$

(Because the logarithmic factor is negative, Eq. 12 is an exponential distribution in the area A swept out. It is related to, but not one of, the extreme value distributions.) For a given set of parameters p_g, A_p, and A_g, as $A/A_g \to \infty$, $P_{srv} \to 0$, as expected. Likewise for a given A, as the probability of cleavage in one grain decreases, or the number of grains in a patch increases, P_{srv} increases toward unity.

For applications, it appears to be worth solving Eq. 12 for the area swept out for a given probability of survival:

$$\frac{A}{A_g} = \left(1 \text{ to } \frac{A_p}{A_g}\right) \frac{\ln P_{srv}}{\ln\left(1 - p_g^{A_p/A_g}\right)} \quad . \qquad (13)$$

With the approximation for small x that $\ln(1-x) \approx -x$,

$$\frac{A}{A_g} = \left(1 \text{ to } \frac{A_p}{A_g}\right) \frac{-\ln P_{srv}}{p_g^{A_p/A_g}} \quad . \qquad (14)$$

For a crack growing across the flange of a large I-beam, A might be 20x200 mm = 4 10^3 mm^2. For a 20 μm grain size, with $A_g = 4\ 10^{-4}$ mm^2, this would give $A/A_g = 10^7$. With a probability of survival of $P_{srv} = 0.999999$, $-\ln P_{srv} = 10^{-6}$. Since the relative cleavage-sensitive patch area of practical interest turns out to be less than $A_p/A_g = 10$, from Eq. 14 the material-, stress-, and temperature-dependent patch probability must be less than $p_g^{A_p/A_g} = 10^{-12}$. There is no way that such low probabilities can be determined directly from experiments. Rather, the following procedure might be developed:

a) From microfractography of stably tearing plates, measure the fraction of grains cleaved, p_g. Do these have orientations near critical?

b) From fractography and from micromechanics including dynamics and rate effects, estimate the patch size (area of contiguous cracked grains) needed to trigger macroscopic cleavage for the conditions of the stable macrocrack.

c) Use those numbers, along with the desired probability of survival, in Eq. 14 to estimate the allowable area swept out before macroscopic cleavage fracture.

For example, if one can determine from fractography that at a given temperature the probability of cleavage of an individual grain is no more than $p_g = 10^{-3}$; if a patch size of $A_p/A_g = 4$ is required for macrocleavage; and if the probability of survival is to be at least 0.999999, Eq. 14 indicates that the crack must not grow beyond $A/A_g =$ (1 to 4) 10^6. This means that for a grain size of 20 μm, the area swept out by the hole growth micromechanism of fracture must be limited to $A < 400$ to 1600 mm^2, a rather severe restriction for steel structures. Other values are presented in Table VI.

Table VI Area Swept, A/A_g, from Eq. 14 for Various Probabilities of Global Survival, P_{srv}, Critical Patch Sizes A_p, Grain Areas A_g, and Grain Cleavage Probabilities p_g.
For test specimens typically $A/A_g = 10^5$
For 20 by 200 mm crack growth in a structure, $A/A_g = 10^7$

Patch Size, A_p/A_g	p_g	Global survival probability, P_{srv} 0.999999999	0.999999	0.999	0.5
3	0.01		1	1e3	0.7e6
			3	3e3	2.1e6
	0.001		1e3	1e6	0.7e9
			3e3	3e6	2.1e9
	0.0001		1e6	1e9	0.7e12
			3e6	3e9	2.1e12
4	0.01	100e-3	100	100e3	0.1e9
		400e-3	400	400e3	0.3e9
	0.001	1e3	1e6	1e9	0.7e12
		4e3	4e6	4e9	2.8e12
	0.0001	10e6	10e9	10e12	7e15
		40e6	40e9	40e12	28e15
7	0.01	100e3	100e6	100e9	
		700e3	700e6	700e9	
	0.001	1e12	1e15	1e18	
		7e12	7e15	7e18	
	0.0001	10e18	10e21	10e24	
		70e18	70e21	70e24	

Discussionof Statistics of Delayed Cleavage

The limited numbers of specimens available for laboratory tests dictate that survival probabilities only of the order of $P_{srv} = 0.1$ - 0.9 can be observed. With ordinary-sized specimens, plastic cracks typically grow only over 10^5 grains. The phenomenon of delayed cleavage due to statistical effects is encountered only if critical patch sizes are about 3 grains, and the probability of single-grain cleavage is of the order of $p_g = 0.01$.

For a structure with plastic crack over 10^7 grains and an assured survival probability of even only 0.999, if the critical patch size were 3 grains, p_g would have to be dropped to 0.001, or 0.003 for a 4-grain patch. These values of p_g would be very tedious to measure on the fracture surfaces of specimens. To assure $P_{srv} = 0.999999$, for the 3-grain patch p_g would have to be dropped to 0.0001, or to 0.001 for a 4-grain patch. These results are very sensitive to critical patch size, so a method for determining it is essential, if high assurance is to be given against the statistical mechanism of delayed cleavage in large structures. The difficulty of determining the critical patch size seems to mean that for some time to come, the design of structures for high reliability must remain subjective, aided by extrapolation using various statistical distribution functions.

Conclusions

Models have been developed for two of many different aspects of cleavage fracture of polycrystalline BCC metals. For the lower shelf, where the macrocrack growth work per unit area arises from plastic tearing of the ligaments between cleavage cracks, a model is developed in terms of the grain size and orientation, and the difficulty of cracking across grain boundaries with a twist misorientation, in contrast to a pitching misorientation. The resulting microcrack paths are tortuous and branching. The work required to tear ligaments due to height differences between adjacent facets determines the critical stress intensity factor for crack growth. For an alloy with a given hardness, the value of this critical factor decreases as the square root of the grain size. It is comparable to those observed for cleavage crack initiation after blunting of a fatigued pre-crack. The model macrocrack was grown by only six grain diameters, insufficient to estimate the growth of roughness, any fractal dimension, and the effect of roughness on work of fracture.

For delayed cleavage that interrupts quasi-steady plastic crack growth, a model was developed for cleavage by encountering a rare agglomeration of grains with orientations favoring cleavage. A relation was worked out and tabulated for the probability of survival as a function of the area swept out by the plastic cracking, the grain size, the probability of cleaving an individual grain, and the number of contiguous grains to trigger macrocleavage. The single-grain probability might be accessible by microfractography of specimens tested under service conditions, but the critical number of contiguous grains seems to require fracture micromechanics.

It is hoped that these two models will add to the understanding that has grown from the great achievements at two stages of George R. Irwin's career: his introduction of fracture mechanics in terms of the critical work per unit area of fracture, and his more recent attention to fracture surfaces.

Acknowledgments

This work was supported in part by the Office of Basic Energy Sciences, Department of Energy, Grant DE-FG02-85ER13331, and in part by the Lockheed Idaho Technology Company, Subcontract K97-177064. This support, and discussions with A. S. Argon, D. M. Parks, and S. Ganti are all very much appreciated.

References

1. M. Toyoda, "How Steel Structures Fared in Japan's Great Earthquake", Welding Journal, December 1995, 31-42.

2. F. A. McClintock, "Reduced crack growth ductility due to asymmetric configurations", Int. J. Fracture, 42(1990), 357-370.

3. M. G. Dawes, M. G., "Significance of Locally Intensified Strain Ageing to the Fracture Toughness of Welded Steel Structures", Fracture Mechanics, 26th Volume, ASTM STP 1256, ed. W. G. Reuter, J. H. Underwood, and J. C. Newman (Philadelphia, PA: American Society for Testing and Materials, 1995), 350-360.

4. F. A. McClintock, Y.-J. Kim, and D. M. Parks, "Tests for Fully Plastic Fracture Mechanics of Plane Strain Mode I Crack Growth", Fracture Mechanics, 26th Volume, ASTM STP 1256, ed. W. G. Reuter, J. H. Underwood, and J. C. Newman (Philadelphia, PA: American Society for Testing and Materials, 1995), 199-222.

5. F. A. McClintock, K. L. Kenney, S. Jung, W. G. Reuter, and D. M. Parks, "Asymmmetric, Fully Plastic Crack Growth Mechanics and Tests for Structures and Piping", Development, Validation, and Application of Inelastic Methods for Stuctural Analysis and Design, PVP - Vol. 343, ed. R. F. Sammataro and D. J. Ammerman, (New York: American Society of Mechanical Engineers, 1996), 153-167.

6. C. F. Elam Tipper, "Fracture of Mild-Steel Plate", Iron and Coal Trades Review, 47(1948), 829-834.

7. C. F. Tipper, "The Fracture of Metals", Metallurgia, 39(1949), 133-137.

8. R. O. Ritchie, J. F. Knott, and J. R. Rice, "On the Relationship between Critical Tensile Stress and Fracture Toughness in Mild Steel", J. Mech. Phys. Solids, 21(1973), 395-410.

9. V. T. Troshchenko, V. V. Pokrovsky, and P. V. Yasniy, "Unstable Fatigue Crack Propagation and Fatigue Crack Fracture Toughness of Steels", Fatigue Fract. Eng. Mater. Struct., 17(1994), 991-1001.

10. V. Tvergaard and A. Needleman, "An Analysis of the Brittle-Ductile Transition in Dynamic Crack Growth", Int. J. Fracture, 59(1993), 53-67.

11. L. Xia and C. F. Shih, "Ductile Crack Growth - III. Transition to Cleavage Fracture Incorporating Statistics", J. Mech. Phys. Solids, 44 (1996), 603-639.

12. J. Besson and A. Pineau, "Numerical Simulation of Ductile Rupture: Analysis of Experimental Scatter and Size Effect", Recent Advances in Fracture, ed. R. K. Mahidhara, A. B. Geltmacher, P. Matic, and K. Sadananda (Warrendale PA: The Minerals, Metals, & Materials Society, 1997), 125-136.

13. F. A. McClintock and M. Clerico, "The Transverse Shearing of Single-Grooved Specimens", J. Mech. Phys. Solids, 28(1980), 1-16.

14. A. P. Green, "A Theory of the Plastic Yielding Due to Bending of Cantilevers and Fixed-Ended Beams. Part I", J. Mech. Phys. Solids, 3(1954), 1-15.

15. T. Lyman, ed., Forming, Metals Handbook Vol. 4, (Metals Park, OH: American Society for Metals, 1969), 33.

16. W. T. Matthews, Plane Strain Fracture Toughness (K_{Ic}) Data Handbook for Metals, Report AMMRC MS 73-6, AD 773-673, (Watertown MA: Army Mechanics and Materials Research Center, 1973).

17. F. A. McClintock and F. Zaverl, Jr., "An Analysis of the Mechanics and Statistics of Brittle Crack Initiation", Int. J. Fracture, 25(1979), 107-118.

18. F. A. McClintock and H. J. Mayson,. "Principal Stress Effects on Brittle Crack Statistics", Effects of Voids on Materials Deformation, ed. S. C. Cowin and M. M. Carrol, (New York: American Society of Mechanical Engineers, 1976), 31-45.

19. F. Xu, A. S. Argon, M. Ortiz, and A. Bower, 1995, "Development of a Variational Boundary Integral Method for the Analysis of Fully Three Dimensional Crack Advance Problems", Computational Mechanics "95, ed. S. N. Atluri, G. Yagawa, and T. A. Cruse, (Berlin: Springer Verlag, 1995), v2, 2874-2889.

20. M. E. Shank, A Critical Survey of Brittle Failure in Carbon Plate Steel Structures other than Ships, Welding Res. Council Bulletin Series, No. 17, (New York: The Welding Society, 1954).

21. J. R. Low, Jr., "A Review of the Microstructural Aspects of Cleavage Fracture", Fracture, ed. B. L. Averbach, D. K. Felbeck, G. T. Hahn, and D. A. Thomas, (Cambridge Mass.: M. I. T. Press and New York: John Wiley and Sons, 1959), 68-90.

22. F. A. McClintock and A. H. Slocum, "Predicting Fully Plastic Mode II Crack Growth from an Asymmetric Defect", Int. J. Fracture, 27(1985), 49-62.

23. F. A. McClintock, "Ductile Fracture Instability in Shear", J. Appl. Mech., 25(1958), 581-588.

Appendix. Detailed Choices of Facet Cracking Sequences and Paths

Applied Stress 2. Bursts 6-13 form by pitching (not twisting) from the original crack front on grains with Orientations 4 and 5. The bursts can be followed not only on Table I, which gives facet heights numerically, but also on the isometric view of Fig. 4. Meandering arrows with bars and heads show the starts and finishes of bursts. The first of the pitching group, Bursts 6 and 7, start between flat facets on either side. Bursts 8-10 start next to flat facets on one side. The two-facet Burst 11 starts next to the oppositely pitched facet from Burst 9. Burst 12 starts in from the original crack tip to avoid the crossing of the twist boundary that would be required if it were to extend Burst 11. Burst 13 is isolated, the last of the pitch facets along the original crack front. Like many of the bursts starting in the first row, its tendency to go deeper, although facilitated by a pitch boundary, is retarded by the tunnel effect.

At about the same applied stress, Burst 14 starts from the tip of a peninsula that leaves two re-entrant corners in the crack, sandwiched between Facets 1,2 and 1,4. It forms laterally by pitching from the pair of flat facets on its right. Burst 15 starts by pitching from the one flat facet on its right. Cracking now extends into the second row, still by pitching, perhaps from the flat facets in Columns 13 and 15, as Bursts 16 and 17. Burst 17 continues on the coincident facet beyond the first. (In Fig. 4, its end is hidden). This leaves flat Grain 2,14 as a peninsula to start the three-facet Burst 18, the first two facets coincident and the third joined laterally by the pitching in behind the facet left by Burst 16. The remaining bursts starting in the second row by pitching are Bursts 19-21. Except for the deep Grain 4,15, any further burst must involve twisting. Even if Grain 4,15 did crack, further growth would be blocked by twist boundaries.

For a simple approximation to a crack that is laterally infinite, assume periodic boundary conditions, so that Column 20 would be the same as Column 1. Then the first row Grain 1,19 is on a two-grain peninsula and is taken to be the first to form a facet by twisting, as Burst 22. Grain 1,17 is a peninsula with two facets on one side, and goes next, by twisting as Burst 23. Grain 2,19 is a peninsula that might crack laterally by twist from either of the flat facets on its sides. (Cracking from its end would require twist and pitch.) Here, this site was not assumed to crack, but if it did, the major burst that follows would have the same pattern as the burst discussed below, although it would have occurred partly in a different order and the heights between its facets and those from earlier bursts would have been very different. A similar situation holds for the re-entrant Grain 2,17. Aside from these, cracking any of the re-entrant corners of the macro crack at Grains 2,3, 2,12, and 2,16 would involve combined pitching and twisting, so an increase in applied stress is needed.

Applied Stress 3, Burst 24. Assume the next facet is formed by twisting from a flat facet in the first row or to a flat grain in the second. The choice makes little difference to the pattern, because any of them will spread laterally to the others by simple pitching. As discussed above, the choice will change the height differences across ligaments between the new facets and those from earlier bursts. The choice of twisting to form the flat Facet 2,10 from 1,10 is made arbitrarily. From this facet, cracking branches out in three directions, making Burst 24 a major one. Follow the left-hand branch first. Cracking proceeds along Row 2 in a series of pitches through Facet 2,4. En route at Facet 2,5 it branches deeper to the coincident Facet 3,5 and then laterally to Facet 3,4, where another branching occurs. The left-hand branch continues to Column 1 and due to the periodic boundary conditions reappears at Column 19. After a branch to one facet on each twig, it is finally stopped by twist boundaries. All grains to its left are cracked except for the remaining Grain 2,3.

From the branch at Facet 3,4 the inward branch leads immediately to the row of coincident Facets 4,3 through 4,6 and back out to Facet 3,6. A set of four flat facets, 5,6, 5,7, 6,6, and 6,7, is now exposed with only a pitch boundary. Although it is at the corner of a blunt tunnel, assume these flat facets crack Then pitching from Facet 5,7 leads back out to the main crack along the coincident pair 4,7 and 3,7. The tunnel broadens further with the formation of Facet 5,3, the pair of Facets 5,5 and 5,4, and Facet 6,5.

Now return to the branch at Facet 2,10, which started Burst 24. The right-hand string of Facets 2,11 and 2,12 completes the advance of the macrocrack through most of Row 2. Tunneling inward is broadened by the coincident pair 3,10 and 3,9. Further tunneling to Facet 4,10 would probably lead to broadening to either side through the coincident string 3,11 through 5,11 and the L-shaped coincident branch 4,9, 4,8, and 5,9.

This leaves Grain 5,10 as a unit peninsula. Its cracking next was overlooked until the paper was in proof. Instead, the crack was taken to spread to the coincident pair of flat facets 5,12 and 6,12. Then it spread back along Row 6 by a string of pitch boundaries, cracking the peninsula of Grain 5,10 on the way. Had Grain 5,10 been taken to crack first, it would have dropped its height and those of the four Facets 6,8 through 6,11 by $2h_0$. It would have left ligaments of $2h_0$ between Facets 6,7 and 6,8, and between 6,11 and 6.12. As will be seen below, these changes would have a negligible effect on the overall result.

Meanwhile, the coincident pair of flat Facets 5,12 and 6,12 cracks from the coincident triplet 3,11 through 5,11. Facet 3,12 and the coincident pair 4,12 and 4,13 are now at the tip of a peninsula. Once they have cracked, lateral spreading can occur to Facets 5,13 and 6,13.

Now comes a critical stage. The set of four coincident orientations of Grains 5, 14, 5,15, 5,16, and 4,16 are taken to provide a tunnel between uncracked grains. Cracking to form flat Facet 4,17 and then the coincident pair 3,17 and 2,17 breaks open the far end of the tunnel. The opening is broadened by cracking deeper to Facet 5,17 and the coincident pair 6,17 and 6,16. The macrocrack grows deeper by cracking along Row 4 to the coincident set (with periodic boundary conditions) 4,19, 4,1, 5,1, 6,1. Branch cracking off this string leads to completing Burst 24, finally with the coincident pair of flat Facets 6,18 and 5,18.

Applied Stress 3, Bursts 25-34. The remaining facets form as shown in Table 1d. Because they are so isolated, most would probably have cracked below the applied stress for Burst 24. Facet 4,15 did not crack when Facet 3,15 did, although it involved only a pitch misorientation, because it was at the tip of a tunnel. The tunnel has now disappeared, so Facet 4,15, hidden in Fig. 4 and here called Burst 25, formed independently sometime during Burst 24. Facet 4,14 is now isolated, so it is likely to crack from its twist orientation to Facet 3,14, as Burst 26. Facet 2,16 is now so exposed that it is likely to form through a pitch-twist misorientation, and continue with Facet 3,16 across a simple twist misorientation, as Burst 27. Burst 28 forms from a twist misorientation from the side. Twist misorientations limit the stress for starting and continuing Burst 29 as Facets 6, 15 and 6, 14.

Its isolated position is likely to cause Burst 30 at Facet 2,3 below the applied stress 3, even though a twist-pitch boundary must be crossed. Likewise with Burst 31 at Facet 3,8 and Burst 32 at Facet 4,2. Facet 5,8 is assumed more likely to form from the crack side with a twist-pitch misorientation than by a twist misorientation on one side. Burst 34 at Facet 6,4 would involve pitch-twist misorientations from either side.

THE ROLE OF PLASTIC DEFORMATION IN CLEAVAGE CRACK PROPAGATION AND ARREST IN FERRITIC STEELS

Edwin Smith
Manchester University/UMIST, Materials Science Centre, Grosvenor Street, Manchester, M1 7HS, United Kingdom

Abstract

The paper reviews and presents new perspectives, related to the role of plastic deformation in the propagation and arrest of cleavage cracks in ferritic steels. Thus the paper addresses, amongst others, the following issues: (a) The interpretation of K_{Ia}, the crack arrest toughness, (b) Temperature versus mechanics related arrest criteria, (c) The role of plasticity in the context of cumulative versus non-cumulative modes of crack extension, (d) The role of shear lips in cleavage crack propagation, (e) The relation between the upper shelf for initiation toughness and the maximum temperature at which a crack is able to propagate by the cleavage mechanism, in the context of the ASME K_{IC} and K_{Ia} curves.

Introduction

It is an accepted fact that steels, as used in engineering structures, contain stress concentrations, which may take a variety of forms. Thus a stress concentration may be a design feature, it may arise as a consequence of welding, or it can be a region of defective material, for example, a region containing a particularly high density of inclusions. Such stress concentrations are directly responsible for probably the most challenging problem that has confronted technologists working with steel structures: catastrophic or brittle failure. When steel engineering structures have failed, the resulting investigations have shown that failure is always associated with a stress concentration, with an unstable fracture being initiated in the vicinity of the concentration (often referred to as the initiation stage), followed by the propagation of a crack (usually by a predominantly cleavage mechanism) into the surrounding structure (usually referred to as the propagation stage). Because it is impracticable to eliminate stress concentrations, although their severities are minimized by adopting careful design principles, reliable welding techniques, adequate stress-relieving procedures and by rejecting particularly defective material, the only rational way of minimizing the risk of a catastrophic failure occurring is to prevent either the initiation of an unstable fracture, or alternatively, assuming that initiation is possible, to limit

George R. Irwin Symposium on Cleavage Fracture
Edited by Kwai S. Chan
The Minerals, Metals & Materials Society, 1997

the extent of crack propagation.

The well established principles of fracture mechanics, founded upon the pioneering work of George Irwin, are used to prevent the onset of unstable fracture (fracture initiation), with the critical size of defect that can be tolerated being related to the applied loadings, and appropriate inspection procedures then being used to ensure that the sizes of actual defects that are present within a structure are less than the critical defect size. When this approach is adopted, there are several factors that should be recognized, for example: (1) it must be recognized that fracture resistance depends on material composition, and consequently in a welded structure the behaviour of weld metal and heat-affected zone metal, as well as the surrounding parent material, must be considered; (2) the interaction between defects in a defective material or the interaction between a defect and a macroscopic stress concentration; (3) residual stresses if there is a likelihood of a structure not having been adequately stress-relieved; (4) allowance must be made for dynamic loading effects if there is a likelihood of such loading occurring in service; (5) consideration must be given to the possibility of a material's properties changing in service, for example, by strain ageing or nuclear irradiation; and (6) allowance must be made for any slow crack growth by fatigue or stress corrosion that might facilitate crack instability. Despite these complicating factors, prevention of unstable fracture initiation by the use of fracture mechanics principles has become a well-established procedure for guarding against a catastrophic failure.

Nevertheless, and primarily because of the complicating factors outlined above, for situations where a possible failure might have extremely serious consequences, it is desirable not to rely entirely on the prevention of fracture initiation. In such circumstances, attempts should be made to develop a back-up position so that extensive propagation of a crack can be prevented, i.e. make sure that we can guarantee crack arrest, allowing for the fact that initiation might occur. Although appreciable effort has been devoted to understanding the phenomenon of crack arrest and, in particular, cleavage crack arrest, the level of understanding is nowhere near the same as that with regard to initiation, due in large part to the obvious complications arising from the dynamical nature of the propagation process. If propagation and arrest were to be better understood, greater emphasis would be given to crack arrest in structural integrity assessments, since the author believes that the existing concentration of attention on the prevention of fracture initiation is due, in some part, to the fact that initiation is reasonably well understood, rather than because of a logically reasoned argument based on the desirability of preventing initiation instead of propagation.

Having therefore argued the case for consideration to be given to the issue of crack propagation and arrest, particularly in situations where a possible failure might have extremely serious consequences, the objective of the paper is to review and present new perspectives, related to the role of plastic deformation in the propagation and arrest of cleavage cracks in ferritic steels; this objective is consistent with the stated aims of this symposium which honours the contributions of George Irwin to the subject. To provide a framework for the considerations, the paper uses the results from an important research programme conducted by the Electric Power Research Institute (EPRI) and Combustion Engineering (CE).

Key Results from the EPRI-CE

Programme

The EPRI-CE experimental programme[1] was based on the testing of unirradiated A533B Class I plate material. The side-grooved moment modified compact tension (MMCT) test specimens (Figure 1) were loaded separately by a set of moment arms to simulate pressure type loadings, and a split wedge to simulate thermal loadings.

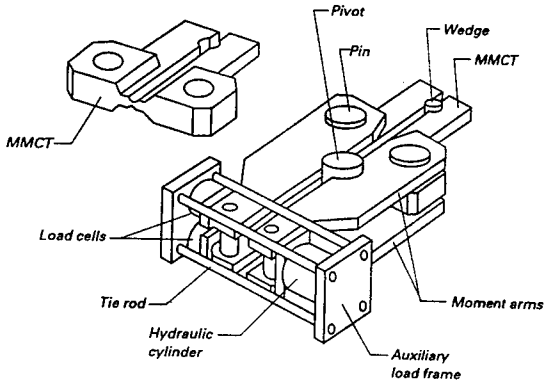


Figure 1. The MMCT test configeration.

Each specimen was chilled at the initial pre-crack end, and was heated at the crack arrest end so as to produce an increasing toughness gradient in the material along the crack path. The test section was ~ 5 cm thick by ~30 cm wide and was ~ 27 cm long, the general stress level acting on the section being ~ 0.3 x the material's tensile yield stress.

Though the number of tests conducted was limited, the specimens were extensively instrumented. Dynamic analysis results, based on crack velocity experimental data, show that a crack, following the onset of crack extension, propagates into the specimen so fast that the bulk of the specimen is unable to respond to the cracks's presence, while detailed observations of the specimen fracture surfaces showed that crack propagation proceeded by predominantly a cleavage mechanism with crack arrest occurring prior to any crack tip blunting. There was little evidence of shear lip formation prior to arrest (remember that the specimens are side-grooved), though the arrested crack front showed some curvature. Because the bulk of the specimen does not have time to respond to the crack's presence prior to arrest, the instantaneous K_I at arrest is much lower, approximately half as much in some cases, than the $K_I = K_I^{ST}$ which is computed via an analysis that is based on the final deformed static state of the cracked specimen. The deformation of the specimen continues as it responds to the presence of the arrested crack (the specimen "rings up"), and this causes the stress intensity K_J to increase to a value which does relate to the final deformed state. If the crack tip parameter does not attain the appropriate initiation value prior to the specimen's peak response, there will be no re-initiation. However, if the initiation value is attained, the crack re-initiates and further crack extension occurs. This type of "immediate" re-initiation, which is associated with inertia effects and with reflected waves returning to the crack tip, occurs very soon (some ms) after arrest.

Noting that the RT_{NDT} of the material is -29°C, the results obtained from the relevant tests in the programme are shown in Table I. Though the first propagation events are seemingly not connected with shear lips and ductile ligaments, it is difficult to draw the same conclusion as regards the second events[1].

Table I

Crack arrest and reinitiation results for the EPRI-CE experiments

Test	Crack jump to 1st arrest mm	Instantaneous K_I at 1st arrest K_I $MPa\sqrt{m}$	K_ISt at 1st arrest $MPa\sqrt{m}$	Temp at 1st arrest RT_{NDT} + °C	Dynamic cleavage reinitiation K_J $MPa\sqrt{m}$	Second crack jump mm	Temp at 2nd arrest RT_{NDT} + °C
6a	187	154	319	68	520	32	83
7a	175	143	273	64	445	29	89
8a	165	115	174	57	No reinitiation MAX K_j : 233	-	-
9a	180	143	297	67	385	29	83

The Role of Plastic Deformation During Cleavage Crack Propagation

As indicated in the preceding section, in the EPRI-CE experimental tests, the first propagation events are seemingly not associated with shear lips, and ductile ligaments, with crack propagation proceeding by predominantly a cleavage mechanism, and with crack arrest occuring prior to any crack tip blunting. The objective of this section is to show how these observations fall within Cottrell's categorization[2] of fracture modes and, in particular, to promote the view that such cleavage crack propagation can be viewed as a cumulative mode.

Cottrell categorized[2] fracture modes into two types: non-cumulative and cumulative. The former in its extreme form, is typified by the behaviour of a sharp slit in a fully ductile solid opening up under plane strain tension; the behaviour is represented by the injection of edge dislocations into the material from the tip along slip lines at about 45° to the tensile loading. The plastic notch widens as it deepens and each dislocation of Burgers vector b, injected into a slip line from the tip, contributes an increment $b/\sqrt{2}$ to both the width and depth of the notch. The plastic zones spread much more readily than the notch across the section, and we therefore have a "non-cumulative" situation in which each increment of growth of the plastic notch requires the injection of more dislocations into the slip lines, and these push the existing dislocations further across the section. The plastic zone increases in size and soon spans the whole load-bearing cross-section, so becoming general yield. We therefore have a stable situation provided the applied stress is below general yield levels. With the extreme form of non-cumulative fracture, the crack growth resistance is high (the slope of the J_R curve is very high) and is manifested by a crack tip opening angle (CTOA) of 90°.

Cottrell[2] also recognized that there are other modes of ductile fracture in which the notch can spread in an unstable manner without the general yield stress ever being reach. Such unstable growth can be understood by considering "cumulative" modes[2], so called because the contribution to fracture made by a dislocation moving through the material ahead of the crack, accumulates continuously with the distance travelled by

the dislocation. Cottrell provided two idealised simple examples: (a) sliding-off by a group of screw dislocations, and (b) plane stress necking by a group of edge dislocations, both in thin sheets. In both cases, the original group of dislocations needed to start fracture has merely to run through the material without adding more dislocations to its number, and the fracture is unstable; this behaviour contrasts sharply with the "non-cumulative" mode described in the preceding paragraph where the fracture is stable. Rapid ductile tearing in thin sheets, e.g. aluminium foil, occurs by such processes. In its extreme form, the J_R curve is perfectly flat when crack propagation proceeds via this mode.

More importantly, with regard to the present paper's considerations, Cottrell[2] also recognized that there are fractures in which microcracks or holes form in the plane of fracture ahead of a crack tip. Now it was concluded earlier that plane strain ductile fractures cannot grow indefinitely until the general yield stress is reached. However, this is no longer the case when the fracture is discontinuous because cumulative plane strain ductile or semi-ductile fracture modes are then possible, the essential requirement, formally, being that the dislocations should advance as edges in the plane of fracture; this involves a climbing motion of the dislocations, not glide, and results in the faces of the fracture plane moving apart. Cottrell therefore argued that plane strain ductile or semi-ductile fracture modes, such as that illustrated schematically in Figure 2 are able to operate in materials where the heterogeneity leads to the formation of microcracks or holes along the fracture path.

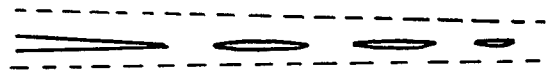


Figure 2. Discontinuous semi-ductile plane strain fracture.

When the discontinuous zone is sufficiently weak that it is able to rupture at stresses at which the surrounding material (i.e. outside the dotted lines in Fig. 2) is still elastic, the fracture is formally of the type described by climbing dislocations. The critical stress is p_*, the average stress at the leading edge of the rupture zone. This can be the stress required to form microcracks or be the stress needed to deform and rupture the bridges between the microcracks, whichever is the larger. In order for the discontinuous mode to operate, p_* must be less than the tensile yield strength σ_y of the material, or otherwise the cumulative mode will not be favoured at the expense of yield of the surrounding material (outside the dotted lines in Fig. 2).

We believe that cleavage crack propagation in the EPRI-CE experiments, at least with regard to the first propagation event, falls into Cottrell's cumulative category, and that p_* is likely to be the stress required to form cleavage cracks in preferentially oriented grains at the leading edge of the rupture zone, with the remaining grains also failing by the cleavage mechanism. Crack arrest is presumed to occur when the dynamic crack tip stress intensity factor K_I^{DYN}, in the limiting case where the crack velocity tends to zero, equates with the limit of the dynamic fracture toughness (K_{ID}), again as the crack velocity tends to zero (this limit can be viewed as the crack arrest

toughness): The dynamic fracture toughness reflects the difficulty of cleaving grains at the crack tip, and increases with increasing temperature because local plasticity at the crack tip is more likely as the temperature increases. The author has shown[3] that this arrest criterion can be expressed in the form $K_I^* = K_{ID}$ (å → o) where K_I^* is the reflectionless stress intensity factor and is given by the expression

$$K_I^* = \sqrt{\frac{2}{\pi}} \int_o^{\epsilon} \frac{p(\lambda)d\lambda}{\sqrt{\epsilon-\lambda}} \qquad (1)$$

where ϵ is the crack extension and $p(\lambda)$ is the tensile stress ahead of the crack tip when it is in its original position at time t = o. Although K_I^* is calculated on the basis of a static stress distribution, i.e. the stress ahead of the crack at the onset of crack extension, it has its origins in a dynamic theory[4-6], based on the assumption that wave reflection effects can be ignored. The author has applied this crack arrest criterion to a range of loading and geometry scenarios during the last five years. An important result arising from this work is the prediction[3] that the arrest crack length in a nuclear reactor pressure vessel, subjected to a hypothetical thermal shock event, can be markedly less than the arrest crack length predicted by the ASME Code crack arrest methodology[7]. This latter methodology is based on static linear elastic fracture mechanics principles, with a crack presuming to arrest when the crack tip stress intensity factor K_I^{ST} falls below the value K_{ID} (å → o), rather than dynamic based principles, as is implicit in the use of the reflectionless stress intensity factor procedure. The author's predictions are consistent with those obtained by Combustion Engineering[1] using a methodology (referred to as the CE-constrained static methodology) which has many similarities with the reflectionless stress intensity factor procedure, as has been demonstrated by the present author[3].

In making these comments regarding crack arrest, it should be emphasized that they refer to the first arrest event, and the possibility of re-initiation has to be addressed. As indicated in the preceding section, with the EPRI-CE experimental tests, at the initial arrest, the deformation of the specimen continues as it responds to the presence of the arrested crack, i.e. the specimen "rings up", and this causes the stress intensity K_I to increase to a value which does relate to the final deformed state. The static value K_I^{ST}, computed via an analysis that is based on the final deformed static state of the cracked specimen, can be as much as a factor of two in excess of the instantaneous K_I at arrest (see the results in Table I). It is important to appreciate that the high values of K_I^{ST} at arrest have nothing to do with a high toughness associated with the propagation and arrest event, but are merely a result of the specimen responding to the presence of an arrested crack.

As indicated in the preceding section, if the crack tip characterizing parameter does not attain the appropriate initiation value prior to the specimen's peak response, there will be no re-initiation, but if the initiation value is attained, then the crack re-initiates and further crack extension occurs. This type of "immediate" re-initiation, which is associated with inertia effects and with reflected waves returning to the crack tip, occurs very soon (some ms) after arrest. If credit is to be taken in an engineering assessment for the shorter crack length at arrest, as predicted by the reflectionless stress intensity factor procedure, then the question of possible reinitiation must be addressed, and there has been progress in this direction[1,8,9].

Interpretation of the Second Crack Propagation and Arrest Events

Cottrell[10] has recently argued that there might be two types of criterion for the arrest of a crack that is propagating by the cleavage mechanism, i.e. stress related and temperature related. The stress related criterion is based upon the matching of the local stress state at a crack tip with the so called crack arrest toughness (see comments in the preceding section), which can be determined via an ASTM standardised procedure[11]. In the light of the comments in the preceding section, the present author envisages that the first arrest events in the EPRI-CE experiments clearly fall within the stress related category.

The temperature related arrest criterion has been discussed in detail by Cottrell[10], building upon his considerations[2] described in the preceding section. Thus he refers to a material's crack arrest temperature, arguing that at this temperature a material has the ability to arrest a crack, irrespective of its length and the stress conditions, which is in contrast to the stress related arrest criterion, which involves both crack length and stress conditions. We will refer to this limiting crack arrest temperature as the material's CAT_* to distinguish it from the arrest temperature (CAT) in an actual experiment which will depend on the stress conditions and the crack length. Cottrell's picture is that small microcleavages form in the grains immediately ahead of the main propagating crack front and these microcleavages join up, but because they are at different levels and inclinations they leave behind initially unbroken ligaments, which thereafter deform plastically. The ligaments will be more pronounced near a free surface where failure proceeds ultimately by the shear lip mode. All these ligaments, which are left unbroken by the advancing brittle crack, support stresses up to their local yield stress which, although not at this stage raised by work hardening, can nevertheless be substanially increased by both plastic constraint and by the short times associated with this rapid fracture. They are therefore able to carry a substantial fraction of the service stress, thus diminishing the effective stress at the crack front, which is driving the crack forward. The higher is the temperature, the greater is the fraction of crack area occupied by these ligaments, and hence the greater is the stress which they are able to support. Cottrell argues that eventually there comes a temperature where the ligaments can support the entire applied stress, even if this is at the general yield level. There is then no stress available to drive forward the brittle crack front, which must therefore stop; Cottrell submits that this is the material's CAT_*. On this basis, he argues that there cannot be a fracture mechanics application to crack arrest at the CAT_* because there is no stress intensity available to drive the crack forward. It is the present author's view that, for a given material, the arrest toughness K_{ID} (å → o) increases with temperature fairly gradually at low temperatures, i.e. low K_{ID} (å → o), but then increases more rapidly as the temperature increases. If this rapid increase is essentially cliff-like, as the author anticipates, then we effectively have a limiting crack arrest temperature and this is CAT_*. This picture is consistent with Cottrell's view.

Against the background of these comments, the present author believes that the EPRI-CE experimental results may be interpreted such that the first arrest conforms to a stress criterion whereas the second arrest occurs at a temperature which approaches CAT_*. The results (compare the K values in columns 3 and 6 in Table I) also clearly demonstrate that arrest of a running cleavage crack and initiation of a running cleavage crack are

mechanistically different phenomena.

Maximum Temperature (CAT_*) for Arrest of a Propagating Cleavage Crack

It has been suggested in the preceding section that the second arrests in the EPRI-CE test programme[1] may be occurring at temperatures approaching CAT_*. Furthermore the results in Table I (last column) suggest that the temperature at which a crack can propagate by a cleavage mechanism may be in excess of RT_{NDT} + 90°C, noting that the maximum temperature associated with a second arrest is RT_{NDT} + 89°C. In reaching this conclusion, it should be noted that the extreme case in an application context, is likely to be where a long axial or long circumferential crack propagates in the through thickness direction in a pressure vessel, when shear lip effects are likely to be minimal. Against this background, it is worth observing that the EPRI-CE test specimens were side grooved (6mm deep with an angle of 90°C) so as to restrict shear lip formation, which would tend to give a high crack arrest temperature. However, set against this, the general applied stress level acting over the test section was only ~ 0.3x the material's tensile yield stress, and the simulated pressure loadings were displacement controlled.

The result that crack propagation by a cleavage mechanism is able to proceed in an unirradiated water cooled reactor pressure vessel steel (heat treated low alloy steel) at a temperature of ~RT_{NDT} + 90°C is not surprising, and is consistent with other crack arrest data[12,13] obtained from large test specimen programmes, which show that cleavage crack propagation can occur at temperatures in excess of RT_{NDT} + 110°C, albeit at high stress levels.

It is against the background of these experimental findings that we now discuss two other ways by which it has been suggested that an assessment might be made of a material's CAT_*: (a) the use of Robertson test or other similar experimental test data, and (b) the use of initiation experimental test data coupled with a comparison of the mechanical processes operative during the initiation and arrest of cleavage cracks.

In the Robertson crack arrest test[14], a wide plate is cooled (with the isothermal version of the test) to the temperature of interest, loaded in tension, and then a brittle running crack is initiated into the plate. The test provides direct evidence of whether or not the crack is able to arrest for a particular combination of temperature and applied transverse stress. There are other similar tests, such as the ESSO test and the Double Tension Test, which have similar characteristics. In using results from tests of these types to estimate the CAT_*, i.e. appropriate to the long crack - pressure vessel situation, it is important to ensure that the test specimens are sufficiently thick to minimize shear lip effects; it has been known for a long time that increasing thickness causes an increase in the CAT. It should also be noted that the CAT may be higher with a pneumatic loading situation (as with the long crack - pressure vessel situation), than the temperature obtained from Robertson-type tests, which are essentially displacement controlled. This means that a degree of caution should be exercised when applying the results from such tests to the pressure vessel situation. In this context it should be noted that a recent survey[13,15] of Double Tension Test results for a range of modern steels and their weldments, has led to the suggestion that the CAT_* can be approximately represented by the relation

$$CAT_* = RT_{NDT} + 30°C \quad (2)$$

However the maximum thickness of the

specimens tested in the survey was 50mm (most of the tests involved 25mm thick specimens), and there was a significant amount of shear (10-20%) on the fracture surfaces in plates that had fractured completely. The author has reservations as to whether relation (2) is applicable to the long crack - pressure vessel situation where the loading is essentially pneumatic, and where shear lip effects are likely to be minimal, particularly since the EPRI-CE (and indeed other) tests have shown that the CAT_* could be in excess of RT_{NDT} + 90°C.

Another way in which a CAT_* assessment has been made is to use initiation test data coupled with a comparison of the mechanical processes operative during the initiation and arrest of cleavage cracks. Lidbury, Druce and Tomkins[16] have used this approach based on Cottrell's considerations[17], and with an unirradiated heat-treated low alloy pressure vessel steel, e.g. a PWR vessel steel, that has a low strain rate sensitivity, have concluded that the CAT_* might not be greater than the onset-of-upper-shelf temperature (OUST) based on initiation data. The issue of the initiation based OUST has received comprehensive consideration by the UK Nuclear Industry Technical Advisory Group on Structural Integrity of Nuclear Plant (TAGSI)[18]. The OUST is defined by TAGSI as the temperature at which there is a predefined probability of failure by cleavage in standard, deep notched bend, plane strain fracture toughness specimens. This temperature can be based on the probability of cleavage not occurring before a specified minimum of ductile tearing, or before a minimum fracture toughness level is reached, or on a combination of these requirements. An example of the definition in relation to an A508 Class 3 PWR pressure vessel forging steel has been presented by Lidbury and Moskovic[19,20], based on a statistical analysis of a data set comprising deep notched bend specimens up to 200mm in thickness. They used a definition based on a required joint probability of 5%, that both a prescribed amount of ductile tearing (Δa) and a given level of fracture toughness (K_J) for the prescribed tearing, are obtained. The results demonstrated that for amounts of tearing of 1mm and above, the estimated OUST is insensitive to toughness level and is determined by the survivor function for Δa. For Δa = 2mm, the estimate of the OUST is RT_{NDT} + 54°C. This estimate is substantially less than the CAT_* (RT_{NDT} + 90°C) observed in the EPRI-CE experiments[1] for a similar heat treated steel and conflicts with Lidbury, Druce and Tomkins' assertion[16] that the CAT_* might not be greater than the initiation based OUST with a steel that has a low strain rate sensitivity. This difference therefore raises questions as to the use of initiation test data for estimating the CAT_*, particularly as the EPRI-CE experimental results also suggest that arrest and initiation of a running cleavage crack are mechanistically different phenomena (see the comments at the end of the preceding section). More generally, the considerations in this section also focus on the need to carefully define the crack arrest temperature, since its magnitude clearly depends on the role played by shear lips; thus with the long crack - pressure vessel situation where shear lip effects are likely to be minimal, the crack arrest temperature (very likely CAT_*) will be higher than in situations where shear lips do have an effect.

Discussion

So as to emphasize the importance of plastic deformation with regard to the propagation and arrest of a cleavage crack, the present paper has appraised results from the EPRI-CE crack arrest test programme[1] on unirradiated A533B Class I plate material (a heat-treated low alloy ferritic steel as used in PWR vessels).

Two main conclusions arising from the appraisal are, firstly, that the results are consistent with Cottrell's assertion[2] that there are two types of cleavage crack arrest criterion: (a) one which is stress related and (b) another which is temperature related. The second type of criterion is more restrictive when applied in a practical context, and against this background, the second main conclusion is that the crack arrest temperature CAT_*, i.e. the maximum temperature at which a crack propagating by the cleavage mechanism can arrest, is high relative to the material's nil-ductility temperature, i.e. it can be in excess of RT_{NDT} + 90°C. The EPRI-CE tests[1] involved the testing of side-grooved specimens which minimised the effect of shear-lips and thus reflect, apart from the loading which is displacement controlled rather than pneumatic, the conditions expected in the long crack - pressure vessel situation where shear lips are likely to have a minimal effect on the propagation and arrest processes. In contrast, a recent survey of Double Tension Test results for a range of modern steels and their weldments has led to the suggestion[13,15] that the $CAT_* \sim RT_{NDT}$ + 30°C. However the maximum thickness of the specimens tested was 50mm and shear lip effects were pronounced. That being the case, the author inclines to the view that the survey CAT_* temperature is likely to be non-conservative, and is inappropriate for application to the long crack - pressure vessel situation. This difference serves to emphasize that it is important to base any assessment of the crack arrest temperature for a given practical situation on data which simulate, as far as possible, the conditions that are likely to be expected in service.

It has also been argued in the preceding section that caution must be exercised in estimating the CAT_* using cleavage initiation test data together with a comparison of the mechanical processes operative at initiation and arrest. Thus, on the basis of such a comparison, Lidbury, Druce and Tomkins[16] have asserted that, with a low strain rate sensitivity steel such as A508 or A533, the CAT_* might not be greater than the initiation based OUST. However, the initiation based OUST for a PWR steel as estimated[19,20] via the TAGSI definition of the initiation based OUST is RT_{NDT} + 54°C, which is substantially less than the highest EPRI-CE crack arrest temperature of RT_{NDT} + 90°C.

In assessing this paper's comments, the author holds the view that, for the case of a long crack in a pressure vessel, the starting point of discussions with regard to the linkage of structural integrity considerations and operational criteria, should be that the CAT_* is markedly in excess of the initiation based OUST. This viewpoint is predicated, for the case of an unirradiated PWR vessel steel, by the EPRI-CE experimental results[1], and also by other crack arrest data[12,13] (see the comments in the preceding section). Whether or not the same conclusion applies to irradiated material or for other steels, remains an open question, in the author's opinion. This view is in sharp contrast with the viewpoint adopted by Lidbury, Druce and Tomkins[16], who suggest that the CAT_* might not be greater than the initiation based OUST.

The fact that the CAT_* exceeds the initiation based OUST is an integral feature of the ASME Code Section III Appendix G philosophy. In the USA, the Code of Federal Regulations: 10 CFR Part 50 governs heat-up and cool-down operations including normal operation of water cooled reactor pressure vessels. The conservatisms required in the fracture assessment of a pressure vessel is defined in Appendix G, which became the standard for defining plant operating limits for

water cooled reactors in 1973, and became mandatory by reference in 10 CFR Part 50. Appendix G postulates the existence of a reference surface flaw, and the governing criterion, based on static LEFM principles, for calculating the allowable pressure-temperature conditions, is that the "driving" stress intensity (with allowance for a margin on the pressure loading) should be less than K_{IR}, a reference fracture toughness, with the K_{IR}-temperature curve being a lower bound of high loading rate and crack arrest data. The use of crack arrest rather than crack initiation data was, in large part, dictated by the possible existence of locally embrittled regions within a vessel that might start off a running cleavage crack and the need to arrest this before it extends far into the vessel wall. The ASME Code K_{IR} and K_{IC} curves, which have a cut-off limit of 220 MPa$\sqrt{m}$ are such that the initiation based OUST is ~ RT_{NDT} + 55°C, which is consistent with the results of Lidbury and Moskovic[19,20] referred to in the preceding section. However, if the OUST is defined with regard to crack-arrest considerations, i.e. it is based on the K_{IR} curve, then the OUST is much higher, i.e. ~ RT_{NDT} + 100°C, a value which is consistent with this paper's CAT_* considerations. It should be emphasised that the ASME Code Section III Appendix G procedure, with its implied use of the K_{IR} (arrest) rather than the K_{IC} (initiation) curve, refers to normal operation of a water cooled reactor vessel and, in particular, a PWR reactor pressure vessel. The temperature margin with regards to normal operation of a PWR vessel is not a consequence of the application of the PTS (pressurized thermal shock) rule, as is believed to be the case in some quarters[20].

If it transpires that application of a CAT_* criterion to the operation of a component is too restrictive, a fall-back position is the development of a limited crack arrest capability, i.e. show that a cleavage crack propagating from a locally embrittled zone or from a local stress raiser, with an assumed upper bound size, is able to arrest using a stress related arrest criterion. Such an approach is implicit in the ASME Code Section III Appendix G methodology, but it is more realistic to proceed beyond the use of the static based arrest procedure implicit in the Appendix G methodology, and use a dynamic based methodology[3] coupled with an assessment of the likelihood of cleavage reinitiation. In following this path, and indeed also with regards to the application of the CAT_* criterion, that as well as guaranteeing the arrest of a cleavage crack, it is important to ensure that an arresting cleavage crack will not continue to propagate by a ductile mechanism. If it transpires that it is not possible to demonstrate a limited crack arrest capability, there is no alternative but to rely on initiation based arguments, and ensure that these are very robust.

Conclusions

- Against the background of the experimental results from the EPRI-CE crack arrest test programme on an unirradiated PWR vessel steel, the paper has addressed several issues associated with the role of plastic deformation in the propagation and arrest of cleavage cracks.

- The results are consistent with Cottrell's view that there are two types of cleavage crack arrest criterion: (a) one which is stress related and (b) one which is temperature related.

- In a practical context the temperature related criterion is more restrictive, and the results show that the limiting crack arrest temperature (CAT_*) is high relative to the nil-ductility temperature, i.e. probably in excess of RT_{NDT} + 90°C.

- Quantification of the crack arrest temperature for a practical situation should be based on data which simulate as far as possible the conditions that are likely to be expected in service, particularly with regards to shear lip/thickness effects.

- Caution should be exercised in using cleavage initiation test data to estimate the CAT_*.

- The ASME Code Section III Appendix G procedure is shown to be consistent with the conclusion that the CAT_* is markedly in excess of the initiation based OUST.

References

1. "Tests and Analysis of Crack Arrest in Reactor Vessel Materials", Final Report NP-5121M prepared by Combustion Engineering Inc. on EPRI Research Project 2180-3, April 1987.
2. A.H. Cottrell, in Fracture, Proceedings of the First Tewksbury Symposium, University of Melbourne, Australia, C.J. Osborn (ed.), 1.
3. E. Smith, Int. Jnl. Press. Vess. and Piping, 42 (1990) 217.
4. J.D. Eshelby, Jnl. Mechs. Phys. Solids, 17 (1969) 177.
5. L.B. Freund,Jnl. Mechs. Phys. Solids, 20 (1972) 151.
6. L.R.F. Rose, Int. Jnl. of Fracture, 12 (1976) 829.
7. ASME, Boiler and Pressure Vessel Code, Section XI, Article A-5300, American Society of Mechanical Engineers, (1975).
8. J. Keeney-Walker and B.R. Bass, PVP-Vol. 233, Pressure Vessel Fracture, Fatigue and Life Management, ASME (1992) p.193.
9. J.D. Sumpter and R.M. Curr, Paper presented at TWI-HSE Seminar on "Crack Arrest Concepts for Failure Prevention and Life Extension", September 1995. Proceedings published by Abington Publishing.
10. Sir Alan Cottrell, Paper presented at TWI-HSE Seminar on "Crack Arrest Concepts for Failure Prevention and Life Extension", September 1995. Proceedings published by Abington Publishing.
11. ASTM E 1221-88: "Standard Test Method for Determining Plane-Strain Crack Arrest Fracture Toughness K_{Ia} of Ferritic Steels", Annual Book of ASTM Standards, 1995.
12. R.M. Gamble, Data presented at EPRI/ASME/NRC Meeting, Anaheim, California, USA, November 1991.
13. C.S. Wiesner and B. Hayes, Paper presented at TWI-HSE Seminar on "Crack Arrest Concepts for Failure Prevention and Life Extension", September 1995. Proceedings published by Abington Publishing.
14. T.S. Robertson, Jnl. Iron and Steel Inst., 175 (1953) 361.
15. C.S. Wiesner, B. Hayes and A.A. Willoughby, Int. Jnl. Press. Vess. and Piping, 56 (1993) 369.
16. D.P.G. Lidbury, S.G. Druce and B. Tomkins, Paper presented at TWI-HSE Seminar on "Crack Arrest Concepts for Failure prevention and Life Extension", September 1995. Proceedings published by Abington Publishing.
17. Sir Alan Cottrell, Int. Jnl. Press. Ves. and Piping, 64 (1995) 171.
18. F.M. Burdekin, Int. Jnl. Press. Ves. and Piping, 64 (1995) 299.
19. D.P.G. Lidbury and R. Moskovic, PVP-Vol. 250, Pressure Vessel Integrity, ASME (1993) p.283.
20. D.P.G. Lidbury, Int. Jnl. Press. Ves. and Piping, 64 (1995) 191.

AN INSTABILITY AND ENERGY RATE MODEL FOR CLEAVAGE FRACTURE

Cedric E. Turner
Mechanical Engineering Department
Imperial College, London.

Abstract

A deterministic model of cleavage fracture is depicted as a multi-stage event, passing from separation of a particular brittle source just ahead of the crack tip, as envisaged by Ritchie *et al*, to an initial instability necessary to allow the crack to extend. The initial event is governed by the ratio of source size to distance ahead of the crack tip, p/t; the subsequent instability is governed by the global (elastic) energy release rate, I, which for some configurations rises well above the lefm rate, G, as plasticity develops. The variability commonly found within a data set even for one geometry is recognised in the data being analysed and is explored in the above light, rather than treated statistically. Several sets of data taken from the literature, each for a particular steel at low temperature with various shallow and deep notch bend (S/DNB), centre-cracked tension (CCT) and compact tension (CT) pieces, are examined closely.

The general patterns of behaviour and differences of J and G values are accounted for in terms of this model, any one result being of course random within that pattern. For high constraint, either initiation or instability can control according to the p/t ratio. With loss of constraint, instability is more likely to be the controlling feature. The upper bound of G is restricted by limit load; the lower bound by the level of K used in fatigue pre-cracking. The minimum toughness at a given temperature is found to be size dependent, and an increase in minimum toughness in so-called low constraint configurations here seems related as much to the fatigue pre-cracking level as to loss of constraint. The range of toughness values, conventionally studied statistically, thus include deterministic configurational effects as well as genuine (micro-structurally based) scatter.

Introduction

In the past decade, there has been a resurgence of interest in cleavage fracture of steels in the transition region. The problem has two distinct aspects. The one is the dependence of the data on test-piece configuration; the other is the wide spread of results even for a given size and configuration. A deterministic criterion is proposed for cleavage fracture, defined as at least a macro-scale jump in crack length. The micro-aspect of the behaviour, to which scatter is closely related, is accepted more or less as currently formulated.

Recently, two rather similar developments have occurred, leading to the two parameter version of J theory. The intent of both is to allow for the changes in crack tip constraint that occur as plasticity spreads, but one method, [1], is expressed in terms of a hydrostatic stress, Q, whereas the other, [2], uses the so called T-stress, which is the stress parallel to the crack or transverse to the normal direction of loading. Irrespective of which is followed, the modified J field is hereafter referred to as J(Q,T). As examples of use, an application of Q to size effects is given [3]; an experimental application of T to configurational effects in cleavage is given [4][5]. A related concept, in which the differences in in-plane constraint are recognised as a modified J, denoted J_o or sometimes J_{ssy}, has been developed for cleavage, [6][7][8], in terms of Q and T, including allowance for finite deformation at the crack tip.

It seems rather generally accepted that initiation is the critical event in causing cleavage fracture. In [9], Landes writes, "It appears from these examples (certain mainly post-yield CT and CCT cases) that although G_{el} may be needed to drive the crack that plenty of energy is available in all cases. What is critical in determining the toughness is the crack tip stress field which initiates the cleavage

George R. Irwin Symposium on Cleavage Fracture
Edited by Kwai S. Chan
The Minerals, Metals & Materials Society, 1997

fracture." The essence of the model used for initiation in [9] is that various combinations of stress level and extent of the inverted bath-tub stress pattern ahead of the tip, can be relevant according to the size and location of particular source defects. Two main groups of sources are recognised in [9], distinguished as giving different statistical distributions within the cleavage data. Sources small and close to the tip are called 'critical damage sites'; those large and more remote from the tip are called 'weak link sites'. A different statistical treatment of the CT data is given in [10] but the CCT data were not there used. The hypothesis that "there is plenty of energy available" is examined in the present work. Such an energetic approach is seen as complementary to the J(Q,T) methods just mentioned, in much the same way as G and K are complementary in lefm. In turning to energy rates, distinction must be made between the lefm rate, G, and the rate of change of elastic energy in the presence of plasticity, I, (after Irwin) as used, [11]. The convention used here is that G relates to linear elastic behaviour only, with the symbol I for the more general case, despite indications in some of Irwin's early work that his intention was not to restrict G to just the lefm regime. Although the term I has been used for ductile instabilities, [12], and more recently set in a wider framework of energy driving and dissipation rates for real elastic-plastic (rep) behaviour, [13–15], it does seem to be widely known. An outline of its derivation is given in the Appendix, together with some other relevant terms. Another key feature in [13–15] was the concept of ductile crack growth as a series of micro-instabilities. That was followed up in [16] as a model for stable ductile growth controlled, for rep material, by the release of elastic energy, leading to the criterion $\alpha\sqrt{G} = H$, where α is a particular measure of the crack tip opening angle, G is the conventional lefm term. For a given material, $H = f(\eta_{el}, \eta_{pl})$, where the η factor scales G or J to work per unit area, for elastic and plastic behaviour respectively. A related approach is followed here, to show that a micro-instability plays a key role in certain cleavage fractures, implying that deterministic factors account for some, though not of course all, of the large scatter seen in cleavage data.

Some Experimental Data

Of the large amount of data collected in [9], only those cases where both G and J are given for more than one configuration are directly useful here. These are for a 20MnMoNi55 type pressure vessel steel, tested at –90°C, where the yield stress, σ_o, is about 550MN/m^2. The configurations are compact tension (CT) pieces, B = 20mm, a/W = 0.55, of three widths, W = 50, 100 and

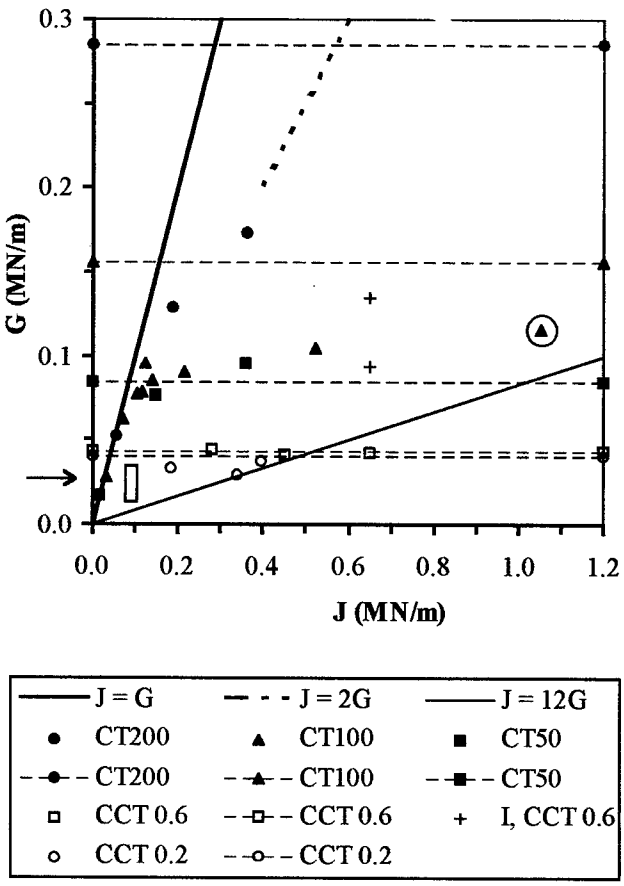


Figure 1: Cleavage data from [9] for CT and CCT pieces, with estimates of G at limit load (dashed lines) added. Estimates of I for the CCT case at the largest J are also marked, +, for D/W = 1.5 (lower) and 2 (upper). See text for points ringed, arrowed and boxed.

200mm (all side grooved to B_n = 16mm) and centre cracked tension (CCT), B = 18mm, overall width W = 90mm, of two crack ratios, 2a/W = 0.22 and 0.61. The relevant data from [9] are shown as points on Fig.1, with various trend lines added here. It should be noted that G was reported in [9] for only a selection of the data in question, usually representative of low, medium and high toughness values. Fig.1 thus clearly shows the trends, but does not always reflect the means, since extra points exist in all of the data sets. Unfortunately, in the data for the case CT100 the key points on Fig.1, minimum (arrowed) and maximum (ringed) are uncertain in that graphical and tabulated results in [9] do not agree and the minimum G for CCT (error box, Fig.1) is not given for either size. The spread between the lowest and highest J in these data is 62 fold. The values of J_{ssy} were given in [9] as derived from [6]. The β correction method, from [17], was also used in [9] to allow for lack of out-of-plane constraint, since for

the CT sizes, b/B varies from 1 to 5. It should be noted that $\beta = (K/\sigma_0^2)/B$ is based on Irwin's early work, [18], where non-plane strain and plane strain data are related by $\beta_c = \beta_{Ic}(1 + 1.4\beta_{Ic}^2)$. It does not relate to the symbol β used in some two parameter analyses as a normalised T. Neither method was applied to the CCT data. Both methods bring all the modified J values for CT within the lines $1 = J/G \leq 2$, as indicated on Fig.1.

A second set of data is taken from [19], where 38 three point bend tests with S/W = 4 or 6, W = 100mm, were made on HSST plate material at various temperatures with $B \approx 50$, 100 and 150mm; G values were provided in the reply to discussion. The data used here, Fig.2, are the six 'production phase' tests that were analysed by computer studies in [19], B = 100mm, made at –40°C (where $\sigma_0 \approx 465 MN/m^2$) for deep notch bending (DNB), $a/W \approx 0.5$ and shallow notch bending (SNB), $a/W \approx 0.1$.

A third set of results, Fig.3, from [4], is for S/DNB with $0.15 \leq a/W \leq 0.7$, ligament b = 25mm (except for a/W = 0.7 where b = 15mm) and CCT with 2a/W = 0.65 and 0.8, total width W = 140mm, using a deliberately chosen lower strength structural steel, BS 4360: 43A, known to be prone to cleavage at the test temperature of –50°C, where $\sigma_0 \approx 300\ MN/m^2$. All the fractures occurred prior to ductile initiation with $0.010 \leq G \leq 0.018$ MN/m though well beyond the lefm regime. Particular attention is later drawn to the revealing differences between the CCT behaviours for the quite different steels in [4] and [9]. A fourth set of results from [20], Fig.4, is for bend tests $0.05 \leq a/W \leq 0.5$ on the same steel as [4], together with the S/DNB data from [4].

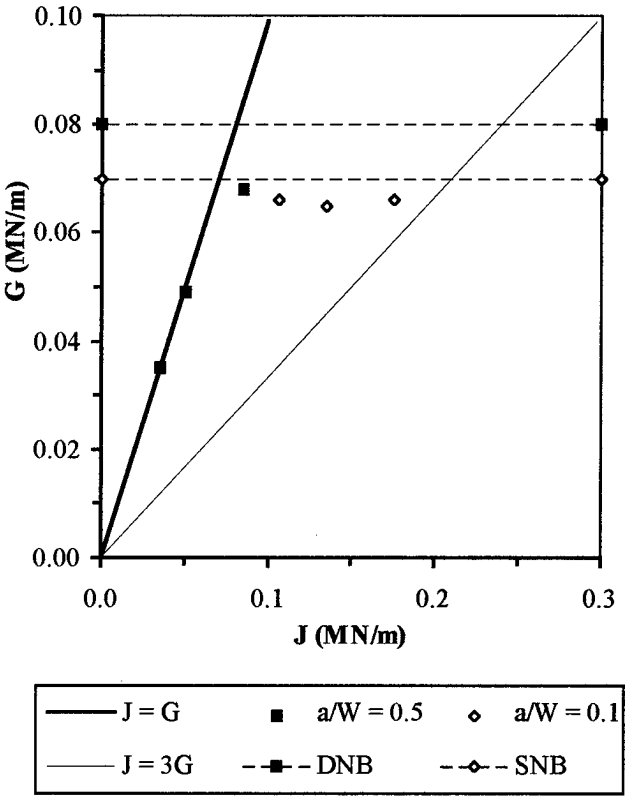


Figure 2: Cleavage data for SNB and DNB from [19], with estimates of G at limit load (dashed lines) added.

Discussion of the Experimental Data

Four questions are asked:-

1) What causes each curve of G rising versus J, which is seen in all the sets of data, Figs.1 and 2? The data of Figs.3 and 4, if plotted in this manner, would also show the same pattern, but individual G values are not given.

2) Why do the curves for G versus J, though of the same generic shape as just discussed, rise to quite different heights, for some of the cases? On Fig.1 the CCT cases are well below the cases CT50 and 100, whilst the case CT200 is well above. In Fig.2, there is no trend for the few points shown. To the contrary, in [4], if plotted as J versus G, a scatter band less than 2 fold in height on the ordinate would cover all the data. This band of values is shown on Fig.3 and an inferred band, on Fig.4.

3) Why are the values of G at fracture so configuration and size dependent in [9] but practically independent of configuration (for a different steel) in [4]?

4) Given that the maximum and minimum values of J reached in each size and/or configuration (and of G in [9]) are so different, can these extreme values represent a material property at all? The recognition that maximum values of J are very size and configuration dependent, is made in [9] by use of J_{ssy} and β, at least for the CT cases; in [19] by J(Q); in [4] and [20], T was used to systematise the S/DNB and CCT data, and in [8], the data of [20] (which includes [4] other than the CCT cases) were treated by J_0. Specifically, taking the plateau data for CT50 or 100 as the datum, with $G \approx 0.1 MN/m$, on Fig.1, the data for CT200 reaches much higher G (roughly double) whereas the CCT data reaches only much lower values (roughly a half). The minimum G values for the side grooved CT tests are 0.017 and $0.057 MN/m^2$ for W = 50 and 200mm respectively, and for CCT, are about 0.030MN/m. It will be recalled that CCT were not side grooved and the lowest cases, included only as J, not G.

Discussion of Question One. The answer to the first question is that the shape is clearly defined by the loading diagram, since G is proportional to load, Q, whereas J reflects both Q and displacement, q. Thus the G versus J lines reflect the random scatter existing over a set of test

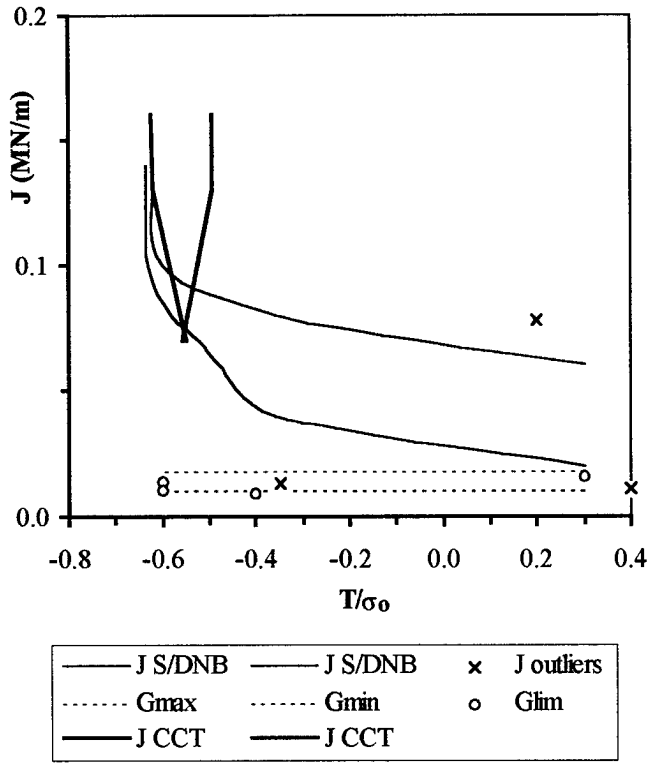


Figure 3: Spread of cleavage data for S/DNB (lines) and CCT (bold) from [4], with experimental range of G at fracture (dotted lines) and estimates of G at limit load, o, added.

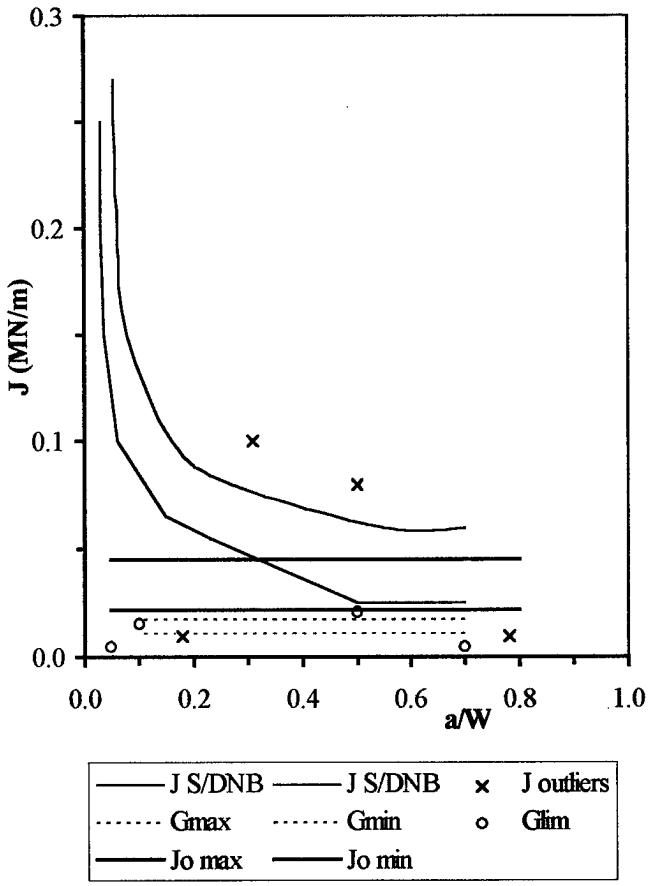


Figure 4: Spread of cleavage data from [20] for S/DNB (lines) with experimental range of G at fracture (dotted lines), where known, and estimates of G at limit load, o, added. The band of J_o values for these data from [8], are also shown.

results, systematised when plotted in the G versus J form. At first sight, J as a criterion for cleavage, seems irrelevant, a remark reinforced by the use of J_{ssy} or β, both of which condense the data to near one line in the quasi lefm regime $1 \leq G/J < 2$ leaving G as the most obvious, if not the only, variable!

Discussion of Question Two. In discussion in [9], relevant to the second question of the different maximum G values attained, some attention is given to thickness effects, since for the cases CT100 and CT200, the ligament to thickness ratio is b/B ≈ 2.5 and 5 respectively. In the absence of side grooves, such cases would be nearer plane stress than plane strain. However, loss of plane strain reduces the plastic constraint factor (or normalised load) L, and thus G, unless the reduction in L were more than offset by work-hardening, implying a degree of deformation associated with ductile rather than cleavage fracture. It is therefore argued here that the evidence of flat, cleavage, fracture shows that an appreciable degree of plane strain remains. The maximum possible load is therefore the plane strain limit load, and that is the feature controlling the maximum possible G, Fig.1. The limit loads are proportional to ligament sizes b, modified by the load constraint factors, L , (L ≈ 1.4 for DNB and CT; L ≈ 1 for CCT) coupled with the lefm shape factor, Y, (higher for DNB and CT than for SNB and CCT) used to convert load to G. Taking the CT case width W = 50mm as a datum, the plateau for W = 100mm is indicated very well (despite the ringed point perhaps relating to –60°C). The much higher curve for CT with W = 200mm, although cut off by the highest toughnesses found in terms of G, is primarily a direct consequence of width, partly offset by less plasticity and thus lower hardening. The much lower plateau of G for CCT, again reflects the combination of ligament size and low L on the limit load for that configuration. Values of G, estimated for the limit state, are shown on Fig.1, increased by 5 to 30% for hardening, according to the degree of plasticity reached at the maximum J.

For the DNB and SNB data of Fig.2, the limit load at

first seems not directly relevant since no case approaches uncontained yield, and the trend may be just part of the scatter, with neither curve defined by sufficient points. In fact, as shown on Fig.2, both cases are approaching a rather similar estimate for G at limit load. Similarly for the data of Figs.3 and 4, estimates of G at limit load, with an allowance for hardening, provide a very reasonable model for the upper bound to the data for G. That is supported on Fig.3 by the known range of G in [4], and on Fig.4 by the inclusion of some data from [4], implying the same limits, together with the estimates of J_0 in [8], which show no trend for the yet smaller a/W values reported only in [20]. Again, in all these cases, J does not seem relevant, G at limit load seeming the dominant variable.

Discussion of Question Three. The reason why the relationship is so different between the maximum G values in the low constraint, CCT, and high constraint CT [9], or S/DNB pieces, [4], which cover a range of constraints, will be clearer after the next section, so is stated here without explanation. It is that the former are in a regime where instability controls cleavage fracture and $I > G$, Eq.1, is very relevant whereas the latter are in a regime where initiation controls it and any exceedance of I over G is not relevant. The very high J values in some cases in [9], up to 0.60 or even 1.0MN/m where $J/G \approx 12$, are well above a ductile initiation toughness. Some stable ductile growth is known to have occurred, allowing the advancing crack to meet a suitable source for cleavage, in due course. In [4], the highest J is only about 0.15MN/m, $J/G \approx 4$, and it is explicitly stated that ductile growth did not occur. These differences are consistent with the reason just given for the two different behaviours. The data in [20] includes tests over a range $0.025 \leq a/W \leq 0.7$ with J up to 0.23MN/m. As seen in answer to Question 2, the limit load values of G differ but little, and at most $I \leq 2G$ for these cases.

Discussion of Question Four. In answer to the first part of the fourth question, the high values of J in all data sets, it is again noted that any treatment, be it either J(Q,T) or β methods, by intent, brings the corrected J back to the regime $1 \leq J/G \leq 2$. The large range of J is lost although the range of G remains, 10 fold on Fig 1, two fold on Fig.3, irrespective of whether the J value has been corrected or not. High G for the case CT200, and low values of G for the CCT cases, or even the differences in the mean values of G for the various configurations, indicates that G cannot be a criterion in its own right. The key is that the driving force with appreciable plasticity is $I > G$. The relationship (see Appendix) is

$$I = G(2(\eta_{ep}/\eta_{el}) - 1) \qquad (1)$$

where η is the factor relating J (or G for the elastic case) to the work done, or area of the loading diagram ($Qq_{el}/2$ in the lefm case). Suffix ep, relates to the intermediate state between elastic (el) and fully plastic (pl) for which the values of η are known, [21] [22]. For the intermediate case, no specific values are known other than by computation or by weighting the elastic and plastic factors appropriately. It so happens that for the CT, DNB and indeed SNB data so far discussed, $I \approx G$, because $\eta_{el} \approx \eta_{ep} \approx \eta_{pl}$. But for CCT, that is not so. The elastic factor is a function not only of a/W but also of D/W where D is the gauge length of the CCT piece, a value not stated in [9]. Assuming it to be either 1.5W or 2W, and using the known ratios of J/G for any particular test, Fig.1, then η_{ep} can be evaluated from the known η_{el} values with $\eta_{pl} = 1$, (see Appendix). These two values of I are marked on Fig.1 for the last point (i.e. highest J) of the CCT 0.6 case. The low plateaux values of G for the CCT cases are not a correct measure of the driving energy for a macro-scale cleavage propagation. Since for DNB and SNB, $I \approx G$, the condensation already seen for the data of [19] and [20] into a single band in terms of G, Figs.2 and 4, is equally valid in terms of I. However, for the data set, from [4], Fig.3, as already seen, G is there constant across CCT, SNB and DNB, within two fold. Transforming to I hardly affects the S/DNB values whereas for CCT, where $D \approx 2.6D$ and $J/G \approx 4$, then $I \approx 3G$, somewhat higher than for the bend pieces.

The reason why $I > G$ is not relevant in that case was stated in Answer 3. That, and the answer to the second part of Question four (are the minimum values of G or J meaningful) will arise after the next section.

Cleavage; Initiation (Stress State) or Instability (Energy) Control ?

Use of G reduces the spread from 62 fold in terms of J to 10 fold in G, for [9]. Use of G in [4], [19] and [20] reduces the scatter from respectively about 8, 5 and 10 fold in J to some 2 to 4 fold in G. Any method, such as the β analysis in [9] or J_{ssy} or J_o, would at best reduce a modified J to G, thus also leaving a spread of 10 fold for [9]. The object of this analysis is to examine that 10 fold spread of the data when expressed in terms of G and the lesser spread in [4], [19] and [20]. The thickness of the pieces discussed will usually be less than that for valid lefm plane strain, but clearly sufficient to give a predominately flat, cleavage mode, of separation. Although much of the discussion centres on post-yield cleavage, three degrees or extents of plasticity will be distinguished;

i) lefm, though here implying that a small plastic zone at the crack tip must be recognised; in the following, this is called 'full' constraint.
ii) contained yield, where J may still be approximated by G but an effect of transverse stress, T, on the plastic zone is recognised; this is called 'relaxed' constraint.
iii) uncontained yield, where J >> G and in appropriate configurations, local triaxiality is lost; this is called 'collapsed' constraint.

In all three cases, an 'eye' of plasticity is formed ahead of the tip. For lefm, the plastic zone (in plane strain) is always of high triaxiality, usually typified by one value, m $\approx$ 3, and of a certain extent, the combination here called 'full' constraint. For contained yield, the major effect is seen as modest loss of the peak triaxiality, m_{max}, with a larger reduction in m at a given size of plastic zone ahead of the tip, relative to lefm, a combination here referred to as 'relaxed' constraint. Examples are shown in terms of $r_m\sigma_o/J$, [6][8][19], where r_m is the distance ahead of the crack tip at which a given level of triaxiality, $m = \sigma_{yy}/\sigma_o$ is reached. For uncontained yield, as pointed out long since by McClintock, [23], the stress field is configuration dependent such that in some cases m_{max} remains high and the extent relatively small so that the constraint is 'full', much as in lefm, whilst in other cases only a low value of m_{max}, approaching one, can be maintained, but extending over a relatively large region. The combination of low m_{max} but large r_m is here called 'collapsed' constraint.

The Initiation Event

The model envisaged for initiation of cleavage at the crystallographic scale is essentially that of Ritchie, Knott & Rice (RKR) [24], where a certain stress, $m_{cl}\sigma_o$, must not only be greater than a material dependent cleavage stress, σ_{cl}, but must be attained over a finite small region just ahead of the tip. If σ_o is the yield stress at the temperature in question, then typically for steel, $m_{cl} > 1.5$ or 2. With crack blunting, the opening stress ahead of the crack, σ_{yy}, first increases to a maximum, $m_{max}\sigma_o$, with $1 \leq m_{max} \leq 3$ from triaxiality plus a further increase by work hardening. It then decreases, $m_{max} \geq m \geq 1$, towards a net section stress (which may of course be less than σ_o), [1][3][23]. It must be noted that in [2] and most of the related T-stress usage, triaxiality is defined as a multiple of the mean stress, $\sigma_{kk}/3$, a term that is about two thirds of m as just defined. As a first event at the micro-scale being considered, a suitably brittle constituent, or possibly a small group of brittle constituents, suitably sized and located, will then crack. This region of the first event is here called the source.

The RKR concept for cleavage, such that a certain level of stresses in the 'eye' of plasticity just ahead of the crack tip must not only be adequate but that the 'eye' at that level of stress must encompass the source of size, p, is expressed here as a reference case, $m_{max} = 3$,

$$m \geq m_{cl}; \quad (r_m)_{ref} \geq t_m + p \qquad (2a,b)$$

where p is the x-direction length of the source, buried beneath the tip at depth, t, to its near end, suffix m implying the particular t for which t + p is just encompassed. The value of p is seen as having a quite restricted range, though possibly existing over more than one range according to the particular type of particles involved, [25][26]. For a given value of the local triaxiality factor, m, r_m is a broad brush description of the x-direction extent of the 'eye' of plasticity, including such slightly off-axis sources as may be. This is shown schematically, Fig.5. As already remarked, the x-direction width of r_m, when normalised as $r_m\sigma_o/J$, is, in general, a function of load or degree of plasticity. Specifically, for all lefm cases, more strictly small scale yielding (ssy) there is no effect of configuration, and then for DNB in both contained and uncontained yield up to the extent of plasticity here encompassed, there is only a small effect so that near full constraint occurs. For SNB there is rather small reduction in m_{max} but $r_m\sigma_o/J$ becomes much smaller as plasticity increases, [19], giving relaxed constraint in contained yield; for CCT, as well as $r_m\sigma_o/J$ becoming much smaller as plasticity increases, m_{max} reduces to about 2, [2][27], with both SNB and CCT experiencing collapsed constraint in uncontained yield. These triaxiality dependent stress states are functions of the hardening exponent, now best described in terms of J(Q,T) from one of the two parameter models, thus leading to the procedures, [5–8] whereby some equivalent value of J is used. Nevertheless, for this exploratory study, a much less detailed picture of the local stress states will be used than in [5–8], but additional physical arguments introduced.

In lefm, the plastic zone size is proportional to G. In epfm, [1][2][6], it scales with J. For simplicity, G is just allowed to grow to J, and as a working approximation, the RKR type requirement, or the first event to trigger the source, is taken in the quasi-lefm form,

$$r_m/t_m = (J/G)r_{ref}/t_m = E'J/2\pi m^2\sigma_o{}^2t_m$$
$$= (J/G)\{(p/t_m) + 1\} \qquad (3a)$$

This is used for values of $m_{max} > m > m_{cl}$, to give a family of reference lines, one for each value of J/G. As seen later, when with plasticity m_{max} may become less

than 3, according to configuration, the reference value must also become a function of the extent of plasticity. The datum lefm case, J/G = 1, implies full constraint with m = m_{max} = 3, so the datum line is

$$r_m/t_m = E'G_{dat}/2\pi m_{max}^2\sigma_o^2 t_m = (p/t_m) + 1 \qquad (3b)$$

Initial Instability

If the first event is to lead to a burst of fracture by cleavage, unstable over at least a few grains, then the criterion must be reached at several sites in succession and these sites connected together. A few extra sites might fracture if stress waves from the first event were just sufficient to trigger the separation, but it seems unlikely that satisfaction of the initial event will in general precipitate what might be called a burst of cleavage, let alone unstable propagation on the macro-scale.

The minimal requirement for actual growth of the crack, is the separation of one or more micro-ligaments between either the first source and the tip or between two more deeply buried sources, later extending back to the tip. If the growth is to be unstable, here taken to imply no increment in external work done, then the driving force can only be the elastic energy, w_{el}, stored in the body. There is of course no guarantee that the initial event will in fact cause unstable growth and it may well be that in some cases a succession of events will be triggered only after there is some non-cleavage crack growth to re-establish the plastic zone over a new region further ahead of the original tip. The simplest case is followed here, in an essentially two dimensional model, where it is envisaged that the initial event is coupled with the separation of the micro-ligament between the original tip and the first source. For a deterministic model, the length, p, of the brittle particle, Fig.5, is therefore kept constant whilst the distance, t, from the crack tip to the particle, is allowed to vary.

Since unloading at constant displacement is an elastic process, the driving force on the micro-ligamant, F per unit thickness, is taken as

$$F(driving) = -\int_t^{t+p} K/\sqrt{(2\pi x)}dx$$
$$= K\sqrt{(2/\pi)}(\sqrt{(t+p)} - \sqrt{t}) = \{\sqrt{(2E'G/\pi)}\}\{(f(p,t)\} \qquad (4)$$

where, introducing g(p/t) to suit what follows,

$$f(p,t) = (\sqrt{(t+p)} - \sqrt{t})$$
$$= \{\sqrt{t}\}\{\sqrt{(1 + (p/t))} - 1\} = \{\sqrt{t}\}\{\sqrt{g(p/t)}\} \qquad (5)$$

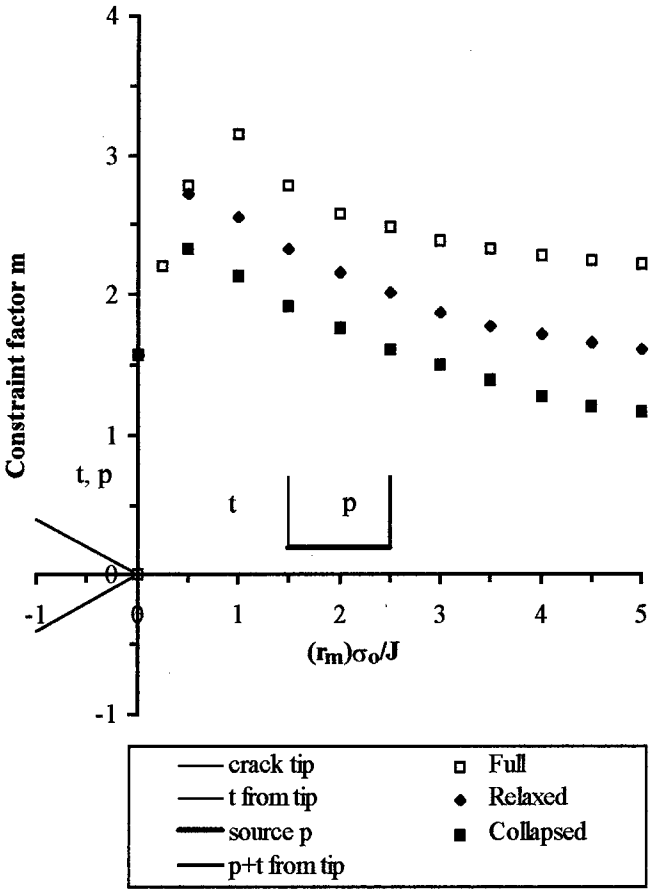


Figure 5: Schematic picture of a brittle source in relation to the cracked tip constraint factor, m, as a function of the distance ahead of the tip, r_m normalised by σ_o/J.

The resisting force on the micro-ligament, F(resist), is

$$F(resist) = m_{av}\sigma_o t_m \qquad (6)$$

where m_{av} is averaged over the micro-ligament. Equating the two forces and using Eq.3, with m = 3 for the lefm plane strain driving force for all configurations, gives

$$\{4E'G/2\pi m_{av}^2\sigma_o^2\}\{g(p/t)\}$$
$$= 4(G/J)(m/m_{av})^2 r_m g(p/t) = t_m \qquad (7)$$

with m_{av} = 3 for unloading according to lefm plane strain, for all configurations, even when m ≤ 3.

However, when plasticity develops, it has already been seen, Eq.1, that the driving force is I, rather than G. If it is assumed that the relationship between the extra elastic energy rate G_p and r_m is the same as for G, then the reference curve for instability becomes,

$$r_m/t_m = E'I(J/I)/ 2\pi m^2\sigma_o{}^2 t$$
$$= (J/I)(m_{av}/m)^2/4g(p/t) \qquad (8a)$$

one of a family for given values of J/I. The datum curve, with $J = G_{dat} = I$, takes the form

$$r_m/t_m = E'G_{dat}/ 2\pi m^2\sigma_o{}^2 = 1/4g(p/t) \qquad (8b)$$

A Burst of Cleavage

The conditions for a small burst of cleavage fracture are therefore taken as:-

i) the pre-requisite that, from typical experience, $m_{cl} \geq 1.5$. That is followed by:-

ii) $r_m/t_m \geq (J/G)$ [(p/t) +1], Eq.3a, for the plastic 'eye' to envelop the source;

iii) $r_m/t_m = (J/I)(m_{av}/m^2)/4g(p/t)$, Eq.8a, for initial instability, once the source is broken.

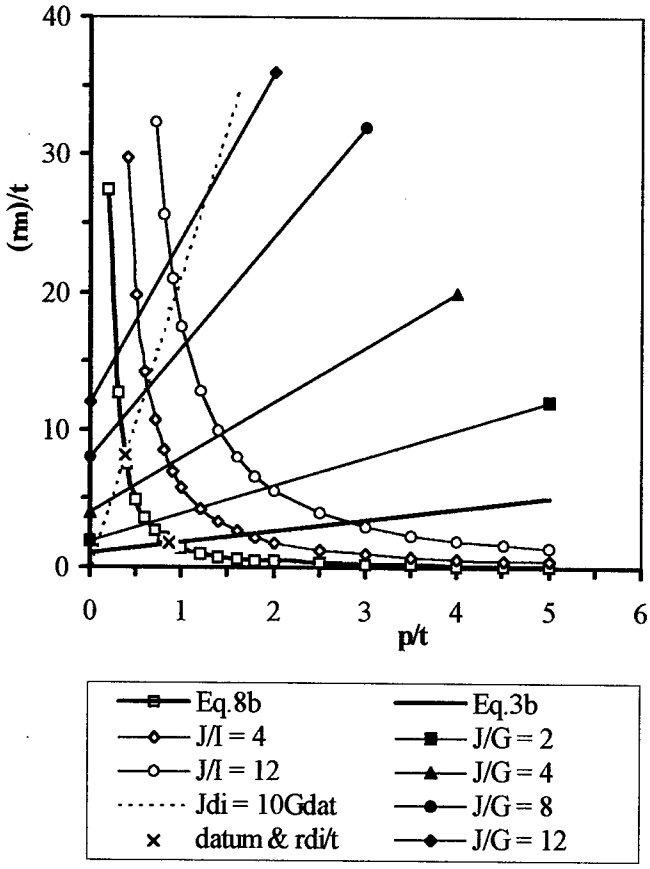


Figure 6: The cleavage diagram of r_m/t versus p/t. The datum cleavage initiation line, Eq.3b, and datum instability curve, Eq.8b, are shown bold; a ductile initiation line is shown dotted, representative of the CT50 case in [9]. (Note curves marked J/I refer to $(J/I)(m_{av}/m)^2$ as used in Eq.8a).

These conditions appear to ensure a burst of cleavage over several grains. The equations for conditions ii) and iii) are shown Fig.6, over the range $0.15 \leq p/t \leq 5.0$, assumed plausible for the particles relevant to the source site. As already said, the initiation line covers any values of m_{cl}. The special case of Eqs.3b and 8b, taken in combination, to imply simultaneous initiation and local instability, gives a datum point at $p/t_m \approx 0.86$, $r_{dat}/t_{dat} \approx 1.86$, which will be used as the basis for discussion of cleavage behaviour. Thus:-

i) to the right of the datum intersection, where $p/t > 0.86$, a burst of cleavage is initiation controlled whereas to the left, for $p/t < 0.86$, it is instability controlled:

ii) a minimum value of G/t_{dat} exists in this datum case, corresponding to r_{dat}/t_{dat} at the datum or intersection point. The value, G_{dat}, will give the connection to actual data.

The relationship between r_m and G_{dat}, can be evaluated from Eqs.3b or 8b, with m = 3; for J, Eqs.3a and 8a are used with m not necessarily 3. The relationship between ssy and lefm valid plane strain does not seem explicit. Here, lefm valid plane strain is taken as the datum, by applying the plane strain criteria, a, b, $B \geq 2.5(E'G/\sigma_o{}^2)$ to the test size. For the piece CT50 from [9], G_{dat} = 0.014MN/m, just below the minimum experimental value of 0.017MN/m. Neglecting that difference, it appears that if the lowest feasible cleavage toughness for the steel and temperature in question has been measured, then t_{dat} = 0.088mm, p = 0.076mm, values perhaps 10 or 20 fold larger than usually anticipated for typical sources, for example, [25][26]. The implication is that the ssy condition, with Eq.2 relevant for a single source leading to fracture, is some 10 or 20 fold below the upper limit of valid lefm for a given size, where fracture must be from a group of adjacent or possibly successive sources.

If plasticity occurs, Eq.8 plots higher on the ordinate, Fig.6, by the amount $(J/I)(m_{av}/m)^2$ which is a function of both extent of plasticity and configuration. Here, J will exceed I (I = G in lefm) when $J > G_{dat}$ although the J(Q,T) studies suggest constraint may be lost as soon as the ssy condition is exceeded. Constraint as measured by m_{max}, can be inferred for more extensive plasticity, as shown later, but is not a parameter specified directly.

A first observation, coupled with the role of plasticity via J/I, is relevant to Question 3 on the difference in trends for the CCT data relative to CT or bend, in Fig.1, from [9] and in Fig.4, from [4]. The implication is that where the plateaux values of G differed in the two configurations, needing the I term to bring them together, Fig.1, the events were stability controlled but where the G values were similar, Fig.4, events were initiation controlled with choice

of G or I as the driving energy, irrelevant. Observations on the values of J, J/G and other points, made later, support this argument.

Ductile Initiation

The discussion cannot continue fruitfully without reference to ductile initiation, taken here as a critical value, J_{di} for which the standard J_{Ic} is a working approximation. Suffix d, reminds that here this ductile initiation event is well above the lefm value at initiation, G_{Ic}, now by definition a cleavage event. Any variation of J_i with constraint is neglected here for simplicity, but could in principle be encompassed by letting J_i be a configuration dependent function of J/I. Considering a fixed source size, p, and a given value of J_{di}, say N_d times the datum value G_{dat}, then, for the datum p/t, J_{di} would plot N_d fold higher on the ordinate, and change directly with t if p/t were some other value. Using sub di to denote ductile initiation, the line is therefore

$$r_{di}/t = 2.16(J_{di}/G_{dat})(p/t) \qquad (9)$$

where $2.16 = 1.86/0.86 = (r_{dat}/t_{dat})/(p/t_{dat})$, the ratio of ordinate to abscissa, at the datum point. Such a line is plotted on Fig.6 for $N_d = 10$, implying a plausible value $J_{di} = 0.14 MN/m^2$ if the datum is valid lefm for CT50 case. It represents a family of lines with slope 2.16N. Note N_d reflects changes in both J_{di} (for instance with temperature and perhaps constraint) and G_{dat} (for instance with size). Clearly, ductile initiation is quite easily reached for the instability controlled regime where $p/t < 0.86$, but is unlikely to be reached for the cleavage initiation controlled regime where $p/t > 0.86$, unless N is about unity. This is in agreement with the deduction already made that much of the beyond-lefm data in [9] is stability controlled, since ductile tearing is referred to in [9], where many J values much exceed J_i. It is also in agreement with the relatively lower J values of [4] being in initiation control, where ductile tearing is most unlikely and was specifically not observed in [4].

Collapse of Constraint

The role of collapse of constraint will now be examined using the CCT case in [9], $2a/W \approx 0.6$, as an example. For that CCT piece, the minimum valid lefm value, $G_{dat} \approx 0.0094 MN/m$, is dictated by the ligament. A priori, there seems no reason why such a value, or even a small fraction of it, might not be observed in the lefm regime; that point will be discussed later. However, as lefm is lost and J

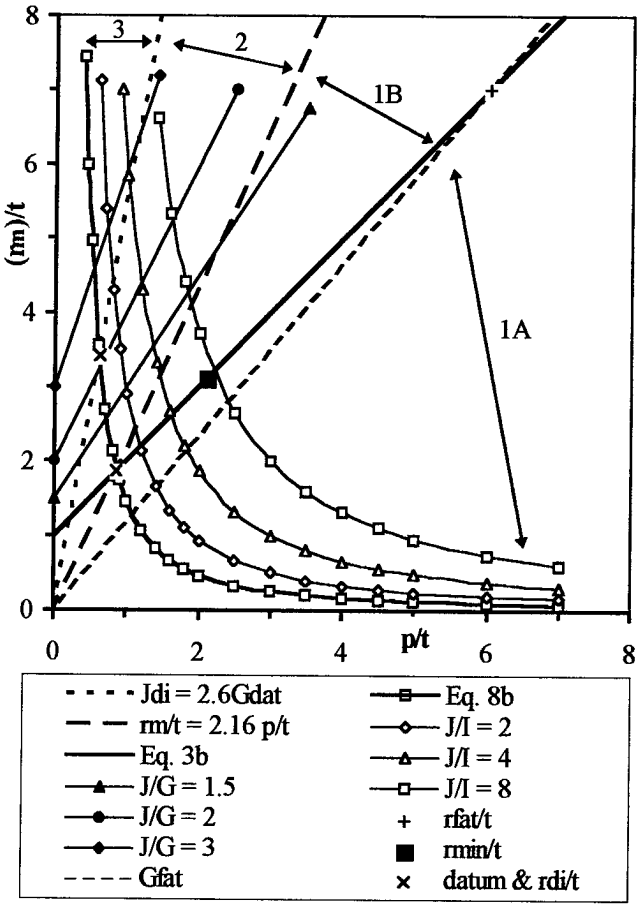


Figure 7: The cleavage diagram divided into three regimes, 1 lefm; 2 post-yield and 3 post ductile initiation, here representative of the CT200 case in [9]. Point + defines r_{fat}/t and thus the maximum p/t available after standard fatigue pre-cracking conditions. The solid square defines maximum p/t available for subsequent cleavage (for $m_{cl} = 1.5$). (Note curves marked J/I in fact refer to $(J/I)(m_{av}/m)^2$ as used in Eq.8a).

exceeds I (and G), two effects seem relevant. Firstly, the cleavage initiation line, Eq.3a, also moves up the ordinate, thereby allowing other sources to be encompassed by the RKR requirement that the plastic zone for a given m_{cl} must envelop the source. Secondly, the micro-ligament is subject to m_{av}, Eq.8a, appreciably higher than the m just encompassed by r_m. These relationships are a complicated function of J(Q,T) and the hardening exponent, as illustrated [1][8]. The smaller loss for m_{max} than for m in SNB, is clearly shown in [19]. Here, a simple model is used to give the required trends. Firstly, retention of triaxiality as plasticity develops, is associated with $\eta_{el} \approx \eta_{pl}$. A near equality is close for DNB, fairly close for SNB but not for CCT, where η_{el} is often much smaller than η_{pl}.

Since G has already been replaced by J on the ordinate of Eq.3, for the effect of plasticity on r_m itself, then where m reduces at a given radius, r_m, it might be inferred as reducing with $\sqrt{(G/J)}$, and intuitively, that suggests that m_{max} might reduce by $\sqrt{(G/I)}$;

$$m_{lc} = m\sqrt{(G/J)}; \quad m_{max} = 3\sqrt{(G/I)} \qquad (10a,b)$$

where m_{lc} is the value to which m has reduced with any loss of constraint. These expressions, though hardly substantiated, are reasonably consistent with no reduction in m or m_{max} for DNB or CT until large scale yielding, probably beyond the cleavage regime, but appreciable, [27] in contained yield CCT. For SNB, both [2] and [19] show only about 5 or 10% reduction in peak constraint, for $\sigma_{kk}/3$ at $T/\sigma_o \approx -0.25$ as in [2], relevant to SNB in [19], or for m_{max} as computed in [19], where a larger reduction is shown in m, for a given relative size of r_m.

Here m is not directly used, but can be inferred, if required, as uncontained yield is approached; for consistency with m = 3, Eq.10 is restricted to $J/G \leq 9$. The value of r_m (where with loss of constraint m < 3) will be appreciably more than r_{dat} (where m = 3) so that, as in Eq.3b,

$$r_m = (3/m)^2 r_{dat} \approx (J/G) r_{dat} \qquad (11)$$

The first part of Eq.11, recognising the effect of loss of constraint, would of course be limited to $J/G \leq 9$. For the second effect, an average value is

$$m_{av} = (m_{max} + m)/2$$
$$= 3\{\sqrt{(G/J)} + \sqrt{(G/I)}\}/2 \qquad (12)$$

and that is used when applying Eq.8a with loss of constraint.

In the CCT case being followed, cleavage was not observed at the lefm condition, J/G = J/I = 1, p/t = 0.86, so the conditions at J > G will be examined. The process is not iterative or cumulative so that large steps may be taken, each referring to a separate test whereby the curve for J versus G, Fig.1, was built up. For the known crack depth ratio, 2a/W, and gauge length taken here as D/W = 2.0, J/I is known if J/G is assumed (see Appendix). Intersection of Eq.8 including the value of $(J/I)(m_{av}/m)^2$ is then sought with Eq.11. J can then be estimated from Eqs.8, 11 and 12, to give an apparent value, G_{app}, based on the original datum. But as p/t decreases, from 0.86 at datum to values nearer 0.5 (see below), there is about a 1.5 fold increase in t. Thus $G_{ref} = (G_{app})t/t_{dat}$. If the β correction is also applied to this CCT case, because, without side grooves it is clearly not in full plane strain, then based on G_{dat} as the lefm plain strain value, G and J rise by about 1.2 fold. The results are:-

For J/G = 4; J/I = 1.64, intersection is found at p/t = 0.58, which, allowing for Eq.12, gives G_{app} = 0.015MN/m and allowing for t/t_{dat} = 1.48, gives G_{ref} = 0.022, whence J = 4G = 0.088; with the β correction, G = 0.027 and J = 0.108MN/m.

For J/G = 8, J/I = 2.51, intersection is found at p/t = 0.51, to give G_{app} = 0.016 and with t/t_{dat} = 1.69, G_{ref} = 0.027 whence J = 0.216; with the β correction, G = 0.030 and J = 0.242MN/m.

For J/G = 12, J/I = 3.16, intersection is found at p/t = 0.47, to give G = 0.022 and with t/t_{dat} = 1.79, G_{dat} = 0.039 whence J = 0.464; with the β correction, G = 0.047 and J = 0.056MN/m.

These three points, β corrected, agree very reasonably with the CCT0.6 data, Fig.1.

A check with Eq.9, where for $G_{dat} \approx 0.010 MN/m^2$ for CCT, N = 14, shows that ductile initiation would not have occurred for these sources until just before the J/G = 12 case. But J = 0.14MN/m soon after the J = 4G case, and allowing for a higher J_{di} for probable loss of constraint and the low temperature in question, makes matters worse. The implication is that J_{di}/G_{dat} must be a much smaller ratio, perhaps only about 4. A possible resolution will emerge after a mechanism whereby pre- or post-initiation cleavage can occur, is considered.

A mechanism for pre- or post-yield cleavage

As seen Eq.9 for the special case of ductile initiation, constant J on the cleavage diagram, Fig.6, plots as a line passing through the origin. In general,

$$J = NG_{dat}; \quad r_m/t = 2.16Np/t \qquad (14a,b)$$

G is a multi-valued function of J – as is clear from such as Figs.1– 4. Along such a line, as it cuts successive initiation lines, Eq.3, with J/G > 1.0, G must decrease since J is fixed. It is seen, Fig.7, that the line for ductile initiation, Eq.9, and Eq.14 used with N = 1 (thereby passing through the datum point) divide the diagram into three regimes, marked 1, 2, 3 on Fig.7, alternative to the cleavage initiation and instability regimes already used on Fig.6:-

Regime 1; between the abscissa and Eq.14:- in the sub-region marked 1A, lefm must prevail in the sense that J cannot yet be distinguished from G, up to the datum line, Eq.3b, where $J/G_{dat} = 1$. For p/t > 0.86, the datum value, a below yield cleavage can occur – indeed, must occur as the

load rises, with potential instability, Eq.8 (used with J = G) satisfied before the initiation condition of Eq.3 is met. The regime is thus initiation controlled. For $p/t < 0.86$, the non-lefm state is entered before Eq.3, let alone Eq.8, can be satisfied. The sub-region marked 1B cannot normally be entered from below since cleavage fracture will have occurred on the datum line.

Regime 2; the middle 'wedge' between Eqs.14 and 9:- this cannot be entered at constant $p/t > 0.86$ since pre-yield cleavage in region 1A) will always have intervened. For a constant $p/t < 0.86$, there is a small region below the datum line where whilst J/G = 1, the absolute value of both terms can be large, for example up to J_{di} or more, implying lefm behaviour up to ductile initiation, as is possible in large pieces. Above the datum line, yield has occurred in the sense that J > G, cleavage initiation will have occurred but the datum curve, or instability condition of Eq.8 with J/I = 1, will not have been met until a higher J is obtained, or more strictly, a higher value of r_m/t. As that crossing is approached, the instability condition must now rise by $(J/I)(m_{av}/m)^2$ times the datum curve, whilst the reference initiation line, Eq.3, also rises by J/G fold above the datum. To satisfy these conditions, J will be driven ever higher until post-yield cleavage will result, with instability as the controlling factor. There can be no ductile crack growth unless $r_m/t \geq r_{di}/t$. In that case, ductile initiation intervenes and in the particular source being studied, p/t increases (see next paragraph) and the source may be annihilated. If so, a new tip will be formed and new sources become available.

The datum point, defined by the lefm validity limit for a given size of B, b or a, as may be, has already been seen to be size dependent. Thus if a bigger size is used, a higher value of G can be measured within lefm. The datum point has the same p/t_{dat} and r_{dat}/t_{dat} values, 0.86 and 1.86 respectively, but the corresponding higher G_{dat} will, for a given J_{di}, make the ratio J_{di}/G_{dat} smaller, with the ductile initiation line therefore plotting at a lower slope. For a sufficiently large piece, G_{dat} can equal J_{di}, so that r_{di} equals r_{dat} and Eq.15 becomes the same as Eq.3, with $J = G = G_{dat}$. Region 2 will then have been squeezed out, leaving only regions 1 and 3. For an even larger size, it appears J_{di} could be smaller than G_{dat}, so that ductile tearing could intervene before cleavage, even within valid lefm. Region 3 would then have overlapped region 1. Of course, there is nothing in the argument so far to prevent either a subsequent, post-yield cleavage or a below yield cleavage, before the valid lefm limit, if only large $p/t > 0.86$ existed.

Regime 3; between the ordinate and Eq.9:- for $p/t > p/t_{di}$, the value for ductile initiation, this region cannot be entered at constant p/t since post-yield cleavage will always have intervened. For $p/t < p/t_{di}$, as load increases, ductile initiation will be met before cleavage instability. As growth occurs, the advancing tip rapidly reduces t and therefore increases p/t. The moving tip is preceded by a plastic zone that advances onto the existing source as an 'eye' of constant extent r_{di} (Eq.9, for initiation) driven by internal energy, rather than as an 'eye' expanding in size with load rising and work being done. But it must still encompass the RKR condition, $r_m \geq p+t$, for cleavage initiation. Thus, at initiation, (see Eq.3 together with Eq.11), r_{dg}, (the suffices implying ductile growth) is

$$r_{dg}/t = r_{di}/t = (J_{di}/G_{dat})(p/t + 1) \qquad (15)$$

Eqs.15 and 3 with 11, become identical, so that cleavage instability is now reached when Eq.15 crosses Eq.8. In other words, with crack growth, the approach to cleavage is along the line of Eq.15, not along a vertical line p/t = constant. If instability does not occur, then that source is annihilated. Another suitable source may then allow more ductile growth. Such a history was followed, with loss of constraint, in the worked example for CCT, despite the still unresolved point that Eq.9 was not then satisfied.

Blunting and the R-curve

The CCT problem allowed a simple mapping of behaviour, other than the inconsistency for the effect of ductile initiation, because the difference between J/G and J/I, gave sufficient conditions to solve the relationships explicitly. For the CT or other high constraint cases where it is assumed G = I, the elevation of both reference initiation lines and reference instability curves is the same leaving the solution at a given p/t indeterminate in J/G, once $J/G_{dat} = 1$ is exceeded. A lower bound on G can be found (next Section) and an upper bound on G is known (neglecting hardening) from limit load. If a guess is made on a plausible p/t less than the datum value, an estimate of J can be made, but it is inconsistent as to how it relates to G or G_{dat}. Such inferred points are quite plausible in relation to Fig.1, for CT200. The missing factor appears to be an R-curve for small growth, so small indeed, that the data would at first be on the blunting line. Very preliminary studies suggest that, at least for self consistency of the model, J_i must be taken as G_{dat} (i.e. much less than the value $J_{di} \approx J_{Ic}$) and then a value $J_b > J_i$ used from the blunting line, for minute amounts of growth. The role of these minute amounts of 'growth' is to allow p/t

to increase by reduction of t, once $J > G_{dat}$. A case being studied can then move away from an initial p/t in a determined way, even though there is still no distinction in value between J/G and J/I.

It is speculated that the lack of modelling of blunting and the R-curve for small growth in the CCT example, is the reason why the J and G values calculated, though satisfactory in themselves, did not map ductile initiation correctly, although another possible reason emerges in the next section where it is seen that the role of fatigue pre-cracking might affect the issue.

Is there a minimum value of cleavage toughness?

It has already been noted in developing the initial instability arguments that the value of p at the datum point, p_{dat}, as calculated from the lefm validity limit, turns out to be about 10 or 20 fold higher than might be expected for steel. That no doubt implies some group of associated particles is having to be broken to establish instability rather than the existence of a very large single source; in short, as noted when the RKR concept for initiation was adopted, p is an effective size of a relevant source, rather than the actual size of an individual particle. If a single particle were envisaged for ssy, then G_{ssy} is some 10 or 20 fold smaller than G_{dat}. As a check on this viewpoint, the maximum value of load to be used for fatigue pre-cracking, is given for the DNB test in the ASTM E1152 test method as $Q(max) = 0.5Bb\sigma_o^2/S$. Combining with the lefm validity requirement shows the maximum G for fatigue cracking, for the DNB case a/W = 0.5, to be $G_{fat} \approx 0.54G_{dat}$. This is well above the range just mentioned for ssy, so that the fatigue pre-cracking level is now taken to set a specifiable starting point for discussion, G_{fat}, rather than the unquantified value G_{ssy}. This is coupled with the suggestion that the stress for cleavage, σ_{cl}, is in reality a term such as G_{cl}/p, where G_{cl} is a material property for cleavage (at least for a given type of source in the material in question). Thus, for p itself constant (or having a few discrete narrow ranges of values as already supposed) then a line as for Eq.14 can be plotted in Regime 1A on Fig.7 to represent the fatigue pre-cracking process, here taken with N = 0.54;

$$r_{fat}/t = 0.54(2.16)p/t \approx 1.17\ p/t \qquad (16)$$

which cuts the datum line (point +, Fig.7) at $p/t_{fat} \approx 6.0$. It should be noted that r_{fat} is the size of the monotonic plastic zone at the maximum load of the fatigue cycle and not the cyclic zone size.

It is now argued that at G_{fat}, the full extent of the plastic zone, r_{fat}, (implying m = 1) will allow dislocations to congregate along the interface of sources within it, so that such a source is nullified since it could not itself be subsequently broken and thus release the energy implied in the instability arguments. Thus, for subsequent cleavage, $t_{min} = m_{cl}^2 r_{fat}$, where the factor m_{cl} allows for the fact that the minimum m for cleavage is expected to be higher than m = 1 at which the congregation of dislocations onto sources has been supposed, perhaps nearer 1.5, and that r_m scales with m^2, Eq.3. Thus, the minimum value of G for cleavage, written as MG_{dat}, is defined by

$$r_{min}/t = ((p/t_{fat}) + 1)/m_{cl}^2 = 7.0/m_{cl}^2 \qquad (17)$$

whence using $m_{cl} = 1.5$, $r_{min}/t = 3.11$, and the line for J = G through that point is $r_{min}/t = 3.11 = 2.16Mp/t$, giving M = 1.44, so that $G_{min} = 1.44G_{dat}$; for $m_{cl} = 1.7$, $G_{min} = 1.12G_{dat}$.

The absolute value of G_{min} is of course also size dependent because G_{dat} depends on size through the lefm validity rule used to define it. For the case CT50, where (to two significant figures) $G_{dat} = 0.014$MN/m, a minimum cleavage toughness for $m_{cl} = 1.5$ is $G_{min} = 0.020$MN/m and for $m_{cl} = 1.7$, $G_{min} = 0.016$MN/m; the minimum experimental value was $G_{expt} = 0.017$MN/m. For CT200, $G_{dat} = 0.054$MN/m, $G_{min} = 0.077$ or 0.060 MN/m with $G_{expt} = 0.057$MN/m.

In general, for $N_{max} > N > N_{min}$ where $N_{max} = 0.86m_{cl}^2/(1.86m_{cl}^2 - 1)$ and $N_{min} \approx 0.86/1.86 \approx 0.463$. $N_{max} \approx 0.61$ for $m_{cl} = 1.5$, increasing as m_{cl} is reduced.

$$M = G_{min}/G_{dat} = N/(2.16N - 1)m_{cl}^2 \qquad (18)$$

For $N \geq N_{max}$, the apparent $r_{min}/t \leq 1.86$ implying $p/t_{min} < 0.86$. A higher G_{min} would occur from intersection of G_{fat} with the datum curve, Eq.8b, instead of with the datum line, Eq.3b. For $N \leq 0.463$, the line $G_{fat} = NG_{dat}$ does not intersect the Eq.3b, the effect of pre-cracking being caused by intersecting Eq.8b, at $p/t_{fat} << 6.0$, to give a lower G_{min}.

In [4] and the related SNB studies of [20], the range of maximum K_{fat} used is stated, giving $0.002 \leq G_{fat} \leq 0.003$MN/m. For the very small a/W cases in [20], the crack length was reduced by machining off the front face after fatigue pre-cracking, so that, for the case a/W = 0.05, the new $G_{dat} \approx 0.00023$MN/m, based on the remaining crack length of about 1.3mm. The experimental J is 0.19MN/m for cleavage. With the original $G_{dat} \approx 0.003$MN/m, $N > N_{max}$ above, for $m_{cl} = 1.5$. The value of p/t_{min} is here assessed on N =1. Cleavage occurs at $J_{cl}/G_{dat} >> 1$. An approximate estimate of an upper bound

of J_{cl} as controlled by fatigue and using $m_{cl} = 1.5$, but which does not satisfy G at limit load is 0.17MN/m.

It is now generally argued that in low constraint situations, the cleavage toughness, including the minimum value, is higher than in full constraint. That is supported for much of the data cited, in terms of J. It is not clear that loss of constraint is relevant to the minimum cleavage toughness, when examined in terms of G. And it will be recalled that most uses of the J(Q,T) analyses via J_o or J_{ssy}, are phrased to eliminate that variation in J, a result, as seen in the discussions of Figs.1–4, more easily obtained by use of G in the first place. Whilst not denying that constraint may be lost as plasticity develops, the value for J_{cl} just quoted has been derived with no allowance for loss of constraint per se, because use of $m_{cl} = 1.5$, in the upper bound for J, is a condition that covers the case where constraint is indeed lost. Clearly more study is needed.

A remark on the statistics

Perhaps most importantly, the implications on any statistical approach that certain aspects of the scatter are deterministic, needs consideration. The argument that G rather than J is the correct yardstick, will no doubt arouse controversy. A first question, even if the energetic approach is not approved of is "why should J, that exceeds G only due to deformation exceeding the elastic value, be relevant to what is agreed by all to be an essentially stress controlled phenomenon, when G is a direct (geometry dependent) measure of load and thus stress?" This paper is an answer to that question, but the immediate point is that any statistical approach should surely be based on G rather than J? The dependence of G_{min} on G_{fat}, if accepted, seems very relevant to a statistical treatment, not only in testing, but also in service where standard test restrictions on the fatigue loading conditions, are not of course relevant. In-service fatigue, if at higher maximum levels of K or G, would imply a smaller value for M and thus give a higher limit for G_{min} for a given size.

The dependence on size of the lefm valid limit, to which G_{dat} and then G_{min} is related, Eq.18, also seems of great importance, again in relation to service as much as testing. As already remarked earlier, the very high J values (which translate to some but not all of the intermediate G or I values) are a consequence of instability control, which on a macro-scale is a system behaviour, not a material property.

In [10], a model is given for the minimum toughness based on even a single test value, and that estimate is compared to various other statistically based estimates. It was applied, inter alia, to the CT data of [9], but not to the CCT data. The formula for the lower bound, J_{LB}, was

$$J_{LB} = J_{fc}[\{\ln [P/(P+1)]/\ln[1/(P+1)]\}]^{1/m} \qquad (19)$$

where J_{fc} is the observed value (preferably not too far removed from lefm to give the best bound), $P = (C/B)(J_{fc}/\sigma_o)$, and C is a constant taken in the light of experience for this type of steel as 1000 and m is the Weibull constant, taken as 2. Applying that to the lowest experimental values, gives

CT50, $J_{LB} = 0.012$ ($J_{fc} = 0.017$), $G_{min} = 0.010$MN/m (as estimated above)

CT200, $J_{LB} = 0.017$ ($J_{fc} = 0.052$), $G_{min} = 0.037$MN/m

CCT0.6, $J_{LB} = 0.016$ ($J_{fc} = 0.062$), $G_{min} \approx 0.012$MN/m (with uncertainty over a number of factors; a β correction for lack of full plane strain raises G_{min} to 0.014MN/m).

It is also shown in [10] that the ASTM assessment of J_{LB}, using the β method and a Weibull analysis, [28], gives $J_{LB} = 0.014$MN/m for CT.

These assessments are all remarkably similar, with the exception of the present G_{min} for CT200. That size effect here appears genuine, provided the fatigue pre-cracking is carried out at a common fraction of G_{dat}, here N = 0.54, of the lefm valid plane strain limit of G for the size in question. It is emphasised that, if that formula, $Q = 0.5Bb^2\sigma_o/S$, were for convenience first translated into a fraction of J_{di} or some size independent G_{Ic} value, then quite different predictions would be made. Of the four sets of data in [9] that show either 3 or 4 different sizes (two side grooved sets with various W, two of proportionally sized) at otherwise common conditions, three show a clear trend of a higher minimum as size increases, the fourth showing no trend.

General discussion

The picture presented is based on very simple algebra, with work-hardening not directly incorporated, but contains two more levels of physical behaviour, a local instability and an effect of fatigue pre-cracking, than has been used in most current models of cleavage behaviour. It is presented in a two dimensional form. The implications of random variations in p/t across the thickness and of more complicated interactions between very small initial instabilities and one large enough to trigger unstable growth over the whole thickness, needs further study. No attempt is made here to discuss a number of other cleavage related features in the light of the present work, notably warm pre-stressing, dynamic fractures or sources between the tip and r for m_{max}.

Nevertheless, it is of interest to follow the likely behaviour of a given material at two different temperatures, one on the lower shelf of brittle behaviour

and one close to the upper shelf. The only variables are the yield stress, σ_o, the work-hardening, possibly σ_{cl} and perhaps the level of fatigue used for pre-cracking, relative to G_{dat} at the test temperature. Fatigue is important to the value of G_{min} and the ratio J_{di}/G_{dat} will affect the onset of cleavage after some small amount of stable growth, a smaller ratio, high on the transition curve, allowing more stable growth. That might interact with the system dependence of I, (see Appendix). In near lefm, on the lower shelf, not only is $I \approx G$ and independent of the system, but the running crack speed will be high and driving energy restricted to that in the test piece. To the contrary, near the upper shelf where the fracture is post-yield, and the higher toughness a mixture of micro-ductile and cleavage events, then $I > G$ and becomes system dependent, whilst the slower crack speeds of the tougher material will begin to allow driving energy from the system beyond the test piece itself. A distinction between a subjectively fast but stable ductile tear and an unstable ductile tear, also arises in that the former is by definition driven by work whereas the latter is driven by internal energy. The former would allow remote slip and loss of constraint in suitable cases whilst the latter would not. The unstable ductile crack, even in such as CCT, would therefore advance with high triaxiality which might thus allow a transition to cleavage, quite apart from any effects of strain rate on the yield strength.

But perhaps, finally, an effect of length on brittle fracture, [29], should be recalled, since it was refuted at the time by Irwin and Kies, [30], on then purely lefm arguments. Subsequent tests, [31], showed no effect on the lower shelf of the appearance transition curve but an extension of the upper shoulder of the curve to higher temperatures. In the light of yielding fracture mechanics, that would surely be consistent with the system dependence of I, just discussed.

Conclusions

An energetic model of cleavage fracture has been made, complementary in general to the existing stress based two parameter J(Q,T) type approaches. On the micro-scale the RKR model is used, in which a plastic zone of size r_m envelops a source, at some stress level $m_{cl}\sigma_o$.

The model shows that cleavage is sometimes controlled by initiation and sometimes by instability, according to the size, p, and distance from the crack tip, t, of the brittle sources involved. A datum value of p/t is given when the two requirements are met simultaneously. Instability governs for p/t smaller than that datum and initiation for p/t larger.

The datum point can be calibrated in terms of toughness, using the lefm valid value for the material, temperature and size in question. The behaviour is then be explored by plotting G versus J, with J/G taken as a variable to characterise the extent of plasticity. That leads to a cleavage fracture diagram of r_m/t versus p/t.

Neither the upper nor lower limits of G (or J or other parameter) for cleavage are, in general, explicit measures of a material property. The former is controlled by limit load; the latter by either instability or initiation of which only the latter represents a material 'property' in the strict sense, and that of course is very scattered. The minimum cleavage toughness, to give at least a small burst of unstable fracture, is a consequence of the ratio of p/t relevant to the source available, and that is strongly affected by the fatigue pre-cracking level.

The algebra used is very simple and quite approximate, but the seemingly more realistic physical model whereby there is an interplay between cleavage initiation, local instability, ductile initiation, level of fatigue pre-cracking and the degree of plasticity (which may cause loss of constraint), seemingly outweighs the simplicity of the formulae used, as witnessed by the quite satisfactory mapping of several data sets existing in the literature.

Appendix

The elastic energy rate available in lefm is G, but with plasticity, becomes the larger term, I (for Irwin). The term I was used to discuss final ductile instability, [11b][12], and has more recently been set in the wider context of an energy dissipation rate model for crack toughness, including stable growth, [13–16]. The term is

$$I = -\partial w_{el}/B\partial a|_q \qquad (A1)$$

where sub q implies fixed displacement, q. Clearly, for lefm, I is identical to G, since |q becomes $|q_{el}$ but as plasticity becomes more extensive, so I exceeds G. The expression for I, [11], is

$$I = G\{(2\eta_{ep}/\eta_{el}) - 1\} \qquad (A2)$$

where η_{ep} is the elastic-plastic case, in general intermediate between the elastic and fully plastic condition. Eq.A2 can alternatively be written

$$I = G + G_{pl} \text{ where } G_{pl} = 2G\{(\eta_{ep}/\eta_{el}) - 1\} \qquad (A3).$$

It should be appreciated that only the energy rate GBda is available for fracture, since G_{pl}Bda is a direct translation

of elastic to plastic energy that occurs as a consequence of crack growth in the plastic state. However, since even the fracture energy, GBda, is converted to plasticity in the Irwin-Orowan model, the distinction is one of understanding rather than of great substance. The component G_{pl} is sensitive to length, through the length dependence of η_{el}. Treating system compliance as an equivalent length, (whilst neglecting inertia for the quasi-static treatment here), makes G_{pl} and thus I, system dependent. Clearly $G_{pl} \rightarrow 0$ and $I \rightarrow G$ for lefm, so that, for well contained yield the three values, G, I and J, do not differ by more that a few percent. For contained yield $J > G$ and for uncontained yield, it is well known that $J >> G$. For the commonly used cases of compact tension (CT), three point deep notch bending (3DNB) and indeed shallow notch bending (3SNB), the values of η_{el} and η_{pl}, though configuration dependent, are nearly equal to each other, so that even for extensive plasticity, $I \approx G$, and the generality that I exceeds G may be overlooked. But for most other configurations, including centre cracked tension (CCT), η_{pl} exceeds η_{el} by appreciable amounts and η_{el} is roughly inversely proportional to gauge length, so that, as extensive yielding is approached, $I > G$, sometimes by several fold.

Algebraic expressions do not exist for $\eta_{ep} = JBb/U$ but approximate values can be estimated by weighting the elastic and plastic terms appropriately, where U is work and w_{el} is elastic energy:

$$\begin{aligned} \eta_{ep} &= (J_{pl} + G)Bb/U \\ &= \{\eta_{pl}(U - w_{el}) + \eta_{el}w_{el}\}/U \\ &= \eta_{pl}\,(J/G)/\{(J/G) + (\eta_{pl}/\eta_{el}) - 1\} \end{aligned} \qquad (A4)$$

whence for any chosen value of J/G, I/G can be evaluated from Eq.A4 and J/I found for use with Eq.8 or 10.

References

1. N. P. O'Dowd and C. Fong Shih, "Two-parameter Fracture Mechanics: Theory and Applications," Fracture Mechanics: Twenty-fourth Volume, STP 1207, (Philadelphia: ASTM, 1994), 21–47.

2. J. W. Hancock, W. G. Reuter and D. M. Parks, "Constraint and Toughness Parameterised by T," Constraint Effects in Fracture, STP 1171, (Philadelphia: ASTM, 1993), 21–40.

3. T. L. Anderson, N. M. R. Vanaparthy and R. H. Dodds, Jr, "Predictions of Specimen Size Dependence on Fracture Toughness for Cleavage and Ductile Tearing," Constraint Effects in Fracture, STP 1171, (Philadelphia: ASTM, 1993), 473–491.

4. J. D. G. Sumpter, "An Experimental Investigation of the T-Stress Approach," Constraint Effects in Fracture, STP 1171, (Philadelphia: ASTM, 1993), 492–502.

5. J. D. G. Sumpter and J. W. Hancock, "Shallow Crack Toughness of HY80 Welds: An Analysis Based on T Stress," Int. J. Pressure Vessels and Piping, 45(1991) 207–221.

6. T. L. Anderson and R. H. Dodds, Jr, "Specimen Size Requirements for Fracture Toughness Testing in the Ductile-Brittle Transition Region," J. Testing and Evaluation, 19(1991), 123–134.

7. M. Y. Kirk, R. H. Dodds, Jr. and T. L. Anderson, "An Approximate Technique for Predicting Size Effects on Cleavage Fracture Toughness (Jc) Using the Elastic T-Stress," Fracture Mechanics: Twenty-fourth Volume, STP 1207, (Philadelphia: ASTM, 1994), 62–86.

8. R. H. Dodds, Jr., C. Fong Shih and T. L. Anderson, "Continuum and Micromechanics Treatment of Constraint in Fracture," (Report Civil Engineering Studies, Structural Research Series 573, Dept. of Civil Engineering, University of Illinois at Urbana-Champaign, 1992).

9. J. D. Landes, "The Effect of Size, Thickness and Geometry on Fracture Toughness in the Transition," (Report GKSS 92/E/43, GKSS, Geesthacht, 1992).

10. J. D. Landes et al., "Single-Specimen Test Analysis to Determine Lower-Bound Toughness in the Transition," Fracture Mechanics: Twenty-fourth Volume, STP 1207, (Philadelphia: ASTM, 1994), 171–185.

11. D. G. H. Latzko, et al. Post-yield Fracture Mechanics, a) (1st ed), Applied Science Pub, 1979; b) (2nd ed), Elsevier Applied Science Pub, 1984.

12. M. R. Etemad and C. E. Turner, "An Investigation of the I and dJ/da Concepts for Ductile Tearing and Instability," Fracture Mechanics: Proc 11th National Symposium, STP 905, (Philadelphia: ASTM, 1979), 614–28.

13. C. E. Turner and O. Kolednik, "A Micro and Macro approach to the Energy Dissipation Rate Model of Stable Ductile Crack Growth," Fat. and Fract. of Eng. Mats. and Structs., 17(9) 1994, 1089–1107.

14. C. E. Turner and O. Kolednik, "Application of Energy Dissipation Rate Arguments to Stable Crack Growth," Fat. and Fract. of Eng. Mats. and Structs., 17(10) 1994, 1109–1127.

15. O. Kolednik and C.E. Turner, "Application of Energy Dissipation Rate Arguments to Ductile Instability," Fat. and Fract. of Eng. Mats. and Structs., 17(10) 1994, 1124–1145.

16. C. E. Turner and O. Kolednik, "A Simple Test Method for Energy Dissipation Rate and CTOA for Large Amounts of Growth and the Study of Size and Transferability Effects," Fat. and Fract. of Eng. Mats. and Structs., (20) 1997. In press.

17. J. G. Merkle "Evaluations of the Irwin β_{Ic} Adjustment for the Small Specimen Fracture Toughness Data," Nucl. Engng. Des. 86(1985), 111–117.

18. G. R. Irwin "Fracture Mode Transition for a Crack Traversing a Plate," J. Basic Engng. 82(1960), 417–425.

19. T. J. Theiss, D. K. M. Shum and S. T. Rolfe, "Interim Results from the Heavy Section Steel Technology (HSST) Shallow-Crack Fracture Toughness Program," Fracture Mechanics: Twenty-fourth Volume, STP1207, (Philadelphia: ASTM, 1994) 131–151.

20. J. D. G. Sumpter and A.T. Forbes, "Constraint Based Analysis of Shallow Cracks in Mild Steel," (Proceedings of the Int. Conf. on Shallow Crack Fracture Mechanics Tests and Applications, TWI, Cambridge, 1992).

21. O. L. Towers, "Stress Intensity Factors, Compliances and Elastic η Factors for Six Test Geometries," (Report, TWI, Abington, Cambridge, 136/1981).

22. J. R. Rice, *et al.* "Some Further Results of J Integral Analysis and Estimates," Progress in Flaw Growth and Toughness Testing, STP 536, (Philadelphia: ASTM, 1973), 231–245.

23. F. A. McClintock, "Effects of Root Radius, Stress, Crack Growth and Rate on Fracture Instability," Proceedings of Royal Society. London: (Series A), 285 (1965), 58–72.

24. R. O. Ritchie, J. R. Rice and J. Knott, "On the Relationship Between Critical Tensile Stress and Fracture Toughness in Mild Steel," J. Mech .Phys. Solids, 21(1973), 395–410.

25. J. F. Knott, Fundamentals of Fracture Mechanics, Butterworths, 1973.

26. S. G. Druce, G. P. Gibson and M. Capel, "Microstructural Control of Cleavage Fracture in an A508 Class 3 Pressure Vessel Steel," Fracture Mechanics: 22nd Symposium, STP1131 (Philadelphia: ASTM, 1992), 682–706.

27. R. M. McMeeking and D. M. Parks, "A Criterion for J-Dominance of Crack-Tip Fields in Large Scale Yielding," Elastic-Plastic Fracture, STP 668, (Philadelphia: ASTM, 1979), 175–194.

28. D. E. McCabe and J. G. Merkle, "Proposed Test Practice (Method) for Fracture Toughness in the Transition Range," ASTM Task Group E24.08.08, Nov 1991.

29. H. de Leiris, "Sur L'influence de la Longeur dans le Phénomène de la Dechirure Semi-fragile," Comptes Rendue de l'Acad. des Sciences, 234(1952), 1125–1126.

30. G. R. Irwin and J. A. Kies, "Critical Energy Rate Analysis of Fracture Strength," Weld. Jour., 334 (April 1954) 193s–198s.

31. R. E. M. Ball and C. E. Turner, Some effects of External Energy on Fracture in the Notch Tensile Test of Mild Steel," Jour. Iron and Steel Institute, 201(1963), 47–53.

DISLOCATION AND ATOMISTIC THEORIES

KINETICS OF THE CRACK-TIP-GOVERNED BRITTLE TO DUCTILE TRANSITIONS IN INTRINSICALLY BRITTLE SOLIDS

A.S. Argon *, G. Xu *†, M. Ortiz ‡
* Massachusetts Institute of Technology, Cambridge, MA 02139
† present address: Terra Tek, Inc, Salt Lake City, Utah 84108
‡ California Institute of Technology, Pasadena, CA 91125

Abstract

Brittle-to-ductile transitions in the fracture of intrinsically brittle solids manifest themselves in two fundamentally different forms. In the first type of solids examplified by the BCC transition metals and some alkali halides in which dislocation mobility against the lattice resistance is governed by double kink nucleation, the corresponding fracture transition appears to be controlled by formation of dislocation embryos at crack tips. In the second type of solids exemplified by Si, and possibly all other compounds, dislocation mobility is governed not only by double kink nucleation but by kink mobility as well. In these solids the B-D transitions are known to be controlled by dislocation mobility. Here we report first on recent simulations of dislocation embryo formation from Mode I cracks in $\alpha - Fe$ as generic cases of BCC transition metals, and then on a new model of the mobility controlled transitions, typically in *Si*. Both models find good experimental confirmation.

Introduction

Abrupt transitions in fracture between energy absorbing ductile forms and brittle cleavage, with decreasing temperature and increasing strain rate have been, and still continue to be of concern in many structural materials. While the phenomenon has been known in engineering practice since at least the celebrated molasses tank fracture in Boston in 1919 (for a discussion of an historical perspective of nonship fractures see Shank, [1]), it became of crisis proportions only during World War II through the rash of major fractures of Liberty ships. In the early post-war years the problem received attention through semi-quantitative studies of notch effects and strain rate [2], and through some studies of effects of microstructure and of alloying to suppress the ductile to brittle transition temperature (for a summary see Parker, [3]). In the 50s and early 60s a fundamental recognition was reached that brittle behavior is usually triggered by deformation induced cleavage microcracks introduced into the system by dislocation pile-ups [4-6] by intersection of deformation twins [7] or by cracking of elongated grain boundary carbides [8]. In the range of the transition temperature a substantial concentration of such microcracks are "injected" into the system. Eventual brittle behavior results when one such microcrack succeeds, without being rearrested, to break through grain boundary barriers and propagates long distances [9-11]. The triggering conditions for this final transition in polycrystalline metals were also studied theoretically [12-15].

A fundamental perspective on the class of materials which are capable of fracture transitions starts with Kelly et al [16], and more specifically with Rice and Thomson [17] who have conceived a fundamental behavior pattern for a theoretical criterion establishing intrinsic brittleness vs intrinsic ductile behavior in materials. According to this criterion an atomically sharp crack has means of governing the behavior of a material in the absence of any other form of plastic response of the background, by either nucleating dislocations from its tip or by propagating in a cleavage mode by virtue of the presence of an energy barrier to the emission of such dislocations. In the first instance the material is designated as intrinsically ductile and incapable of exhibiting a fracture transition, while in the second instance it is designated as intrinsically brittle and capable of undergoing a transition from brittle cleavage to ductile forms at a characteristic transition temperature T_{BD}, affected by the rate of loading. Although many experimental studies have demonstrated that mere nucleation of some dislocations from a crack tip does not assure ductile behavior [18,19], the Rice Thomson mechanism comes close to a threshold process that triggers ductile behavior in a class of intrinsically brittle solids with relatively high dislocation mobility, such as the BCC transition metals and most alkali halides. However, fully satisfactory experimental confirmation of this limiting response is rare, outside of an elegant experiment by Gilman et al. [20] of crack arrest in *LiF*.

In distinction to the nucleation controlled response is the well established response of Si, and presumably, many other covalent materials and compounds with sluggish dislocation mobility, where the transition between brittle to tough behavior is governed by the mobility of groups of dislocations away from the crack tip [21-25]. In either the nucleation or the mobility controlled dislocation emission scenarios it is now well recognized that, emission of such dislocations from a crack tip occurs preferentially from specific crack tip sites and that assurance for full ductile behavior requires that

George R. Irwin Symposium on Cleavage Fracture
Edited by Kwai S. Chan
The Minerals, Metals & Materials Society, 1997

all parts of the crack front be shielded to prevent continued brittle behavior by local break-out of the cleavage crack from unshielded portions of the crack front [24]. Since even the ductile to brittle transition is triggered by the continued propagation of an "injected" cleavage microcrack, it is now widely accepted that the fundamental fracture transition is governed by the behavior of a cleavage crack. Most modeling studies have been developed around this concept.

The fundamental supposition of the brittle-to-ductile transition models based on the Rice and Thomson scenario [17] is that while background plastic relaxations can serve to suppress the transition temperature, the ultimate arbiter of the transition is the ability, of the crack tip to emit dislocations that can shield the entire crack front and trigger widespread plastic deformation before the crack can propagate by cleavage. However, the approach of the Rice and Thomson model in which the activation configuration consisted of a fully developed dislocation line have proved to seriously over estimate the energy barriers to nucleation of dislocations [26], even after incorporating such refinements as crack tip non-linearity and tension softening [27] across the slip plane. This indicated that the activation configurations must involve imperfect dislocations which must incorporate at least a minimum of atomistic information [26].

The accumulating experimental evidence on Si [21-25] and the insight provided by the most recent modeling studies of Schöck and Püschl, [28], Rice and Beltz [29], Xu et al., [30] suggest that the activation configuration of a dislocation embryo is in the form of a double kink of dislocation core matter. The observation permits the identification of two distinct types of B-D transitions. In the BCC transition metals where barriers to kink mobility along the dislocation are low, the B-D transition is likely to be governed directly by the formation of dislocation embryos at the crack tip, resulting in a nucleation-controlled transition. By contrast, in semi-conductors and compounds the evidence suggests [31-35], and modeling verifies [36], that kink mobility is hindered by substantial energy barriers, rendering the B-D transition controlled by dislocation mobility away from the crack tip.

Ultimately, a full understanding of the B-D transitions must come from atomistic models of the formation and outward propagation of the dislocation embryo at the crack tip. Before such modeling can be attempted, however, much progress can be made by recourse to hybrid continuum-atomistic approaches [28-30,37] based on the use of a Peierls interplanar potential [38-40]. In a recent development of this technique by Xu et al. [30], an additional surface production resistance was introduced into the interplanar potential, and the appropriate saddle point configurations of the dislocation embryos were determined by recourse to a variational boundary integral method advanced by Xu and Ortiz earlier [41]. Xu et al. [30] concluded that the energetics of dislocation embryo formation on inclined slip planes containing the crack tip, against an additional surface production resistance, is quite unfavorable and does not explain the known B-D transition temperatures. It was then conjectured that nucleation may be more favorable on oblique slip planes or, may occur heterogeneously at crack front ledges.

In the present communication we first review briefly the recent findings of Xu et al. [30,42] on the dislocation emission processes that most likely govern the brittle to ductile transition in BCC transition metals. These findings demonstrate the power of the special hybrid continuum - atomistic approach, based on the recently developed technique of Rice and coworkers [37], in fairly accurately predicting the transition temperature and the specific modes of dislocation embryo formation that govern it. We then present a new development for the B-D transition in fracture in Si where this transition is governed by dislocation mobility away from the crack tip. It is worth noting that even in this latter case the specific process of dislocation embryo formation at the crack tip will occur and often govern the mode of the crystal plasticity of the crack tip but do not govern the kinetics of the transition.

Modes of Dislocation Nucleation at a Crack Tip

Several alternative modes of dislocation nucleation from crack tips have been contemplated in the past. The modes differ mainly in the relative geometry of the slip plane, the crack surface and the crack front. The configurations considered include: nucleation of dislocations on the extension of the crack surface, Fig. 1a; nucleation on an inclined plane containing the crack front, Fig. 1b; nucleation on an oblique plane, Fig. 1c; and nucleation on a cleavage ledge, Fig. 1d.

Of these modes, that shown in Fig. 1a is the simplest, since it involves no tension across the potential slip plane and no production of a free surface. It has been investigated by Rice, [43] and Rice et al. [37] in a two dimensional setting and by Schöck and Püschl [28] in a three dimensional setting of a simple double kink shaped activation configuration. This was also done by a more elegant perturbation analysis by Rice and Beltz [29]. These analyses that have used a conservative tension-shear potential based on a Peierls-Nabarro model to represent the periodic interplanar shear resistance of a slip plane and a tension softening effect have demonstrated that the activation configuration did indeed consist only of dislocation core matter. In 2-D this produces an inelastic crack tip displacement equal to one half of a Burgers displacement and results in a critical energy release rate equal to the unstable stacking energy associated with a half step shear across the slip plane. Rice et al. [37] have extended their approach to also deal with the mode of Fig. 1b involving dislocation nucleation on an inclined plane-albeit without the affect of surface ledge production. A surface production resistance was incorporated into the Rice model by Xu et al. [30] who have concluded that this effect raises the energy barrier to such a degree that it all but rules out dislocation nucleation on inclined planes.

Experimental observations of Burns and Webb, [18] and considerations of local peak stress levels [26] point to the possibility of nucleating dislocations on oblique planes as shown in Fig.1c. However, approximate analysis of this nucleation mode by the Rice and Thomson method have led to very large energy barriers. This conclusion is reinforced

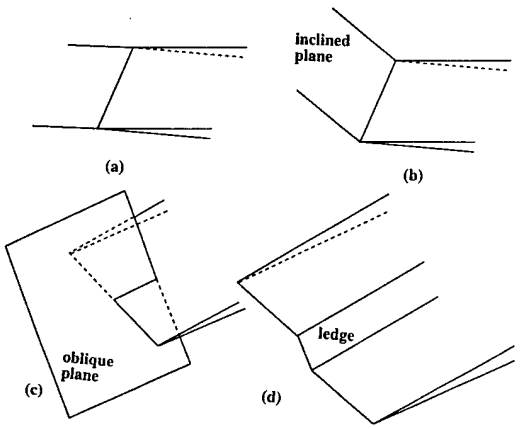


Fig. 1 Alternative modes of dislocation nucleation from a crack tip, ([42], courtesy of Taylor & Francis).

by a more accurate analysis of Xu et al. [42] that we present below. Finally, experimental observations of George and Michot, [25] have indicated that actual dislocation nucleation occurs very frequently on cleavage ledges on the crack front and near free surfaces. This possibility is analysed further below and shows that conditions are indeed quite favorable for it. Since nucleation controlled fracture transitions are likely to be limited only to BCC transition metals and to some alkali halides, the analysis of Xu et al. was performed for $\alpha - Fe$. Figures 2a-2c show the specific geometrical settings for Fe that were considered, where the cleavage plane is (001) and the crack front is parallel to the [110] directions which are the prevalent directions of the crack front in Fe giving a minimum of energy release rate [42].

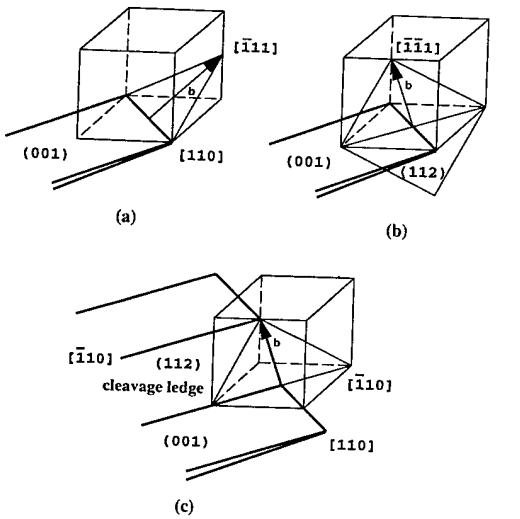


Fig. 2. Modes of dislocation nucleation from crack tips in $\alpha - Fe$: a) inclined plane; b) oblique plane; c) cleavage ledge, ([42], courtesy of Taylor & Francis)

Method of Analysis for Dislocation Embryos

The analysis for dislocation embryos employs a variant of the variational boundary integral method of Xu and Ortiz [41] to encompass problems of dislocation nucleation from atomically sharp cracks. In this model, a slip plane connected to the crack front is viewed as an extension of the crack surfaces with a nonlinear interlayer potential acting across it. Thus, the crack and the slip plane on which the dislocation nucleates are jointly regarded as a three-dimensional crack system embedded in the linear elastic solid. The interlayer potential acting across the slip plane is modeled by combining the universal binding energy relation of Rose et al. [44] with a skewed shear resistance profile [40]. The interplanar displacements and the crack opening displacements are represented by a continuous distribution of curved dislocations. This approach introduces no artificial discontinuity between the elastic crack opening and inclastic interplanar slip and separation. The technique has been described in complete detail by Xu and Ortiz [41] and its application to the present study by Xu et al. [30,42]. In this section, we briefly outline those aspects of the method which are pertinent to the treatment of the special activation configurations described in the previous section.

Consider a semi-infinite cleavage crack and a slip plane intersecting the crack front as shown in Fig. 1b. The crack/slip plane system is loaded remotely by a K-field. The crystallographic slip plane is chosen to be the most advantageous for slip. As the driving force increases, an embryonic dislocation forms progressively until it reaches an unstable equilibrium (saddle-point) configuration. The load corresponding to this unstable configuration is defined as the critical driving force for nucleation. The embryonic dislocation profile is characterized as a distribution of interplanar inelastic displacements, defined by Rice [43] as:

$$\delta = \Delta - \Delta^e \tag{1}$$

where Δ and Δ^e denote the total and the elastic interplanar displacements respectively. The opening displacements $\mathbf{u}$ of the crack surface, including the inelastic displacements along the slip plane, can be written as:

$$u = \overline{u} + \delta \tag{2}$$

where $\overline{u}$ is the displacement of a standard K-field for a reference semi-infinite crack. The term $\overline{u}$ matches the behavior of the opening displacements of the crack far away from the crack tip and serves as a boundary condition of the system. Consequently, the additional term δ, modifying the former, and being the primary unknown in the analysis, is expected to decay rapidly to zero with distance away from the crack tip in either direction. In this manner, δ can be considered in a finite domain around the crack front on the crack surface and on the slip plane connected to the crack.

Following the procedure introduced by Xu et al. [30,42], the potential energy of the whole system can be written in the form.

$$\Pi[\overline{u}+\delta] = W[\overline{u}+\delta] + V[\delta]$$
$$= W_1[\overline{u}] + W_1[\delta] + W_2[\overline{u},\delta] + V[\delta], \qquad (3)$$

where we identify $W_1[\overline{u}]$ as the elastic strain energy of the system, free of inelastic modifications, $W_1[\delta]+V[\delta]$ as the self energy of the system of inelastic modifications consisting of the distributed dislocations and the interplanar interaction energy on the slip plane, and $W_2[\overline{u},\delta]$ is the interaction energy of the initial unmodified system with the second system of modifications. Of these energies the ones of relevance in the variational approach are those that depend on the unknown inelastic modification δ. Their specific forms have been given elsewhere [30, 42].

The potential energy $V[\delta]$ of the interplanar inelastic deformation on the slip plane is a key ingredient of the method and is given as:

$$V[\delta] = \int_{\hat{S}_s} \Phi[\delta] dS, \qquad (4)$$

where $\Phi[\delta]$ is the interplanar tension/shear potential, defined per unit area of the slip plane, $\hat{S}_s$. It adopts the constrained displacement hypothesis of Rice [43] and Sun et al. [45], in which the interplanar shear displacement Δ_r is constrained along the Burgers vector direction. The shear and tension separation resistances, τ and σ respectively, follow as functions of the inelastic shear displacements δ_r and tensile separation displacement δ_θ on the slip plane. The associated traction-displacement relation has been modeled by Rice et al. [37] and was modified by Xu et al. [30] to incorporate an element of skewness and a surface production resistance. The resulting forms have been presented in detail elsewhere [30].

The unknown displacements follow by rendering the potential energy$\Pi[\overline{u}+\delta]$ stationary. This is achieved by discretizing the integral equation with six noded elements distributed on the crack surface. The non-linear equations are solved by a Newton-Raphson iteration. The saddle-point configurations are activated by introducing a small perturbation into the system at the bifurcation point, based on the solution of a first-order eigen-value problem if necessary. Solutions are obtained by recourse to interplanar displacement control, achieved through the introduction of Lagrange multipliers [30,42].

The material constants for α-Fe used in the present calculations are given in Table I.

Table I. Material Properties for α-Fe [42]

slip system	T (°K)	μ (10^5MPa)	c	$\gamma_{us}^{(u)}$ (Jm^{-2})	$2\gamma_s$
$(1/2)[111](1\bar{1}0)$	4.2	0.756	3.125	0.517	3.33
$(1/2)[\bar{1}\bar{1}1](112)$	4.2	0.756	3.125	0.581	3.80

where
- μ shear modulus
- c uniaxial strain elastic modulus
- $\gamma_{us}^{(u)}$ unrelaxed unstable stacking energy
- γ_s surface energy

Embryo Configurations and Energies

Nucleation of Dislocations from a Shear Crack in Mode II

This configuration which is easiest to analyse was the one considered first by Rice[43] to establish that in the athermal limit of emission of a straight dislocation, the critical configuration consists entirely of dislocation core material with a total inelastic crack-tip shear displacement of one half Burgers displacement and an energy G_{IIcd} equal to the unrelaxed unstable stacking energy $\gamma_{us}^{(u)}$. It is of little realistic interest, even in its 3-D saddle point forms at driving forces $G_{II} < G_{IIcd}$ that were analysed by Xu et al. [30,42].

Nucleation of Dislocations on Inclined Planes in Mode I.

The nucleation of a dislocation on any inclined slip plane passing through a Mode I crack will occur under a mixture of effective Modes II and Mode I where the local effective Modes I and II are related to the overall Mode I acting across the crack by [46],

$$K_I^{eff} = K_I cos^3(\theta/2) \;\; \therefore K_{II}^{eff} cos^2(\theta/2) sin(\theta/2) \qquad (5a,b)$$

To better appreciate this mixture of modes we have examined the general modifying effect on K_{II} of a K_I^{eff} acting across a slip plane, that is required to achieve an athermal 2-D release of a straight dislocation on this plane. This result is given in Fig. 3 [30] and demonstrates that while the effect of a K_I^{eff} acting across the slip plane does indeed produce some reduction in the required K_{II}^{eff}, this reduction is relatively minor. Xu et al. [30] have shown that this comes about from the lack of spatial coincidence of the non-linear opening displacements and shear displacements at the crack tip.

On any inclined slip plane the nucleation of a dislocation must produce a free surface ledge after the dislocation is emitted and has been sent into the background. During the actual nucleation process when the incipient surface is not

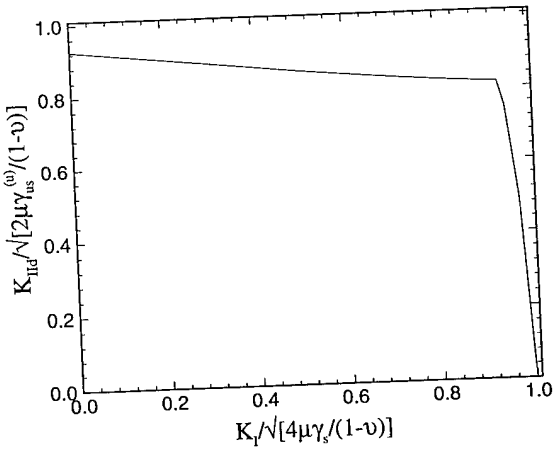


Fig. 3. Dependence of critical K_{II} for dislocation emission on K_I present on the $\frac{1}{2}[\bar{1}\bar{1}1](112)$ system of α-Fe ([30], courtesy of Taylor & Francis).

yet relaxed the effect must be considered as an additional surface production resistance to be added to the shear resistance of the tension shear potential [30, 47] to at least the first row of atoms that will be bared as a free surface. The result of a specific analysis of this effect is shown in Fig. 4 again for the release of a straight dislocation from the crack

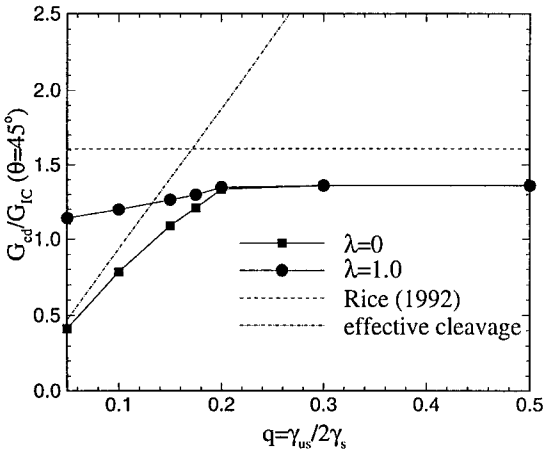


Fig. 4. Dependence of the critical energy release rate G_{cd}/G_{IC} on the factor $q = \gamma_{us}/2\gamma_s$ for dislocation nucleation at 45°, ([30], courtesy of Taylor & Francis).

tip onto an inclined plane making an angle of 45° with the crack plane. The dependence of the critical energy release rate G_{cd}, normalized with the crack driving force G_{IC} on the parameter $q = \gamma_{us}/2\gamma_s$ is shown for a case with no surface production resistance ($\lambda = 0$) and for a surface production resistance affecting substantially only the first row of atoms ($\lambda = 1$). The slanted dash-dotted line shows a somewhat more approximate estimate of Rice for no surface production resistance [43], while the horizontal dashed line gives the condition where cleavage is obtained on the slip plane. $G_{cd}/G_{IC} < 1.0$ indicates nucleation of a dislocation prior to propagation of the crack. The solutions including the surface production resistance indicates that for all values of q crack propagation on the cleavage plane will precede athermal release of a dislocation on the 45° inclined plane. Values of q range from 0.081 for Al to 0.091 for Ni (both for Shockley partial dislocations) to 0.217 for $\alpha - Fe$ and 0.376 for Si (Shockley partial) [30]. Since all cases lie above G_{cd}/G_{IC} of 1.0, it must be concluded that homogenous nucleation of dislocations on inclined planes is not possible prior to crack propagation for any material, regardless of whether it is intrinsically brittle or ductile [30].

Nucleation of Dislocations on an Oblique Plane.

Dislocation nucleation on oblique planes has frequently ben suggested as a likely mode. Approximate analyses based on the Rice and Thomson method have led to estimates of the B-D transition temperatures several orders of magnitude higher than what is experimentally observed, prompting suggestions that nucleation should involve a fractional dislocation [26].

The problem of the formation of a dislocation embryo on an oblique plane in $\alpha - Fe$ in the configuration of Fig. 2c was considered.

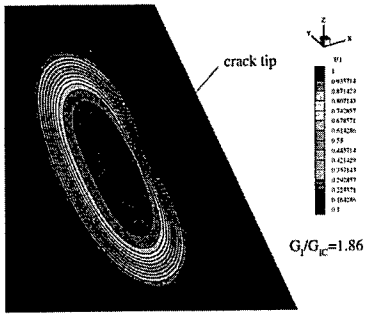


Fig. 5. Saddle-point configuration of a dislocation embryo emitted from a crack tip on an oblique plane, ([42], courtesy of Taylor & Francis).

A typical saddle-point configuration of such an embryonic dislocation loop emanating from the crack tip is shown in Fig. 5. The resulting calculated dependence of the activation energy on the crack driving force, near the athermal threshold is shown in Fig. 6. The critical driving force at the athermal threshold, and the attendant activation energies are so high that they render the nucleation mechanism most unlikely. The activation energy at $G_I/G_{IC} = 1.0$ can be estimated from the extrapolated curve, and forms an adequate basis for reaching a firm negative conclusion on the likelihood of nucleating a dislocation in the interior by this mechanism. A very different conclusion can be reached, however, for this mechanism where the crack front reaches a free surface. Here, no plane strain stress constraint exists and the resolved shear stresses on the oblique planes become much higher. An estimate of this is readily obtained by re-scaling the driving forces in Fig. 6 in proportion to

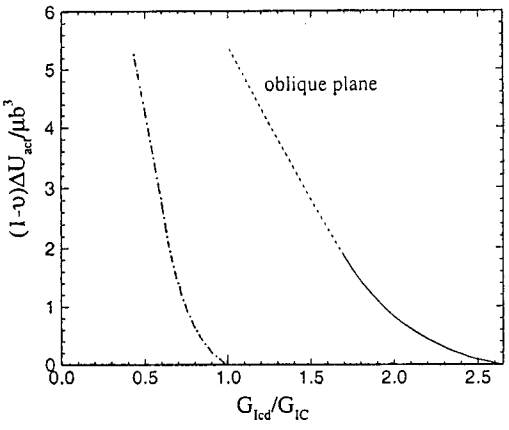


Fig. 6. Activation energies for dislocation nucleation on an oblique plane. Dash-dotted curve for such a plane near the surface, ([42], courtesy of Taylor & Francis).

the resolved shear stresses on the oblique slip planes near the surface vs those in the interior as (for the geometry of Fig. 2b):

$$\frac{G_{Is}}{G_{Ii}} = \left(\frac{3-4\nu}{3}\right)^2 \tag{6}$$

where G_{Is} and G_{Ii} are the respective energy release rates for initiation near the surface and in the interior. The result for *Fe* with $\nu = 0.291$ is shown as the dash-dotted curve in Fig. 6, which now suggests almost spontaneous nucleation near the surface. This, however, is not quite the case since in this instance some surface ledge needs to be produced on the side surfaces which will make the nucleation more difficult, but presumably still much easier than in the interior.

Nucleation of Dislocations on a Cleavage Ledge

Cleavage surfaces in metallic crystals invariably contain ledges parallel to the direction of crack propagation. These are likely to form when the direction of the principal tension driving the crack deviates slightly on a local scale, requiring the crack to make small adjustments along its front. This unavoidable micro-roughness of the cleavage surface depends on the crystallography of the cleavage planes and the crack propagation direction, as well as on temperature. The height of the observed ledges can range from several atomic spacings to microns. Numerous observations [24,25,48] have revealed that dislocation nucleation at a crack front is a relatively rare phenomenon associated with such crack front heterogeneities [49].

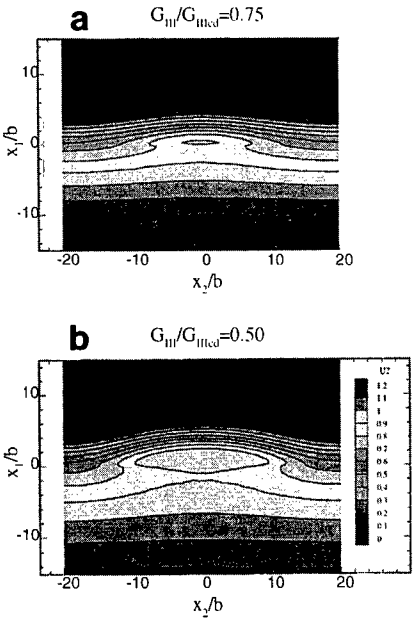
Consider a cleavage crack propagating under Mode I loading, and containing ledges of a width of roughly a hundred atomic spacings distributed along its front. The presence of a considerable local Mode III stress intensity factor acting on the ledge, the fact that no free surface is produced, and that the nucleated embryo will be nearly screw in nature are all expected to promote such nucleation.

The distribution of stress intensity factors on the crack front can be readily calculated by the boundary element method [41]. On the ledge, the dominant stress intensity factors are $K_I^{ledge} \sim 0.81 K_{IC}$ and $K_{III}^{ledge} \sim 0.35 K_{IC}$ at the verge of brittle propagation of the crack.

The athermal condition for nucleating a dislocation in Mode III loading, as it exists on the ledge, was determined by Rice [43], as:

$$\begin{aligned} K_{IIIcd} &= \sqrt{(1-\nu)\gamma_{us}/2\gamma_s} K_{IC} \\ &= 0.357 K_{IC} > 0.350 K_{IC} \end{aligned} \tag{7}$$

This result suggests that dislocation formation on crack front cleavage ledges should be close to spontaneous according to this simple estimate. However, we merely conclude that it should be in the range to initiate thermally assisted embryo formation. To analyse such thermally assisted embryo formation a saddle point analysis of a crack in pure Mode III, to apply to the problem at hand, of the cleavage ledge loaded in Mode III. Figures 7a and 7b show the saddle point configuration under normalized load levels of



Figs. 7a & b. Saddle-point configurations of a dislocation embryo on a cleavage ledge at $G_{III}/G_{IIIcd} = 0.75$, and 0.5, ([42], courtesy of Taylor & Francis).

G_{III}/G_{IIIcd} of 0.75 and 0.5 respectively. The resulting dependence of the activation energies for such configurations on actual normalized crack driving forces G_I/G_{IC} are shown in Fig. 8, for a case with no K_I component acting across the ledge (∇) and the case with the appropriate K_I component of $0.81 K_{IC}$ (o) acting across the ledge, as it should be the case of the geometry of Fig. 2c. The differences are small.

The B-D Transition Temperature in α-Fe

The preceding results can be used to estimate the B-D transition temperatures attendant to the three main nucleation modes considered. No precise experimental measurements of the transition temperature of single crystal $\alpha - Fe$ are available. The transition temperature for polycrystal low carbon steel is about $250^o K$, as determined from Charpy impact experiments [50]. Based on this, we take the transition temperature for $\alpha - Fe$ to be in the range of $250 - 300^o K$. A B-D transition scenario proposed by Argon [26] consists of the arrest, at T_{BD}, of a cleavage crack propagating with a velocity v against a temperature gradient. This gives the relation,

$$T_{BD} = \left[\frac{ln(c/v)}{\alpha} + \eta\frac{T_o}{T_m}\right]^{-1} T_o \tag{8}$$

where $T_o \equiv \mu b^3/k(1-\nu) \sim 1.2\text{x}10^5 K$; the melting temperature $T_m = 1809K$ for $\alpha - Fe$; $\alpha = (1-\nu)\Delta U_{act}/\mu b^3$ is the normalized activation energy; c is speed of sound; $v \sim 1\ cm/s$ is a typical crack propagation velocity, giving $\ln(c/v) \sim 10; \eta \sim 0.5$ is a coefficient describing the temperature dependence of the shear modulus which, to a first approximation, is taken to be of the form $\mu = \mu_o(1-\eta(T/T_m))$.

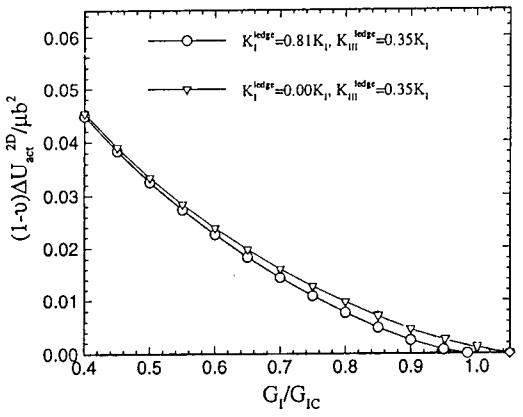


Fig. 8. Activation energies for dislocation nucleation on a cleavage ledge, ([42], courtesy of Taylor & Francis).

The activation energy at the critical driving force for cleavage , i.e., at $G_I/G_{IC} = 1$, determines the transition temperature through Eqn. 8. This relation is plotted in Fig. 9 together with reasonable ranges of activation energies for nucleation on inclined planes, oblique planes and on crack tip ledges. The results for the oblique plane near a free surface should be close to that for crack tip cleavage ledges. Also shown in the figure is the value of the transition temperature for polycrystalline *Fe* and its melting temperature. It is evident that only nucleation on cleavage ledges and on oblique planes near a free surface result in transition temperatures that approach the expected value for $\alpha - Fe$. The dislocation loops which eventually shield the entire crack are apparently emitted from ledges distributed along the crack front as was noted by George and Michot [25].

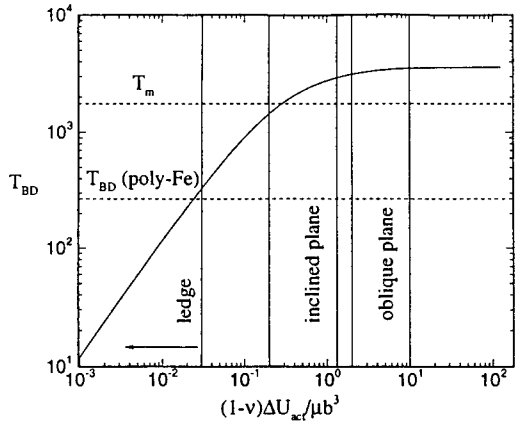


Fig. 9 Estimates of T_{BD} in $\alpha - Fe$, vis-a-vis the three primary nucleation configurations considered, ([42], courtesy of Taylor & Francis).

Dislocation Mobility Controlled B-D Transitions in Si

Stress Relaxation and Crack-Tip Shielding

That the B-D transition in *Si* single crystals is controlled by dislocation mobility is well established. The meticulously performed stress relaxation experiments of George and Michot [25] carried out at $K_I < K_{IC}$ levels have demonstrated that the development of crack tip shielding by the emitted dislocations leading to an eventual fracture transition is associated with a complex set of dislocations moving away from the crack tip on several crystallographic planes. The best available analyses of the spread of dislocations from the crack tip [51-53] have been too idealized and stylized to represent the real situation. Here we present a more homogenized approach that is based on the developments of Riedel and Rice [14] for sharp Mode I cracks undergoing stress relaxation by power-law creep from an initially elastic response. In their extensive characterization of the inelastic response of *Si* at elevated temperature Alexander and Haasen [55] have demonstrated that, once an initial stage of dislocation multiplication is completed, the steady state creep response of *Si* can be given by a nearly perfect power-law form of Eqn. 9 with a stress exponent of $n = 3$.

$$\dot{\epsilon} = \alpha exp\left(-\frac{U}{kT}\right)(\sigma/\sigma_o)^3 \tag{9}$$

where $\alpha/\sigma_o^3 = 1.34\text{x}10^3 MPa^{-3}s^{-1}$ and the activation energy $U = 2.4$ eV/atom.

The Riedel and Rice solution gives for creep stress relaxation around a Mode I crack at time t, for the tensile stress $\sigma_{\theta\theta}$ at the crack tip at $\theta = 0$ and $r = r_c = b$ the following form [56].

$$\sigma_{\theta\theta} = \sigma_o \left(\frac{K_I^2(1-\nu^2)/E}{\sigma_o \alpha exp(-U/kT) I_n (n+1) r_c t}\right)^{\frac{1}{n+1}} \tilde{\sigma}_{\theta\theta}^c(\theta, n) \tag{10}$$

where I_n is a well defined integration constant and $\tilde{\sigma_{\theta\theta}^c}(\theta, n)$ is another constant defining the angular dependence of the stress field around the crack. For the present purpose for *Si* with n=3 we represent the relaxing stress $\sigma_{\theta\theta}$ in a different form of

$$\sigma_{\theta\theta}(r_c) = \sigma_{ic}\tilde{\sigma}_{\theta\theta}^c(0,3)\left[\left(\frac{K_I}{K_{IC}}\right)^2 \frac{(1-\nu)^2}{\sigma_{ic}^2 E I_3}\left(\frac{\pi}{2}\right)\left(\frac{\sigma_o^3}{\alpha}\right)\frac{1}{t exp(-\frac{U}{kT})}\right]^{0.25} \tag{11}$$

where we have introduced the ideal cohesive strength σ_{ic}, determined from the universal binding energy relation of Rose et al [57].

$$\sigma_{ic} = \frac{1}{e}\sqrt{\frac{2\chi_s E}{(1-\nu^2)b}} = \frac{K_{IC}}{\sqrt{2\pi r_c}} \tag{12}$$

This permits a simple statement of the time dependent development of creep-strain-induced-crack-tip-shielding ΔK_{ISh} as

$$\left|\frac{\Delta K_{ISh}}{K_{IC}}\right| = \frac{K_I}{K_{IC}} - \tilde{\sigma}_{\theta\theta}^c(0,3)\left[\left(\frac{K_I}{K_{IC}}\right)^2 \frac{(1-\nu)^2}{\sigma_{ic}^2 E I_3}\left(\frac{\pi}{2}\right)\frac{\sigma_o^3}{\alpha t exp(-\frac{U}{kT})}\right]^{0.25} \tag{13}$$

The utility of this expression can be tested first to explain the recent stress relaxation experiments of Xin and Hsia [58]

on Si single crystals containing cracks subjected to stress intensities $K_I < K_{IC}$ for 20 hrs at 500C followed by subsequent measurement of increases of K_{IC} to fracture the samples at room temperature. As reproduced in Fig. 10, Xin and Hsia have noted that above a threshold of $K_I = 0.4K_{IC}$ increasing crack tip shielding develops in 20 hrs of stress relaxation with increasing K_I. Xin and Hsia attribute the stress intensity threshold to result from initiation of crack tip dislocation nucleation at this stress intensity at 500C over this period of holding. While this interpretation is, no doubt correct, we use the observation in our framework as a level of K_I/K_{IC} at which, over the period of holding, no significant crack tip shielding develops, and proceed to obtain a fit from Eqn(13) by solving for α/σ_o^3 for the well defined physical and simulation parameters of $n = 3, I_3 = 5.386, \sigma_{ic} = 17.7GPa, E = 147GPa, \nu = 0.215, \tilde{\sigma}^c_{\theta\theta}(0,3) = 1.9$. The choice is for $\alpha/\sigma_o^3 = 2.94x10^{-2}$ MPa^{-3} sec^{-1} and a factor of $2.19x10^{-5}$ smaller than the steady state value reported by Alexander and Haasen [55] and given above. While this discrepancy, at first sight, appears depressing, it is quite within expectations if it is recognized that in the Alexander and Haasen creep experiments the mobile dislocation density was $4.9x10^{11}m/m^3$. In the experiments of Xin and Hsia as well as on other B-D transition experiments performed on initially perfect crystals of Si the dislocation density starts out from zero and builds up in a slow transient. Thus, the value of α/σ_o^3 obtained from the fit amounts to a local mobile dislocation density at the time of transition to about $10^7m/m^3$ which is quite acceptable. Using this value, the subsequent levels of K'_{IC} at fracture reported by Xin and Hsia following the stress relaxation treatments can be determined simply from,

$$\frac{K'_{IC}}{K_{IC}} = 1 + \left(\frac{\Delta K_{ISh}}{K_{IC}}\right) \tag{14}$$

This result is plotted in Fig. 10 as the slanted dashed line and shows a similar nearly linear rise of K'_{IC}/K_{IC} with increasing K_I/K_{IC}, used in the stress relaxation experiment, but at a level of about 0.42 of what was reported by Xin and Hsia. Since there is no real or operational means of accommodating this finding by another adjustment in the developments of Eqns. (11-14), we attribute the difference

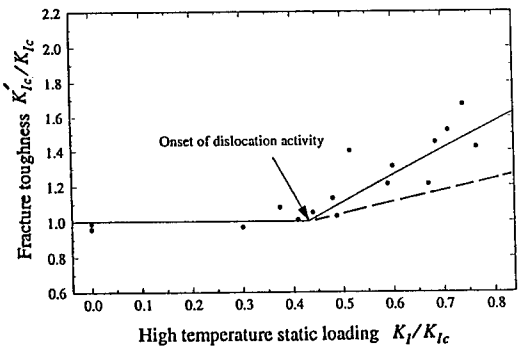


Fig. 10 Effect of crack tip stress relaxation at 500C for 20 hrs. for a cleavage crack on the (110) cleavage plane parallel to a [100] direction, on the subsequent fracture toughness. Dashed line represents Eqn. (14) (after Xin and Hsia [58], courtesy of Pergamon Press).

to a geometrical effect of fracture surface roughening, while the calculated effect presumably is what can be attributed to stress relaxation alone. Micrographs of fracture surfaces presented by Xin and Hsia show roughness levels that can readily account for the difference.

Brittle-to-Ductile Transitions in Constant Loading Rate Experiments

The B-D transition model presented by Brede [52], while quantitatively somewhat deficient, provides important insight into the dislocation-mobility-controlled-fracture-transition in Si. It demonstrates that a monotonic increase of the applied stress intensity factor K_I together with a concurrent crack tip stress relaxation results in a systematic reduction in the crack tip tensile stress from an otherwise linear increase with K_I in the absence of crack tip creep. At the range of the B-D transition, $\sigma_{\theta\theta}$ just manages to reach the ideal cohesive strength σ_{ic}, but the rate of increase in $\sigma_{\theta\theta}$ with time (orK_I) becomes zero. Thus, the B-D transition is a competition between elastic stress increase with a creep-induced-stress-relaxation process at a crack tip point $r = r_c$. Thus, the increase in the crack tip tensile stress $\sigma_{\theta\theta}(r = r_c)$ is,

$$d\sigma_{\theta\theta} = \left(\frac{\partial\sigma_{\theta\theta}}{\partial K_I}\right)_t dK_1 + \left(\frac{\partial\sigma_{\theta\theta}}{\partial t}\right)_{K_I} dt \tag{15}$$

where

$$\left(\frac{\partial\sigma_{\theta\theta}}{\partial K_I}\right)_t = \frac{1}{\sqrt{2\pi r_c}} = \frac{\sigma_{ic}}{K_{IC}} \tag{16a}$$

and

$$\left(\frac{\partial\sigma_{\theta\theta}}{\partial t}\right)_{K_I} = -\frac{\sigma_{ic}A}{4}\left(\frac{K_I}{K_{IC}}\right)^{\frac{1}{2}}\left(\frac{1}{t^5 exp(-\frac{U}{kT})}\right)^{\frac{1}{4}} \tag{16b}$$

obtainable directly from Eqn. (11) with,

$$A = \tilde{\sigma}^c_{\theta\theta}(0,3)\left|\frac{(1-\nu^2)}{\sigma_{ic}^2 E I_3}\left(\frac{\pi}{2}\right)\frac{\sigma_o^3}{\alpha}\right|^{\frac{1}{4}} = 1.28x10^{-3}(sec)^{0.25} \tag{16c}$$

for the quantities of Si given above.

At the B-D transition,

$$\sigma_{\theta\theta}(r = r_c) = \sigma_{ic} \quad \therefore \frac{d\sigma_{\theta\theta}(r = r_c)}{dt} = 0 \tag{17}$$

These two conditions with $t = K_I/\dot{K}_I$ and the use of Eqns. (15-16c) give a simple dependence of the brittle to ductile transition temperature T_{BD} on loading rate K_I as,

$$T_{BD} = T_o/ln(\dot{K}_o/\dot{K}_1) \tag{18}$$

where

$$T_o = \frac{U}{k} = 2.78x10^4 K \text{ and}$$

$$\dot{K}_o = \frac{4K_{IC}}{A^4} = 1.42x10^{12}\frac{MPa\sqrt{m}}{sec}$$

Moreover, the actual level of fracture toughness K'_{IC} at the verge of the fracture transition in units of the intrinsic frac-

ture toughness K_{IC} can be given as,

$$\frac{K'_{IC}}{K_{IC}} = \frac{1}{4}\frac{\dot{K}_o}{\dot{K}} exp(-U/kT) \qquad (19)$$

The experimental support of Eqn (18) is very good. Eqn. (18) gives,

$$\frac{dln\dot{K}_1}{d(1/T_{BD})} = -T_o = -2.78\text{x}10^4 K \qquad (20)$$

while the values of this dependence reported by Brede and Haasen[22] range from 2.08 x 10^4K(G)[21] to 2.32 x 10^4K(E) and 2.67 x 10^4K(F)[62], and 2.10 x 10^4K(A)[22] all for intrinsic *Si*.

While this agreement of the predicted dependence of T_{BD} on $\dot{K}_I$ is pleasing, a check of the accuracy of the absolute value of T_{BD} through Eqn. (18) reveals a further discrepancy. The use of Eqn. (18) with the values for *Si* listed above adjusted to the experiment of Xin and Hsia, would give the characteristic line (1) plotted on Fig. 11 showing the various experimental results reported by Brede and Haasen [22]. A better fit given by line (2) would require a different adjustment for α/σ_o^3 to 1.63 x 10^{-4} MPa^{-3} sec^{-1} and a corresponding change of $\dot{K}_o$ to 7.89 x 10^9 MPA$\sqrt{m}$/sec. This would imply an even smaller dislocation density in the experiments of the fracture transition investigations [21,22,25] whose data is given in Fig. 11, below those required in the stress relaxation experiment of Xin and Hsia. This is not unlikely if it is noted that all the data reported in Fig. 11 involves a fracture transition on the {111} cleavage plane with the crack front being parallel to the <112> direction, while in the Xin and Hsia experiment the cleavage crack is on the {110} plane with the crack front being parallel to the <100> direction. The slip distribution for these two geometries is radically different [25].

Experimental verification of Eqn. (19) is more difficult since when a successful transition is initiated it follows continuously to much tougher behavior.

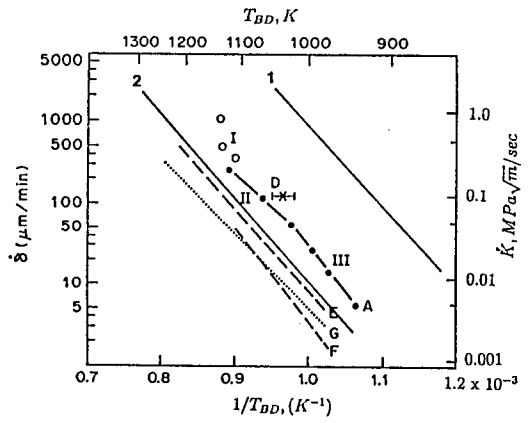


Fig. 11 Dependence of T_{BD} on loading rate $\dot{K}_1$ for a cleavage crack on (111) plane parallel to a [112] direction. Data from [22]. Line (1) results of Eqn. (18) based on Xin and Hsia data. Line (2) with adjustment for α/σ_o^3 more appropriate to the fracture transition experiments (after Brede and Haasen [22], courtesy of Pergamon Press).

Discussion

The models presented here relate to the fracture transition in both dislocation nucleation controlled solids, such as BCC transition metals and some alkali halides including *LiF, NaCl*, as well as in dislocation-mobility-controlled solids where *Si* is a principal example. In either case the processes are of key nature - more so in the initation-controlled solids then in the mobility-controlled solids where the actual toughening results from subsequent large scale plastic response, governed by extensive dislocation multiplication and spreading, rather than by the key process itself. The insight offered by the newly proposed approach using the Riedel-Rice solutions of continuum creep stress relaxation is particularly useful. It provides a good phenomenological framework in separating the two proccesses. Recently Roberts and coworkers[53,59] have advocated that all fracture transitions, including those in BCC transition metals, are governed by dislocation mobility on the basis of a good correspondence of the kinetics of the transition to the kinetics of dislocation mobility. We find this not convincing, first because the kinetics of dislocation glide in BCC metals exhibits a very different form from that in *Si*. In such materials the activation energy of glide against the lattice resistance is strongly stress dependent, manifesting itself in a very large phenomenolgical stress exponent in the range of 30-50 rather than 3, and a stress independent activation energy as is the case in *Si*. The resulting formalism following Eqns (11-19) while still useful, will indicate a near threshold type behavior in the fracture transitions. Nevertheless, the subject is still in need for further exploration in which our new developments could prove useful.

The two different adjustments that were necessary to the factor α/σ_o^3 representing the effective mobile dislocation density points out a number of important problems. First, in the range of transition to fully plastic behavior the evolution of a dislocation density is a complex process and as important as the kinetics of glide. Second, the actual B-D transition temperature (although not its dependence on loading rate) can depend sensitively on the particular kinematical distribution of the slip systems at the crack tip which is associated with the geometry of crystal plasticity and governs the effective density of dislocations that accomplish the transition. Finally, the adjustment exercise also points out the important role of mobilizable background dislocations, which through their polarization, will play a role in the crack tip shielding process. This is evident from the two cases considered. A formal increase in α/σ_o^3 shifts the T_{BD} toward lower levels.

There are many microstructural aspects of a B-D transition in polycrystalline solids in which microcrack, nucleation and processes of crack arrest at grain boundaries become very important, and will modulate the actual B-D transition temperature. Definitive understanding of these processes are still lacking. They too can benefit from more fundamental approaches of the type presented here.

Finally, we note that the ability of dislocation nucleation at the crack tip to account for the exceedingly sharp transitions observed in materials such as *Si* has been questioned by Khanta et al. [60, 61] who have advocated a critical phenomena approach, akin to defect- mediated melting where dislocation loops form and collapse in thermal equilibrium. The preponderance of the experimental evidence is against this proposition and supports the crack-tip dislocation mechanisms. Indeed, the detailed and meticulous direct X-ray imaging experiments of George and Michot [25] of the stages of evolution of the crack-tip plastic response, starting from nucleation at crack tip heterogeneities and followed by the very rapid spread and multiplication of dislocation length from such sources, is a convincing direct demonstration of the vast numbers of degrees of freedom available to dislocations for populating the highly stressed crack-tip zone. We know of no present experimental evidence nor any fundamental justification for the large thermal equilibrium concentrations of stiffness-attenuating dislocation dipoles that are predicted by the model of Khanta et al.

Acknowledgments

This research was supported by the Office of Naval Research (ONR) under contracts N00014-92-J-4022 and N00014-96-1-0629 with additional support from the ARO under Grant No. P-33768-MA-RIP for computer equipment acquisitions.

REFERENCES

1. M.E. Shank, *Mech. Eng., 76*, 23 (1954).
2. E. Orowan, in *Repts. Prog. Physics, vol 12*, p.185 (1949).
3. E.R. Parker, "*Brittle Behavior of Engineering Structures*", J. Wiley, New York (1957).
4. C. Zener, in "*Fracturing of Metals*", ASM, Metals Park Ohio, p.3 (1949).
5. A.N. Stroh, *Proc. Roy. Soc., A223*, 404, (1954).
6. A.N. Stroh, *Proc. Roy. Soc., A232*, 548 (1955).
7. D. Hull, *Acta Metall, 8*, 11 (1960).
8. C. McMahon, "*Micromechanisms of Cleavage Fracture in Polycrystalline Iron*", *ScD Thesis, M.I.T.*, Cambridge, MA (1963).
9. G.T. Hahn, B.L. Averbach, W.S. Owen, and M. Cohen, in "*Fracture*", edited by B.L. Averbach et al. MIT Press, Cambridge, MA, p. 91 (1959).
10. J.F. Knott and A.H. Cottrell, *J. Iron Steel Inst., 201*, 249 (1963).
11. M. Cohen and M.R. Vukcevich, in "*Physics of Strength and Plasticity*", edited by A.S. Argon, MIT Press, Cambridge, MA p.295 (1969).
12. A.N. Stroh, *Adv. Phys., 6*, 418 (1957).
13. R.O. Ritchie, J.F. Knott and J.R. Rice, *J. Mech. Phys. Solids, 21*, 395 (1973).
14. T. Lin, A.G. Evans and R.O. Ritchie, *J. Mech. Phys. Solids, 34*, 477 (1986).
15. T. Lin, A.G. Evans and R.O. Ritchie, *Met. Trans.,18A*, 641 (1987).
16. A. Kelly, W.R. Tyson and A.H. Cottrell, *Phil. Mag., 15*, 567 (1967).
17. J.R. Rice and R. Thomson, *Phil. Mag., 29*, 73 (1974).
18. S.J. Burns and W.W. Webb, *J. Appl. Phys., 41*, 2078 (1970).
19. S.J. Burns and W.W. Webb, *J. Appl. Phys., 41*, 2086 (1970).
20. J.J. Gilman, C. Knudsen and W.P. Walsh, *J. Appl. Phys., 29*, 600 (1958).
21. C. StJohn, *Phil. Mag., 32*, 1193 (1975).
22. M. Brede and P. Haasen, *Acta Metall, 36*, 2003 (1988).
23. P.B. Hirsch, J. Samuels, and S.G. Rloberts, *Proc. Roy. Soc., A421*, 25 (1989).
24. P.B. Hirsch, S.G. Roberts, J. Samuels and P.D. Warner, in *"Advances in Fracture Research"* edited by K. Salama et al. Pergamon, Oxford vol 1, p.139 (1989).
25. A. George and G. Michot, *Mater. Sci. Engng., A164*, 118 (1993).
26. A.S. Argon, *Acta Metall., 35*, 185 (1987).
27. K.S. Cheung, A.S. Argon and S. Yip, *J. Appl. Phys., 69*, 2088 (1991).
28. G. Schöck and W. Püschl, *Phil. Mag., A64*, 931 (1991).
29. J.R. Rice and G.E. Beltz, *J. Mech. Phys. Solids, 42*, 333 (1994).
30. G. Xu, A.S. Argon and M. Ortiz, *Phil. Mag., 72*, 415 (1995).
31. K. Sumino, in "*Structure and Properties of Dislocations in Semiconductors*", edited by S.G. Roberts et al, Inst. Phys., Bristol, England, p.245 (1989).
32. K. Maeda and Y. Yamashita, same as Ref. 31, p.269 (1989).
33. I. Yonenaga, U. Oriose and K. Sumino, *J. Mater. Res., 2*, 252 (1987).
34. I. Yonenaga, K. Sumino, G. Izawa, H. Watanabe and J. Matsui, *J. Mater. Res., 4*, 361 (1989).
35. I. Yonenaga, and K. Sumino, *J. Mater. Res., 4*, 355 (1989).
36. V.V. Bulatov, S. Yip, and A.S. Argon, *Phil. Mag., 72*, 452 (1995).

37. J.R. Rice, G.E. Beltz, and Y. Sun, in "*Topics in Fracture and Fatigue*", edited by A.S. Argon, Springer, Berlin, p.1 (1992).

38. R.E. Peierls, *Proc. Phys. Soc., A52*, 34 (1940).

39. F.R.N. Nabarro, *Proc. Phys. Soc., A59*, 256 (1947).

40. A.J. Foreman, M.A. Jaswon, and J.K. Wood, *Proc. Phys. Soc., A64*, 156 (1951).

41. G. Xu and M. Ortiz, *Intern. J. Num. Methods Engng., 36*, 3675 (1993).

42. G. Xu, A.S. Argon and M. Ortiz, *Phil. Mag., 75*, 341 (1997)

43. J.R. Rice, *J. Mech. Phys. Solids, 40*, 235 (1992).

44. J.H. Rose, J. Ferrante and J.R. Smith, *Phys. Rev. Letters., 47*, 675 (1981).

45. Y. Sun, G.E. Beltz and J.R. Rice, *Mater. Sci. Engng., A170*, 67 (1993).

46. B. Cotterell and J.R. Rice, *Intern. J. Fract., 16*, 155 (1980).

47. Y. Juan, Y. Sun and E. Kaxiras, *Phil. Mag. Lett., 73*, 233 (1996).

48. Y-H, Chiao, and D.R. Clarke, *Acta Metall., 47*, 203 (1989).

49. S.J. Zhou and R. Thomson, *J. Mater. Res., 6*, 639 (1991).

50. F.A. McClintock and A.S. Argon "*Mechanical Behavior of Material*", Addison Wesley, Reading MA (1966).

51. J. Samuels and S.G. Roberts, *Proc. Roy. Soc., A421*, 1 (1989).

52. M. Brede, *Acta Metall., et Mater., 41*, 211 (1993).

53. B. Devincre and S.G. Roberts, *Acta Material, 44*, 2891 (1996)

54. H. Riedel and J.R. Rice, in "*Fracture Mechanics: Twelfth Conference*" ASTM STP 700, edited by P.C. Paris, ASTM: Philadelphia PA p. 112, (1980).

55. H. Alexander and P. Hassen, in "*Solid State Physics*", edited by F. Seitz and D. Turnbull, Academic Press: New York, Vol. 22 p. 28 (1968)

56. H. Riedel, "*Fracture at High Temperatures*", Springer: Berlin (1987).

57. J.H. Rose, J. Ferrante, and J.R. Smith, *Phys. Rev. Letters, 47*, 675 (1981).

58. Y.-B. Xin and K.J. Hsia, *Acta Material, 44*, 845 (1996).

59. S.G. Roberts, M. Ellis and P.B. Hirsch, *Mater. Sci. Engng., A164*, 135 (1993).

60. M. Khanta, D.P. Pope and V. Vitek, *Phys. Rev. Letters, 73*, 684 (1994).

61. M. Khanta, D.P. Pope and V. Vitek, *Scripta Metall et Mater., 31*, 1349 (1994).

62. G. Michot and A. George, in *"Strength of Metals and Alloys"*, edited by H.J. McQueen et al. Pergamon: Oxford, Vol. 2, p. 1187 (1985).

MODELLING CRACK TIP PLASTIC ZONES AND BRITTLE-DUCTILE TRANSITIONS

P.B. Hirsch & S.G. Roberts
Department of Materials
University of Oxford
Parks Road, Oxford
OX1 3PH, U.K.

Abstract

Plasticity at crack tips has been modelled as self-organising arrays of dislocations emitted from a source near the crack tip. The model takes into account dislocation shielding, but not blunting. For materials where dislocation motion is slow, and the friction stress is high, the modelled arrays are far from equilibrium. The brittle-ductile transition is then controlled by dislocation velocity. If dislocation motion is fast, and there is a substantial dislocation pinning stress, τ_p the arrays are quasi-static, and the model predicts behaviour very similar to those of earlier static models. A power-law relation connects the shielded crack tip stress intensity, k, to the pinning stress, τ_f, the length of the dislocation array, d, and the size of the "dislocation free zone" near the crack tip. Close to the crack tip, the stress $\sigma_{yy} \propto k.(x^{-1/3})$. Using either of two fracture criteria, (a) $k = K_{Ic}$, or (b) the stress at some point ahead of the crack tip exceeds a local fracture stress, the variation of stress intensity at fracture K_F with temperature is predicted to be controlled by the temperature variation of the yield stress: $K_F \propto \sigma_y^{-0.57}$.

George R. Irwin Symposium on Cleavage Fracture
Edited by Kwai S. Chan
The Minerals, Metals & Materials Society, 1997

Introduction

Many crystalline solids fail by cleavage at low temperatures, and by plastic processes at high temperatures. In the transition region, cleavage occurs at stresses which increase with increasing temperature. The most frequently observed transition is of a gradual nature, where the fracture stress increases over a range extending over the order of 100 K or more [1]. BCC metals [2,3], intermetallics [4-6], MgO [7], and many other materials exhibit this type of transition. In some cases, e.g. for Si [8-11] and Al_2O_3 (sapphire) single crystals [12], the transition is very sharp, occurring over a temperature range of <10 K. The transitions are strain-rate dependent; for BCC metals the strain-rate dependence is small [2,3]; for Si single crystals, increasing the strain-rate by a factor of ten increases the temperature of the transition typically by 100 K [8-11].

It is well known that the increase in fracture stress / toughness with temperature is associated with a decrease in the yield stress, σ_y, in the same temperature range, resulting in an increasing amount of plasticity around the crack tip. Irwin [13] and Orowan [14] independently modified the original Griffith criterion for the propagation of a sharp crack by assuming that plastic work γ_p has to be done in addition to the generation of free surfaces (energy 2γ), ie, in plane stress:

$$\frac{\sigma_f \sqrt{\pi a}}{E} = 2\gamma + \gamma_p \qquad (1)$$

where σ_f is the fracture stress, a the crack length and E is Young's modulus. The l.h.s. is the driving force for crack extension, G; the r.h.s. is the material's resistance to crack extension, G_c. Thus the condition for crack extension is $G = G_c$. Using Westergaard's cracked body solution [15], Irwin [16] showed that $G = K^2 / E'$ where $E' = E$ in plane stress and $E / (1-\nu^2)$ in plane strain (ν = Poisson's ratio), and K is the stress intensity factor, where $K = f\ \sigma\ (\pi a)^{1/2}$, where f is a parameter depending on geometry. Irwin [17] also made the first quantitative estimate of the plastic zone size, e.g. $r_y = K^2 / (6\ \pi\ \sigma_y^2)$ in plane strain. These three steps have been quite fundamental to the development of fracture mechanics, and Professor Irwin is justly recognised as the founder of this important science.

Since then, the plastic zone has been modelled in various ways:

1) by continuum mechanics, using analytical and finite element techniques [18-20];
2) by the yield strip model [21];
3) by representing the crack and yielded zone in the yield strip model by a continuous distribution of dislocations [22]; and
4) by an array of discrete dislocations in static equilibrium with a shear yield stress τ_f (e.g. [23-27]);
5) by a self- organising array of dislocations emitted from a source, and moving outwards according to a velocity / stress / temperature law, and velocities determined by the stress on each one; these arrays are not at equilibrium [1,28,29].

This last type of model differs from the others in that it assumes that plasticity is generated by the operation of sources in the crystal. It takes into account the discrete nature of the dislocation network, i.e. the source spacing and strength, (which become important at small distances from the crack tip). The model automatically includes workhardening, which results from the back stress of the plastic zone at the source. In the model developed so far crack tip shielding is included but blunting is neglected. This paper gives a brief review of this model and describes recent developments in which a velocity law includes a minimum stress for dislocation motion. The predictions of dislocation distributions from this model are shown to give results equivalent to those from models of types (1) and (2).The model therefore can be used to describe a large range of dislocation behaviour near crack tips, independent of whether dislocations are far from or close to equilibrium positions. The model also computes the shielding effects of dislocation arrays on the crack tip, and can be used to make predictions of brittle-ductile transition behaviour.

The basic model

We simplify the crack tip plastic zone as a single slip plane which intersects the crack plane along the line of the crack tip (see figure 1). The angle between the slip plane and the crack plane, θ, in the modelling reported here was 70.5°, this being the plane subjected to the maximum shear stress in mode I loading. A dislocation source is positioned on the slip plane at a fixed distance, x_c, ahead of the crack tip (50b - 5000b for these simulations).

The source emits a single edge dislocation when the stress on a dislocation at the source is sufficient to move it away from the crack tip. The stress τ_{x_i} on a dislocation at x_i is given by:

$$\tau_{x_i} = \alpha \frac{K}{(2\pi x_i)^{1/2}} - \beta \frac{\mu b}{x_i} + \sum_{ij} \tau_{ij} \qquad (2)$$

The first term is the crack tip field stress (α depends on θ) at an applied stress intensity K, the second term is the image stress (given by Lakshmanan and Li [27]), the third term is the stress arising from dislocation - dislocation / image interactions [27], μ is the shear modulus, b the Burgers vector.

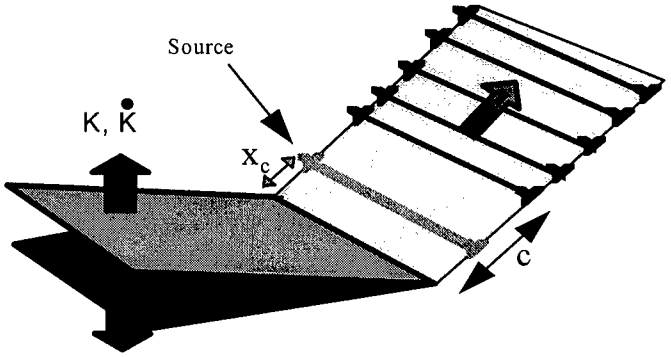


Figure 1: Configuration of models. An edge dislocation may be emitted from a source onto a slip plane inclined to the crack plane when the stress at the source is high enough to move a dislocation away from the crack.

The model requires a dislocation velocity law to function. When the velocity is controlled by the lattice friction, the relation:

$$v_i = \frac{dx_i}{dt} = A\left(\frac{\tau_{x_i}}{\tau_0}\right)^m \exp\left(\frac{-U}{kT}\right) = {\tau_{x_i}}^m v_0 \qquad (3)$$

is appropriate, where v_0 contains the temperature dependent term. We can rewrite the l.h.s. of eqn. 2 in the form:

$$\tau_{x_i} = \left(\frac{\dot{K}}{v_0}\right)^{1/m} \left(\frac{dx_i}{dK}\right)^{1/m} \qquad (4)$$

The model then runs at a fixed dK/dt ($\dot{K}$), and in each program cycle (equivalent to a short time interval δt) examines the source to see if a dislocation should be nucleated (i.e. whether $\tau_{xc} > 0$), calculates the stress on all dislocations and moves them a distance $\delta t\ v_i$. K is increased by $\delta t \dot{K}$, and the next cycle begins. At each cycle, the model uses the positions of the dislocations to calculate the local crack tip stress intensity, k, which is lower than the applied K because of the "shielding" effect of the emitted dislocations and their images.

$$k = K + K_D \qquad (5)$$

Expressions for K_D (which is negative for dislocations emitted outwards from the source into the "plastic zone") are given in [27]. As time and applied K increase in the model, k increases, as the increasing back stress from the already emitted dislocations restricts further emission from the source (this is effectively equivalent to work-hardening).

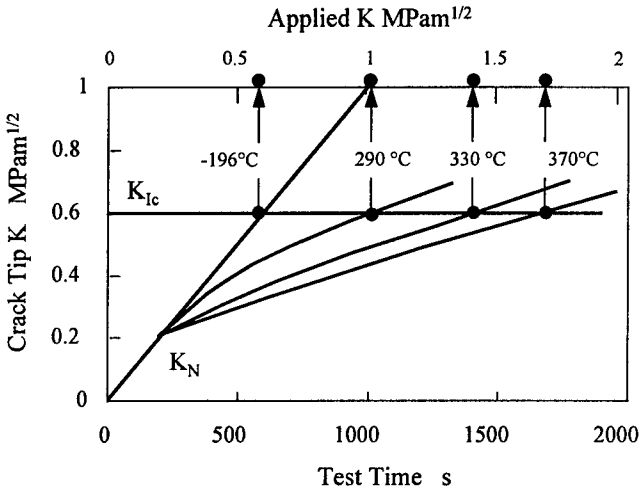
To determine K at fracture (K_F), a fracture criterion has to be assumed. When the fracture event is the propagation of the original crack, and blunting is negligible, a local Griffith criterion can be used, i.e.

$$k = K_{Ic} \tag{6}$$

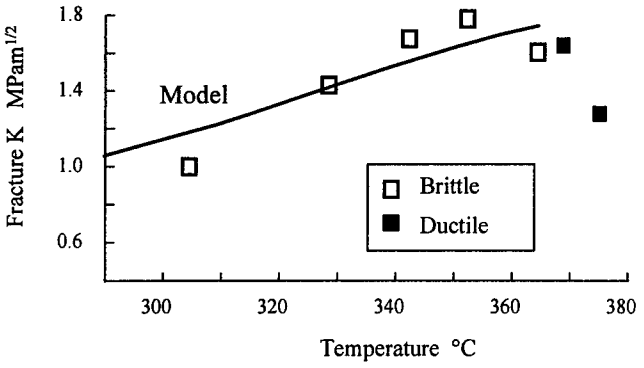
This has been used for Si, Ge, Al_2O_3, Mo single crystals. (For reviews see [30-32]). When the fracture event is the nucleation of cracks ahead of the main shielded crack, as is the case for steels [33], the condition is

$$\sigma_{yy}(x_R) = \sigma_f \tag{7}$$

where x_R is some microstructural distance (e.g. grain size) and σ_F is the fracture stress of a carbide.



a)



b)

Figure 2: Modelling the BDT in germanium: (a) predicted crack tip K during simulated tests at various temperatures; (b) predicted fracture K vs. temperature.

Fig. 2a shows k as a function of time or K for Ge at various temperatures [34], using the known dislocation velocity law . k increases with increasing K, and fracture occurs when $k = K_{Ic}$, which is also known for Ge. The corresponding values of K_F are indicated on the K scale at the top of the diagram.

Fig. 2b shows these calculated values of K_F as a function of temperature, and the experimental results. The agreement is reasonable.

The strain-rate dependence of the BDT can be inferred from eqns. (2) and (4). For a given K the dislocation positions and therefore the shielding K_D and hence k, depend only on ($\dot{K}$ / v_0); i.e. T at a given K_F depends on K according to:

$$\ln \dot{K} = -U_v / k_B T + \text{constant} \tag{8}$$

Two curves of K_F against T corresponding to two strain-rates $\dot{K}_1$, $\dot{K}_2$ are shifted relative to each other on the temperature axis by:

$$\left(\frac{1}{T_2} - \frac{1}{T_1}\right)\frac{U_v}{k_B} = \ln\left(\dot{K}_1 / \dot{K}_2\right) \tag{9}$$

Applying this expression to experiments (e.g. Ge), U_v has been found to be equal to the activation energy for dislocation velocity.

In some materials (notably silicon), the transition is not of this form; rather, K_F rises abruptly from K_{Ic} at the transition temperature. The experimental evidence indicates that this is a result of a very low density of dislocation sources in the material, and especially along the crack tip [35,36]. Models taking this into account produce K_F / T curves that closely fit the experimental results . This paper is not concerned with this rare type of behaviour; further details are to be found in [28, 35-37].

Model with pinning / yield stress

The dislocation velocity relation (eqn. 3) was modified to include a dislocation pinning stress:

$$\left|\tau_{x_i}\right| \le \tau_f \Rightarrow v_i = 0 \tag{10}$$

$$\left|\tau_{x_i}\right| > \tau_f \Rightarrow v_i = \left(\frac{\tau_{x_i} - \tau_f}{\tau_{x_i}}\right) A \left(\frac{\tau_{x_i}}{\tau_0}\right)^m \exp\left(\frac{-U}{kT}\right) \tag{11}$$

Above the pinning stress (τ_f) the velocity rises rapidly. The modification is a purely empirical way of ensuring that the dislocation velocity rises smoothly above τ_f from zero towards the value given by eqn. 3, so that the simulation process is stable (a steplike rise in velocity would require a very small δt to ensure that dislocations did not substantially "overshoot" in a single program cycle; the ratio of CPU time to simulated time would become unusably large).

For convenience, the velocity parameters used were those previously used for simulations of the BDT in molybdenum: $A = 8.61 \times 10^{-3}$ ms^{-1}, τ_0 = 1 MPa, U = 0.491 eV and m = 3.4 + 333.6 / T, giving the best fit to the screw dislocation velocity data of Imura et al. [38]. It should be emphasised that this does not mean that the results presented here apply only, or indeed particularly, to molybdenum. As will be seen, the behaviour of the model is controlled predominantly by τ_f and the applied K. The dislocation velocity parameters used are simply to provide a self-consistent and typical range of mobilities; the "temperature" used was always 180 K (this is close to the normal BDTT for molybdenum, so the velocities at a given stress are in the range of velocities in the transition temperature range).

Dislocation arrays

Figure 3 shows the results of a typical simulation, for a source distance $x_c = 50b$, and τ_f = 100 MPa, with $\dot{K}$ = 1000 Pa $m^{1/2}$ s^{-1} up to K = 10 MPa $m^{1/2}$, with K then being held steady.

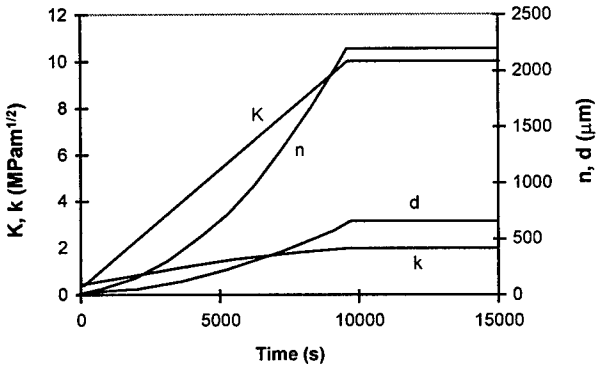


Figure 3: Results of model using τ_f =100 MPa, dislocation mobility parameters as for Mo at 180 K. K = applied stress intensity, k = crack tip stress intensity. The dislocation array, length d, containing n dislocations, is in quasistatic equilibrium at all stages of the simulation.

At K=10 MPa $m^{1/2}$, $\dot{K}$ =0, the array is clearly in equilibrium: there is no further change in array length (d) or number of dislocations emitted from the source (n). Also, the crack tip stress intensity, k, does not change once K reaches 10 MPa $m^{1/2}$, indicating that the positions of all dislocations within the array stay fixed.

This quasi-static behaviour was shown by all the simulations at T = 180 K for $\tau_f > \sim 80$ MPa. For lower values of τ_f, n and d are less than the quasi-static values at a given applied stress intensity, K, and at a constant K, both n and d increase with time to the eventual equilibrium value. It is interesting to note that if $\tau_f = 0$, the non-equilibrium values of d and n have a different dependence on K. At any given K, $d \propto K^{2(m+1)/(m+2)}$, and $n \propto K^{(2m+3)/(m+2)}$; for large m these dependencies approach asymptotically the static equilibrium values.

We would expect from the results of continuum fracture mechanics (see e.g. [39]) that, for a constant yield stress σ_y (i.e. if all dislocations in the array are in equilibrium against a friction stress $\tau_f = \sigma_y/\sqrt{3}$), then:

a) the crack opening displacement, COD $\propto$ n $\propto (K^2/\sigma_y)$, and
b) the plastic zone size $\equiv$ d $\propto (K/\sigma_y)^2$.

Figure 4 shows typical data from the model with τ_f = 100 MPa; d and n are proportional to K^2 at all stages of the growth of the dislocation array. The values for d and n produced by the model vary only slightly with x_c: e.g. for K = 10 MPa $m^{1/2}$ and τ_f = 100 MPa, with x_c = 5000 b, d = 595 μm (625 μm for x_c = 50b) and n = 1925 (2170 for x_c = 50b).

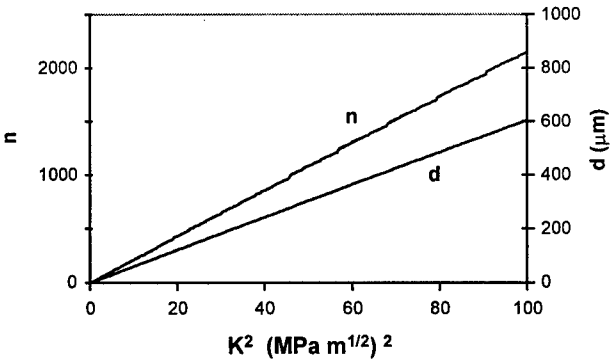


Figure 4: Evolution of dislocation array for τ_f = 100 MPa, up to K = 10 MPa $m^{1/2}$. Both the number of dislocations in the array, n and the array length, d , are proportional to K^2.

For x_c = 50 b, and τ_f between 100 and 600 MPa (i.e. σ_y between 173 and 1040 MPa) $d / (K/\sigma_y)^2 = 0.188 \pm 3\%$; if we take COD = n.b.sin 70.5°, then $COD / (K^2/E\sigma_y) = 0.345 \pm 4\%$. The corresponding values from finite element analyses [40,41] are $d / (K/\sigma_y)^2 = 0.175$ and $COD / (K^2/E\sigma_y) = 0.425$.

Fig. 5 shows a typical dislocation distribution along the slip plane, for x_c = 50b, τ_f = 100 MPa, K = 10 MPa $m^{1/2}$; it is in the form of an inverted pile-up strongly peaked near the crack tip, as expected from previous studies of arrays of dislocations in equilibrium near a crack tip [22,27]. Contrary to the results from [22], the dislocation density drops to zero at the end of the dislocation free zone, at c from the crack tip (see fig. 1); this is not visible in fig.5, since c = 0.24μm.

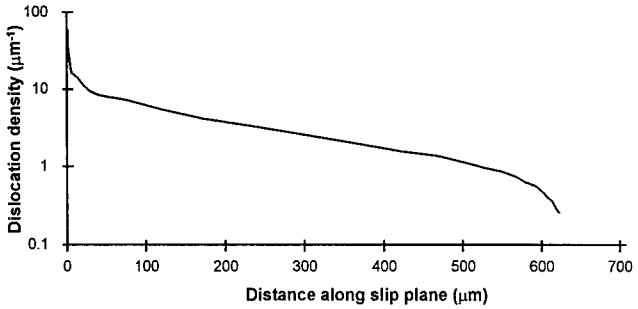


Figure 5: Dislocation distribution along the slip plane, for x_c = 50b, τ_f = 100 MPa, K = 10 MPa $m^{1/2}$.

Shielding

The stress fields produced by the dislocations in the plastic zone reduce the crack tip stress intensity, k (and thus raise the applied stress intensity, K, required to produce fracture at $k = K_{Ic}$). In mode III loading an approximate solution exists [25] for k as a function of the friction stress, τ_f , the plastic zone size, d, and the "dislocation free zone" size, c (the distance between the crack tip and the innermost dislocation in the array); for d > c :

$$k = \frac{3}{\pi}\sqrt{\frac{2}{\pi}}\,\tau_f\sqrt{c}\left(\ln\left(\frac{4d}{c}\right)+\frac{4}{3}\right) \qquad (12)$$

For the case of shielding by edge dislocations on an inclined slip plane, no such solution exists. We examine here the form of such shielding, using the equations of Lakshmanan and Li [27] to calculate the crack tip stress intensity, k, from the dislocation distributions resulting from the model for each value of τ_f and K, and thus with varying resultant values of d and c. Results are shown in figure 6, plotted as $k / (\tau_f c^{1/2})$ as a function of ln(d/c).

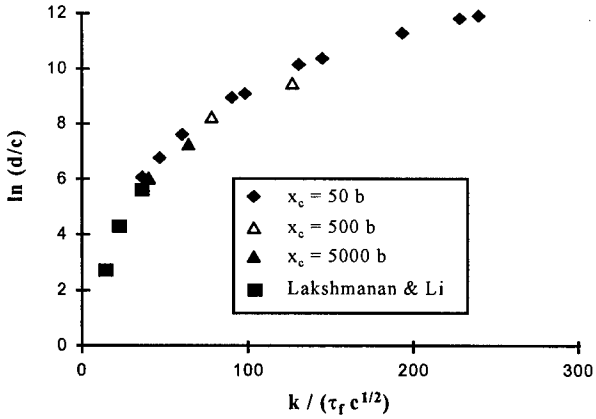


Figure 6: Dislocation array size data for simulations with 100 MPa $\leq \tau_f \leq$ 600 MPa, 10 MPa $m^{1/2} \leq K \leq$ 40 MPa $m^{1/2}$. Data from Lakshmanan and Li [27] are also shown. d = array length, c = dislocation free zone size, x_c = distance of dislocation source from crack tip.

If eqn. 12 is followed, as for mode III, then the data would lie on a straight line; instead, for these edge dislocations on an inclined slip plane in mode I loading, the data are found to lie on a single curve (only slight deviations from the curve result from using different dislocation source positions, x_c). Data derived from [27] for equilibrium dislocation arrays on the 70.5° slip plane are also shown.

Figure 7 replots these data as ln(d/c) against ln ($k/(\tau_f c^{1/2})$): the data lie on a straight line indicating a power law dependence. A best fit line through these data give a relation as follows:

$$\frac{k}{\tau_f c^{1/2}} = 5.38\left(\frac{d}{c}\right)^{0.317} \qquad (13)$$

Thus, given that $d / (K/\sigma_y)^2 = 0.188$, with $\sigma_y = \sqrt{3}\,\tau_f$,

$$k = 1.82\, K^{0.634}\, \sigma_y^{0.366}\, c^{0.183} \qquad (14)$$

Or in terms of the plastic zone size d,

$$\frac{k}{K} = 1.32\left(\frac{c}{d}\right)^{0.183} \qquad (15)$$

This shows clearly that the residual local stress intensity factor k depends on the ratio c/d. The smaller c, the greater the shielding for a given K; when c=0, the crack is completely shielded.

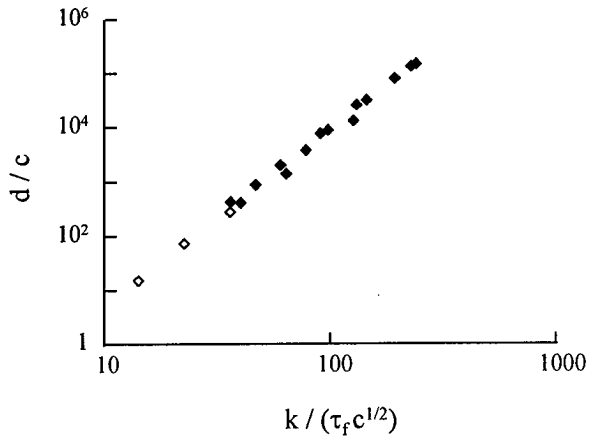


Figure 7: Data of fig. 6 replotted to show power-law relation between d/c and $k/(\tau_f c^{1/2})$.

Thus from eqn. 14, for a material with a given (near) crack-tip dislocation source configuration, there is a well-defined relation between crack tip stress intensity, k, applied stress intensity, K, and the yield stress, σ_y, or minimum stress to move dislocations, τ_f. If we assume that fracture occurs when at $k = K_{Ic}$, then the fracture K, K_F, is given by:

$$K_F = B\, K_{Ic}^{1.58}\, \sigma_y^{-0.57} \qquad (16)$$

where B depends weakly on c, and is effectively a constant. The values of the constants in eqns. 13, 14 and 15 may vary slightly with the elastic constants and Burgers vector of the material (values for molybdenum are used here), since these will affect the strength of dislocation interactions. However, they will not depend on the details of the dislocation velocity law, as long as the dislocations move quickly enough (and σ_y is high enough) for the arrays to be close to their static equilibrium configurations.

The dislocation free zone size, c, is found to be relatively insensitive to τ_f and K for a given value of x_c; see fig 8. For other values of x_c, the DFZ size is similarly always slightly greater than x_c.

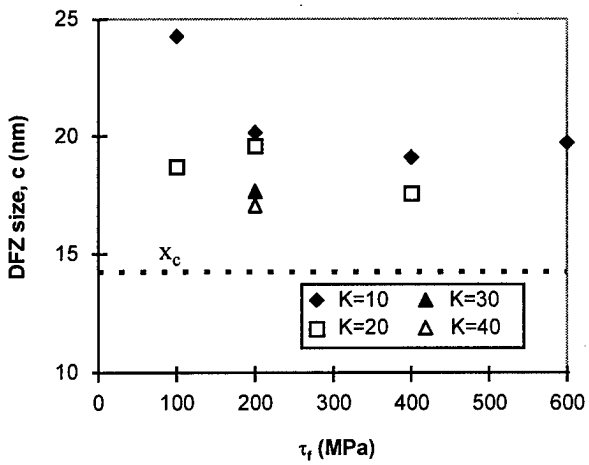


Figure 8: Variation of dislocation free zone size, c, with τ_f and K (MPa $m^{1/2}$)

Stresses ahead of the crack

Figure 9 shows the form of the stress fields ahead of a crack tip loaded to 10 MPa $m^{1/2}$, with τ_f =100 MPa (i.e. σ_y = 173 MPa). The figure shows the stress σ_{yy} along the continuation of the crack plane, from (a) the applied stress intensity, K; (b) the shielding caused by the dislocations on the slip plane : (c) the images of the dislocations; (d) the resulting total stress σ_{yy}. The dislocations themselves actually increase the stress σ_{yy} on this plane ahead of the crack; it is their image dislocations that provide the shielding which reduces k below the applied stress intensity. The forms and relative magnitudes of the stress / position curves are the same for all τ_f and K.

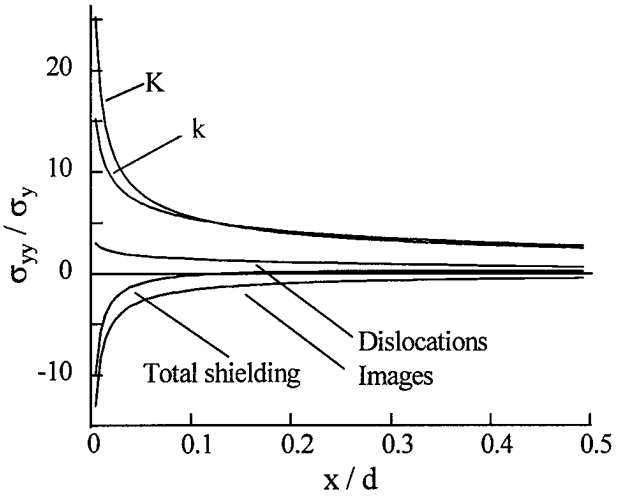


Figure 9: σ_{yy} stresses on the crack tip plane, ahead of a crack tip loaded to 10 MPa $m^{1/2}$, with τ_f =100 MPa (σ_y = 173 MPa).

The stress field near, but not at, the crack tip no longer has $\sigma_{ij} \propto x^{-1/2}$. If we examine the variation of σ_{yy} on the continuation of the crack plane, taking $\sigma_{yy} \propto x^{-n}$, the exponent n varies with x. Near to the crack tip, where the dislocation image stress field varies rapidly ($x < \sim d/30$), n is very close to 1/3. With increasing x, the local value of n increases to a value exceeding 1/2, before reaching 1/2 asymptotically as x increases further. In the near crack tip region σ_{yy} (y = 0) is proportional to k, and for $x_c = 50b$ is given by:

$$\frac{\sigma_{yy}}{\sigma_y} = 9.76\frac{k}{x^{1/3}} \qquad (17a)$$

$$= 17.8\,c^{0.183}\left(\frac{K^2}{\sigma_y{}^2}\right)^{0.317}\left(\frac{1}{x}\right)^{1/3} \qquad (17b)$$

It is important to note that σ_{yy} is determined by the local k field. The proportionality factor 9.76 in eqn. 17a is only weakly dependent on c; increasing x_c from 50b to 5000b reduces it by a factor of only 2.5. This change is compensated for by the $c^{0.183}$ term in eqn. 17b, so that the dependence of σ_{yy}/σ_y on K, σ_y and x in eqn. 17b is almost independent of c. The $x^{-1/3}$ variation of σ_{yy} is the same as that from the Hutchinson, Rice and Rosengren (HRR) continuum model [18,19] for a workhardening exponent of 2. The exponent of the $(K/\sigma_y)^2$ term is also very close to 1/3, the value expected from continuum mechanics for the same workhardening exponent. In our model, the workhardening arises because of the influence of the dislocations in the array on the operation of the source; as more dislocations are emitted, their back-stresses raise the K at which the next dislocation can be nucleated. This is a consequence of the criterion for dislocation emission being that a critical stress must be exceeded at a source positioned ahead of the crack tip.

If fracture is controlled by a critical micro-fracture event ahead of the main crack tip, (e.g. nucleation of cracks at carbides), which occurs at a fixed distance x_R from the crack tip, as proposed by Ritchie, Knott and Rice (RKR) [33], when $\sigma_{yy} = \sigma_F$, a critical local fracture stress, the condition for fracture becomes

$$K_F \propto x_R{}^{0.50}\,\sigma_f{}^{1.57}\,\sigma_y{}^{-0.57} \qquad (18)$$

The form of the variation of K_F with σ_y is the same as that where the fracture criterion is $k = K_{Ic}$ (eqn 16). Fig. 10 compares the variation of K_F with temperature predicted from our model with the RKR model [33], with the proportionality constant in eqn. 18 fitted to the RKR data at -140°C. The temperature variation of σ_y is taken from the same paper [33]. The result is similar to that obtained with the continuum mechanics solutions.

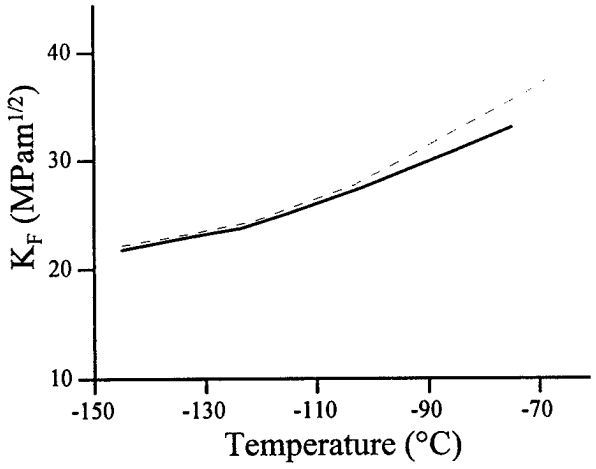


Figure 10: Comparison of fracture K (K_F) of mild steel predicted by the model presented here (dashed line) and that of RKR [33] (solid line).

Warm prestressing

Figure 11 shows a loading cycle ("load, unload, cool, fracture", or LUCF) in which a cracked component is loaded to an applied stress intensity factor K_1 and temperature T_1, unloaded at T_1 to a stress intensity factor K_{1U}, cooled to T_2, and re-loaded to failure by cleavage at K_{2f}. K_{2f} is found in general to exceed K_{2c}, the normal critical stress intensity factor for cleavage at T_2 in the absence of prestressing at a higher temperature. This is the warm-prestressing effect.

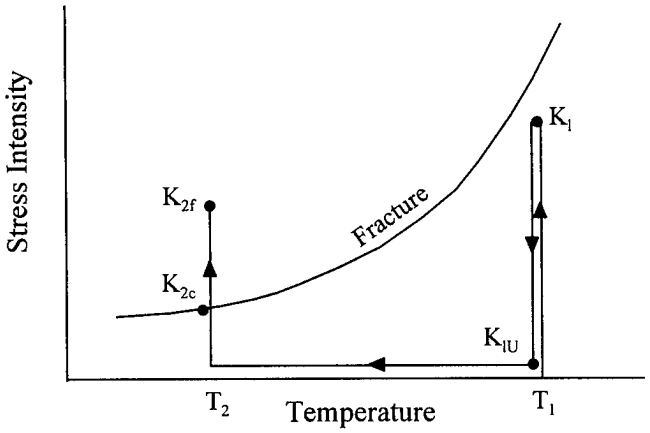


Figure 11: LUCF cycle.

Chell, Haigh and Vitek [42], Curry [43], and Smith and Garwood [44] have modelled the effect by assuming the principle of plastic superposition [45], according to which the stresses and strains of the final state are obtained by the superposition of three independent states: the original loaded state characterised by K_1 and a yield stress σ_{y1}, a reverse loading state characterised by $(K_{1U} - K_1)$ and an effective yield stress $2\sigma_{y1}$ (any reverse flow at T_1 has to overcome an internal stress σ_{y1} and a friction / yield stress σ_{y1}), and a re-loading state characterised by $(K_{2f} - K_{1U})$ and an effective yield stress (σ_{y1} plus σ_{y2}); any forward flow has to overcome an internal stress σ_{y1} and a fiction / yield stress σ_{y2} appropriate to T_2). The case most commonly considered is where the lengths of the plastic zones corresponding to the three states, d_1, d_{1U} and d_{21} are in the order $d_1 > d_{1U} > d_{21}$ (see Figure 12, for the case of complete unloading, i.e. $K_{1U} = 0$, and for the plastic zone model discussed in this paper).

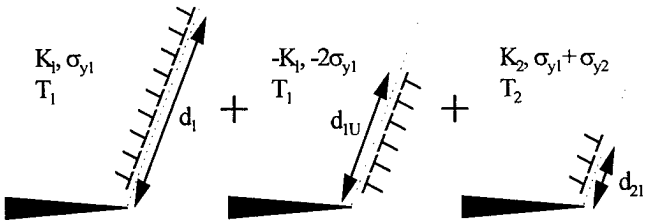


Figure 12: Plastic superposition for a LUCF cycle with $K_{1U} = 0$. The final state is a superposition of three independent states: loading, (K_1, σ_{y1}, T_1), unloading ($-K_1$, $-2\sigma_{y1}$, T_1) and reloading (K_2, $\sigma_{y1} + \sigma_{y2}$, T_2).

Assuming the RKR [33] fracture criterion that the local tensile stress exceeds the cleavage fracture stress σ_f over a characteristic distance x_0, and noting that according to equation 17, σ_{yy} is a function only of the local k and x, provided the distance of the operating source is at the same distance from the crack tip in all three loadings, the condition for fracture on loading at T_2 is given by:

$$k_{21} + k_1 - k_{1U} = k_{2c} \qquad (19)$$

where k_1, k_{1U}, k_{2l}, k_{2c} are local crack tip stress intensities for loading at T_1, unloading at T_1, reloading at T_2 and loading at T_2 without prior warm prestressing. Using equation 17 we find:

$$\frac{K_{2F}}{K_{Ic}} = \left[\Sigma^{0.366} + 0.29\left(K_1 / K_{2c}\right)^{0.634} \right]^{1.58} (1+\Sigma)^{-0.58} \qquad (20)$$

Figure 13 compares predictions of equation for $\Sigma = 2.4$, with experimental data for steels in the literature collected by Professor Burdekin, and also with the predictions of previous models [42, 44, 46].

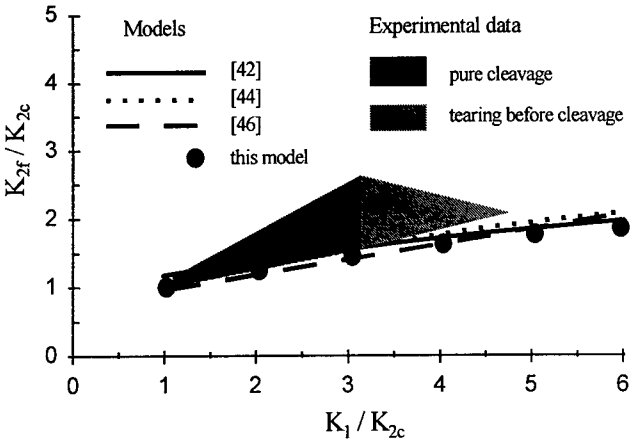


Figure 13: Comparison of predictions of the model for LUCF cycle warm prestressing with the models of [42, 44, 46]. The range of experimental data for steels is also shown.

All the models predict very similar values which appear to be a lower bound to the experimental results. In their model, Smith and Garwood [44] superimposed stresses from the three cycles, and applied the Ritchie, Knott and Rice criterion for fracture. They used the small scale yielding and strain hardening solutions of Hutchison [19] and Rice and Rosengren [18], and the curve of their predictions in Figure 13 is for a strain hardening exponent equal to 10. The present treatment is similar to that of Smith and Garwood, but the stresses are based on equation 17, which corresponds closely to the HRR solutions for n = 2.

Summary

Plasticity at crack tips may be modelled as self-organising arrays of dislocations emitted from a source near the crack tip. The model takes into account shielding by the emitted dislocations, but not blunting. For materials where dislocation motion is slow, and any friction stress is high (e.g. semiconductors, ceramics), the modelled arrays are far from equilibrium (measured dislocation array lengths in, e.g. silicon, correspond closely to these predicted lengths [47]). Under these conditions the increase in fracture toughness with increasing temperature in the brittle-ductile transition can be modelled in terms of a dislocation velocity / stress / temperature law without a pinning stress. The brittle-ductile transition and its strain rate dependence are then controlled by the activation energy of dislocation velocity. If dislocation motion is fast, and there is a substantial dislocation pinning stress, τ_f, as expected in b.c.c. metals, the arrays are quasi-static, and the model predicts behaviour very similar to those of earlier static models. The behaviour of the model is relatively insensitive to the characteristics of the dislocation source.

The dislocation array length, d, was then found to be given by: $d = 0.188\,(K/\sigma_y)^2$, where K is the applied stress intensity and σ_y is the yield stress of the material (taken to be $\sqrt{3}\,\tau_f$).

The form of the stress fields ahead of the crack tip was investigated. Close to the crack tip, $\sigma_{yy} \propto k\, x^{-1/3}$, characteristic of a "plastic zone" with a work-hardening exponent of 2. The shielding arises from the action of dislocation images; the dislocations themselves (on a 70° slip plane) increase the stresses ahead of the crack tip.

A power-law relation has been found connecting the shielded crack tip stress intensity, k, to the pinning stress, τ_f, the length of the dislocation array, d, and the size of the "dislocation free zone" near the crack tip, c:

$$\frac{k}{\tau_f\, c^{1/2}} = 5.38\left(\frac{d}{c}\right)^{0.317}$$

The value of c is relatively insensitive to K and τ_f, but depends on the position of the dislocation source relative to the crack tip. Thus, using a fracture criterion either $k = K_{Ic}$, or that the stress at some point ahead of the crack tip exceeds the local fracture stress, the variation of stress intensity at fracture K_F with temperature is predicted to be:

$$K_F \propto \sigma_y^{-0.57}$$

The simple k-controlled stress/distance power law has been used to determine the warm prestressing effect in steels, in good agreement with previous models. The model is also be used to describe fatigue [48]. Future developments planned include the extension to slip on both sides of the crack tip and, most importantly, to take account of blunting. Stable crack extension will also be considered.

Acknowledgements

Our thanks are due to Professor Burdekin FRS for permission to use his data in Figure 13.

References

1. S.G. Roberts, "Modelling the Brittle to Ductile Transition in Single Crystals", Computer Simulation in Materials Science - nano / meso / macroscopic space and time scales, edited by H.O. Kirchner, L.P. Kubin & V. Pontikis, NATO ASI series, series E (applied sciences), 308, Kluwer Academic Publishers, 1996, p 409-434.

2. M. Ellis, "The Ductile to Brittle Transition in BCC Metals", D.Phil thesis, University of Oxford, 1991.

3. D. Hull, P.Beardmore and A.P. Valintine, "Crack Propagation in Single Crystals of Tungsten", Phil. Mag. 14 (1965) 1021-1041.

4. S.G. Roberts and A.S. Booth, "The Brittle-Ductile Transition in γ-TiAl Single Crystals", Acta. Mater. 45 (1997) 1045-53.

5. F.C. Serbena, "The Ductile to Brittle Transition in NiAl Single Crystals", D.Phil thesis, University of Oxford, 1995.

6. H. Vehoff, "Fracture Mechanisms in Intermetallics", in Ordered Intermetallics - Physical Metallurgy and Mechanical Behaviour, NATO Advanced Science Institutes Series vol 213 (Series E, Applied Sciences) eds. C.T. Liu, R.W. Cahn and G. Sauthoff (Kluwer Academic Publ, Dordrecht, Netherlands, 1992), p299-320.

7. A.S. Booth and S.G. Roberts, "Dislocation Activity, Stable Crack Motion and the Warm-prestressing Effect in Magnesium Oxide", J. Am. Ceram. Soc., 77 (1994)1457-66.

8. J. Samuels and S.G. Roberts, "The Brittle-Ductile Transition in Silicon. I. Experiments", Proc. R. Soc. Lond. A 421 (1989) 1-23.

9. G. Michot and A. George, "In-situ observation by X-ray Synchotron Topography of the Growth of Plastically Deformed Regions around Crack Tips in Silicon under Creep Conditions", Scripta Metall. 16 (1982) 519-523.

10. M. Brede and P. Haasen, "The Brittle to Ductile Transition in Doped Silicon as a Model Substance", Acta Metall. 36 (1988) 2003-18.

11. C. St. John, "The Brittle to Ductile Transition in Pre-cleaved Silicon Single Crystals", Phil. Mag. 32 (1975) 1193-1212.

12. S.G. Roberts, H.S. Kim and P.B. Hirsch, "The Brittle-Ductile Transition and Dislocation Mobility in Silicon and Sapphire", Proc. Ninth Intl. Conf. on the Strength of Metals and Alloys, Haifa, July 1991, eds. D.G. Brandon, R. Chaim and A. Rosen (Freund Publishing, London, 1991), p317-324.

13. G.R. Irwin, "Fracture Dynamics", Fracturing of Metals (Cleveland, Ohio: American Society of Metals 1948), 147-166.

14. E. Orowan, "Fracture and Strength of Solids", Reports on Progress in Physics, 12 (1948), 185.

15. H.M. Westergaard, "Bearing Pressures and Cracks", Trans. Amer. Soc. Mechanical Engineers, 61 (1939), A49-53.

16. G.R. Irwin, "Analysis of Stresses and Strains near the End of a Crack Traversing a Plate", Journal of Applied Mechanics, 24 (1957), 361-364.

17. G.R. Irwin, J.A. Kies and H.L. Smith, "Fracture Strengths Relative to Onset and Arrest of Crack Propagation", Proc. Amer. Soc. for Testing Materials 58 (1958), 640-657.

18. J.R. Rice and G.F. Rosengren, "Plane Strain Deformation near a Crack Tip in a Power-law Hardening Material", J. Mech. Phys. Solids 16 (1968) 1-12.

19. J.W. Hutchinson, "Plastic Stress and Strain Fields at a Crack Tip", J. Mech. & Phys. Solids 16 (1948) 337-347.

20. D.M. Tracey, "Finite Element Solutions for Crack-tip Behaviour in Small Scale Yielding", J. Engin. Mater. Technol. 98 (1976) 146-151.

21. D.S. Dugdale, "Yielding of Steel Sheets Containing Slits", J. Mech. & Phys. Solids. 8 (1960) 100-108.

22. B.A. Bilby, A.H. Cottrell and K.H. Swinden, "The Spread of Plastic Yield from a Notch", Proc. Roy. Soc. Lond. A272 (1963) 304-314.

23. B.S. Majumdar and S.J. Burns, "Crack Tip Shielding - an Elastic Theory of Dislocations and Dislocation Arrays near a Sharp Crack", Acta metall. 29 (1981) 579-588.

24. S.-J. Chang and S.M. Ohr, "Dislocation-free Zone Model of Fracture", J. Appl. Phys. 52 (1981) 7174-81.

25. J. Weertman, I.-H. Lin and R. Thomson, "Double Slip Plane Crack Model", Acta metall. 31 (1983) 473-482.

26. R. Thomson, "Physics of Fracture", Solid State Physics 39, ed. H. Ehrenreich and D. Turnbull (London: Academic Press., 1986), 1-129.

27. V. Lakshmanan and J.C.M. Li, "Edge Dislocations Emitted along Inclined Planes from a Mode I Crack", Mat. Sci. & Eng. A104 (1988) 95-104.

28. P.B. Hirsch, S.G. Roberts and J. Samuels, "The Brittle-Ductile Transition in Silicon: II Interpretation", Proc. Roy. Soc. Lond. A 421 (1989) 25-53.

29. M. Brede, "The Brittle-Ductile Transition in Silicon", Acta metall. mater. 41 (1993) 211-228.

30. S.G. Roberts, P.B. Hirsch, A.S. Booth, M. Ellis and F.C. Serbena, "Dislocations, Cracks and Brittleness in Single Crystals", Physica Scripta T49 (1993) 420-426.

31. S.G. Roberts, A.S. Booth and P.B. Hirsch, "Dislocation Activity and Brittle-Ductile Transitions in Single Crystals", Mat. Sci. & Eng. A176 (1994) 91-98.

32. P.B. Hirsch, "Crack-tip Plasticity and Quasi-brittle Fracture of Single Crystals", Plastic Deformation of Ceramics, ed. R. Bradt, C. Brooks and J. Routbort (New York; Plenum Press, 1995) 1-20.

33. R.O. Ritchie, J.F. Knott and J.R. Rice, "On the Relationship between Critical Tensile Stress and Fracture Toughness in Mild Steel", J. Mech. Phys. Solids 21 (1973) 395-410.

34. F.C. Serbena and S.G. Roberts, "The Brittle-to-Ductile Transition in Germanium", Acta metall. mater. 42 (1994) 2505-10.

35. H. Azzouzi, G. Michot and A. George, "In-situ Synchotron X ray Topography Observation of Crack Tip Plasticity and the Brittle-Ductile Transition in Silicon", Proc. 9th Intll. Conf. on Strength of Metals and Alloys, ed. D.G. Brandon, R. Chaim and A. Rosen (Freund, London, 1991) 783-789.

36. P.D. Warren, "The brittle-ductile Transition in Silicon: the Influence of Pre-existing Dislocation Arrangements", Scripta Metall. 23 (1989) 637-642.

37. P.B. Hirsch and S.G Roberts, "The Brittle-Ductile Transition in Silicon", Phil. Mag. A64 (1991) 55-80.

38. T. Imura, K. Noda, H. Matsui, H. Saka, and H. Kimura, "Direct Measurement of Mobility of Dislocations in High Purity Molybdenum", Dislocations in Solids ed. H. Suzuki, T. Ninomiya, K. Sumino and S. Takeuchi (Yamada Science Foundation, University of Tokyo Press 1985) 287-290.

39. John F. Knott, Fundamentals of Fracture Mechanics. (London: Butterworths,1973).

40. N. Levy, P.V. Marcal, W.J. Ostergren and J.R. Rice, "Small Scale Yielding near a Crack in Plane Strain: a Finite Element Analysis", Int. Journ. Fracture Mechanics 7 (1971) 143-156.

41. J.R. Rice and M.A. Johnson, Inelastic Behaviour of Solids ed. M.F. Kanninen et al. (New-York: Mc Graw-Hill.1970) 641.

42. G.G. Chell, J.R. Haigh and V. Vitek, "A Theory of Warm Prestressing: Experimental Validation and the Implications for Elastic-Plastic Failure Criteria", International Journal of Fracture, 17 (1981) 61-81.

43. D.A. Curry, "A Micromechanistic Approach to the Warm Prestressing of Ferritic Steels", International Journal of Fracture, 17 (1981) 335-43.

44. D.J. Smith and S.J. Garwood, "Application of Theoretical Methods to Predict Overload Effects on Fracture Toughness of A533B", International Journal of Pressure Vessels and Piping, 41 (1990) 833-357.

45. J.R. Rice, "Mechanics of Crack Tip Deformation and Extension by Fatigue", in Fatigue Crack Propagation, STP 415 (Philadelphia, P A: American Society for Testing Materials, 1967) 247-309.

46. G.G. Chell and J.R. Haigh, "The Effect of Warm Prestressing on Proof Tested Pressure Vessels", International Journal of Pressure Vessels and Piping, 23 (1996) 121-132.

47. P.B. Hirsch, S.G. Roberts, J Samuels and P.D. Warren, "Dislocation Dynamics and the Brittle-Ductile Transition in Precracked Silicon", Structure and Properties of Dislocations in Semiconductors 1989, ed. S.G. Roberts, D.B. Holt and P.R. Wilshaw. (Bristol, Institute of Physics, Conf. Ser. 104, 1989) 373-384.

48. A.J. Wilkinson and S.G. Roberts, "A Dislocation Model for the Two Critical Stress Intensities Required for Threshold Fatigue Crack Propagation", Scripta Mater. 35 (1996) 1365-1371.

Inside the crack tip

M. Marder

Department of Physics and Center for Nonlinear Dynamics
The University of Texas at Austin, Austin TX 78712

Abstract

This article reviews analytical results for dynamic brittle fracture at the atomic level. It explains in detail the analysis of the simplest one-dimensional model, and explains some of the phenomena that arise in more realistic two-dimensional cases, as well as mentioning unanswered questions.

Introduction

Fracture mechanics as transformed into a working tool by Irwin[1] is immensely successful because it strips the problem of strength down to essentials. Resistance of a body to fracture is characterized by a single number, the critical stress intensity factor, that can be obtained in laboratory specimens, and used to investigate the safety of arbitrarily large and complicated structures. Despite the immense number of refinements of the basic theory[2], and despite the absence of a completely reliable numerical tool to handle general three-dimensional cases, the problem of fracture is essentially solved.

This solution however only reaches down to a certain level of understanding. Condensed matter physics inquires how properties of a material arise from its atomic arrangement. For some simple types of solids, and some simple properties, detailed calculations are possible. For example, the elastic constants of crystals can accurately be obtained from the conventional approximations to Schrödinger's equation, as can many other properties, such as specific heat, or electrical resistivity[3]. Coming from such a background, it is natural to ask for the atomic origins of fracture toughness. This problem is more difficult than any calculation involving a homogeneous solid, and rarely has been tackled on a realistic stage. One reason for the difficulty is that a body with a crack is no longer a perfect periodic crystal, and therefore many of the most powerful tools of solid state physics must instantly be abandoned. A rather separate reason for the difficulty is that the possibility of crack motion at the atomic level cannot be separated from a careful understanding of the dynamics of atoms around the crack tip when it decides to move. That is, it is not enough to have some sort of rough criterion for when a crack might decide to leap into motion. At the atomic level, there is no substitute for asking when the atoms actually begin to move apart to allow the crack to pass. In fact, as will be discussed below, no simple criterion captures the conditions under which crack motion begins in the cases that are best understood.

The goal in this article is to review analytical and numerical work[4, 5] that has permitted a complete description of fracture toughness in some exceedingly simple solids under rather idealized conditions. Some of the mathematics duplicates previous publications, but there are some points which readers have found confusing that are spelled out in detail for the first time. In addition, I will discuss some of the experimental evidence that the theoretical picture is incomplete.

A Paradox

As a practical procedure for characterizing materials and predicting the onset of crack motion, fracture mechanics has been tested beyond question. Nevertheless, it rests upon some puzzling conceptual inconsistencies. One of these concerns the direction of crack motion. The prescription by which fracture mechanics predicts crack paths begins with the calculation of stresses ahead of the tip. One finds the stress σ_{rr} for a variety of angles, and predicts that the crack moves along the line where σ_{rr} is maximal[6]. Although this prescription has been verified experimentally in some detail, it does not make sense. The idea behind the calculation is that one should find that line in the material ahead of the crack along which the stresses are the largest; this line will open and the crack will extend. Unfortunately, for the elastic fields of linear elastic fracture mechanics, that line is not parallel to the crack line, but tends to be perpendicular to it[7, 8].

This unsettling claim is easily proved. Let us look at σ_{xx}/σ_{yy} right on the crack line. Using the established forms of the singular crack fields[1], and defining

$$\alpha = \sqrt{1 - v^2/c_l^2}; \quad \beta = \sqrt{1 - v^2/c_t^2}, \tag{1}$$

with c_l and c_t longitudinal and transverse wave speeds, one finds that

$$\frac{\sigma_{xx}}{\sigma_{yy}} = \frac{(\beta^2+1)(1+2\alpha^2-\beta^2) - 4\alpha\beta}{4\alpha\beta - (1+\beta^2)^2} \tag{2}$$

$$= \frac{2(\beta^2+1)(\alpha^2-\beta^2)}{4\alpha\beta - (1+\beta^2)^2} - 1. \tag{3}$$

George R. Irwin Symposium on Cleavage Fracture
Edited by Kwai S. Chan
The Minerals, Metals & Materials Society, 1997

The Taylor expansion of Eq. (3) is

$$1 + \frac{v^2(c_t^4 + c_l^4)}{2c_l^2 c_t^2 (c_l - c_t)(c_l + c_t)} + \ldots, \qquad (4)$$

and Eq. (3) is always greater than unity. Therefore, if one wanted to adopt the rule that a crack always opens along the direction perpendicular to maximum stresses, one would have to conclude that any crack moving at nonzero speed always moves perpendicular to itself. This conclusion is ridiculous, but it is not easy to see exactly where it goes wrong. For example, Ching, Langer, and Nakanishi[7] have shown that if one probes beyond the asymptotic forms of the stress fields, for example with a Barenblatt or Dugdale zone, the conclusion is not altered.

One-Dimensional Atomic Model

To begin resolving the paradox, it is helpful to have a case in which the fracture problem can be solved, analytically, all the way down to the atomic level. With such a setting for the problem, there is no longer any uncertainty about how or when the crack should move, nor are there any divergent stress fields left whose precise significance is open to interpretation. The main doubt about such an approach is whether it could be possible at all, or whether one is forced to resort purely to numerical calculation, which carries its own types of uncertainties. However, Slepyan[9, 10] showed that there is a class of solvable problems if the interatomic potential is chosen properly. The solvable cases include two-dimensional triangular crystals breaking under mode I loading. Since the algebra becomes very elaborate[5], so it is advisable to start with the simplest possible case, which is a one-dimensional model[11, 12, 13, 5].

Definition and Energetics

In order to mimic the motion of a crack in a strip, including the effects of underlying discreteness, but otherwise making the calculation as simple as possible, consider the model shown in Figure 1. One can view it as a model for the atoms lying just along a crack surface. They are tied to nearest neighbors by elastic springs, with spring constant $K = 1$, and tied to a line of atoms on the other side of the crack line by similar springs, which however snap when extended past some breaking point. The lines of atoms are being pulled apart by weak springs of spring constant $K = 1/N$. These weak springs are meant schematically to represent N vertical rows of atoms pulling in series, and in more elaborate calculations can be treated more realistically. The equation which describes the upper row of mass points in this model is

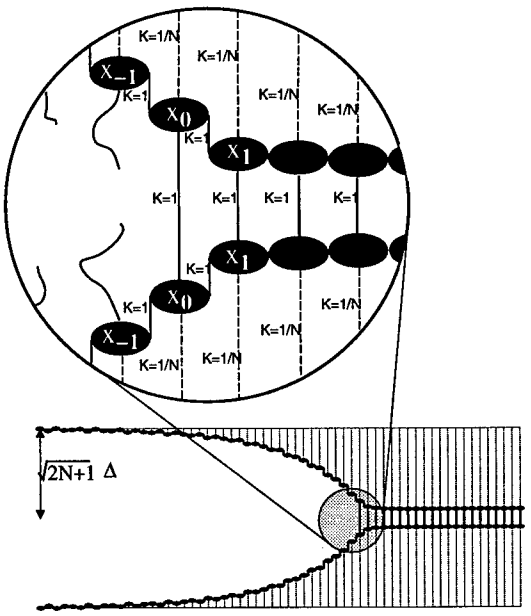


Figure 1: This one-dimensional model mimics the motion of a crack in a strip, incorporating effects of discreteness. One can view it as a model for the atoms lying just along the surface of a crack. The mass points are only allowed to move vertically, and are tied to their neighbors with springs which break when they exceed a certain extension. The lower portion of the figure shows an actual solution of the model, using Eq. (32), at $v = 0.5$, b=0.01.

$$\ddot{u}_{l,+} = \qquad (5)$$
$$\begin{cases} u_{l+1,+} - 2u_{l,+} + u_{l-1,+} \\ +\frac{1}{N}(U_N - u_{l,+}) \\ +(u_{l,-} - u_{l,+})\theta(2u_f - |u_{l,-} - u_{l,+}|) \\ -b\dot{u}_{l,+} \end{cases}$$

There are a few terms that need discussion. First, θ is a step function, and the term containing it describes bonds which snap when their total extension reaches a distance $2u_f$, where u_f is a fracture distance. Second, a small amount of dissipation has been added, the term proportional to b. The amount of dissipation will usually be taken to be vanishingly small. Third, the height that mass points reach after the crack has passed is U_N, and this term describes the force driving crack motion.

As N varies, the natural scale on which a displacement U_N is able to drive crack motion varies, so one should find the natural dimensionless constant which governs crack motion. The question to ask is, *when is enough energy stored in the strip, per lattice spacing far*

to the right of the crack, to break one bond along the crack line? An important physical quantity to define in answering this question is obtained by going far to the right of the crack, and taking the ratio of the displacement of the atom just above the crack line, $U_{\rm right}$ to the total displacement at the top of the strip U_N. Denote this ratio by

$$Q_0 \equiv \frac{U_{\rm right}}{U_N}. \tag{6}$$

Suppose that mass points far to the left and far to the right of the crack are stationary, and that dissipation is negligible. Far to the right of the crack, one has that $U_{\rm right} = u_{l+} = -u_{l-}$, and so balancing forces on masses with location $l \gg 0$ gives

$$2U_{\rm right} = \frac{1}{N}(U_N - U_{\rm right}) \tag{7}$$

$$\Rightarrow Q_0 = \frac{1}{2N+1}. \tag{8}$$

Remembering a factor of two for the upper and lower halves of the strip, the energy per bond for location $l \gg 0$ is therefore

$$2\frac{1}{2}\frac{1}{N}(U_N - U_{\rm right})^2 + \frac{1}{2}(2U_{\rm right})^2 \tag{9}$$

$$\Rightarrow E_{\rm right} = 2Q_0(U_N)^2. \tag{10}$$

Far to the left of the crack, one simply has that

$$U_{\rm left} = U_N. \tag{11}$$

The energy per bond for $l \ll 0$ is just that needed to stretch the spring between u_{l+} and u_- from rest to breaking, and is just

$$E_{\rm break} = 2u_f^2 \tag{12}$$

Assuming there is no other sink of energy, one must have that

$$2Q_0(U_N)^2 = 2u_f^2. \tag{13}$$

Therefore, the minimum value of U_N at which enough energy is stored to the right of the crack so as to be able to snap the bonds along the crack line is

$$U_N^c = \frac{u_f}{\sqrt{Q_0}}. \tag{14}$$

For this reason, it is convenient to define a dimensionless measure of how far one has pulled the edges of the strip,

$$\Delta \equiv \frac{U_N\sqrt{Q_0}}{u_f}. \tag{15}$$

By definition, energy balance requires that steady crack motion is only possible for $\Delta \geq 1$, and a system in which a crack moved when $\Delta = 1$ would have to be perfectly efficient in turning potential energy into crack motion.

Wiener-Hopf solution for steady states

While the preceding calculations motivate the definition Eq. (14), they are based upon false assumptions. When a crack moves in steady state, Slepyan[9]first showed that the mass points far from its tip are necessarily in motion. As a result the energy accounting carried out above is wrong, and crack motion is only possible for $\Delta > 1$. The goal now is to examine steady states in detail.

A steady state in a lattice is more complicated than one in a continuum; it is a configuration which repeats itself after a time interval $1/v$, but moved over by one lattice spacing. In steady state, one has the symmetries

$$u_{l+} = -u_{l-}, \tag{16}$$

$$u_{l+}(t) = u_{0+}(t - l/v), \tag{17}$$

which means that all spatial behavior is contained in the time history of any single mass point. Take this mass point to be u_{0+}, and denote it simply by $u(t)$. Using Eq. (17) and Eq. (16) in Eq. (6) gives

$$\begin{aligned}\ddot{u} &= u(t-1/v) - 2u + u(t+1/v) \\ &+\frac{1}{N}(U_N - u) - 2u\theta(2u_f - 2|u|) - b\dot{u}.\end{aligned} \tag{18}$$

Eq. (18) can be solved analytically using Wiener-Hopf methods. Here is the solution.

There must be some first time at which $u(t)$ rises to 1 and the θ function vanishes. Let us take this time to be $t = 0$. Assuming that u rises above the height of 1 once and remains above it for good, one can write

$$\begin{aligned}\ddot{u} &= u(t-1/v) - 2u + u(t+1/v) \\ &+\frac{1}{N}(U_N e^{-\alpha|t|} - u) - 2u\theta(-t) - b\dot{u}.\end{aligned} \tag{19}$$

Eq. (19) does not quite follow from Eq. (18), since the factor $\exp(-\alpha|t|)$ has appeared. It is introduced just to make Fourier integrals converge, and α will tend to zero at the end of the calculation.

Everything in Eq. (19) can be Fourier transformed in a straightforward way except for the term $\theta(t)u(t)$. Simply define

$$U^-(\omega) = \int dt e^{i\omega t}\theta(-t)u(t) \tag{20a}$$

$$U^+(\omega) = \int dt e^{i\omega t}\theta(t)u(t) \tag{20b}$$

so that $U(\omega)$, the Fourier transform of $u(t)$, is

$$U(\omega) = U^+(\omega) + U^-(\omega) \tag{21}$$

The crucial observation is that U^+ is free of poles in the upper half complex ω plane, while U^- is free of poles in the lower half plane, since the integrals Eq. (20) are obviously convergent in these cases.

Using these definitions, Eq. (19) can be transformed to read

$$\begin{aligned} -\omega^2 U &= 2(\cos\omega/v - 1)U \\ &\quad + \frac{U_N}{N}\left\{\frac{1}{\alpha + i\omega} + \frac{1}{\alpha - i\omega}\right\} \\ &\quad - \frac{U}{N} - 2U^- + i\omega b U. \end{aligned} \tag{22}$$

$$\begin{aligned} \Rightarrow U(\omega)\, F(\omega) - 2U^-(\omega) \\ = \frac{U_N}{N}\left\{\frac{1}{\alpha + i\omega} + \frac{1}{\alpha - i\omega}\right\} \end{aligned} \tag{23}$$

with

$$F(\omega) = \omega^2 + 2(\cos\omega/v - 1) - \frac{1}{N} + i\omega b. \tag{24}$$

Solving for U^- with the aid of Eq. (21) gives

$$\begin{aligned} U^+(\omega)\frac{F(\omega)}{F(\omega) - 2} + U^-(\omega) \\ = -\frac{U_N}{N[F(\omega) - 2]}\left\{\frac{1}{\alpha + i\omega} + \frac{1}{\alpha - i\omega}\right\}. \end{aligned} \tag{25}$$

Define

$$Q(\omega) = \frac{F(\omega)}{F(\omega) - 2} \tag{26}$$

and use the fact that α is vanishingly small, so one only needs the value of $F(0) = -1/N$ on the right hand side of Eq. (25) to write

$$\begin{aligned} Q(\omega)\, U^+(\omega) + U^-(\omega) \\ = Q_0 U_N\left\{\frac{1}{\alpha + i\omega} + \frac{1}{\alpha - i\omega}\right\}. \end{aligned} \tag{27}$$

Here Q_0 is given by Eq. (8), and one can easily check that

$$Q_0 = Q(0). \tag{28}$$

The Wiener-Hopf technique directs one to write

$$Q(\omega) = \frac{Q^-(\omega)}{Q^+(\omega)}, \tag{29}$$

where Q^- is free of poles and zeroes in the lower complex ω plane and Q^+ is free of poles and zeroes in the upper complex plane. One can carry out this decomposition with the explicit formula

$$Q^{\pm}(\omega) = \exp[\lim_{\epsilon\to 0}\int \frac{d\omega'}{2\pi}\frac{\ln Q(\omega')}{i\omega \mp \epsilon - i\omega'}]. \tag{30}$$

Now separate Eq. (27) into two pieces, one of which has poles only in the lower half plane, and one of which has poles only in the upper half plane:

$$\begin{aligned} \frac{U^+(\omega)}{Q^+(\omega)} - \frac{Q_0 U_N}{Q^-(0)}\frac{1}{(-i\omega + \alpha)} \\ = \frac{Q_0 U_N}{Q^-(0)}\frac{1}{(i\omega + \alpha)} - \frac{U^-(\omega)}{Q^-(\omega)}. \end{aligned} \tag{31}$$

Because the right and left hand sides of this equation have poles in opposite sections of the complex plane, they must separately equal a constant, C. The constant must vanish, or U^- and U^+ will behave as a delta function near $t = 0$. So

$$U^-(\omega) = U_N\frac{Q_0 Q^-(\omega)}{Q^-(0)(\alpha + i\omega)}, \tag{32a}$$

and

$$U^+(\omega) = U_N\frac{Q_0 Q^+(\omega)}{Q^-(0)(\alpha - i\omega)}. \tag{32b}$$

One now has an explicit solution for $U(\omega)$. Numerical evaluation of Eq. (30), and $U(t)$ from Eq. (32) is fairly straightforward, using fast Fourier transforms. However, in carrying out the numerical transforms, it is important to analyze the behavior of the functions for large values of ω. In cases where functions to be transformed decay as $1/i\omega$, this behavior is best subtracted off before the numerical transform is performed, with the appropriate step function added back analytically afterwards. Conversely, in cases where functions to be transformed have a step function discontinuity, it is best to subtract off the appropriate multiple of $e^{-t}\theta(t)$ before the transform, adding on the appropriate multiple of $1/(1 - i\omega)$ afterwards. A solution of Eq. (32) constructed in this manner appears in Figure 1.

Relation between Δ and v

There is an important point which has been forgotten. This solution is only correct if in fact

$$u(t) = u_f \text{ at } t = 0 \tag{33}$$

because this is supposed to be the moment at which the bond between u_{0+} and u_{0-} breaks. The only parameter in the problem one is free to vary is U_N, so the condition

Eq. (33) chooses a value of U_N, or its dimensionless counterpart, Δ. Once one assumes that the crack moves in steady state at velocity v, there is a unique Δ which makes it possible.

To obtain Eq. (33), one needs to require that

$$\lim_{t\to 0^-} \int \frac{d\omega}{2\pi} e^{-i\omega t} U^-(\omega) = u_f. \tag{34}$$

This integral can be evaluated by inspection. One knows that for positive $t > 0$,

$$\int d\omega \exp[-i\omega t] U^-(\omega) = 0, \tag{35}$$

and that any function whose behavior for large ω is $1/i\omega$ has a step function discontinuity at the origin. Therefore, Eq. (34) and Eq. (32a) become

$$u_f = U_N Q_0 \frac{Q^-(\infty)}{Q^-(0)}. \tag{36}$$

Since from Eq. (26) follows that $Q(\infty) = 1$, one sees from Eq. (30) that

$$Q^-(\infty) = Q^+(\infty) = 1. \tag{37}$$

As a result, one has from Eq. (36) and the definition of Δ given in Eq. (15) that

$$\Delta = \frac{Q^-(0)}{\sqrt{Q_0}}. \tag{38}$$

To make this result more explicit, use Eq. (30) and the fact that $Q(-\omega) = \bar{Q}(\omega)$ to write

$$Q^-(0) = \exp[\int \frac{d\omega'}{2\pi} \frac{1}{2} [\frac{\ln Q(\omega')}{\epsilon - i\omega'} + \frac{\ln Q(-\omega')}{\epsilon + i\omega'}]] \tag{39}$$

$$= \exp[\int \frac{d\omega'}{2\pi} [\frac{1}{-2i\omega'} \ln \left\{ \frac{Q(\omega')}{\bar{Q}(\omega')} \right\} + \frac{\epsilon}{\epsilon^2 + \omega'^2} \ln Q(0)]] \tag{40}$$

$$\Rightarrow Q^-(0) = \sqrt{Q_0} \exp[-\int \frac{d\omega'}{2\pi} \frac{1}{2i\omega'} \ln \left\{ \frac{Q(\omega')}{\bar{Q}(\omega')} \right\}]. \tag{41}$$

Placing Eq. (41) into Eq. (38) gives

$$\Delta = \exp[-\int \frac{d\omega'}{2\pi} \frac{1}{2i\omega'} \ln \left\{ \frac{Q(\omega')}{\bar{Q}(\omega')} \right\}]. \tag{42}$$

In order to record a final expression that is correct not only for the one-dimensional model considered here, but for more general cases, rewrite Eq. (42) as

$$\Delta = C \exp[-\int \frac{d\omega'}{2\pi} \frac{1}{2i\omega'} \left\{ \begin{array}{c} \ln Q(\omega') \\ -\ln Q(\omega') \end{array} \right\}], \tag{43}$$

where C is a constant of order unity that is determined by the geometry of the lattice, equaling 1 for the one-dimensional model considered here, 1 for a triangular lattice loaded in Mode III, but $2/\sqrt{3}$ for a triangular lattice loaded in Mode I. When written in this form, Eq. (43) is suitable for numerical evaluation, since there is no uncertainty relating to the phase of the logarithm.

When b becomes sufficiently small, Q is real for real ω except in the small neighborhood of isolated roots and poles that sit near the real ω axis. Let r_i^+ be the roots of Q with negative imaginary part (since they belong with Q^+), r_i^- the roots of Q with positive imaginary part, and similarly $p_i^\pm$ the poles of Q. Then one can rewrite Eq. (43) as

$$\Delta = C \sqrt{\prod \frac{r_i^- p_i^+}{r_i^+ p_i^-}}, \text{ for } b = 0. \tag{44}$$

One may derive Eq. (44) as follows: away from a root or pole of Q, the integrand of Eq. (43) vanishes. Consider the neighborhood of a root r^+ of Q which falls to the real axis from the negative side as $b \to 0$. For the sake of argument, take the imaginary part of this root to be $-ib$. In the neighborhood of this root, say within a distance $\sqrt{b}$, the integral to compute for Eq. (43) is

$$-\frac{1}{2\pi} \int_{r^+ - \sqrt{b}}^{r^+ + \sqrt{b}} \frac{d\omega'}{2i\omega'} \left[\begin{array}{c} \ln(\omega' - (r^+ - ib)) \\ -\ln(\omega' - (r^+ + ib)) \end{array} \right]. \tag{45}$$

Defining $\omega'' = \omega' - r^+$, and integrating by parts gives

$$-\frac{1}{2\pi} \int_{-\sqrt{b}}^{\sqrt{b}} \frac{d\omega''}{2i} \ln[\omega'' + r^+] \frac{2ib}{\omega''^2 + b^2} \tag{46}$$

$$= -\frac{1}{2} \ln r^+ + \mathcal{O}\sqrt{b}. \tag{47}$$

Similar integrals over other roots and poles of Q finally produce Eq. (44).

Together with Eq. (32), Eq. (43) and Eq. (44) constitute the formal solution of the model. Since Q is a function of the steady state velocity v, Eq. (42) relates the external driving force on the system, Δ, to the velocity of the crack v.

Cherenkov radiation

It is interesting to plot the function $\Delta(v)$ obtained from Eq. (44) (Figure 2). Because all steady states occur for $\Delta > 1$, one necessarily concludes that not all energy stored to the right of the crack tip ends up devoted to snapping bonds. The fate of the remaining energy depends upon the amount of dissipation b, and the distance from the crack tip one inspects. In the limit of vanishing dissipation b, traveling waves leave the crack

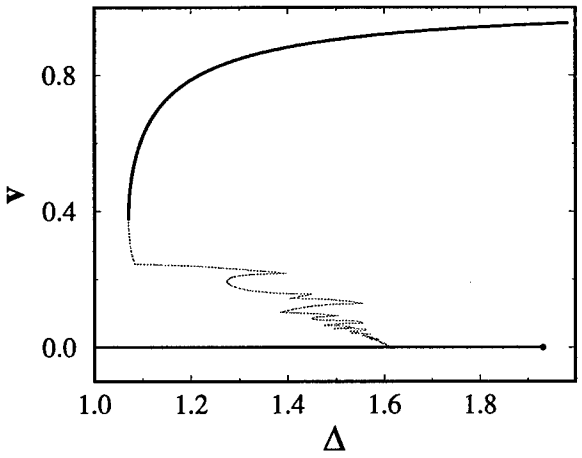


Figure 2: The velocity of a crack v is plotted as a function of the driving force Δ for the one-dimensional model. The calculation is carried out using Eq. (44) for $N = 100$ and $v = 0.5$. The thick upper line indicates physically realizable solutions, and the line along $v = 0$ indicates the range of lattice-trapped solutions[11]; that is, solutions which are stationary and metastable.

tip and carry energy off in its wake; the amount of energy they contain becomes independent of b. Such a state is depicted in Figure 1, which shows a solution of Eq. (32) for $v = 0.5$, $N = 9$, and $b = 0.01$. For all nonzero b, these traveling waves will eventually decay, and the extra energy will have been absorbed by dissipation, but the value of b determines whether one views the process as microscopic or macroscopic.

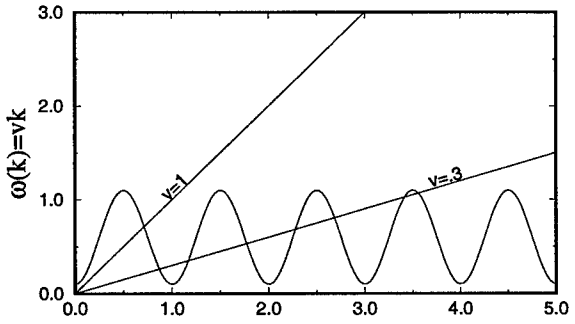


Figure 3: Graphical solution of Eq. (51), showing that for low velocities, a large number of resonances may be excited by a moving crack.

The frequencies of the radiation emitted by the crack have a simple physical interpretation as Cherenkov radiation. This argument is quite general. Consider motion of a particle through a lattice, in which the phonons are described by the dispersion

$$\omega_\alpha(\vec{k}). \tag{48}$$

If the particle moves with constant velocity $\vec{v}$, and interacts with the various ions according to some function $\mathcal{I}$, then to linear order the motions of the ions can be described by a matrix D which describes their interactions with each other as

$$m\ddot{u}^l_\mu = -\sum_{\nu l'} D_{\mu\nu}(\vec{R}^l - \vec{R}^{l'})u^{l'}_\nu + \sum_{l'} \mathcal{I}_\mu(\vec{R}^{l'} - \vec{v}t). \tag{49}$$

Multiplying everywhere by $e^{i\vec{k}\cdot\vec{R}^l}$, summing over l, letting $\vec{K}$ be reciprocal lattice vectors, and letting Ω be the volume of a unit cell gives

$$m\ddot{u}_\mu(\vec{k}) = \sum_\nu D_{\mu\nu}(\vec{k})u_\nu(\vec{k}) + \frac{1}{\Omega}\sum_{\vec{K}} e^{i\vec{v}\cdot(\vec{k}+\vec{K})t}\mathcal{I}_\mu(\vec{k}+\vec{K}). \tag{50}$$

Inspection shows that the lattice frequencies excited in this way are those which in the extended zone scheme[3] obey

$$\omega(\vec{k}) = \vec{v}\cdot\vec{k}. \tag{51}$$

In the case of the one-dimensional model described here, there are two phonon dispersion relations to consider. One gives the conditions for propagating radiation far behind the crack tip, and the other gives the conditions for propagating radiation far ahead of the crack tip. The first of these is given by the roots of

$$\omega^2(k) + 2(\cos k - 1) - \frac{1}{N} + i\omega(k)b = 0, \tag{52}$$

while the second is given by the roots of

$$\omega^2(k) + 2(\cos k - 1) - \frac{1}{N} - 2 + i\omega(k)b. \tag{53}$$

Looking through the definitions in Eqs. (24) and (26), one sees that the roots of $Q(\omega)$ correspond exactly to the case where the dispersion relation Eq. (52) obeys the Cherenkov condition Eq. (51), while the roots correspond to the case where Eq. (53) obeys this condition. That is the reason for the appearance of these roots and poles in Eq. (44). However, Eq. (44) not only describes the frequencies excited by the moving crack but also the magnitude of the energy they radiate away. I do not know if Eq. (44) is more than approximately correct for particle interactions more general than linear snapping bonds use in Eq. (6).

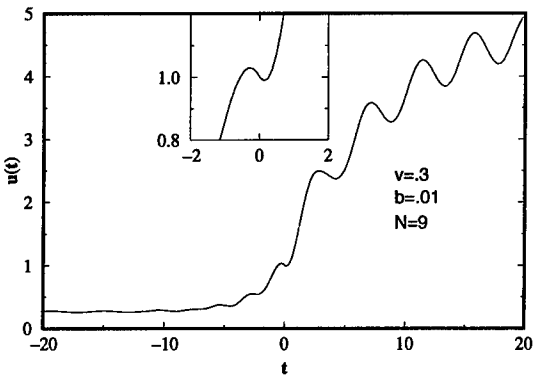


Figure 4: The height of u_{0+} is plotted as a function of time for $v = .3$, $b = .01$, and $N = 9$. Notice that u rises above $u_f = 1$ before $t = 0$, and is actually descending at the moment when it again passes height u_f and is supposed to have broken.

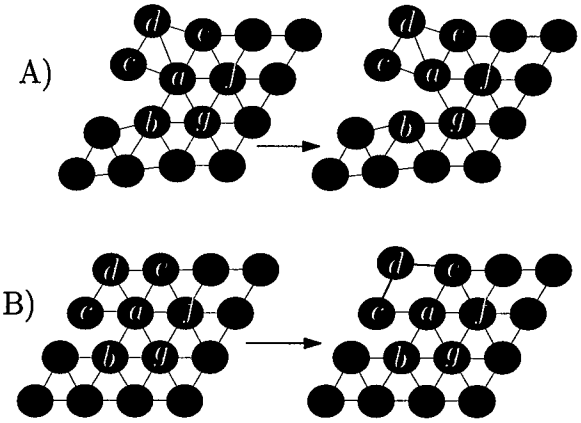


Figure 5: When particle displacements at the moment of bond snapping are comparable to interparticle spacing, particle c effectively pulls up on particle a, and snaps the $a-b$ bond, as in A). However, if bonds break when displacements are small, c is ineffective in pulling up on a, and the $a-d$ bond will be the first to break, as indicated in B)

Forbidden velocities

The jagged structure of Figure 2 makes it appear that many different states, emitting different quantities of radiation, can coexist for some values of Δ. This conclusion is largely incorrect, for two reasons. In Ref. [5], it is shown that states are linearly unstable whenever v is a decreasing function of Δ. So all the backward-traveling portions of the curve can be ruled out. In addition a final condition has been neglected. Not only must the bond between u_{0+} and u_{0-} reach length u_f at $t = 0$, but this must be the first time at which that bond stretches to a length greater than u_f. For $0 < v < 0.3\ldots$ (the precise value of the upper limit varies with b and N) that condition is violated. The states have the unphysical character shown in Figure 4. Masses rise above height u_f for t less than 0, the bond connecting them to the lower line of masses remaining however intact, and then they descend, whereupon the bond snaps. Since the solution of Eq. (19) is unique, but does not in this case solve Eq. (18), no solutions of Eq. (18) exist at all at these velocities.

This argument shows that no steady state in the sense of Eq. (17) can exist. It is also possible to look analytically for solutions that are periodic, but travel two lattice spacings before repeating. No solutions of this type exist. Numerically, one can verify that if a crack is allowed to propagate with Δ right above the critical threshold, and Δ is then very slowly lowered through the threshold, the crack stops propagating. It does not slow down noticeably; suddenly the moving crack emits a burst of radiation that carries off its kinetic energy, and stops in the space of an atom. There is a forbidden band of velocities.

Two-Dimensional Models

The techniques of the previous section can, with some effort, be extended to more complicated two-dimensional models, and such calculations were first performed by Slepyan and co-workers[10]. Just as before, cracks enter steady state, and there is a forbidden band of velocities starting at 0, and proceeding up to some minimum critical velocity. There is however a new feature of the problem which enters, and which is nothing but the reflection, on the atomic level, of the tendency for cracks to move perpendicular to themselves. A crack only proceeds in perfectly brittle fashion if it snaps one by one the bonds that lie along the crack line. However, there is no necessary reason that these bonds should be the first to snap as the crack moves. If they are not, then the crack suffers some type of instability, which might cause it to blunt and stop, to begin emitting dislocations, or to generate microcracks perpendicular to the main direction of motion.

These instabilities were first described theoretically in a two-dimensional lattice loaded in Mode III. In this case, adopting a rule that bonds which once break are not allowed to re-heal, the main crack throws out a dendritic thicket of microcracks. Despite the pleasing resemblance of the pictures obtained in this way to those found in experiments on brittle amorphous materials[14], it is necessary to proceed on to consider lattices loaded in Mode I, and here the situation is more complicated. The simplest case to study is a triangular lattice with purely central forces between nearest neighbors; unfortunately, this model does not permit ideal brittle crack

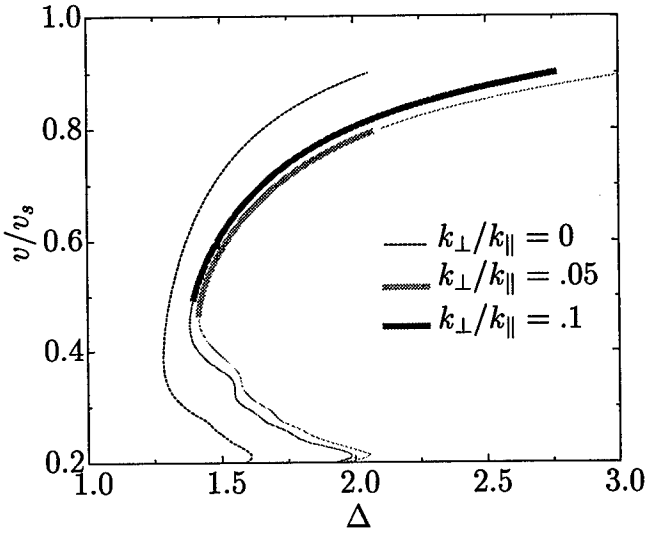


Figure 6: Crack velocity versus loading parameter Δ for different ratios of $k_\perp/k_\parallel$. Thin lines show unstable states that cannot physically be realized, thick lines stable states.

propagation at any speed. The reason for the difficulty is illustrated in Figure 5. The interactions between neighboring particles are only linear in the limit where the distance particles have to move to snap bonds is very small compared to the inter-particle spacing. However, in this limit, particles along the crack line cannot effectively transfer forces to their neighbors, and bonds off the crack line snap. The prediction of linear elasticity is correct; these cracks try to move perpendicular to themselves, and therefore cannot efficiently move at all. However, although this result does accurately describe a class of possible crack tip instabilities, it arises in this case from the rather artificial demand that interactions between neighbors be purely linear. If everything about the model is left the same, with forces between neighbors proportional to their distance to the point of snapping, but with bonds breaking only after particles travel a noticeable fraction of the nearest-neighbor separation brittle crack propagation is possible. In numerical experiments, the "noticeable fraction" is around .2.

There is a second way to stabilize ideal brittle fracture, and that is to allow non-central forces. Then particle c can pull upwards on particle a in Figure 5, and allow crack propagation. The model can still be solved analytically in this case, and some results appear in Figure 6. The definition of the parameters $k_\parallel$ and $k_\perp$ is this: consider two particles, let the vector connecting them in equilibrium be $\vec{R}$, and let the vector connecting them in general be $\vec{R}+\vec{u}$. Let $\hat{n}_\parallel$ be a unit vector parallel to $\vec{R}$, and $\hat{n}_\perp$ a unit vector perpendicular to $\vec{R}$. Then the force of one particle on another is given by $\vec{F} = k_\parallel \hat{n}_\parallel \cdot \vec{u} + k_\perp \hat{n}_\perp \cdot \vec{u}$. Anisotropy in such a form that bonds perpendicular to the cleavage plane are weaker than other bonds would also clearly tend to promote stable rapid fracture, but no analytical calculations along these lines have been performed.

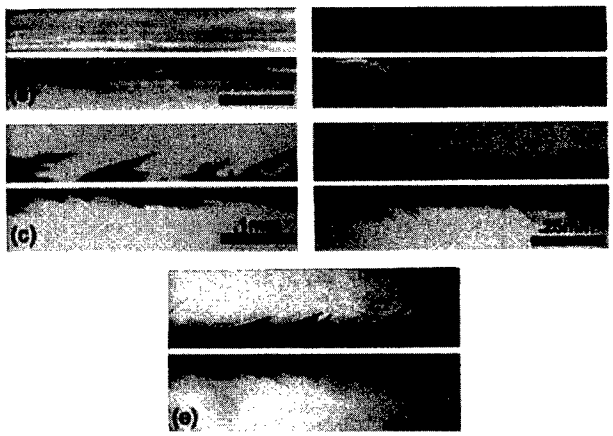


Figure 7: Photographs of subsurface structure generated by cracks traveling at various speeds in Homalite. The crack traveled from left to right. Courtesy of J. Hauch.

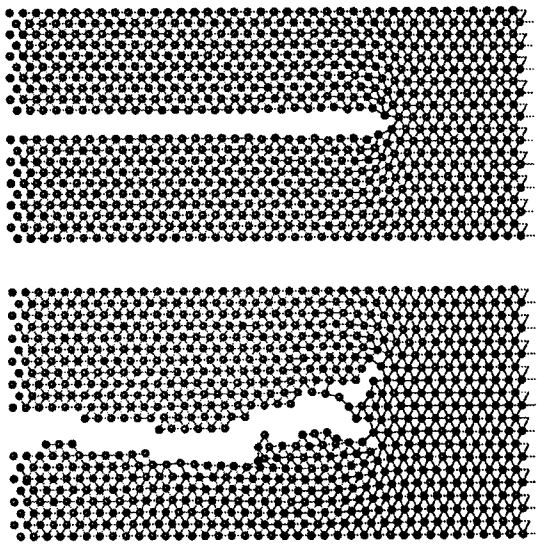


Figure 8: Molecular dynamics in a simple two-dimensional model display a transition between smoothly moving cracks and a violent branching instability that is surprisingly similar to experiment. The upper image shows stable crack motion driven by Δ below the critical threshold, while the lower image shows unstable motion once Δ passes the threshold.

Figs. 7 and 8 compare the subsurface microcracks from experiments in Homalite, and two-dimensional mol-

ecular dynamics in a simple crystalline model where atoms interact by the UBER potential. However, this sort of comparison is not satisfying because Homalite has nothing to do with a triangular lattice. All the qualitative predictions of these two-dimensional calculations are borne out in molecular-dynamics simulations of three-dimensional atomic systems with realistic three-body potentials for silicon or silicon oxide. Cracks find it impossible to travel at velocities below a minimum critical threshold, adopt periodically repeating steady states above it, and finally become unstable above a critical energy release rate. This work is still in progress, so I cannot describe it in detail here.

Conclusion

The calculations discussed in this paper reveal qualitative features of crack motion that can only be understood thoroughly at the atomic level. The effects persist up to the macroscopic scale, just as the anisotropy of an underlying crystal makes itself felt in the anisotropy of bulk elastic constants. They determine whether a brittle fracture can stably propagate or not, and how much energy it consumes if it does so, and where exactly the energy goes. The comparison of these results with experiment has not completely been worked out, but the following points are worth mentioning:

- Anisotropy and non-central forces are predicted to tend to stabilize crack motion. This prediction is in accord with the fact that ionic and covalently bonded solids tend to be brittle, and that crack motion at speeds up to the Rayleigh wave speed has been observed in crystals, and along weak interfaces[15, 16].
- The dendritic microbranching patterns observed in brittle amorphous solids after the cracks go unstable are very similar to the patterns observed in the simple models.
- The band of forbidden velocities predicted by all the analytical models has never been observed. J. Hauch and I have performed experiments clearly showing that it is not present in amorphous materials at room temperature. Experiments to test the prediction in crystals at low temperature are in progress, but no results are yet available.

Eventually it may be possible to start at the atomic level, to predict whether a material should be brittle or ductile, and calculate the factors contributing to its dynamic fracture energy. Right now, some of the ingredients needed for this task are evident, but it is far from complete.

References

[1] H. Tada, P. C. Paris, and G. R. Irwin, *The Stress Analysis of Cracks Handbook* (Paris Productions, St. Louis, 1985).

[2] M. F. Kanninen and C. Popelar, *Advanced Fracture Mechanics* (Oxford University Press, New York, 1985).

[3] N. Ashcroft and N. D. Mermin, *Solid State Physics* (Saunders, Fort Worth, 1976).

[4] M. Marder and X. Liu, Physical Review Letters **74**, 2417 (1993).

[5] M. Marder and S. Gross, Journal of the Mechanics and Physics of Solids **43**, 1 (1995).

[6] E. H. Yoffe, Philisophical Magazine **42**, 739 (1951).

[7] E. S. C. Ching, J. S. Langer, and H. Nakanishi, Physical Review E **53**, 2864 (1996).

[8] E. S. C. Ching, H. Nakanishi, and J. S. Langer, Physical Review Letters **76**, 1087 (1996).

[9] L. I. Slepyan, Soviet Physics Doklady **26**, 538 (1981).

[10] S. A. Kulakhmetova, V. A. Saraikin, and L. I. Slepyan, Mechanics of Solids **19**, 101 (1984).

[11] R. Thomson, C. Hsieh, and V. Rana, Journal of Applied Physics **42**, 3154 (1971).

[12] R. Thomson, Solid State Physics **39**, 1 (1986).

[13] M. Marder, Physica D **66**, 125 (1993).

[14] E. Sharon, S. P. Gross, and J. Fineberg, Physical Review Letters **74**, 5096 (1995).

[15] J. J. Gilman, C. Knudsen, and W. P. Walsh, Journal of Applied Phyics **29**, 601 (1958).

[16] B. Cotterell, Applied Materials Research **4**, 227 (1965).

A NEW MODEL OF THE BRITTLE-TO-DUCTILE TRANSITION BASED ON A COLLECTIVE DISLOCATION GENERATION INSTABILITY

Robert H. Folk, II, Steven M. Labovitz, and David P. Pope
Department of Materials Science and Engineering,
University of Pennsylvania, Philadelphia, Pa. 19104

Abstract

A new model of the brittle-to-ductile (BDT) transition has been proposed based on a cooperative mechanism of dislocation generation. In the existing models, the BDT is assumed to be either controlled by the nucleation of a single dislocation or the mobility of a group of dislocations. The effects of temperature enter these models only via thermally activated generation or motion of dislocations. In contrast, the model advanced in this work suggests that the BDT corresponds to a combined thermal-and-stress induced cooperative instability of a large number of dislocation loops. The analysis is carried out in the framework of statistical mechanics and is closely related to the well-known Kosterlitz-Thouless type dislocation instability. The new model not only identifies the specific role of the crack tip in the BDT but also suggests that a sudden onset of plasticity at a certain temperature is possible in crack-free crystals. There is ample evidence in the literature for this.

We have performed experiments to check the model, looking for the onset of sudden massive plasticity at the BDT. In order to minimize the uncertainties in the stress distribution, the experiments are performed on homogeneously stressed, nearly dislocation-free silicon. Results obtained on highly stressed Si/Ge epitaxial overlayers on silicon are very encouraging. We see a sudden onset of stress relaxation in the overlayer during heating in which the mobile dislocation density increases from near-zero to 10^{11} over a small temperature interval and corresponds to the onset of dislocation activity in the film, leading to the production of interfacial dislocations.

George R. Irwin Symposium on Cleavage Fracture
Edited by Kwai S. Chan
The Minerals, Metals & Materials Society, 1997

Introduction

The mechanism governing the brittle-to-ductile transition (BDT) has been the subject of debate for some time. Existing models view this transition as a change in a material's response to loading brought about by the nucleation of a single dislocation in the vicinity of a crack tip, or, by the activation of a mobile population of preexisting dislocations. Rice and Thomson [1] were the first to provide a theoretical treatment of brittle versus ductile behavior in materials using crack tip dislocation processes as a foundation. Materials were categorized as being either intrinsically brittle or intrinsically ductile depending on the magnitude of the activation energy for dislocation nucleation. Here it was assumed that an atomically sharp crack is necessary to generate the stresses required for dislocation nucleation. Materials found to have large activation energies, such as silicon, were thought to be intrinsically brittle and unable to plastically deform even at high temperatures. In contrast, many of the face-centered cubic metals such as silver and copper were determined to be capable of spontaneous dislocation emission regardless of temperature. The rate of dislocation nucleation in this model is given by an exponential function. However there were several problems with this initial model. In addition to the unrealistic activation energies predicted by the model, it did not explicitly treat thermal effects. To address these shortcomings, Rice and Beltz [2, 3] recast the original Rice-Thomson model in a Peierls framework. This modification of the model did produce more realistic activation energies without significantly altering the underlying assumptions.

During the evolution of the Rice-Thomson model, a second model was developed by Hirsch and Roberts [4, 5] to explain the apparent strain-rate dependence of the BDT. This model is based on the assumption that sufficient Frank-Read type dislocation sources already exist near the crack tip. These sources become active when the local stress approaches the Griffith stress for cleavage fracture. The BDT occurs when a sufficient number of emitted dislocations are able to move rapidly enough to shield the crack tip. Here an Arrhenius type equation is used to describe the thermally activated motion of the dislocations.

Although both methods described above are reasonable approaches to the BDT problem, neither model adequately describes the range of observations reported in the literature. Early experiments on whiskers demonstrate the characteristics of a brittle-to-ductile transition, although at the time the results were not associated with it. Pearson, Read, and Feldmann [6] conducted three-point bending experiments on silicon whiskers at various temperatures. Their research showed that dislocation-free whiskers could deform elastically at room temperature to stresses that approach the theoretical limit for silicon before brittle failure occurs. However if the whiskers were tested above 600°C a sharp yield point was observed followed by a substantial load drop. These results are similar to observations made by Brenner [7, 8] on silver, copper, and iron whiskers. Although Brenner only conducted experiments at room temperature, all of the whiskers supported large elastic strains. When the elastic limit was exceeded the iron whiskers fractured whereas the silver and copper whiskers yielded and a substantial load drop accompanied the yielding in these samples. The importance of these results is their resemblance to observations made during BDT experiments on bulk silicon. Many researchers [9-11] have studied the BDT in silicon using various experimental techniques and conditions. However all of their results possess characteristics similar to the findings in the whisker research: 1) dislocation-free silicon is able to withstand very large elastic strains prior to failure, 2) the failure mode changes from brittle fracture to ductile yielding over a very narrow temperature range, 3) in constant strain-rate tests, a large load drop occurs upon yielding, and 4) the onset of yielding requires the nucleation of many dislocations in the initially dislocation-free material. More recently, research conducted on the relaxation of strained SiGe epitaxial layers has yielded similar results [12]. Massive dislocation nucleation with concomitant strain relaxation in the film appears to occur when a critical temperature is achieved. Preliminary results from our current research on the mechanical behavior of silicon beams also corroborate these findings. Collectively, these observations have led to the development of a new approach to describing the BDT.

We propose that the BDT is one example of a more general phenomenon in which dislocation activity changes dramatically above some critical point. The Khantha-Pope-Vitek (KPV) model reviewed here provides a new perspective on the BDT problem. According to the KPV model, many dislocation loops are homogeneously nucleated in a material when a critical combination of stress and temperature is reached. This nucleation event follows from the interaction of many dislocation loops that are sub-critical in size. The avalanche of dislocations results in macroscopic yielding of the material. The KPV model makes no assumptions about the mode of loading or the preexistence of a crack.

This paper is organized as follows: First we will outline the prominent features of the Rice-Thomson dislocation nucleation model and the Hirsch-Roberts dislocation mobility model, and highlight their general predictions. Following this we will review the Khantha-Pope-Vitek model of the BDT. Finally, experimental observations from BDT related research will be discussed and compared with predictions from the three models.

Theoretical Background

In their early paper on the subject of brittle and ductile material behavior, Rice and Thomson [1] proposed that materials exhibit either brittle fracture or ductile failure depending on the ease with which individual dislocation loops can be nucleated at an atomically sharp crack tip. The nucleation event was viewed to be a competition between the applied shear stress acting to expel a fully formed dislocation half-loop from the crack tip and the combined effect of ledge surface energy and the image force acting to pull the dislocation back into the crack. The dislocation must achieve a radius corresponding to the equilibrium point of these competing forces in order for it to be able to expand unstably under the influence of the applied shear stress. If this equilibrium distance falls within the elastic core cut-off distance, then spontaneous emission of dislocations can occur, thereby blunting the crack tip. Materials capable of spontaneous emission were classified as intrinsically ductile and included many of the face-centered cubic metals such as copper and silver. If the equilibrium distance is greater than the cut-off distance, an energy barrier exists which prohibits spontaneous emission. Rice and Thomson used the calculated activation energies to determine the degree to which these materials were brittle. For some materials the calculated activation energy was small, for example the activation energies of sodium and iron are 0.02 and 2.2 eV, respectively. Such low activation energies would permit thermally activated dislocation nucleation. However the energy barrier in most of the materials classified as brittle is quite large (e.g. 111 eV in silicon), eliminating the possibility of thermally activated dislocation generation, and hence ductile behavior is prevented even at very high temperatures.

Since the model was first proposed, several researchers have taken steps to extend Rice and Thomson's work to more accurately portray experimental observations. Most recently Rice and Beltz [2, 3] have modified the model using the Peierls concept of a periodic stress field on the slip plane. Here the elastic core cut-

off distance of the original Rice-Thomson model is eliminated through the application of a periodic shear displacement emanating from the crack tip. In this model an incipient dislocation will be emitted from the crack if the Griffith energy release rate exceeds the unstable stacking energy, γ_{us}. Conversely, brittle fracture will occur if the Griffith energy for cleavage is exceeded first. Dislocation nucleation can occur below the critical energy release rate with the assistance of thermal activation. Although this enhancement to the Rice-Thomson model did address some of the problems of the earlier work, it did not change many of the underlying assumptions. First, it is assumed that an atomically sharp crack is necessary to generate sufficient stress for dislocation nucleation and that the crack tip intersects a suitable slip plane. In addition, the nucleation rate is believed to be described by an exponential function, indicating a gradual emission of dislocations as the temperature is increased. Finally it is assumed that if one dislocation can be nucleated, then whatever number of dislocations necessary to arrest the crack will also be nucleated.

An alternative approach has been developed by Hirsch and Roberts [4, 5] to address the strain-rate dependence of the BDT. Here it is assumed that dislocation nucleation is not a limiting factor; sufficient Frank-Read or other sources are present near the crack tip. These sources become active when the local stress near the crack tip approaches the Griffith stress for cleavage fracture. However the emission of dislocations does not directly result in the BDT. The BDT will only occur when the emitted dislocations move rapidly enough to shield the advancing crack indefinitely. The BDT is therefore a result of the thermally activated motion of dislocations near the crack tip. The velocity of the dislocations is described by an Arrhenius type equation and, as in the Rice-Thomson model, the existence of a crack is an integral part of their description of the BDT. Also, information must be known about the locations of the dislocation sources relative to the crack front.

The KPV model differs from the above models in that it describes a transition in which many dislocations are homogeneously nucleated in a material. The homogeneous nucleation event results from a thermally-driven, stress-assisted instability of many dislocation loops. Below we will outline the KPV model and qualitatively discuss some of its predictions. A complete treatment of the KPV model, from which the following passages are taken, can be found in [13] with additional information available in [14-16].

Unless the stress approaches the theoretical limit, the energy required to nucleate a single dislocation loop and expand it to its critical diameter is generally too large to permit thermal activation. However if one considers the formation of dislocation loops (dipoles in two dimensions) smaller than the critical size for unstable expansion, nucleation events become probable even without the elevated levels of stress associated with an atomically sharp crack. In an unloaded solid the enthalpy of formation of a loop with a radius close to the cut-off radius for linear elastic behavior, is on the order of 0.1-2.0 eV. Due to the small energy associated with these atomic size loops, an equilibrium population of loops will exist in a solid due to thermal fluctuations. The density of loops at a temperature T, is proportional to $\exp[-H(r)/k_BT]$, where H(r) is the enthalpy of formation of a loop with radius r and k_B is the Boltzmann factor. Here it can be seen that small reductions in the self-energy of the loops or an increase in temperature results in an exponential increase in the density of the loops. Associated with each loop is a component of plastic strain resulting from the expansion and contraction of the loop during formation and annihilation. If the loops do not glide through the solid, the plastic strain is small and the stress-strain relationships remain linear. The increase in total strain resulting from the plastic strain can be accounted for by replacing the moduli used in the purely elastic stress-stain relationships with reduced moduli, referred to here as 'effective moduli'. The energy of a dislocation loop formed in a medium described by stress-strain relations given in terms of the effective moduli is proportional to the effective moduli. This description is completely equivalent to the well-known energy of an isolated dislocation loop being proportional to the elastic moduli. At low temperatures, the density of loops is low and the effective moduli do not differ greatly from the elastic moduli. As the temperature is increased there is a rapid increase in the density of loops and a concomitant increase in the plastic strain introduced into the system. The resulting reduction in moduli lowers the self-energy of the loops thereby providing feedback for the formation of subsequent loops in the vicinity of preexisting loops. This feedback process in turn results in a further increase in the density of loops. It is important to note that this cooperative dislocation screening process increases the dislocation density at a rate much greater than an exponential function would allow. As the density of loops increases, there is also a rapid increase in the configurational entropy. At the critical point, the reduction in the enthalpy of the loops and the increase in the entropy of the system results in a negative free energy and unstable expansion of the loops occurs. In the absence of an external stress field, this avalanche of dislocations corresponds to the Kosterlitz-Thouless (K-T) description of a dislocation mediated phase transition that occurs just below the melting temperature of the material.

The KPV model presented here, uses the K-T result as a basis for the description of dislocation generation in a loaded medium. In a loaded solid, the enthalpy of formation for a dislocation loop is reduced by an amount proportional to the work done by the applied shear stress. For a fixed load, the additional reduction in the self-energy of the loops causes the system to reach the critical point for unstable loop expansion at a temperature that is well below the K-T transition temperature. The avalanche of dislocations produced at the critical point is sufficient to produce macroscopic yielding of the sample. In the limiting case of an applied shear stress approaching the theoretical limit for the material, the transition temperature is reduced to 0°K. The problem then becomes one of nucleating a single fully formed dislocation loop without thermal activation, and the original Rice-Thomson model result is recovered. In the absence of an applied shear stress, the K-T result is recovered and dislocation nucleation occurs near the melting point of the material. Between these two extremes, dislocation nucleation occurs at a critical combination of stress and temperature. The stress to drive the instability decreases with increasing temperature until at some temperature it becomes equal to the fracture stress. We take this to be the BDT.

Experimental Evidence

In reviewing the experimental evidence in the literature we have included research that is typically ignored in discussions of the BDT because its relevance is not immediately apparent. Specifically, we have chosen to include research on the yielding of whiskers and the problem of misfit dislocation generation in strained epitaxial films in our discussion. A comparison can be made between these research areas and traditional BDT experiments because the state of stress generated in a homogeneously loaded whisker (or a strained epitaxial film) is comparable to that found at the tip of a crack. In fact, the information gained from the whisker experiments may prove more valuable because the results are free from the uncertainties introduced during the pre-cracking of samples and due to the difficulty in calculating the interaction of a crack tip stress field with dislocations.

Insight into the nature of the BDT can be found in early research conducted on whiskers. Pearson, Read, and Feldmann [6] conducted three-point bending tests on silicon whiskers grown

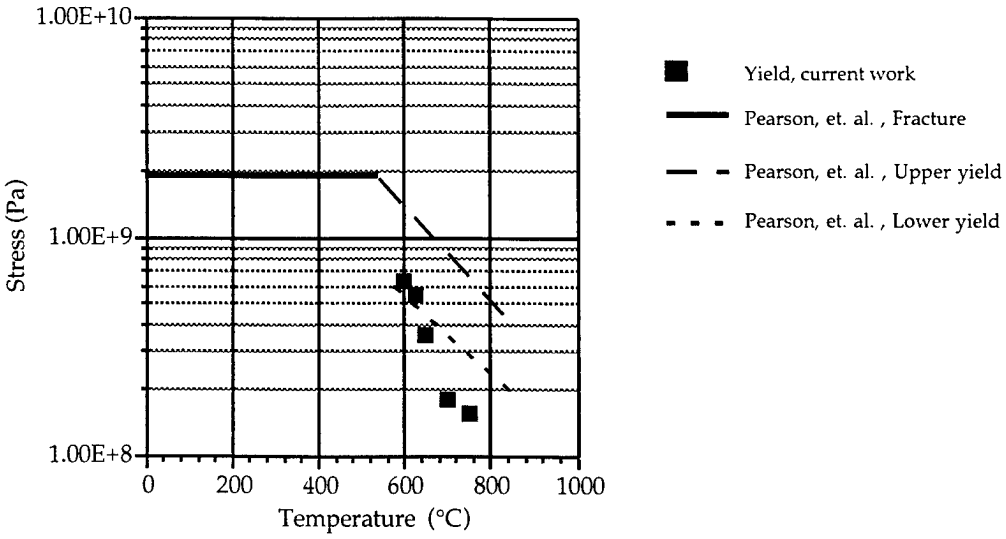


Figure 1: Fracture, yield stress of silicon whiskers and beams, silicon whisker data from Pearson, et. al. [6] .

from the vapor and small silicon rods cut from bulk silicon. Samples tested at room temperature were capable of enduring elastic strains up to 2.6 percent prior to fracture. The whiskers displayed this stress-strain behavior up to test temperatures as high as 600°C. However as the test temperature was increased above 600°C many samples displayed a distinct yield point followed by a load drop, after which the samples began to flow and deformed into a sharp vee-shape. Increasing the test temperature resulted in lower yield points. These results are presented schematically in Figure 1. Although comparable experiments were only carried out on the rods at room temperature and 800°C, the rods displayed characteristics similar to the whiskers. The maximum stress to fracture and to yield were lower in the rods, which may be attributable to surface defects introduced into the rods during their preparation. From these results, Pearson, et. al. are unable to explain the temperature dependence of the yield-point in silicon and concluded that even their smallest whiskers must contain many dislocation sources. Also shown in Figure 1 are preliminary results from our experiments on beams cut from semiconductor-grade silicon wafers. These samples were also tested in three-point bending. At this time only the high temperature experiments have been completed, however a trend similar to the whisker results is evident. Our measured yield points may be depressed relative to Pearson's data due to surface defects introduced during sample preparation. Further experiments will be carried out at lower temperatures and steps will be taken to minimize the effect of surface defects.

The results of Pearson, et. al. are further corroborated by research conducted contemporaneously by Brenner [7, 8]. Brenner conducted two studies on the mechanical properties of iron, silver, and copper whiskers using tensile tests. Although his reported experiments were only conducted at room temperature, his results are in qualitative agreement with the silicon results. The iron whiskers tested reached elastic strains between 3.6 and 4.8 percent prior to fracture. The tensile test results varied with sample size indicating a variation in sample quality. The experiments involving the silver and copper whiskers also displayed large elastic strains, however these samples yielded, followed by a substantial load drop. This load drop was as great as 80-to-1 for the copper whiskers as shown in Figure 2. In addition, the plastic deformation was confined to sharp slip bands in the whisker. Brenner found that if the sections containing slip bands were removed and the shorter whiskers reloaded, the whiskers achieved the same level of elastic strain before yielding again. Brenner ruled out dislocation locking as an explanation for the sharp yield points due to low impurity levels in the whiskers (<30 ppm in the silver whiskers) and due to the magnitude of the yield drop.

One of the earliest investigators to specifically study the nature of the BDT in silicon was St. John [9]. St. John studied the notch sensitivity of silicon through a series of plane-strain fracture experiments using tapered double-cantilever beam samples. Both the strain-rate and the test temperature were systematically varied during these experiments. Two significant results from St. John's work are the narrowness of the transition temperature range and the strain-rate dependence of the transition temperature; these results are shown in Figure 3. Using x-ray topography, St. John was able to demonstrate that the dislocation density in the silicon samples increased from nil to a level sufficient to arrest crack

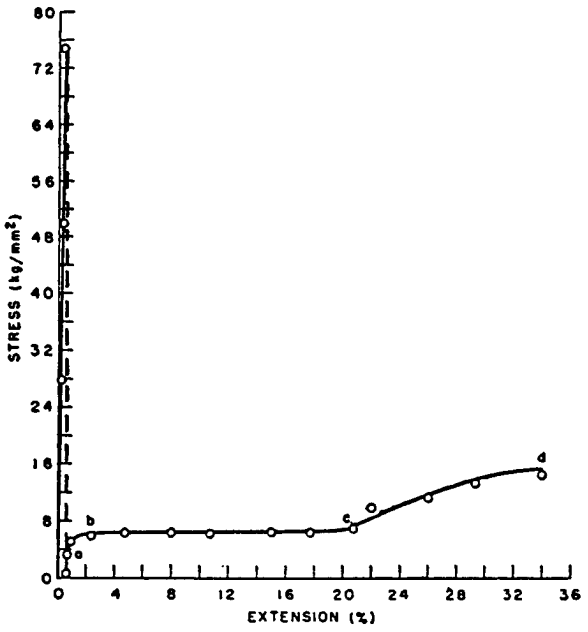


Figure 2: Stress-extension curve of a copper whisker, from Brenner [8].

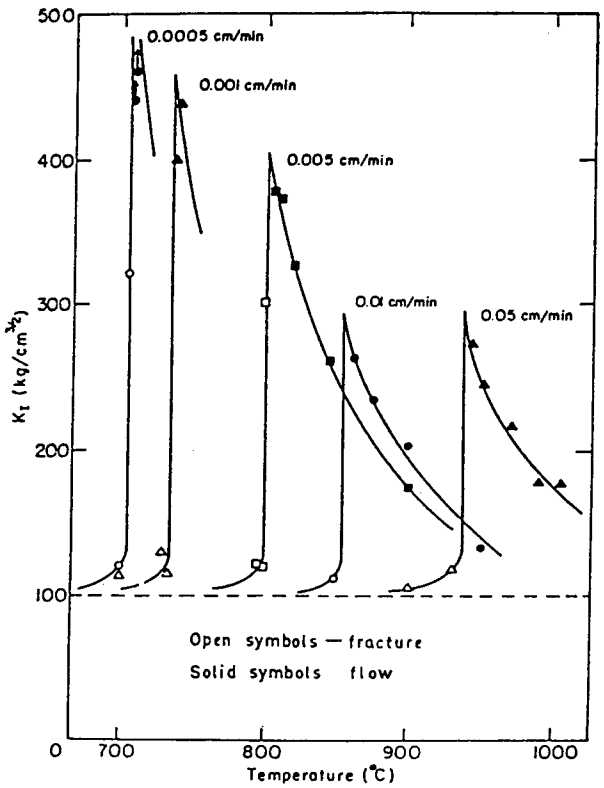


Figure 3: Strain-rate dependence of the BDT in silicon, from St. John [9]

propagation over a temperature range of approximately 5°C. The strain-rate dependence of the transition temperature led St. John to associate the BDT with the mobility of dislocations in the diamond cubic lattice. The experimental procedure of St. John was also used by Brede and Haasen [10] in their study of the BDT in silicon. They furthered this work by evaluating the effect of n-type dopant concentration on the dislocation velocity and the resulting transition temperature.

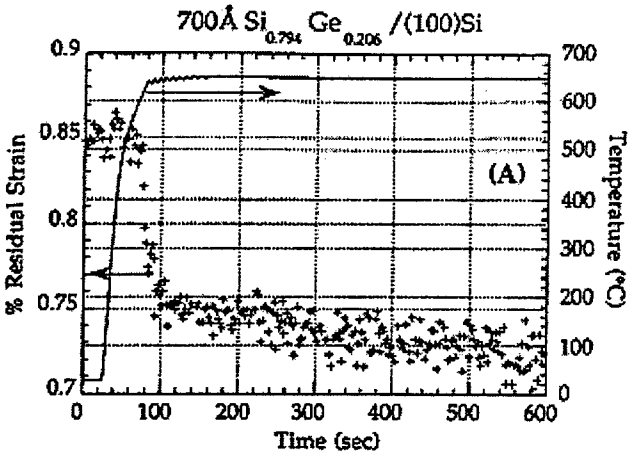


Figure 4: Strain relaxation during rapid thermal anneal, from Labovitz [12].

More recently, Samuels and Roberts [11] investigated the BDT by conducting four-point bending experiments on pre-cracked Si samples. In addition to strain-rate and test temperature, they also varied the dopant concentration of their samples. Their results concur with St. John's. Upon examination of the fracture surfaces of their samples, they note essentially no dislocation activity below the transition temperature and extensive dislocation activity just above it. Although the focus of their work is on the strain-rate dependence of the BDT they do comment that their results: "suggest that at T≈Tc a 'nucleation' event precedes the generation of avalanches of dislocations when $K \approx K_{Ic}$."

Further evidence of a sudden 'nucleation event' can be found in recent experiments on strained SiGe epitaxial layers [12]. These films were prepared in a manner that virtually eliminated heterogeneous dislocation sources. Here a crack tip is not present and the compressive biaxial state of stress in the film prohibits crack growth. However the composition of the Si/Ge overlayer is such that stresses in the GPa range and elastic strains up to 4.2% are produced in the film. To induce relaxation of the stresses, the films were heated at 300°C/min. Figure 4 is a plot of residual strain and temperature versus time. Here it can be seen that a sudden relaxation occurs between 500 and 550°C. This relaxation event reduces the elastic strain by 20 percent. Not only were a large number of dislocations nucleated very rapidly, but the nucleation event also appears to have occurred homogeneously. The initial dislocation densities necessary to carry the plastic strain rate is in the range of $10^{11}/cm^2$.

Discussion and Conclusions

If the experimental results described above are looked at collectively, several features of the BDT become apparent. The most obvious feature of the BDT is that it is a sharp transition; the failure mode in silicon can change from brittle fracture to massive shear within a temperature range as small as 5°C. For silicon, this precludes thermal activation of dislocation sources. If the dislocation sources were thermally activated one would expect to see a gradual change in fracture mode as indicated by the Arrhenius type equation used to describe the nucleation rate. In addition, the mechanism governing the BDT must be capable of generating a sufficient density of dislocations to accommodate massive plasticity of the sample without preexisting dislocation sources. The large number of dislocations nucleated at the onset of plasticity is also indicated by the significant load drops displayed by the copper, silver, and silicon whiskers upon yielding. It is not clear in the Rice-Thomson model how dislocation nucleation could suddenly be activated over such a small temperature interval nor is it clear how the model would explain the onset of plasticity in the materials that did not contain cracks or other suitable stress concentrators. In the Hirsch-Roberts model, the nucleation event is not treated explicitly, it is simply assumed to occur. Nucleation is only discussed in the context of how dislocation velocity may influence the rate of nucleation. Although the mobility of nucleated dislocations is an important aspect of any model of dislocation processes, a source for the dislocations must be identified first. We propose that the KPV model may provide an explanation for the nucleation event in all materials that have been studied thus far. An advantage to this approach is that it provides a solution that is not dependent on the specifics of the loading conditions or on the method of sample preparation, i.e. pre-cracked or not.

A second characteristic of the BDT is its apparent strain-rate dependence. Any model that deals solely with the issue of nucleation will not adequately describe the BDT. Presently none of the nucleation based models, including the KPV model presented here, address dislocation dynamics. The Hirsch-Roberts model

provides a description of the strain-rate dependence of the BDT that does agree well with the experimental results from the silicon studies. However this model requires preexisting dislocation sources and knowledge of their geometric relation to the crack tip. These factors may limit its applicability to other material systems and arbitrary loading situations. Our future work will involve incorporating dislocation dynamics into the KPV model. In addition the effect of preexisting dislocation sources will be evaluated.

Acknowledgments

We would like to acknowledge Dr. Khantha of the University of Pennsylvania for many discussions on the KPV theory. This research was supported by the U.S. Air Force Office of Scientific Research grant 95-1-0143.

References

1. J.R. Rice and R. Thomson, "Ductile Versus Brittle Behavior of Crystals," Philos. Mag., 29 (1974), 73-97.

2. J.R. Rice, "Dislocation Nucleation From a Crack Tip: An Analysis Based on the Peierls Concept," J. Mech. Phys. Solids, 40(2)(1992), 239-271.

3. J.R. Rice and G.E. Beltz, "The Activation Energy for Dislocation Nucleation at a Crack," J. Mech. Phys. Solids, 42(2)(1994), 333-360.

4. P.B. Hirsch, S.G. Roberts and J. Samuels, "The Brittle-Ductile Transition in Silicon. II. Interpretation," Proc. R. Soc. Lond. 421A(1989), 25-53.

5. P.B. Hirsch and S.G. Roberts, "The Brittle-Ductile Transition in Silicon," Philos. Mag. A, 64(1)(1991), 55-80.

6. G.L. Pearson, W.T. Read Jr. And W.L. Feldmann, "Deformation and Fracture of Small Silicon Crystals," Acta Metall., 5(April)(1957), 181-191.

7. S.S. Brenner, "Tensile Strength of Whiskers," Journal of Applied Physics, 27(12)(1956), 1484-1491.

8. S.S. Brenner, "Plastic Deformation of Copper and Silver Whiskers," Journal of Applied Physics, 28(9)(1957), 1023-1026.

9. C. St. John, "The Brittle-to-Ductile Transition in Pre-Cleaved Silicon Single Crystals," Philos. Mag., 1193-1212.

10. M. Brede and P. Haasen, "The Brittle-to-Ductile Transition in Doped Silicon as a Model Substance," Acta Metall., 36(8)(1988), 2003-2018.

11. J. Samuels and S.G. Roberts, "The Brittle-Ductile Transition in Silicon. I. Experiments," Proc. R. Soc. Lond., 421A(1989), 1-23.

12. S.M. Labovitz, "Dislocation Nucleation in Strained Epitaxial Layers" (Ph.D. Thesis, University of Pennsylvania, 1996).

13. M. Khantha and V. Vitek, "Mechanism of Yielding in Dislocation-Free Crystals at Finite Temperatures: I. Theory" Acta Metall. (In press).

14. M. Khantha, D.P. Pope and V. Vitek, "Mechanism of Yielding in Dislocation-Free Crystals at Finite Temperatures: II. Applications to the Deformation of Whiskers and the Brittle-to-Ductile Transition" Acta Metall., (In press).

15. M. Khantha, D.P. Pope and V. Vitek, "Dislocation Screening and the Brittle-to-Ductile Transition: A Kosterlitz-Thouless Type Instability," Physical Review Letters, 73(5)(1994), 684-687.

16. M. Khantha, D.P. Pope and V. Vitek, "The Brittle-to-Ductile Transition I: A Cooperative Dislocation Generation Instability," Scripta Metall. et Mat., 31(10)(1994), 1349-1354.

ATOMISTIC SIMULATIONS OF FRACTURE

Diana Farkas
Virginia Polytechnic Institute and State University
Department of Materials Science and Engineering
Blacksburg, VA 24061

Abstract

Embedded atom interaction potentials are used to simulate the atomistic aspects of the fracture process. Simulations are presented for the behavior of cracks in pure metals and intermetallics, near the Griffith condition. The materials considered include Fe, Cu, Ni as well as Fe, Ni, Co, and Ti aluminides. The work focuses on the comparative study of fracture behavior in the different materials. The role of the atomic relaxation at the crack tip and of lattice trapping phenomena is analyzed.

George R. Irwin Symposium on Cleavage Fracture
Edited by Kwai S. Chan
The Minerals, Metals & Materials Society, 1997

ATOMISTIC STUDY OF THREE-DIMENSIONAL FRACTURE AND DEFORMATION:

S. J. Zhou
D. M. Beazley
P. S. Lomdahl
B. L. Holian
D. Preston
Los Alamos National Laboratory
Applied Theoretical Division and Theoretical Division
Los Alamos, NM 87545

Abstract

Fracture behavior of metals and intermetallics is closely related to cracks, dislocations, and their interactions. However, cracks and dislocations are intrinsically three-dimensional (3D) defects and their core regions must be characterized with atomistic simulations. With the advance of computer power, the full dynamical and atomistic nature of this problem can be revealed. In this talk, we will report two studies in a f.c.c. single crystal with 3D molecular dynamics simulations with up to 35 million atoms: (1) 3D fracture and (2) intersection of two dislocations. We observed a variety of dislocation emission modes in a sample that was sufficiently thick that we could be sure that the results did not depend on the thickness. The sequence of dislocation emission in the crack blunting process strongly depends on the crystallographic orientation of the crack front and differs strikingly from anything previously conjectured. This finding is essential to make more quantitative an intrinsic ductility (i.e., dislocation emission) criterion. More detailed results on this ongoing work will be reported in the meeting.

George R. Irwin Symposium on Cleavage Fracture
Edited by Kwai S. Chan
The Minerals, Metals & Materials Society, 1997

EFFECT OF IMPURITIES ON CLEAVAGE FRACTURE: H, C, B, AND S IN Ni_3Al:

Nicholas Kioussis
G. Lu
California State University Northridge
Department of Physics
Northridge, CA 91330-8268,*

M. Ciftan
US Army Research Office
Research Triangle Park, NC 27709

A. Gonis
Lawrence Livermore National Laboratory
Livermore, CA 94550

Abstract

The Ll_2 intermetallic Ni_3Al exhibits unique mechanical properties that make it attractive for high temperature structural applications. Understanding the origins in the electronic structure of the impurity-induced strengthening or impurity-induced environmental embrittlement in Ni_3Al is of practical importance. The effects of hydrogen, carbon, boron, and sulfur impurities on the ideal cleavage fracture properties of Ni_3Al under tensile stress are investigated using total-energy full-potential electronic structure calculations with a repeated slab arrangement of atoms simulating an isolated cleavage plane. Results for the stress-strain relationship, cleavage energies, ideal yield stress and strains with and without impurities are presented, and the electronic mechanism underlying the contrasting effects of impurities on the ideal cleavage of Ni_3Al is elucidated. *Supported by US Army Research under contract No. DAAH04-93-G-0427.

George R. Irwin Symposium on Cleavage Fracture
Edited by Kwai S. Chan
The Minerals, Metals & Materials Society, 1997

MICROMECHANICAL AND MICROSTRUCTURAL MODELING

RECENT ADVANCES IN THE MICRO-MODELLING OF CLEAVAGE FRACTURE IN STEEL

John F. Knott

School of Metallurgy and Materials
The University of Birmingham

Abstract

The paper covers two aspects of the modelling of cleavage fracture in steels. The first relates to events at the microstructural scale, where fracture initiators are smaller than 10μm (usually, smaller than 5μm) in size. Here, the discussion focuses on the ways in which the local cleavage fracture stress depends on microstructure. Attention is drawn to behaviour in weld metals, where initiation sites can be clearly identified on fracture surfaces. The relation of local fracture stress to fracture toughness relies on the identification of a "critical distance" and the uniqueness of this "distance" when dealing with cleavage following warm prestressing, or cleavage ahead of a growing fibrous crack, is questioned. Comparisons are made with the so-called "local approach" which is statistically based. The second aspect covers events at the meso-scale: specifically, the ways in which fracture toughness results should be analysed, when the microstructure comprises a two-phase mixture of tough and brittle areas, of order 50-200μm in size. The traditional Weibull approach is challenged, because it does not represent physical reality and because it produces ultra-pessimistic lower-bound values. The re-examination of the Weibull approach has implications with respect to micro-scale modelling.

Introduction

The quantitative relationship of plane strain fracture toughness, K_{IC}, to features of a material's microstructure and to the micro-mechanisms of fracture has developed, over the last thirty years, in a number of steps. The critical local tensile fracture stress, σ_F, for transgranular cleavage fracture, in *blunt-notched* bars was established by Knott (1): here, the critical microstructural fracture was identified as the ferrite grain size. Following the work of McMahon and Cohen (2), Smith (3) developed a theory of cleavage fracture which incorporated both the length of a dislocation pile-up (grain-size) and the thickness of grain-boundary carbides. The elastic/plastic analysis of Knott's notched bars, using finite element techniques, was published by Griffiths and Owen (4). This clarified the distribution of stresses in the plastic zone, but the assumption still had to be made that σ_F was equal to the maximum value of tensile stress in the zone, i.e. that the fracture-initiating nucleus was located at the position of maximum tensile stress.

In 1972, Ritchie, Knott and Rice (5) employed similar concepts to predict the variation of K_{IC} with temperature, from known values of σ_F and yield stress, σ_Y, which is a function of temperature, T: σ_Y decreases as T increases, and the size of the plastic zone has to increase with temperature to ensure that sufficient tensile stress is available to propagate a microcrack. This is the RKR model. The dimensions of σ_F (stress) and K_{IC} (stress $\sqrt{}$length) are such that any relationship between them must involve a length: in the RKR model, this is the *critical distance* X. The RKR results suggested a value of X very close to two grain diameters, but no especial significance is to be attached to this particular value, because subsequent work by Curry and Knott (6) demonstrated that X was not a unique function of grain size, and that fracture behaviour was related to the thicknesses of grain-boundary carbides. The final reconciliation between the "grain-size" microstructural feature and the "carbide-thickness" microstructural feature was made by demonstrating that, for as-cooled microstructures, there was a monotonic relationship between carbide thickness and grain size, since both were controlled by common diffusion processes, Curry and Knott (7).

Curry and Knott (8) proceeded to study cleavage fracture in spheroidised carbide microstructures and were able to define X in terms of a *statistically-averaged distance*. A *microstructure* could be characterised in terms of the histogram of number density (per unit volume, or per unit area in 2-D) of carbides as a function of carbide

George R. Irwin Symposium on Cleavage Fracture
Edited by Kwai S. Chan
The Minerals, Metals & Materials Society, 1997

radius. The local value of σ_F (as determined in notched bars) was calculated for each radius in the histogram. Reference was then made to the tensile stress distribution in the process zone ahead of a crack loaded to a given stress-intensity factor, K, and the stress "available" at a given position r, θ was compared with the probability that, at this position, there would be a carbide of radius sufficiently large for a newly-initiated (penny-shaped) microcrack to propagate at this level of local stress. If this were not the case for all values of r, θ for a given applied K, the value of K would have to be increased until the condition *was* met (at $K = K_{IC}$). Any statistical variation in K_{IC} (scatter) could then be related to the distribution of carbide sizes. For the spheroidised steels studied (small specimens, fully austenitised, uniformly quenched and fully tempered) such a distribution is smooth and continuous (uni-modal) and there is a high probability that a "typically coarse" (say, 95th percentile) carbide will be found *consistently* in an equivalent σ (r, θ) position for a given applied K value, so that scatter should be small. This conclusion is supported also for other fine-scale, *quasi-homogeneous* microstructures, as described later.

An alternative, statistical treatment (Beremin) was described by Pineau (9). Here, a number of cylindrically notched testpieces (for which elastic/plastic stress analyses are available) are fractured and the (nominal) fracture stresses are assigned to a Weibull distribution. Stress distributions around a crack tip at a given K-level are analysed and the probability that the stress at a given r, θ position in the plastic zone exceeds the "Weibull stress" (measured in the notched bars) is assessed. The *maximum local stress* in a cylindrically notched testpiece is a monotonic function of applied stress and could be used in a similar manner: this would then be equivalent to the original RKR model. The concept of a "critical distance" is still necessary, to reconcile the dimensions of stress and fracture toughness, and is, in one example, of order 0.25mm (in the original RKR, using σ_{max}, X = 0.12mm). In a sense, the Beremin modelling of K_{IC} is statistically based, since it relies on the "Weibull stress" treatment for applied fracture stress (or even, local (maximum) fracture stress). It does not, however, relate such variation to microstructural features, such as carbide distributions. Recent work by Cardinal at Birmingham demonstrates that the Beremin "statistically-based distance parameter" has no more detailed, microstructural significance than that of the RKR model.

Over the last fifteen years or so, significant advances have been made in terms of relating, (for cleavage fractures) local fracture stress and fracture toughness to microstructural features. The first main area is that of weld metals, in which it is found that non-metallic inclusions (deoxidation products) are of great importance, and in which the concept of "critical distance" can be tested directly. The second is that of mixed (tough: brittle) microstructures, in which the spatial distribution of the more brittle component is highly significant. Here, there is particular interest in choosing appropriate macroscopic statistical distributions to represent material properties faithfully, so that extrapolations to "lower bounds" (say 10^{-3} probability) from limited data-sets, can be made sensibly. Blind adherence to Weibull-distribution fits can prove to be ultra-pessimistic.

Cleavage Fracture In Ferritic Steel Weld-Metals

The microstructures of common (C-Mn) weld metals are generally quite complex, incorporating both ferrite/carbide mixtures and a distribution of non-metallic inclusions, such as oxides or silicates, which form as solid deoxidation products in the molten weld pool. The typical, as-deposited, ferrite/carbide morphology comprises grain-boundary ferrite, which is carbide-free, perhaps ferrite "sideplates" (akin to upper bainite morphologies), and "acicular" ferrite, which nucleates independently within grains, at the interfaces between the non-metallic inclusions and the matrix (which is, of course, austenite, before transformation). The acicular ferrite adopts a crystallographic, "basket-weave" morphology, which is often on a fine-scale, imparting high strength (because the effective grain-size is small) and good toughness, because microcracks find it difficult to propagate through acicular ferrite boundaries. The carbon contents of the weld metal are low (<0.1%; often <0.05%) so that the carbides are generally much thinner than they are in (as-rolled or normalised) parent-plate, section or tube. Reheating into the intercritical (α + γ) region (e.g in a multi-pass weld) may permit partition of carbon into the γ-phase, so that high-carbon "patches" or "islands" can be produced, which can subsequently transform to high-carbon MAC (Martensite, {retained} Austenite, Carbide) products; possibly outlining prior austenite grain-boundaries.

Generally, however, it is found that the sizes of inclusions are significantly greater than those of carbides or MAC and the pioneering work of Tweed (10) showed that the inclusions in low-carbon weld metals provided the sites on which "virulent" micro-cracks could be nucleated. In notched bars, it was possible to measure values of σ_F at the site of an inclusion and to relate these to the radius, c of the (penny-shaped) microcrack nucleus, in terms of the "local" Griffith criterion:

$$\sigma_F = \{\pi E \gamma_p / 2(1-\nu^2)c\}^{1/2} \qquad 1)$$

where E is Young's modulus, ν is Poissons ratio and γp is the effective work of fracture.

Using data generated by Tweed and by McRobie (11), it is possible to demonstrate that the $c^{-1/2}$ relationship is followed, and that the appropriate value of γp is some 9-14 Jm^{-2}, as found by Curry for spheroidised carbide microstructures. An interpretation of this value, in terms of local micro-crack-tip fracture mechanisms, has been given by Knott (12) and relates to the local stiffness of the array of atoms in the crack-tip region. The macroscopic value, K_{1c}, is a measure of all the plastic work that is done in the "process zone" ahead of the macro-crack tip as a necessary *precursor* to setting up the critical condition for nucleating and propagating the micro-crack. The results of detailed studies by Tweed, McRobie, Reed (13) and Bose (14) - well over a hundred observations in total - have shown that the critical nuclei in notched-bars are situated right at, or nearer to the notch-root than, the elastic/plastic boundary. This is consistent with the requirement for: a) slip to nucleate the microcrack by exerting very high local stresses (from dislocation "pile-ups", or other arrays) on the inclusion; b) sufficient tensile stress to be present to propagate the microcrack as soon as it nucleates.

McRobie also made measurements of the temperature-dependence of σ_F and showed that, when account was taken of a variation of size of the initiating inclusion, any temperature-dependence was weak. This implies that the local "γp" in equation 1) is sensibly independent of temperature, which adds support to a very local micro-crack tip separation mechanism, involving atomic reorganisation ("shuffling"), occurring at stresses of order $\mu/10$, which are so high that thermal fluctuations (at sub-zero temperatures) can have no significant effect. At this stage, the situation with respect to inclusion-initiated fracture in weld metals is similar to that treated by Curry and Knott (8) for spheroidised carbide microstructures. For "intrinsic" inclusion distributions, which are produced as a result of deoxidation processes in the weld pool, it is reasonable to anticipate a smooth, "well-behaved" inclusion size distribution: typical, experimental data indicate that the 95th percentile of "significant" inclusions is of order 2-2.5μm. From this distribution, it should be possible to predict the K_{1c} probabilistic distribution, given a (statistically-based) "critical distance", X.

It is important to be aware of the possible existence of "outliers" to the distribution, given by the presence of "rogue" or "exogenous" inclusions arising from sources other than the deoxidation processes. In Tweed's original work (10), it was found that some fractures initiated from inclusions of sizes (between 5μm and 12μm) which clearly lay outside the "well-behaved" distribution and which also *possessed a different chemistry*. Specifically, they were found to contain the elements Ca and K, which were not included as deoxidants in the weld. They were, however, present in the compounds used to bind the electrode coating to the mild steel core and it appears that particles containing these elements simply dropped into the weld pool. Awareness of, and close attention to control of, such effects led to the production of weld deposits of consistently better toughness properties.

Table I Comparison of Measured Values of Critical Distance, X, with RKR Predictions (after (11))

Test Temperature °C	Yield Strength MPa	K_Q $MPam^{0.5}$	X (observed) μm	X(RKR) μm
-173	650	44	34	188
-150	585	49	56	220
-120	505	55	57	217
-100	460	63	190	204

Inclusion Distribution: Mean Diameter 1.17μm standard deviation 0.54μm 95th percentile 2.25μm

Observations: -173°C 1.4μm; -150°C, 3μm; -120°C, 1.4μm; - 100°C 2.1μm

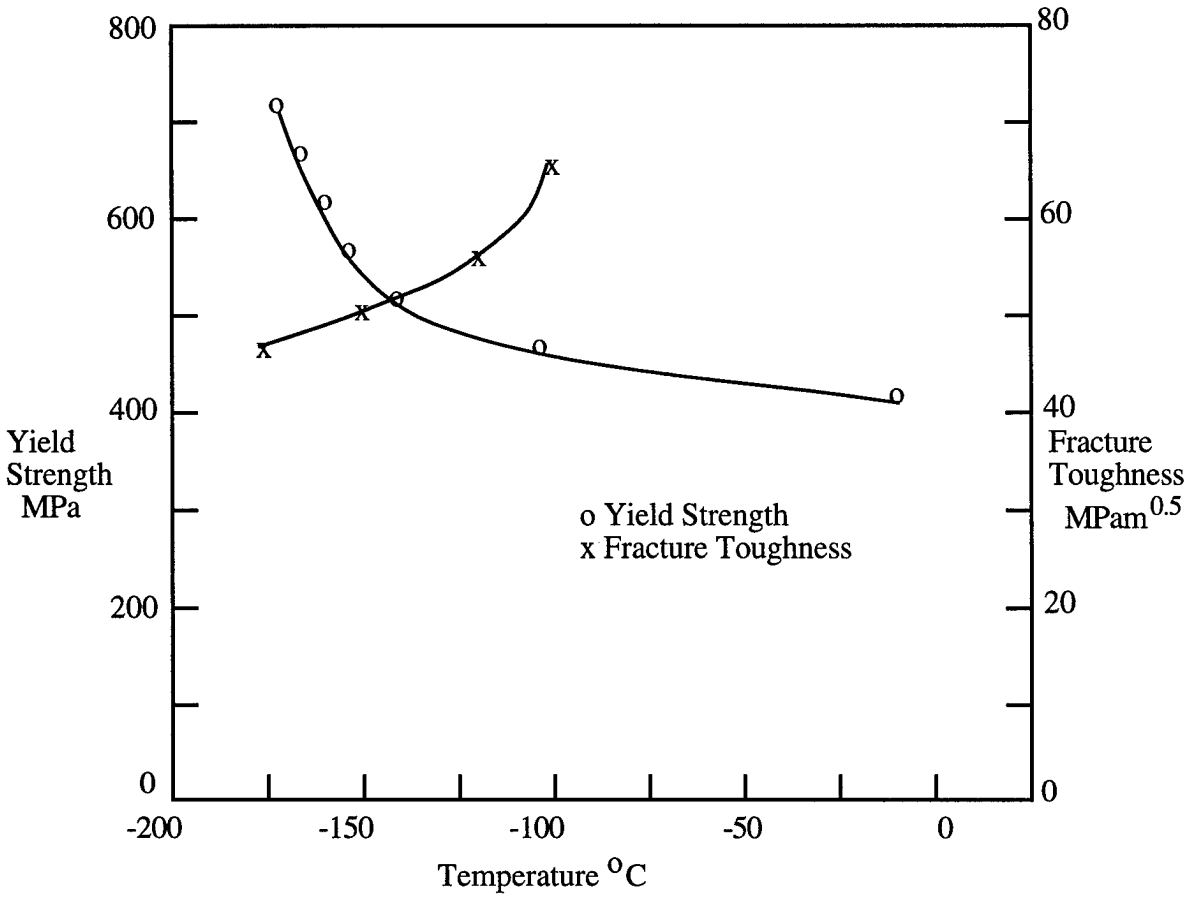


Figure 1. Variation of Yield Strength and Fracture Toughness with Temperature for C/Mn Weld Metal (after Dr D E McRobie ref. 11)

The next step taken by McRobie was to calculate a "critical distance" from a comparison of σ_F and K_{1c} (for a "well-behaved" inclusion distribution) and then to locate the position of the fracture-initiating inclusion in a fracture-toughness testpiece, to obtain an experimental value for the distance. The results of the comparison are given in Table 1, from which it is clear that agreement is poor, except at the highest test temperature, where agreement (within experimental errors) is good. It must be borne in mind that all fatigue precracking was carried out at room temperature, where the yield stress is 400 MPa. If the maximum value of K during precracking was, for example, 31 MPam$^{1/2}$ at room temperature, corresponding to $K = 0.63\sigma_Y B^{1/2}$, (BS 5762), with B = 15mm, this would produce a plastic zone size at -173°C equivalent to a K-value of 50 MPam$^{1/2}$ (since $r_Y \propto (K/\sigma_Y)^2$). The possibility of a significant "warm-prestressing" (WPS) effect exists and, as is reported below, such an effect can radically *alter* the "critical distance".

The effects of WPS have been studied in A508 weld metal by Reed (13, 15). Here, the matrix microstructure is effectively quenched-and-tempered, so that the ferrite grain-size is small. This makes it somewhat more difficult to locate the major fracture-initiation site by tracing-back river-lines, but Reed's careful work demonstrated again that cleavage fracture was initiated from non-metallic inclusions (at σ_F values of approx. 1800 MPa). Warm prestressing involves loading a pre-cracked testpiece at a high temperature (*above* the transition temperature) to a load greater than the observed, low-temperature, fracture-load, followed by cooling directly to the low temperature and then loading to failure (LCF cycle) or by unloading, cooling to low temperature, and then re-loading to failure (LUCF cycle).

In both cases, there is an increase in the low-temperature fracture load. For the LCF cycle, it is necessary to exceed the pre-load (to initiate a new, virulent microcrack at low temperature): for the LUCF cycle, the subsequent low-temperature load is increased above its initial value, but not to such a large extent. The enhancement of fracture load/fracture toughness can be attributed to the compressive residual stress distribution generated during the prestressing and unloading sequence. Further

evidence is given by studies made on bars containing blunt notches, for which a prestrain with the notch in compression generates *residual tension* on unloading: this gives rise to a *reduction* in the subsequent low-temperature fracture load. It is possible to obtain a positive WPS effect for a (tensile) pre-load smaller than the non-WPS fracture load at low temperature, provided that the pre-stress plastic-zone size is larger than that associated with non-WPS fracture at low temperature.

A second, most important observation is that, whereas the fracture initiation sites for non WPS fractures correspond to the largest inclusions (in a "well-behaved" distribution) the initiation sites for WPS fractures are associated with inclusions of a size closer to the mean of the size distribution see (Table II) and large inclusions are observed to have voids around them. It is deduced that, during the pre-stressing treatment, the inclusion/matrix interfaces for large inclusions are decohered at low strain, so that the inclusions are rendered "benign" (non-virulent) with respect to subsequent cleavage fracture (since a micro-crack needs to run at speed through the inclusion and continue dynamically into the ferrite matrix through a well-bonded interface). This may be because the larger inclusions have a duplex character: possibly an oxide/silicate core surrounded by a sulphide "shell" (produced by sulphide precipitation on inclusions as the weld cools through the austenite region). Subtle effects of inclusion interface chemistry and the relative thermal expansions of inclusion and matrix need to be considered.

Whatever the precise details of decohering during prestressing, it is clear from Table II that a *different inclusion distribution* is responsible for cleavage fracture after WPS than that associated with fracture in the non WPS condition. It follows that the *statistically-determined critical distance* must also be different. This is at variance with the assumption made by Beremin/ Pineau (1981). Although low-temperature fracture loads are higher, because both compressive residual stresses have been generated and large inclusions have been rendered "benign", it may be deduced that the "critical distance" will *decrease*, because there are many more inclusions of size closer to the mean (of "significant" inclusions) than at the 95th percentile. If, therefore, the fatigue-precracking procedures used by McRobie to obtain the results given in Table I did, indeed, introduce a measure of a WPS effect, it is not surprising that the observed value of critical distance was significantly lower than that predicted.

An even more dramatic example of a change in the "critical distance" is given by considering the conditions leading to the onset of cleavage fracture ahead of a fibrous fracture (at temperatures towards the top end of the ductile/brittle transition). Such a change in fracture mechanism can occur because the fibrous crack accelerates as increasing load is applied to a testpiece, and the local maximum tensile stress ahead of the accelerating crack tip increases, as a result of the dynamic elevation of the yield stress. Suppose that the material is a typical low-carbon steel, with a microstructure of ferrite and grain-boundary carbide. At a low temperature, of say -140°C, the fracture toughness value might typically be $50MPam^{1/2}$ with a yield stress of 500MPa. The CTOD at fracture, δ_c is given by:

$$\delta_c = K_{1c}^2 / 2\sigma_Y E \qquad \text{.....2)}$$

Table II Effect of Warm Prestressing on Inclusion-Initiated Cleavage Fracture (after ref. 13)

	General Inclusion Population	Non-WPS Fracture-initiating inclusions	WPS Fracture initiating inclusions
Population size	295	23	28
Mean Inclusion Diameter	0.89μm	1.53μm	0.94μm
Standard Deviation	0.48μm	0.75μm	0.52μm
Confidence intervals (95% confidence limits)	0.83-0.94μm	1.23-1.84μm	0.74-1.13μm

With E = 200GPa, δ_c is approx. 12.5μm. The peak of the stress distribution ahead of the blunted crack tip is at 1.9δ (approx. 25μm) but the RKR model focuses attention on a region extending up to typically, 8δ *ahead* of this position. The linear dimension of the process zone size is therefore some 2-10δ = 25 - 125μm and the plastic strains within this zone are small. In contrast, the value of δ_i for a low carbon steel is likely to be at least 0.25mm, so that the linear dimension of any process zone relevant to cleavage is 500-2500μm and the strains within this zone approach 100% at the blunted crack tip and are approx. 25% at 500μm ahead of the tip (16). Any carbide microcrack produced at near yield-point strain will have blunted to an extent such that it can no longer operate as a cleavage micro-crack nucleus and any micro-crack nuclei have to be *newly-formed*, in a conceptually different set of particles, with a different, statistically averaged, "critical distance". The situation is illustrated in fig. 2.

The situation in weld-metals illustrates this change in "critical distance" with clarity. Work by Yunquan Zhang in low-carbon, C/Mn weld-metal, demonstrates that, *at low temperature*, cleavage fracture is nucleated by inclusions (of size corresponding to the top end of a "well behaved" distribution). For cleavage fracture ahead of a growing fibrous, however, *all* inclusions have been rendered "benign" by the high strains and it is then necessary to nucleate fracture from other particles, such as carbides or MAC product. An example of such nucleation ahead of a growing fibrous fracture is given in fig. 3. It is clear that the "critical distance" associated with fracture at -100°C does not equate to that ahead of a fibrous fracture, and that any statistical analysis needs to be re-addressed.

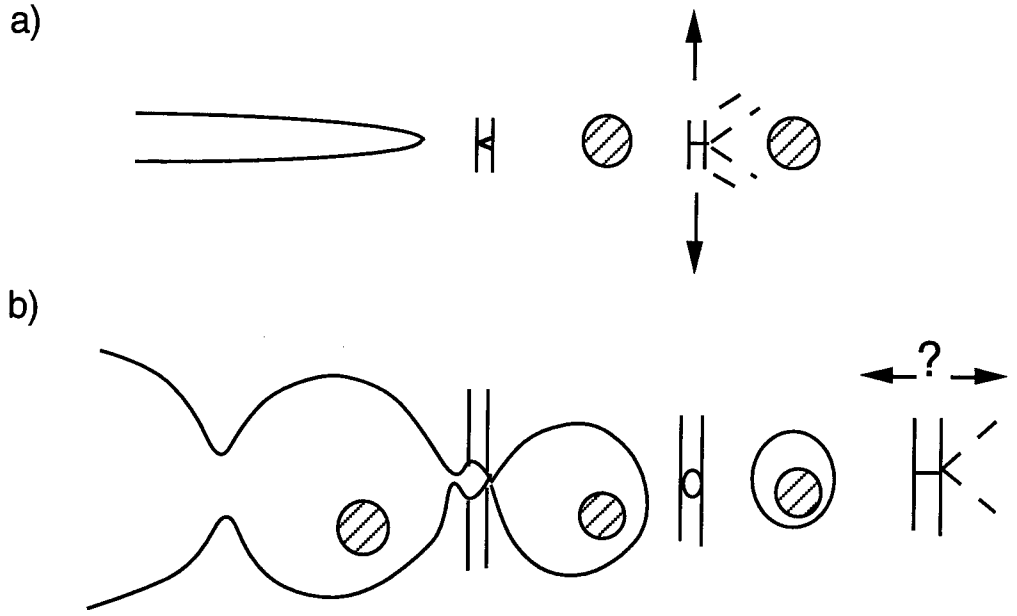


Figure 2. Initiation of Cleavage Fracture in Wrought Steel containing Inclusions:

a) At low temperature, where the macro-scale fatigue-crack is only slightly blunted and no significant voids have formed round the inclusions: crack nuclei are formed in carbides at low strain.

b) Cleavage crack nucleation ahead of a growing fibrous crack. Micro-crack nuclei near the macro-crack tip have blunted-out due to the high local strains, so any critical distance must change.

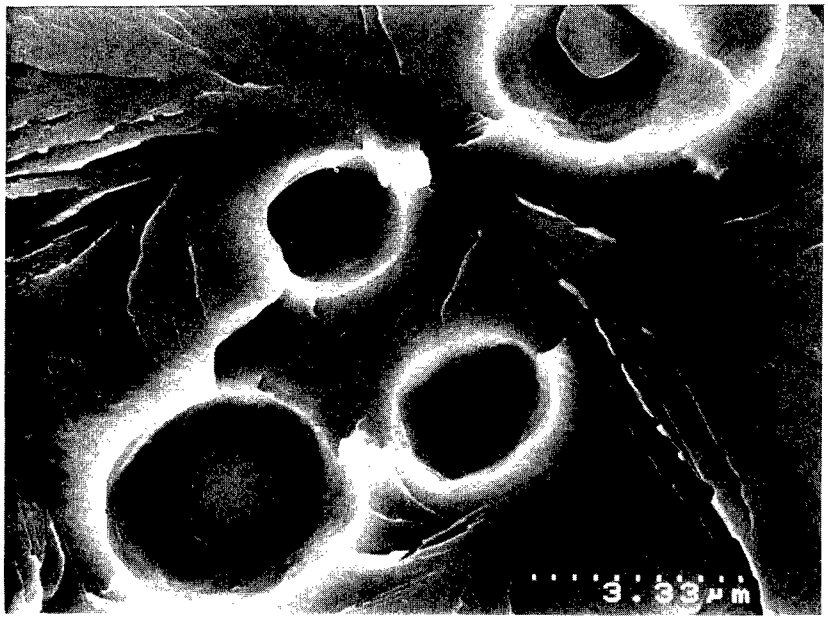


Figure 3. Initiation of Cleavage Fracture ahead of a Growing Fibrous Crack in C/Mn Weld Metal (courtesy Dr Y Zhang). Note that: whereas at low temperatures, cleavage fracture is nucleated on the (brittle) inclusions); ahead of the growing fibrous crack, voids have formed around the inclusions and cleavage is nucleated (probably on MAC products) *between* inclusions. See also Figure 2.

Cleavage Fracture in Quasi-Homogeneous and Inhomogeneous Microstructures

The previous sections have concentrated on cleavage fracture nucleated on inclusions or on carbide particles, often deliberately coarsened to make observation easier. The work of Bowen (17) has demonstrated that, in A533B nuclear pressure vessel steel (0.25 C) in the as-quenched (auto-tempered) martensitic condition, the microstructural factor controlling cleavage fracture at low temperatures is the thickness of inter-lath carbides. These are of fine size (thickness <30 nm) and are closely spaced (lath widths some 2-3 μm in size) so that the spatial density in any given area is high. It is of interest to compare these figures with the dimensions of a notional process zone ahead of a (blunted) crack tip loaded to a stress-intensity factor equal to the material's fracture toughness, K_{1c}, and to try to deduce the resulting degree of predicted scatter in K_{1c} values.

Following the general concepts of the RKR model, the area of interest is that immediately beyond the stress (σ_{max}/σ_Y) intensification maximum, which is located at 1.9δ (CTOD) ahead of the crack tip. If ±2% is allowed on the value of (σ_{max}/σ_Y) at a nominal value of 3.0, i.e. a range from 3.06 to 2.94, the corresponding linear spread in distance, ΔX, is $0.003\ (K_{1c}/\sigma_Y)^2$. For Bowen's steel at -120°C, K_{1c} was 51.4 $MPam^{1/2}$ and σ_Y was 1340 MPa, giving a value for ΔX of 4.4μm. The area subjected to quasi-constant (±2%) maximum stress is then of order $20\mu m^2$, compared with the microstructural unit size (in 2-D) of approx. $6\mu m^2$. Thus, approx. 3 units are sampled by the quasi-constant stress in 2D, and the sampling is increased if consideration is given to further neighbouring units in the thickness direction. Throughout a total thickness of, say 10 mm, some 4000 units are sampled. At the 95th percentile of carbide thickness, approx. 200 carbides will experience quasi-constant stress, The argument is that, at a given K-value, the thickest carbide fractures, but, almost instantaneously, the next thickest fractures and an "avalanche" of micro-cracking occurs at a "constant" K (corresponding to ±2% on local stress). For the quasi-homogeneous microstructure, the fracture toughness distribution is predicted to be essentially single-valued.

A convenient way to visualise probability distributions is to make use of "normal" probability paper. The predicted single-valued function (as a "probability density function" pdf) would plot as a single "spike" or delta

function: as a "cumulative distribution" CDF (the integral of the pdf) it would plot as a step function, i.e. no failures below a critical value of K_{1c}; 100% failures above the critical value. These functions do not take account of random error. The *central limit theorem* predicts that the delta-function pdf is modified by random errors to become a Gaussian (normal) distribution: the CDF step-function is modified to become an error function (erf). In linear co-ordinates, the error function is a symmetrical, sigmoidal curve, but, since it has a defined algebraic form, the ordinate can be scaled accordingly, such that the sigmoidal curve plots as a straight line. This scaling produces "normal" probability paper, with spacing about the 50% mark scaled in a Gaussian manner. The standard deviation (s.d) is directly observable as the spread on the abscissa corresponding to values which are 34% either side of the mean (i.e. either 16% or 84%).

To test for quasi-homogeneous behaviour in a test material, it is first necessary to set appropriate limits to the s.d corresponding to the random errors associated with a fracture-toughness test. The work of Neville (16) claimed errors of order ±2%, but these were associated with tests carried out with high precision on specimens machined with great care. More generally, one might expect errors of fixed values, rather than as percentages. A "pragmatic" value of ±2MPam$^{1/2}$ (for one s.d) is suggested: this is, of course, ±2% of a K_{1c} value of 100MPam$^{1/2}$, but assumes a higher percentage for lower values. The proposal is that if the CDF for cleavage fracture-toughness values plots as a single, straight line on normal probability paper, with a s.d of no more than 2MPam$^{1/2}$, the material is deemed to be "quasi-homogeneous".

Given this definition, it is possible to test different databases, starting with fine-scale microstructures similar in nature to that in Bowen's A533B steel. Figure 4 shows results for 300M forging steel (courtesy Dr J E King). It is clear that the distributions plot as straight lines and that, in each case the s.d is of order 2MPam$^{1/2}$ such that "quasi-homogeneous" behaviour (within the limits of random experimental errors) is established. The points would, of course, plot equally well as straight lines on Weibull probability paper; but association with a Weibull distribution does not give significant further insight: Weibull arguments have been related to "weakest-link" concepts, but it is not clear that these really hold for very fine-scale microstructures, in which an "avalanche" may occur at a K-value only marginally higher than that at which the most virulent microcrack propagates.

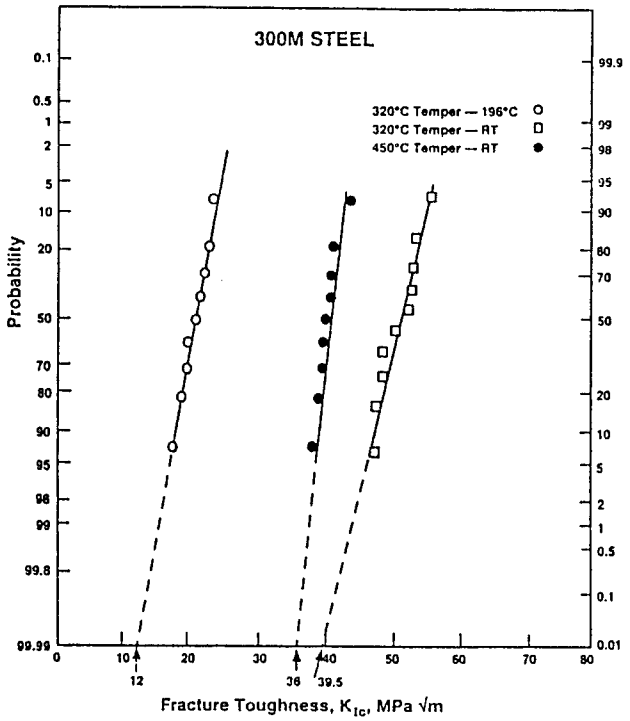


Figure 4. Cumulative Distributions for the Distribution of Fracture Toughness in 300M Quenched-and-Tempered Steel, given different Tempers and tested at -196°C (data, courtesy Dr J E King).

The description of a material as "quasi-homogeneous" is not a just a matter of academic definition. In many cases involving structural-integrity assessment, it is necessary to produce "lower-bound" fracture toughness values. These may be expressed as 2s.d or 3s.d below the mean or values at a given probability level, e.g. 0.1% (10^{-3}) or 0.01% (10^{-4}). Given "quasi-homogeneous" distributions of the form shown in fig. 4, it is possible to extrapolate the straight lines to these lower probability levels with a degree of confidence, noting that the degree of quality-control in material specification, processing and heat-treatment is such that significant outliers should not occur. *Any* extrapolation technique can, of course, be related only to a specific (and limited) data set, although perhaps drawing information from *comparable* data generated for other application.

The number of data points required is of interest. The median ranking used in fig. 4 is based on the good approximation:

$$F_n = (n - 0.3)/(N + 0.4) \qquad \text{.....3)}$$

so that, for 10 specimens, the first value is (1-0.3)/(10+0.4) = 0.067 (6.7%); for 30 specimens, it is 0.7/30.4 = 0.023 (2.3%); for 100 specimens, it is 0.7/100.4 = 0.7%. All these probabilities are significantly greater than 0.01%. An increase in number of test specimens increases somewhat the goodness of fit to a straight line and thence may (doubtfully) improve on a (safe) "10 specimen lower-bound minus 10% of that value", but its main value is to test quality control (the absence of outliers). If quality-control of consistency can be established by other means (e.g. combining data-sets from alloys made by the same supplier and processes, but for different applications) only 10-20 tests may be needed for "lower-bound" predictions.

The situation with respect to quasi-homogeneous materials should be contrasted sharply with that for (spatially) inhomogeneous materials. Following the earlier work of Hagiwara (19) and Neville (18), the situation is best described with respect to research being carried out by X Zhang at Birmingham. He has measured cleavage fracture-toughness values at -80°C for A508 pressure-vessel steel, heat-treated to generate three microstructures: a) 100% (autotempered) martensite: b) 100% (coarse) upper bainite, β, c) 40%β, 60% α′, all with a prior austenite grain size of 250μm. The CDFs for the K_{1c} distributions for 100%α′ and 100%β plot as reasonable "quasi-homogeneous" functions, leading to lower bounds, at the 0.1% level, extrapolated as 65 $MPam^{1/2}$ and 22 $MPam^{1/2}$ respectively. The interest, however, lies in the behaviour of the 40%β 60%α′ mixture (see fig. 5).

As a result of carbon and alloy segregation in the melt and during processing, the hardenability of the material is not completely uniform, in a spatial sense, and the resulting microstructure consists of a "patchy" mixture of "brittle" bainite (β) and "tough" martensite (α′). In a fracture-toughness test, the critical region ahead of the crack tip encounters sometimes a preponderance of "brittle" bainite and sometimes a region of "tough" martensite, see fig. 6.

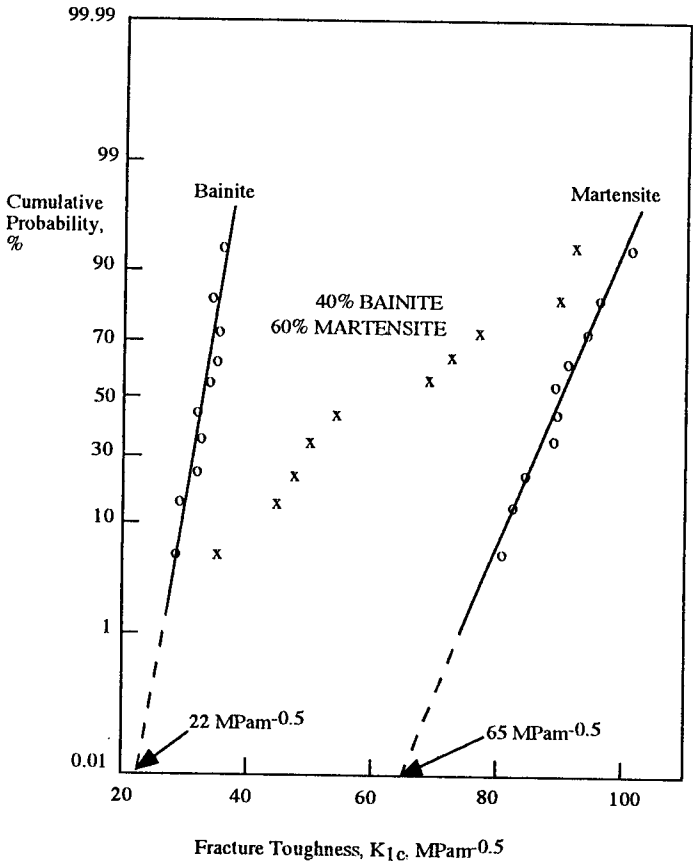


Figure 5. Cumulative Probability Distribution Functions (CDF) for "Quasi-Homogeneous" Microstructures (Martensite and Upper Bainite) and for a "Mixed" Microstructure. Note that both the martensites are relatively well-behaved, so that extrapolation to 0.01% can be made with a degree of confidence. If *only* the "mixed" microstructure data were available, extrapolation would give a value close to zero (or even negative), which is physically unreasonable.

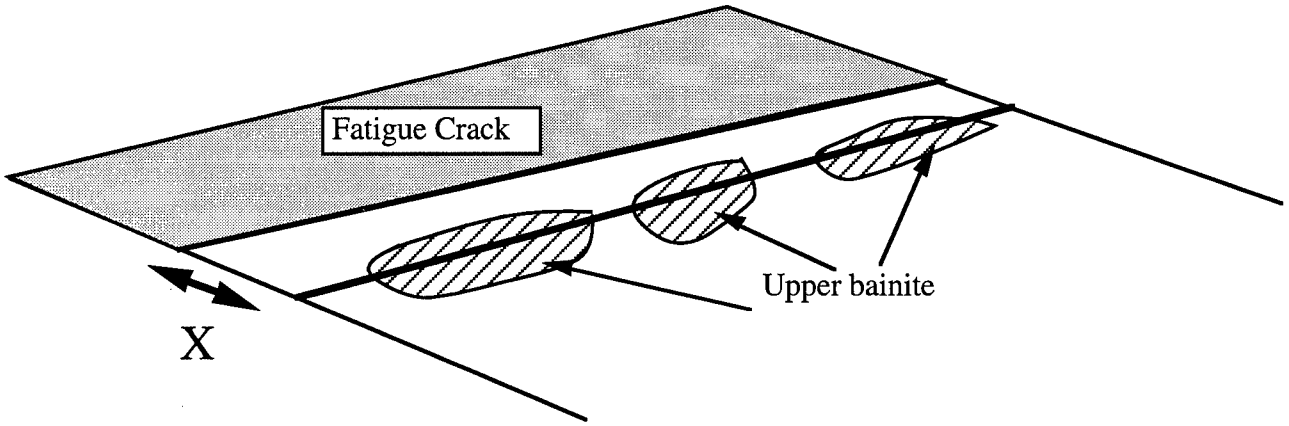


Figure 6a. Illustration of Spatial Distribution of Phases ahead of a Fatigue-Crack Tip in a mixed Martensite/Upper-Bainite Microstructure. In some testpieces a high volume fraction of upper-bainite will be present at the critical distance X; in others, the volume fraction of upper-bainite could be small.

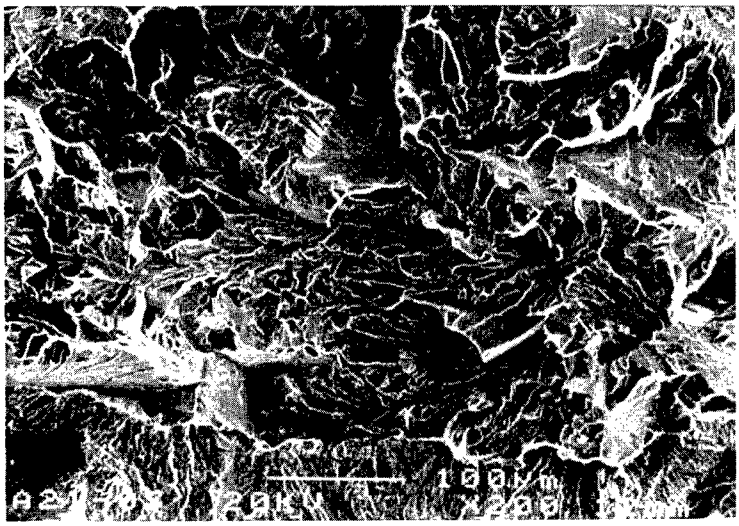


Figure 6b. Fractograph of Crack-Tip Region for Mixed Microstructure of Fracture Toughness 32 MPam$^{0.5}$

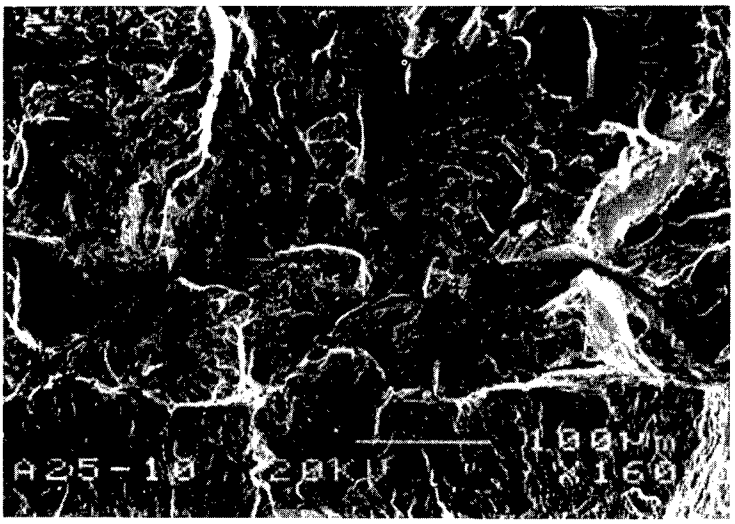


Figure 6c. Fractograph of Crack-Tip Region for Mixed Microstructure of Fracture Toughness 91 MPam$^{0.5}$

Given a measure of dynamic effect with respect to "brittle" initiation, it might then be expected that the (K_{Ic}) CDF for the mixed microstructure might fall between "tramlines", bounded by the CDF for β and that for α′, respectively. This is, indeed, the case (fig. 5). A line could be drawn through the data-points, but it would not be straight, and even a "best-fit" line would exhibit a s.d. much greater than 2MPam$^{1/2}$. The material is not "quasi-homogeneous" and the physical reason for this is clear. Extrapolation to 0.01% probability gives a value much lower than the lower-bound for *the more brittle constituent!* Consider now, the situation that the only data-set available is that for 40%β 60%α′ material. It does not give a straight-line fit on normal probability paper, so there is a great temptation to fit it to a Weibull distribution. Fig.7 shows the results of doing this for a two parameter Weibull (lower-bound, "cut-off" value zero). Sensitivity studies, as used by Neville and Knott (1986) would deduce the "cut-off" value to be zero or even negative, in agreement with the putative extrapolation of the data-points in fig.5. It is clear that what is reasonable for extrapolations for quasi-homogeneous material is unsupportable for (spatially) inhomogeneous material.

Zhang's work has been carried out on a metallurgical system, carefully-designed to demonstrate a point of general applicability to "heterogeneous" microstructures. These include not only micro/meso-scale variations in heat-treated forging steels, but also meso/macro-scale variations in coarse-grain/fine-grain weld metals and nano/micro/meso-scale variations in the segregation of "embrittling" species (such as P, Sn, Sb) to grain boundaries in quenched-and-tempered steels. Fig. 8 shows CDF plots for some of Reed's (13, 15) warm pre-stressing (WPS) results. In general, the CDFs show slightly greater scatter than that for high-quality wrought material (fig. 4) but are still reasonably well-behaved. The plots do however indicate clear outliers which would require detailed investigation. There is much scope for future research.

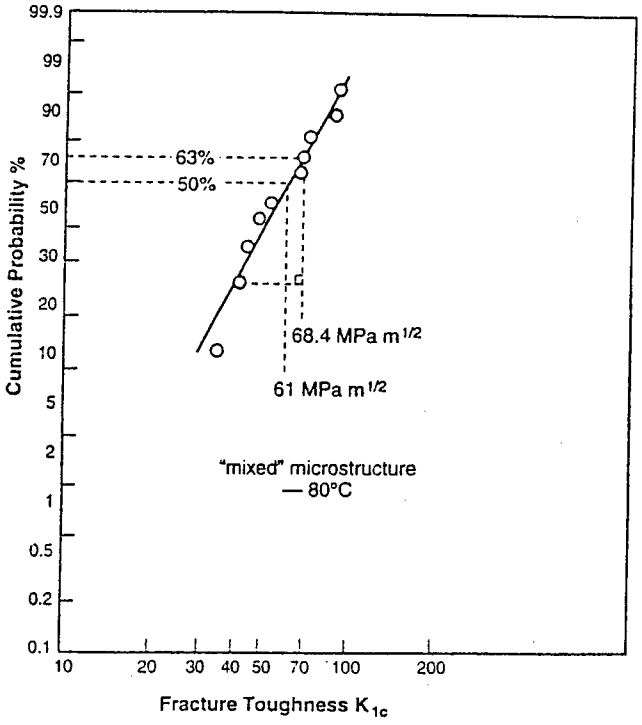


Figure 7. The Result of Fitting the "Mixed" Microstructure Fracture Toughness Data (Figure 5) to a Weibull Distribution. Note that extrapolation of this distribution to a cumulative probability of 0.01% indicates a "lower bound" toughness close to zero.

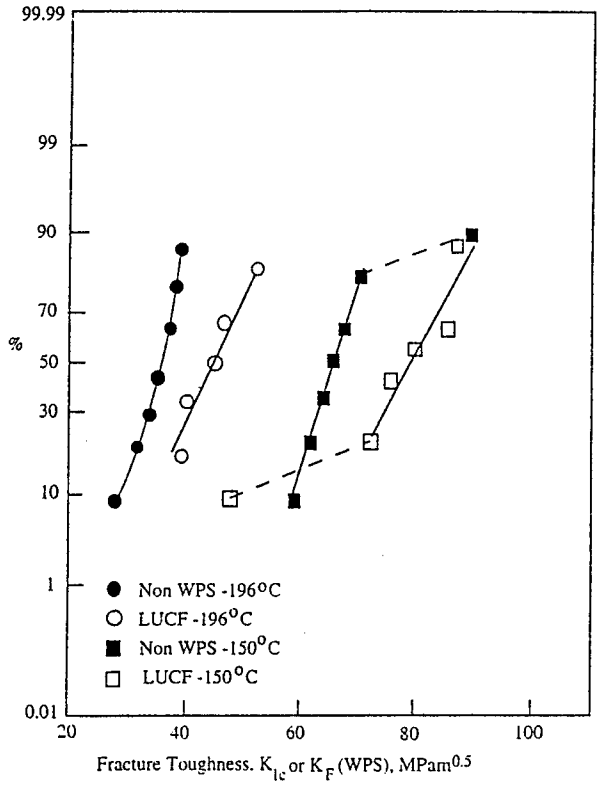


Figure 8. Cumulative Distribution for Fracture Toughness Distributions in A533B Weld Metal, tested at -196°C and -150°C in the Non-Warm Pre-stressed (Non WPS) condition and after Load/Unload/Cool/Fracture WPS sequences. Note first that the benefits of WPS are clearly demonstrated, despite overlap of individual K_{Ic} values (WPS and non-WPS); second, that one WPS point at -150°C and one LUCF point at -150°C are clearly outliers (requiring further investigation).

Acknowledgements

I am grateful to Professor P Bowen for many useful discussions and to dr J E King, Dr D E McRobie, Dr Y Zhang and Mr X Zhang for permission to use their experimental data.

References

1) Knott, J F. "Some Effects of Hydrostatic Tension on the Fracture Behaviour of Mild Steel", Jnl. Iron and Steel Inst., 1966, 204, pp 104-111.

2) McMahon, C J and Cohen, M. Acta Met, 13, p 591 (1965).

3) Smith, E. Proc. Conf. "Physical Basis of Yield and Fracture" pp 36-46, Inst. Phys, Phys. Soc. (1966).

4) Griffiths J R and Owen D R J. J. Mech. Phys. Solids,19, 1971, p 419.

5) Ritchie, R O, Knott J F and Rice J R, "On the Relationship between Critical Tensile Stress and Fracture Toughness in Mild Steel", Jnl. Mech. Phys. Solids, 1973, 21, p 395.

6) Curry, D A and Knott J F, "The Relationship between Fracture Tougness and Microstrucutre in the Cleavage Fracture of Mild Steel", Metal Science, 1976, 10, p 1.

7) Curry, D A and Knott, J F, "The Effects of Microstructure on the Cleavage Fracture Stress in Steels", Metal Science, 12, 1978, p 511.

8) Curry, D A and Knott, J F, "The Effect of Microstructure on the Cleavage Fracture Toughness of Quenched and Tempered Steels", Metal Science, 1979, 13, p 341.

9) Pineau A. Proc. 5th Intl. Conf. on Fracture (ed. D Francois), Pergamon, Vol 2, p 533, 1981

10) Tweed, J H and Knott J F, "Micromechanisms of Failure in C-Mn Weld Metals" Acta. Met., 1987., 35, pp 1401-1414.

11) McRobie D E, "Cleavage Fracture in C-Mn Weld Metals", PhD thesis - Cambridge 1985.

12) Knott, J F, "The Science and Engineering of Fracture" in "Advances in Fracture Research and Structural Integrity", Proceedings ICF8, Ed V V Panasyuk et al, Pergamon, 1994, pp 13-49.

13) Reed, P A S and Knott, J F, "An Investigation of the Warm Prestressing (WPS) Effect in A533B Weld Metals", Fatigue and Fracture of Engineering Materials and Structures, 15, No 12, pp 1251-1270, 1992.

14) Bose W. PhD Thesis - "Micromechanisms of Brittle Fracture in High Strength Low Alloy Steel in Weld Metals" . The University of Birmingham. December 1995.

15) Reed, P A S and Knott, J F, "Investigation of the Role of Residual Stresses in the Warm Pre-stress (WPS) Effect. Fatigue and Fracture of Engineering Materials and Structures: Part I, 19, pp 485-500, Part II, 19, pp 501-512, 1996

16) Ritchie, R O, Smith, R F and Knott, J F. Metal Science, 9, 1975, p 485.

17) Bowen, P, Druce, S G and Knott, J F. "Micromechanical Modelling of Fracture Toughness", Acta Metall. 1987, 35, pp 1735-1746.

18) Neville, D J and Knott, J F, "Fracture of Homogeneous and Inhomogeneous Materials, "Part I: "Homogeneous Materials"; Part II: "Inhomogeneous Materials"; Part III: "The Transition Region", Jnl. Mech. Phys. Solids, 1986, 34, pp 243-291.

19) Hagiwara, Y and Knott, J F, "Cleavage Fracture in Mixed Microstructures", 5th Intl. Conf. on Fracture (ed. D Francois), Pergamon 1981 p 707.

An Application of the J-Q Model for Estimating Cleavage Stress in the Brittle to Ductile Transition

John D. Landes and Carlos A. J. Miranda,
University of Tennessee, Knoxville, TN
and IPEN, São Paulo, Brazil

Abstract

A recent model has been proposed by the authors to predict cleavage failure in the transition for steels based on a weak link mechanism and a crack tip stress field modified for planar constraint by the J-Q theory. The model uses the distribution of toughness results at a single temperature to predict the same at a different temperature or for a different geometry. In this model a material cleavage stress is needed to predict when the weak link fracture is triggered. This cleavage stress is a key input for the application of the model but is not a property that is routinely measured and is hence not available for most steel alloys. Using a characteristic of the model this cleavage stress can be estimated from the result of two distributions of toughness values tested at two different temperatures in the transition. In this paper the method to estimate a value of cleavage stress is presented and the result is used to predict the toughness distributions for structural component models. Examples are given for several steels to show that a measured value of cleavage stress and one determined from the model result in nearly the same prediction of cleavage fracture toughness from the model.

George R. Irwin Symposium on Cleavage Fracture
Edited by Kwai S. Chan
The Minerals, Metals & Materials Society, 1997

Introduction

Predicting the fracture behavior of steels in the ductile to brittle transition region has been a problem because the toughness exhibits size and geometry effects as well as extensive scatter [1]. One way to handle size effects and scatter is through the application of statistical models. The use of Weibull statistics and a master curve concept [2] has led to the development of a uniform standard test procedure as well as a way to handle the statistical treatment of the data and temperature effects in a reproducible manner. In addition the development of the two parameter fracture characterization [3-6] has allowed fracture behavior to be predicted with a fracture locus concept [7].

The master curve is used to predict the temperature effect on toughness for the test specimen geometry. It does not give guidance on the prediction of fracture in a structural component with a different geometry from that of the test specimen. The fracture locus concept has also been observed to have a geometry dependency that might cause difficulty in the prediction of fracture behavior for component geometries [8]. Therefore the problem of the geometry effect on toughness has not been completely solved by these methods. An approach that can be used is a mechanistic one rather than the traditional correlative approach. Mechanistic models could use a local crack tip fracture criterion to predict global fracture in a component.

Models for the prediction of brittle cleavage fracture in steels have been based on the attainment of a critical stress at some characteristic distance. Wilshaw et. al [9] proposed a model for brittle failure in notched bar under a bending loading. Ritchie et. al [10] proposed a model for the brittle fracture of cracked bodies based on the attainment of a critical stress over a critical distance. Heerens et. al [11] proposed a model based on the attainment of a critical cleavage stress at the point where a weak link existed in the material. To apply these models some knowledge of the stress field in front of the notch or crack is needed. Wilshaw et al [9] based the stress distribution on the slip line field analysis. Rice and Johnson [12] analyzed the stress distribution in front of a blunted crack tip with a slip line field analysis which included large deformation effects; this was used in the Ritchie et. al model [10]. Heerens et. al [11] based the stress distribution on an analytical model developed by Schwalbe [13]. These stress models did not account for constraint differences that would be caused by large scale yielding or the effect of the geometrical shape of the body being analyzed.

The recent development of the two parameter fracture mechanics models [6-9] allows the determination of crack tip stresses as a function of constraint. Hence the influence of size, geometry and thickness can be included in the calculation of crack tip stress as a constraint effect. With the development of the two parameter fracture characterization it is possible to reformulate the traditional stress based cleavage failure model to reflect the influence of such things as geometry or loading conditions. A recent model has been proposed by the authors to predict cleavage failure in the transition for steels based on a weak link mechanism and a crack tip stress field modified for planar constraint by the J-Q theory [8,14]. The model uses the distribution of toughness results at a single temperature to predict the same at a different temperature or for a different geometry. In this model a

material cleavage stress is needed to predict when the weak link fracture is triggered. This cleavage stress is a key input for the application of the model but is not a property that is routinely measured and is hence not available for most steel alloys. Using a characteristic of the model this cleavage stress can be estimated from the result of two distributions of toughness values tested at two different temperatures in the transition. In this paper the basic components of the model will be presented. Then the method to estimate a value of cleavage stress is presented and the result is used to predict the toughness distributions for structural component models. Examples are given for several steels. Examples are given for several steels to show that both measured and predicted values of cleavage stress result in nearly the same prediction of cleavage fracture toughness from the model.

Review of Model

The model is based on a weak link failure mechanism. It is assumed that a weak link exists at some distance from the crack tip. The weak link requires a given value of stress, labeled here the cleavage stress, σ_c, to trigger failure. Once the failure of the weak link is triggered, the entire specimen fails. The cleavage stress is a material constant with a fixed value that is not influenced by temperature. However, other material properties such as the yield stress are a function of temperature. The crack tip stress is determined by a large strain numerical analysis which allows crack tip blunting and is put in the format of the J-Q model [4,5].

A schematic of how the model works is given in Fig. 1. The crack tip stress field has the characteristic pattern which can be developed numerically for large strain analysis. Distance from the crack tip in Fig. 1 is normalized by the blunted crack tip opening. The normalized parameter that gives the distance is $r/J/\sigma_o$, where r is distance from the crack tip, J is the crack tip loading parameter and σ_o a yield or flow stress. In terms of the normalized distance from the crack tip the stress pattern is stationary. An absolute distance r moves into the crack tip as loading is increased, that is J as is increased. A weak link at a given distance, r, from the crack tip will move into the stress pattern. If the stress peak is greater than the cleavage stress, the weak link will eventually touch the stress distribution at some point, that is, the stress level at the weak link will be greater than the cleavage stress needed to cause failure of the weak link. At that point a global failure will be triggered. The absolute level of the peak is not a factor in the failure if it is above the stress needed to trigger the failure, σ_c.

The maximum peak of the $\sigma_{\theta\theta}$ stress is scaled to the yield stress σ_o. As the yield stress decreases with temperature increase, the stress peak will eventually drop below the level needed for cleavage. In this regard the model is similar to others which have been proposed [11, 15]. The additional feature is that the stress peak is also scaled by the Q parameter where the value of Q is given by

$$Q = \left[\frac{\sigma_{\theta\theta}}{\sigma_o}\right] - \left[\frac{\sigma_{\theta\theta}}{\sigma_o}\right]_{(SSY)} \qquad (1)$$

As the loading is increased, hence J is increased, the constraint may begin to decrease and the peak of the stress field can decrease as illustrated in Fig. 2. The

value of Q also depends on the geometry and mode of loading of the body so the level of the crack tip stress distribution depends on the overall geometry of the body being analyzed as well as the loading condition and temperature.

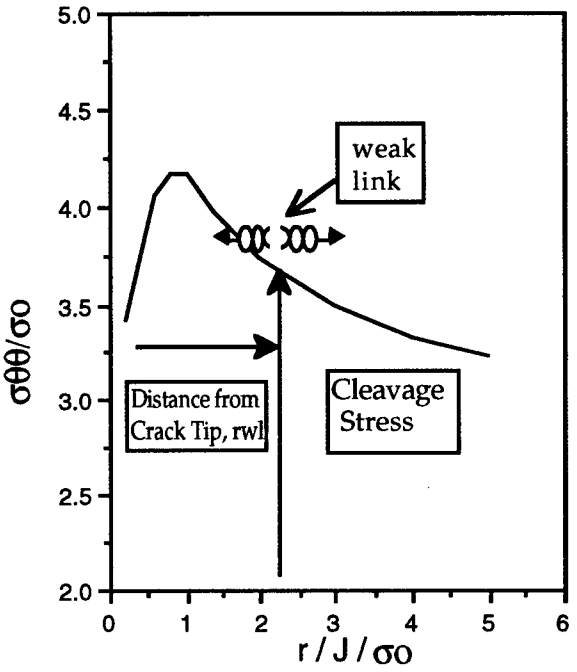


Fig. 1 - J-Q Based Weak Link Model

As the loading is increased, hence J is increased, the constraint may begin to decrease and the peak of the stress field can decrease as illustrated in Fig. 2. The value of Q also depends on the geometry and mode of loading of the body so the level of the crack tip stress distribution depends on the overall geometry of the body being analyzed as well as the loading condition and temperature. The presentation of the stress distribution in Figure 2 is different from that in Figure 1 in that the abscissa is not normalized but is absolute. Therefore the stress distribution moves to the right and down with loading.

The material characteristic in the model that quantifies the toughness scatter is the distance from the crack tip to the weak link. To make a prediction of fracture toughness an input set of fracture toughness values from a given geometry at a fixed temperature are used [8]. For the material a value of cleavage stress is determined separately [11]. The yield strength is measured at the temperature for which the model is applied. Then for each toughness given in terms of a J value, a distance from the crack tip to the weak link can be determined, here labeled r_{WL}. This determination uses a crack tip stress, $\sigma_{\theta\theta}$, which has been adjusted for Q. In the previous work [8] the Q values were taken from the work of O'Dowd and Shih [4, 5]. To predict the toughness distribution for a different temperature or geometry, a new value of σ_o corresponding to the new temperature is needed as well as a set of Q calibrations for the geometry. The value of cleavage stress is the same as before; it is assumed to be independent of temperature. From a value of r_{WL} determined above, the value of J which causes the crack tip stress, $\sigma_{\theta\theta}$, to reach the cleavage stress at r_{WL} is the toughness value for the predictive case. Then from the set of input toughness values, that is a set of r_{WL} values, a scatterband of toughness values can be predicted for the new temperature and/or geometry.

An important input to the model is the invariant cleavage stress. It can be measured by separate experiments [11], but is not often measured or reported in the literature. It would be desirable to make an estimate of the cleavage stress from other measurements. Using the fracture toughness results from tests at two different temperatures, an estimate of the cleavage stress can be made that gives

reasonable results when used in the model. This procedure is discussed in the next section.

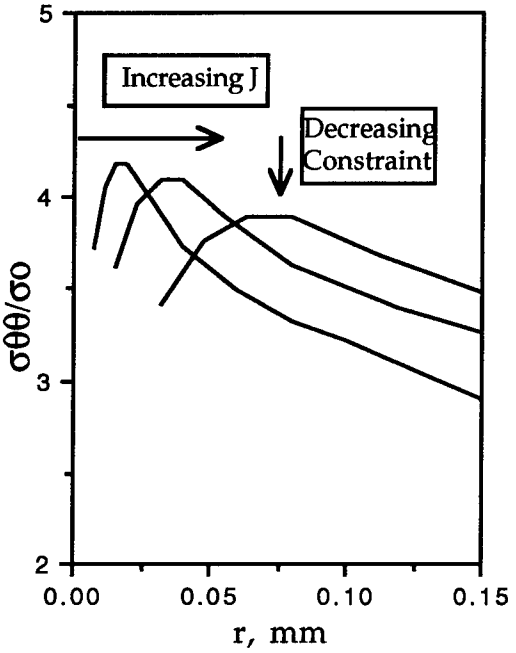


Fig. 2 - Change in Crack Tip Stress with Increasing J and Decreasing Constraint

Prediction of the Cleavage Stress

The cleavage stress, σ_c, is a key input to the model and is a material property that must be measured; it cannot be predicted from theory. Using the result of the model, that is that given a cleavage stress, a fracture toughness can be predicted at one temperature from a toughness value at another temperature, a method to predict a cleavage stress value was developed. If two toughness values exist at two different temperatures, it should be possible to predict the cleavage stress by an application of the model where cleavage stress and not toughness is the unknown. Since the toughness values measured at a given temperature show a lot of scatter, it would not work well to predict this cleavage stress from two single values of toughness at two temperatures. Rather a number of tests should be conducted at each temperature and an average or median value of toughness used for the prediction.

In the case studied here a median value of toughness was used for sets of data containing 10 or more data points. Two materials were used to evaluate σ_c, a CrMoV steel [15, 16] and a 20MnMoNi55 steel [15, 17]. For both of these steels a cleavage stress had been measured separately so that a comparison could be made. The approach was to use the median toughness at one temperature and try to predict the median toughness at the second temperature by guessing a cleavage stress and applying the model in the normal way. The guess of the cleavage stress was incremented and a second application of the model made. This procedure was continued until a range of predictions was made. It was discovered that in incrementing the cleavage stress to make a prediction, a local minimum or maximum was reached at the appropriate value of toughness, hence the correct cleavage stress. The prediction made from a higher temperature to a lower one causes a minimum and a prediction from a lower temperature to a higher one causes a maximum.

Examples are given for the two steels in Figures 3 and 4. For the case of the CrMoV steel the prediction was made from 80°C to 100°C and visa versa, Figure 3. For the 20MnMoNi55 steel the prediction was made from -90°C to -60 °C steel and visa versa, Figure 4. The prediction value of J_c in the figures was

normalized by the absolute minimum or maximum in the group to allow comparisons to be made on the same scale. These normalized predictions are plotted as a function of the guessed value of σ_c. For the 20MnMoNi55 steel the local minimum and maximum are clearly seen and they occur at about a cleavage stress of 1600 MPa. For the CrMoV steel the minimum and maximum were not as distinct but they occurred at about 2000 MPa. The measured values of σ_c were about 1750 for the 20MnMoNi55 steel and 1900 MPa for the CrMoV steel. The predictions were not much different from the measured values.

In applying the model with these values of cleavage stress the result is not very sensitive to a variation in terms of predicted toughness. The model is sensitive to the value of σ_c for the prediction of the end of the transition region. This prediction corresponds to a point where the cleavage stress is higher than the crack tip stress predicted numerically and altered by the constraint as given by Q. Therefore a lower cleavage stress extends the transition temperature to higher temperatures. However, the actual toughness values predicted at not sensitive to values of σ_c as will be illustrated in the next section.

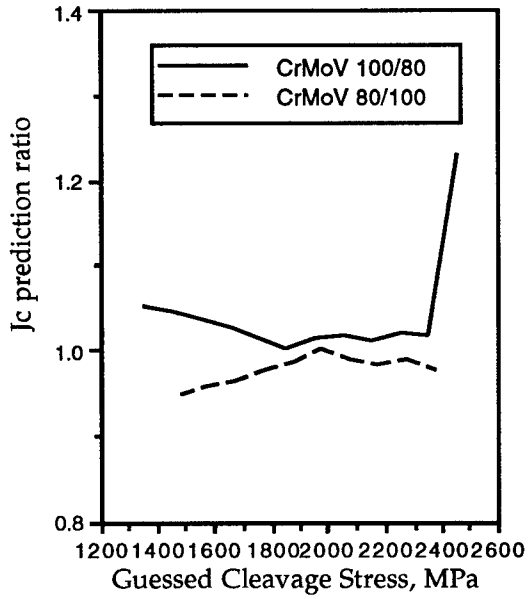


Fig. 3 - Ratio of Jc Predicted versus Guessed Cleavage Stress for CrMoV Steel

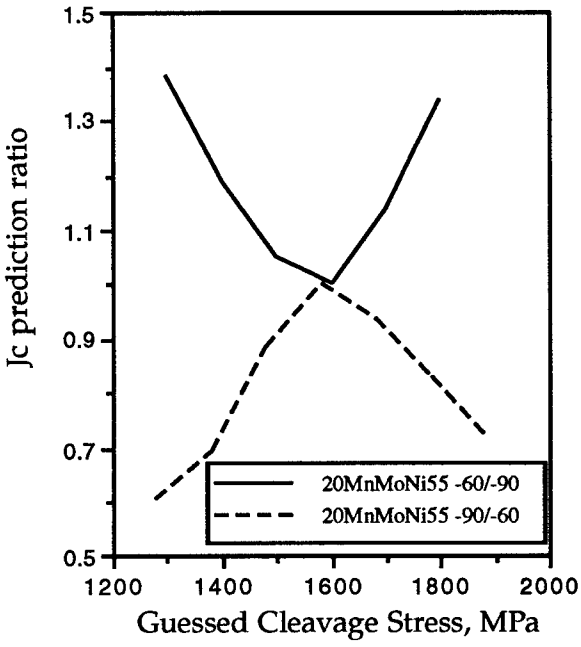


Fig. 4 - Ratio of Jc Predicted versus Guessed Cleavage Stress for 20 MNMoNi55 Steel

Demonstration of Model Predictions

Some examples of the application of the model are given first to illustrate how it works and second to compare the model predictions with different values of σ_c. The examples are given only for the 20MnMoNi55 steel where the difference between the measured and estimated values of σ_c were greatest. In Figure 5 a prediction is given for the fracture toughness of the 20MnMoNi55 steel at through the transition from input data at -90°C. The predictions are made from the median toughness value and from the upper and lower bound values of toughness at -90°C. The input data are the closed points, the predictions are given as trend lines. Measured values of cleavage fracture toughness at -60 °C are given as open points. Also on this figure the prediction of the end of the transition is given as a closed square. These features in Figure 5 illustrate the types of things that can be predicted from the model.

The predictions in Figure 5 are made for the measured value of σ_c 1750 MPa. To illustrate the effect of the cleavage stress on the prediction, the same predictions are made for the estimated value of σ_c, 1600 MPa. In Figure 6 the prediction of the range of cleavage toughness values at -60 °C is made using the two values of σ_c. As can be seen the scatterbands predicted from the -90 °C input data set are nearly identical. Also the predicted median value is not much different. In this case the predicted median toughness is 250 kJ/m^2 from with the 1750 MPa σ_c and 300 kJ/m^2 with the 1600 MPa σ_c. The overall effect of the value of cleavage stress is reflected more in the prediction of the end of the transition. This prediction is illustrated in Figure 7. The two values of σ_c are used to predict the end of the transition and a third value, 1900 MPa, is added to illustrate the trend of the prediction of the end of the transition. As can be seen in this Figure, there is an effect of the σ_c value on the temperature predicted as the end of the transition. Between the measured and estimated values of σ_c this is 20°C. Although this is visible on the figure, it is not a large effect for such a prediction. The actual end of the transition was not carefully measured for this material and is usually difficult to measure accurately. At the end of the transition the data include both test results that exhibit cleavage fracture, sometimes at surprisingly low values of toughness and those tests that are completely ductile fracture, exhibiting large values of toughness. in this regard the ability to predict the end of the transition could be valuable.

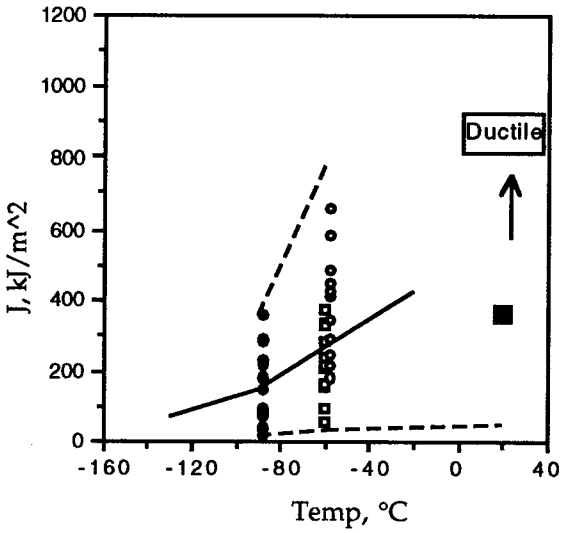


Fig. 5 - Transition Fracture Toughness Prediction for 20MnMoNi55 Steel

The result of these two predictions with the measured σ_c and the value obtained from the model are not very different.

For the prediction of actual toughness values the difference in the range of toughness predicted from a scatterband of input toughness value is very small. The prediction of the end of the transition is influenced more by the σ_c value but is also not very great. Therefore for materials that do not have a measured σ_c the prediction model for the σ_c would be satisfactory. However two sets of cleavage fracture toughness values at two different temperatures is needed as input. This is often available for materials whose transition fracture toughness trends has been studied [15].

Summary

The model to predict cleavage failure in the transition for steels requires a value of cleavage stress to make the prediction of a cleavage fracture toughness at one temperature from input at another. This value of cleavage stress can be estimated using the model from two sets of toughness values at two different temperatures. The values estimated for two different steels were reasonably close to the measured values. When the predicted and measured values of cleavage stresses were used with the model, the difference in the predicted toughness was not much. When the two different values of cleavage stress were used to predict the end of the transition a larger effect resulted but it was not a very significant one when compared with the uncertainty of test results.

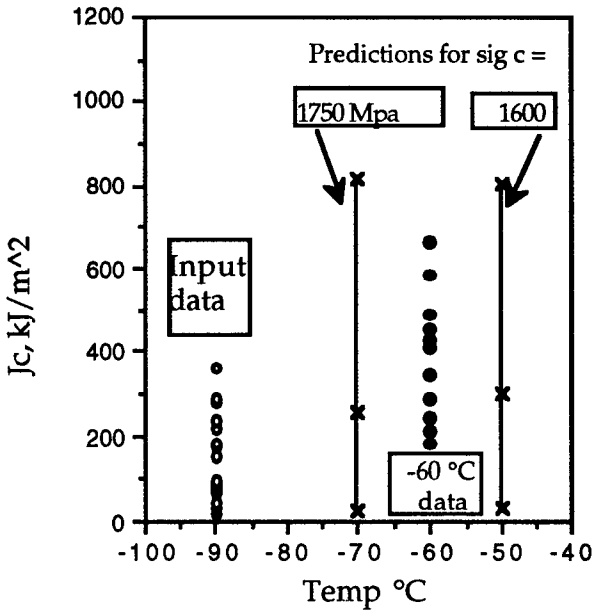


Fig. 6 - Prediction of Transition Cleavage with Different Cleavage Stresses

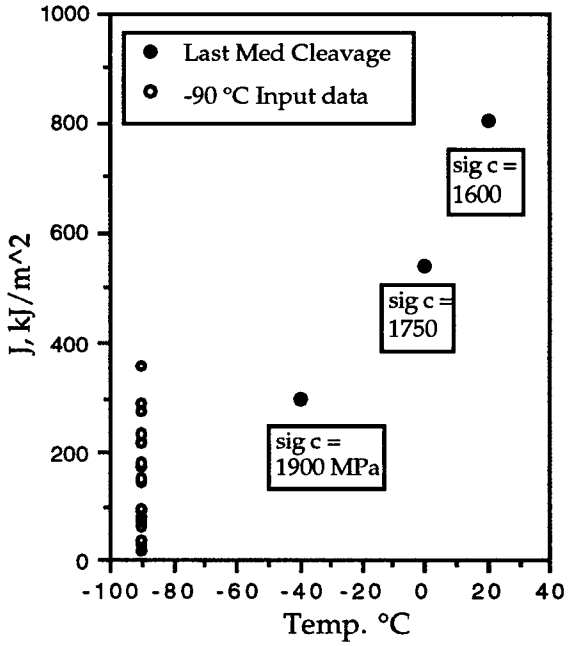


Fig. 7 - Prediction of Transition End with Different Cleavage Stresses

References

1. J. D. Landes and D. H. Shaffer, (1980) "Statistical characterization of fracture in the transition region", Fracture Mechanics: Twelfth Conference, ASTM STP 700, ASTM, pp. 368-382.

2. Wallin, K., (1991) "Fracture toughness transition curve shape for ferritic structural steels", Proceedings of the Joint FEFG/ICF International Conference on Fracture of Engineering Materials, Singapore, August 6-8, pp. 83-88.

3. J. W. Hancock, W. G. Reuter, and D. M. Parks, (1993), "Constraint and toughness parameterized by T", Constraint Effects in Fracture, ASTM STP 1171, E. M. Hackett, et. al. Eds, ASTM, pp. 21-40.

4. N. P. O'Dowd and C. F. Shih, (1991), "Family of crack-tip fields characterized by a triaxiality parameter: part I - structure of fields", J. Mech. Phys. Solids, Vol. 39, pp. 989-1015.

5. N. P. O'Dowd and C. F. Shih, (1992), "Family of crack-tip fields characterized by a triaxiality parameter: part II - fracture applications", J. Mech. Phys. Solids, Vol. 40, 939-963.

6. T. L. Anderson and R. H. Dodds,, (1991), " Specimen Size Requirements for Fracture Testing in the Transition Region", Journal of Testing and Evaluation, JTEVA, American Society for Testing and Materials, Philadelphia, Vol. 19, pp. 123-134.

7. Shih, C. F., O'Dowd, N. P. and Kirk, M. T., (1993) "A Framework for Quantifying Crack Tip Constraint" Constraint Effects in Fracture, ASTM STP 1171, E. M. Hackett, et. al. Eds., American Society for Testing and Materials, Philadelphia, pp. 2-20.

8. J. D. Landes, "Application of a J-Q Model for Fracture in the Ductile-Brittle Transition" (to be published in an ASTM STP).

9. T. R. Wilshaw, C. A. Rau and A. S. Tetelman (1968) "A general model to predict the elastic-plastic stress distribution and fracture strength of notched bars is plane strain bending", Engineering Fracture Mechanics, Vol. 1 No. 1, June, pp. 191-211.

10. R. O. Ritchie, J. F. Knott and J. R. Rice, (1973) "On the relationship between critical tensile stress and fracture toughness in mild steel", Journal of the Mechanics and Physics of Solids, Vol. 21, pp. 395-410.

11. J. Heerens, D. T. Read, A. Cornec and K-H. Schwalbe, (1991) "Interpretation of fracture toughness is the ductile-to brittle region by fractographic observations" Defect Assessment in Components - Fundamentals and Applications, ESIS/EGF 9, (Edited by J. G. Blauel and K.-H. Schwalbe), Mechanical Engineering Publications, London, pp. 659-678.

12. J. R. Rice and M. A. Johnson, (1970) "The role of large crack tip geometry changes in plane strain fracture", Inelastic Behavior of Solids, Eds. M. F. Kanninen et. al., pp. 641-672.

13. K.-H. Schwalbe, (1977) "Comments on finite element solutions of crack-tip behavior in small scale yielding," Transactions of ASM, April, pp. 186-188.

14. J. D. Landes (1993), "A two-criteria statistical model for transition fracture

toughness", Fatigue Fract. Engrg. Mater. Struct., Vol. 16, No. 11, pp. 1161-1174.

15. J. D. Landes, (1992). "The effect of size, thickness and geometry on fracture toughness in the transition", GKSS Report, GKSS 92/E/43.

16. J. Heerens, (1991) Unpublished CrMoV Data.

17. J. Heerens and B. Petrovski, (1991) unpublished 20MnMoNi55 data.

MODELING A CLEAVAGE-CHARACTERISTIC STRESS (S_{CO}) OF FERRITIC STEELS

D. M. Li and M. Yao*

School of Materials Science & Engineering, Harbin Institute of Technology, Box 433, Harbin 150001, P. R. China

*Materials Science Department, Yanshan University, Qinhuangdao 066004, P. R. China

Abstract

The cleavage fracture behavior of ferritic steels has been studied under different specimen geometry (smooth, notched and cracked bars/sheets), loading mode (plain tension, three-/four-point notch/crack bending and cracked sheet tension) and strain rate (quasi-static to impact tests) conditions. Data of mechanical property testing, fractographic observation and FEM calculation are incorporated to model and substantiate a "cleavage-characteristic stress" S_{co} as a parameter representing the cleavage fracture resistance of a material. A concept of "effective plastic zone" has been emphasized in constructing the proposed probabilistic fracture model. On the basis of this important parameter (S_{co}), a unified cleavage fracture criterion is established under the different conditions involved.

George R. Irwin Symposium on Cleavage Fracture
Edited by Kwai S. Chan
The Minerals, Metals & Materials Society, 1997

Introduction

Despite the fact that cleavage fracture has received, among other mechanisms in the fracture family, the most attention from scientists in different areas, controversy still exists regarding such important issues as the fracture criterion and the characteristic parameter measuring the cleavage fracture resistance of a material.

The build-up of cleavage fracture criterion requires a fundamental understanding of the fracture process and hence, of the micromechanism. Early physical models (1-5) assume the formation of cleavage cracking in basically ferritic structures as a result of interaction of dislocation movement with microstructural discontinuities, e.g. phase/grain boundaries (1-2) or brittle second phase (typically carbide) particles (3-4), or directly with weak (low index) crystal planes (5) (cleavage planes). The intersection of deformation twins has also been proposed to be alternative mechanism for cleavage crack forming at very low temperatures or high strain rates (6). For steels with less simple microstructures, other phase elements have also been assumed to be the sources for cleavage crack nucleation (7-12). These include martensitic packet (7-8), bainitic packet (9), pearlitic packet (10) and inclusions (11-12). While these various models can reasonably provide possible mechanisms for cleavage crack nucleation, they are not always adequate to predict cleavage fracture as a whole process considering the fact that arrested grain-sized microcracks have frequently been found in specimens of ferritic steels (13-21).

The critical tensile stress theory (22-29) is still prevailing today in describing cleavage fracture criterion for notched or cracked specimens. It is proposed by this theory (22-29) that cleavage fracture occurs when the maximum principal stress ahead of notch (crack) tip reaches a critical value σ_f^* which is assumed to be temperature and strain rate independent. Then σ_f^* is assumed to be a characteristic cleavage fracture stress of the material. However, it should be noted that the value of σ_f^* thus defined is remarkably higher than the cleavage fracture stress determined by plain tensile bars at different temperatures (19, 30, 31). In other words, there is not a unified criterion of cleavage fracture between smooth and notched (cracked) specimens, contradicting the fact that the same physical process, *i.e.* cleavage fracture, occurs in both types of specimens.

The RKR model (32) is established based on detailed analysis of the near crack-tip field (33-36). It is indicated by this model that for cleavage fracture to occur in a precracked specimen the critical stress σ_f^* should be reached or exceeded over a microstructurally significant distance ahead of crack-tip called "characteristic distance" (X_0) which is assumed to be temperature independent and is originally taken as two times grain size. Besides presenting a cleavage fracture criterion, this model is used to predict the temperature dependence of fracture toughness K_{IC} in the corresponding regime. In a later study (37) it is found that the prediction works in a quantitative manner if and only if X_0 is temperature independent. However, further investigations have indicated the temperature dependence of X_0 (37) or a random distribution of the crack nucleation location (38) or no simple relationship between X_0 and such microstructural parameters as grain size (39). Moreover, since the parameter σ_f^* is invariably adopted in the RKR model, the problems involved with σ_f^*, as explained earlier, still exists. Nevertheless, by presenting a characteristic distance, the RKR model (32) does trigger a statistical viewpoint to consider the probabilistic aspects in the confined plastic zone ahead of crack-tip, which has been adopted in principle afterwards. Based on these findings (32-39), some statistical models (40-48) have been developed, which are fundamentally on the weakest link assumption. Inherent to these models is the recognition of a known distribution of potent microcrack nuclei (brittle second phase particles). Most of these models assume the propagation of the particle-sized microcrack into the matrix to be a critical event (40-46), whereas a subsequent study by Lin *et al* (47) accounts for the possibility of a cleavage fracture governed by the propagation of grain-sized cracks into neighboring grain but assuming independent roles of grains and particles. A recent model (48), which emphasizes a combined role of particles and grains, reveals that the microcrack nucleation due to carbide cracking is directly proportional to its diameter but the probability of nucleation by this mechanism is just around 10^{-4}. If this is the case, it may be worth while considering such a question as why the grain-sized nuclei, whose scale is order(s) larger than that of particle size, should not be included as primary "building blocks" in the construction of the statistical model, since arrested grain-sized cracks are often evidenced (13-21, 45-47). Clearly the principal issue concerning the critical event in cleavage fracture process has not been clarified with these statistical models (40-48). Furthermore, while these models can give a reasonable lower bound prediction of K_{IC}, they have not been capable of doing so for the cleavage fracture occurring in the ductile-brittle transition regime or in the case of general yielding. As is concluded elsewhere (48), current probabilistic models have a weak support and further experimental efforts are needed.

In the present paper the cleavage fracture behavior in ferrite-based steels is modeled and verified, incorporating analytical and experimental results obtained by the present authors and their co-workers in the past decade. It is justified here that there should be a unified criterion for cleavage fracture occurring under different specimen geometry (smooth, notched and cracked), loading mode and strain rate conditions, in a view to maintain a consistent physical nature of cleavage fracture. A major effort is focused on the development of a parameter of material – cleavage-characteristic stress (S_{co}).

Plain Tensile Fracture Behavior: Background of S_{co}

Similar to other forms of fracture, cleavage fracture is assumed to be a result of the interaction between the inherent (characteristic) resistance of a material to cleavage fracture and the stress-strain field under a given environment. For the determination of the stress-strain field, there have been various experimental and analytical methods nowadays in an era of fracture mechanics. Determining the characteristic resistance parameter of the material is not, however, so straightforward due to the well-documented complicated effects of stress state (*e.g.* constraint), specimen geometry (*e.g.* notch, crack, *etc.*) as well as crack-tip blunting on the fracture behavior. These typical influencers can confuse the manifestation of somewhat more inherent properties of the material. Nevertheless, since it is convinced by the present authors that cleavage fracture is physically ONE process regardless of the mechanical conditions involved, there should be a distinct revelation of the characteristic resistance of the material to cleavage fracture in the case of a homogeneously strained smooth specimen fractured without crack-tip blunting prior to catastrophic propagation. Consequently cleavage fracture behavior is first probed through plain tensile tests at a series of temperatures to have a background understanding and then, to determine the material-characteristic parameter mentioned.

Fig. 1 shows the variation of plain tensile yielding and fracture behavior representative of our previous experimental results (19, 30, 31, 49-51) obtained mainly in low-carbon steels (C ≤ 0.19 wt.%) with both annealed and precipitation-hardened ferrite-based microstructures. T_{cf} represents the lowest temperature at which a fibrous fracture by micro-void coalescence initiates before a cleavage crack can propagate. As such, when temperature decreases to a value $T < T_{cf}$, cleavage fracture occurs as a dominant gross fracture process and hence, the present study will be concentrated on the fracture behavior in the temperature range of $T < T_{cf}$. As is evidenced in Fig. 1, while yield strength σ_y increases and reduction of area (RA) decreases monotonically, fracture stress S_f varies with temperature in different trends, as temperature decreases in this range. When $T_{co} < T < T_{cf}$, macro-scale plastic deformation, indicated by a definite amount of RA, precedes cleavage fracture and thus, the fracture is ductile in an engineering sense. RA decreases with decreasing temperature and approaches a zero value when temperature reaches T_{co}. When $T < T_{co}$, no nonlinear stage is evident on the experimentally recorded load-elongation curve, or the curve ends at the serrated "yield plateau" for steels exhibiting the physical yielding. The data points of S_f thus obtained falls on a curve which is well justified as the extension of σ_y *vs* temperature curve. In consequence, the fracture in this case is considered macroscopically brittle. Then it is clear that the ductile-brittle transition of cleavage fracture takes place at a critical temperature T_{co}. T_{co} is defined as the ductile-brittle transition temperature for plain tension. At T_{co}, cleavage fracture stress reaches a minimum value, S_{co}, termed "cleavage-characteristic stress". S_{co} is assumed to represent the characteristic resistance of the material to cleavage fracture and this will be verified further.

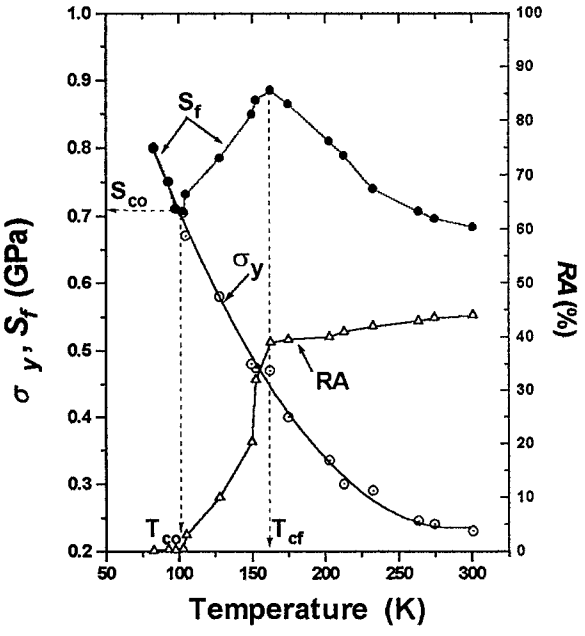


Fig. 1: Yield strength (σ_y), fracture stress (S_f) and reduction of area (RA) as functions of temperature in plain tension.

As is stated earlier, the establishment of a cleavage fracture model should be based on a confirmed physical clarification of cleavage fracture process. To begin with, there should be no question on the assumption that cleavage fracture is preceded by plastic deformation to some scale, since a dislocation- or deformation-induced mechanism has been proposed in almost all models on cleavage crack nucleation (1-12). By means of longitudinal sectioning (19-21), cracks nucleated by various mechanisms have been evidenced to be left near the main crack plane, including cracked carbides, inclusions and pearlitic packets, cracks triggering from the center but ending at the boundary of a ferritic grain, and ferritic grain-sized cracks. The fact that cracks can be nucleated by different mechanisms in one steel implies that the crack nucleation is a stochastic process in cleavage fracture. The observations of arrested ferritic grain-sized cracks (13-21, 45-47) indicate that the propagation of the grain-sized crack across the grain boundary should be the critical event for the gross fracture process. This is justified considering the fact that more work is required in crossing the crystallographically discontinuous boundary area and in forming "steps" (constituents of the "river" pattern) due to a mismatch between cleavage planes in adjoining grains (19, 20, 30). While there exist more than one ferritic grain-sized cracks, it is the propagation of the most "eligible" one that determines the gross fracture. The most "eligible" crack is defined as the "cleavage fracture origin" (CFO) whose condition is most favorable for the catastrophic propagation regarding (a) its size (approaching the largest available), (b) its orientation with the principal stress axis (approaching 90° as possible) and (c) its orientation with the neighboring cleavage plane (approaching 0° as possible) (19-21). From a statistical viewpoint CFO represents the crack having the largest comprehensive probability for its unstable propagation. Here "comprehensive" is emphasized because a practically available CFO cannot always be the most favorable in all aspects: (a) through (c). Then the cleavage fracture process in ferritic steels should consist of three fundamental stages (19-21, 49): (i) yielding, (ii) crack nucleation in those grains where stress concentration is adequate and (iii) unstable propagation of CFO across the grain boundary. In relating the parameter S_{co} to microscopic fracture process, it is proposed that S_{co} should reflect the minimum stress corresponding to the stress level required for the catastrophic propagation of the unblunted CFO.

Based on this hypothesis, the cleavage fracture behavior (Fig. 1) can have a reasonable interpretation as follows. When $T > T_{co}$, yield strength $\sigma_y < S_{co}$. Then initial cracks become blunted before they can propagate with the minimum stress S_{co}. As a result, unstable crack propagation has to take place at a stress level (S_f) higher than S_{co}. When $T < T_{co}$, $\sigma_y > S_{co}$. In this case S_{co} has only got a potential meaning since cleavage fracture cannot occur without yielding as is seemingly justified by the stress balance. Consequently, as yielding initiates and thus the probability of crack nucleation is provided, the overwhelming stress condition makes the above-mentioned three stages complete in instant succession. That is, the fracture is yielding-controlled or nucleation-controlled and thus it occurs with CFO in an unblunted (sharp) state. T_{co} is the highest temperature for the occurrence of the yielding-controlled cleavage fracture. Therefore fracture stress S_f can obtain its minimum value S_{co} at T_{co}. At T_{co}, the ductile-brittle transition of cleavage fracture occurs with the criterion:

$$\sigma_y (T_{co}) = S_{co} \qquad (1)$$

Fracture Behavior of Notched/Cracked Specimens: Verification of S_{co}

To verify the effects of specimen geometry and stress state on cleavage fracture, the plastic deformation and fracture behavior have been studied by mechanical tests of single-edge notch (crack) three-/four-point bending (19, 30-31, 49-51), center-cracked sheet tension (52), and surface-crack three-point bending (53) at a series of temperatures. An identical experimental law has been found for these different types of tests regarding the variation of the deformation and fracture properties with test temperature. This is examplified in Fig. 2 which gives a similar behavior as reported by other investigators (29, 54-55). In Fig. 2, σ_{fn} is the nominal fracture stress, σ_{gy} is the general yield stress calculated by a slip-line field solution (29, 56), T_{gy} is the critical temperature for cleavage fracture at general yielding, T_c is the temperature at which σ_{fn} gets a minimum or trough, and T_{cf} is, as in the plain tension, the temperature for the onset of fibrous fracture, below which a complete cleavage fracture occurs. At temperatures $T < T_{gy}$, cleavage fracture happens prior to the general yielding of the notched/cracked cross-section, *i.e.* with confined plastic zone ahead of notch/crack. In the temperature range of $T_{gy} \sim T_c$, while cleavage fracture happens after general yielding, σ_{fn} well approaches σ_{gy} and the amount of plastic deformation is not evident, as reflected by a small value of *COD*. In an engineering sense the fracture in this range is also regarded as a macroscopically brittle fracture. When $T > T_c$, however, σ_{fn} increases steeply with temperature and so does the macroscopic deformation prior to fracture, *e.g.* indicated by *COD*. Clearly T_c represents the temperature for the occurrence of ductile-brittle transition of cleavage fracture in notched/cracked specimens.

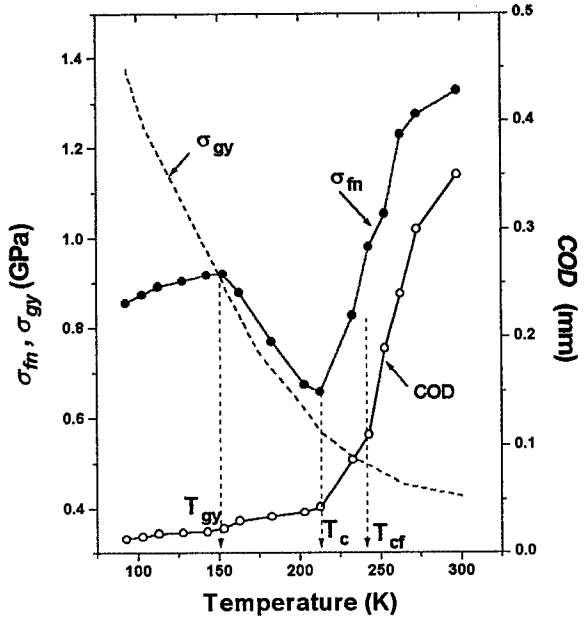


Fig. 2: Temperature dependence of nominal fracture stress (σ_{fn}), general yield stress (σ_{gy}) and crack-tip opening displacement (*COD*) for the notched specimens in bending tests.

It is assumed that the existence of notch or crack should not change the physical inherence of cleavage fracture process, though it does form a highly localized stress-strain field with the building-up of a plastic zone ahead of notch/crack. As a matter of fact, experimental observations (19-21) confirm that the cleavage fracture process in notched/cracked specimens should also consist of the same three fundamental stages as described in the preceding section. However, it should be indicated that the probabilistic aspect should not be neglected in constituting the cleavage fracture criterion for notched/cracked specimens because of the stress-strain localization involved. In the case of plain tension, by contrast, yielding can spread the whole cross-section of a specimen and hence, probabilistic condition for crack formation can be satisfied at the moment of the stress condition is satisfied. That is to say, probabilistic aspect is hidden by the unique feature of stress-strain field in plain tensile tests. To consider the probabilistic requirement of cleavage fracture in notched/cracked specimens, the concrete meaning of "yielding" in stage (i) of the fracture process should be the formation of a yield zone large enough to enclose an "effective yield zone" (EYZ) ahead of a notch/crack-tip. EYZ is defined as the part of the yielded material volume within which the principal stress reaches or exceeds the "cleavage-characteristic stress" S_{co} and the probability of finding CFO is unity. A one-dimensional illustration of EYZ is given as its width r_e in Fig. 3 in which the principal stress distribution is one of the results of the finite element method (FEM) (19, 30, 57). The FEM calculation was based on an incremental law of plastic flow (58) and both the von Mises and the Tresca yield criteria were adopted in the calculation. Only the result by the Tresca criterion is given Fig. 3 due to its better prediction for our case. If the stress intensification factor (Q) at X_e, the near-tip edge of EYZ (Fig. 3), is Q_e, the criterion for cleavage fracture at temperatures $T \leq T_{gy}$ can be expressed as :

$$\begin{cases} Q_e \sigma_y = S_{co} \\ r = r_e \end{cases} \qquad (2)$$

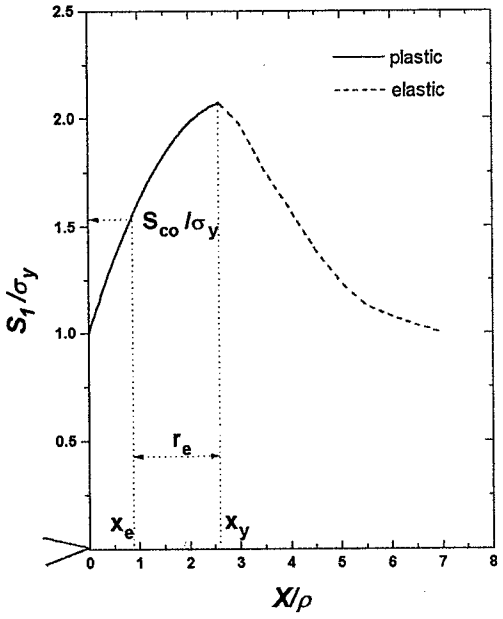


Fig. 3: A one-dimensional illustration of the location of the "effective yield zone" (EYZ) for cleavage fracture in notched/cracked specimens based on the FEM calculation results (19).

Since the whole fracture process consists of the above-mentioned three stages, it is convenient to conduct the probabilistic evaluation individually for each stage. By assuming EYZ, the probability for stage (i) is automatically implied. Then only the probabilities for stages (ii) and (iii) should be considered for modeling. Let the probability for the crack nucleation in a ferritic grain to be P_n and that for the propagation of an "eligible" initial crack to be P_p, then the probability for the whole fracture process, P_e, can be written as:

$$P_e = \int_0^{V_e} P_n P_p \frac{dv}{V} = 1 \qquad (3)$$

where V_e is the volume of EYZ and V is the volume of a ferrite grain. P_n reflects the possibility of finding the stress concentrators in a grain, *e.g.* grain size determining the slip-band pile-up, morphology, size and distribution of particles acting as obstacles to local dislocation movement, *etc.* Therefore P_n is primarily dependent on microstructural characteristics of a material and is considered a constant for a given material. P_p consists of two parts: the probability for the propagation over the grain-boundary area, P_{p1}, and the probability for the propagation across the neighboring mismatched cleavage planes, P_{p2}. Then

$$P_p = P_{p1} P_{p2} \qquad (4)$$

P_{p1} is determined by the microstructural configuration of grain boundary and hence, is also regarded as a constant for a given material. P_{p2} is determined by the mismatch of cleavage plane systems between neighboring grains and is dependent on the included angle between the initial (cleavage) crack plane and the cleavage plane in the neighboring grain, α. If the stress to separate the cleavage plane is S_t, the condition for the crack propagation across the neighboring cleavage plane is

$$hS_1 \cos^2 \alpha = S_t \qquad (5)$$

where h is the microstructure-determined stress concentration factor and S_1 is the first principal stress ahead of a notch/crack. On the other hand, as a special case in plain tension, the corresponding condition for the crack propagation under the stress S_{co} is

$$hS_{co} \cos^2 \alpha_0 = S_t \qquad (6)$$

where α_o represents the critical value of α. In the case of homogeneous straining of the specimen cross-section in plain tension, there are numerous initial cracks nucleated prior to final fracture (19-21) and only the crack (*i.e.* CFO) with the minimum value of α can propagate catastrophically, following the least energy principle. Accoding to the physical implication of S_{co} stated ealier, it is suggested that α_o should take a very small value approaching zero. For a first order approximation, let $\cos \alpha_o = 1$. Dividing Eq. 6 by Eq. 5 gives the largest permissible α qualified for crack propagation under the principal stress S_1 in a notched/cracked specimen:

$$\cos \alpha = \sqrt{\frac{S_{co}}{S_1}} \qquad (7)$$

or

$$\alpha = \cos^{-1} \sqrt{\frac{S_{co}}{S_1}} \qquad (7')$$

Because the cleavage plane system {100} is an orthogonal system, the largest included angle between an initial crack plane and a cleavage plane in the neighboring grain is $\alpha_{\max} = \cos^{-1} \frac{1}{\sqrt{3}}$. Spatially this α_{max} forms a cone-spheroid whose volume is proportional to $1 - \cos(\cos^{-1} \frac{1}{\sqrt{3}})$, *i.e.* $1 - \frac{1}{\sqrt{3}}$. This cone-spheroid determines the largest possible spatial range in which the initial crack plane intersects with a cleavage plane in the neighboring grain. A similar cone-spheroid can be defined for α, whose volume is proportional to $(1\text{-}\cos\alpha)$. Consequently P_{p2} can be calculated according to the principle of geometrical probability and using Eq. 7:

$$P_{p2} = \frac{1 - \cos \alpha}{1 - \frac{1}{\sqrt{3}}} = \frac{3 + \sqrt{3}}{2} \left(1 - \sqrt{\frac{S_{co}}{S_1}}\right) \qquad (8)$$

In Eq. 3, the volume of a ferritic grain is statistically estimated as $V = \lambda D^3$ where D is the grain diameter and λ is a proportionality constant of the material. Considering the singularity of the stress distribution near the main crack plane, it is reasonable to assume that the fracture is primarily dependent on the layer of grains at the main crack plane. Then $dv = \beta BD\, dx$ where B is the

specimen thickness and β is another proportionality constant of the material. Here, x is a non-dimensional coordinate (relative to coordinate X) along the specimen width direction, *i.e.* $x = X/\rho$ where ρ is the radius of curvature of a notch/crack-tip. Substituting Eq. 3 by Eqs. 4 and 8 as well as these expressions of V and dv, we have

$$\int_{x_e}^{x_y} (1-\sqrt{\frac{S_{co}}{S_1}})dx = C \qquad (9)$$

where x_e and x_y are respectively the starting and ending edges of EYZ (Fig. 3) and C is a constant for a given specimen and

$$C = \frac{3-\sqrt{3}}{3}\frac{\lambda D^2}{\beta B P_{p1} P_n} \qquad (10)$$

Using the FEM calculation results (19, 30, 57) the function $S_1 / \sigma_y = f(x)$ can be expressed as a quadratic approximation:

$$\frac{S_1}{\sigma_y} = 1 + ax - bx^2 \qquad (b>0) \qquad (11)$$

with a and b as constants. The values of a and b depend on specimen geometry and loading mode, *e.g.* for a V-notch with ρ = 0.25 mm in three-point bending, $a \approx 0.75$, $b \approx 0.13$ and for a pseudo-crack with ρ = 0.1 mm in the same loading mode, $a \approx 1.19$, $b \approx 0.18$. When Eq. 9 is substituted by Eq. 11 and integrated, we have

$$(x_y - x_e) = C + \frac{\Phi}{\sqrt{b}}(\sin^{-1}\frac{2bx_y - a}{\sqrt{a^2+4b}} - \sin^{-1}\frac{2bx_e - a}{\sqrt{a^2+4b}}) \qquad (12)$$

where $$\Phi = \sqrt{\frac{S_{co}}{\sigma_y}} \qquad (13)$$

It has been a mathematical principle for approximation that $\sin^{-1} u \approx u$ when $|u|$ is small enough, where u is an arbitrary variant. Considering the range of values x_e, x_y, a and b in the present case, the error is less than 3% by adopting this principle. Therefore Eq. 12 is simplified through this approximation to be:

$$(1-\frac{2\Phi\sqrt{b}}{\sqrt{a^2+4b}})(x_y - x_e) = C \qquad (14)$$

When $T \le T_{co}$, $\sigma_y \ge S_{co}$, then EYZ coincides with the whole yield zone and we have

$$x_e = 0 \quad (T \le T_{co}) \qquad (15)$$

When $T \ge T_{co}$, x_e is determined using Eq. 11 by assuming $S_1 = S_{co}$:

$$x_e = \frac{a + \sqrt{a^2 + 4b(1-\Phi^2)}}{2b} \qquad (16)$$

The constant C can be determined using data obtained at $T = T_{co}$: Φ = 1 (Eqs. 1 and 13) and x_e = 0 (Eq. 15). Thus Eq. 14 gives

$$C = (1-\frac{2\sqrt{b}}{\sqrt{a^2+4b}})x_{y(T=T_{co})} \qquad (17)$$

In Eq. 17, $x_y (T = T_{co})$ can be determined by the value of σ_{fn} measured at T_{co} and the FEM calculation results (19, 30, 57) which provide a relation of x_y against σ_{fn}. As such it is possible to use Eq. 14 to estimate the value of x_y qualified for cleavage fracture. And, x_y thus calculated determines the width of EYZ when it is combined with the value of x_e. Here, two approaches are made to verify the validity of the probabilistic criterion for cleavage fracture of notched/cracked specimens. First, the center of CFO is located as the non-dimensional distance x_r (= X_r/ρ) by scanning electron microscopy (SEM) (21) and is compared with the data of x_y calculated by Eq. 14 and x_e calculated by Eqs. 15-16. A typical comparison of these data is given in Table I. It is clear from Table I that $x_e < x_r < x_y$, *i.e.* the observed CFO always falls within the calculated range of EYZ.

Table I. Calculated (ca.) and measured (me.) data on the range of EYZ

Specimen Type	*A: V-notch, ρ = 0.25 mm*					*B: pseudo-crack, ρ = 0.06 mm*				
Temp. / K	93	103	113	128	143	83	98	113	133	148
x_e *(ca.)*	0	0	0.12	0.38	0.64	0	0	0.21	0.49	0.94
x_v *(ca.)*	1.81	1.92	2.13	2.71	3.12	1.62	1.95	2.57	3.24	3.81
x_r *(me.)*	1.17	0.93	1.85	1.59	2.71	0.98	1.16	2.49	3.02	2.91

Note: data for a mild steel with 0.18 wt.% C, annealed at 1423 ℃, solution heated at 933 ℃ and aged at 473 ℃, with grain size D = 0.094 mm and S_{co} = 705 MPa

As an alternative approach, nominal fracture stress σ_{fn} is calculated by the FEM results (19, 30, 57) on σ_{fn} as a function of x_y which, in turn, is calculated by Eq. 14. Calculated and measured values of σ_{fn} are compared in Table II. It is found that a fairly satisfying agreement is achieved between the calculated and the measured values of σ_{fn}, with a relative error of less than 2.5 %.

Table II. Calculated (ca.) and measured (me.) values of nominal fracture stress σ_{fn}(MPa)

Specimen Type	*A: V-notch, ρ = 0.25 mm*					*B: pseudo-crack, , ρ = 0.06 mm*				
Temp. / K	93	103	113	128	143	83	98	113	133	148
σ_{fn}*(ca.)*	863	878	887	912	941	510	574	637	668	721
σ_{fn}*(me.)*	856	875	892	905	917	503	581	625	673	716

Note: material's data as noted in Table I.

Both approaches prove the validity of the probabilistic model of cleavage fracture as expressed by Eq. 2 or Eq. 3. Since the model is based on the assumption of S_{co} as the characteristic parameter of the material, the success in performing the two approaches establishes that S_{co} also controls the cleavage fracture behavior of notched/cracked specimens as well as of smooth specimens.

Strictly speaking, the effect of notch/crack-tip blunting should be taken into account for cleavage fracture at temperatures $T \geq T_{co}$. However, experimental observations (19, 30, 49, 52) indicate that the blunting effect is not evident so long as $T \leq T_{gy}$. When $T > T_{gy}$, this effect has to be evaluated since the fracture occurs after general yielding. This is done by introducing an increment ΔS_c, caused by notch/crack-tip blunting, into S_{co}, *i. e.* by replacing S_{co} with $(S_{co} + \Delta S_c)$ in Eqs. 12-14. ΔS_c depends on the amount of plastic deformation prior to fracture and is determined by the increment $(S_f - S_{co})$ in the temperature range $T_{co} \leq T \leq T_{cf}$ (Fig. 1). It is emprically related to the true plastic strain ε_f as:

$$\Delta S_c = m \varepsilon_f^{\,n} \tag{18}$$

where m and n are constants, *e. g.* $m \approx 75$ and $n \approx 0.65$ for a mild steel with 0.18 wt.% carbon (19). This correlation for the notch/crack-tip blunting effect has also been proved to be successful in the prediction of the cleavage fracture behavior of notched/cracked specimens in the temperature range of $T_{gy} < T \leq T_c$ (19, 30, 57).

Special attention is due to the cleavage fracture at T_c where the stress intensification factor Q_e reaches its maximum value $Q_{e,max}$. Then the cleavage fracture

criterion at T_c can be expressed, in a simplified form but with adequate engineering accuracy, as

$$\begin{cases} Q_{e,\max}\sigma_{y(T_c)} = S_{co} \\ r = r_e \end{cases} \qquad (19)$$

in replacing Eq. 2. For instance, experimental ratio of $S_{co} / \sigma_{y(T_c)}$ for a V-notched bend specimen and a pseudo-crack ($\rho = 0.06$ mm) bend specimen are 2.15 and 2.37 respectively, well approaching 2.12 and 2.36 calculated separately by FEM for $Q_{e,max}$. It is worth while noting that $Q_{e,max}$ = 1 for plain tension. In other words, Eq. 1 is just a special case of Eq. 19, indicating the consistency of the ductile-brittle transition behavior among different specimen geometries.

With a further increase in temperature, the probabilistic condition for cleavage fracture cannot be met without inducing evident work-hardening of the yield zone. So the nominal fracture stress σ_{fn} now turns to increasing steeply with temperature and finally this leads to the onset of fibrous fracture by micro-void coalescence. Therefore Eq. 19 is also a presentation of the criterion for the macroscopic ductile-brittle transition of cleavage fracture.

In concluding this section, it is established that cleavage fracture criterion can be unified among smooth, notched and cracked specimens by assuming S_{co} as the characteristic parameter of the material controlling the physically identical fracture process in different mechanical loading conditions.

Fracture under Dynamic Load: Further Confirming S_{co}

For S_{co} to qualify a characteristic resistance of the material to cleavage fracture, it is assumed to be independent of both temperature and strain rate. The temperature independence of S_{co} has been clarified by successful verification of the modeling of the cleavage fracture behavior of notched/cracked specimens in the preceding section. The effect of strain rate on S_{co} and S_{co}-based cleavage fracture model has yet to be investigated. In the present work the dynamic aspects of cleavage fracture behavior is also studied under different mechanical conditions using smooth, notched and cracked specimens.

As is demonstrated earlier, a direct measurement of S_{co} is achieved by performing the plain tensile test at various temperatures (Fig. 1). Hence this type of test has been conducted at different strain rates ranging $10^{-4} \sim 10^{1}$ s^{-1} to investigate the response of fracture behavior to dynamic loading (59-60). It is found that (59-60) as strain rate increases, the yield strength σ_y *vs* temperature curve shifts upward to a higher stress level and, as a result, the ductile-brittle transition temperature T_{co} shifts to a higher temperature, as is shown in Fig. 4. Nevertheless, the value of S_{co} is virtually insensitive to strain rate variation, with a change of less than 2% (59-60) within the rate range tested. As is illustrated in Fig. 4, the mechanism by which high strain rates intensify the low-temperature embrittlement, as is frequently encountered, is not due to a degradation of the characteristic resistance of the material to cleavage fracture (S_{co}), but to an elevation of the ductile-brittle transition temperature (T_{co}), which, in turn, is caused by an increase in yield strength. With the strain rate independence of S_{co}, it is reasonably assumed that S_{co} should also control the cleavage fracture behavior under dynamic loading conditions, and this is to be examined by probing into the dynamic fracture characteristics of notched and cracked specimens, as described below.

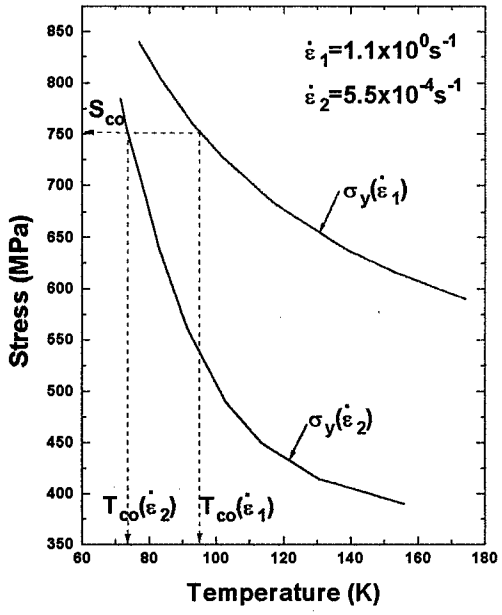


Fig. 4: The effects of strain rate on yield stress, cleavage fracture stress and ductile-brittle transition temperature (60-61).

Impact tests have been conducted using the instrumented Charpy impact testing machine (60). The specimens used are mainly of two types: one is the standard Charpy V-notch (CVN) specimen (ASTM E-23) and the other is the pseudo-crack specimen (with the crack sawn by an electrical charge release cutting machine, giving a crack-tip radius of 0.06 mm) (60). It is found from these tests that the fracture load varies with test temperature in a similar manner as is shown in Fig. 2 for the case of static loading and especially, the fracture load exhibits a similar trough at a definite temperature T_c. Here T_c also represents the temperature for the ductile-brittle transition as in the static loading conditions. For now T_c corresponds to the temperature at which both fracture load and the absorbed impact energy show a transition. The similar macromechanical behavior makes it plausible to assume the micromechanism of the dynamic fracture based on that of the static fracture.

To verify whether S_{co} is still effective in controlling cleavage fracture behavior of notched/cracked specimens under dynamic loading, it is convenient to check whether the cleavage criterion as described by Eq. 2 or Eq. 19 is still valid for the corresponding conditions. For this verification the independence of S_{co} on strain rate is assumed together with the probabilistic requirement of forming EYZ as in the static loading conditions. Here attention is put on the variation in the yield strength σ_y as a result of the damping of the strain rate across the notch/crack section even under a definite (external) loading rate. Then it is crucially important to determine the strain rate distribution across the notch/crack section, especially in EYZ. The automatic dynamic incremental nonlinear analysis (ADINA) program (61) has been adopted as an FEM tool to calculate this strain rate variation as functions of both the loading time and the distance from notch/crack-tip (60). It is predicted by the results of the calculation (60) that there exists a steep distribution of the equivalent strain rate $\dot{\varepsilon}$ (corresponding to the equivalent strain) along the distance from notch/crack-tip: $\dot{\varepsilon}$ decreases steeply with increasing the distance. To examine Eq. 2 or Eq. 19, the value of $\dot{\varepsilon}$ at the near-tip edge of EYZ (x_e), $\dot{\varepsilon}_e$, has to be estimated in order to determine the corresponding value of σ_y. As a typical example, the fracture behavior at T_c as expressed by Eq. 19 is examined here. For the instrumented Charpy impact test using the CVN specimen, the value of $\dot{\varepsilon}_e$ is approximately 3 s^{-1}. Then $\sigma_y(T_c, \dot{\varepsilon}_e)$, the effective yield strength at temperature T_c and strain rate $\dot{\varepsilon}_e$, is estimated as follows.

The yield strength of steels at a strain rate $\dot{\varepsilon}$ under a temperature T can be expressed as (62-63)

$$\sigma_y(\dot{\varepsilon},T) = A(T) + B(T)\ln\dot{\varepsilon} \quad (10^{-4} < \dot{\varepsilon} < 10^{3}) \qquad (20)$$

where $A(T)$ and $B(T)$ are temperature-dependent constants. By conducting plain tensile tests at two different strain rates $\dot{\varepsilon}_1$ and $\dot{\varepsilon}_2$ but at the same temperature T to give $\sigma_y(\dot{\varepsilon}_1, T)$ and $\sigma_y(\dot{\varepsilon}_2, T)$ and using the combination

$$\begin{cases} \sigma_y(\dot{\varepsilon}_1,T) = A(T) + B(T)\ln\dot{\varepsilon}_1 \\ \sigma_y(\dot{\varepsilon}_2,T) = A(T) + B(T)\ln\dot{\varepsilon}_2 \end{cases} \qquad (21)$$

the constants $A(T)$ and $B(T)$ can be determined. Then Eq. 20 becomes

$$\sigma_y(\dot{\varepsilon},T) = \sigma_y(\dot{\varepsilon}_1,T) + \\ +[\sigma_y(\dot{\varepsilon}_2,T) - \sigma_y(\dot{\varepsilon}_1,T)]\frac{\ln\dot{\varepsilon} - \ln\dot{\varepsilon}_1}{\ln\dot{\varepsilon}_2 - \ln\dot{\varepsilon}_1} \qquad (22)$$

Let $T = T_c$, then, for a mild steel 16Mn (60), we have

$$\dot{\varepsilon}_1 = 5.5 \times 10^{-4}\ s^{-1},\ \sigma_y(\dot{\varepsilon}_1, T_c) = 270\ \text{MPa}$$
$$\dot{\varepsilon}_2 = 5.5 \times 10^{-2}\ s^{-1},\ \sigma_y(\dot{\varepsilon}_2, T_c) = 328\ \text{MPa}$$

Let $\dot{\varepsilon} = \dot{\varepsilon}_e \approx 3\ s^{-1}$ for the case of the CVN specimen, then Eq. 22 gives the corresponding effective yield strength as

$$\sigma_y(\dot{\varepsilon}_e, T_c) = 378\ \text{MPa}$$

Take S_{co} = 745 MPa as is assumed to be strain rate independent, resulting in $S_{co}/\sigma_y(\dot{\varepsilon}_e, T_c)$ = 1.97, fairly approaching the theoretical value of $Q_{e,max}$ = 1.96 calculated by FEM for a standard CVN specimen (60). In the case of the pseudo-crack specimen mentioned above, $\dot{\varepsilon}_e \approx 50\ s^{-1}$. Following the same procedure, it is found that $S_{co}/\sigma_y(\dot{\varepsilon}_e, T_c)$ = 2.37, also fairly approaching the FEM result of $Q_{e,max}$ = 2.36 for this type of specimen (60). This agreement of $S_{co}/\sigma_y(\dot{\varepsilon}_e, T_c)$ with $Q_{e,max}$ justifies the consistence in cleavage fracture criterion (Eq. 19) between static and dynamic loading conditions.

Note that the verification is made by assuming the strain rate independence of S_{co} and the validity of the EYZ-based probabilistic cleavage fracture model. Therefore S_{co} is believed to control cleavage fracture behavior under dynamic loading as well as under static loading.

Summary

The present paper concentrates on building up a unified criterion for cleavage fracture based on the establishment of the "cleavage-characteristic stress" S_{co} as the characteristic resistance of the material to cleavage fracture. Assuming an identical physical implication of cleavage fracture process, the concept of S_{co} is initiated from the results of plain tension (Fig. 1 and Eq. 1). The microscopic analysis identifies the existence among initial cracks of the "cleavage fracture origin" (CFO) which is the most advantageous in the combination of stress concentration, crack dimension and crack orientation. S_{co} is micromechanically regarded as the minimum stress for the propagation of the unblunted CFO. Then S_{co} is verified in the loading conditions with stress concentration and constraint as in notched and cracked specimens. By defining the "effective yield zone" (EYZ) ahead of a notch/crack, a probabilistic cleavage fracture model is formulated and examined by experimental data as predicting satisfactorily the location of CFO and the fracture load in the temperature range involved. Regarding the dynamic aspect of cleavage fracture, the strain rate independence of S_{co} is primarily verified by experimental measurement in plain tensile tests and further confirmed by test results obtained from notched and cracked specimens. The strain rate distribution in the region corresponding to EYZ is used to determine the effective yield strength therein and the agreement between experimental and analytical data justifies the consistence in cleavage fracture behavior under static and dynamic loading.

Acknowledgment

The present study has been supported mainly by the State Natural Science Foundation through the contract 58870042.

References

1. C. Zener, "The Micromechanism of Fracture," Trans. ASM, 40A (1948), 3-4.

2. A. N. Stroh, "The Formation of Cracks as a Result of Plastic Flow," Proceedings of the Royal Society, A223 (1954), 404-414.

3. E. Smith, "The Nucleation and Growth of Cleavage Microcracks in Mild Steels," in Proceedings of Conference on Physical Basis of Yield and Fracture, (Oxford: Institute of Physics and Physical Society, 1966), 36-39.

4. E. A. Almond, D. H. Timbres and J. D. Embury, "The Influence of Second Phase Particles on Brittle Fracture," in Fracture 1969 (Proc. of ICF2), (London: Chapman and Hall, 1969), 253-256.

5. A. H. Cottrell, "Theory of Brittle Fracture in Steel and Similar Materials," Trans. AIME, 212 (1958), 192-195.

6. D. Hull, "Twinning and Fracture of Single Crystals of 3% Silicon Iron,"Acta Metall., 8 (1960), 11-16.

7. J. P. Naylor and P. R. Krahe, "Cleavage Planes in Lath Type Bainite and Martensite," Metall. Trans. A, 6A (1975), 594-598.

8. J. P. Naylor and R. Blondeau, "The Respective Roles of the Packet Size and the Lath Width on Toughness," Metall. Trans. A, 7A (1976), 891-894.

9. P. Brozzo, G. Buzzichelli, A. Mascanzoni and M. Mirabile, "Microstructure and Cleavage Resistance of Low-Carbon Bainitic Steels," Met. Sci., 11 (1977), 123-127.

10. Z. E. Liu and Q. G. Cai, "The Application of Fracture Physics Parameter σ_F* in Controlled Rolling," Iron and Steel Sinica, 17(1) (1982), 12-17.

11. D. E. McRobie and J. F. Knott, "Effects of Strain and Strain Aging on Fracture Toughness of C-Mn Weld Metal," Mater. Sci. Tech., 1 (1985), 357-365.

12. T. J. Baker, F. P. L. Kavishe and J. Wilson, "Effect of Non-Metallic Inclusions on Cleavage Fracture," Mater. Sci. Tech., 2 (1986), 576-583.

13. W. S. Owen, B. K. Averbach and M. Cohen, "Brittle Fracture of Mild Steel in Tension at 196 °C," Trans. ASM, 50 (1958), 634-640.

14. C. J. McMahon Jr and M. Cohen, "Initiation of Cleavage in Polycrystalline Iron," Acta Metall., 13 (1965), 591-598.

15. L. E. Kaechele and A. S. Tetelman, "A Statistical Investigation of Microcrack Formation," Acta Metall., 17 (1969), 463-471.

16. M. Cohen and M. R. Vukcevich, Physics of Strength and Plasticity (Cambridge, Mass.: MIT Press, 1969).

17. J. R. Rice and R. Thompson, "Ductile versus Brittle Behavior of Crystals," Philosophical Magazine, 29 (1974), 73-80.

18. J. D. G. Groom and J. F. Knott, "Cleavage Fracture in Prestrained Mild Steel," Met. Sci., 9 (1975), 390-396.

19. D. M. Li, "Cleavage Fracture and Low-Temperature Embrittlement of Mild Steels" (Ph. D. Thesis, Harbin Institute of Technology, 1987).

20. D. M. Li, M. Su and M. Yao, "Microscopic Analysis of the Cleavage Crack Origin in a Mild Steel," Metal Science and Technology Sinica, 7(4) (1988), 8-14.

21. D. M. Li and M. Yao, "A Metallographic and Fractographic Study of the Origin of Cleavage Fracture in Mild Steel," Materials Characterization, 36 (1996), 27-33.

22. J. F. Knott, "Some Effects of the Hydrostatic Tension on the Fracture Behavior of Mild Steels," JISI, 204 (1966), 104-111.

23. T. R. Wilshaw, "Deformation and Fracture of Mild Steel Charpy Specimens," JISI, 204 (1966), 936-942.

24. T. R. Wilshaw, C. A. Rau and A. S. Tetelman, "A General Model to Predict the Elastic-Plastic Stress Distribution and Fracture Strength of Notched Bars in Plane Strain Bending," Engng Fract. Mech., 1 (1968), 191-199.

25. G. Oates, "Effect of Hydrostatic Stress on Cleavage Fracture in a Mild Steel and a Low-Carbon Maganese Steel," JISI, 206 (1968), 930-935.

26. G. Oates, "Effect of Temperature and Strain Rate on Cleavage Fracture in a Mild Steel and a Low-Carbon Maganese Steel," JISI, 207 (1969), 353-358.

27. J. R. Griffiths and D. R. J. Owen, "A Elastic-Plastic Stress Analysis for a Notched Bar in Plane Strain Bending," J. Mech. Phys. Solids, 19 (1971), 419-427.

28. J. F. Knott, "Mechanics and Mechanisms of Large-Scale Brittle Fracture in Structural Metals," Mater. Sci. Eng., 7 (1971), 1-36.

29. J. F. Knott, Fundamentals of Fracture Mechanics (London: Butterworths, 1973).

30. Y. K. He, "The Cleavage Fracture Behavior in Notched Specimens of Mild Steels" (Master Degree Thesis, Harbin Institute of Technology, 1982).

31. M. Yao, Y. K. He and D. M. Li, "A Mechanical-Metallurgical Analysis of the Cleavage Fracture Criterion in Notched Specimen of Mild Steels," Iron and Steel Sinica, 19(12) (1984), 10-18.

32. R. O. Ritchie, J. F. Knott and J. R. Rice, "Further Study on the Mechanism of Cleavage Fracture at Low Temperatures," J. Mech. Phys. Solids, 21 (1973), 395-410.

33. J. R. Rice and G. F. Rosengren, "Plane Strain Deformation near a Crack Tip in a Power-Law Hardening Material," J. Mech. Phys. Solids, 16 (1968), 1-12.

34. J. W. Hutchinson, "Singular Behavior at the End of a Tensile Crack in a Hardening Material," J. Mech. Phys. Solids, 16 (1968), 13-22.

35. J. R. Rice and M. A. Johnson, Inelastic Behavior of Solids (New York: McGraw-Hill, 1970).

36. N. Levy, P. V. Marcal, W. Ostergren and J. R. Rice, "Small Scale Yielding near a Crack in Plane Strain: A Finite Element Analysis," Int. J. Fracture, 7 (1971), 143-152.

37. P. Bowen, S. G. Druce and J. F. Knott, "Micromechanical Modeling of Fracture Toughness," Acta Metall., 35 (1987), 1735-1744.

38. J. H. Chen, G. Z. Wang and L. Zhu, "Further Study on the Scattering of the Local Fracture Stress and Allied Toughness Values," Metall. Trans. A, 22A (1991), 2287-2296.

39. D. A. Curry and J. F. Knott, "Effects of Microstructure on Cleavage Fracture Stress in Steel," Met. Sci., 12 (1978), 511-514.

40. D. A. Curry and J. F. Knott, "Effect of Microstructure on Cleavage Fracture Toughness of Quenched and Tempered Steels," Met. Sci., 13 (1979), 341-346.

41. A. Pineau, "Review of Fracture Micromechanisms and a Local Approach to Predicting Crack Resistance in Low Strength Steels," in Advances in Fracture Research

(Proc. of ICF5), ed. D. Francois *et al* (Oxford: Pergamon Press, 1981), vol. 2, 553-560.

42. A. G. Evans, "Statistical Aspects of Cleavage Fracture in Steel," Metall. Trans. A, 14A (1983), 1349-1357.

43. F. M. Beremin, "A Local Criterion for Cleavage Fracture of a Nuclear Pressure Vessel Steel," Metall. Trans. A, 14A (1983), 2277-2287.

44. C. X. Hou, Q. G. Cai, Y. Su and X. Y. Zheng, "Volume Effect On Cleavage Strength, Microstructure And Fracture Micromechanism of Welded 15MnVN Steel,"in Advances in Fracture Research (Proc. of ICF6), ed. S. R. Valluri *et al* (Oxford: Pergamon Press, 1984), vol. 2, 1415-1422.

45. T. Lin, A. G. Evans and R. O. Ritchie, "A Statistical Model of Brittle Fracture by Transgranular Cleavage," J. Mech. Phys. Solids, 34 (1986), 477-497.

46. T. Lin, A. G. Evans and R. O. Ritchie, "Statistical Analysis of Cleavage Fracture ahead of Sharp Cracks and Round Notches," Acta Metall., 34 (1986), 2205-2214.

47. T. Lin, A. G. Evans and R. O. Ritchie, "Stochastic Modeling of the Independent Roles of Particle Size and Grain Size in Transgranular Cleavage Fracture," Metall. Trans. A, 18A (1987), 641-651.

48. A. Martín-Meizoso, I. Ocaña-Arizcorreta, J. Gil-Sevillano and M. Fuentes-Pérez, "Modeling Cleavage Fracture of Bainitic Steels," Acta Metall. Mater., 42 (1994), 2057-2068.

49. M. Yao, D. M. Li, Z. Huang and C. Z. Zhou, "Cleavage-Characteristic Stress S_{co} and its Role in Low-Temperature Fracture Behavior of Mild Steel," in Proceedings of Sino-Japanese Symposium on Materials Science , ed. T. C. Lei and N. Igata (Harbin: HIT Press, 1986), 205-214.

50. D. M. Li and M. Yao, "Effect of Precipitation and Grain Size on Ductile-to-Brittle Transition in Mild Steels," Mater. Chem. Phys., 24 (1989) 157-162.

51. D. M. Li and M. Yao, "Effect of Hardening Mechanism on Cryogenic Brittleness of Steel," Metal Science and Technology Sinica, 9(3) (1990), 18-23.

52. D. M. Li and M. Yao, "Critical Crack Size for Low-Temperature Brittleness of Mild Steel in Tension of Center-Cracked Sheet," Mater. Chem. Phys., 24 (1990), 429-434.

53. Z. Huang and M. Yao, "Research into Brittle/Ductile Transition Temperature," Scripta Metall., 23 (1989), 2137-2144.

54. J. F. Knott, "Effects of Notch Depth on the Toughness of Mild Steel," in Fracture 1969 (Proc. of ICF2) (London: Chapman-Hall, 1969), 205-218.

55. A. S. Tetelman and T. R. Wilshaw, "A Criterion for Plastically Induced Cleavage after General Yield in Notched Bend Specimens", in Fracture 1969 (Proc. of ICF2) (London: Chapman-Hall, 1969), 219-228.

56. R. Hill, The Mathematical Theory of Plasticity (Oxford, 1950).

57. Z. Huang and M. Yao, "Calculation of Cleavage Fracture Stress in Low-Carbon Steel," Metal Science and Technology Sinica, 6(2) (1987), 1-9.

58. R. Wang, Fundalmentals of Mechanics of Plasticity (Beijing: Science Press, 1981).

59. W. S. Lei and M. Yao, "Effect of Strain Rate on Cleavage Fracture of Mild Steel in Plain Strain Tension Testing," Scripta Metall. Mater., 25 (1991), 2669-2670.

60. W. S. Lei and M. Yao, "The Cleavage-Characteristic Stress for Steels" (HIT Technical Report for SNSF Project 58870042, Harbin Institute of Technology, 1992).

61. X. H. Zhao, translated from: K. J. Bathe, ADINA/ADINAT User's Manual (Beijing: Mechanical Industry Press, 1986).

62. Z. E. Liu and Q. G. Cai, "Determination of Dynamic Yield Strength σ_{ys}* and Cleavage Fracture Stress σ_f* Using Instrumentated Charpy Tests," Physical Mechanical Testing Sinica (Physics Branch), 6 (1981), 15-21.

63. Y. N. Liu, J. H. Zhu and H. J. Zhou, "Strength of a Low Carbon Steel at Different Temperatures and Strain Rates," Materials Science Progress Sinica, 4(4) (1990), 285-291.

SHEAR-INDUCED CLEAVAGE FRACTURE

Kwai S. Chan

Southwest Research Institute
P. O. Drawer 28510
San Antonio, Texas 78228-0510

Abstract

Experimental evidence shows that shear-induced cleavage fracture is prominent in many intermetallic alloys and in-situ composites, as well as in other brittle materials. In materials with a plastically deformable matrix, the characteristics of shear-induced cleavage fracture generally include planar slip, slipband decohesion, and cleavage crack formation. In contrast, shear cracks with wing-tip cleavage cracks dominate in plastically nondeformable materials subjected to compressive loads. In this article, the phenomenon of shear-induced cleavage fracture is revisited. Theoretical analyses of the driving force for the fracture process are summarized to illustrate the salient features of shear-induced cleavage fracture and to derive the critical condition for crack instability. Applications of the brittle fracture theory to treating shear-induced cleavage in TiAl alloys, Nb-Cr-Ti alloys, rock salt, and alumina scales on overlay coatings are presented with experimental verifications.

Introduction

The instigation of cleavage fracture by shear is quite well known. The nucleation of a cleavage crack by a linear array of dislocation pileup was first analyzed by Stroh [1-3]. This analysis was subsequently generalized by Smith [4-6] to consider crack nucleation by several dislocation pileup configurations under a stress gradient. The onset of crack nucleation by cleavage and slipband decohesion was determined from an energy balance and the Griffith fracture criterion [7]. These analyses show that cleavage crack nucleation ahead of a dislocation pileup is energetically feasible when the elastic energy release rate exceeds the energy expenditure in creating the fracture surfaces.

The failure of brittle materials subjected to compression frequently occurs through the development of wing cracks, which are cleavage cracks at the tip of shear cracks [8-15]. Nucleated by the tensile stress of the near-tip field of the shear crack, the wing cracks are aligned almost parallel to the maximum compressive stress direction [8-10]. The nucleation and propagation of the wing cracks have been analyzed using a continuous dislocation approach as well as by analytical approaches [11-15]. The continuous dislocation approach is rigorous, but the governing singular integral equations must be solved numerically [8-10]; the analytical approaches lead to approximate solutions in closed form expressions [11-15].

Recent experimental evidence indicates that slipband decohesion and cleavage are the predominant fracture mechanisms in TiAl-based intermetallic alloys [16, 17] and

George R. Irwin Symposium on Cleavage Fracture
Edited by Kwai S. Chan
The Minerals, Metals & Materials Society, 1997

Nb-Cr-Ti solid solution alloys [18, 19]. In both cases, dislocation pileups play an important role in the fracture process. In materials such as rock salt [20], the predominant fracture process under compression appears to be the propagation of cleavage cracks (wing cracks) induced at the tip of shear cracks. These experimental findings provide evidence that shear-induced cleavage fracture is an important fracture mechanism in both brittle and ductile materials. While cleavage fracture in brittle materials is fairly well understood, the formation of cleavage cracks in the presence of plastic flow is not. The simultaneous occurrence of slipband decohesion, which is mode II fracture, and cleavage fracture, which is mode I fracture, in TiAl alloys and Nb-Cr-Ti solid solution alloys [18, 19] is still poorly understood.

In this paper, experimental evidence of shear-induced cleavage fracture and slipband decohesion is presented. The salient features of these fracture processes are analyzed by extending the Stroh approach to include the presence of plastic flow during crack nucleation. Analyses are presented for both slipband decohesion and cleavage fracture. The analytical results are used to elucidate the conditions for the onset of slipband decohesion and cleavage fracture in TiAl-based and Nb-Cr-Ti alloys as well as cleavage fracture in rock salt and in the brittle oxide scale formed in metallic surfaces and coatings at elevated temperatures.

Shear-Induced Fracture Mechanisms

Two distinctly different fracture mechanisms can be induced by the action of a dislocation pileup subjected to a shear stress: cleavage fracture and slipband decohesion. The driving forces for these two distinctly differently fracture processes are illustrated in Figure 1 (a) and (b), which show the shear and normal stresses associated with a shear crack [21]. The stress field of a shear crack is essentially identically to that of a dislocation pileup [22]. Both tensile and compressive normal stresses exist at the tip of a dislocation pileup. The tensile stress serves as a driving force for the initiation and propagation of a pair of cleavage cracks, while the shear stress on the dislocation pileup serves as the driving force for decohesion along the slip plane. In case of the shear crack, the near-tip tensile stress acts to initiate and propagate the cleavage cracks, while the shear stress tends to propagate the shear crack itself. Shear-induced cleavage cracks, which have also been referred to as wedge cracks, wing cracks, or Stroh's cracks [1-3], are usually aligned normal to the direction of the maximum tensile stress, which occurs at an angle of 70.5° measured from the tip of the shear crack or the dislocation pileup [1-3]. Since the driving force is the stress field of the dislocation pileup or the shear crack, shear-induced cleavage and decohesion are operative both in tension and in compression.

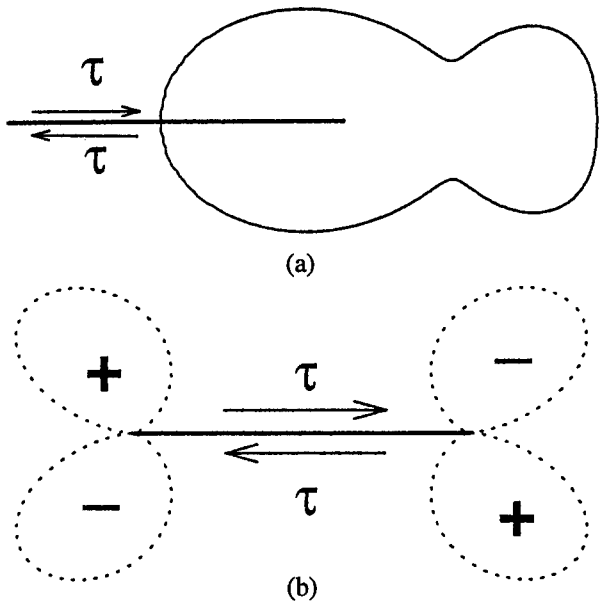


Figure 1: Shear and normal stresses ahead of a dislocation pileup or a shear crack: (a) shear stress, and (b) normal stress.

The formation of slipband cracks is common in planar slip materials such as α+β Ti alloys [23], Ni-base superalloys [24], and Nb-based alloys [18]. Intermetallic alloys based on Ti_3Al [25] and TiAl [16, 17] also exhibit planar slip and slipband cracking. The formation of a crystallographic crack by decohesion along a slip plane in a lamellar TiAl alloy is illustrated in Figure 2, which shows a crack

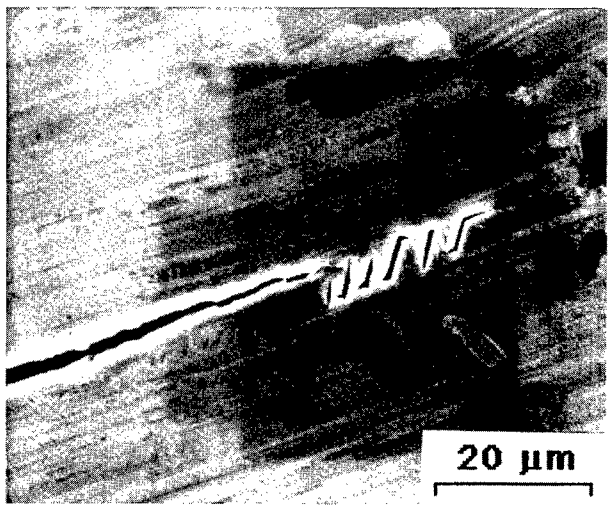


Figure 2: A crystallographic crack propagated along a slip plane in a lamellar TiAl alloy by decohesion of a slipband into a mixed mode crack. Microcracks are also formed near the tip of the slipband crack.

nucleated and propagated along a planar primary slipband in a smooth specimen loaded under tension. Microcrack formation near the slipband crack is also evident in Figure 2. Slipband decohesion has also been observed to occur ahead of a crack tip after a significant amount of plastic deformation. For a solid solution Nb-Cr-Ti alloy [18], the formation of an intense planar slipband ahead of the crack tip occurred at a stress intensity factor, K, of 77 MPa$\sqrt{m}$, Figure 3(a). Upon further loading, the slipband decohered to form a slipband crack at K=82 MPa$\sqrt{m}$, which, in turn, induced the formation of a cleavage crack ahead of the slipband crack, Figure 3(b). The extension of the cleavage crack was unstable and led to fracture.

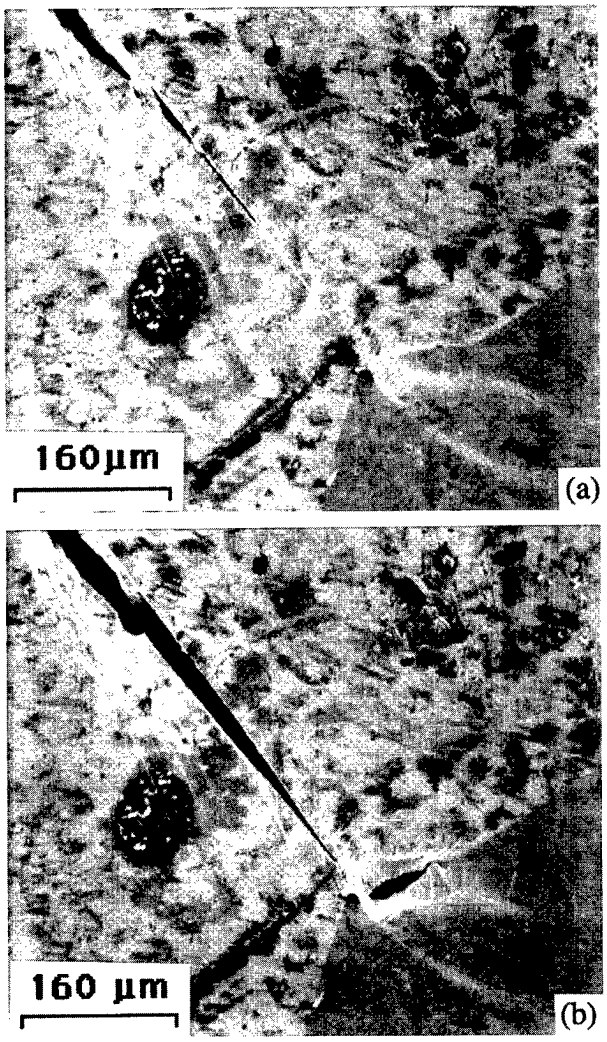


Figure 3: Evidence of slipband decohesion and shear-induced cleavage in an Nb-Cr-Ti solid solution alloy: (a) the decohesion of a slipband into a shear crack in the plastic zone of a mode I crack at K = 77 MPa $\sqrt{m}$, and (b) the nucleation of a cleavage crack at the tip of the slipband shear crack at K = 82 MPa $\sqrt{m}$. From Chan [18]. Loading direction is vertical.

Experimental evidence indicates that slipband decohesion, which is driven by shear, and cleavage fracture, which is driven by the normal stress, can occur concurrently in the presence of substantial plastic flow [18]. Aspects of this fracture process analyzed and summarized in this paper include: (1) the nucleation and growth process of the slipband crack, (2) the nucleation and growth process of the cleavage crack, and (3) the synergisms between plastic flow, slipband crack, and cleavage fracture.

Initiation of Slipband Cracks

Slipband decohesion can be modeled by considering the formation of linear arrays of dislocation pileups on several slip planes within a slipband, Figure 4. According to an analysis by Stroh, the shear stress, τ, acting on a single dislocation pileup on a particular slip plane is given by [2]

$$\tau = \frac{m\tau_o}{2}\left(\frac{L}{r}\right)^{1/2}\left(2\cos\frac{\theta}{2} - \sin\theta\,\sin\frac{3\theta}{2}\right) \qquad (1)$$

where τ_o is the applied shear stress, L is the pileup length, r and θ are the distance and angle measured from the tip of the dislocation pileup, and m is the number of slip planes with dislocation pileups that exert a force on the particular dislocation pileup of interest. For slipband decohesion, θ can be taken as zero. The mode II stress intensity factor acting at the tip of the dislocation pileup is given by [5]

$$K_{II} = \tau\sqrt{2\pi r} \qquad (2)$$

leading to

$$K_{II} = M\tau_o\sqrt{2\pi L} \qquad (3)$$

when Eqs. (1) and (2) are combined with $\theta = 0$. The material is considered to be isotropic and to obey power-law hardening. As described in the Ramberg-Osgood constitutive equation, the applied shear stress is related to the flow stress, σ_o, according to

$$\tau_o = \frac{\sigma_o}{\sqrt{3}} = \frac{\sigma_y}{\sqrt{3}}\left(\frac{\epsilon_p}{\alpha\,\epsilon_y}\right)^{1/n} \qquad (4)$$

where ϵ_p is the plastic strain; σ_y is the yield stress; ϵ_y is the yield strain, n is the inverse of the strain hardening exponent; α is a material constant in the Ramberg-Osgood equation. Substituting Eq. (4) into Eq. (3) and imposing the condition of $K_{II} = K_{IIC}$ leads one to

$$\epsilon_p (d)^{\frac{n}{2}} = \alpha \left(\frac{\sigma_y}{E} \right) \left(\frac{\sqrt{3} K_{IIC}}{\sqrt{\pi m} \sigma_y} \right)^n \qquad (5)$$

when the pileup length, 2L, is taken to be the grain size, d, and the yield strain is expressed as the ratio of the yield stress to the Young's modulus, E.

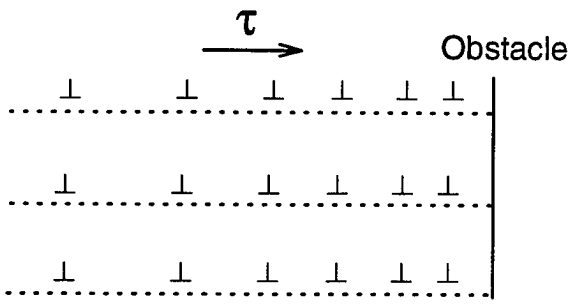


Figure 4: Stroh's model of decohesion of a slip plane by dislocation pileups on multiple slip planes [2].

If fracture is controlled by initiation of a slipband crack, the plastic strain, ε_p, at fracture can be predicted from Eq. (5) if the values of K_{IIC}, σ_y, n, α, and E are known. The calculated fracture strain also depends on the number of pileups, m, involved in the decohesion of the slip plane. Decohesion strain calculation was performed for lamellar TiAl alloys using experimentally determined values of material constants as follows: σ_y = 329.6 MPa, E = 1×10^5 MPa, n = 6, α = 0.58, and K_{IIC} = 18 MPa$\sqrt{m}$. The value of K_{IIC} was assumed to be identical to the K_{IC} value at which crack extension by decohesion of slipbands occurred in lamellar TiAl alloys. Unrealistically large values of ε_p were obtained for $m \leq 3$. As a result, the value of m was chosen to be 4; the calculated values of the fracture strain is shown as a function of grain size in a log-log plot in Figure 5, with the experimental data of tensile ductility. A slope of $-n/2$ is expected based on Eq. (5), but the experimental slope is about -1. Since ε_p depends on K_{IIC}/m, the high calculated values of ε_p for $m \leq 3$ might imply the value of K_{IIC} is considerably less than 18 MPa$\sqrt{m}$ or high decohesion strain is possible if interactions of dislocation pileups on parallel planes could be minimized (i.e., $m < 4$). In either case, the result in Figure 5 suggests that initiation of slipband crack can take place in the presence of a large plastic strain, but it does not appear to be limiting mechanism controlling the ductility of lamellar TiAl alloys for colony size > 100 μm. For colony size < 65 μm, the agreement between the crack nucleation and experimental data is reasonably good that crack nucleation might be the mechanism limiting ductility for fine-grained (< 50 μm) lamellar TiAl alloys.

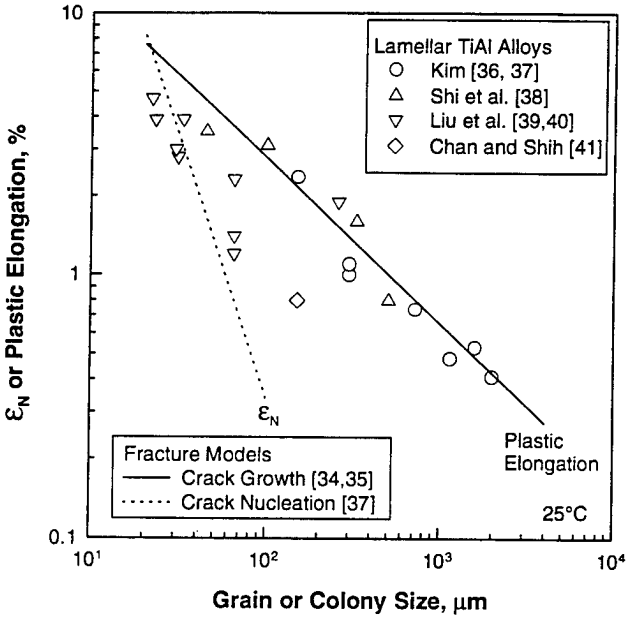


Figure 5: Calculated values of tensile ductility based on microcrack nucleation (slipband decohesion) and microcrack growth (J_{IC} criterion) models compared against experimental data of lamellar TiAl alloys showing different dependence on grain (colony) size. The comparison suggests that the tensile ductility of lamellar alloys is controlled by crack instability and not by microcrack nucleation, except for grain size <50 μm.

Growth of Slipband Cracks

The growth of a slipband crack occurs under mixed mode conditions. The crack-tip stress state associated with the propagation of a mixed mode crack along a crystallographic plane has been analyzed by Koss and Chan [26]. The salient feature of a mixed mode slipband crack is the formation of a plastic zone containing slip on a plane that is coplanar with the crack plane and a region of both coplanar and out-of-plane slip, as shown in Figure 6. The size of the coplanar slip zone is considerably larger han that of the out-of-plane slip zone, but the latter is located closer to the crack tip. The shear stresses within the plastic zone are relaxed and limited by coplanar slip. The coplanar slip, however, does not relax the normal stresses. Consequently, the normal and hydrostatic stresses within the plastic zone continue to build up until out-of-plane slip is activated near the crack tip, resulting in an elastic-plastic stress field described by [26]

$$\sigma_{ij} = \begin{bmatrix} \overset{+}{\sigma}_{xx} & \overset{*}{\sigma}_{xy} & \overset{*}{\sigma}_{xz} \\ \overset{*}{\sigma}_{xy} & \overset{+}{\sigma}_{yy} & \overset{*}{\sigma}_{yz} \\ \overset{*}{\sigma}_{xz} & \overset{*}{\sigma}_{yz} & \overset{+}{\sigma}_{zz} \end{bmatrix} \tag{6}$$

where $\overset{*}{\sigma}_{xz}$, $\overset{*}{\sigma}_{yz}$, and $\overset{*}{\sigma}_{xz}$ are the shear stresses relaxed by coplanar slip, and $\overset{+}{\sigma}_{xx}$, $\overset{+}{\sigma}_{yy}$, and $\overset{+}{\sigma}_{zz}$ are the normal stresses that must be relaxed by out-of-plane slip. At the out-of-plane slip plastic zone [26]

$$\overset{+}{\sigma}_{xx} = \overset{+}{\sigma}_{yy} = \frac{\overset{+}{\sigma}_{zz}}{2\nu} = \frac{K_I}{\sqrt{2\pi r_p^s}} \tag{7}$$

where ν is Poisson's ratio, and r_p^s is the out-of-plane plastic zone size. The presence of the large normal and hydrostatic stresses at the crack tip provides the driving force for continual propagation of the mixed mode crack along the slip plane and the formation of cleavage-like fracture facets, despite the occurrence of coplanar slip directly ahead of the crack plane.

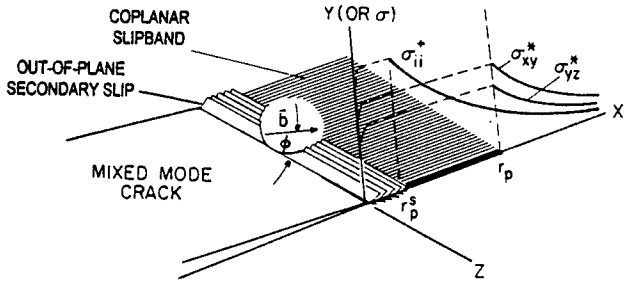


Figure 6: A schematic illustration of the stress state ahead of a mixed mode crack with a coplanar slipband characterized by a slip vector $\bar{b}$ at an angle ϕ to the crack front. The coplanar slip extends to r_p, while out-of-plane secondary slip is activated to r_p^s. From Koss and Chan [28].

The local driving force for propagating a slipband crack can be evaluated using the J-integral approach pioneered by Rice [27]. First, a fictitious cut is made to extend the slipband crack into the out-of-plane slip zone. The newly created crack surface is then superimposed with appropriate normal and shear tractions. Evaluating the J-integral around the crack surface by taking a counter-clockwise path gives

$$J_c = \overset{+}{\sigma}_{yy}\delta_y + \overset{*}{\sigma}_{xy}\delta_x + \overset{*}{\sigma}_{xz}\delta_z \tag{8}$$

where $\overset{+}{\sigma}_{yy}$ is the normal traction; $\overset{*}{\sigma}_{xy}$ and $\overset{*}{\sigma}_{xz}$ are the shear tractions on the extended crack surfaces; δ_y, δ_x and δ_z are the corresponding crack tip opening displacements. At the onset of crack extension, the J-integral is represented by a critical value, J_c, as a measure of the material's resistance against fracture. The $\overset{+}{\sigma}_{yy}\delta_y$ term in Eq. (8) corresponds to the work done in opening up the slipband crack, which contains both the surface energy, Γ_s, and the plastic energy, Γ_o, dissipated by out-of-plane slip, while the $\sigma_{xy}\,\delta_x$ and $\sigma_{xz}\,\delta_z$ terms correspond to the plastic energy, Γ_c, dissipated by coplanar slip. The condition at the onset of slipband fracture is thus given by

$$J_c = \Gamma_s + \Gamma_o + \Gamma_c \tag{9}$$

which corresponds to the effective surface energy [28] or to the work of crack separation per unit area [29]. For small-scale yielding, the J_c parameter is equivalent to the critical strain energy release rate, G_c, which, in turn, is related to the critical stress intensity factor [27, 30].

The distinction between types of slip in the plastic zone provides valuable insight into the slipband cracking process. A significant implication of Eq. (9) is that the Γ_c term due to coplanar slip is essentially decoupled from the mode I fracture term, which is the sum of Γ_s and Γ_o. In general, the fracture resistance of a slipband crack depends on the plastic energy dissipated by both out-of-plane and coplanar slip. In the extreme limit that out-of-plane slip is difficult, the out-of-plane slip zone is negligibly small ($\Gamma_o = 0$), and mode I opening of the slipband crack occurs when $\overset{+}{\sigma}_{yy}\,\delta_y = \Gamma_s$. Since coplanar slip takes place before the condition of $\overset{+}{\sigma}_{yy}\,\delta_2 = \Gamma_s$ is attained, the resulting J_c has a value equal the sum of Γ_s and Γ_c, with $\Gamma_c >> \Gamma_s$. Hence, the fracture resistance of the slipband crack is dictated by plastic energy dissipated by coplanar slip, even though mode I opening of the slipband crack, which occurs elastically, controls the crack surface separation process. As a result, slipband fracture is characterized by intense slip lines that are parallel to the cleavage-like fracture facets [23]. In the other extreme that out-of-plane slip is easy, the size of the out-of-plane slip zone can exceed that of coplanar slip; the plastic constraint near the crack tip is drastically reduced and the work of fracture is increased significantly. The consequence is that crack extension along the coplanar slip band becomes increasingly difficult with increasing out-of-plane slip [31].

Initiation of Cleavage Cracks

In this section, the condition for the initiation of cleavage cracks at the tips of a dislocation pileup is considered. Since a dislocation pileup can be treated as a shear crack, the problem is equivalent to the formation of a small

kinked crack at the tip of a mode II shear crack, as shown in Figure 7(a). Using the kinked crack solutions of Cotterell and Rice [32], the mode I stress intensity factor, K_I^c, acting on an incipient cleavage plane located at angle, ϕ, from the tip of the shear crack is given by [19]

$$K_I^c = C_{12}(\phi) K_{II}^s \tag{10}$$

where

$$C_{12}(\phi) = -\frac{3}{4}[\sin(\phi/2) + \sin(3\phi/2)] \tag{11}$$

and K_{II}^s is the mode II stress intensity factor of the shear crack. Since K_{II}^s is given by Eq. (3), combining Eq. (8) with Eqs. (3) and (4) leads one to

$$\varepsilon_p(d)^{\frac{n}{2}} = \alpha \left(\frac{\sigma_y}{E}\right)\left(\frac{\sqrt{3}\,K_I^c}{\sqrt{\pi}\,C_{12}(\phi)\,m\,\sigma_y}\right)^n \tag{12}$$

for slip-induced cleavage fracture, which differs from Eq. (5) for slipband decohesion by only the $C_{12}(\phi)$ term. Thus, nucleation of a cleavage crack in a plastic field is feasible as long as the K_I induced at the tip of a shear crack on dislocation pileup exceeds the K_{IC} value.

In many materials, the dislocation pileup occurs at a slipband located at the tip of a mode I crack, as shown in Figure 7(b). Initiation of a cleavage crack at the tip of such a slipband requires relating the mode II stress intensity factor for the slipband, which is again treated as a mode II shear crack, to the stress intensity factor of the mode I crack. Applying the Cotterell-Rice kinked crack solution leads one to [19]

$$K_{II}^s = C_{21}(\theta) K_\infty \tag{13}$$

where K_∞ is the applied stress intensity factor,

$$C_{21}(\theta) = \frac{1}{4}[\sin(\theta/2) + \sin(3\theta/2)] \tag{14}$$

and θ is the angle between the slipband and the cleavage crack. Eq. (13) can be combined with Eq. (10) to give [19]

$$K_I^c(\phi) = C_{12}(\phi) C_{21}(\theta) K_\infty \tag{15}$$

which indicates that the stress intensity factor on the incipient crack depends on the orientations of the incipient cleavage crack and the slipband, as well as the applied stress intensity factor.

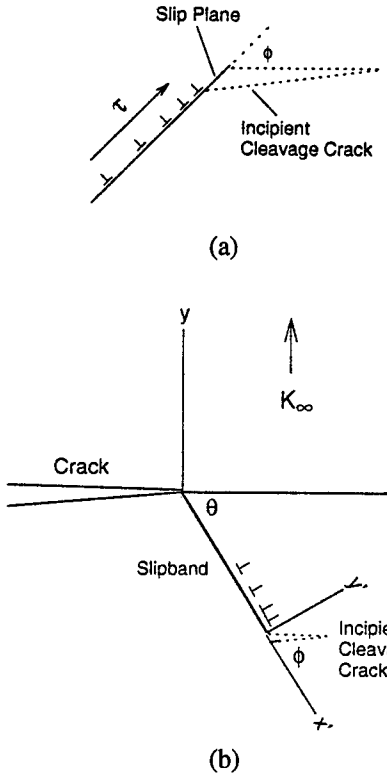


Figure 7: Nucleation of a cleavage crack by shear: (a) ahead of a dislocation pileup or a shear crack, (b) ahead of a slipband located in the plastic zone of a mode I crack.

Figure 8 presents the calculated results of the mode I and II stress intensity components associated with an incipient slipband crack normalized by the applied stress intensity factor, K_∞. The normalized K_I^s value decreases with the angle, θ, of the slipband, while the normalized K_{II}^s component exhibits a maximum at $\theta = 70.5°$. These results indicate that crack deflection along the direction of $\theta = 70.5°$ would maximize the mode II component and lead to a reduction in the K_I^s value. The dashed-double dotted curve in Figure 8 shows the result for K_I^c/K_{II}^s, which indicates that the K_I^c component at the tip of the slipband is a maximum at $\phi = 70.5°$. This angle of maximum K_I^c is a well-known result previously obtained by Stroh [1] and by Smith and Barnby [5]. If the slipband is aligned along the maximum mode II direction (θ=70.5°), the value of K_I^c/K_∞ is a maximum at ϕ=70.5° also, as shown by the dotted curve in Figure 8.

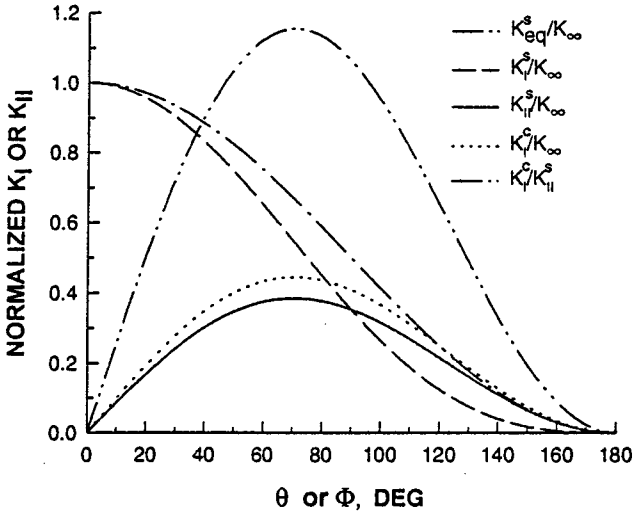


Figure 8: Mode I and II stress intensity factors associated with incipient slipband and cleavage cracks as a function of crack orientation [19].

The crack-tip stress field for a mode I crack is such that the maximum K_{II} component occurs at an angle, θ, of 70.5° measured from the crack tip. If a shear band develops in this orientation, the maximum K_I component occurs also at an angle, ϕ, of 70.5° [19] measured from the tip of the slipband. Because of the stress distributions, deflection of a mode I crack by a slipband would likely occur when the slipband is located at an angle of 70.5° measured from the tip of the main crack, Figure 7(b). After crack deflection on the slipband, the most likely orientation for the formation of a cleavage crack ahead of the slipband crack is also 70.5° measured from the tip of the slipband. Formation of such a cleavage crack would deflect the slipband crack to lie normal to the applied stress, Figure 9(a). Further deflection of the cleavage crack can occur by the formation of a slipband crack at either +70.5° in the counterclockwise direction or at −70.5° in the clockwise direction, depending on the sense of shear. In the former case, alternate slipband cracking and cleavage fracture leads to crack growth approximately in the original mode I crack direction, Figure 9(a). In the latter case, alternative slipband decohesion and cleavage leads to the formation of staircase fracture steps, Figure 9(b). A significant aspect of the proposed alternate slipband decohesion and cleavage fracture process is that crystallographic cracking and cleavage occur at the presence of plastic flow, with the consequence that the associated fracture toughness can be quite high, despite the presence of cleavage facets on the fracture surface [19].

Experimental evidence for the proposed fracture mechanism of alternate slipband decohesion and cleavage fracture is presented in Figure 3, which shows that the

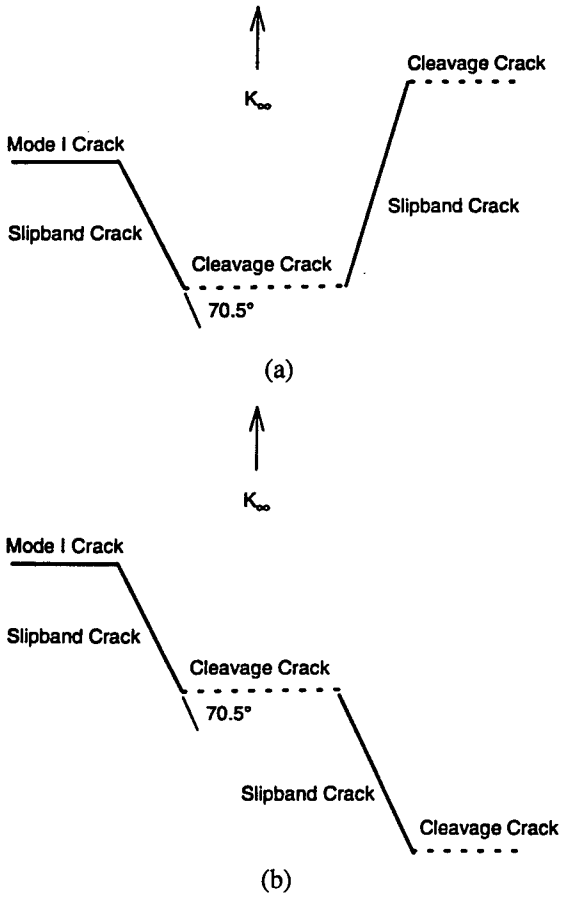


Figure 9: Two failure processes postulated for shear-induced cleavage fracture in Nb-Cr-Ti alloys: (a) alternate slipband cracking and cleavage that leads to cleavage accompanied with large plastic flow and high fracture resistance; (b) formation of staircase cleavage fracture steps with shear ridges by alternate slipband cracking and cleavage. From Chan [18].

main crack deflected to propagate along the (112) slip plane, induced a cleavage crack in a neighboring grain, and then deflected to propagate on the cleavage plane [18]. A macroscopic view of the deflected crack path associated with this alternate slipband cracking and cleavage process is presented in Figure 10 [18]. An important point to be noted here is that slipband cracking occurs in the direction of maximum K_{II}, while cleavage fracture occurs in the direction of maximum K_I. Note also that the cleavage plane could be a slip plane. Fracture on a slip plane is considered cleavage when fracture is dominated by the K_I component, but is considered slipband decohesion when fracture is initially dominated by the shear, or K_{II}, component. Once the slipband decoheres, cracking along the localized slipbands occurs under a mixed mode I and II condition.

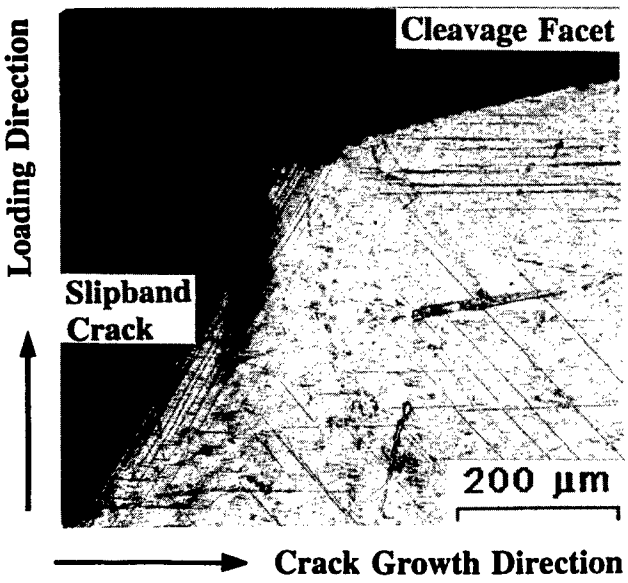
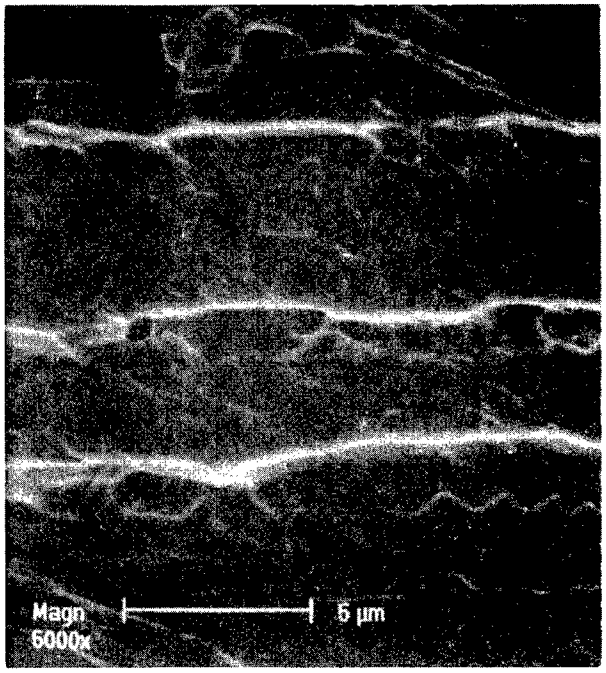


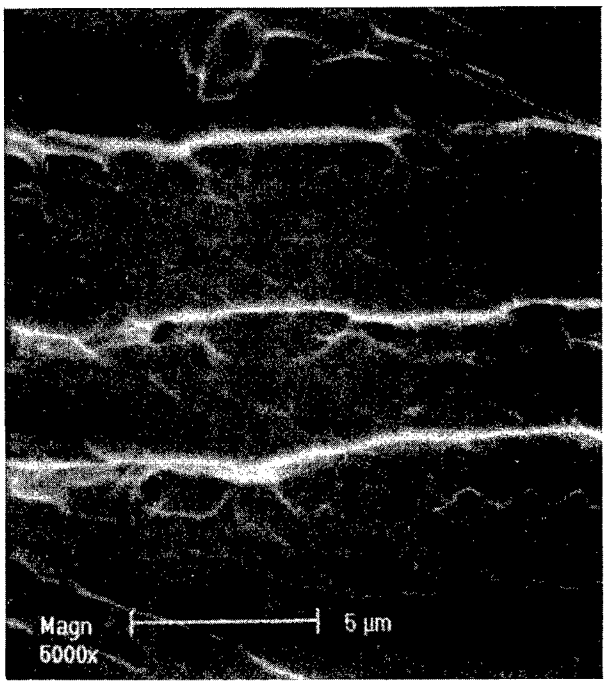
Figure 10: This optical micrograph shows cracking on a plane parallel to coarse planar slip planes and cleavage fracture on a plane that is oriented at ≈74° from the slip plane in an Nb-Cr-Ti alloy [18].

Staircase fracture steps were observed in the cleavage surface of the Nb solid solution alloy. A stereo-pair fractograph of these stairstep fracture steps is shown in Figure 11 [18]. Four fracture steps slanting from top to bottom with the highest elevation at the top are present in Figure 11. Each step is separated from the next one by a vertical plane that shows evidence of shear, i.e., a shear ridge. The cleavage fracture surface in the Nb_{SS} alloy was covered with shear ridges. In Figure 11 there are features that resemble dimples at regions near the shear ridges. Thus, the results provide the evidence to support the notion that alternate slipband decohesion and cleavage occurs in the Nb solid solution alloy, as well as an explanation for the high fracture toughness value.

In many materials the cleavage planes are also the slip planes. For example, TiAl alloys decohere (by shear stress) and cleave (by normal stress) on the (111) planes [16, 17]. Nb-Cr-Ti alloys appear to decohere and cleave on the (112) planes [18]. The fracture process involved is illustrated in Figure 12, which shows dislocation pileup on one set of slip plane, S_1, induces a high normal stress, σ_{yy}, on another slip plane, S_2, that is oriented at about 70.5° from the first one. Note that the induced normal stress, σ_{yy}, is normal to the Burgers vector, b_2, of the dislocations resided on the second plane, S_2; as a result, the S_2 dislocations are not able to relax the normal stress, σ_{yy}, because σ_{yy} exerts zero Peach-Koehler [33] force on the S_2 dislocations. Thus, the condition for cleavage here is similar to that encountered during propagation of a mixed mode crack along a slip plane. In both cases, elastic normal stresses are present to cause separation of the slip plane, despite concurrent slip.



(a)



(b)

Figure 11: This pair of stereo fractographs shows four staircase cleavage fracture steps separated by three shear ridges in an Nb-Cr-Ti alloy. Features that resemble dimples are observed near the shear ridges: (a) 0° tilt and (b) 7° tilt [18].

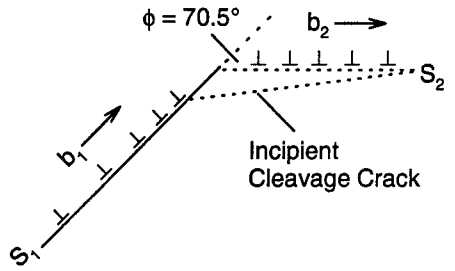


Figure 12: Nucleation of a microcrack on an active slip plane, S_2, due to impingement of intersecting slip on another active slip plane, S_1, oriented at an angle of 70.5° from each other. The induced normal stress, σ_{yy}, on S_2 due to S_1 cannot be relaxed by slip on S_2 because σ_{yy} is normal to the Burgers vector, b_2, and results in a zero Peach-Koehler force on the dislocations on S_2.

Cleavage Crack Growth in Tension

Once nucleated and a sufficient length attained, the growth of the wing will eventually be dictated by the remote stress field. The growth of a cleavage crack in tension is governed by the instability conditions of $J \geq J_{IC}$ and $T \geq T_R$, where J_{IC} is the critical value of the J-integral, T is the applied tearing modulus, and T_R is the tearing modulus of the material [34].

In many intermetallic alloys, tensile ductility is limited by the unstable growth of one or more microcracks nucleated either by slipband decohesion or cleavage during plastic deformation. According to an analysis by Chan, the plastic elongation at fracture, ε_{1f}, for K_{IC}-controlled fracture of tensile specimens can be approximated by [34, 35]

$$\varepsilon_{1f}(d)^{\frac{n}{1+n}} = \left[\frac{1.65\,(1-\nu^2)\sqrt{1+3/n}\,(\alpha\,\varepsilon_y)^{1/n}K_{IC}^2}{\pi\,\sigma_y E}\right]^{\frac{n}{1+n}} \quad (16)$$

which is applicable when the plastic contribution to the J-integral is much greater than the elastic one [34]; otherwise, it is an approximation that tends to overpredict the tensile ductility because the elastic contribution to the J-integral is ignored. Eq. (16) indicates that a slope of $-n/(1+n)$ should be observed in a log-log plot of ε_{1f} versus grain size, d, providing that K_{IC} is independent of the grain size. For TiAl alloys, K_{IC} depends weakly on the grain size. This dependence causes a change of exponent in the ε_{1f} and d relation that was verified by performing calculations using the full tensile ductility model described in [34, 35]. The result, which is shown as the solid line in Figure 5, is in good agreement with the experimental data [36-41], except at grain size less than 65 μm where crack nucleation dominates. The important implications of these results are: (1) tensile ductility is limited by the growth of shear-nucleated microcracks, and (2) increasing the grain size leads to a decrease in plastic elongation.

Wing Crack Growth in Compression

Figure 13 shows a schematic of the wing crack problem considered by Chan et al. [15]. A shear crack or dislocation pileup of length $2l_o$ is subjected to a predominantly compressive stress field of principal stresses σ_1, σ_2, and σ_3, with tension taken to be positive.[1] Specifically, σ_1 is the maximum principal stress, σ_3 is the minimum principal stress, and σ_2 is the intermediate principal stress. As the stress increases, sliding along the surfaces of the shear crack (or a dislocation pile-up) causes the formation of a pair of symmetric wing cracks at the tips of the shear crack, as shown in Figure 13. Wing cracks developed at the tips of a shear crack are generally curved [8-10], Figure 13(a). For simplicity, the wing cracks are assumed to be straight and aligned parallel to the σ_3 direction, as shown in Figure 13(b). The length of the wing cracks is l, and the angle between the shear crack and the σ_3 axis is ψ.

Analyses of the stress intensity factor for both short and long wing cracks in an infinite plate were considered by Chan et al. [15]. The stress intensity factor at the tip of the wing cracks include contributions from the stress field of the shear crack and the far-field stress field acting normal to the wing cracks. The loading due to the shear crack is represented as a point force, F, as shown in Figure 13(c). The mode I stress intensity, K_I, at the tip of the long wing crack is then computed based on the point force, F, acting at the center of the crack and the confinement stress, σ_1, acting over the length of the crack, leading to [15]

$$K_I = \frac{2(\tau_n - \mu\,\sigma_n)l_o \sin\psi}{\sqrt{\pi\,(l+\kappa\,l_o)}} + \sigma_1\sqrt{\pi\,l} \quad (17)$$

where τ_n and σ_n are the shear and normal stresses acting on the shear crack; μ is the coefficient of friction; κ is a parameter obtained by matching the long crack solution with the short crack result, correcting for the transition of the short crack solution to the long crack solution. The growth of the wing crack was assumed to occur when $K_I = K_{IC}$. Applying this criterion to Eq. (17) and rearranging the terms leads to [15]

[1] The convention used here is opposite of that used in Chan et al. [15].

$$\sigma_1 - \sigma_3 = \frac{\sqrt{\pi L}\sqrt{\pi (L + \kappa)}}{\sin 2\psi \sin \psi}\left[\frac{K_{IC}}{\sqrt{L}\sqrt{\pi l_o}} - \sigma_1\right] \quad (18)$$

which can be used to examine the growth of the wing cracks from an initial length of L_o to a large L value (e.g., $L > 10$), where L_o and L are normalized crack lengths [15].

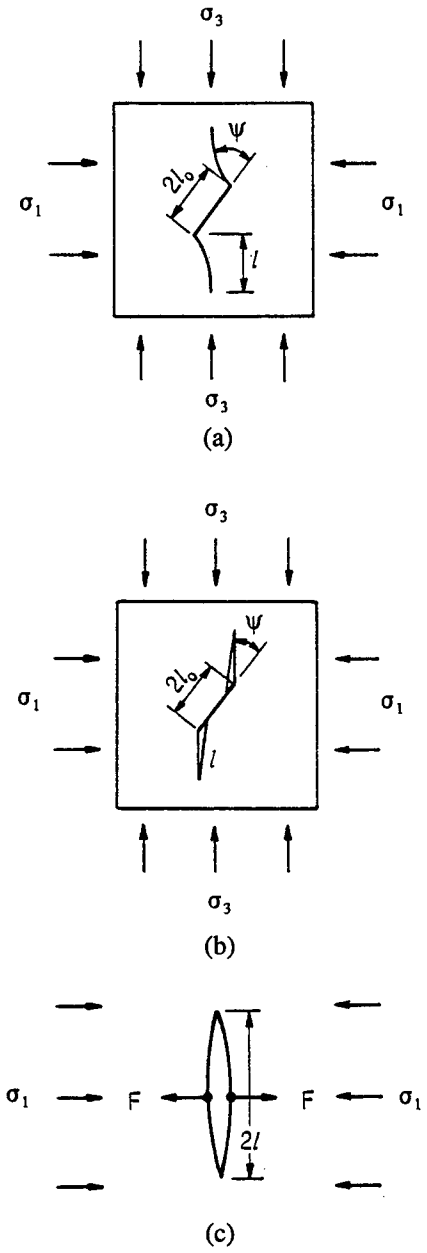


Figure 13: Geometries of short and long wing cracks at the tips of a shear crack of length $2l_o$: (a) curved short wing cracks, (b) straight short wing cracks, and (c) long wing cracks subjected to a point force, F (Chan et al. [15]).

Relations between the stress difference, tensile stress, and the normalized crack length at the onset of unstable crack growth are derived from Eq. (18) by imposing the condition that

$$\frac{\partial K}{\partial l} = 0 \quad (19)$$

at crack instability. This leads one to [15]

$$\frac{-P}{\sigma_1 - \sigma_3} = \frac{\sqrt{L}\sin\psi \sin 2\psi}{\pi (L + \kappa)^{1.5}} \quad (20)$$

for the case of frictionless sliding ($\mu = 0$). This particular value of μ has been chosen because shear along a slip plane leading to nucleation by dislocation pileup is most likely in salt in the dislocation creep regime. Eq. (20) is then substituted into Eq. (18) to give [15]

$$\sigma_1 - \sigma_3 = \frac{\pi (L+\kappa)^{1.5} K_{IC}}{(2L + \kappa)\sqrt{\pi l_o}\sin\psi \sin 2\psi} \quad (21)$$

and

$$P = -\frac{K_{IC}\sqrt{L}}{(2L + \kappa)\sqrt{\pi l_o}} \quad (22)$$

as the expressions for the critical stress difference and tensile stress at the onset of unstable cleavage fracture.

Theoretical failure loci for cleavage fracture of rock salt have been calculated using the wing crack model. The calculated curve shows that the critical tensile stress decreases with increasing stress difference, as shown in Figure 14 [15]. For uniaxial tension where $|\sigma_1 - \sigma_3| = \sigma_1$, the fracture mechanism changes from wing crack to Griffith crack fracture [7]. Figure 14 shows that cleavage fracture changes from the wing crack to the Griffith crack process at $|\sigma_1 - \sigma_3| = \sigma_1 = 3.38$ MPa. Independent experimental data [15, 20, 42-44] in Figure 14 also indicate that the tensile strength of rock salt decreases with increasing stress difference. Although not exactly in accordance with the best fit to the experimental results, the calculated curve is an acceptable and possible approximation to the data. The discrepancy between the calculated curve and experimental data arose because the different rock salts probably do not exhibit identical cleavage fracture strength at a given stress difference.

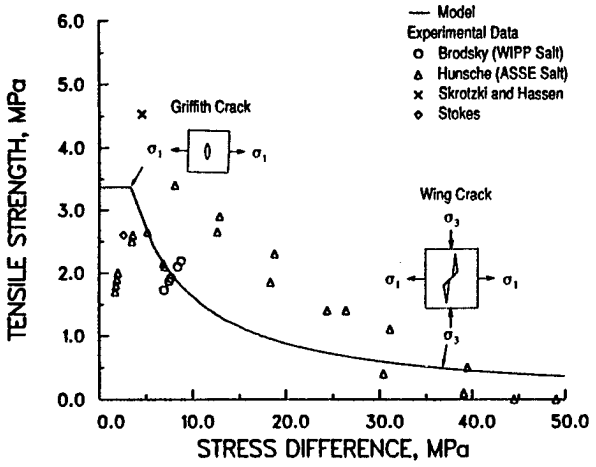


Figure 14: Comparison of calculated and measured values of tensile strength of rock salt as a function of stress difference. Experimental data of WIPP salt and other data are from Chan et al. [15], Hunsche [42], Skrotzki and Haasen [40], and Stokes [41]. Figure is from Chan et al. [15].

The theoretical and experimental fracture strength results are compared in Figure 15, which shows the fracture loci in the σ_1 vs. σ_3 stress space. Figure 15 also shows the creep and creep fracture regions for rock salt from the Waste Isolation Pilot Plant (WIPP) site [15, 45-48]. Within the triaxial compression region, the elastic stress field associated with a shear crack or a dislocation pileup is sufficient to introduce cleavage wing cracks at low levels of stress difference in rock salt if creep deformation by dislocation mechanisms does not occur at ambient temperature [15]. Because of creep, the onset of wing-crack formation is delayed until the creep fracture boundary is exceeded. The propagation of a wing crack is always stable in the presence of a confining pressure [15]. Consequently, the relevant damage processes in the creep fracture regime are the initiation, stable propagation, and coalescence of wing cracks for triaxial compression. In the presence of a small tensile stress, creep-induced wing cracks can propagate as unstable cleavage cracks if the combination of stress difference and tensile stress exceeds that required for crack instability (i.e., the cleavage fracture boundary). The important implications are: (1) cleavage cracks in salt can occur in the presence of a tensile stress that is less than the tensile strength, and (2) cleavage fracture initiation in salt is the culmination of a ductile deformation (slip) process and micromechanical damage (microcrack) accumulation, even though salt is often considered a brittle material in tension. The tensile stress required to trigger unstable cleavage fracture decreases with increasing stress difference. Because of this, both stress difference and tensile stress levels are important in considering possible failure by shear-induced cleavage in a salt structure.

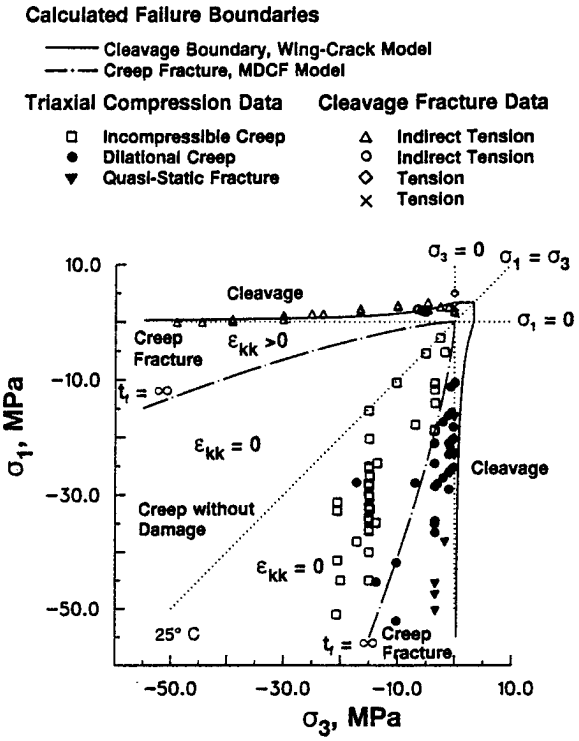


Figure 15: Comparison of calculated fracture mechanism map against experimental data of rock salt. The cleavage fracture data are from Chan et al. [15], Hunsche [42], Skrotzki and Haasen [40], and Stokes [41]. The triaxial creep data are from Van Sambeek et al. [46], Senseny [43], Fossum et al. [44], Wawersik and Hannum [45]. The quasi-static triaxial comparison data are from Wawersik and Hannum [45]. Figure is from Chan et al. [15].

Wing Crack Growth Under Compressive Thermal Stresses

In many engineering applications, brittle coating materials are subjected to compressive thermal stresses induced as the result of differences in the coefficient of thermal expansion, which, in turn, leads to spallation of the coating materials. Some examples are the spallation of oxide scales on high-temperature alloys and thermal barrier coatings. In some instances, spallation of the oxide scale and thermal barrier coating can be treated on the basis of the growth of shear-induced wing cracks.

The spallation of an oxide scale from an overlay coating or a metallic substrate was treated by Chan [49] as a wing crack growth failure process, as shown in Figure 16. In this case, the driving force for crack growth is the compressive thermal stress, σ_c, induced as the result of a difference in the coefficients of thermal expansion between the oxide and the coating (or substrate). The wing crack growth analysis gives the mode I stress intensity, K_I, at the wing crack, leading to

$$K_I = \frac{\sigma_c \sqrt{\pi l_o}\ \sin 2\psi\ \sin\psi}{\pi \sqrt{L + \kappa}} = K_{ox} \qquad (23)$$

when detachment of the oxide spalls is assumed to occur at $K_I = K_{ox}$, where K_{ox} is the critical stress intensity factor (i.e., fracture toughness) of the oxide. Eq. (23) leads to the prediction of a critical temperature drop, ΔT_c, for the onset of oxide spallation, which is given by

$$\Delta T_c = \frac{\pi \sqrt{L + \kappa}\ K_{ox}}{E_{ox} \Delta\alpha \sqrt{\pi l_o}\ \sin 2\psi\ \sin\psi} \qquad (24)$$

where E_{ox} is the Young's modulus of the oxide, and $\Delta\alpha$ is the difference in the CTE between the oxide and the coating or the substrate.

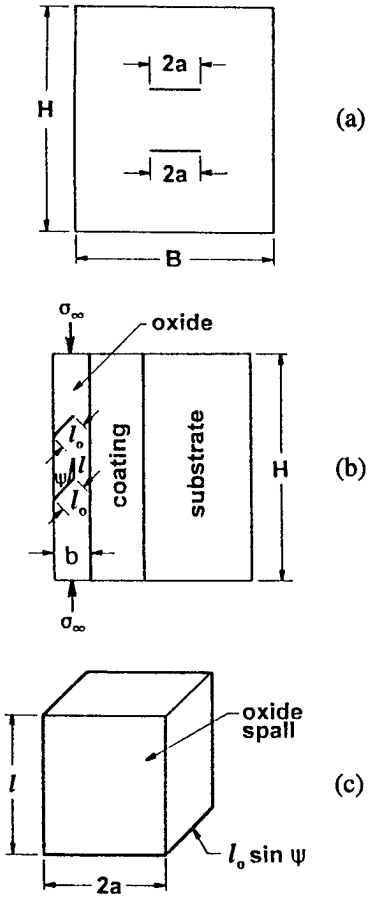


Figure 16: A schematic of the oxide spallation process by the propagation of a wing crack between two shear cracks: (a) front view of the shear cracks, (b) side view of shear cracks and a wing crack, and (c) the volume of a spall formed when the wing crack joins with the two shear cracks. From [47].

The concept of a critical temperature drop for the onset of spallation has been incorporated into a recent oxide spallation analysis to obtain an explicit relation between weight of oxide spalled, W_s, and weight of oxide, W_{ox}, formed on the coating (or substrate), which is

$$W_s = q(\Delta T - \Delta T_c)^2 H(\Delta T - \Delta T_c)\left[\frac{W_{ox}}{W_o}\right]^{1+m} \qquad (25)$$

where

$$q = \frac{\zeta_o W_o \sin^2 2\psi \sin^3\psi}{\pi}\left[\frac{E_{ox}\Delta\alpha\sqrt{l_o}}{K_{ox}}\right]^2 \qquad (26)$$

and ζ_0 is the reference crack density; W_0 is the reference weight; H is the Heaviside function; m is the crack density exponent.

Equations (25) and (26) have been used as part of a cyclic oxidation model to calculate the weight change curves for a coated IN718 [50] under three temperature change conditions. The results are compared against the experimental data [50] in Figure 17, which indicate the amount of weight change as a function of time for ΔT values of 0, 780, and 1093°C. For $\Delta T = 0$, the weight change is entirely due to weight gained resulting from the formation of oxide on the coating at a constant temperature. Spallation of the oxide occurs when $\Delta T > \Delta T_c$. The amount of oxide spalled increases with $(\Delta T - \Delta T_c)^2$; consequently, the weight change becomes negative when the weight of oxide spalled exceeds that of weight gained due to oxide formation.

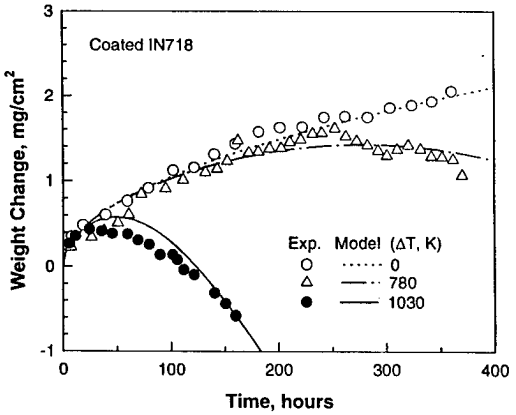


Figure 17: Comparison of calculated and measured weight change curves [50] for two different levels of temperature drop (ΔT) in cyclic oxidation and for isothermal oxidation. The amount of spallation increases with increasing temperature drop, resulting in a larger weight loss observed in cyclic oxidation with a larger ΔT.

Conclusions

Experimental evidence indicates that shear-induced cleavage occurs in both ductile and brittle materials. In ductile materials, stress concentration at a dislocation pileup can lead to slipband band decohesion or cleavage fracture. Slipband decohesion is controlled by mode II fracture toughness, while cleavage fracture is controlled by mode I. Cleavage fracture process can be unaffected by slip activities that are coplanar with the crack plane. As a result, cleavage fracture can take place in the presence of plastic flow and be accompanied by a high toughness value. In brittle materials, shear-induced cleavage is driven by the tensile stresses associated with the stress field of a shear crack and is an important failure mechanism in solids subject to a predominantly compressive stress field.

Acknowledgements

Preparation of this manuscript was supported by the Air Force Office of Scientific Research (AFSC) under Contract No. F49620-95-0043, Dr. Charles H. Ward, Program Monitor. Work described in this paper was supported by AFOSR (TiAl and Nb-Cr-Ti), DOE (rock salt), and EPRI (oxide spallation). The United States Government is authorized to reproduce and distribute reprints for governmental purposes notwithstanding any copyright notation hereon. Clerical assistance by Ms. Patty A. Soriano of Southwest Research Institute is appreciated.

References

1. A. N. Stroh, Proc. Roy. Soc. A, 223 (1954), 597-606.

2. A. N. Stroh, Proc. Roy. Soc. A, 232 (1955), 548-561.

3. A. N. Stroh, Phil. Mag., 3 (1958), 597-606.

4. E. Smith, Acta Metall., 14 (1966), 985-996.

5. E. Smith and J. T. Barnby, Metal Science Journal, 1 (1967), 56-64.

6. E. Smith, Metal Science Journal, 1 (1967), 119-121.

7. A. A. Griffith, Phil. Trans. R. Soc. A, 221A (1920), 163-198.

8. S. Nemat-Nasser and H. Horii, J. Geophys. Res., 87 (1982), 6805-6821.

9. H. Horii and S. Nemat-Nasser, J. Geophys. Res., 90 (1985), 3105-3125.

10. H. Horii and S. Nemat-Nasser, Phil. Trans. Roy. Soc. London A, 319 (1986), 337-374.

11. M. L. Kachanov, Mech. Mat., 1 (1982), 29-41.

12. P. Steif, Eng. Fract. Mech., 20 (1984), 463-473.

13. M. F. Ashby and S. D. Hallam, Acta Metall., 34 (1986), 497-510.

14. S. D. Hallam and M. F. Ashby, Deformation Processes in Minerals, Ceramics, and Rocks, ed. D. J. Barber and P. G. Meredith (New York, NY: Routledge Chapman & Hall, 1990), Ch. 4, 84-108.

15. K. S. Chan, D. E. Munson, S. R. Bodner, and A. F. Fossum, Acta Met. Mat., 44 (1996), 3533-3565.

16. K. S. Chan and Y.-W. Kim, Metall. Trans A, 23A (1992), 1663-1677.

17. K. S. Chan and Y.-W. Kim, Metall. and Mat. Trans. A, 25A (1994), 1217-1228.

18. K. S. Chan, Metall. Trans. A, 27A (1995), 2518-2531.

19. K. S. Chan, Micromechanics of Advanced Materials, edited by S. N. G. Chu, P. K. Liaw, R. J. Arsenault, K. Sadananda, K. S. Chan, W. W. Gerberich, C. C. Chau, and T. M. Kung (Warrendale, PA: TMS, 1995), 113-120.

20. K. S. Chan, N. S. Brodsky, A. F. Fossum, D. E. Munson, and S. R. Bodner, ASME Transactions, J. Eng. Mat. Tech., 1997 (submitted).

21. P. C. Paris and G. C. Sih, Fracture Toughness Testing and Its Applications, ASTM STP381 (Philadelphia, PA: ASTM, 1964), 30-83.

22. H. W. Liu, J. Appl. Mech., 36 (1965), 1468-1470.

23. K. S. Chan and D. A. Koss, Mat. Sci. Eng., 443 (1980), 177-186.

24. M. Gell and G. R. Leverant, Acta Metall., 16 (1968), 553-561.

25. K. S. Chan, Metall. Trans. A, 21A (1990), 2687-2699.

26. D. A. Koss and K. S. Chan, Acta Metall., 28 (1980), 1245-1252.

27. J. R. Rice, Fracture: An Advanced Treatise, edited by H. Liebowitz (New York, NY: Academic Press, 1968), Vol. 2, 191-311.

28. E. Orowan, Welding Journal, 34 (1955), 1575-1605.

29. V. Tvergaard and J. W. Hutchinson, J. Mech. Phys. Solid, 40 (1992), 1377-1397.

30. G. R. Irwin, J. Appl. Mech., 24 (1957), 361-364.

31. K. S. Chan, Proceedings of International Symposium on Structural Intermetallics II, edited by R. Darolia et al. (Warrendale, PA: TMS, 1997), in press.

32. B. Cotterell and J. R. Rice, Int. J. Fracture, 16 (1980), 155-169.

33. M. D. Peach and J. S. Koehler, Phys. Rev., 80 (1950), 436-439.

34. K. S. Chan, Metall. Mat. Trans. A, 25A (1993), 299-308.

35. K. S. Chan, Scripta Met., 24 (1990), 1725-1730.

36. Y.-W. Kim, JOM, 46(7) (1994), 30-39.

37. K. S. Chan, in Gamma Titanium Aluminides, edited by Y.-W. Kim, R. Wagner, and M. Yamaguchi (Warrendale, PA: TMS, 1995), 835-847.

38. J. D. Shi, Z. J. Pu, and K. H. Wu, in Gamma Titanium Aluminides, edited by Y.-W. Kim, R. Wagner, and M. Yamaguchi (Warrendale, PA: TMS, 1995), 709-716.

39. C. T. Liu, J. H. Schneibel, P. J. Maziasz, J. L. Wright, and D. S. Easton, Intermetallics, 4 (1996), 429-440.

40. C. T. Liu, P. J. Maziaz, D. R. Clemens, J. H. Schneibel, V. K. Sikka, T. G. Nieh, J. Wright, and L. R. Walker, in Gamma Titanium Aluminides, edited by Y.-W. Kim, R. Wagner, and M. Yamaguchi (Warrendale, PA: TMS, 1995), 679-688.

41. K. S. Chan and D. S. Shih, Metal. Mat. Trans. A, 28A (1997), 79-90.

42. W. Skrotzki and P. Haasen, Deformation of Ceramic Materials II, edited by R. Tressler and R. C. Brandt, Mat. Sci. Res. Symp. Proc., Vol. 18 (New York, NY: Plenum Press, 1984), 429-444.

43. R. J. Stokes, Proc. British Ceram. Soc., 6 (1966), 189-207.

44. U. E. Hunsche, Seventh Symp. on Salt, edited by H. Kakihana et al., Vol. 1 (New York, NY: Elsevier Science Pub., 1993), 59-65.

45. P. E. Senseny, Triaxial Compression Creep Tests on Salt from the Waste Isolation Pilot Plant, SAND85-7261 (Albuquerque, NM: Sandia National Laboratories, 1986).

46. A. F. Fossum, N. S. Brodsky, K. S. Chan, and D. E. Munson, Int. J. of Rock Mech. Min. Sci. and Geomech. Abstr., 30 (1993), 1341-1344.

47. W. R. Wawersik and W. Hannum, Interim Summary of Sandia Creep Experiments on Rock Salt from the WIPP Study Area, Southern New Mexico, SAND79-0115 (Albuquerque, NM: Sandia National Laboratories, 1979).

48. L. L. Van Sambeek, A. F. Fossum, G. Callahan, and J. Ratigan, Seventh Symp. on Salt, edited by H. Kakihana et al. (New York, NY: Elsevier Science Pub., 1993), Vol. 1, 127-134.

49. K. S. Chan, Metall. Trans. A, 1997 (in press).

50. D. L. Deadmore and C. E. Lowell, Oxidation of Metals, 11(2) (1977), 91-106.

CLEAVAGE-QUASI CLEAVAGE IN FERRITIC AND MARTENSITIC STEELS:

G. R. Odette
K. V. Edsinger
G. E. Lucas

University of California Santa Barbara
Department of Mechanical Engineering
Santa Barbara, CA 93106-5070

Abstract

Confocal microscopy-fracture reconstruction and SEM were used to characterize the sequence-of-events leading to cleavage in a low alloy pressure vessel steel and two 8-12Cr martensitic steels as a function of temperature. While differences between the steels were observed, they shared some common characteristics that differ from the conventional view of cleavage. Most notably cleavage does not occur as a single weakest link event; rather it is the consequence of a critical condition when a previously nucleated dispersion of microcracks suddenly coalesce to form a large, rapidly propagating macroscopic crack. It is argued that the critical event can be treated as a bridging instability. The stabilizing effect of the ductile ligaments separating the cleavage facets increases with increasing temperature. Indeed, even in the ductile tearing regime cleavage facets form a significant fraction of nuclei for larger microvoids.

George R. Irwin Symposium on Cleavage Fracture
Edited by Kwai S. Chan
The Minerals, Metals & Materials Society, 1997

STATISTICAL AND CONSTRAINT FACTORS IN CLEAVAGE INITIATION

G. R. Odette
K. V. Edsinger
G. E. Lucas

University of California Santa Barbara
Department of Mechanical Engineering
Santa Barbara, CA 93106-5070

Abstract

The size dependence of effective cleavage initiation toughness $K_c(T)$ (defined by the load-displacement conditions at initiation) of steels are mediated by both statistical and constraint factors. Statistical effects are controlled by the total high stress volume even under plane strain, small scale yielding, e.g., $K_{Ic} \propto 1/B^{-1/4}$. Constraint loss and reductions in the stress fields occurs for shallow cracks, large scale yielding and deviations from plane strain. The interplay between these factors is examined by analyzing the observed $K_c(T)$ behavior for specimens with different W, B and a/W using FEM simulations of the crack tip fields and confocal microscopy, fracture reconstruction and SEM characterization of the sequence-of-fracture-events. Observed versus actual sequences and complications such as crack tip strain, the transition to ductile tearing and ultimate loss of specimen capacity are discussed.

George R. Irwin Symposium on Cleavage Fracture
Edited by Kwai S. Chan
The Minerals, Metals & Materials Society, 1997

THE FRACTOGRAPHY-MODELING LINK IN CLEAVAGE FRACTURE

Anthony W. Thompson

Lawrence Berkeley National Laboratory
Materials Sciences Division
University of California
Berkeley, CA 94720

Abstract

Cleavage fracture has historically been modelled, out of necessity, in rather idealized terms. In real materials, however, there are a number of difficulties in linking such models with metallographic and fractographic observations. Some of the most vivid examples occur for α_2 titanium aluminide alloys, in which, when the microstructure contains primary α_2 particles, the primary particles crack first. When "basketweave" or Widmanstätten structures of α_2 laths comprise the microstructure, it appears that individual laths crack first. And in colony structures, cracking occurs first across the α_2 lath colonies. Both detailed fractographic observations, and also a statistical model for brittle fracture by failure of weakest links, have been developed. The extent to which this can be interpreted in classical cleavage terms will be discussed. This work has been supported by the U. S. Air Force Office of Scientific Research.

George R. Irwin Symposium on Cleavage Fracture
Edited by Kwai S. Chan
The Minerals, Metals & Materials Society, 1997

FRACTURE MECHANISMS

MICROMECHANISMS OF CLEAVAGE FRACTURE

A. R. Rosenfield
Rosenfield & Rosenfield
1650 Ridgway Pl.
Columbus OH 43212

Abstract

Starting with recent work of Irwin and Zhang [1], evidence is reviewed showing that cleavage fracture in steel is essentially a series of burst/pause events. The bursts are propagation of cleavage cracks formed ahead of the main crack, while the pauses are ductile rupture of unbroken ligaments behind the crack tip. While there are differences in detail, the processes of initial crack extension and rapid crack propagation have significant similarities. In particular, the concept of local dynamic elastic loading on the micro-scale may be useful for the analysis of both phenomena.

Introduction

In 1995 Irwin and Zhang [1] published a summary of their microscopic observations of cleavage fracture of steel along with some discussion of the implications regarding the fracture mechanism. The object of this paper is to combine a discussion of their analysis with a review of our research at Battelle. The review extends over several decades, since concerted research into cleavage fracture of steel began with the World War II Liberty Ship failures. It is convenient to divide the subsequent interval into a 'classic' period up to around 1970 (dominated by metallurgy and concentrating on smooth-bar behavior) and a later 'modern' period (combined metallurgy and mechanics approaches, concentrating on pre-cracked specimens).

Crack Initiation

In 1966 we summarized the 'classic' picture of the mechanism of cleavage fracture of steel [2]. According to this approach each steel has a yield stress which is dependent on temperature, strain

George R. Irwin Symposium on Cleavage Fracture
Edited by Kwai S. Chan
The Minerals, Metals & Materials Society, 1997

rate, and microstructure and a cleavage stress which is dependent on microstructure alone. Figure 1 plots constitutive relations for carbon and low-alloy steels and indicates that cleavage occurs when the yield stress reaches the cleavage stress. If the test conditions are at point 'A', yielding will occur and lead to dimpled rupture (upper-shelf behavior). In order to achieve cleavage the effective stress must be increased so that it exceeds the cleavage stress. As indicated in Figure 1, the increase is made possible by greater constraint, higher loading rate, or lower temperature, either singly or in combination.

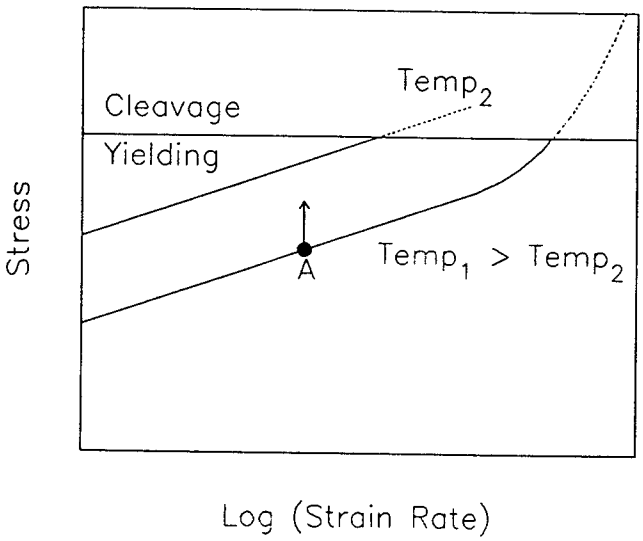


Figure 1. Schematic Constitutive Relations for Steel. ↑ = Constraint Effect

The second aspect of the 'classic' approach arose from a number of observations, reviewed by Hahn in 1984 [3], which showed that cleavage is triggered by the slip-induced fracture of brittle particles. The mechanisms that were developed required the intersection of a slip band (represented by a dislocation pile-up) with the particle. The large stress at the head of the pile-up is believed sufficient to crack the particle. Because non-propagating microcracks were observed microscopically, it was concluded the particle fracture was a necessary, but not sufficient, condition for cleavage failure. The pile-up stress has to be sufficient to both crack the particle and drive the cleavage into the surrounding ferrite. A corollary of this picture is that the local stress will be significantly higher than the applied stress.

The 'modern' approach to cleavage concentrates on pre-cracked specimens. This approach is complicated because of the gross stress/strain non-uniformity within the crack-tip plastic zone. In addition, within the ductile/brittle transition region, cleavage failure occurs after some stable crack growth. As shown in Figure 2, a variation in cleavage fracture toughness arises because there are varying amounts of ductile crack growth prior to the onset of cleavage

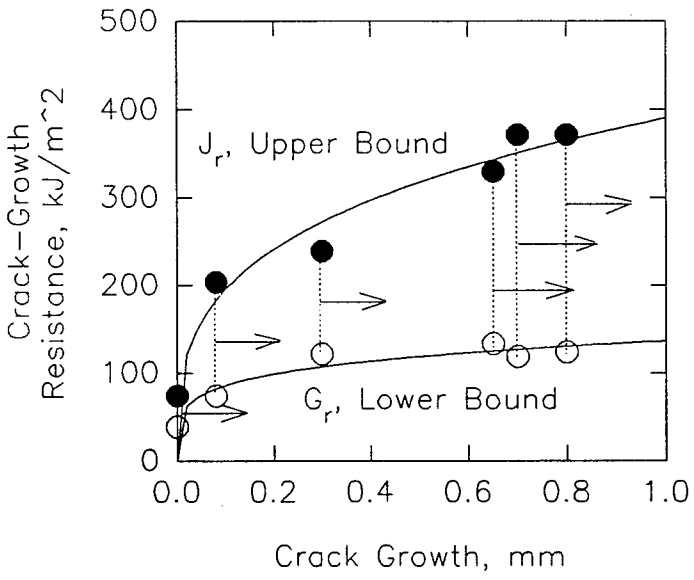


Figure 2. Crack Growth Data of Rosenfield and Shetty [5]. Points Represent Conversion to Cleavage.

under nominally-identical test conditions. This behavior, which can be denoted subsequent-mechanism fracture, contrasts with the mixed-mode mechanism in Charpy specimens tested in the transition region. Viewed in this context, the lower shelf in fracture toughness tests is where there is no stable crack growth prior to fast fracture and the upper shelf is where there is complete failure by stable crack growth.

Because the J-integral is undefined for a growing crack, there is also a problem in using transition-temperature data to verify any theoretical analysis. Neither J (solid points in Figure 2) nor G (open points curve in Figure 2) is likely to be the correct value. An additional problem in developing a theoretical analysis is that the dimpled-rupture crack tip is not the ideal sharp crack envisioned in fracture-mechanics analyses. We [4],[5] adopted the position that the value of G (elastic strain energy release rate) is appropriate for engineering purposes in this situation, because it is the lower bound of toughness for a growing crack [6]. As discussed below, there may be a physical basis for G-controlled crack initiation.

Even when transition-temperature data are eliminated, it is difficult to relate smooth-bar data to pre-cracked-specimen data. Two important differences are present, one associated with the non-uniform stress/strain distribution in the crack-tip region and one associated with the difference in the plastically-deformed volumes in the two geometries. The initial consideration of the stress/strain non-uniformity came from Ritchie, et al. [7], who accommodated the fact that the highest local stress does not occur at the crack-tip, but some distance ahead of it (e.g. [8]), and predicted that cleavage-crack growth would be initiated at a 'characteristic microstructural dimension' ahead of the main crack. This approach implies a fracture mechanism triggered by formation of a microcrack and that the main crack initially grows when the backwardly-propagating microcrack meets the fatigue pre-crack.

We [9],[10] verified the essentials of Ritchie's prediction experimentally using ASTM-A508, a quenched and tempered low alloy steel and made two major findings:

A1. Cleavage is triggered at a particle ahead of the main crack, either by fracture or decohesion. In contrast to the 'classic' focus on large carbides, subsequent research has revealed a rich variety of trigger sites [11],[12]. Additionally, we found that the nature of the trigger particle changed with test temperature.

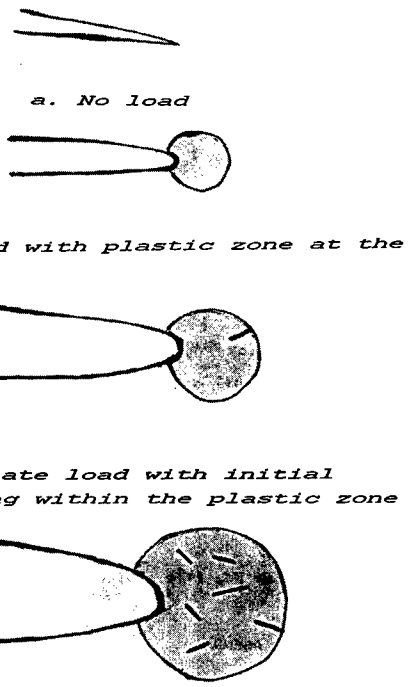
A2. The distance from the fatigue-crack tip to the trigger particle is a variable and not a 'characteristic microstructural dimension'.

The latter observation introduces a reason to adopt a statistical variation of cleavage toughness. According to this approach, cleavage obeys the Weibull theory [13]. This theory implies that successful trigger points are sufficiently rare that the probability that a given volume contains one has to be taken into account. However, Zhang, et al. [14] have pointed out that the microstructure typically contains a much greater density of trigger sites than would be expected if triggering is sufficiently rare to require us to invoke Weibull statistics.

There have been some suggestions for escaping this dilemma. Irwin

and Zhang [1] emphasize the need for high strain rate to elevate the yield stress so as to inhibit plastic flow and allow cleavage. They point out that even when initiation occurs at a low imposed strain rate, micro-cleavage or particle debonding can induce the necessary high strain rates locally to trigger cleavage. If this idea is correct, it suggests that the cleavage-initiation process is locally controlled by dynamic elastic stresses, lending plausibility to our concept of G-controlled cleavage-crack initiation as discussed in connection with Figure 2, above.

They also argue that cleavage can be affected by local stress concentrations associated with non-uniformity of the shape of the fatigue pre-crack and with microstructural inhomogeneities (e.g. carbide banding). This possible role of dimensions in addition to the trigger particle size is reminiscent of the analyses of the 1970's, which include the mean free path of slip lines [3].



a. No load

b. Small load with plastic zone at the crack tip

c. Intermediate load with initial microcracking within the plastic zone

d. Load just prior to fracture with microcrack cloud within the plastic zone

Figure 3. Schematic Diagram of Microcracking Accompanying Loading of Steel

A second explanation for the relative rarity of successful triggering arises from the work of Chen and Wang [15]. They examined pre-cracked specimens that had been unloaded prior to fracture and found blunted cavities near the pre-crack. Within the plastic zone, but beyond the peak stress, they found cleavage microcracks. The observation of non-propagating microcracks is consistent with the evidence on smooth bars cited above.

Chen and Wang's [15] picture is illustrated by Figure 3. As the load is increased a plastic zone forms and grows. Eventually microcracks are generated within it. The number of microcracks continually increase with increasing load. Eventually one microcrack rapidly expands in all directions, joining the main crack and leading to unstable rapid fracture.

Based on their observations, Chen and Wang [15] suggested that there are three criteria that must be obeyed for cleavage to be triggered:

B1. a sufficient local plastic strain to cause particle fracture or decohesion.

B2. a sufficiently high local stress constraint to inhibit relaxation of the resulting local stress concentration. The high loading rate idea of Irwin and Zhang [1] supplements this requirement by adding the idea of insufficient time for stress relief by plastic flow to the exis-

tence of a high hydrostatic stress.

B3. a sufficiently high local peak stress to equal or exceed the cleavage stress for the material.

Because it is difficult to fulfill all of these conditions simultaneously, the volume where cleavage triggering is possible becomes quite small. This volume may contain sufficiently few particles that statistical theories are necessary to describe the onset of fracture.

Crack Propagation and Arrest

In a recent historical review [16], I pointed out that serious study of crack arrest began with Irwin and Wells' suggestion [17] that crack arrest is the reverse of crack initiation. Perhaps the most interesting aspect of the Irwin and Zhang paper [1] is their discussion of the commonality in mechanism of both initiation and arrest, providing a mechanistic expansion on that idea. Although the crack arrest toughness is significantly less than the static crack initiation toughness the dynamic initiation toughness is close to the crack-arrest toughness [18] providing support for Irwin's concept. In effect, initiation due to dynamic loading inhibits plastic flow and makes the large-scale stress/time history at the crack tip closer to the local stress/time history associated with initiation due to static loading. Rapid crack propagation also induces dynamic elastic stresses at the crack tip and arrest occurs when these stresses are no longer able to sustain the cleavage mechanism.

More insight into the crack-propagation process comes from morphological observations on arrested cracks [19], which were based on earlier Battelle work on Fe-3%Si [20] and ASTM A-508 [21] steels. The Fe-3%Si studies were particularly useful since the employed the etch-pit technique to detect patterns of plastic deformation. Our observations were:

C1. The tip of the arrested crack had a very small plastic zone, indicating a very low crack-tip stress intensity after arrest. This observation, combined with measurements of the thickness variation of crack-arrest toughness [22], provides support for having a less restrictive thickness requirement of the ASTM crack arrest toughness standard (E1221) than for linear elastic fracture toughness (E399).

C2. Plasticity was concentrated at ligaments behind the crack tip. The ligaments close to the crack tip remained unbroken.

C3. The remainder of the flanks of the crack in Fe-3%Si were almost completely dislocation-free, suggesting that cleavage segments of the run/arrest event were accompanied by little or no plastic flow.

C4. Ligaments fail by a dimpled-rupture mechanism.

C5. The percentage of fracture surface containing dimpled rupture increases as the test temperature increases, accounting for the rise in toughness.

Figure 4 shows Irwin and Zhang's propagating crack concept [1]. Note the broken ligaments far behind the advancing crack and the unbroken ligaments just behind the crack tip. Irwin and Zhang suggest that cleavage crack propagation occurs in a series of bursts and halts, which can be termed sequential initiation. A burst

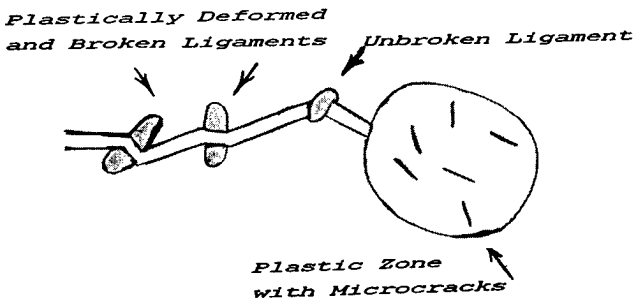


Figure 4: Schematic Diagram of a Rapidly Propagating Cleavage Crack in Steel

occurs when an already-formed microcrack goes unstable and jumps forward or when a new microcrack, formed in the crack-tip plastic zone, jumps forward. In either case an unbroken ligament is left behind. This ligament reduces the crack tip stress intensity until such time that it stretches and breaks. Bursts happen so rapidly that little or no plastic stress relief is possible during the cleavage components of the run/arrest event. This suggestion is consistent with our observation no. C3, above. Irwin and Zhang also assume an invariant cleavage burst velocity and that a lower overall velocity results from a longer pause.

Although there is no direct evidence for this mechanism in steel, we [23] did observe a burst/pause mechanism of crack propagation in a brittle plastic (Figure 5). The observations were of slow crack growth of a wedge-loaded specimen as observed in a light microscope when the average velocity is about 10^{-7} m/s. Here there is a jump accompanied by the formation of a new 'plastic zone', consisting of craze material. Rupture of the ligament transfers more stress on the crack-tip region facilitation craze stretching in preparation for a new jump.

Concluding Remarks

The contribution of Irwin and Zhang [1] is to envision the region at the crack tip as a damage zone, where the damage consists of microcracks. Both initial crack extension and crack growth are viewed as unstable growth of a microcrack within the damage zone. Eventually this extended microcrack joins with the main crack via a process of ligament rupture. Accordingly modelling cleavage fracture as the simple translation of a linear crack tip must be incorrect. Furthermore, models must take into account dynamic elastic effects even in nominally-static situations.

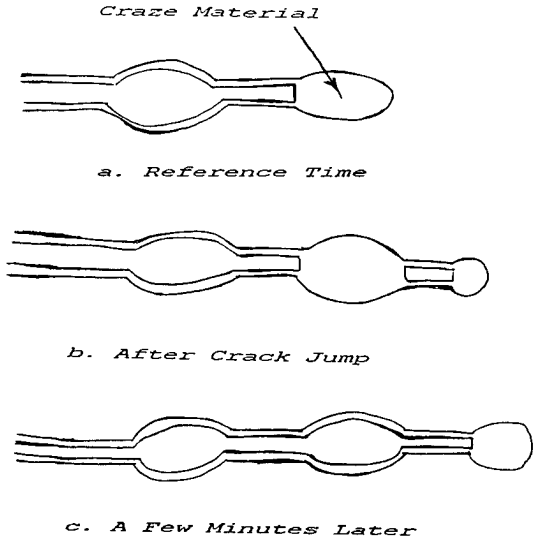


Figure 5. Slow Crack Growth in PMMA Brittle Plastic. After Mincer and Rosenfield [23]

Acknowledgments

The research reported here reflects the long-time cleavage-fracture studies at Battelle done in collaboration with valued colleagues. I am particularly fortu-

nate to have worked with Dick Barnes, George Hahn, Paul Held, Dick Hoagland, Mark Landow, Bhaskar Majumdar, Al Markworth, Charlie Marschall, Paul Mincer, Carolyn Pepper, Dinesh Shetty, and Andy Skidmore. Dr. Marschall read the manuscript and offered several useful comments. Dr. F. W. Brust of Battelle also provided some valuable insights on solid mechanics analysis. In addition my association with George Irwin on the ASTM Crack Arrest Task Group remains a cherished memory.

References

1. G. R. Irwin and X. J. Zhang, "Cleavage Behavior in Structural Steels," Int. J. Solids Structures, 32(1995) 2447-2456

2. A. R. Rosenfield and G. T. Hahn, "Numerical Descriptions of the Ambient Low-Temperature, and High-Strain Rate Flow and Fracture Behavior of Plain Carbon Steel," Trans ASM, 59(1966) 962-980

3. G. T. Hahn, "The Influence of Microstructure on Brittle Fracture Toughness," Metall. Trans. A, 15A(1984), 947-959

4. A. R. Rosenfield and D. K. Shetty, "Lower-Bound Fracture Toughness of a Reactor-Pressure-Vessel Steel," Engg. Fracture Mech., 14(1981) 833-842

5. A. R. Rosenfield and D. K. Shetty, "Cleavage Fracture of Steel in the Upper Ductile-Brittle Transition Region," Engg. Fracture Mech., 17(1983) 461-470

6. C. E. Turner, "A J-Based Engineering Usage of Fracture Mechanics," D. Francois, et al., eds., Advances in Fracture Research vol. 3 (Oxford, Pergamon Press, 1981), 1167-1189

7. R. O. Ritchie, J. F. Knott, J. R. Rice, "Ont the Relationship between Critical Tensile stress and Fracture Toughness in Mild Steel," J. Mech. Phys. Solids, 21(1973) 395-410

8. S.-X. Wu, Y.-W. Mai, and B. Cotterell, "Ductile-Brittle Fracture Transition as a Result of Increasing In-Plane Constraint in a Medium Carbon Steel," ASTM STP 1207, (1994) 376-386

9. A. R. Rosenfield, D. K. Shetty, and A. J. Skidmore, "Fractographic Observations of Cleavage Initiation in the Ductile-Brittle Transition Region of a Reactor-Pressure-Vessel Steel," Metall. Trans. A, 14A(1983), 1934-1937

10. A. R. Rosenfield and D. K. Shetty, "Cleavage Fracture of Steel in the Ductile-Brittle Transition Region," ASTM STP 856, (1985) 196-209

11. A. R. Rosenfield and B. S. Majumdar, "Micromechanisms and Toughness for Cleavage Fracture of Steel," Nucl. Engg. Des., 105 (1987), 51-57

12. X. J. Zhang, R. W. Armstrong, and G. R. Irwin, "Stereo (Scanning Electron Microscopy) Section Fractography of Isolated Cleavage Regions in Nuclear Vessel Steels," Metall. Trans. A, 20A (1989), 2862-2866

13. K. Wallin, et al., "The Effect of Loading Rate upon Irradiation Embrittlement Measured by Fracture Mechanical Properties," ASTM STP 1175, (1993)

14. X. J. Zhang, et al., "Fractographic Study of Isolated Cleavage Regions in Nuclear Pressure Vessel Steels and their Weld Metals," ASTM STP 1085, (1990) 89-101

15. J. H. Chen and G. Z. Wang, "Study of Mechanism of Cleavage Fracture at Low Temperature," Metall. Trans A, 23A(1992) 509-517

16. A. R. Rosenfield, "A Note on the Development of the ASTM Crack Arrest Test," H. P. Rossmanith, ed., Fracture Research in Retrospect - George R. Irwin Anniversary Volume, (in press)

17. G. R. Irwin and A. A. Wells, Metallurgical Reviews vol. 10 (Metals Park OH: American Society for Metals, 1965)

18. A. R. Rosenfield, "Suggested Toughness/Temperature Relations for Reactor Pressure Vessel Steels," Nucl. Engg. Design 14-4(1993) 487-496

19. A. R. Rosenfield and B. S. Majumdar, "A Micromechanical Model for Cleavage-Crack Reinitiation," Metall. Trans. A, 18A(1987) 1053-1059

20. R. G. Hoagland, A. R. Rosenfield, and G. T. Hahn, "Mechanisms of Fast Fracture and Arrest in Steels," Metall. Trans., 3(1972) 123-135

21. G. T. Hahn et al., "Fast Fracture Toughness and Crack Arrest Toughness of Reactor Pressure Vessel Steel," ASTM STP 711, (1980) 289-320

22. A. R. Rosenfield et al., "Recent Advances in Crack-Arrest Technology," ASTM STP 833,(1984) 149-164

23. A. R. Rosenfield and P. N. Mincer, "Crack Propagation and Arrest in PMMA," Polymer Science Symposium, 32(1971) 283-296

AN INVESTIGATION INTO THE MECHANISM OF CLEAVAGE FRACTURE IN A DUAL PHASE STEEL

Wei-Di Cao

ALLVAC
An Allegheny Teledyne Company
2020 Ashcraft Avenue
Monroe, NC 28110-0531

Abstract

The cleavage fracture behavior in notched and precracked specimens of a dual phase steel was studied as a function of grain size and test temperature. It was found that critical cleavage fracture stress σ_F is roughly proportional to the reciprocal square root of bainite packet size, but the dependency is weaker in comparison with other types of steels. The σ_F is relatively temperature independent within the test temperature range. The cleavage fracture toughness K_{IC} decreased with increasing grain size, but rose again after passing a critical grain size, leading to a minimum in K_{IC} - grain size dependence. A strong temperature dependence of K_{IC} was observed at higher test temperature near the transition temperature of cleavage - dimple fracture.

To explain the observed behaviors, a detailed fracture process observation was conducted by using acoustic emission monitoring, cross section observation and fractography on interrupted test specimens. It was found that the cleavage fracture mechanism could change with the type of test specimen and test temperature. The grain size and temperature dependencies of yield stress, plastiscity effect, and changes in fracture mechanisms all contributed to observed behaviors.

A comparison was made with major available theories and a modeling methodology is suggested to better explain the experimental phenomena.

Introduction

The cleavage fracture of steels as an academically and technologically important problem has been intensively studied over the past several decades. This work has led to a better understanding of many important issues such as the mechanisms of cleavage fracture, relationship of cleavage fracture characteristics, material microstructures and test conditions, and modeling of the cleavage fracture process. However, a number of basic problems are not yet completely understood, despite this great progress. Two of these issues are as follows:

1. The microstructural unit controlling the occurrence of cleavage fracture - An understanding of cleavage mechanisms was gained mainly from steels with a rather simple microstructure, such as mild steels and steels with spherical carbide particles. The critical events of cleavage fracture in steels with complex microstructures, such as martensite and bainite, are not determined conclusively. A number of investigators[1-2] suggested that cleavage fracture is controlled by the nucleation of a micro crack, but most people suggested that propagation of the critical micro crack is controlling[3-6]. It was agreed that the critical micro crack is always associated with a specific microstructural unit in those steels. Various microstructural constituents, including martensite or bainite packet[3,4], undissolved or tempered carbide particles, and nonmetallic inclusion particles[5, 6], etc., have been suggested to be the critical unit, but the conditions under which a specific microstructural unit will dominate the occurrence of cleavage fracture have not been

George R. Irwin Symposium on Cleavage Fracture
Edited by Kwai S. Chan
The Minerals, Metals & Materials Society, 1997

clearly defined. Moreover, Petch[7] pointed out the possibility that both grain size and grain boundary carbide sizes could be controlling factors for cleavage fracture in mild steels. It is not clear as to what features control cleavage fracture in steels with complex microstructures. This problem is particularly interesting for dual phase steels which have become an important class of steels. Many dual phase steels consist of a ferrite matrix and martensite-austenite (M-A) island dispersed in the matrix. So far, much evidence[8,9] has demonstrated that micro cracks form at M-A islands during the cleavage process, and M-A particle-sized micro cracks control the occurrence of cleavage fracture in these types of steels. Much less attention has been paid to the role of grain size of a ferrite matrix of these steels. Since the ferrite matrix has a packet structure in some types of dual phase steels with a bainite ferrite matrix, the packet size could become an important factor in the occurrence of cleavage fracture in these steels. However, this problem has not been studied in any detail.

2. The interrelationship between cleavage mechanism and test conditions - The cleavage fracture mechanism is regarded to be independent of test conditions as long as the mechanism of plastic deformation (slip or twin) is identical, i.e., the cleavage mechanism is independent of test temperature, strain rate and specimen geometry. This assumption is held in almost all the available theories discussing temperature and specimen geometry dependencies of cleavage fracture characteristics (critical cleavage fracture stress or cleavage fracture toughness). However, this assumption has not been fully proven by detailed experimental work. Our previous exploratory work demonstrated that the cleavage fracture mechanism could be different in different specimen geometries, such as notched and precracked specimens, and can change with test temperature and even the grain size. Further studies are obviously needed.

An extensive research program has been initiated to study all the relevant issues, and the detailed results will be published elsewhere[10-12]. This paper will report the major results generated from this study.

Experimental Procedures

The test material was a C-Mn-B steel containing 0.12%C, 3.08%Mn and 0.007%B. The test steel was heat treated to have different grain sizes but with an identical microstructure consisting of dislocated lathe ferrite in packets and M-A islands (so-called granular bainite), see Figure 1. Since all the microstructural constituents other than grain/packet size (size and volume fraction of M-A islands, content of retained austenite and nonmetallic inclusion particles) were identical, this material provided an opportunity to study the true effect of grain or packet size on cleavage fracture in this type of dual phase steel. The microstructural parameters of test steels are listed in Table 1. The relationship between grain size and packet size can be expressed as $dp = k D^n$, with an exponent n of about 2/3, which is in good agreement with Ref. 13.

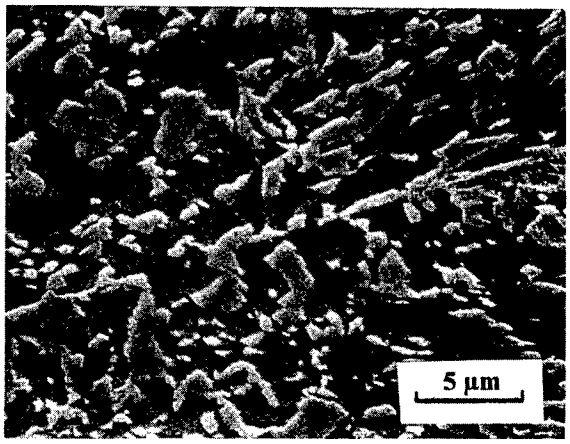


Figure 1: Microstructure of test steel.

Table I Microstructural Parameters of Test Steels

Heat Treatment		A	B	C	D	E	F	G	H	I
Grain Size (μm)		245.0	180.0	80.0	40.1	20.7	15.8	12.3	10.4	8.5
Packet Size (μm)		56.0	48.0	26.0	16.4	10.8	9.0	7.8	6.7	6.0
M-A Phase	f_V (%)	37.1	n.d.	n.d.	35.9	36.1	n.d.	n.d.	37.5	n.d
	L (μm)	1.8	n.d.	n.d.	1.9	1.6	n.d.	n.d.	1.6	n.d.
γ_R (%)	24° C	1.4	2.1	1.4	1.8	1.7	2.3	2.0	2.1	1.9
	- 120° C	1.3	n.d.	n.d.	1.6	1.7	n.d.	n.d.	1.9	n.d.

* f_V is the volume fraction of M-A islands and L its average intercept length.
** n.d. — not determined.

Fracture tests were performed on test steels at different test temperatures from -120°C to 10°C. The tests performed included a 45° V- notched four point bending test to determine critical cleavage fracture stress[14], and three point bending tests of precracked specimens for fracture toughness determination.

The fracture tests were monitored by acoustic measurement to trace the development of cleavage fracture process at different test conditions. Some tests were interrupted at different load levels before final fracture, and the interrupted test specimens were sectioned and examined to gain the information of the micro cracking process by cross section metallographic observation.

Experimental Results

Critical Cleavage Fracture Stress

The critical cleavage fracture stress was determined at -80°C and -120°C, and the results are shown in Figure 2 as a function of grain and packet size. The cleavage stress is roughly proportional to the reciprocal square root of bainite packet size, indicating that the packet size does affect the cleavage fracture of this steel.

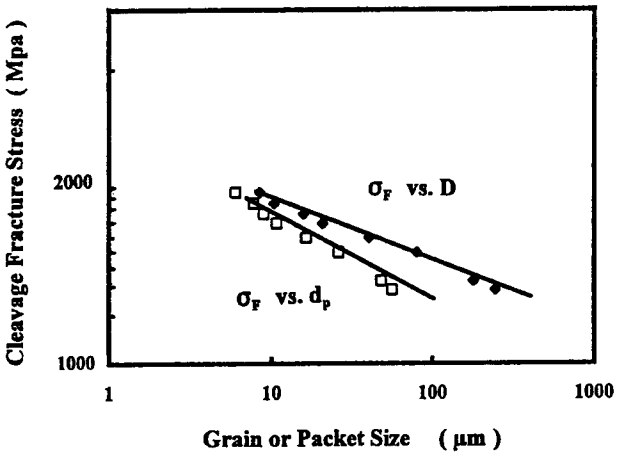


Figure 2: Grain Size and Packet size dependencies of cleavage fracture stress.

Cleavage Fracture Toughness

Figure 3 shows the packet size dependence of fracture toughness at different test temperatures. It can be seen from this figure that the fracture toughness decreases with increasing packet size up to a critical packet size and reverses this tendency at packet sizes greater than this critical value. This trend holds at almost all the test temperatures with a weaker packet dependence at lower temperatures. The packet size dependence of fracture toughness in the region of packet sizes finer than a critical value can be approximately given by a $d_p^{-1/2}$ relation except for the results obtained at 10°C in steels with fine grain size, as marked in Figure 3. This deviation was caused by the change in fracture mode, i.e., the fracture mode in this region was not fully cleavage fracture; instead, there was a dimple fracture band immediately ahead of the blunted crack tip. Therefore, these data should be excluded from analysis.

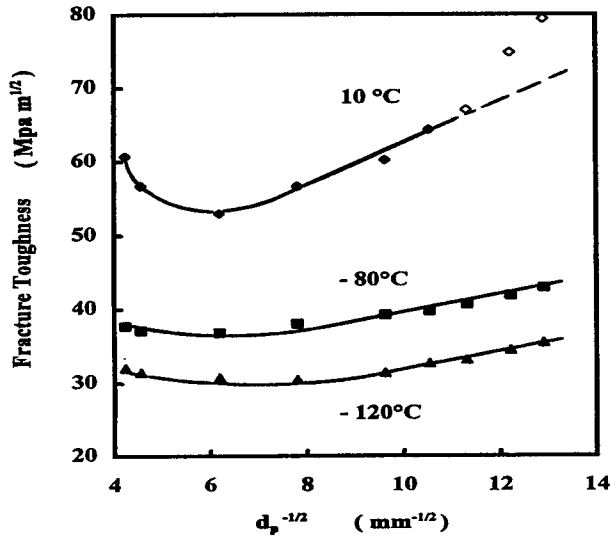


Figure 3: Cleavage fracture toughness as a function of bainite packet size at different test temperatures.

The temperature dependence of fracture toughness was more carefully studied in steels with a grain size of 20.7 and 80 μm, and the results are shown in Figure 4. A very rapid increase in fracture toughness was seen at higher test temperatures, i.e., from -40°C to 10°C. This rapid increase in fracture toughness is not due to the effect of change in frac-

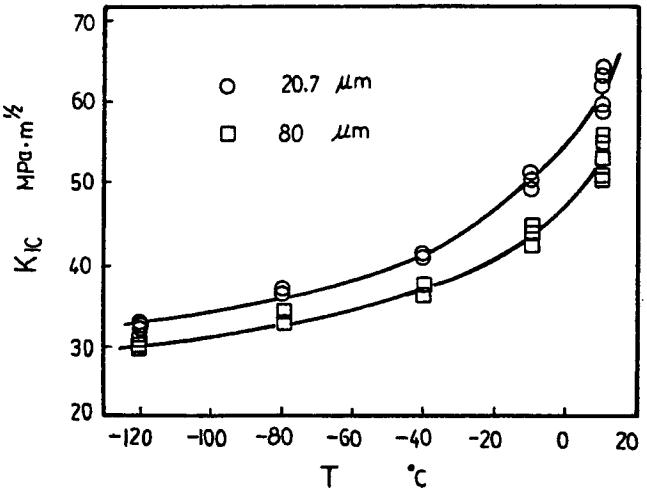


Figure 4: Temperature dependency of cleavage fracture toughness

ture mode because the fracture mode was cleavage in all the cases studied in this figure except for one data point obtained at 10°C in steel with D=20.7μm where a very narrow dimple fracture band existed at the crack tip.

Cleavage Fracture Process Observation

The observation of cleavage process was not very successful in notched specimens. The strong AE signal burst can be picked up only immediately before final fracture, and the abrupt breakage of test specimens frequently led to the damage of the AE sensor. However, this fact at least indicates that the occurrence of cleavage micro cracking associated with strong AE signals was almost concurrent with bulk breakage of notched specimens. The cross section observation on specimens unloaded at ~ 0.95 fracture load at which strong AE signals occurred found some micro cracks formed at the interfaces between M-A islands and matrix, see Figure 5. No packet sized micro crack was found.

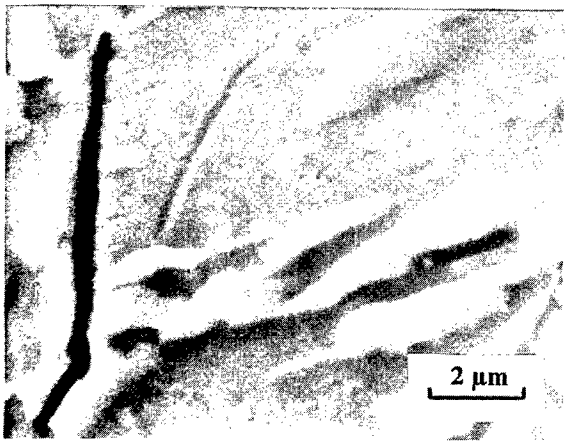


Figure 5: Micro cracks formed at M-A island and bainite-ferrite interfaces.

Much more information was obtained in precracked specimens. The AE activity was significantly different from that in notched specimens; strong AE activity was picked up at load levels much lower than the pop-in load. A parameter K_i was determined from the deflection point in accumulated AE energy vs. K_i curves, following the method suggested in Reference 15. It was believed that K_i indicates the onset of cleavage micro cracking. This has been proved in our cross section study. Figure 6 shows K_i, together with K_{IC}, as a function of grain size. It can be seen that K_i is much lower than K_{IC}, particularly in coarse grained steels, and monotonically decreases with increasing grain size in contrast with the behavior of K_{IC} at coarse grain region.

The cross section observation on interrupted precracked specimens revealed many interesting aspects of cleavage

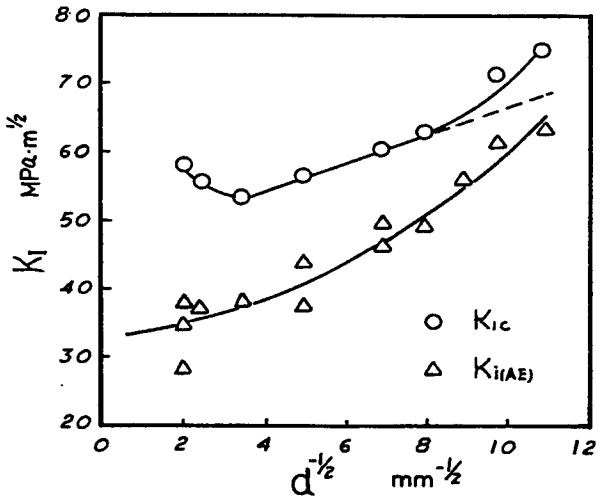


Figure 6: Initiation K_I of acoustic emission burst as a function of grain size.

fracture occurrence in this specimen geometry. The major results can be summarized as follows and are shown in Figure 7:

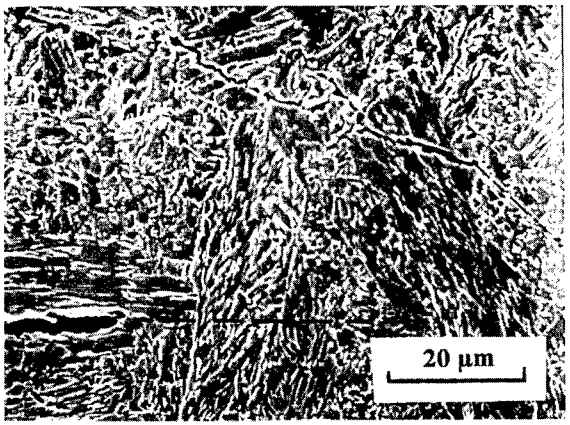
a. A few stable micro cracks with a size equivalent to packet size formed ahead of the macro crack tip at the load well below the pop-in load. The stress intensity factor for the onset of micro cracking was roughly coincident with K_i in Figure 6.

b. The first micro crack formed at the location having a certain distance from the crack tip and with a certain angle to the macro crack plane, see Figure 7 (a).

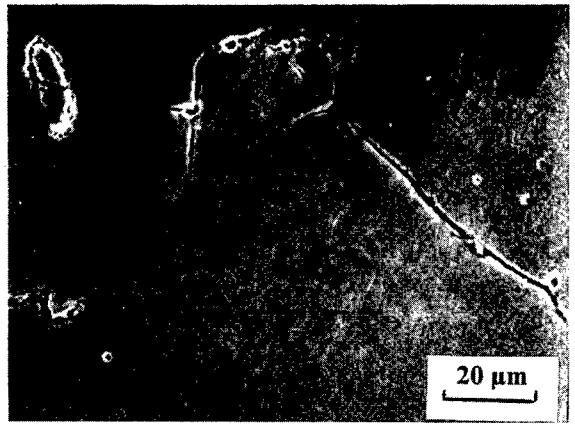
c. Increasing the load caused the micro cracking to extend into a region further away from the crack tip and turn back to the macro crack plane. A significant blunting of the tip of micro cracks occurred at higher test temperatures. The micro cracks could connect each other in the micro cracking zone, but ligament zones still existed between the micro cracking zone and macro crack tip, see Figure 7 (b), although the connection of micro cracks and the macro crack tip could occur at a few localized regions.

d. Final propagation of the macro crack was realized by cleavage cracking of ligament zones, started either at the macro crack tip, or more frequently from blunt micro crack tips, Figure 7 (c). This catastrophic connection occurred at pop-in load, leading to abrupt propagation of macro crack over a larger distance, Figure 7 (d).

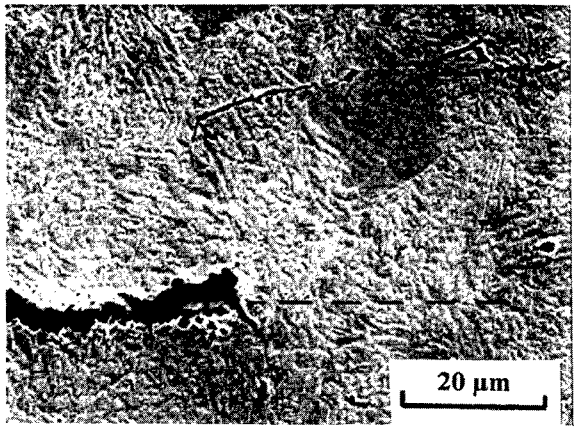
In order to quantitatively characterize the distance and angle between the macro crack tip and the nearest micro crack, a measurement was made and the results are shown in Figure 8. It can be seen that the distance and angle are the function



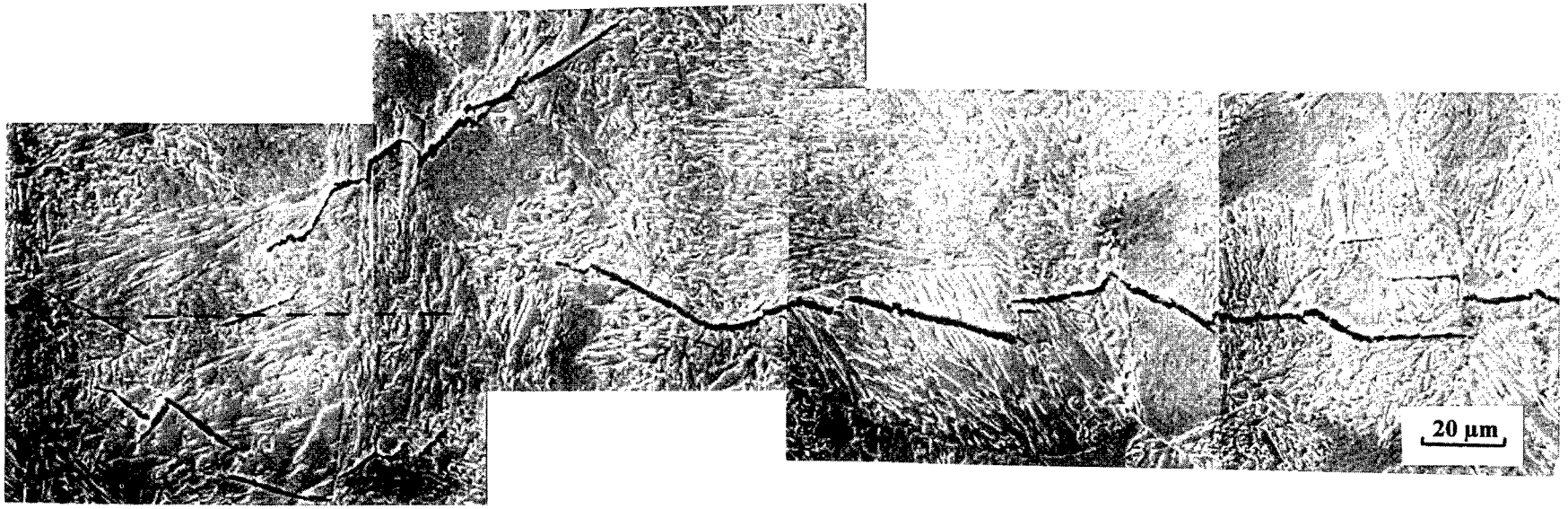
(a)



(b)



(c)



(d)

Figure 7: Process of cleavage fracture in precracked specimens (a) micro crack formed in the front of macro crack at certain angle to the macro crack plane, (b) micro cracking turned back to the extension of macro crack plane, (c) connection between micro and macro cracks by cleavage fracture of ligament started at the micro crack tip, (d) macro crack propagation over a larger distance at pop-in load.

of test temperature and grain size; with increasing test temperature, the angle between the macro crack plane and the nearest micro crack became greater, but the distance between micro and macro crack tips only modestly increased. The major change caused by increased grain size was the increase in the distance between macro crack tip and micro crack. It is believed that these phenomena, together with the blunting of the micro crack tip, exerted a great influence on the onset of propagation of the macro crack, and therefore the fracture toughness. These results clearly showed that the basic mode of cleavage process may not change with test conditions and grain size of test steels in precracked specimens, but the detailed mechanism may be significantly different.

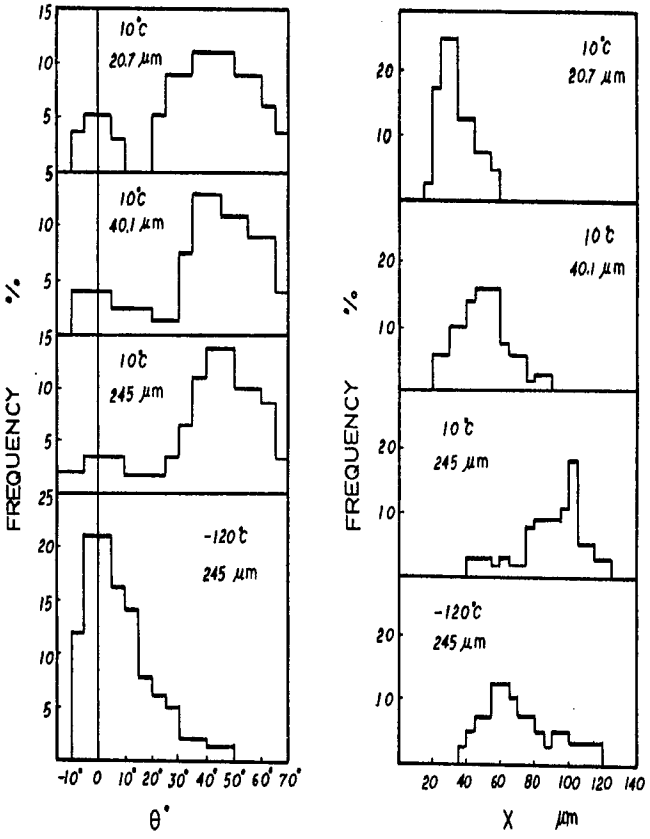


Figure 8: Results of the measurements on cross section. Θ-angle of micro crack to macro crack plane and X-distance of micro crack to the tip of macro crack.

Discussion

The cross section observation seemingly implied that the controlling mechanism in notched specimens would be the propagation of an M-A island sized micro crack. The calculation of microscopic critical cleavage fracture stress appears to support this mechanism. Following the arguments adopted in most previous studies, the σ_F obtained by the bending test is very close to the microscopic critical cleavage fracture stress and can be expressed as:

$$\sigma_F = \{ 4E\gamma_p/\pi (1-\nu^2) a \}^{1/2} \qquad (1)$$

Where "γ_p" is the effective surface energy for micro crack propagation and "a" is the size of critical micro crack, i.e., M-A island or packet size, as appropriate. Substituting relevant values into equation (2), γ_p of 14 - 20 J m^{-2} or 100-120 J m^{-2} were obtained if taking "a" as M-A island size or bainite packet size. The former value is closer to the reasonable effective surface energy for cleavage fracture, indicating that the M-A island might be the controlling microstructural unit.

However, this is contradictory with the packet size dependency of critical cleavage fracture stress because the M-A island size does not change with grain size, and a packet size independent cleavage stress should be found if M-A islands are the only controlling microstructural constituent. To show the concurrent effect of both M-A island size and packet size on cleavage fracture stress, the σ_F is plotted as a function of packet size in Figure 9 on the basis of data obtained in this study and from literature. According to the above equation, there should be a linear relation passing through the origin point in the σ_F vs. $a^{-1/2}$ plot, and the γ_p can be determined by the slope of σ_F and $a^{-1/2}$ line. However, the σ_F and $a^{-1/2}$ line obtained in this study does not pass through origin, and the γ_p cannot be derived from this line. This result is difficult to explain by single microstructural unit (either M-A island or packet) controlling mechanism and may be more properly explained by a mechanism suggested by Petch[7] for mild steels, i.e., both grain size and particle size contribute to the cleavage fracture.

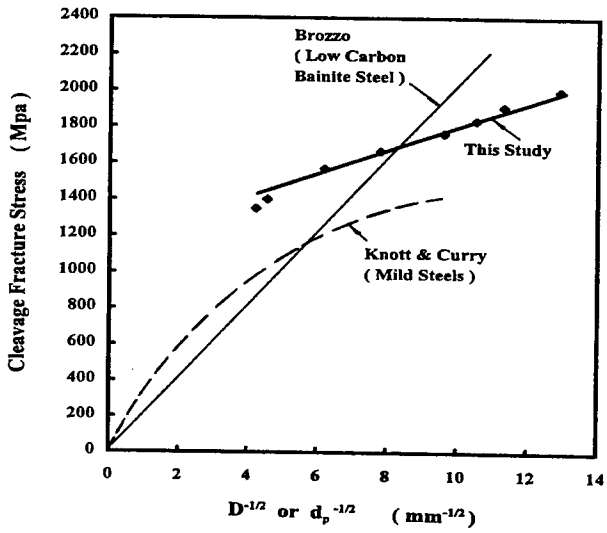


Figure 9: Comparison of cleavage fracture stress obtained in this study with other results.

This study also illustrates that both direct and indirect fracture process observation techniques employed in this study, such as acoustic emission and cross section observation, are not able to expose the interaction between the microstructure and cleavage fracture process in notched specimens and failed to provide an explanation of how the M-A island-matrix interface and the packet boundary worked together to prevent the cleavage propagation of micro cracks.

On the other hand, these indirect and direct fracture process observation techniques provided much new information on the cleavage process in precracked specimens. The most striking result from this study is that the mechanism of cleavage fracture could change with specimen geometry and test conditions.

1. In notched specimens, the propagation of M-A island sized micro cracks immediately led to the catastrophic cleavage failure of bulk specimens, but in precracked specimens, this localized cleavage fracture (formation and propagation of micro cracks) could occur far before the propagation of macro crack, which was more likely controlled by the bulk connection, not local connection, between the macro crack and localized cleavage zone. This picture is obviously against many cleavage fracture models, such as the weakest linkage model[16-18], and in support of the so-called process zone model[19,20].

2. The detailed process of the formation of the micro cracking zone ahead of, and its connection with, the macro crack varied with test conditions, especially the test temperature and microstructure. With increasing test temperature, the distance to macro crack tip and the angle to macro crack plane of the micro cracking zone increased, and blunting of micro crack tip developed. These observations are at odds with the assumptions adopted in many theoretical models, for example, the micro crack formation at the extension of the macro crack plane with maximum tensile stress.

The cleavage fracture process features above have not been included in most available models of K_{IC}. Most available theories applied the elastic-plastic stress distribution of a crack tip obtained by continuum mechanics analysis with the assumption of a cleavage mechanism independent of specimen geometry and test conditions to model the cleavage fracture in precracked specimens. For example, the temperature dependence of K_{IC} derived in most theories, such as the weakest linkage theory, can be expressed as:

$$K_{IC}(T_2) / K_{IC}(T_1) = [\,\sigma_{ys}(T_2) / \sigma_{ys}(T_1)\,]^{m/4-1} \qquad (2)$$

Where $\sigma_{ys}(T_2)$, $K_{IC}(T_2)$ and $K_{IC}(T_1)$, $\sigma_{ys}(T_1)$ are fracture toughness and yield stress at T_2 and T_1, respectively. "m" is a constant of ~ 22.

Equation (2) indicates that the temperature dependency of K_{IC} is controlled by that of yield stress. Eq. (2) is plotted in Figure 10 by using the results of this study and significant deviation from eq. (2) can be seen at higher test temperatures. This deviation is believed to be caused by the changes in the fracture mechanism with specimen geometry and test conditions. An early occurrence of local micro cracking, increased distance and angle of the micro cracking zone to macro crack tip, and the blunting of the micro crack tip, all contribute to the observed temperature dependency which is stronger than that predicted by available theories. The packet size dependency with a minimum of K_{IC} can be similarly explained by taking the changes in the geometry of the micro cracking zone relative to the macro crack. The detailed analysis on the temperature and grain size dependencies was reported in References 11 and 12.

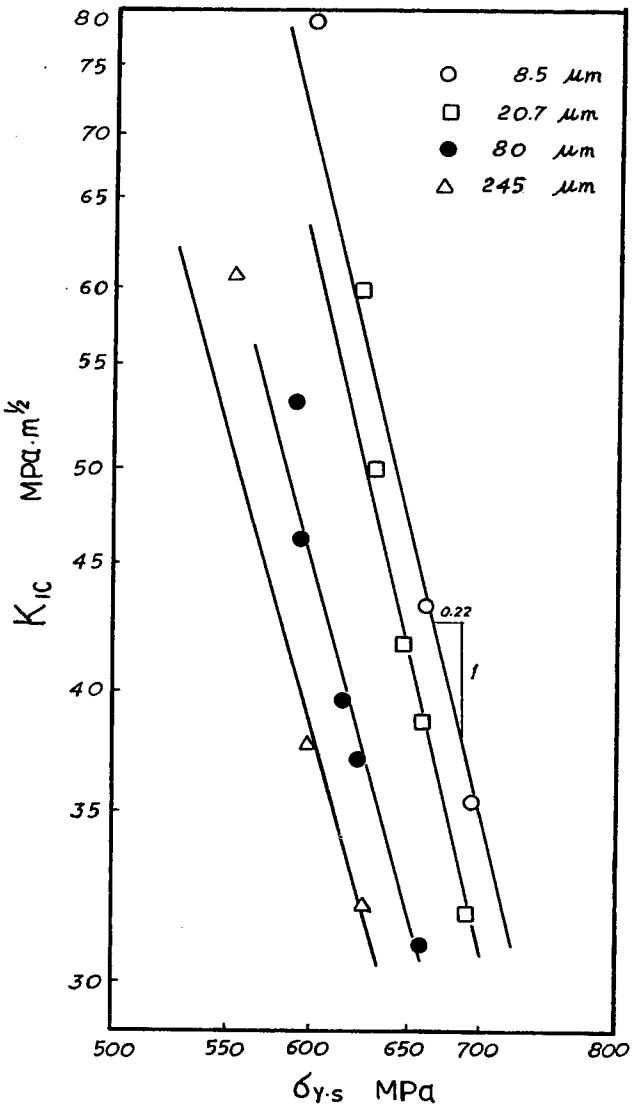


Figure 10: Temperature dependency of fracture toughness expressed as a function of yield stress.

In order to build up a model of cleavage fracture in precracked specimens consistent with actual fracture process and mechanical behaviors observed experimentally, it is important to take the following factors into account:

a. Screen effect of the micro cracking zone to the macro crack

b. Side formation of micro cracks, i.e., the angle of micro crack to macro crack plane

c. Distance between micro crack and macro crack tip

d. Blunting of both macro crack and micro crack tips

This model is under development and assumes the critical condition for the propagation of a stationary macro crack to be the attainment of critical tensile stress over the ligament between the macro crack tip and micro cracking zone, and the tensile stress over the ligament is affected by the above stated factors. The detailed discussion on the proposed modeling approach can be found in Reference 12.

Conclusions

The cleavage fracture mechanisms were studied in a dual phase steel consisting of a bainite ferrite matrix and M-A islands. The only microstructural variable in test steels was the bainite grain or packet size with the size of M-A islands being nearly constant. The following conclusions can be derived from this study:

1. The cleavage fracture in notched specimens occurred immediately after initiation of the micro cracking process, and the fracture process observation revealed stable M-A island sized micro cracks which formed by the separation at the M-A island and matrix interface. The calculation of effective surface energy from measured critical cleavage fracture stress supported the island sized micro crack controlling mechanism.

2. The critical cleavage fracture stress of this steel is roughly proportional to the reciprocal square root of packet size, indicating that the matrix - matrix interface also played a role in retarding the cleavage propagation of the micro crack, and therefore a dual microstructural barrier of micro crack cleavage propagation is possible.

3. A unique grain/packet size dependency of K_{IC} was found in this steel with a K_{IC} minimum at some critical grain/packet size. A stronger K_{IC} - test temperature dependency was also established.

4. The cleavage fracture mechanism in precracked specimens involved micro crack formation and propagation ahead of the crack tip at a K_I level much lower than K_{IC}, and the catastrophic fracture at K_{IC} was controlled by the cleavage connection between the macro crack tip and the nearest micro cracks. This is totally different from that in notched specimens where the micro crack propagation controls the occurrence of cleavage fracture.

5. The details of micro crack formation, propagation and their connection with the macro crack tip varied with changing test conditions and grain size. With increasing test temperature, the angle of micro cracks to macro crack plane became greater (side formation of micro cracks) and blunting of not only the macro crack tip, but also the micro crack tips intensified. The distance from micro cracks to the macro crack tip increased with increasing grain/packet size.

6. A cleavage model in precracked specimens could be developed by taking the above factors into account, i.e., screen effect of early micro cracking, distance from macro crack tip and angle to macro crack plane of the nearest micro crack and blunting of both macro crack and micro crack tips.

References

1. D. A. Curry, Metal Science, 1982, vol. 16, 435-40.

2. D. A. Curry, Metal Science, 1984, vol. 18, 67-76.

3. P. Brozzo, G. Buzzichelli, A. Mascanzoni and M. Mirabile, Metal Science, 1977, vol. 11, 123-29.

4. H. Kotilainen, K. Torronen and P. Neonen, "Advances in Fracture Research," D. Francois, ed., Pergamon Press, 1982, vol. 2, 723-30.

5. P. Bowen and J. F. Knott: Metal Science, 1984, vol. 18, 225-35.

6. P. Bowen, S. G. Druce and J. F. Knott: Acta Metal., 1986, vol. 34, 1121-31.

7. N. J. Petch, Acta Metall., 1986, vol. 34, 1387-93.

8. O. M. Akselsen, Φ-Grong and J. K. Solberg, Mater. Sci. Technol., 1987, vol. 3, 649-55.

9. C. L. Davis and J. E. King, Metall. Trans. A., 1994, vol. 25A, 563-73.

10. W. D. Cao and X. P. Lu, "A Fundamental Study of Cleavage Fracture in a Dual Phase Steel, I. Cleavage Fracture Characteristics," unpublished work.

References (Con't)

11. W. D. Cao and X. P. Lu, "A Fundamental Study of Cleavage Fracture in a Dual Phase Steel, II. Cleavage Fracture Mechanisms," unpublished work.

12. W. D. Cao and X. P. Lu, "A Fundamental Study of Cleavage Fracture in a Dual Phase Steel, III. Comparison with Available Theories," unpublished work.

13. T. E. Swarr and G. Krause, "Grain Boundaries in Engineering Materials," J. L. Walter, J. H. Westbrook and D. A. Woodford, eds., Claitor's Publishing Division, 1975, 127-38.

14. J. Griffith and D. R. J. Owen: J. Mech. Phys. Solids, 1971, vol. 19, 419-31.

15. M. A. Khan, T. Shoji and H. Takahashi, Metal Science, 1982, vol. 16, 118-26.

16. A. Pineau, "Advances in Fracture Research," D. Francois, ed., Pergamon, New York, NY: 1981, vol. 2, 553-76.

17. F. M. Beremin, Metall. Trans. A, 1983, vol. 14A, 2277.

18. T. Lin, A.G. Evans and R. O. Ritchie, Metall. Trans. A, 1987, vol. 18A, 641.

19. W. W. Geberich, et al., Metall. Trans. A, 1987, vol. 18A, 1861-75.

20. W. W. Geberich, "Metallurgical Aspects of Crack-Tip Failure Process," D. T. Read and R. P. Reed, eds., ASTM STP945, ASTM, Philadelphia: 1988, 5-18.

BRITTLE FRACTURE IN HIGH-STRENGTHENIHG SINGLE CRYSTALS OF AUSTENITIC STAINLESS STEELS

Yu. I. Chumlyakov, I. V. Kireeva, E. I. Litvinova, V. I. Kirillov, N. S. Surikova
Siberian Physico-Technical Institute, Revolution sq., 1, Tomsk, 634050 Russia
chum@phys.tsu.tomsk.su

Abstract

Single crystals of austenitic stainless steels with a stacking fault energy γ_{sf}=0.02-0.2 J/m^2, fcc heterophase Cu-Al-Co, bcc heterophase Fe-Cr-Co-Mo and titanium nickel crystals were investigated in order to find out the deformation and fracture dependence on crystal orientation, test temperature, nitrogen content, size and volume fraction of second phase particles. It was shown that the plastic deformation mechanism (slip and twinning) and strength level play the main role in the formation conditions of the brittle fracture. In the high-strengthening fcc single crystals the "ductile-to-brittle" transition (DBT) was found. DBT is caused by the combination of the twinning deformation with the high strength level. It was made the generalization of obtained results for the case of bcc crystals and titanium nickel B2-intermetallides.

George R. Irwin Symposium on Cleavage Fracture
Edited by Kwai S. Chan
The Minerals, Metals & Materials Society, 1997

Introduction

In fcc poly- and single crystals with a stacking fault energy γ_{sf}=0.02-0.2 J/m^2 the achievement of the high strength level leads to the appearance of new peculiarities of mechanical behavior as compared with the low-strengthening crystals of pure fcc metals and substitution alloys [1,2]. The combination of the high strength level with a low stacking fault energy γ_{sf}=0.04-0.02 J/m^2 leads to the deviation from the Boas-Schmid law (the appearance of the strong orientation dependence and asymmetry of τ_{cr}), which is not observed in the low-strengthening fcc crystals [1,2]. It was experimentally determined two types of non-schmid phenomena, which are different each from other by their nature. First type is connected with the splitting of the a/2<110> dislocation into the Shockley a/6<211> partials according to reaction [3]

$$a/2[\bar{1}01]=a/6[\bar{2}11]+a/6[\bar{1}\bar{1}2] \qquad (1)$$

Crystals of [111] tension axis and other orientations, which are on the right from the large circle passing over [113]-[012] poles, are "soft", because of the elastic interaction of the impurity atoms and disperse particles with the strongly extended dislocations. However, on the left from the circle above-mentioned, on contrary, the dislocation splitting decreases, unextended dislocations interact with obstacles. Such crystals are "hard" [1, 2].

The change of effective stacking fault energy γ_{eff} is estimated in the theory of dislocations [3,4]

$$\gamma_{eff}=\gamma_{sf}\pm 0.5*(m_2-m_1)*\sigma*b_1 , \qquad (2)$$

where m_2, m_1 are the Schmid factor for the leading a/6[211] and trailing a/6[112] Shockley dislocations; σ is the external stress applied to the crystals; b_1 is the Burgers vector module of the partial dislocation; plus and minus signs take into considerations the tension and compression deformation, respectively (Fig.1).

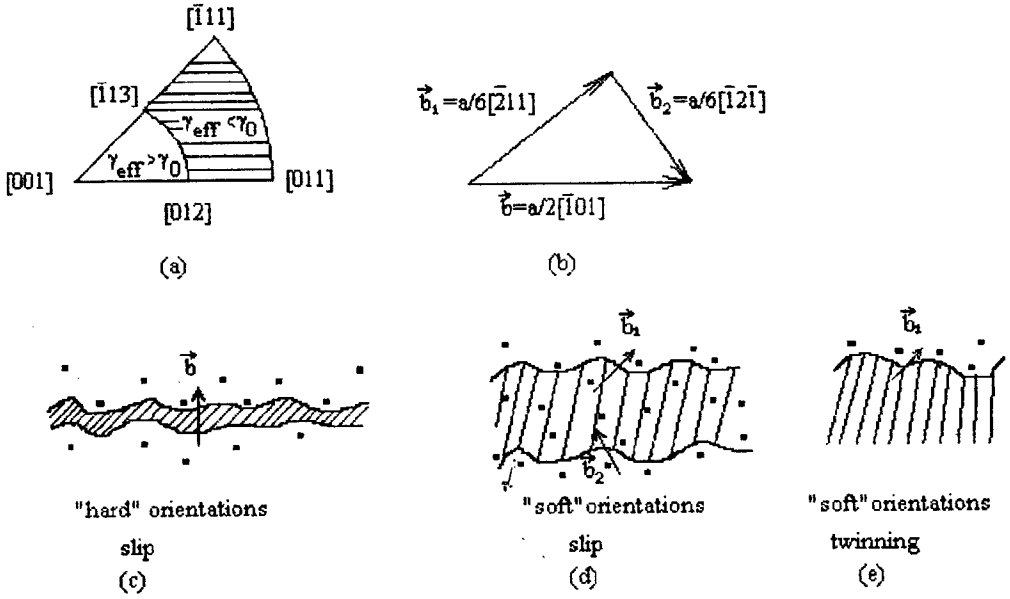


Figure 1: The a/2<110> dislocation splitting into the a/6<211> Shockley partials in the external stress field (a, b); the interaction with obstacles at slip and twinning in "soft" and "hard" orientations (c, d, e).

The orientation dependence analysis of the splitting of the a/2<110> dislocation into the Shockley partials is experimentally confirmed by number of works [1, 2, 5], and it is taken as a principle of the orientation dependence of τ_{cr}. Using works over the calculation of the τ_{cr} dependence on the splitting of dislocations at the cutting of coherent particles [6], the by-passing of plastically non-deforming second phase precipitation [7], the estimate of the solid solution hardening by interstitial atoms [8], non-schmid effects may be explained both qualitatevely and quantitatively.

Second type of non-schmid phenomena is connected with the orientation dependence of the plastic deformation mechanism (slip and twinning). In "soft" [111] orientations the slip deformation is changed by twinning, which develops from the first deformation stages and is the single deformation mechanism at T=77-673K [1, 2, 9]. In "hard" [001] orientations the deformation realizes by slip of unextended dislocations. In high-strengthening crystals the slip-to-twinning transition may be regarded as the loss of stability of extended dislocations to the splitting into Shockley partials according to reaction (1). Consequently, in high-strengthening crystals the single dislocations may

be regarded as sources of stacking faults in accordance with the idea of the "slip source" [10].

In present work single crystals of austenitic stainless steels strengthened by nitrogen and disperse particles, high-strengthening heterophase copper base Cu-Al-Co single crystals were investigated in order to find out the role of strength level, the deformation mechanism (slip and twinning), the tension axis orientation in the development of a plastic deformation and fracture. Such investigations exactly on single crystals are very important. At first, single crystals permit to overcome difficulties connected with grain boundaries and their orientation in the field of applied stresses. Secondly, single crystals give a possibility to model an influence of important material parameters (γ_{sf}; the deformation mechanism: slip and twinning; the strength level) on the magnitude of the strain-hardening coefficient Θ, the plasticity, the localization of plastic flow and the fracture mechanism. Such investigations permit to find out necessary conditions for the fracture mechanism change from ductile, which is usually observed in pure fcc crystals and their solid solutions, to brittle in high-strengthening fcc crystals.

Experimental

Single crystals were grown by the Bridgman technique in inert gas atmosphere and then were homogenized at T=0.8-0.9 T_m (T_m - the melt alloy temperature). Test samples of a preselected orientation were spark-cut ; all samples were mechanically ground, chemically etched , and electrolytically polished to remove damaged surface layers. The crystal orientation was determined using X-ray diffraction. The dislocation structure was investigated by a Tesla BS-500 electron microscope at 90 kV. The crystal fracture surface was observed by a scanning electron microscope REM-200.

Results and Discussion

1. Mechanical properties and fracture of single crystals of austenitic Cr-Ni stainless steels with a high nitrogen content

1.1 Tension of [001] crystals at T=77K

Austenitic stainless steels : I-Fe-18%Cr-12%Ni-2.3%Mo; II- Fe-24%Cr-18%Ni-2.2%Mo; III-Fe-18%Cr-16%Ni-10%Mn; IV-Fe-26%Cr-32%Ni-3.3%Mo (wt.%) were investigated to find out the dependence of mechanical properties, plasticity, fracture mechanism on tension axis orientation, nitrogen concentration (γ_{sf}=0.020 J/m^2 for I-III steels; γ_{sf}=0.20 J/m^2 for IV steel) at the test temperature T-77K.

The stress-strain curves of I-IV steels of [001] orientation in dependence on the nitrogen concentration are presented in Figure 2. Alloying by nitrogen up to C_N=0.5 wt.% of I steels leads to the increase of σ_{cr} 2.5 times as compared with the nitrogen-free crystals (Fig. 2a, 1-3 curves). Stages of stress-strain curves and plasticity change insignificantly as compared with nitrogen-free crystals. It is observed the small decrease of Θ on the early deformation stages ε<10% at C_N=0.4 wt.%. It should be noted that at C_N=0.5 wt.% the small section of the stress-strain curve with Θ~0 appears, which is connected with deformation by the Lüders band.

At ε>5% the shear develops in several slip systems simultaneously, the precession of the crystal axis is absent. At ε<4% dislocations form planar pile up in several slip systems. And at ε>10% dislocation structure may be characterized as a homogeneous distribution of unextended dislocations; deformation twins and stacking faults are not observed (Fig.3 a, b). At C_N=0-0.5 wt.% the fracture of I crystals is ductile, it occurs by necking (Fig. 4), the fracture surface is non-perpendicular to tension axis, crystallographic planes are close to the (111) plane. At C_N=0-0.5 wt.% both in II-III crystals with a low stacking fault energy γ_{sf} and in the IV crystals with a high γ_{sf} the stress-strain curve evolution, the plasticity change are analogous those of above-mentioned (Fig. 2a, 1-3 curves). In II-IV crystals the increase of C_N>0.5 wt.% is accompanied by the increase of Θ, the plasticity decrease up to ε=4% (Fig. 2a, curve 4; Fig. 2b, curve 3). In this case the crystal fracture occurs without necking, perpendicularly to the tension axis along the {100} planes. It observed the fracture change from ductile at C_N<0.5 wt.% to cleavage (Fig. 3a, b) or to mixed fracture type (the combination of dimples and cleavages). Thus, strengthening of [001] crystals of austenitic stainless steels by nitrogen leads to the crystal plasticity decrease and the fracture mechanism change from ductile at C_N<0.5 wt.% to mixed or brittle at C_N>0.5 wt.%. This peculiarity is common for crystals with different γ_{sf}=0.020-0.20 J/m^2.

1.2 Tension along [111], [011] axes at T=77K

Nitrogen-free crystals of I steel of [111], [011] tension axis are plastic. It is observed the ductile fracture by necking after ε=25% and ε=40%, respectively (Fig. 5a, curve 1). In the neck of [011] crystals two systems of macroscopic shear bands form along which the fracture by cut occurs. X-ray investigations shown that within localization bands material is disoriented relatively the homogeneously deformed crystal part approximately 9^0, the localization bands are approximately 5-7^0 to slip planes (111). In consequence, the "geometrical softening" occurs, that is the increase of Schmid factor for slip systems in macroscopic shear band as compared with the homogeneously deformed part of crystal [11, 12]. This circumstance is the cause of anomalous shear localization in the bands which leads to the fracture by cut (Fig.6a).

Alloying by nitrogen to C_N<0.4 wt.% leads to the increase of τ_{cr} , the change of stress-strain curve stages , plasticity and fracture mechanism. Metallographic, TEM

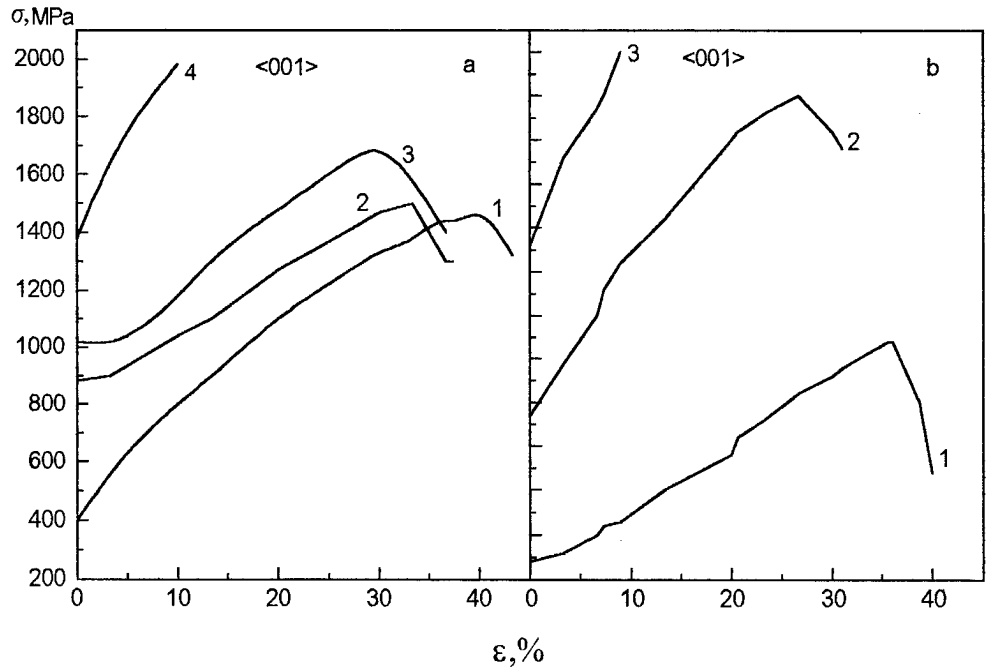


Figure 2: The stress-strain curves of austenitic stainless steels at tension along [001] axis at T=77 K in dependence on nitrogen content (a)- low γ_{sf}=0.02 J/m^2: 1-without nitrogen; 2- 0.4 wt.%; 3- 0.5 wt.% (I steel); 4- 0.7 wt.% (III steel);
(b)- high γ_{sf}=0.20 J/m^2: 1-without nitrogen; 2- 0.3 wt.%; 3- 0.7 wt.% (IV steel).

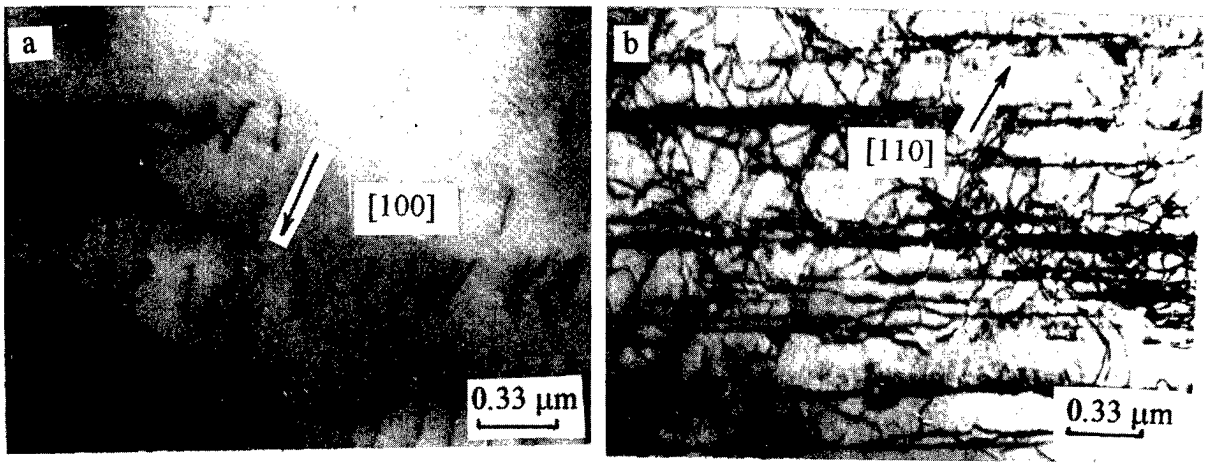


Figure 3: The dislocation structure of [001] single crystals of I steel at tension (C_N=0.5 wt.%, T=77 K)
a-planar pile up, ε=3%; b-homogeneous distribution of unextended dislocations, ε=15%

investigations of the dislocation structure, X-ray measuring of the crystal axis precession shown that the early deformation stages ε<13% correspond to the slip deformation development by planar dislocation pile up in several slip systems. Abrupt fall of stress is connected with the deformation transition in single slip system and with the further motion of Luders band up to ε=20-25%. The increase of Θ is connected with transition again to multiple-slip at ε>20-25%. At C_N<0.35 wt.% fracture occurs by necking , and at C_N>0.4 wt.% the neck is absent. On the fracture surface at C_N=0.35 wt.% parts of ductile and brittle fracture are observed. It should be noted that at the increase of the nitrogen content C_N the fraction of the brittle fracture increases.

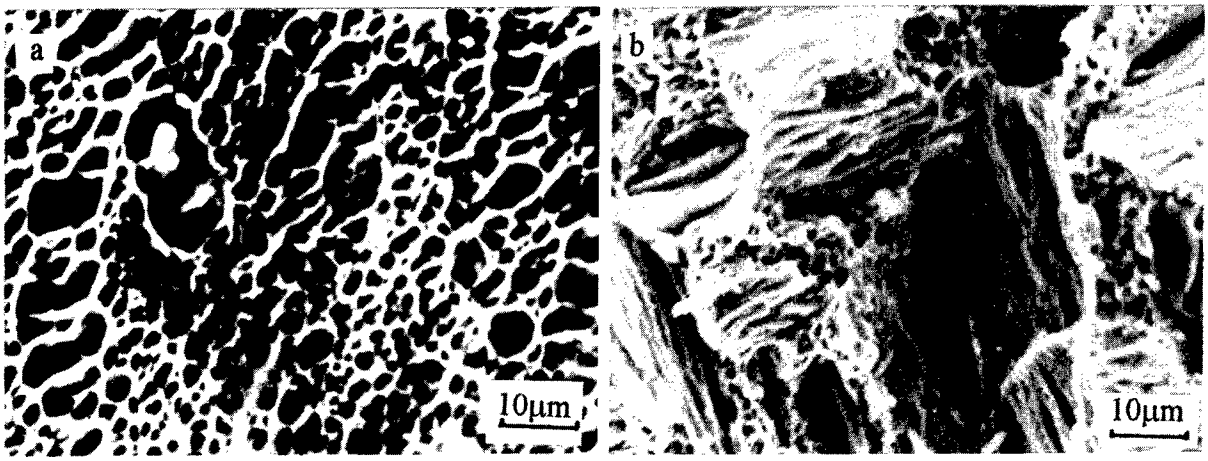


Figure 4: The fracture of [001] single crystals of high-nitrogen steels at T=77 K
(a)-I steel; C_N=0.5 wt.%; (b)-IV steel, C_N=0.7 wt.%.

At C_N>0.5 wt.% in I-II crystals the increase of Θ, the change of σ(ε) curve stages occur. It should be noted that the abrupt decrease of plasticity is observed (Fig. 5a). It was X-ray determined the crystallographic orientation of fracture planes. They are close to {111} planes. The plastic slip deformation before the mechanical twinning ε_t decreases at the nitrogen content increase : at C_N<0.3 at ε_t=20%, at C_N=0.5 wt.% ε_t=5%, and at C_N=0.7 wt.% the twinning deformation occurs from the most beginning of the plastic flow and holds in the temperature interval T=77-773K. Since at C_N>0.7 wt.% at tension of [111] crystals the plasticity is equal to zero, in such orientations the dislocation structure was investigated at compression of [001] crystals. It was shown that at tension of [111] crystals at C_N=0.4 wt.% dislocations form planar pile up. It is observed extended dislocations, stacking faults and twins (Fig. 7). It should be noted that at tension of [111] crystals at C_N=0.6 wt.% and at compression of [001] at C_N=0.7 wt.% the twinning deformation develops from the earlier deformation stages in several slip systems. The thickness of twins is d=0.2 μm, the density of twins and the number of twin intersections of two systems increase as the deformation growth. And this circumstance is the cause of the abrupt increase of the stress-hardening coefficient Θ.

At tension of [111] crystals the temperature dependence τ_{cr}(T) changes at the nitrogen content increase. At C_N>0.7 wt.% τ_{cr}(T)~G(T) (Fig. 8, curve 2) in the temperature interval T=77-773K and, consequently, the thermally activated part of flow stresses is absent, and deformation is athermal.

This peculiarity of the temperature dependence τ_{cr}(T) is characteristic for the twinning [1, 2], and at the slip deformation in the [111] crystals (Fig. 8, curve 1) the τ_{cr}(T) dependence is significantly different from that of abovementioned: it's observed the strong temperature dependence τ_{cr}(T). The comparison of τ_{cr} for [111] and [001] crystals at the same test method, for example, at tension, allow to make the following conclusion. There is the strong orientation dependence of τ_{cr},, τ_{cr}<111> < τ_{cr}<100>, and <111> orientations are "soft", but <100> crystals are "hard" ones. At the same crystal orientation, e.g., <100>, τ_{cr}^{ten}<100> > τ_{cr}^{com}<100>, consequently, asymmetry of τ_{cr} is observed [1, 2].TEM investigations showed that at C_N<0.5wt.% non-schmid effects are connected with the influence of the external stress field on the splitting dislocations. In "hard" orientations ([001] crystals at tension, [111] ones at compression) the extended dislocations are not observed, while in the "soft" orientations (tension along [111] axis, compression of [100] crystals) dislocations are splitted into the Shockley partials.

At C_N=0.6-0.7 wt.% it was found the second type of non-schmid effects connected with the orientation dependence of the deformation mechanism (slip at tension of [001] crystals and at compression [111]; twinning at tension along [111] orientation and at compression of [001] crystals).

Thus, at tension of [111] crystals of I-III austenitic stainless steels with a low stacking fault energy γ_{sf} the strong dependence of strain-hardening coefficient Θ, plasticity, slip and twinning deformation mechanism, fracture mechanism on nitrogen concentration was found. The combination of the high strength level with the low stacking fault energy at C_N<0.4 wt.% leads to the change of the dislocation splitting. This circumstance determines the preferable development of shear in single slip system, in spite of crystal orientation for multiple slip. The transition to activation of slip and twinning is accompanied by the increase of Θ, the plasticity decrease. At C_N>0.7 wt.% the twinning deformation leads to the cleavage along (111) planes without macroscopic plastic deformation. In order to separate the role exactly of the high strength level from twinning deformation single crystals of IV steel [111] orientation with a high γ_{sf} were investigated. In this

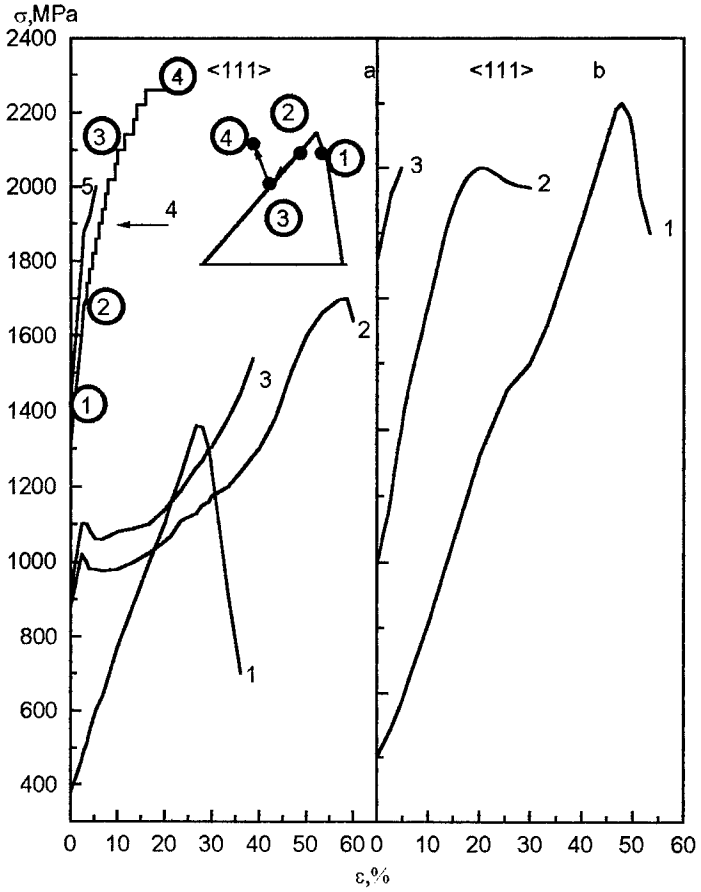


Figure 5: The stress-strain curves of austenitic stainless steels at tension along [111] axis at T=77 K in dependence on nitrogen content (a)- low γ_{sf}, I steel: 1-without nitrogen; 2- 0.35 wt.%; 3- 0.4 wt.%; 4- 0.5 wt.%; 5-0.7 wt.% (III steel); figures in circle show crystal axes in dependence on deformation; (b)- high γ_{sf}, IVsteel: 1-without nitrogen; 2- 0.3 wt.%; 3- 0.7 wt.%.

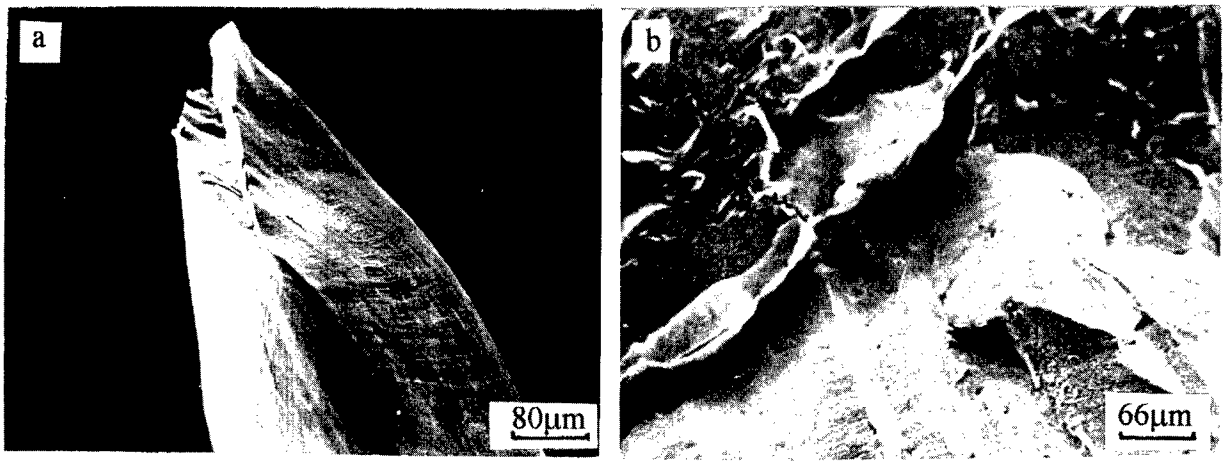


Figure 6: The fracture of [011] single crystals of I steel at T=77 K
(a)-without nitrogen; (b)- C_N=0.5 wt.%,

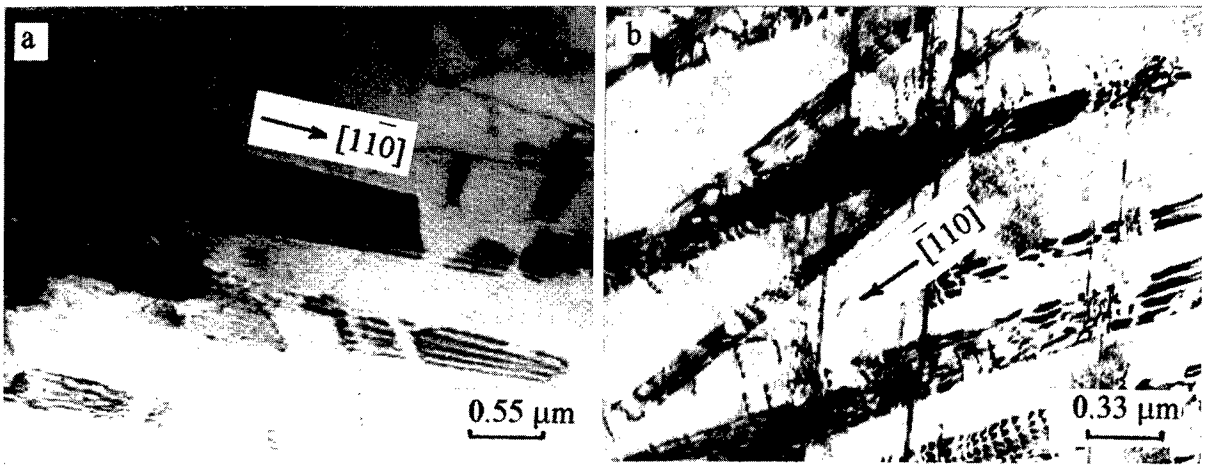


Figure 7: The dislocation structure of [111] single crystals of I steel at tension (C_N=0.5 wt.%, T=77 K) (a)-stacking faults, ε=3%; (b)-deformation twins, ε=20%.

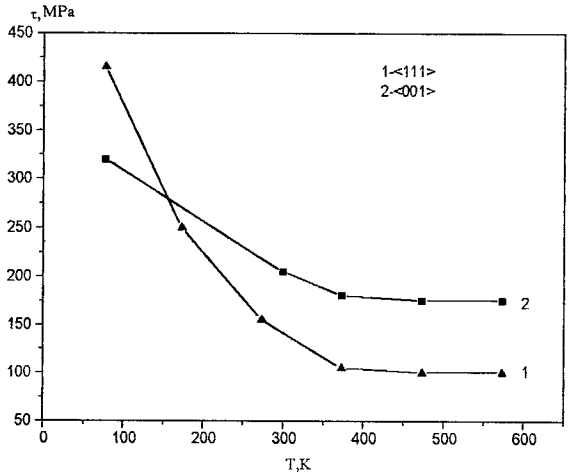


Figure 8: The temperature dependence of τ_{cr} of III steel at compression at C_N=0.7 wt.%: 1- [111]; 2- [001].

steel the twinning deformation is not expected because of high γ_{sf}. It was shown (Fig. 5b) that in absence of twinning in [111] crystals, the abrupt plasticity decrease is observed at the increase of C_N. At C_N=0.7 wt.% the crystal fracture is brittle, it occurs along (111) planes after homogeneous deformation ε=4%. Hence, suppression of twinning at fracture of high-strengthening crystals of austenitic stainless steels with a high γ_{sf} is not accompanied by the plasticity increase as compared with twinning crystals. Therefore, the high strength level plays the main role at forming of brittle fracture conditions.

1.3 The "ductile-to-brittle" transition (DBT) in high-nitrogen single crystals of austenitic stainless steels with different stacking fault energy

In nitrogen-free crystals of I-IV steels and C_N<0.3-0.4 wt.% at tension of [001] and [111] orientations DBT is not observed based on both deformational and fractographic criteria (Fig. 9a). At C_N=0.5-0.6 wt. % in [111] orientation of I-III steels in the temperature interval T=77-120 K the abrupt increase of the homogeneous elongation is observed, which is accompanied by the appearance of the ductile fracture component (Fig. 9b). It should be noted that at T>300 K the fracture is ductile. In [001] crystals the plasticity change is not observed. In this case DBT is determined over the fracture change and crystallography of fracture surface (Fig. 9b, curves 6, 8).

At C_N>0.6 wt.% in the IV steels DBT is observed, in [111] crystals the plasticity at T=77 K gradually increases from ~3% up to ~20% at 473 K. In the temperature interval T=123-281 K the plasticity increase is accompanied by necking at ε=3% at T=123 K and at ε=5.6% at T=291 K (Fig. 9b, curve 5). Then deformation occurs in the neck and the crystal fracture is mixed; on the fracture surfaces there are both brittle and ductile components. At the increase of T the fraction of ductile component increases, and at T-473 K the fracture is ductile.

At C_N=0.7 wt.% in [001] crystals of the same steel (Fig. 9b, curve 6) the homogeneous elongation strong changes at test temperature increase from 77 K up to 300 K.

Thus, in crystals with a low stacking fault energy γ_{sf} the achievement of the high strength level at C_N>0.5 wt.% leads to DBT over fractographic criterion independently of the crystal orientation. In [111] orientations the plasticity, changes from nought up to ~16% at the temperature increase. In this case, twinning is the main deformation mechanism. According to the deformation criterion at the slip deformation in [001] crystals DBT takes place in the temperature interval T=77-300 K (Fig. 9b).

In the IV crystals with a high γ_{sf} at C_N>0.7 wt.% DBT is observed in both [001] and [111] orientations (Fig. 9b, 5,

6 curves). In the table the temperature dependence of the crystallographic fracture surfaces is presented. The comparison of the fracture plane orientation change for all crystals at C_N>0.7 wt.% irrespective of γ_{sf} and orientation allows to find out the following common conformity, namely, at the low temperature T=77-123K the fracture occurs without necking, it is brittle, the crystal orientation is determined by the crystal orientation.

1.4 The "ductile-to-brittle"transition in aged Fe-22Cr-17Ni-2.3Mo-0.6N single crystals

The precipitation of FeN, CrN disperse particles leads to the increase to the strength properties in the temperature interval T=77-773 K, preservation of the orientation dependence of τ_{cr}, twinning in [111] crystals and slip deformation in [100] (Fig. 10, 1, 2 curves). Both at the twinning

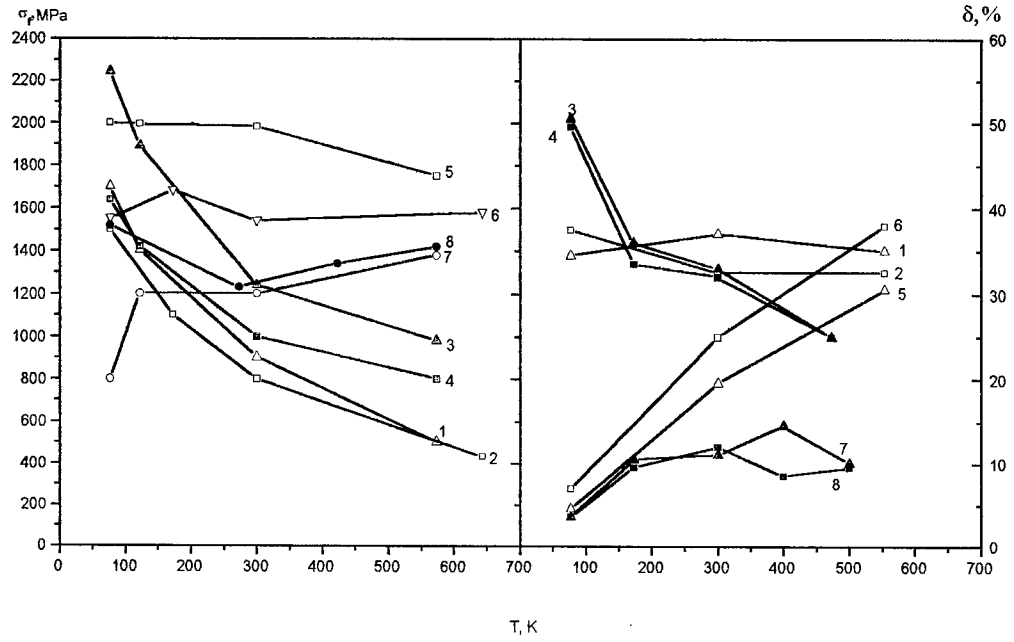


Figure 9: The temperature dependence of plasticity and fracture stresses in dependence on nitrogen content: (a)- low γ_{sf}, I steel: 1, 2-σ_f at C_N=0.4 wt.%; 3, 4- σ_f at C_N=0.5 wt.%; 5, 6- δ at C_N=0.4 wt.%; 7, 8- δ at C_N=0.5 wt.%. 1, 3, 5, 7-[111] tension axis; 2,4,6,8-[001] tension axis.(b)-1, 2, 5, 6- high γ_{sf}, I steel: C_N=0.7 wt.%; 1, 2-σ_f; 5, 6- δ; 3, 4, 7, 8– low γ_{sf}; C_N=0.7 wt.%; 3, 4- -σ_f; 7, 8- δ; 1, 3, 5, 7-[111] tension axis; 2,4,6,8-[001] tension axis.

Table Crystallographic fracture planes in austenitic stainless steels with different γ_{sf} in dependence on nitrogen content and test temperature

Steel	γ_{sf}, J/m^2	C_N, wt.%	Tension axis orientation	T, K	Fracture surface
18Cr-12Ni-2Mo	0.02	0	[001]	77-300	{111}
		0.4	[001]	77-300	{111}
		0.5	[001]	77-300	{111}
		0.7	[001]	77-300	{001}
		0	[111]	77-300	{111}
		0.4	[111]	77-300	{111}
		0.5	[111]	77-300	{111}
		0.7	[111]	77-300	{111}
26Cr-32Ni-3Mo	0.2	0.7	[001]	77-300	{001}
		0.7	[111]	77-300	{111}

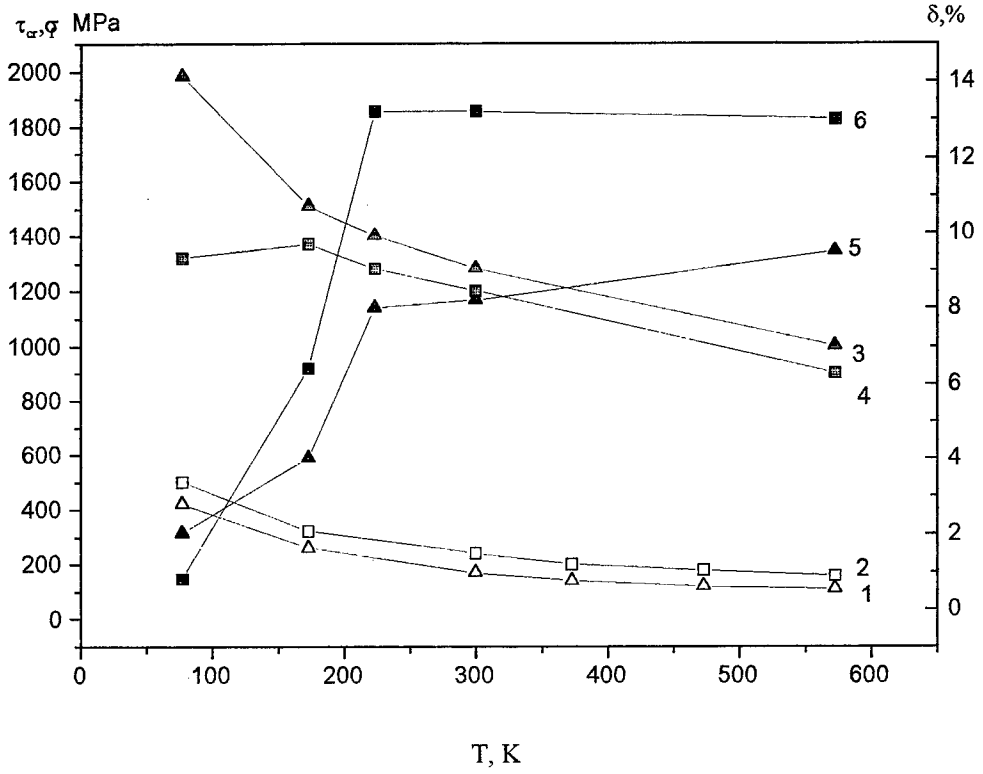


Figure 10: The temperature dependence of plasticity, critical resolved shear stresses and fracture stresses in II steel at C_N=0.6 wt.% at ageing at 923 K for 10 hr.: 1, 2- τ_{cr}; 3, 4-σ_f, 5, 6- δ; 1, 3, 5-[111] tension axis; 2,4,6-[001] tension axis.

in [111] orientations and at the slip in [001] at T<173 K the crystal fracture is brittle without necking. It is observed cleavage after small plastic deformation Θ=1-2%. At T>223 K the abrupt plasticity increase up to 10-13 % is observed. On the fracture surface the ductile component appears, the fraction of which increases at the test temperature increase. It should be noted that at T>300 K the fracture is ductile in all investigated orientations (Fig. 10, 4-6 curves).

Thus, the precipitation of disperse particles, the increase of the resistance to dislocation motion as compared with particles-free crystals and the strong temperature dependence τ_{cr}(T) create conditions of the brittle fracture of crystals at T<123 K. The "ductile-to-brittle" transition takes place at T>273 K. These results are in accordance with those of above-mentioned over plasticity and brittle fracture in the steels strengthened by interstitial atoms, where the achievement of the critical strength level leads to the brittle fracture irrespective of crystal orientation and deformation mechanism (slip or/and twinning). At the increase of T the abrupt decrease of τ_{cr} two to three times because of the strong temperature dependence τ_{cr}(T) is the cause of DBT, as it is usually observed in bcc poly and single crystals [13].

1.5 Orientation dependence of fracture mechanism and "ductile-to-brittle" transition in high strengthened Cu-15%Al-2%Co single crystals with non-coherent particles

The combination of the low γ_{sf}=0.004 J/m^2 with the high level of τ_{cr} on account of non-coherent plastically non-deforming CoAl particles leads to the strong orientation dependence of τ_{cr}. In [111], [123] crystals at τ_{cr}>140-180 MPa deformation takes place by the twinning in the temperature interval T=77-673 K [1-9]. At 77 K the twinning in [123] crystals in single <211>{111} system leads to the high plasticity. Deformation develops in two stages: the first stage is one at ε<2.5-3.5% with the high Θ, it is characterized by the complete reversibility of plastic flow. This stage is stipulated by the elastic twinning phenomenon. On this stage after "loading-unloading" cycle on the polished crystal surface any slip lines are not observed. The TEM investigations show the availability of the high density of stacking faults. At ε>ε_{cr} the loading stage, connected with the nucleation and following motion of the Lüders band from the residual twins over crystals, is observed. At ε=37% total crystals pass into the twinning orientation and only the nucleation of the second twinning systems near holds leads to the cleavage along [111] planes. In [111] crystals at T=77 K the plastic deformation is limited by the first hardening stage with the high Θ. On this stage complete deformation is reversible (Fig. 11). It is

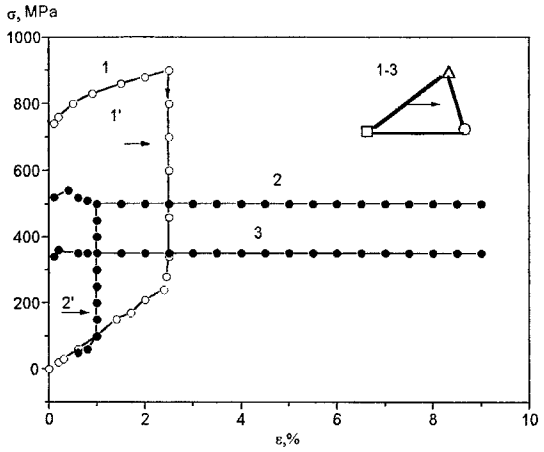


Figure 11. The stress-strain curves (1-3) and mechanical hysteresis curves (1', 2') of Cu-15%Al-2%Co single crystals.Ageing at 773 K for 67 hr.

observed the cleavage over the {111} plane system at $\varepsilon > \varepsilon_{cr}$ (Fig. 12). It is coincided with the appearance of residual twinning lamella, the interaction of which each with other leads to the nucleation and rapid growth of crack along the twinning boundaries. At the temperature increase DBT takes place at the preservation of twinning as single deformation mechanism (Fig. 13).

The temperature dependence of twinning critical resolved shear stresses τ_{cr}^{tw} at $T > T_{brittle}$ is stronger than that of shear module G(T). It connected with the development of diffusion process of internal stress relaxation caused by incompatibility of the plastic deformation of twinning matrix and plastically non-deforming particle (Fig. 13). At twinning the strong temperature dependence of reversible deformation ε_{rev} is evidence of the internal stress relaxation at temperature increase. The plasticity increase takes place in the temperature interval ΔT of the decrease of superelasticity effects and, consequently, internal stress fields [1].

In [001] crystals deformation occurs by slip. It should be noted that in this case at the more high level of τ_{cr} the fracture is ductile, and DBT is not observed [1]. For the first time in the fcc high-strengthening crystals the fracture mechanism orientation dependence caused by the that of the slip and twinning deformation mechanism was obtained At twinning deformation in alloys with the plastically non-deforming particles the fine structure of deformation twins plays the important role because of accumulation of the high density of dislocations in twin and the appearance of internal stresses.

1.6 The "ductile-to-brittle" transition in bcc heterophase Fe-26%Cr-10%Co-3%Mo and titanium nickel single crystals

For the clarification of community of conditions of the brittle fracture appearance in the high-strengthened crystals, distinction of mechanical twinning role as the factor decreasing the crystal plasticity the investigations of the plasticity orientation dependence, DBT of bcc heterophase crystals were carry out. In these alloys the strength level may be changed in the wide ranges on account of the coherent particles (Fig.14, 15).

At tension of [100] crystals the twinning deformation really occurs at the achievement of the critical stress level

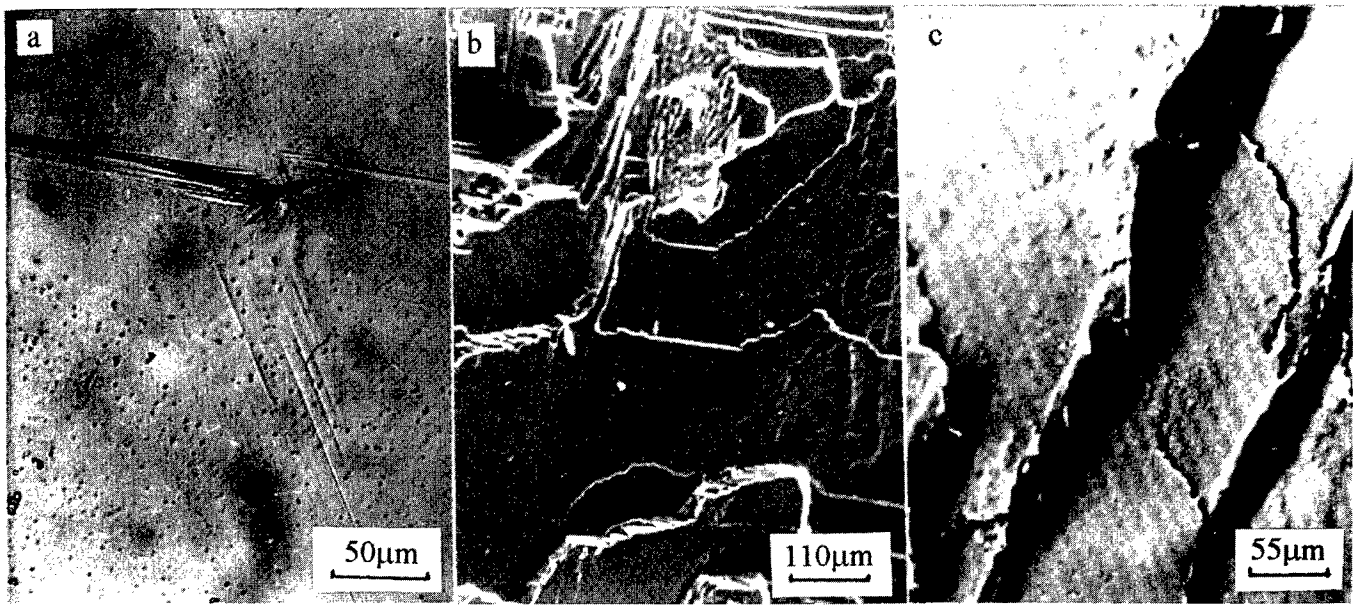


Figure 12: (a)-Optical micrograph of crack nucleation of [111] crystals of Cu-15%Al-2%Co alloy; (b, c)-fracture surface of [111] crystals of Cu-15%Al-2%Co alloy at T=77K

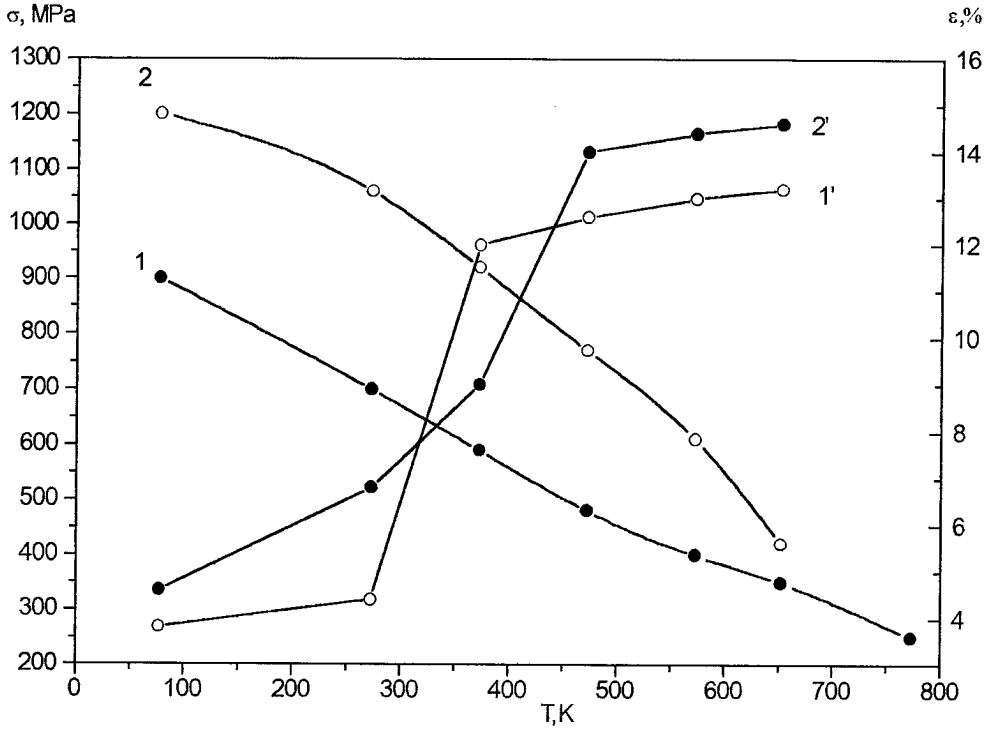


Figure 13: The temperature dependence of plasticity (curves 1', 2') and twinning stresses (curves 1, 2) of [111] Cu-15%Al-2%Co single crystals:
1, 1'- ageing at 773 K for 67 hr.; 2, 2'-ageing at 723 K for 10 hr.

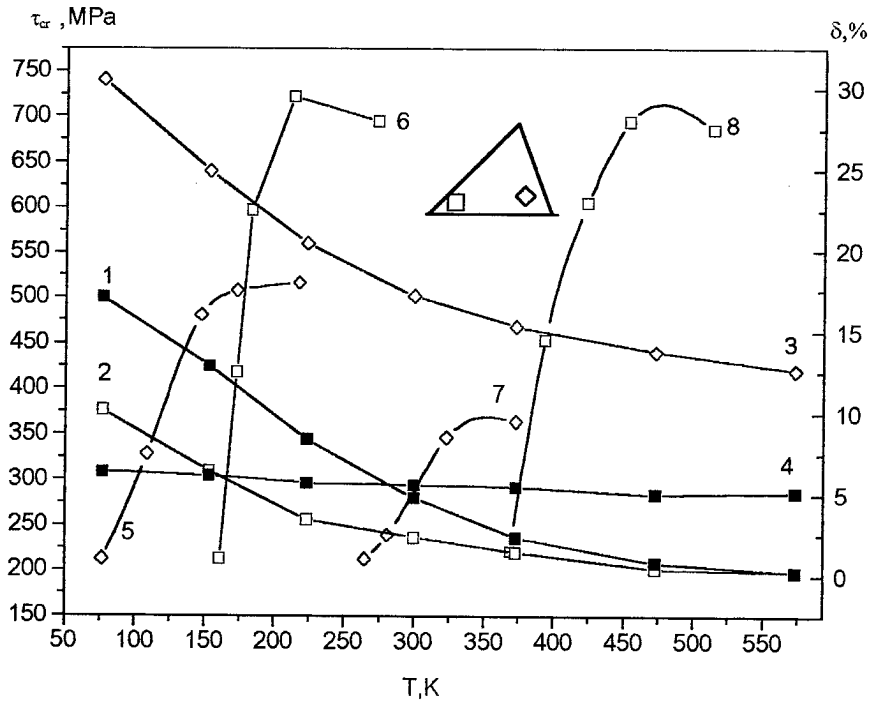


Figure 14: The temperature dependence of critical resolved shear stresses and plasticity of Fe-Cr-Co-Mo single crystals:
1, 2, 5, 6-ageing at 893 K for 2 hr.; 3, 4, 7, 8- 813 K for 16 hr.;1, 3, 5, 7-near [011] tension axis; 2,4,6,8-near [001] tension axis.

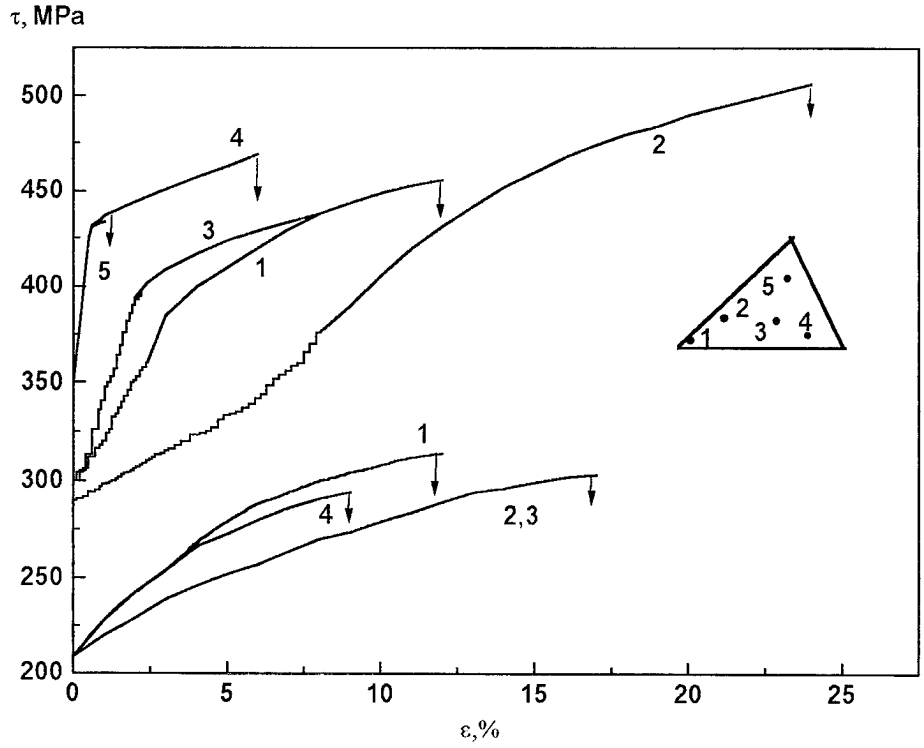


Figure 15. The stress-strain curves of Fe-Cr-Co-Mo of different orientations with the temperature ageing 833 K for 3 hr. (the upper curves) and ageing at 893 K for 2hr.(the lower curves). Tension at 473 K. Shaded parts correspond to mechanical twinning.

on account of coherent particles. The stress-strain curves are saw-shaped at high temperatures T>473 K (Fig.15). Deformation is accompanied by sound clicks. It is TEM observed the deformation twins in two systems. At $T>T_{DBT}$ in such crystals DBT takes place (Fig. 16). At the strength

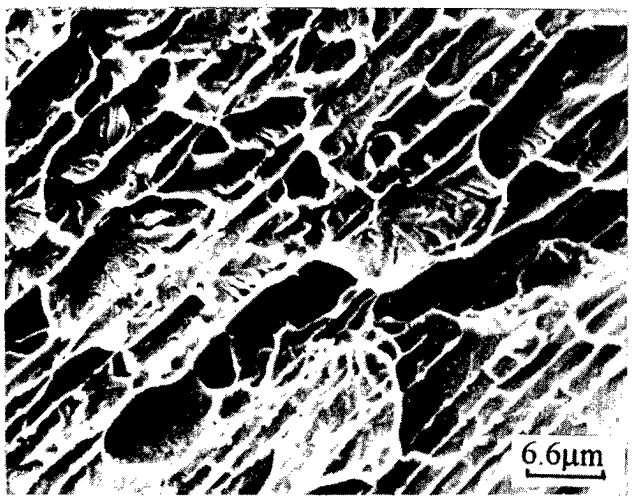


Figure 16: Fracture of [001] Fe-Cr-Co-Mo crystals (ageing at T=813 K for 16 hr.). Test temperature is 77 K.

level increase on account of the change of the disperse particles size and alloying elements content in both phase and matrix, the increase of T_{DBT} occurs. These changes are 300 K (Fig. 14). In [011], [111] crystals of antitwinning orientation at the slip deformation DBT is observed at significantly lower temperatures as compared with the twinning crystals. This distinction holds in the whole tested interval of τ_{cr} (Fig. 14).

Other distinction is the fracture peculiarity at $T> T_{DBT}$ in crystals of different orientations: the fracture of [011] orientations occurs by nucleation in the neck of the macroscopic shear band, deformation localization is observed and, fracture occurs by cut. In the twinning crystals such peculiarity at $T> T_{DBT}$ is not observed.

In the titanium nickel alloys with thermoelastic transformations, in the high-temperature B2 phase the slip takes place in the <100>{110} slip systems.

Therefore, it was experimentally found out the brittle fracture (Fig. 17a) at tension of crystals with a {100} axis. The plastic deformation is only observed at T>300 K, when DBT occurs (Fig.18). The crystals with a [111] tension axis are plastic, deform up to Θ=40-60%, the fracture is ductile (Fig. 17b). Thus, at $T> T_{DBT}$ the absence of critical resolved shear stresses in slip system in [001] crystals leads to the rapid achievement of the fracture stress as compared

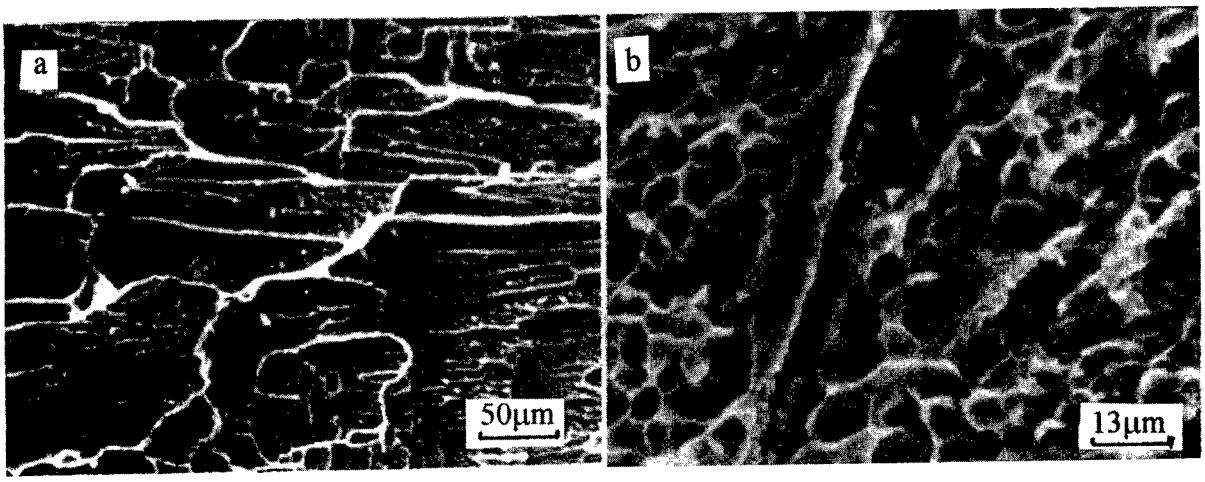


Figure 17: Fracture of Ti-Ni-Mo at tension at 473 K.
(a)-[011]; (b)-[111]

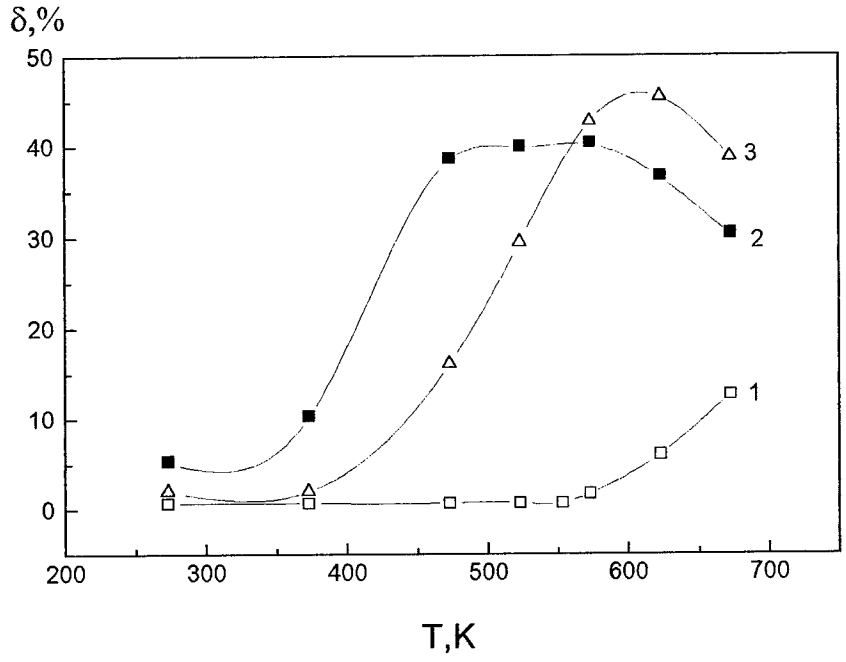


Figure 18: The homogeneous elongation dependence δ on test temperature for Ti-50.8at.%Ni-0.5at.%Mo with shape memory effect

with the activation of other possible slip systems a<111>{110}.

It is only very likely the dislocation climb processes lead to the plastic flow and ductile fracture.

It is very interesting that in the temperature interval of stress-induced martensite in a [001] crystals the plastic deformation connected with the martensite transformations is not observed. Hence, the nucleation of the first martensite crystal, the its fast growth non-limited by grain boundaries create the conditions for the achievement of fracture stresses even at $T \sim M_s$ (M_s is the temperature of the start of the martensite transformation at cooling).

The fracture stress σ_f changes with T according to Clapeyron-Clausius equation. It confirms the assumption that the nucleation and growth of martensite crystal are the cause of the brittle fracture.

In the plastic crystals with a [111] tension axis such peculiarities are not observed. Crystals deform in the interval of stress-induced martensite transformations. Therefore, only at conditions of slip deformation suppression in

B2 phase the martensite crystal is the source of brittle fracture.

2. Discussion

Experimental data analysis over the nitrogen influence on the strength properties and fracture of polycrystals shows that at C_N=0.31 wt.% at T=77 K the fracture is ductile [14-19]. However, the important role in the fracture mechanism plays the plastic flow localization caused by both the planar type of dislocation structure (because of the high friction level) and the adiabatic heating effects.

In consequence, the deformation localization leads to fracture along the localization bands. In steel with C_N=0.37 wt.% the test temperature decrease up to 4K leads to the ductile fracture along {111} planes. At C_N>0.6-0.9 wt.% DBT is observed. Nearly the room temperature polycrystals are plastic, the fracture is ductile [16, 19]. In such steels deformation mechanism investigation shows that twinning is the main deformation mechanism, cracks form in places of deformation twins intersection and move over twinning boundaries [19, 20].

On the other hand, in austenitic stainless steels with the high content of the interstitial atoms the high strength level caused by short range interaction of slip dislocations, peculiarities of core structure of slip dislocation create the temperature dependence of high-nitrogen polycrystals which is close to that of bcc poly- and single crystals [13]. Therefore, the temperature dependence of plasticity , DBT in fcc polycrystals may be explained with position developed for bcc metals. The main idea is following: the deforming stress is approximately equal to the fracture one [16, 18]. In this case the twinning role as the main factor of brittle fracture of austenitic stainless steels requires the special analysis.

Experiments on single crystals of austenitic stainless steels with the different stacking fault energy γ_{sf}=0.02-0.2 J/m^2 and C_N=0-0.7 wt.% allow to solve this problem.

First, at T=77 K in crystals of austenitic stainless steels with the high stacking fault energy γ_{sf}, where the mechanical twinning is not observed, at C_N>0.7 wt.% the fracture is brittle after small plastic deformation in any investigated orientation [001], [111] (Fig. 4b). The nitrogen content decrease is accompanied by the plasticity increase, and the fracture is ductile (Fig. 2b).

Secondly, at twinning suppression on account of the choice of [001] orientation at tension in crystals with the low γ_{sf}=0.02 J/m^2 at T=77 K the plasticity abrupt decrease, fracture is brittle. Additional strengthening of steels with the low γ_{sf}=0.02 J/m^2 by disperse particles brings to nought the plasticity without twinning deformation in [001] orientation (Fig. 10).

Thus, at the strength increase the abrupt plasticity decrease is not connected with the plastic deformation mechanism change, but it is determined by the achievement of high strength level on account of hardening by nitrogen atoms. This level is close to that of the fracture stresses. In these crystals DBT is connected, as in bcc metals, with the strong temperature dependence of τ_{cr}(T), the slip dislocation mobility increase and relaxation of appearing stress concentrators [1, 2, 16].

The structure of slip dislocation, its splitting into Shockley partials, the appearance of stacking faults, the deformation mechanism change from slip to twinning influence on plasticity and fracture mechanism of [111], [001] crystals of steels the low γ_{sf} (Fig. 5a, 9a).

Already at C_N<0.3 wt.% the motion of extended dislocations leads to the preferable development of slip in single system in spite of crystal orientation for multiple slip (Fig. 7a). Consequently, the dislocation splitting into the Shockley partials makes difficulties for the dislocation intersection processes. The shear preferably develops in the single system. Consequently, the stress-hardening coefficient decreases, the plasticity increases, fracture is ductile, it occurs along the macroscopic shear bands (Fig. 5, 2-3 curves). Mechanical twinning, which develops at T=77 K and C_N>0.5 wt.%, significantly decreases plasticity and leads to the appearance of brittle fracture surfaces (Fig. 5a, 4 curves, Fig. 6b). At C_N=0.35-0.4 wt.% the comparison of [001] with [111] crystals, deformed at T=77 K, shows that at the middle nitrogen-hardening level, when the brittle fracture conditions are not achieved in [001] at slip near the yield strength, twinning is the factor promoting to the brittle fracture in [111] crystals [19, 20]. In [111] crystals at C_N=0.5 wt.% intensive twinning leads to the plastic flow instability (saw-shaped $\sigma(\varepsilon)$ diagrams, the abrupt Θ increase, the plasticity decrease, the cleavage along (111) planes). While in [001] crystals the fracture is ductile or mixed. Only insignificant part , approximately ~20% of fracture surface, is presented by brittle component. That is there is the strong orientation dependence of fracture mechanism: the brittle fracture is in [111] twinning crystals and the ductile one is in [001] orientation at slip (Fig. 2a, 2 curve, Fig. 5a, 3-4 curves).

At last, at hardening by nitrogen and disperse particles the father increase of τ_{cr} leads to the brittle fracture both at twinning of [111] crystals and at slip in [001] orientation with the low γ_{sf} at C_N=0.7 wt.% (Fig. 9b).

Consequently, at high nitrogen content, the precipitation of disperse particles τ_{cr} are achieved, at which fracture conditions realized independently of deformation mechanism (slip, twining).

At multiple-twinning of [111] crystals at C_N=0.5-0.7 wt.% the high stress-hardening coefficient Θ may be connected with particularities of fine twin structure in fcc single crystals with high interstitial atom concentration [20, 21]. At shear on b_1=a/6<211> interstitial atoms from octahedral interstitial position, which impurities occupied before twinning, transit to tetrahedral places. Consequently, twin is strengthened, since tetrahedral interstitial is two times smaller than octahedral one. Therefore, dislocations appearing at intersection of twin coherent boundary in accordance with [21] will experience the additional

resistance to their motion. High Θ caused by twinning leads to the achievement of high strength level, which is close to the fracture stress. In these conditions the intersections of two systems of twins are the crack nucleation places, as it was noted earlier [1, 2, 19, 20].

At creation of brittle fracture conditions the more clearly the role of intersection of two twinning systems is shown by experiments over fracture of heterophase fcc Cu-Al-Co (Fig. 11-13) single crystals. At T=77 K the fine structure of deformation twins is characterized by high density of the "geometrically necessary " Shockley partial dislocations, which accumulate in twins as they bypass plastically non-deforming particles [23]. Gradients of plastic deformation over "twin-particles" boundary lead to the appearance of high back stress level caused by reversible motion twins. Intersection of such strengthened twins is difficult. Therefore, in places of contact of two twin systems the high stress concentration appears, cracks nucleate, and grow along twins boundaries. Consequently, the cleavage is observed at $\varepsilon<3\%$, suppression of second system of twins increase plasticity up to ~37%.

At slip in [001] high-strengthening Cu-Al-Co crystals the abrupt plasticity increase is observed, the fracture is ductile [1].

It is obvious that at precipitation of by-passing disperse particles in [111] crystals of austenitic stainless steels strengthened by nitrogen at aging both factors may be observed simultaneously: at twinning the solid solution changes its structure because of the interstitial atom position changing, the dislocation accumulation in twins will occur. The abrupt increase of Θ, the parabolic dependence of $\sigma(\varepsilon)$, the absence of visible slip lines at metallographic investigations are indirect evidence of by-passing processes in aging steels [2, 3]. Therefore, in crystals oriented for multiple twinning brittle fracture is achieved at the small deformation degrees.

In the twinning orientation of austenitic stainless steels with nitrogen, fcc heterophase Cu-Al-Co crystals the "ductile-to-brittle" transition is not connected with the deformation mechanism change from twinning at low T to slip at high T. Structural investigations show that twinning is the main deformation mechanism , the twinning shear transference processes over coherent twin boundary make easy. The internal stress relaxation is the main factor making easier the twinning shear transference processes in fcc crystals, whiles in austenitic stainless steels with nitrogen the softening of twins on account of reverse jumping of interstitial atoms from tetrahedral positions into octahedral ones, the external stress level decrease, the stress-hardening coefficient Θ are factors making easier the twinning shear crossing processes [1, 2, 20].

The development mechanical twinning in [001] bcc Fe-Cr-Co-Mo heterophase crystals is the cause of shear of the "ductile-to-brittle" transition temperature (T_{DBT}) in side of more high temperatures as compared with antitwinning crystals [14].

In these alloys the change of strength level on account of precipitation of second phase particles changes T_{DBT} - the "ductile-to-brittle" transition temperature in very wide ranges from T=77 K in low-strengthening crystals up to ~473 K in high-strengthening ones [14].

The strength level increase in Ti-Ni crystals on account of choice of [001] orientation at tension, in which Schmid factor for slip systems a <100>{110} is close to zero, leads to cleavage in B2 phase. High local stress concentration because of nucleation and growth of martensite crystals determines brittleness in the temperature interval of stress-induced martensite transformations (Fig. 17, 18). Hence, an earlier developed approach to explanation of brittle fracture of bcc metals may be applied to the high-strengthening fcc crystals, titanium nickel based B2 -intermetallides. The "ductile-to-brittle" transition is connected with the strength level decrease at increase of T.

Conclusions

1. On single crystals of austenitic stainless steels the systematical investigation of the fracture mechanism was made in order to find out the dependence on the nitrogen content, test temperature, tension axis orientation, stacking fault energy γ_{sf}. It was shown that the achievement of high strength level on account of solid solution hardening at $C_N>0.6$-0.7 wt.% and disperse hardening leads to the "ductile-to-brittle" transition independently of crystal orientation, magnitude of stacking fault energy γ_{sf}, deformation mechanism of slip and twinning.

2. At $C_N=0.45$-0.5 wt.% in crystals with a low stacking fault energy γ_{sf} oriented for multiple-slip [111] the twinning deformation leads to brittle fracture, while at slip in [001] crystals the fracture is ductile. Optimal combination of high strength with plasticity achieves in [111], [011] crystals at $C_N=0.3$ wt.% because of deformation development in single slip system caused by both the high friction level and the influence of external stress field on the magnitude of splitting of extended dislocation into the Shockley partials.

3. In high-strength fcc heterophase Cu-15%Al-2%Co single crystals with non-coherent particles the orientation dependence of fracture mechanism was determined. In [111] crystals deformation occurs by twinning. At $T< T_{brittle}$ twinning is the case of brittle fracture. The "ductile-to-brittle" transition is connected with the development of relaxation process in twins.

4. In high-strengthening bcc heterophase Fe-Cr-Co-Mo crystals the strength level change leads to the alteration of T_{DBT} approximately 300K. The twinning of [001] crystals increases T_{DBT} nearly 100-120K as compared with the slip in [011] orientations. Suppression of slip deformation in a <100>{110} slip systems in B2 phase of titanium nickel crystals with a [001] tension axis leads to the achievement of fracture stresses earlier than for slip. Nucleation and rapid growth of martensitic crystals leads to the brittle

fracture at the decrease of external stress level two to seven times.

Acknowledgments

The research described in this publication was made due to the financial supports of Grant - 95-02-03500 from Russian Fond on Fundamental Investigations and Grant from State Committee of Higher Educational School (UGTU-UPP, Ekaterinburg, Grant from MGTU named Bauman, Moscow).

References

1. Yu. I. Chumlyakov, A. D. Korotayev, "Physics of plasticity and fracture of high-strengthening crystals," Isvestiya Vuz. Fizika (Russian Physics Journal), 35 (9) (1992), 3-24.

2. Yu. I. Chumlyakov, I.V. Kireeva, A. D. Korotayev, E. I. Litvinova, Yu. L. Zuev, "Mechanisms of the plastic deformation, hardening and fracture of single crystals of austenitic stainless steel with nitrogen," Izvestiya Vuz. Fizika (Russian Physics Journal), 39 (3) (1996), 5-32.

3. J. P. Hirth, J. Lothe, Theory of dislocations (Moscow: Atom Publishing Company, 1972), 599.

4. S. M. Copley, B. N. Kear, "The dependence of the width of a dislocation on dislocation velocity," Acta Metall., 16 (2) (1968), 227-231

5. H. J. Kestenbach, "The effect of applied stress on partial dislocation separation and dislocation substructure in austenitic stainless steel," Phil. Mag., 36 (1977), 1506-1515.

6. E. Nembach, "Hardening by coherent precipitates having a lattice mismatch: the effect of dislocation splitting," Scripta Metall., 18 (1984), 105-110.

7. M. F. Ashby, "Results and consequences of a recalculation of the Frank-Read and Orowan stress," Acta Metall., 14 (1966), 679-681.

8. O. V. Ivanova, Yu. I. Chumlyakov, "Solid solution hardening of austenitic stainless steel crystals with high nitrogen content," ISIJ Int., 36 (12)(1996), 1494-1499.

9. A. D. Korotayev, Yu. I. Chumlyakov, V. F. Esipenko et al., "Superelasticity effect in single crystals of Cu-15%Al-2%Co with non-coherent particles due to twinning," Phys. Status Solidi (a), 82 (4)(1984), 405-412.

10. J. A. Venables, "The nucleation and propagation of deformation twins," J. Phys. and Chem. Solids, 25 (7) (1964), 693-700.

11. Y. W. Chang, R. I. Asaro, "An experimental study of shear localization in aluminum-copper single crystals," Acta Metall., 29 (1)(1981), 24-257.

12. G. Gonzalez-Doncel, M. Torralba, O. A. Ruano, "Fracture of Al-4%Cu-0.1%Fe single crystals," Journal of materials science, 24 (1989), 2594-2602.

13. V. N. Trefilov, Yu. V. Mil'man, S. A. Firstov, "Physical principle of strength of refractory metal"(Kiev: Naukova Dumka, 1975), 315.

14. J. D. Diffilippi, K. G. Brickner, and E. M. Gilber, "Ductile to brittle transition in austenitic chromium-manganese-nitrogen stainless steels," Transaction of the metallurgical Society of AIME, 245(1969), 2141.

15. R. L. Tobler and D. Meyn, "Cleavage-like fracture along slip planes in Fe-18Cr-3Ni-13Mn-0.37N austenitic stainless steels," Metallurgical Transaction, 19 (A)(1988), 1626.

16. J. B. Vogt, A. Messai and J Foct, "Cleavage fracture of austenitic induced by nitrogen supersaturation," Scripta Metall.Mater., 31 (1994), 548.

17. R. J. Ilola, H. E. Hannienen and K. M. Ullakko, "Mechanical properties of austenitic high-nitrogen Cr-Ni and Cr-Mn steels at low temperatures," ISIJ International, 36 (7)(1996), 873-877.

18. J. B. Vogt, A. Messai and J Foct, "Sensitivity of a high nitrogen austenitic stainless steel to fatigue crack initiation," ISIJ International, 36 (7)(1996), 862-866.

19. P. Mullner, C. Solenthaler, P. J Uggowitzer and M. O. Speidel, "Brittle fracture in austenitic steel," Acta Metall.Mater., 42 (7)(1994), 2211-2217.

20. L. Remy, "The interaction between slip and twinning systems and the influence of twinning on the mechanical bechaviour of fcc metals and alloys," Metallurgical Transactions A, 12 (A)(3)(1981), 387-408.

21. J. W. Chan, "Thermodynamic and structural changes in deformation twinning of alloys," Acta Met., 25 (1977), 1021-1026

22. P. H. Adler, G. B. Olson and W. S. Owen, "Strain hardening of Hadfield manganese steel," Metal. Trans., 17 (A)(1986), 1725-1737.

23. M. F. Ashby, "The deformation of plastically non-homogeneous materials," Phil. Mag., 21 (1970), 399-424.

INFLUENCE OF TiN PARTICLES AND MICROSTRUCTURE ON CLEAVAGE FRACTURE IN SIMULATED HAZ

L. P. Zhang, C. L. Davis and M. Strangwood

School of Metallurgy and Materials
The University of Birmingham
Edgbaston, Birmingham B15 2TT, U. K.

Abstract

Thermally stable TiN particles can effectively pin austenite grain boundaries in weld heat affected zones (HAZs), thereby improving toughness, but can also act as cleavage initiators. The effects of prior austenite grain size and matrix microstructure on the cleavage fracture of simulated HAZs in steels with two Ti levels (0.045 and 0.1wt%) have been investigated using two peak temperatures (T_p) and three cooling times ($\Delta t_{8/5}$) by a Gleeble 1500TCS. Coarse (1-6μm) and fine (35-400nm) TiN particles were identified in both steels and it was found that the mean size in both ranges increased with increasing Ti content at a constant number density. Higher T_p (1350°C vs. 1100°C) for the same cooling time gave austenite grain growth and decreased toughness significantly. However, increasing cooling time from 8s to 90s changed the matrix microstructure from bainite to ferrite-pearlite with little variation in toughness. For both steels cleavage initiation was observed to occur at large TiN particles. For this range of variables, austenite grain size dominates toughness, although further investigation is required on steels with a lower Ti level, thereby avoiding coarse TiN particles, to determine the relative role of TiN particles on grain size and cleavage initiation and hence on toughness.

Introduction

The problem of sudden brittle fracture at low temperatures is a concern in structural material applications, particularly in welded structures where failure is often found to initiate in the heat affected zone (HAZ). The thermal cycle experienced during single-pass welding results in four characteristic regions in the HAZ: a coarse-grained region (CGHAZ), a fine-grained region (FGHAZ), an intercritical region (ICHAZ) and a subcritical region (SCHAZ). The CG HAZ is generally the location of initiation for brittle fracture. This is due to its large prior austenite grain size, which increases the ductile to brittle transition temperature (DBTT), and the presence of low toughness microstructures in this region, causing it to have the lowest toughness in the HAZ [1-3]. An important approach to improving HAZ toughness is to restrict austenite grain coarsening near the fusion boundary through the use of finely dispersed particles. One of the most effective precipitates in pinning the grain boundaries is titanium nitride. Compared with the nitrides of Al, Nb or V, TiN precipitates have a higher thermodynamic stability, i.e. low solubility in the matrix and high resistance to particle coarsening [4-6]. In order to pin the grain boundaries more effectively, it is emphasised that the TiN

George R. Irwin Symposium on Cleavage Fracture
Edited by Kwai S. Chan
The Minerals, Metals & Materials Society, 1997

precipitate distribution should be the largest volume fraction and smallest particle size possible. According to recent research work [7-9], however, a high Ti content promotes the formation of coarse TiN particles with sizes over 0.5μm. These coarse TiN particles are ineffective in pinning the grain boundaries and can act as cleavage nucleation sites. Therefore, the problem of conflict between the beneficial effect of fine particles inhibiting grain growth and the possibility of coarse particles impairing toughness needs to be solved. In addition to the coarse grain size in the CGHAZ region, the balance of microstructural constituents, such as martensite, bainite and various ferrite phases, also affects the fracture toughness. In order to investigate the relationship between microstructure and fracture toughness in the HAZ, thermal cycle simulation techniques can be used. Crack tip opening displacement (CTOD) tests on simulated HAZ specimens can then be used in design and material selection.

Experimental Procedure

Two steels, of the same nominal composition except for the Ti additions, were used in this study and the composition of steels is shown in Table I. Steel 1 has 0.045wt% Ti and steel 2 has 0.1wt% Ti. The grain size (equivalent diameter), TiN particle size (side length), number density and area fraction were measured using an image analyser. Carbon extraction replicas were used in a Philips CM20 TEM to investigate the size distribution of the fine TiN particles (sizes less than 400nm) and SADP (selected area diffraction pattern) analysis was used to determine the particle crystal structure. Samples, measuring 10x10x55mm, were simulated with peak temperatures of 1100°C and 1350°C corresponding to the FGHAZ and CGHAZ regions respectively. The cooling times used from 800°C to 500°C, $\Delta t_{8/5}$, were 8s, 32s and 90s for both peak temperatures. Single cycle simulations and the long cooling time ($\Delta t_{8/5}$ of 90s) were used since the aim of this investigation is to relate microstructural features to fracture behaviour.

Samples, after thermal cycle simulation, were machined with V notches (45°) and then prefatigued in three point bend in accordance with the procedures laid down in BS 7448 [10]. A ratio of minimum to maximum stress intensity factors, K_{min} and K_{max} respectively, of 0.1 was used for all pre-fatigue cracking. Crack tip opening displacement (CTOD) tests were carried out at temperatures from -196°C to room temperature for steel 2 samples simulated with peak temperatures of 1100°C and 1350°C; and cooling times of 8s and 90s. The values of CTOD were then calculated according to BS 7448. The fracture surfaces were investigated using a JEOL scanning electron microscope (SEM).

Results and Discussion

Microstructure Examination

The base plate microstructure of steels 1 and 2 consists of banded ferrite and pearlite (volume fraction of pearlite is about 4%). Typical microstructures for simulations with peak temperatures of 1100°C and 1350°C and a cooling time of 90s are shown in Figure 1(a, b). As T_p increases, the microstructure changes from an equiaxed ferrite-pearlite structure, with a very small amount of bainite, to a more complex microstructure consisting primarily of bainite with
smaller areas of Widmanstätten ferrite (WF), grain boundary ferrite (GF) and intragranular ferrite (IF). The grain size increases from 6 to 110μm with the increase in peak temperature from 1100°C to 1350°C for the same cooling time of 90s. The influence of cooling time on the microstructure can be seen in Figure 1(b, c). For a cooling time of 8s, the microstructure is a nearly 100% bainite, with the other transformation phases tending to be suppressed at this faster cooling rate.

TiN Particles

In the steels investigated, the particles were observed to have a cubic morphology. The size of the TiN particles, examined using optical and transmission electron microscopy, varies from 35nm to 6μm. The particles with sizes in the range 35-400nm and 1-6μm are classified as fine and coarse particles respectively. SADP analysis revealed that the particles have a NaCl structure with a lattice parameter of 0.423nm. Considering the composition of the steel, the lower combination energy between Ti-N compared to Ti-C and the particles morphology [11, 12], the particles with a cubic and rectangular-prism shape are determined to be titanium nitride precipitates.

For the coarse particles, the distributions of TiN particle size and density (particle number/mm^2) in the base plates are shown in Figure 2 for both steels. With increasing Ti content from 0.045 to 0.1wt%Ti, the particles coarsen slightly from 1.78±0.88μm to 2.08±1.45μm but do not change much in number density. After simulation, the coarse particle mean size and density hardly change with peak temperatures and cooling times. Compared to the base plate, all simulated samples with a Ti content of

Table I Composition of Steels Used in the Investigation, wt%

	C	Si	Mn	P	S	Cr	Mo	Ni	Al	Cu	N	Nb	Ti	V
Steel 1	.093	.01	1.50	.010	.002	<.02	<.005	<.02	.026	<.02	.0045	.050	.045	<0.005
Steel 2	.089	.21	1.50	.010	<.002	<.02	<.005	<.02	.026	<.02	.0048	.053	.10	<0.005

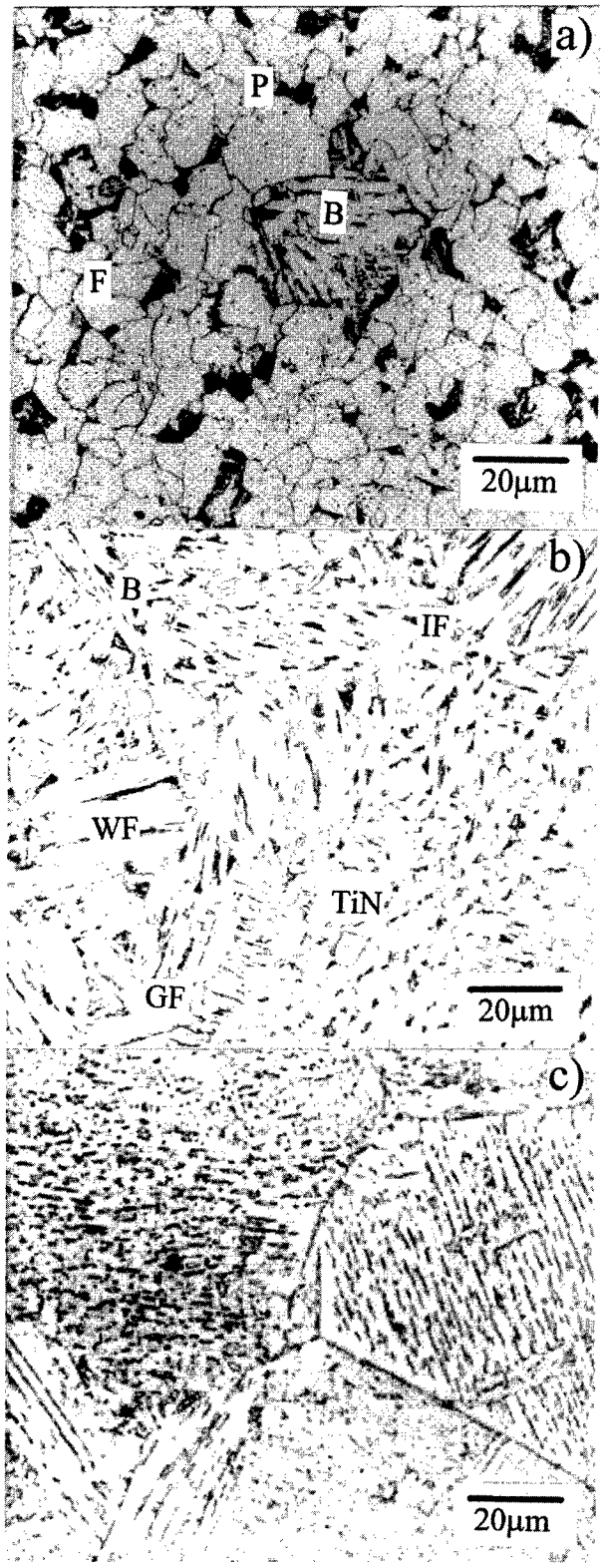


Figure 1: Microstructure in samples simulated with T_p and $\Delta t_{8/5}$ of: a) 1100°C, 90s b) 1350°C, 90s c) 1350°C, 8s

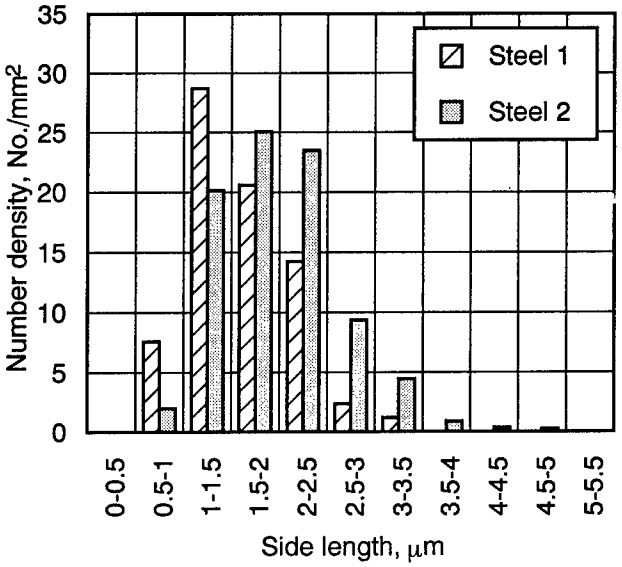


Figure 2 Distributions of coarse particle number density in the base plates (measured through plate thickness)

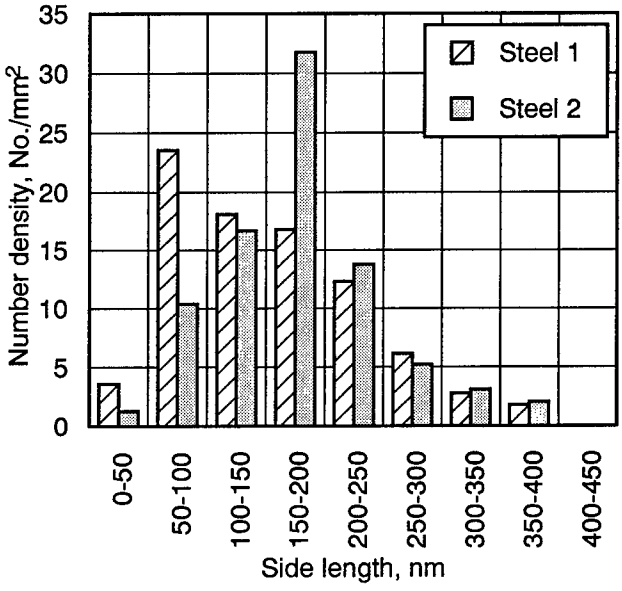


Figure 3 Distributions of fine particle number density in the base plates

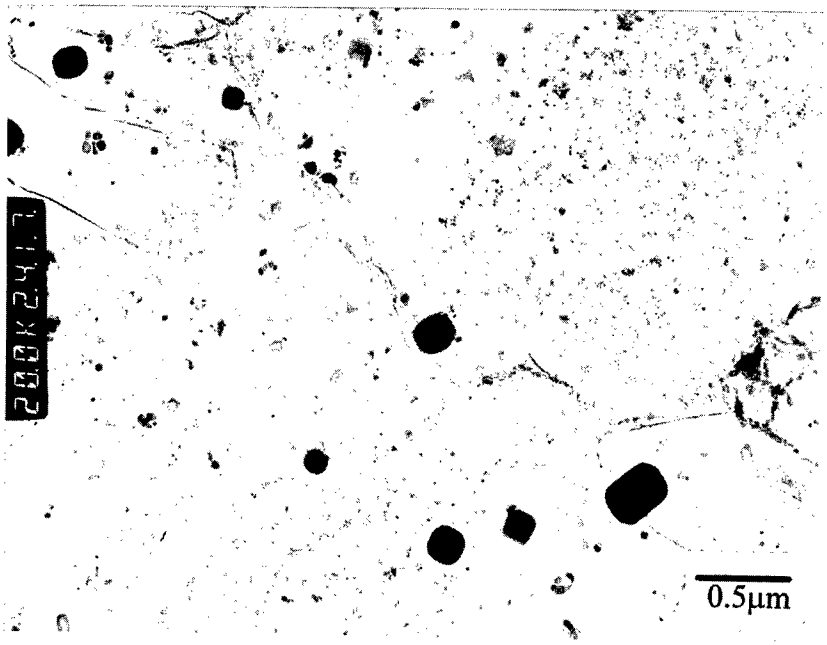


Figure 4 Carbon replica showing the morphology and distribution of the fine TiN particles (1100°C, 32s)

0.1wt% show a small increase in mean particle size and a small decrease in number density.

For the fine particles, with the increasing Ti content from 0.045 to 0.1wt%, the mean size of the TiN particles in the base plate increases from 163±153nm to 175±116nm, but with a similar number density in both steels, about $8.4x10^5$ particles/mm^2, as shown in Figure 3. The area fraction of fine particles in steel 2 is 0.023% and in steel 1 0.020%. After simulation, some particles with a size smaller than 100nm are dissolved in the matrix due to the high peak temperature experienced. For steel 2, the area fraction decreases from 0.018% to 0.009% and the number density decreases from $5.61x10^5$ to $2.25x10^5$ particles/mm^2 with the increase in peak temperature from 1100°C to 1350°C and the same cooling time. The morphology and distribution of the fine particles extracted by carbon film, with a peak temperature of 1100°C and a cooling time of 32s, is shown in Figure 4.

Fracture Toughness

The CTOD values of the base plate and simulated samples were tested and calculated according to BS 7448 only for the steel 2 due to the small difference in microstructure and TiN particles distribution between the two steels. The CTOD values are plotted in Figure 5. When the peak temperature increases from 1100°C to 1350°C, the CTOD values decreased significantly, for example decreasing from 0.245mm to 0.037mm at room temperature for the samples with a cooling time of 90s. The morphology of the respective fracture surfaces changes from a ductile fracture mode to a cleavage fracture mode. The ductile-brittle

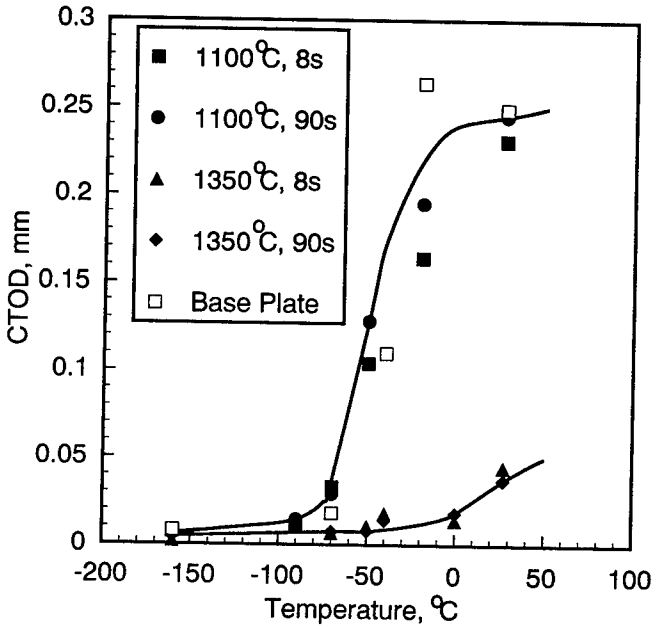


Figure 5 CTOD test results of the base plate and simulated samples (steel 2)

transition temperature (DBTT) is shifted from -50°C to above 20°C when the simulation peak temperature increases from 1100°C to 1350°C. At both peak temperatures of 1100°C and 1350°C, the CTOD values and the DBTT are similar when the cooling time varies from 8s to 90s. In addition, the CTOD values of the samples with a peak temperature of 1100°C are quite similar to those of base plate.



Figure 6 Matching micrographs showing a TiN particle (a) or its hole (b) acting as a cleavage nucleation site (-70°C)

Influence of Microstructural Features on Fracture Toughness

The two peak temperatures used during thermal cycle simulation result in two very different grain sizes, and the three cooling times produce microstructures containing different amounts of ferrite-pearlite phase, IF, GF, WF and bainite for each peak temperature, as shown in Figure 1. The fracture toughness (CTOD) of the HAZ depends on the complex interplay between grain size and microstructure at the same TiN particle distribution. When the peak temperature increases from 1100°C to 1350°C, with a similar microstructure and the same coarse TiN particle distribution for each cooling time, the grain size increases significantly, e.g. from 6μm to 110μm at a cooling time of 90s, leading to a marked decrease in CTOD values and a shift in DBTT from -50°C to above 20°C. Therefore, the grain size affects the fracture toughness significantly. For both peak temperatures of 1100°C and 1350°C, when the cooling time increases from 8s to 90s, with the similar grain size and TiN particle distribution, the matrix microstructure changes from bainite to ferrite-pearlite for the low T_p, and from a completely bainite structure to a microstructure consisting of bainite with various ferrite phases (GF, WF and IF) for the high T_p. The values of CTOD are similar and the DBTT hardly changes with increasing cooling time at each T_p, so the microstructures, compared to the grain size, have a less marked influence on the toughness. Therefore, the increase in grain size is the major reason impairing the fracture toughness for variables investigated.

An example of the influence of coarse TiN particles on the fracture behaviour can be seen in Figure 6(a, b). River patterns originate from a coarse TiN particle or from its hole on the other, matching, fractured surface, i.e. coarse TiN particles can act as cleavage nucleation sites. The influence of TiN particles within different matrix microstructures on the fracture toughness needs to be ascertained through the use of a much lower (0.01wt%) Ti containing steel. This forms part of ongoing research. Considering the fine and coarse particle size distributions in the base plates, as shown in Figures 2 and 3, although a lower Ti content of 0.045wt% is better than the higher Ti content of 0.1wt% in promoting the formation of smaller size particles, it is still a high Ti level because many coarse particles are also formed in this steel. Therefore titanium content control is very important and a much lower Ti content is suggested to avoid the formation of coarse particles.

Titanium Content Control

From Zener's theory [13], the suppression of grain growth by TiN particles depends on the particle size and volume fraction. Small particles are more effective in pinning the grain boundaries. It was reported that the distribution of TiN particle size is largely determined by the Ti content in a steel [14, 15]. According to alloy thermodynamics, the equilibrium equation of TiN dissolution in liquid or solid steel is described as [1]:

$$\log\{[X_{Ti}-X_{TiN}][X_N-X_{TiN}]\} = -A/T + B \qquad (1)$$

where X_{Ti} and X_N are the contents of Ti and N in the steel in at%, X_{TiN} is the atomic percentage of TiN formed in the liquid or solid state at the temperature T (K); A and B are constants, for the liquid state, A=16586 and B=6.57; for the solid state, A=8000 and B=1.0. Figure 7 shows the relationship between Ti content and the atomic percentage of TiN formed in the liquid or solid state. For the steels investigated, the liquidus and solidus temperatures are about 1800K and 1760K respectively. The minimum Ti contents to form the TiN particles in the liquid states before and during the solidification and in the solid state after solidification are 0.1wt% (0.116at%), 0.062wt% (0.073at%) and 0.013wt% (0.015at%) respectively. For steel 1, since the Ti content, 0.045wt%, is between the Ti contents of 0.062wt% and 0.013wt%, some TiN particles must have formed in the solid state when the steel is cooled to 1760K. For steel 2, since the Ti content, 0.1wt%, is between 0.1wt% and 0.062wt%, the TiN particles very likely precipitate in the liquid steel during solidification but not in the liquid steel prior to solidification. The particles formed at high temperatures (above the solidus temperature) usually have a large size [9, 16], therefore some coarse particles (>0.5μm) can be seen in both steels. In addition, the initial TiN particles in steel 2 precipitate at relatively high temperatures (in liquid state) compared to that (in solid state) in steel 1 due to the higher Ti content, therefore the coarse particle mean size in

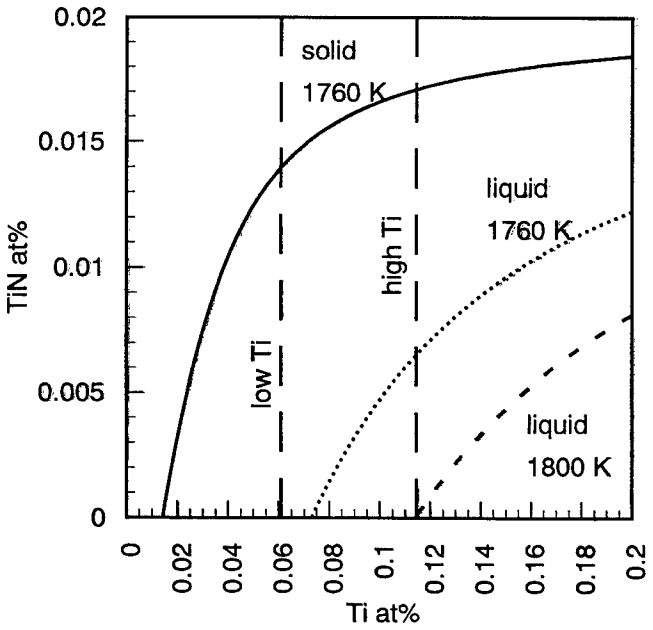


Figure 7 Relationship between Ti content and TiN formed at different temperatures under equilibrium conditions (determined using Eq. 1)

steel 2 is larger than that in steel 1, i.e. 2.08μm in steel 2 and 1.78μm in steel 1. A much lower Ti content, e.g. 0.005-0.01wt%, may promote formation of finely dispersed particles. This is because the Ti contents in this range are all lower than the Ti content of 0.013 wt%, therefore the initial TiN particles will precipitate in the solid state after solidification, hence having a small size.

In the steels investigated, because the Ti content is much higher than the N content, 0.0048wt%, the number of TiN nuclei formed in the liquid steel is determined by the N content, and therefore does not change with the increasing Ti content. On the other hand, from Figure 7, the TiN, at%, formed in the liquid steel increases with the increasing Ti content. Therefore, when the Ti content is much higher than the N content, the TiN particle size will increase with increasing Ti content due to the constant number of TiN nuclei. This may be another reason to explain that the increasing Ti content increases the particle size.

Conclusions

1) For the two steels investigated, an increase in Ti content is not conducive to forming more fine particles but instead makes the particles coarser. When the Ti content increases from 0.045wt% to 0.1wt%, the particle mean size increases from 163 to 175nm for fine particles (with a size of 35-400nm) and from 1.78 to 2.08μm for coarse particles (with a size of 1-6μm), but the particle number density hardly changes, with about 81 particles/mm^2 for the coarse particles and 8.4x10^5 particles/mm^2 for the fine particles.

2) Increasing cooling time from 8s to 90s for a similar grain size and TiN particle distribution causes the matrix microstructure to change from bainite to ferrite-pearlite for the low T_p (1100°C) simulation and from a completely bainitic structure to a microstructure comprised of bainite with various ferrite phases, such as grain boundary ferrite, Widmanstätten ferrite and intragranular ferrite, for the high T_p (1350°C) simulation. The CTOD values and the ductile-brittle transition temperature (DBTT) do not vary significantly with cooling time for a constant T_p. Increasing peak temperature from 1100°C to 1350°C with a cooling time of 90s for a similar matrix microstructure, however, increases prior austenite grain size from 6μm to 110μm, leading to a shift in DBTT from -50°C to above 20°C. Therefore, the fracture toughness is relatively insensitive to matrix microstructure but is impaired significantly by increasing grain size.

3) SEM investigation of the fracture surfaces after CTOD testing shows that some river patterns during cleavage fracture originate from coarse TiN particles with a size over 0.5μm, indicating that these coarse particles can act as cleavage nucleation sites.

Acknowledgements

The authors wish to acknowledge Professor I. R. Harris for the provision of research facilities and the financial support and provision of material from British Steel plc.

References

1 Kenneth E. Easterling, Introduction to the Physical Metallurgy of Welding, (Oxford, U.K.: Butterworth-Heinemann Ltd, 1992) 167-169

2. Ø. Grong and D. K. Matlock, "Microstructural development in mild and low-alloy steel weld metals" International Metals Reviews, 31(1) (1985), 27-48

3. H. Cerjak, ed., Mathematical Modelling of Weld Phenomena 2, (The Institute of Materials, 1995), 162-171

4. J. Strid and K. E. Easterling, "On the Chemistry and Stability of Complex Carbides and Nitrides in Microalloyed Steels" Acta Metall., 33(11) (1985), 2059

5. K. A. El-Fawakhry et al., "Characterization of Precipitates in Vanadium and Titanium Microalloyed Steels" ISIJ International 31(1991), 1020-1025

6. S Suzuki., G. C. Weatherly and D. C. Houghton "The Response of Carbo-Nitride Particles in HSLA Steels to Weld Thermal Cycles" Acta Metall., 35(2) (1987), 341-352

7. M. A. Linaza et al. "Cleavage Fracture of Microalloyed Forging Steels" Scripta Metallurgica et Materialia, 32(3) (1995), 395-400

8. M. A. Linaza, "Influence of the Microstructure on the Fracture Toughness and Fracture Mechanisms of Forging Steels Microalloyed with Titanium with Ferrite-Pearlite Structures" Scripta Metallurgica et Materialia, 29(1993), 451-456

9. J. Y. Li and W. Y. Zhang, "Effect of TiN Inclusion on Fracture Toughness in Ultrahigh Strength Steel" ISIJ International, 29(2) (1989), 158-164

10. British Standard, Fracture Mechanics Toughness Test (Draft), (BS 7448, part 1, 1991), 11-23

11. F. C. Liao, S. Liu and Olson D. L. Olson, "Effect of Titanium Nitride Precipitates on the Weldability of Nitrogen Enhanced Ti-V Microalloyed Steels" 35th MWSP CONF. PROC., ISS-AIME, XXXI (1994), 511-522

12. B. Loberg et al. "The Role of Alloy Composition on the Stability of Nitrides in Ti-Microalloyed Steels during

Weld Thermal Cycles" Metall. Trans. 15A(1) (1984) 33-41

13. C. Zener, Personal Communication to C. S. Smith, American Institute of Mining and Metallurgical Engineers, 15, 1949, 175

14. G. L. Tang et al., "Grain Coarsening in V-Ti-N Microalloyed Steel" Acta Metall., 25(6) (1989), A414-419

15. Guangkui Xu and Jingjue Chen, "V-Ti Casting Iron and Steel", (China, Metallurgy Industry Publishing Ltd, 1995), 6-7

16. F. B. Pickering, "Titanium Nitride Technology" 35th MWSP CONF. PROC., ISS-AIME, XXXI (1994), 477

A New Tool for Crystallographic and Topographic Analysis of Cleavage Fracture Surfaces

C. O. A. Semprimoschnig, O. Kolednik, R. Pippan

Erich-Schmid-Institute for Solid-State-Physics of the Austrian Academy of Sciences
Jahnstraße 12, A-8700 Leoben, AUSTRIA

Abstract

A new experimental method is presented for the combined topographic and crystallographic analysis of cleavage fracture surfaces which is a powerful tool for quantitative fractographic investigations.
The new method combines the Electron Back Scatter Diffraction technique with a system for automatic surface reconstruction. It enables to perform a *crystallographic fractometry*, i.e. cleavage fracture surfaces can be crystallographically surveyed.

Introduction

So far no comprehensive model has been developed which can explain the initiation as well as the propagation of cleavage fracture in polycrystals [1-4]. However, studies of cleavage fracture surfaces by means of classical fractography have contributed significantly to the development of models about this type of fracture. Common tasks for which fractography is used include tracing river patterns to determine the crack propagation direction on a cleaved facet and searching for cleavage fracture initiation sites [5,6]. The distance of the latter regarding a stress concentrator such as a fatigue pre-crack has been used to calculate cleavage fracture stresses. This procedure has often been applied to C-Mn steels, when fracture was produced close to the transition region [7-8]. It should be noted that further below the transition region multiple initiation can occur which make it very difficult to determine *the* critical fracture stress.

Despite the progress which has been achieved with fractographical investigations some crucial questions can not be tackled by classical methods. Such questions include: How does a cleavage fracture propagate in a polycrystal, how is the micro and the macro crack propagation direction correlated to each other, how are fractographic features on a cleavage fracture facet related to the crystallographic orientation of a facet etc. Therefore we felt that a new method is needed with which cleavage fracture surfaces could be crystallographically surveyed.

In this paper we will describe a new technique for the combined crystallographic and topographic analysis of cleavage fracture facets. The developed method we call *crystallographic fractometry* [9] as it enables to crystallographically survey cleavage fracture surfaces.

The method is based on the information fusion of the Electron Back Scatter Diffraction (EBSD) technique with which the crystallographic orientation of cleavage facets can be determined and a system for automatic surface reconstruction (ASRS) with which the topography of surfaces can be analysed. In the following chapters a few aspects of both techniques concerning cleavage fracture will be outlined. Then some examples of our investigation on a model material will be presented.

Aspects of the crystallographic analysis

The EBSD-technique has established itself as an important technique regarding orientation measurements [10]. EBSD-patterns are similar to Kikuchi lines known from transmission electron microscopy but are recorded in the backscattering mode in a SEM. They form when a focused electron beam impinges upon a crystal specimen. As a result of the interaction between the incoming electrons and the crystalline specimen diffraction cones for each crystal plane form. These diffraction patterns are recorded on a phosphor screen and monitored via a highly light sensitive camera. The EBSD-patterns are digitally captured and the orientation of the inspected crystal is evaluated with a special software. With the usual operating conditions of a SEM a spatial resolution of approximately 0.2 μm can be reached. The angular accuracy for orientation measurements lies between 1° and 2° for absolute orientation measurements, for relative orientation measurements (misorientation between neighbouring grains) an angular accuracy of about 0.5° can be reached. Some general information about the necessary calibration and evaluation procedures of this technique can be found in [10]. Details about the used experimental set-up can be found in [9,11].

George R. Irwin Symposium on Cleavage Fracture
Edited by Kwai S. Chan
The Minerals, Metals & Materials Society, 1997

Cleavage facets are very suitable for EBSD measurements as they are accompanied only by a small amount of plasticity in comparison to ductile fracture surfaces. This is important as the EBSD technique is surface sensitive, i.e. the information is gained from a small interaction volume of the electron beam and the crystal of the inspected grain. (It should be noted that it is also possible to observe the effect of local plastic strain on the pattern quality, i.e. the increasing diffusivity with increasing plastic strain. However, a quantitative measurement of the dislocation density is not yet state-of-the-art. [12-14]) An example of a typical EBSD-pattern from a cleavage facet is shown in Fig. 1.

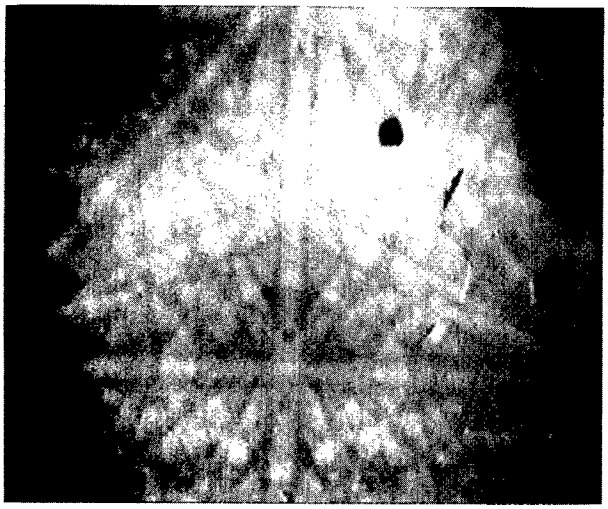


Fig. 1: Example of EBSD-pattern from a cleavage facet.

The EBSD-technique enables to determine the crystallographic orientation of individual cleavage facets. This orientation is given as an 3x3 orientation matrix which relates the crystal co-ordinates to a fixed reference co-ordinate system in the Scanning Electron Microscope (SEM).

Aspects of the topographic analysis

The ASRS which is based on the method of computer assisted stereophotogrammetry is a powerful tool to analyse fracture surfaces [15]. It uses stereoimage pairs taken in the SEM to compute a digital elevation model (DEM) of a fracture surface. Stereoimage pairs are two digital fractographs taken from one area of interest with two different tilting angles. The resolution of such a digital fractograph is 1024x768 pixels at 256 grey levels. The essential part of the image processing system is a matching algorithm which automatically finds homologue points on the two stereophotograms. Some time ago such a matching procedure has been done by hand which was a very time consuming and strenuous task [16]. This has limited the broad application of the method in the past.

Details about the applied algorithm are described in [17]. After the homologue points on the stereoimage pairs have been found, the 3D co-ordinates of each point can be determined applying Piazessi's algorithm [18]. Necessary input parameters for the computation are the magnification, the working distance and the tilting angle. The result is a DEM which contains about 7000 to 20000 points. From DEMs parameters can be computed which are used to describe and to analyse the fracture behaviour of materials [19]. In the case of ductile fracture analysis COD_i values can be determined and in the case of fracture by fatigue the height and spacing of striations can be measured.

For the topometric analysis of cleavage fracture DEMs are used to determine the 3-dimensional location of a cleavage plane in respect to a fixed reference co-ordinate system in the SEM. To compute the location of a cleavage plane a profile has to be extracted from the DEM which contains a representative amount of data points of that plane, i.e. the profile should include at least one obtuse angle. With these data points a normal vector of the plane can be calculated with a 3D interpolation. To compute the direction on a cleavage plane a similar procedure, this time with a 3D-line regression, is followed. An example of a DEM of a cleavage facet is shown in Fig. 2. The corresponding fractograph is presented in Fig. 3. A profile base line is superimposed on that on that image. The starting point of the profile is indicated with „1". The corresponding profile is shown in Fig. 4.

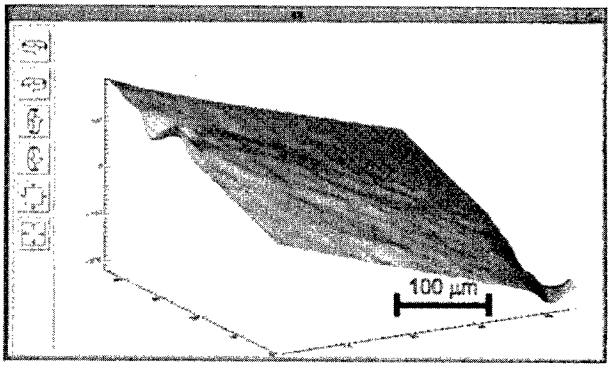


Fig. 2: DEM of a cleavage fracture facet. (x-y, in pixels, z in [mm].)

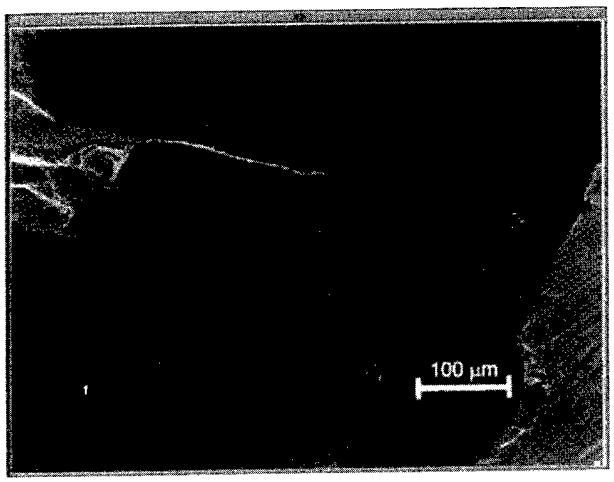


Fig. 3: Corresponding fractograph to Fig. 2. including profile base line.

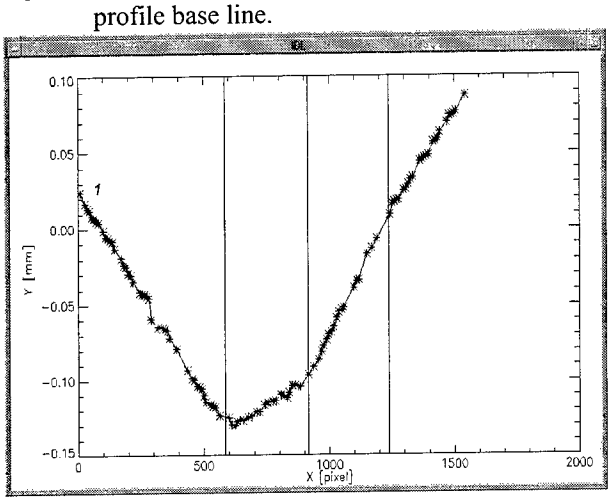


Fig. 4: Height profile from the base line in Fig. 3. (Height in [mm].)

Combined crystallographic and topographic analysis

A necessary prerequisite for a combined crystallographic and topometric analysis is that the results from both methods have to be related to the same reference co-ordinate system of the SEM. This is achieved when the edges of a specimen are accurately aligned in respect to that co-ordinate system. To make things easy one normally uses the fixed co-ordinate system of the specimen stage as the reference co-ordinate system.

Then the multiplication of the orientation matrix of the cleaved crystal with a 3D-vector describing either a cleavage plane or a direction on such a plane yields the crystallographic nature of cleavage planes and/or of directions on such planes. So the crystallographic nature of cleavage planes as well as of directions on such planes can be determined. Thus, it can be decided whether cleavage planes are of {001}, {110} etc. type and whether local crack propagation directions or of <001>, <110> etc. type.

Examples of combined analysis

In this chapters some results gained with the new tool will be presented. As a model material we used ARMCO iron (pure iron) with a grain size between 700 and 800 µm. The fracture mechanics tests were performed at 77K according to ASTM 399 on a pre-fatigued Compact Tension specimen. After the first cleavage crack propagation, i.e. first pop-in, the test was stopped and the specimen was fractured by post-fatigue as described in [9, 20].

As a first example a cleavage fracture surface is shown in Fig. 5. By tracing the river patterns it can be found that cleavage fracture initiated close to the fatigue pre-crack in „grain I". After initiation the crack crosses a grain boundary and cleaves grain II. From the post-fatigue fracture surfaces within grain II it can be concluded that grain II was not fully fractured by cleavage. Some ligaments were constraining the cleavage crack during its first propagation. For a further crack propagation additional energy should have been provided. This was not the case in the current test procedure. From both grains EBSPs were recorded and the orientation, i.e. the orientation matrices, of the crystals from both facets were determined. It was found that the misorientation between the two cleaved grains is close to 32.3° with a vector of rotation of [0.114, 0.021, 0.993]. Then stereoimage pairs of the fracture surface around the crossing between grain I and grain II were recorded. With the ASRS a DEM of the area of interest was determined. The DEM of the crossing is shown in Fig. 6. Another DEM of the same area computed from fractographs taken at a higher magnification is shown in Fig. 7. From that DEM we extracted several profiles and determined vectors describing the location of both cleaved facets as well as of directions on both facets. Then the vectors were multiplied with the corresponding orientation matrices which yields the crystallographic nature (index) of the vector. To determine an index we allow a deviation of 5° from an ideal crystallographic index such as [100]. This worked well for our calculations. (It is not the intention of this paper to go into further details about the procedures we apply to check the accuracy of the calculations.) For both grains we found a {001} type of cleavage plane. It is interesting that the cleavage fracture did not follow the macroscopic crack propagation direction. On a microscopic scale the crack spread into two <110> directions. This can be inferred from the shape of the tongues on both cleavage facets. A reason for this spreading could be that the local crack resistance on a {001} cleavage plane is lower in two <110> directions than in one <100> direction. Note that for both grains of

Fig. 8 the macroscopic crack propagation direction lies close to a <100> type direction. The determined indices are superimposed on the fractograph of Fig. 8.

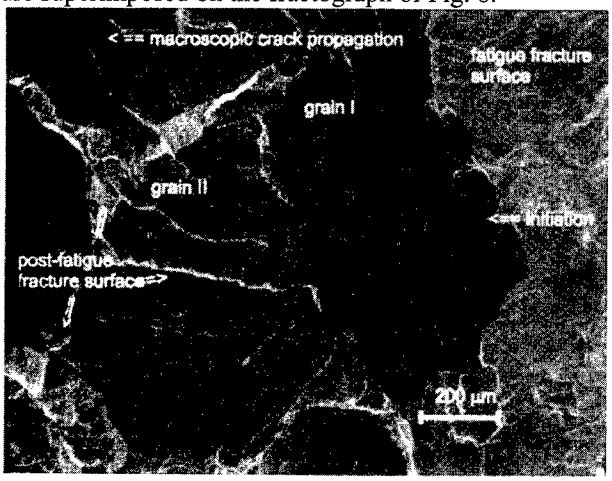


Fig. 5: Cleavage fracture surface.

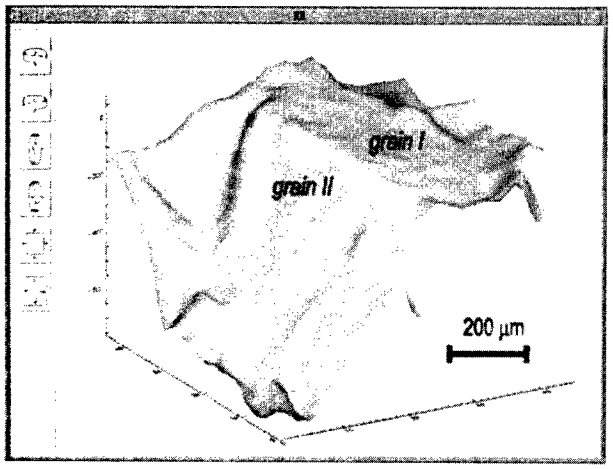


Fig. 6: DEM of Fig. 5 (low magnification). (x-y in pixel, z in [mm].)

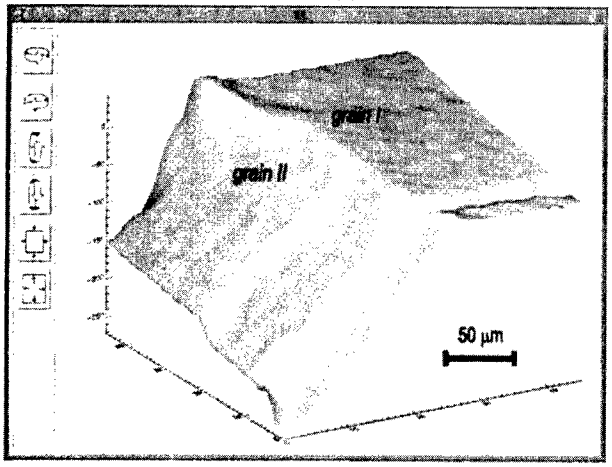


Fig. 7: DEM of Fig. 5 (high magnification). (x-y in pixel, z in [mm].)

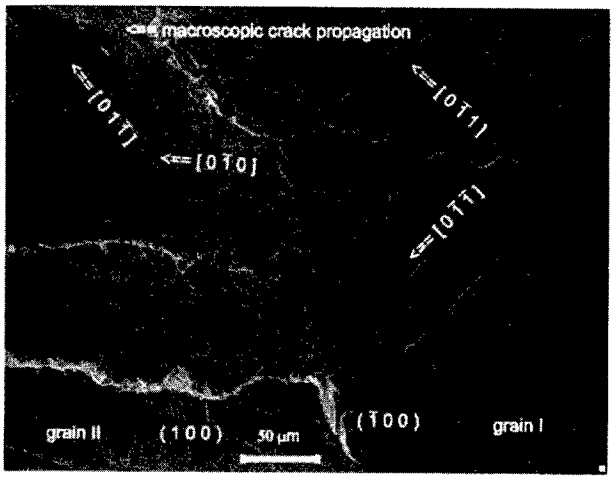


Fig. 8: Crossing between grain I and grain II with superimposed crystallographic indices.

Another application of our tool is the analysis of fracture markings sometimes observed on cleavage facets. A well known example are deformation twins which are commonly called tongues. With the developed tool we are able to determine the operating systems of such twins. Furthermore it may be even possible to decide whether the twins were a source for crack nucleation. This topic will be a subject of a forthcoming paper. An example of such an analysis is shown in Fig. 9. On a (001) cleavage plane we found two types of deformation twins. The big one at the bottom is a ($\bar{1}\ \bar{1}\ 2$) [111] and the small ones at the upper part belong to ($\bar{1}\ 1\ 2$) [1 $\bar{1}$ 1]. According to the convention of Schmid and Boas [21] they belong to the type I respectively type VII twinning system.

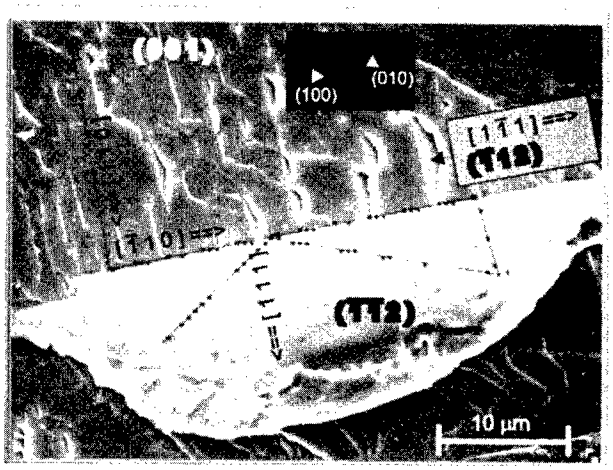


Fig. 9: Determination of twinning systems of tongues on a cleavage facet.(Indices are superimposed.)

A third application of our technique is to analyse the crystallographic and topometric relations between the fracture halves of one broken specimen.

It was found that between the cleavage facets of one grain the misfit between the orientation matrices was significantly larger than the misfit between the normal vectors. The latter were calculated from the DEM and described the location of both facets in space. It should be noted that for such analysis the EBSD-patterns have to be taken from the same corresponding areas on both fracture halves and the profiles have to use base lines with the same corresponding reference points on both fracture halves. We determined that the difference between two orientation matrices taken from the two cleavage facets of one grain was between 5° and 10°, whereas the difference between the two normal vectors describing the location of the two cleavage facets in space was less than 2,5°. This misorientation might be coming from a plastic deformation during the crack propagation of a cleavage crack. The reason is that plasticity induces a local rotation of the crystallographic orientation of a grain close to the fracture surface. Thus, if a significant misfit between the crystallographic orientation between two cleavage fracture facets of one grain is measured it might be due to a dislocation emission process from the crack tip during crack propagation.

A model how an orientation misfit might be related to a dislocation emission process during crack propagation is presented in Fig.9 [9]. The first line shows a crystal in space shortly before it will be cleaved on the bold printed cleavage plane. The second line shows one specimen half (A) after cleavage fracture and the third line shows the other specimen half (B) after cleavage. This is the position how both specimen halves are surveyed on the specimen stage in the SEM. (Note that the specimen half B is mirrored in relation to the specimen half A. For the drawing the mirror axis is the horizontal of the sheet of paper.) Now three possibilities can be distinguished. All of them are analysed with a stereographic projection. (Note that in the stereographic projection only *the* [100] direction („central pole") is shown which is closest to the centre of the stereographic projection. The centre of the stereographic projection describes the direction of the specimen normal. For the drawing the direction of the specimen normal is the vertical of the sheet of paper. It is lying in the plane of the sheet of paper.):

Case 1, left column: *Ideal cleavage fracture of a crystal at central position, same position of central pole, no misfit.* One [100] direction lies exactly in the direction of the specimen normal. As no plasticity occurs the crystal cleaves in an ideal manner. The „central pole" from both specimen halves point in the direction of the specimen normal. No misfit can be measured.

Case 2, central column: *Ideal cleavage fracture of a crystal at arbitrary position, symmetric position of the central pole around the specimen normal, no misfit.* The cleaved crystal lies at an arbitrary position. As no plasticity occurs the central pole from both specimen halves lies symmetrically around the central pole. No misfit can be measured.

Case 3, right column: *Cleavage fracture of a crystal at arbitrary position, plasticity leads to a rotation of the cystal, a misfit between the two specimen halves can be measured.* The cleaved crystal lies at an arbitrary position. During the crack propagation dislocations are emitted from the crack tip and lead to a small rotation of the crystal close to the fracture surface. Due to this misfit between the two specimen halves the „central pole" of each crystal does not lie symmetrically around the specimen normal of the stereographic projection. Thus, in the stereographic projection, the deviation from the symmetrical position between both fracture halves is a measure for the amount of plasticity occurred. How this amount of plasticity depend on variables such as orientation of crystals, micro and macro crack propagation directions etc. will be a subject for future research.

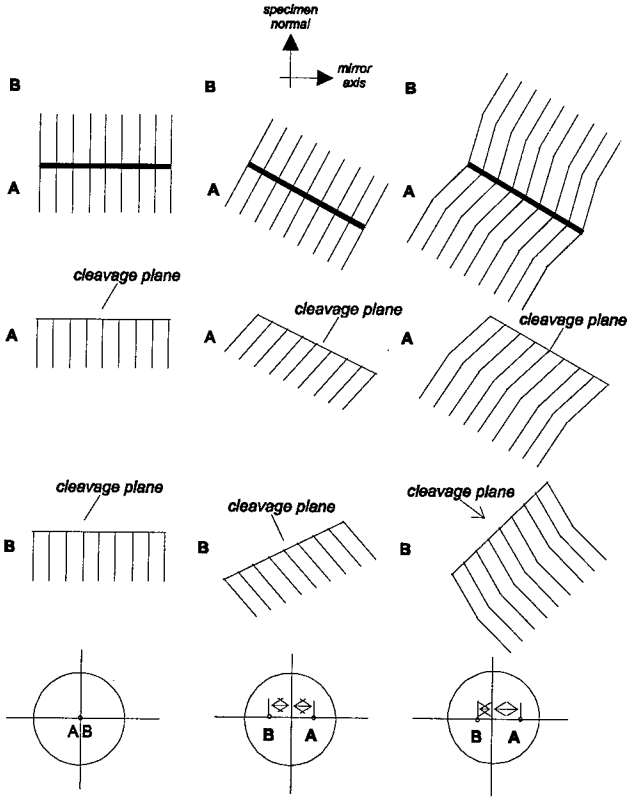


Fig. 10: Orientation misfit due to dislocation emission.

Conclusions

The combination of crystallographic and topographic information provides a powerful tool to investigate

cleavage fracture surfaces of polycystals. We call this type of fractography a *crystallographic fractometry*. As long as EBSD-patterns and DEMs can be recorded we can crystallographically index cleavage planes as well as directions on such planes. Moreover, the method can be applied to study plasticity which occurs during the crack propagation process.

Acknowledgements

The test material was kindly provided by the Armco corporation.

References

[1] G. T. Hahn: „The influence of microstructure on brittle fracture toughness", *Metallurgical Transactions* **15A** (1984) 947-959

[2] A. W. Thompson, J.F. Knott: „Micromechanics of brittle fracture", *Metallurgical Transactions* **24A** (1993) 523-534

[3] R. O. Ritchie, J.F. Knott, J.R. Rice: „On the relationship between critical tensile stress and fracture toughness in mild steel", *J. Mech. Phys. Solids*, **Vol.21** (1973) 395-410

[4] W. W. Gerberich, S.-H. Chen, C.-S. Lee, T. Livine: „Brittle fracture: weakest link or process zone control?" *Metallurgical Transactions* **18A** (1987) 1861-1875

[5] ASM Metals Handbook Vol 12 9th ed.: Fractography, ASM International, Ohio, USA 1987

[6] ASM Metals Handbook Vol 9 8th ed.: Fractography and Atlas of Fractographs, ASM International, Ohio, USA 1974

[7] D. A. Curry, J.F. Knott: „Effects of microstructure on cleavage fracture stress in steel", *Metal Science* **11** (1978) 511-514

[8] D. A. Curry: „Influence of microstructure on yield stress and cleavage fracture stress at -196°C of SA508 class 2 pressure vessel steel", *Metal Science* **18** (1984) 67-76

[9] C. O. A. Semprimoschnig, „Die kristallographische Fraktometrie - Entwicklung einer Methode zur quantitativen Analyse von Spaltbruchflächen" (Ph.D. thesis, Montanuniversität Leoben, 1996)

[10] D.J. Dingley, V. Randle:"Microtexture determination by electron back-scatter diffraction", *Journal of Material Science* 27 (1992) 4545-4566

[11] C. O. A. Semprimoschnig, O. Kolednik, R. Pippan "Spaltbruchuntersuchungen mit dem EBSP-Verfahren und computerunterstützter Stereophotogrammetrie *28. DVM-Arbeitskreis Bruchvorgänge*, Bremen, Germany (1996)

[12] A.J. Wilkinson, D.J. Dingley: Quantitative Deformation Studies using Electron Back Scatter Patterns, *Acta metall. mater*. Vol 39 12 (1991) 3047-3055

[13] A.J. Wilkinson, D.J. Dingley: The Distribution of plastic deformation in a Metal Matrix Composite caused by straining transverse to the fibre direction, *Acta metall. mater*. Vol 40 12 (1992) 3357-3368

[14] W. Buchgraber:"Untersuchung des Einflusses von Versuchsparametern und plastischer Verformung auf die Linienschärfe von Electron Back Scatter Diffraction Patterns", Master thesis, Montanuniversität Leoben 1996

[15] J. Stampfl et al., „Reconstruction of surface topographies by scanning electron microscopy for application in fracture research, *Applied Physics A*, in print

[16] O. Kolednik, H.P. Stüwe: The Stereophotogrammetric Determination of the Critical Crack Tip Opening Displacement, *Engr. Frac. Mech*. **21** (1985) 145-155

[17] R.T. Frankot, S. Hensley, S. Shafer: Noise resistant estimation techniques for SAR image registration and stereomatching, Int. Geoscience and Remote Sensing Symp. IGARSS (1994) 1151-1153

[18] G. Piazessi, : Photogrammetry with the scanning electron microscope, *J. of Phys. E* **Vol.6** (1973) 392-396

[19] J. Stampfl et al.: „The stereophotogrammetric determination of the plastic work for ductile fracture", Proceedings. ECF 11, Poitiers, France (1996)

[20] C.O.A. Semprimoschnig et al. „Micro-Fractography of Cleavage Fracture by EBSP Technology and Computer Assisted Stereophotogrammetry, Proceedings ECF 11, Poitiers, France, (1996)

[21] Schmid, E., W. Boas: „Kristallplastizität mit besonderer Berücksichtigung der Metalle", Springer Verlag, 1935

A FRACTOGRAPHIC STUDY OF THE LOW TEMPERATURE FRACTURE OF A HIGH Mn, HIGH N AUSTENITIC STAINLESS STEEL

J.I. Dickson§, J.-B. Vogt*, A. H. Messai * and J. Foct*
§ Ecole Polytechnique, P.O. 6079, Sta A, Montreal , Que., Canada, H3C 3A7
* Laboratoire de Métallurgie Physique (URA.CRNS 234), Université de Lille, F-59655 Villeneuve d'Ascq, France

Abstract

Results are presented on the occurrence of low temperature cleavage cracking in a high Mn, high N austenitic stainless steel. A considerable amount of macrocleavage occurs on {111} planes and a small amount on {100} planes. Another fractographic feature often observed on this steel consists of microcleavage which formed on mainly parallel {111} planes with the microcleavage facets then being opened partially or totally into dimple-like features on crystallographic facets. These facets corresponded often to {211} planes, and often to a {211} plane perpendicular to the {111} microcleavage plane. The increase with increasing strain amplitude in the amount of such microcleavage on the final fracture portion of fatigue specimens clearly indicates that plastic strain favours the nucleation of such {111} cleavage, which at times has been termed "slip band" cracking. The present results in which most large {111} facets were approximately perpendicular to the tensile axis, however, indicate that crack propagation occurs by true cleavage.

Introduction

The alloying of austenitic stainless steels with relatively large amounts of nitrogen (e.g., 0.35-0.9 wt %) can result in cleavage-like crystallographic cracks being observed on fracture surfaces produced at relatively low temperatures (1-7). The preferential cleavage plane has been reported as {111} in high Mn, high N austenitic stainless steels (1-4, 6, 7), while room-temperature cleavage in austenite was observed in a relatively low Ni, low Mn, high Cr duplex stainless steel (5), with the observations indicating f.c.c. cleavage primarily on {100} planes. The {111} crystallographic cracking has been at times referred to as slip-band cracking or cleavage-like cracking (1-3) because the observations often indicate that the {111} cracking generally occurs on planes on which slip has been produced previously. In agreement with such observations, {111} cleavage-like fractures in low temperature tensile tests on high N austenitic stainless steel single crystals (8) never were perpendicular to the tensile axis but were always on a plane on which an important shear stress was present.

The present paper reports and discusses the fractographic features produced at low temperatures during tensile and Charpy-V impact tests as well as in the rapid final fracture region produced during fatigue tests carried out on a high nitrogen polycrystalline austenitic stainless steel, designated as P900, in which the usual cleavage plane was previously identified as {111} (7).

The objectives of this paper are to characterize the microfractographic features in this steel and to identify the crystallography of this low temperature cracking by scanning electron microscopy observations as well as to comment on the implications which these observations suggest concerning the cracking mechanisms.

Experimental Procedure

The composition of the steel studied was 19.1 % Mn, 18.7% Cr, 0.45% Ni, 0.45% Si, 0.06% Mo, 0.016% P, 0.90% N and 0.04% C. The average grain size was approximately 80 microns. The tests performed were tensile and low cycle fatigue tests at 77K and Charpy-V impact tests at 197 and 77K. Tests were also performed at room temperature but cleavage-like facets were not obtained at this temperature although some intergranular facets were obtained. In the low cycle fatigue tests, the total strain ranges employed (twice the fully-reversed strain amplitudes) were 1.0%, 1.6%, 2.0% and 2.5%.

Stereographic fractographs taken at angles which differ by 6° were generally employed to observe the three-dimensional features of the microfractographic facets and to determine whether a fracture facet was approximately parallel or considerably inclined with the fracture plane, which was perpendicular to the tensile axis and generally perpendicular to the average viewing direction. On facets which are considerably inclined to the average fracture plane, the measured angles can differ considerably from the true angles. It was therefore only on facets which were approximately perpendicular to the average viewing direction that the angles measured between fractographic features were considered as approximating well the true angles. For a small number of inclined facets, controlled tilting was performed to view the facets in a direction approximately perpendicular to their orientation.

George R. Irwin Symposium on Cleavage Fracture
Edited by Kwai S. Chan
The Minerals, Metals & Materials Society, 1997

Quantitative observations were carried out on the plane strain portion of the fracture surfaces of the fatigue specimens to determine the percentage of surface (viewed perpendicularly to the stress axis) corresponding to the different types of fracture. These observations were limited to the final fracture, plane strain region of the fatigue specimens and did not include the portion of fatigue cracking.

Observations and Results

From the angles which the traces on the fracture surfaces made with each other, two different orientations of large crystallographic facets having features typical of cleavage were clearly identified. As well, facets were present which were crystallographic, quasi-crystallographic or which had crystallographic portions and which presented discontinuous crystallographic lines often in the shape of fine, elongated slots but which in many cases could be recognized well as conforming to elongated dimples.

{111} Cleavage

Large, relatively flat {111} facets, often of a size similar to that of grains, were identified frequently from the angles of 60° and 120° which crystallographic lines on these facets made with each other (Fig. 1). These angles are consistent with such lines corresponding to traces of other {111} planes intersecting the fracture surface along <110> directions. At times two different {111} cleavage facets within a grain met each other along such a line. Some of these lines presented fine tongues (Fig. 2), indicating the presence of thin deformation twins on {111} planes cutting the fracture surface. At times, the stereographic observations indicated that the {111} fracture facets became slightly inclined near some of the <110> lines on these facets, suggesting that this may be associated with the intersection of some {111} twins which were too fine to produce visible tongues or that the fracture plane deviated slightly to follow the intersected {111} plane for a short distance. In other cases, crystallographic steps were present along such <110> river lines with the fracture plane following a second {111} plane along these steps, thus indicating some secondary cleavage (Fig. 3).

On the fracture surfaces of specimens tested in fatigue at 77K, such large {111} fracture facets were present mainly on the plane strain portion of the fracture surface produced during the final fracture, although a few such facets were also present on the portion of the fracture surface produced during fatigue cracking. Such relatively large {111} facets were generally approximately perpendicular to the tensile axis and the fracture initiation site within grains generally appeared to be in a grain boundary region.

Some difficulty was encountered in trying to determine the local crack propagation direction from the river lines on {111} facets. On some {111} facets, no or very few river lines were present leaving some ambiguity as to the site of cleavage crack initiation in that grain (Fig. 1). Also in the center of many grains, river lines would at times appear to coalesce together and then to resplit apart (Figs. 2 and 4).

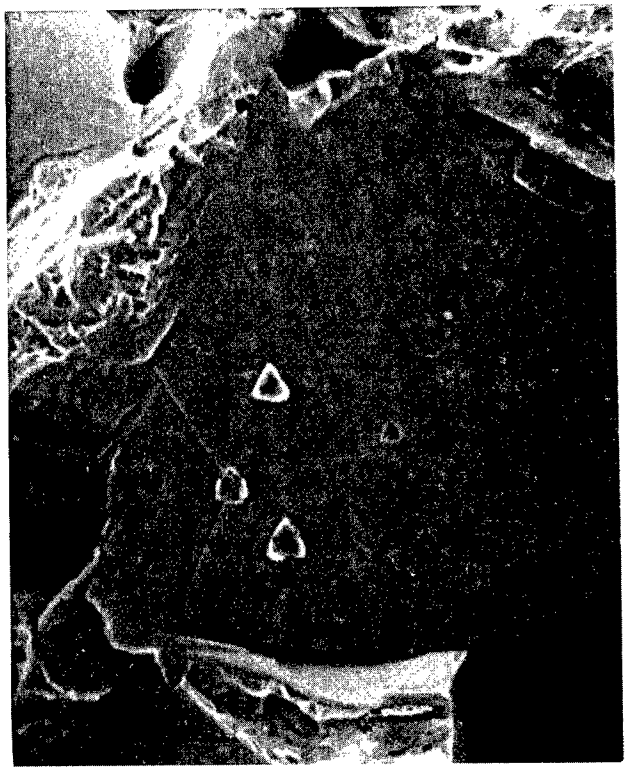


Fig. 1 Flat {111} facet in a tensile specimen fractured at 77K, showing a quasi-absence of river lines.



Fig. 2. {111} cleavage facet observed on a Charpy-V specimen tested at 197K. Very thin tongues are present along two sets of <110> traces indicating fine {111} deformation twins. Parallel to one of these traces the fracture surface at times makes small jumps to a parallel {111} plane before coming back to the original plane. The river lines present show the frequent difficulty observed for river lines to coalesce on these {111} facets.

This was associated with river lines coming very close to each other without actually coalescing and then redeviating from each other. That the river lines had not actually coalesced often was difficult to see because of the brightness of the image obtained at the river line (but was easier to see if the image was viewed with low contrast or if a lower accelerating voltage was employed in the scanning electron microscope) or because the side of the river line became inclined at less than 90° with the facet and then often became hidden from view when the river lines became very close together. The crack propagation direction indicated by the coalescence of large river lines near a grain boundary generally indicated the correct propagation direction within a grain. Such coalescence of large river lines generally occurred near the grain boundary at which cleavage had initiated in a grain. Coalescence of river lines with a line parallel to a <110>, however, occurred relatively easily when such coalesence produced a secondary {111} cleavage facet (Fig. 3). Fig. 4 does not contradict this statement because the propagation direction is from top to bottom.



Fig. 3. Large river lines parallel to a trace of a <110> on a {111} facet. In this case, coalescence of river lines occurs easily and the plane of the river lines is also a {111} facet. Therefore the continued cracking on the river line occurs by cleavage on this secondary facet.

The shape of tongues which were approximately perpendicular to the local river lines could also be employed to determine the correct local crack propagation direction. The formation of a tongue, the base of which is approximately perpendicular to the local crack front, should only occur in the direction of crack propagation. The correct crack propagation direction is then indicated by the angle of more than 90° between the fracture surface and that of a tongue which starts at a line approximately perpendicular to a river line. Tongues with bases which are approximately parallel to the local propagation direction, however, provide no information on this direction. Tongues with bases approximately perpendicular to river lines generally indicated the same crack propagation direction as did the coalescence of the river lines. In a few cases, where the coalescence of the river lines on a facet suggested that crack propagation in neighbouring regions were in opposite directions, suitably orientated tongues when present indicated that crack propagation was in only a single direction and thus appeared a more reliable indicator of the local crack propagation direction in this material in which the coalescence of river lines occurred with difficulty. In a few cases, {111} cleavage initiation in a grain had occurred in two different regions near different grain boundaries, which was easy to recognize by the large step where the fractures on the parallel cleavage planes came together.

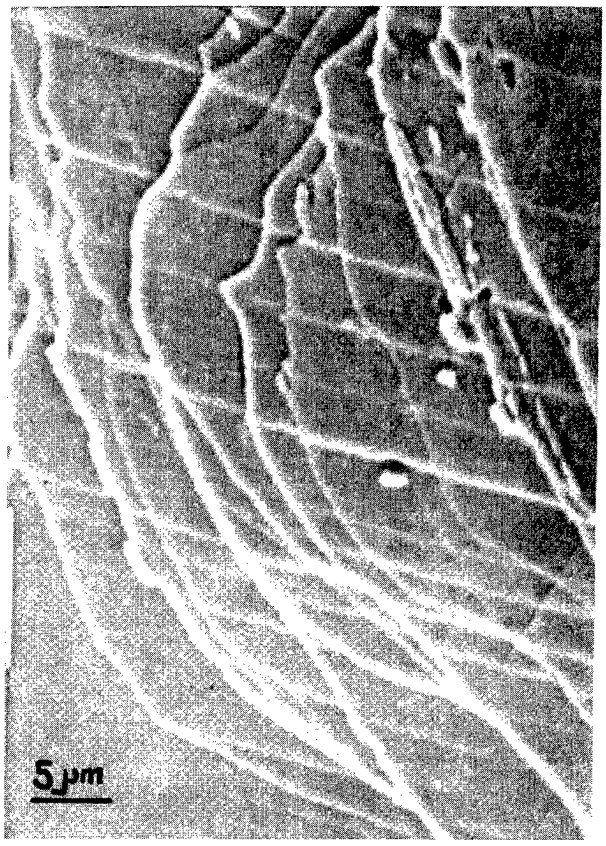


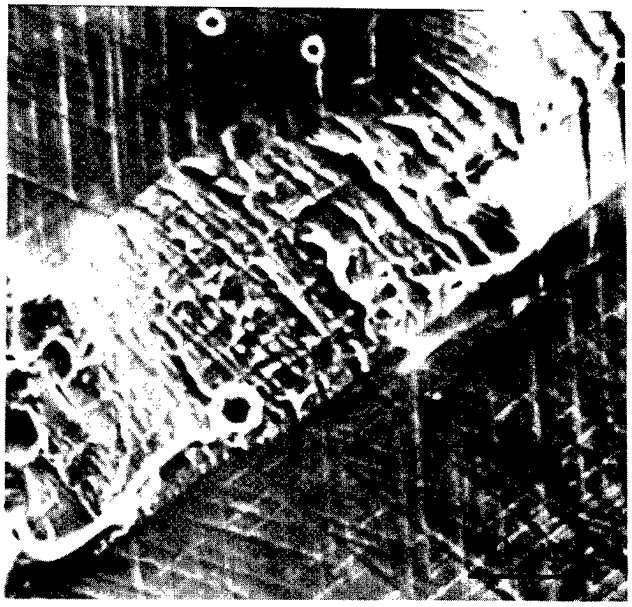
Fig. 4. River lines observed on a {111} facet. These lines appear to coalesce in both directions, because of the difficulty for river lines non parallel to a <110> direction to truly coalesce on such facets. The actual local crack propagation direction in this region is from top to bottom.

On some of the {111} facets observed on Charpy specimens, thin flat regions were at times present along some of the <110> traces, indicating that along these regions, the fracture surface changed to a parallel {111} plane before coming back to the original plane (Fig. 2). In other cases, this change along a short distance to a plane parallel to the original fracture plane occurred at a number of discontinuous small points along a <110> line. Since these features differ from tongues, it appears improbable that these regions could be associated with mechanical twinning. Indeed in many cases tongues were present in addition to these changes to a parallel cleavage plane (Fig. 2). One possibility is that this change to a parallel fracture plane along a thin band or along a line of fine points could be associated with sites at which martensite has formed on a {111} slip band intersecting the original cleavage plane and favouring a temporary local change in fracture plane following this slip band. Grazing X-ray diffraction of fracture surfaces of fatigue specimens tested at 77K (9) indicated the presence of both ε and α' martensite in the fracture region, however, such local changes in the fracture facets on the final fracture region of these fatigue specimens were generally not observed.

In two grains of a Charpy-V specimen tested at 197K, the fractographic facet presented the three sets of lines making angles of 60° with each other, with the features of these lines typical of <110> lines on a {111} cleavage facet in this steel. On these facets, however, three additional sets of lines were present and made angles of 20° with those which had the features of <110> lines, with two of these sets appearing parallel to tongues indicative of twins. Part of this region is presented in Fig. 5. These additional sets of lines suggest the occasional presence of slip and twin traces which probably correspond either to {210} or to {211} planes and which do not agree with traces of {111}, {100} or {110} planes.

{100} Cleavage

A small number (approximately 3% of the fracture surface) of large crystallographic facets had an orientation, which was identified as {100}, from the angles of 45° and 90° that the crystallographic sets of lines on these facets made with each other. Generally three or four sets of such lines being present (Fig. 6). The sets of lines corresponding to <011> traces could generally be recognized since tongues were often present along certain of these lines indicating the presence of presumably {111} deformation twins. The lines corresponding to <001> traces at times corresponded to sharp steps on the fracture surface, which could be easily be mistaken for tongues. Careful high magnification stereographic observations permitted unambiguously to distinguish such steps from tongues. Such observations also showed that these steps were perpendicular to the {100} primary facet and therefore also corresponded to {100} surfaces. On some of these facets, the crack propagation direction appeared to correspond to a <100>, while on others, it appeared to correspond to a <110>. Some large cleavage-like crystallographic facets had features indicating that they could correspond to {100} facets, with an additional set of lines (which only occasionally corresponded to tongues) present, the orientations of which were consistent with traces of {210} or {211} planes.



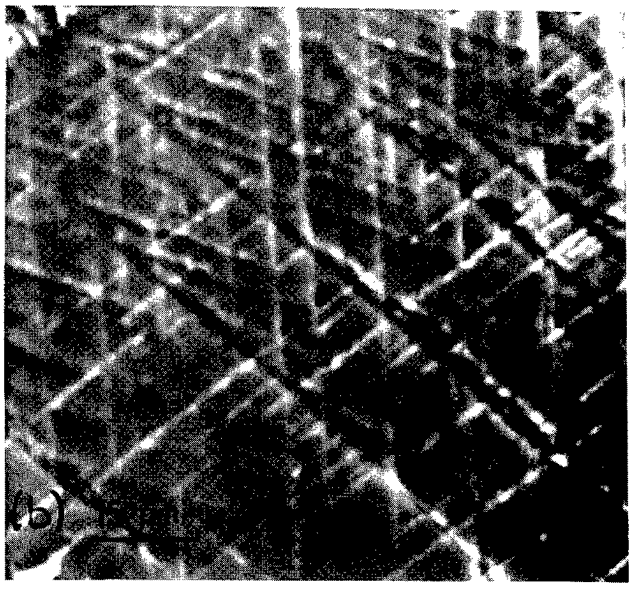


Fig. 5. Lines observed on a {111} facet in the vicinity of an annealing twin (Fig. 5a) on a Charpy-V specimen fractured at 197K. In addition to the three sets of lines corresponding to <110> traces, a set of lines generally in the shape of tongues (Fig. 5b) are present approximately perpendicular to the interface of the annealing twin. Two other sets of such lines were observed in other regions of this cleavage facet.

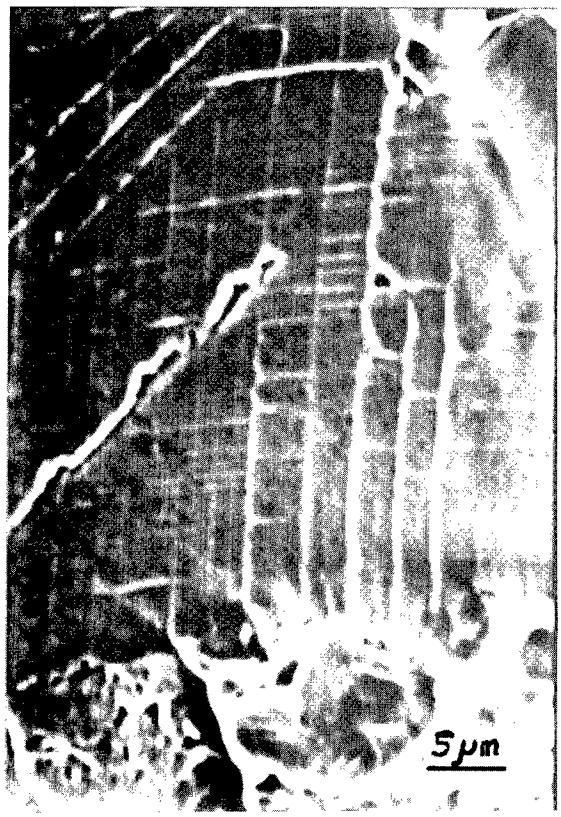


Fig. 6. {100} cleavage facet observed on the fast fracture region of a specimen cycled in fatigue at a strain range of 1% at 77K. Stereographic observations showed that the horizontal and vertical lines corresponded to steps on the facets, while the lines at approximately 45° to the vertical corresponded to tongues and thus indicate mechanical twins, probably of {111} orientation.

{111} Microcleavage

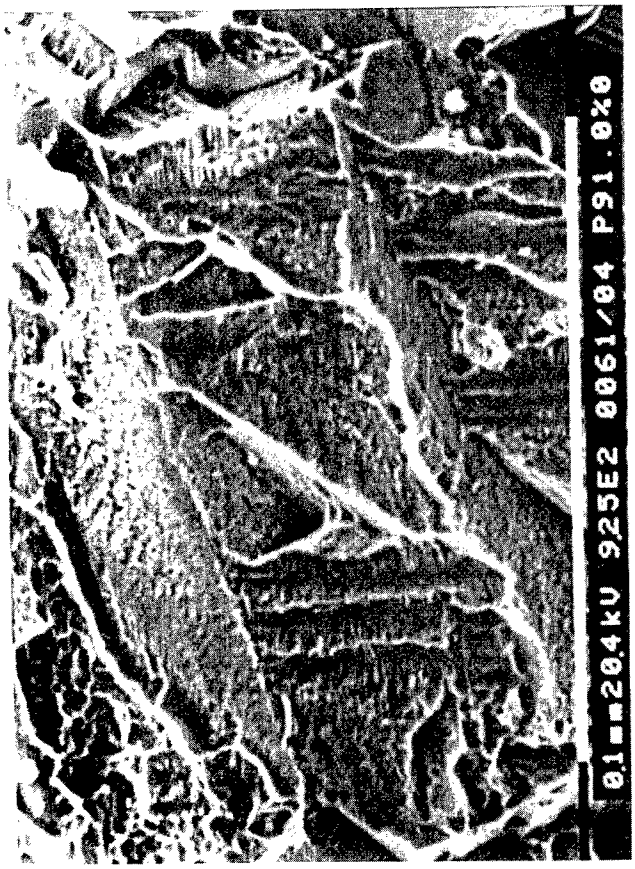
Besides these large, very crystallographic facets which had typical features of cleavage, numerous crystallographic or approximately crystallographic facets presented parallel straight lines of small facets considerably inclined with respect to the average orientation of the larger facets. These microscopic facets were always identified as corresponding to {111} from frequent stereofractographic observations (e.g., Fig. 7) of grains in which both a large crystallographic {111} facet was present as well as microfacets parallel to this macrofacet. A {211} or near-{211} orientation was frequently identified for the macrofacets containing {111} microfacets, with both sharing a common <110> direction. Often on such {211} macrofacets, most of the microfacets had a {111} orientation perpendicular to that of the macrofacet. An example is presented in Fig. 8 and other examples can be seen in Fig. 7. The striation-like lines on these macrofacets correspond to {111} microcleavage facets, which have been partly opened towards fine elongated dimples, as indicated by the shape and orientation of these small dimple-like features.

The macroscopic fracture plane containing {111} microfacets was not always very crystallographic, although generally at least some small regions were approximately crystallographic. In many cases in which the macroscopic fracture plane was less crystallographic, the microscopic {111} facets were seen to have been opened up into well recognizable, elongated dimples (Fig. 9). Even in some cases where the macroscopic fracture facet was rather crystallographic, the {111} microfacets had been opened up in quite easily recognizable elongated dimples.

Some elongated approximately crystallographic facets covered with dimples were often present on the shear lip near the interface between this lip and the plane strain fracture region. Several facets of two or more orientations were present, which shared a common crystallographic line approximately orientated towards the free surface. Although the orientation of these facets was not always very crystallographic, the usual angle between two such facets was approximately 60° (or 120°), with a few facets at times making an angle of approximately 90° with another set of facets. In some grains, all three sets of such facets making angles of 60° with each other were present (Fig. 10), all of which met each other along a single parallel crystallographic set of lines orientated towards the free surface. The dimples on these facets were in the shape of full dimples (rather than the half dimples expected on the shear lip) and were elongated perpendicularly to this common set of lines, with these dimples often crossing such a line and being on two or three different facets. These observations strongly suggest that these dimples are elongated along a {111} plane and that the sets of fracture facets normal to this plane primarily correspond to {110} or {211} facets, since these make angles of 60° with each other. The observations suggest that both of these orientations may be present but that one is dominant.

Such observations appear rather similar to the {211} facets presenting a set of {111} microfacets perpendicular to the macrofacets found in the plane strain region, except that in the plane strain region the {111} microfacets generally have not been strongly stretched into dimples. In contrast, in the plane stress region, the dimples along parallel {111} traces are so strongly stretched that no physical evidence remains to indicate that they initiated by the occurrence of {111} microcleavage other than the similarities with the features observed in the plane strain region. These similarities are sufficiently strong to indicate that it is very probable that most of the dimpled facets at the start of the shear lip also correspond to {211} facets.

On the large {111} cleavage facets in the plane strain region, which are often approximately perpendicular to the tensile axis and which were generally viewed parallel to the tensile axis, the stereographic micrographs taken were found actually to indicate a number of cases of three {110} facets perpendicular to a large {111} cleavage facet as shown in Fig. 11, but with the former facets being approximately parallel to the viewing direction, resulting in the dimpled features on these {110} facets usually being visible (and usually only barely) on only one of these sets of {110} facets. In contrast, on the shear lip, these sets of dimpled {110} facets were always very clearly visible since they were on planes of important shear stress.



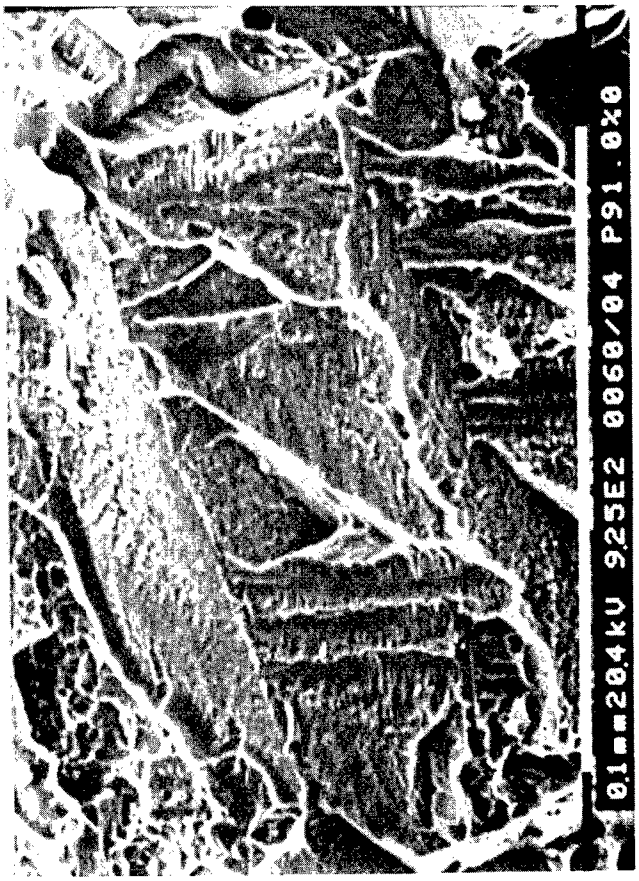


Fig. 7. Stereographic pair of micrographs taken from a grain in the final fracture region of a specimen cycled at a strain range of 1% at 77K. Two {111} facets, indicated A and B are seen and some of the dimpled facets can be recognized as corresponding to {211} planes.



Fig. 8. A {211} facet perpendicular to the large inclined {111} facet seen at the left of the micrograph, with the microfacets on the {211} parallel to this large {111} facet.

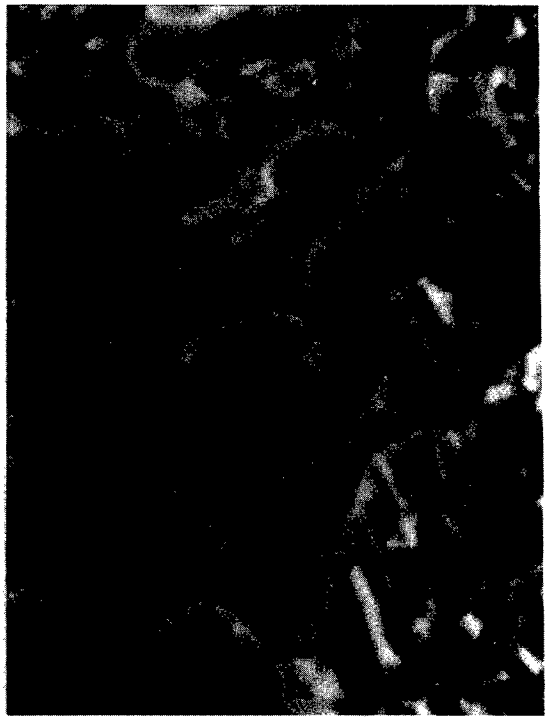


Fig. 9. Region in the final fracture zone of a fatigue specimen (strain range = 2.0%) which is not very crystallographic but with microfacets recognized as corresponding to elongated, crystallographic dimples.

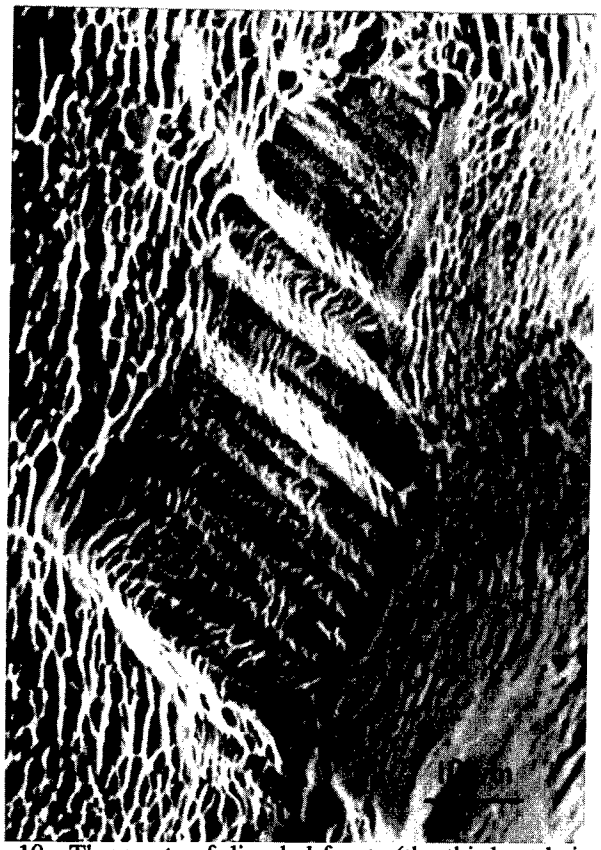


Fig. 10. Three sets of dimpled facets (the third set being near the extremity of these features at right) making angles of approximately 60° are present at the start of the shear lip on a specimen fractured in a tensile test at 77K. The dimples on these features are full dimples which are often present on two or three facets and which are perpendicular to the common direction shared by these facets. These observations indicate that these macrofacets share a common <111> with the dimples elongated on the plane perpendicular to this direction.



Fig. 11. Two dimpled crystallographic planes approximately perpendicular to a large {111} facet are seen as well as a dimpled crystallographic plane inclined approximately 20° to this {111} facet The three dimpled each share a different <110> with the {111} facet. These observations indicate that each of the three dimpled facets corresponds to a different {211}.

Intergranular cracking

A sizeable portion of the fracture surface comprised of intergranular facets. For some grains, such facets were partly intergranular, partly transgranular. In the plane strain, final fracture portion of the specimens tested in fatigue at 77K, the intergranular portion of fracture surface decreased with increasing strain range while the portion corresponding to a crystallographic or quasi-crystallographic plane presenting dimples which had formed as microcleavage facets on a {111} plane increased with increasing strain range.

Quantitative fractographic analysis

The results of the quantitative fractographic analysis performed on the plane strain region of the specimens tested in fatigue at 77K are reported in Table I. It is seen that the features with {111} microfacets (often on {211} or near-{211} macrofacets) increased continuously with increasing strain range, going from 6% for a range of 1.0% to 19% for one of 2.5%. This increase was compensated by a continuous decrease in the amount of intergranular facets with increasing strain range, which went from 41% for a range of 1.0% to 30% for a range of 2.5%. The sum of these two types of facets was approximately constant and corresponded to 47.5% ± 2.5% for the four strain ranges studied.

These observations therefore indicate that as the fatigue strain range increases the amount of intergranular cracking decreases and is compensated by a corresponding increase in the amount of facets which present fine dimples, with these dimples having formed as microcleavage facets on one or more sets of {111} planes. In contrast, the surface area occupied by the other microfractographic features observed does not vary significantly with strain range. These observations therefore strongly suggest that, as the strain range increases, the number of grains in which a considerable amount of slip occurs increases and that this increased slip per cycle favours the obtention of macrofacets presenting fine {111} microfacets.

Table 1: Analysis of the plane strain portion of the fracture surfaces of fatigue specimens tested at 77K

strain range	1.0%	1.6%	2%	2.5%
{111} macrofacets	44%	47%	43%	43%
{111}microfacets	6%	8%	16%	19%
intergranular facets	41%	37%	34%	30%
{100}facets	4%	3%	3%	2%
unidentified facets	2%	2%	2%	3%
ductile tearing dimples	3%	3%	3%	3%

Role of slip in producing cleavage

The present results therefore indicate that slip on {111} planes favours the initiation of {111} cleavage, in agreement with the conclusions of previous studies on these high nitrogen austenitic stainless steels (1-3). That slip on {111} planes facilitates the nucleation of cleavage is also in agreement with low temperature tensile test results on single crystals of high nitrogen austenitic stainless steels, in which {111} cleavage-like facets were produced but never on a plane perpendicular to a <111> crystal axis (8). That the large cleavage facets were generally almost perpendicular to the tensile axis in the present study indicates that in grains having a {111} plane almost normal to the tensile axis, this cleavage, once initiated, occurred easily at sufficiently low temperatures, since these planes were well oriented for cleavage. The results on the fatigue specimens however indicated that in grains not well oriented for cleavage, an increasing plastic strain range favoured the initiation of {111} microfacets but little influenced the percentage of large {111} macrofacets. This result strongly suggests that the role of slip is to strongly favour the initiation of {111} cleavage but to have little influence on its propagation.

The present results showed that crystallographic cracking along {211} planes also occurred but the {211} macrofacets were apparently always intersected by {111} microfacets, often oriented perpendicularly to these {211} facets. The {100} cleavage facets often indicated traces consistent with the occurrence of {211} slip. The large {111} cleavage facets only rarely presented lines taken as {211} traces (Fig. 5), but six of the {211} planes intersect a {111} plane along the same <110> directions as the other {111} planes. The observations also indicated that the {211} facets found were frequently those which shared a <110> direction with a large {111} cleavage facet (Fig. 11). These results therefore suggest that the {211} slip probably nucleates by a dislocation reaction at a <110> direction common with a {111} plane or, in spite of the very planar slip, as cross slip from this {111} plane. The numerous {111} microfacets generally intersecting {211} facets also suggest a tendency for slip to return to {111} planes intersected by the {211} slip plane, with this slip tending to initiate cleavage on both planes.

As well with the indicated role of slip in nucleating {111} and apparently {211} cleavage, a simple explanation can be offered for the reported (2, 3} tendency for a decreasing grain size to increase the ductile-brittle transition temperature. A decreasing grain size causes an increase of the volume of material near grain boundaries, and it is in the grain boundary regions that accommodation effects can produce slip perpendicularly to the tensile stress, with this slip favouring the initiation of cleavage on this plane.

Conclusions

The present results allow one to conclude that {111}, {100} and {211} cleavage were produced at low temperatures in the high nitrogen austenitic steel studied, with the nucleation of cleavage along {111} and {211} planes favoured by slip.

Acknowledgments

The authors are grateful to VSG GmbH, Essen, Germany for providing the stainless steel. JID acknowledges research support from NSERC (Canada) and FCAR (Quebec.)

Refcrences

1. J. D. Defilippi, K. G. Brickner, and E.M. Gilbert, "Ductile-to-Brittle Transition in Austenitic Chromium-Manganese-Nitrogen Stainless Steels," Trans TMS-AIME, 245 (1969), 2141-2148.
2. R.L. Tobler and D. Meyn, "Cleavage-Like Fracture along Slip Planes in Fe-18Cr-3Ni-13Mn-0.37N Austenitic Stainless Steel at Liquid Helium Temperature," Metall. Trans., 19A (1988) 1626-1631.
3. Y. Tomata and S. Endo, "Cleavage-like Fracture at Low Temperatures in an 18Mn-18Cr-0.5N Austenitic Steel," ISIJ Intern., 30 (1990) 656-662.
4. P. J. Uggowitzer, N. Paulus and M. O. Speidel, "Ductile-to-Brittle Transition in Nitrogen Alloyed Austenitic Stainless Steel," Applications of Stainless Steels 92, Jernkontoret, 1 (1992) 62-72.
5. J. Foct and N. Akdut, "Cleavage-like Fracture of Austenite in Duplex Stainless Steel," Scripta Met. et Mat., 29 (1993) 153-158.
6. R. J. Ilola, H. E. Hänninen and K. M. Ullakko, "Mechanical Properties of Austenitic High-Nitrogen Cr -Ni and Cr-Mn Steels at Low Temperatures," ISIJ Intern. 36 (1996) 873-877.
7. J.-B. Vogt, H. Messai, and J. Foct, "Cleavage Fracture of Austenite Induced by Nitrogen Supersaturation," Scripta Met. et Mat., 31 (1994) 549-554.
8. Yu. Chumljakov, Siberian Physical-Technical Institute, Tomsk, Russia, personal communication.
9. A. H. Messai, "Analyse fractographique de la rupture fragile d'un acier inoxydable austénitique très chargé en azote," Doctoral thesis, Université des Sciences et de Technologies de Lille, 1996.

OXIDE FILM EFFECTS ON CLEAVAGE:

W. W. Gerberich
N. R. Moody[+]
M. D. Kriese

University of Minnesota
Minneapolis, MN 55455

[+]Sandia National Laboratories
Livermore, CA

Abstract

When cleavage nucleates from crack tips containing oxide layers or when time-dependent, subcritical crack growth occurs by a brittle cleavage or intergranular process, what is the role of an oxide film? The mechanism of stress corrosion cracking by a film rupture process has been postulated for some time. In addition, film-induced cleavage has been proposed more recently by Sieradzki and Newman. While either or both of these may exist, is there yet an even more general effect which must be considered? That is, either along with these mechanisms or in some cases *in lieu* of them, must we consider how oxide films affect dislocation emission which then becomes involved in shielding effects on cleavage or time-dependent failure? What we do know is that oxide films greatly affect the yield load occurring under a sharp indenter. Might this not also affect yield behavior at a crack tip since both represent sharp stress concentrators? For example, indentation induced yield excursions can vary by an order of magnitude in Fe-3wt%Si and tungsten with different oxide films. Plans for sorting this out are underway using companion experiments undergoing cleavage as well as indentation. Results on NiAl single crystals will be reported.

George R. Irwin Symposium on Cleavage Fracture
Edited by Kwai S. Chan
The Minerals, Metals & Materials Society, 1997

SURFACE FILM SOFTENING AS A PROBLEM OF CLEAVAGE FRACTURE

R. Gibala

University of Michigan
Department of Materials Science and Engineering
Ann Arbor, MI 48109-2136

Abstract

We have examined experimental data on the phenomenon of surface film softening of quasi-brittle metals and intermetallics in the context of cleavage fracture and its interaction with the intrinsic plasticity of these materials. Surface film softening is manifested as increased plasticity and, in many instances, as reduced flow stresses of a substrate material due to enhanced dislocation generation associated with film-substrate constraint under applied stress. Nominally ductile refractory metals such as Nb and Ta can be substantially ductilized by surface films to the point of exhibiting appreciable free strain. More brittle metals, such as Mo or W exhibit film-enhanced plasticity, some evidence of free strain, and associated changes in fracture mechanisms. Intermetallic alloys and compounds, e.g. NiAl, FeAl, and $MoSi_2$, can exhibit film-enhanced plasticity but usually without significant changes in fracture behavior.

George R. Irwin Symposium on Cleavage Fracture
Edited by Kwai S. Chan
The Minerals, Metals & Materials Society, 1997

CLEAVAGE MECHANISM IN VANADIUM ALLOYS

G. R. Odette
E. Donahue
G. E. Lucas

University of California Santa Barbara
Department of Mechanical Engineering
Santa Barbara, CA 93106-5070

Abstract

The effect specimen geometry, loading rate and irradiation on the ductile-to-brittle transition in a V-4Ti-4Cr alloy were evaluated and modeled. Confocal microscopy-fracture reconstruction and SEM were used to characterize the sequence-of-events leading to cleavage, as well as the CTOD at fracture initiation. This alloy undergoes normal stress-controlled transgranular cleavage below a transition temperature that depends primarily on the tensile properties and constraint. Thus an equivalent yield stress model is in good agreement with observed effects of loading rate and irradiation hardening. Predicted effects of specimen geometry based on a critical stress-area criteria and FEM simulations of crack tip fields were also found to be in agreement with experiment. Some interesting characteristics of the fracture process are also described.

George R. Irwin Symposium on Cleavage Fracture
Edited by Kwai S. Chan
The Minerals, Metals & Materials Society, 1997

CLEAVAGE FRACTURE IN ALUMINIDES AND CERAMICS

FRACTURE AND FRACTURE TOUGHNESS OF DIRECTIONALLY SOLIDIFIED TiAl-BASED TWO-PHASE ALLOYS

N. Akiyama, S. Yokoshima, D. R. Johnson, K. Kishida, H. Inui and M. Yamaguchi

Department of Materials Science and Engineering, Kyoto University
Sakyo-ku, Kyoto 606-01, Japan

Abstract

The TiAl(γ)/Ti_3Al(α_2) lamellar microstructure in γ -based two-phase alloys are of special interest since γ -based alloys having a fully lamellar microstructure exhibit good creep and fracture resistance at temperatures up to 800℃. We have introduced a new approach for studying the γ / α_2 lamellar microstructure by producing polysynthetically twinned (PST) crystals with the lamellar microstructure derived from a single α grain and thus with the same lamellar orientation over the entire crystal by means of directional solidification techniques. We have been working on the deformation behavior of such PST crystals to understand the mechanical properties of the lamellar microstructure in γ -based two-phase alloys at a fundamental level. Recently, we have extended our study of mechanical properties of PST crystals to directionally solidified ingots composed of columnar grains with the lamellar structure aligned parallel to the growth direction. In this paper, the fracture behavior, fracture surface morphology and fracture toughness of PST crystals and directionally solidified ingots are discussed as a function of lamellar orientation, test environment, loading rate and alloy composition.

Introduction

Extensive work has been made on the microstructural characteristics and property/microstructure relationships of γ -based two-phase alloys in the last decade [1-5]. Based on these achievements, various engineering γ -based two-phase alloys have been developed and industries are seeking to accomplish their introduction for various structural components. The mechanical properties of γ -based two-phase alloys strongly depend on their microstructure, which is usually in the lamellar or the duplex form. Fine and homogeneous duplex structures result in good ductility, although their fracture toughness and high-temperature strength are rather poor. By contrast to such duplex structures, lamellar structures are poor in ductility; however, they are generally superior to the duplex structures in other mechanical properties such as fracture toughness, fatigue resistance and high-temperature strength. Fracture toughness of γ -based two-phase alloys in the lamellar form has been known to increase with increasing the size of lamellar grains. On the other hand, the ductility decreases with increasing the lamellar grain size [6-9]. This is typically shown in Fig.1 [3].

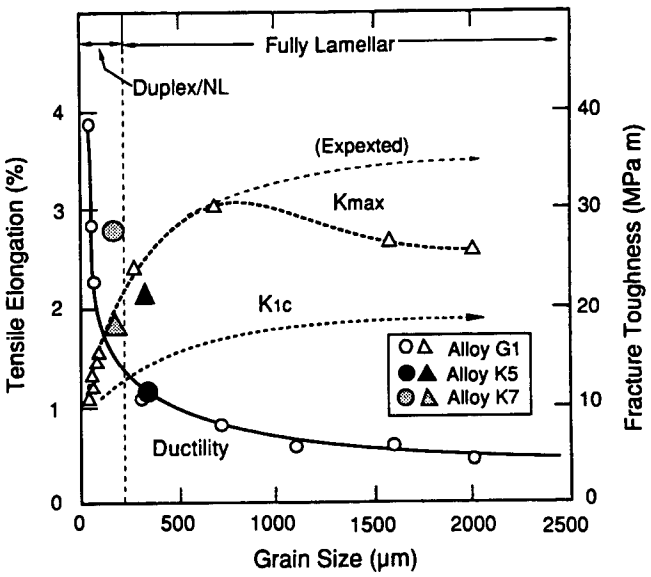


Figure 1: Inverse ductility/toughness (K_{IC} and K_{MAX}) relationships observed in some γ -based alloys[3].

George R. Irwin Symposium on Cleavage Fracture
Edited by Kwai S. Chan
The Minerals, Metals & Materials Society, 1997

One approach to minimize such inverse relationship between tensile properties and fracture toughness is to develop a microstructure consisting of refined lamellar grains so that reasonably high ductility and fracture toughness are achieved. Thermomechanical processing routes such as hot isostatical pressing followed by hot working procedures are generally used to produce materials with a finer distribution of lamellar grains [3]. In fact, a series of new generation alloys with refined lamellar structures have been reported to exhibit balanced mechanical properties for higher performance and temperature capabilities [3, 10, 11].

Another approach with a potentially greater payoff is to use directional solidification techniques to produce a columnar grain material with the lamellar orientation aligned parallel to the growth direction. During the last few years, the fundamental properties of the γ / α_2 lamellar microstructure such as microstructure [12], deformation [13, 14], fracture toughness [15] and macroscopic flow behavior [16] have been extensively researched by PST crystals . With such a data base now available, if γ -based two-phase alloys can be processed such that the microstructure is composed of columnar grains all having the lamellar microstructure aligned parallel to the growth direction with each grain rotated about its longitudinal axis, the resulting material would exhibit a good combination of strength, ductility, and toughness. A schematic representation of such an ingot is shown in Fig. 2.

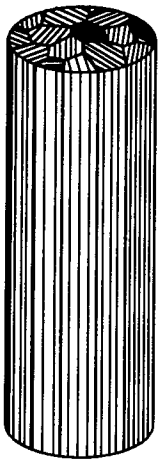


Figure 2: Directionally solidified ingot composed of columnar grains whose γ and α_2 lamellae are aligned along the growth direction.

Unfortunately, simple casting operations usually result in the opposite situation with the lamellar boundaries perpendicular to the dendritic growth direction. The reason for this is that the preferred growth direction of α -phase dendrites is parallel to the [0001] direction during solidification. Upon cooling, the lamellar microstructure is then formed from the parent α phase such that $(0001)_\alpha // (111)_\gamma$ and $<11\bar{2}0>_\alpha // <110>_\gamma$ [12, 17]. Hence, to control the final orientation of the lamellar microstructure, the orientation of the high temperature α -phase must first be controlled. Recently, we found that the γ / α_2 lamellar microstructure can be aligned parallel to the growth direction in a number of directionally solidified TiAl-based alloys by using an appropriately oriented seed from the TiAl-Si system. Studies on the deformation and fracture behavior of such directionally solidified ingots are presently in progress. In this paper, the results of studies on the fracture and fracture toughness of PST crystals and some directionally solidified ingots are presented. The fracture behavior and fracture toughness of PST crystals are discussed as a function of lamellar orientation, test environment, loading rate and alloy composition.

Experimental

Specimens for fracture toughness measurements

Specimens in the PST form PST crystals approximately 70 mm long and 10 mm in diameter were grown from arc-melted ingots with nominal compositions of Ti-49.3Al, Ti-47.0Al and Ti-48.9Al-0.4Cr (at%) using an ASGAL FZ-SS35W optical-floating zone furnace at a growth rate of 5 mm/h under Ar gas flow. Three-point bend specimens with five different notch orientations (Fig.3) were prepared from these as-grown PST crystals. However, most of fracture experiments were done for PST crystals of Ti-49.3Al alloy and thus the term PST crystals will mean those of Ti-49.3Al alloy unless otherwise stated. Types I, II and III are crack arrester, crack divider and crack delamination orientations with respect to the lamellar boundaries. In Fig.3, the direction normal to the lamellar boundaries is assigned to be [111], and the $<11\bar{2}>$ and $<1\bar{1}0>$ Miller indices indicate the directions normal to the notch plane with respect to γ lamellae. Indices of the notch plane can not be specified even though the lamellar boundaries are assigned to be parallel to (111) because of the domain structure in the γ phase [15].

A Chevron notch with a sharp tip was introduced in each specimen with a dimension of 20 x 4 x 3 mm^3 (Fig.4). Except for those of type III, the notched specimens were then fatigue-precracked, as shown in Fig.4, using an automated electro-servo-hydraulic testing machine operating under load control at a sinusoidal frequency of 15 Hz and a load ratio of R = 0.1. Fatigue-precracked specimens were side-grooved by spark machining such that the ratio of B_N/B is 0.7 so as to evaluate their J_{IC} values using the simple method for determining J_{IC} proposed by Server, Wullaert and Ritchie [18] and applied for various different materials including a two-phase TiAl alloy by Mutoh and his colleagues [19-21]. If side grooving is made properly, the J integral corresponding to the maximum load point on the load-displacement curve reasonably approximates the JIC of the specimen [19-21].

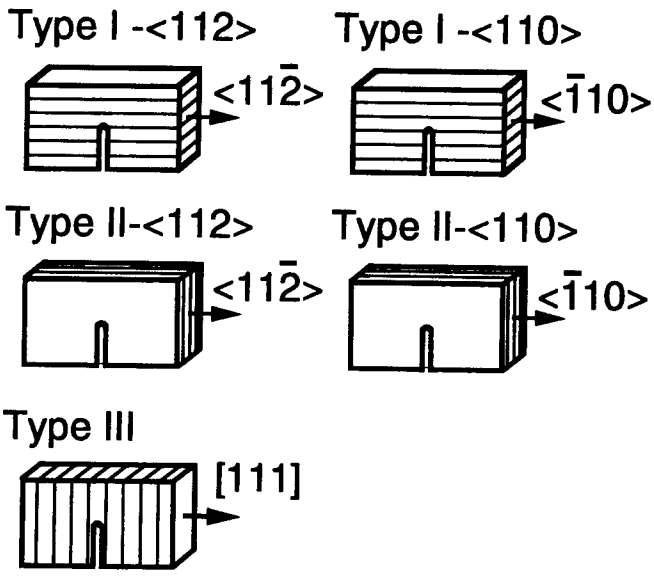
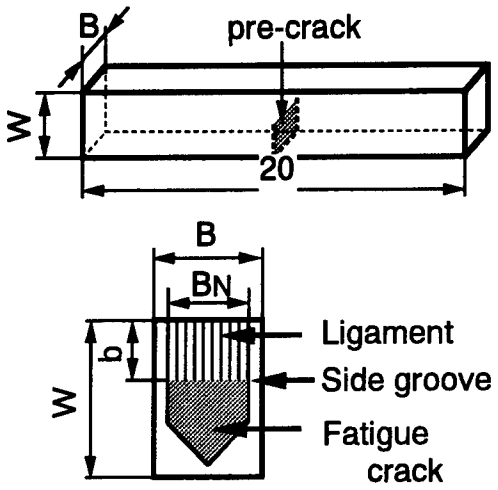


Figure 3: Orientations of PST specimens.

Directionally solidified ingots Directional solidification was performed using the same optical-floating zone furnace at a growth rate of 100 mm/h under argon gas flow. The initial master ingots of Ti-43Al-3Si alloy approximately 10 mm diameter and 80 mm in length were prepared by arc-melting. From directionally solidified ingots, bend specimens with dimensions of 14x4x3 mm^3 were cut and a 1.5 mm notch was cut into each specimen in the crack delamination or the crack arrester orientation by spark machining and a fatigue crack was not initiated at the notch tip.



Span for three point bending : 14mm

W = 4 mm

B = 3 mm

b = 0.4W

BN = 0.75B

Figure 4: Geometry of PST specimens.

Fracture toughness measurements and fracture surface observations

Specimens in the PST form Specimens were tested in three-point bending with a span length of 14 mm. Bending tests were conducted at load-line displacement rates of 0.02 and 10 mm/min at room temperature in three different environments, i.e. in air, in a scanning electron microscopy (SEM) with a loading stage evacuated to 1.33×10^{-2} Pa by a diffusion pump and in a vacuum chamber evacuated to 1.33×10^{-3} Pa by a turbo-molecular pump. Loading in the SEM was conducted in situ monitoring the sequence of events that accompany crack extension. Load-line displacement (hereafter, simply called displacement) was measured using a laser scan micrometer. JIC was approximated by the value given by $J = 2A/B_e b$, where A is the area under the load-displacement curve ($0 \leqq$ load $\leqq$ the maximum load) that is rectified with respect to the jig compliance, and B_e is the effective width of a ligament which is given by $1.1x(B \cdot B_N)^{1/2}$ [15, 20]. Fracture surface examinations were made using a SEM. Specimens of type III were not fatigue-precracked because of the brittleness. They were just notched and side-grooved by spark machining and then tested in bending.

Directionally solidified ingots All specimens were tested in three-point bending at a load-line displacement rate of 0.02 mm/min at room temperature in air. In all cases, the load versus displacement curve was linear until fracture. The fracture toughness values were calculated using the K calibration for 3-point bending and the load at fracture [22].

Results and discussion

Fracture behavior and fracture toughness

Specimens in the PST form Figure 5 shows load-displacement curves for PST crystals with five different notch orientations in air. For specimens of types I and II, load increases even after the load-displacement linearity is lost, reaches a maximum, and then decreases gradually with increasing displacement. This indicates that the lamellar structure provides significant resistance to propagation of a crack whose tip intersects the lamellar boundaries, as has been observed in the polycrystalline lamellar γ -based two-phase alloys [7, 8, 23-25]. On the other hand, specimens of type III can bear only a very small load.

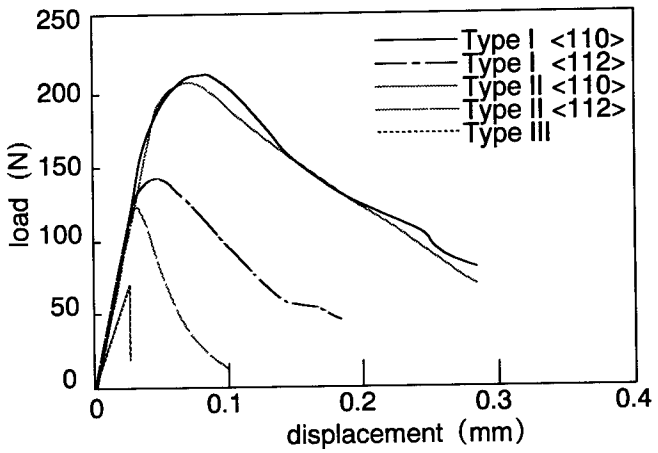


Figure 5: Load versus load-line displacement curves for three point bending of PST specimens of Ti-49.3Al alloy at a displacement rate of 0.02mm/min in air [15].

Figure 6 shows load-displacement curves for PST crystals tested in vacuum of two different levels. The results in air are shown together with those in vacuum for purposes of comparison. Except specimens of type III, the maximum load for each load-displacement curve in vacuum, in particular in a vacuum of 1.33×10^{-3} Pa is much higher than that for the corresponding load-displacement curve in air. This is the most significant difference between load-displacement curves in air and in vacuum. In addition, there are some other notable differences in the load-displacement behavior between in air and in vacuum. When tested in air, the general trend of the load-displacement behavior for specimens of types I and II depends on neither the type of notch nor the orientation of notch plane, although the maximum load depends on the orientation of notch plane. The maximum load is much higher for specimens with the {110}-type notch plane than those with the {112}-type notch plane. When tested in vacuum, the trend of load-displacement behavior depends on the type of notch, but it does not depend on the orientation of notch plane. The trend of load-displacement curves for specimens of type II is the same as in air. However, load-displacement curves for specimens of type I in vacuum are quite different from those for specimens in air and for specimens of type II in vacuum. For type I, load decreases in a complicated manner after it reaches a maximum. This suggests that crack propagation for the crack arrester-type orientation is much harder in vacuum than in air.

J values corresponding to the maximum load of load-displacement curves in Figs. 5 and 6 are shown in Fig.7. For $J = J_{IC}$, the specimen size requirements given by

$$B, b \geqq 50\{J/(\sigma_y + \sigma_u)\}$$

should be satisfied, where σ_y and σ_u are yield stress and tensile strength, respectively. The yield stress, fracture stress and tensile elongation for unnotched PST crystals tested along <110> parallel to the lamellar boundaries are plotted as a function of test environment and strain rate in Fig.8 [26]. The figure shows that the yield stress and the tensile strength are higher than 250 and 350 MPa, respectively when tested in air or in vacuum. Thus, J values obtained in the present investigation should reasonably approximate J_{IC} values of PST crystals. K_{IC} values corresponding to measured J_{IC} values can be calculated using the J_{IC}-K_{IC} relationship, $J_{IC} = K_{IC}^2(1-\nu^2)/E$ [22], E = 176 GPa and ν = 0.26[27-29]. K_{IC} values corresponding to the highest J_{IC} obtained for type I-<110> in a vacuum of 1.33×10^{-3} Pa and the lowest one for type II-<112> in air are 58.5 and 8.7 MPa$\sqrt{m}$, respectively. The K_{IC} values for specimens of type III ranges from 3.0 to 4.0 MPa$\sqrt{m}$ both in air and in vacuum and they are in good agreement with those obtained using CT-specimens of binary PST crystals with the same orientation and about the same composition [30].

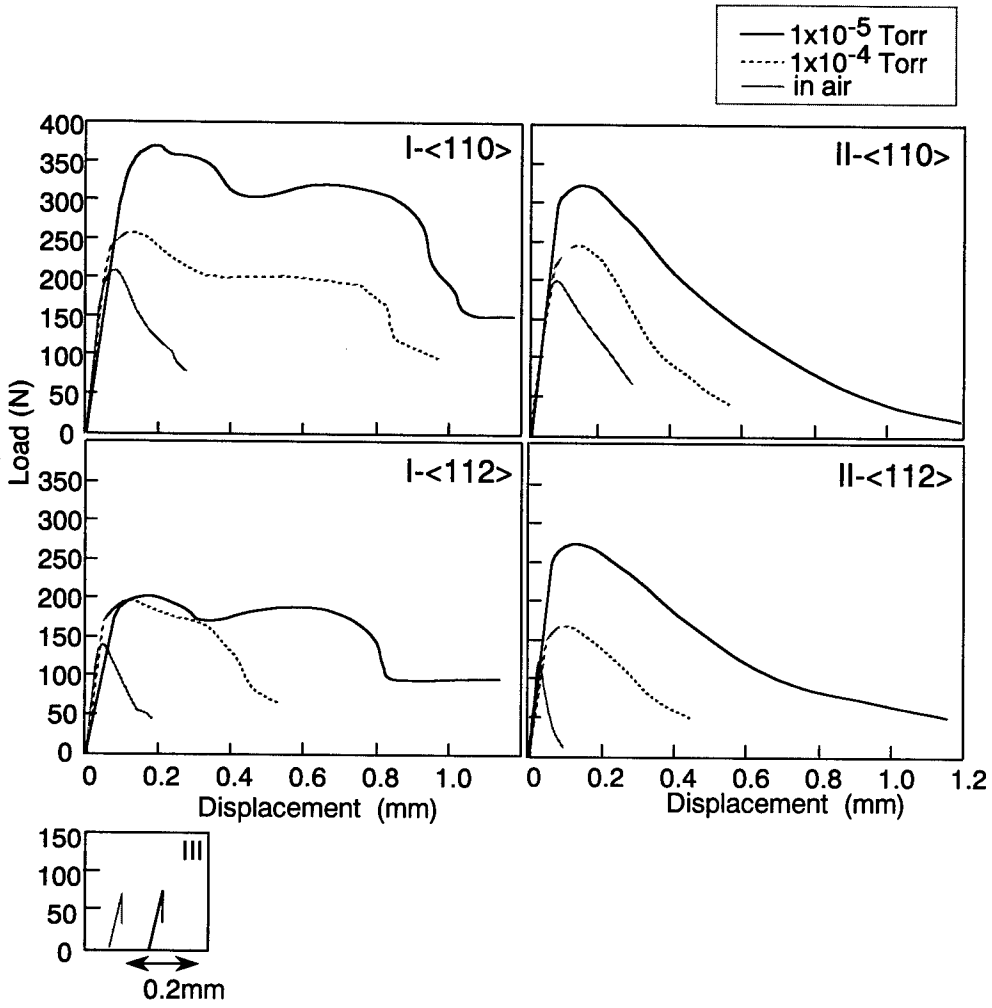


Figure 6: Load versus load-line displacement curves for three point bending of PST specimens of Ti-49.3Al alloy at a displacement rate of 0.02mm/min in vacuum and in air.

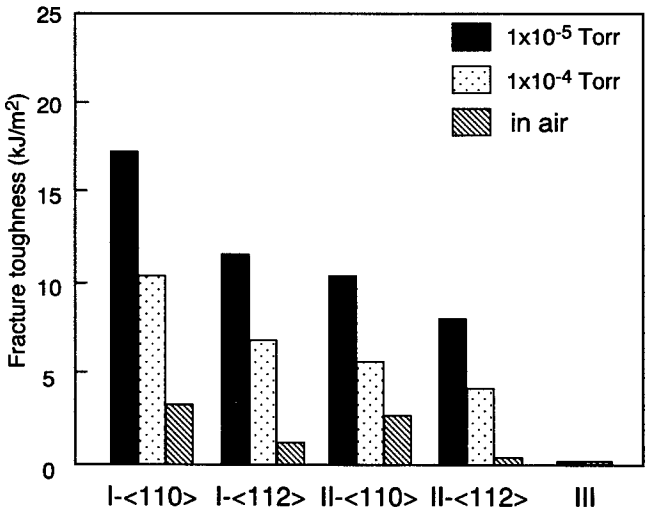


Figure 7: Fracture toughness (J values) of PST crystals of Ti-49.3Al alloy in air and in vacuum.

Directionally solidified ingots Examinations of tensile and fracture properties of a directionally solidified ingot of Ti-43Al-3Si (at%) alloy were performed in parallel. This alloy was chosen because the lamellar orientation could be controlled by using a seed crystal [31, 32]. Tensile specimens were cut from a directionally solidified ingot with the lamellar microstructure at different orientations relative to the tensile axis. Each tensile specimen contained approximately five columnar grains all with the same orientation of the lamellar microstructure. Similarly to binary PST crystals, tensile test results greatly varied depending upon the loading orientation. However, the best combination of strength and ductility was found for a loading orientation parallel to the lamellar boundaries. The very large Ti_5Si_3 particles found in this alloy are obviously detrimental to the ductility. However, the smaller silicide particles probably from an eutectoid reaction may be beneficial to the fracture toughness. The fracture surface shown in Fig.9 was taken from a specimen tested in the brittle orientation with the lamellar orientation perpendicular to the loading axis. Evidence of crack bridging and fiber-pull out by the small rod-shaped eutectoid silicide particles are visible as indicated by the arrows in Fig. 9.

Bend specimens were cut from a directionally solidified Ti-43Al-3Si ingot and from a PST crystal of Ti-48Al alloy for comparison. The notch was oriented either parallel or perpendicular to the lamellar boundaries. For the PST-crystal, the notch was oriented almost parallel to the lamellar boundaries. These test results are shown in Fig.10. For the brittle orientation with the notch parallel to the lamellar boundaries, the silicon containing alloy was considerably tougher than the binary alloy with a

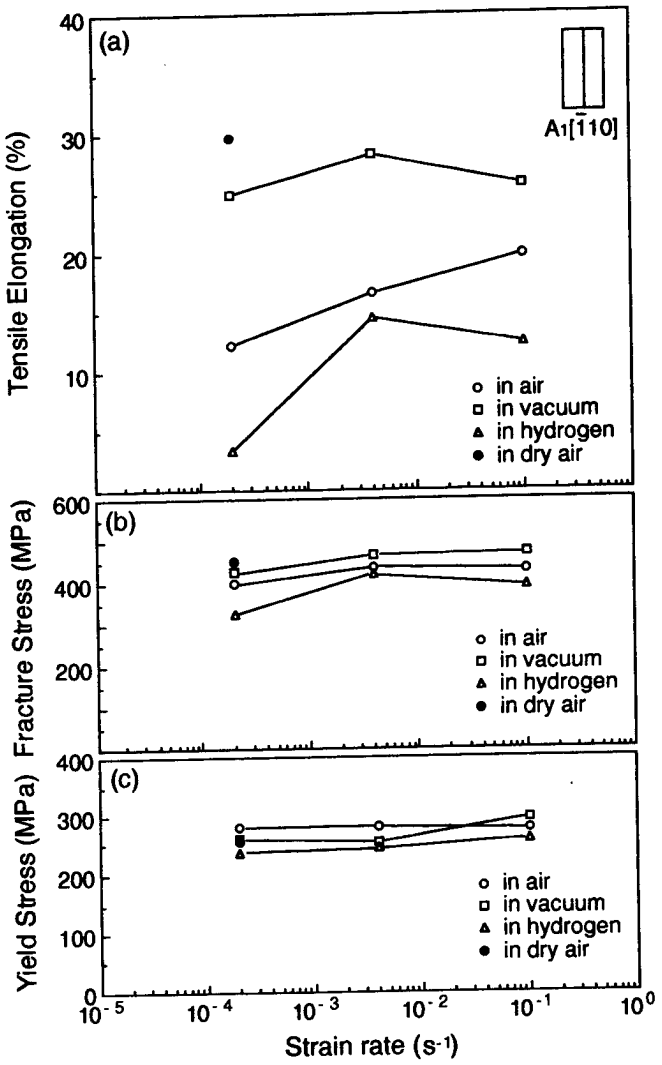


Figure 8: Test environment and strain rate dependence of (a) tensile elongation, (b) fracture stress and (c) yield stress of PST crystals of Ti-49.3Al alloy tested along <110> parallel to the lamellar boudaries [26].

value of Kq=8.9 MPa$\sqrt{m}$ compared to about 4 MPa$\sqrt{m}$ for the PST-crystal. The fracture toughness values for the PST crystals are in good agreement with the K_{IC} value for type III calculated from Fig.7. For this brittle orientation, fracture occurs by delamination parallel to the lamellar boundaries. However, considering that the fracture surface of the Ti-43Al-3Si alloy specimen is rough in comparison to fracture surfaces of binary PST crystals [31], the small silicide particles visible on the fracture surface of the Ti-43Al-3Si alloy specimen may play a positive role in toughening the microstructure. The small silicide particles may direct the propagating crack away from the plane parallel to the lamellar boundaries increasing the energy needed for fracture. The lamellar grain size for this alloy was measured at 400 μm; however, the difference between the fracture surfaces of PST crystals and the TiAl-Si alloy for the brittle orientation is on a much finer scale. Thus, the boundary between neighboring lamellar grains in the directionally solidified Ti-43Al-3Si alloy may not play a major role in the fracture process for the brittle orientation.

The fracture toughness value of Ti-43Al-3Si alloy for the notch orientation perpendicular to the lamellar boundaries is comparable to that for binary PST crystals with the I-<112> type notch in air. Currently, we are working to clarify the similarities and differences in the fracture behavior and fracture toughness between PST crystals and directionally solidified ingots for the crack arrester and crack divider orientations.

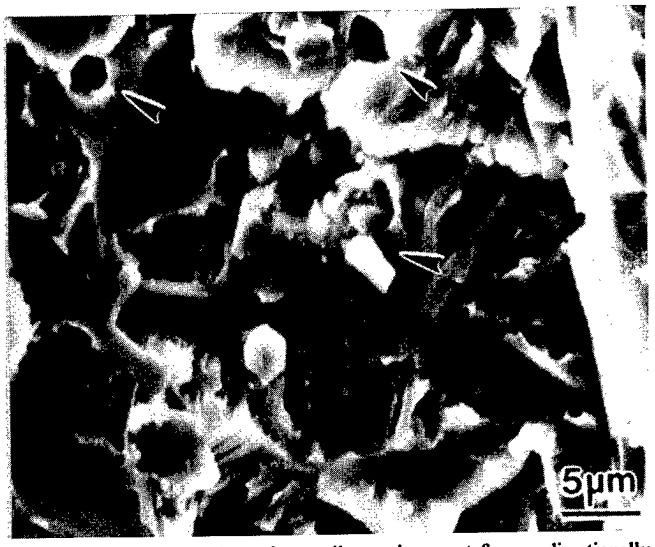


Figure 9: Fracture surface of a tensile specimen cut from a directionally solidified Ti-43Al-3Si alloy tested in the brittle orientation with the lamellar boundaries perpendicular to loading axis. Arrows indicate regions of crack-bridging/fiber pull-out [31].

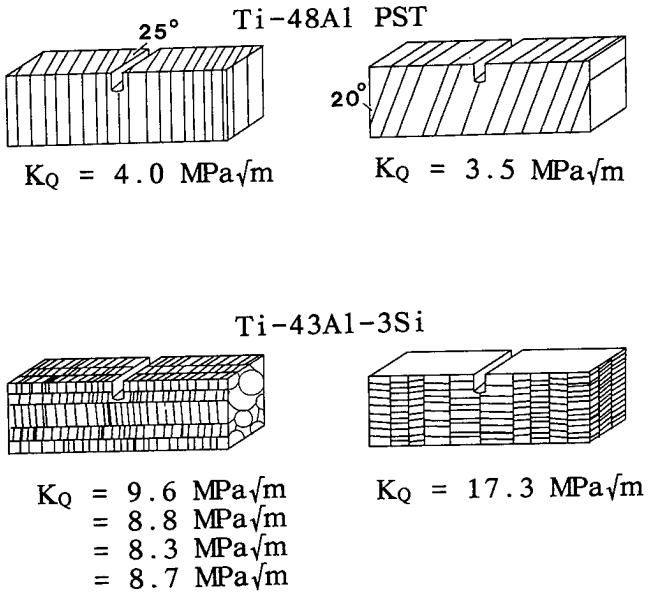


Figure 10: Bend test results from a PST crystal of Ti-48Al alloy and from a directionally solidified Ti-43Al-3Si ingot [31].

Fracture surfaces

Figure 11 shows fracture surfaces of specimens with five different notch orientations tested in a vacuum of 1.33 x 10^{-3} Pa. They were observed in a SEM at low magnification. In each specimen, the crack propagated from right to left. Fracture surfaces for specimens of types I and II consist of the fatigue-precracked region and broken ligament. No stretch zone is observed. The fracture surface of type III specimen consists only of the broken ligament since it was not fatigue-precracked. The macroscopic features of fracture surfaces shown in Fig.11 are quite similar to those of fracture surfaces of specimens tested in air [15]. However, when the surfaces of specimens of types I and II fractured in vacuum are examined at higher magnification, they are found to be significantly different from those of specimens fractured in air with respect to both the frequency of delamination parallel to the lamellar boundaries and the fracture habit planes.

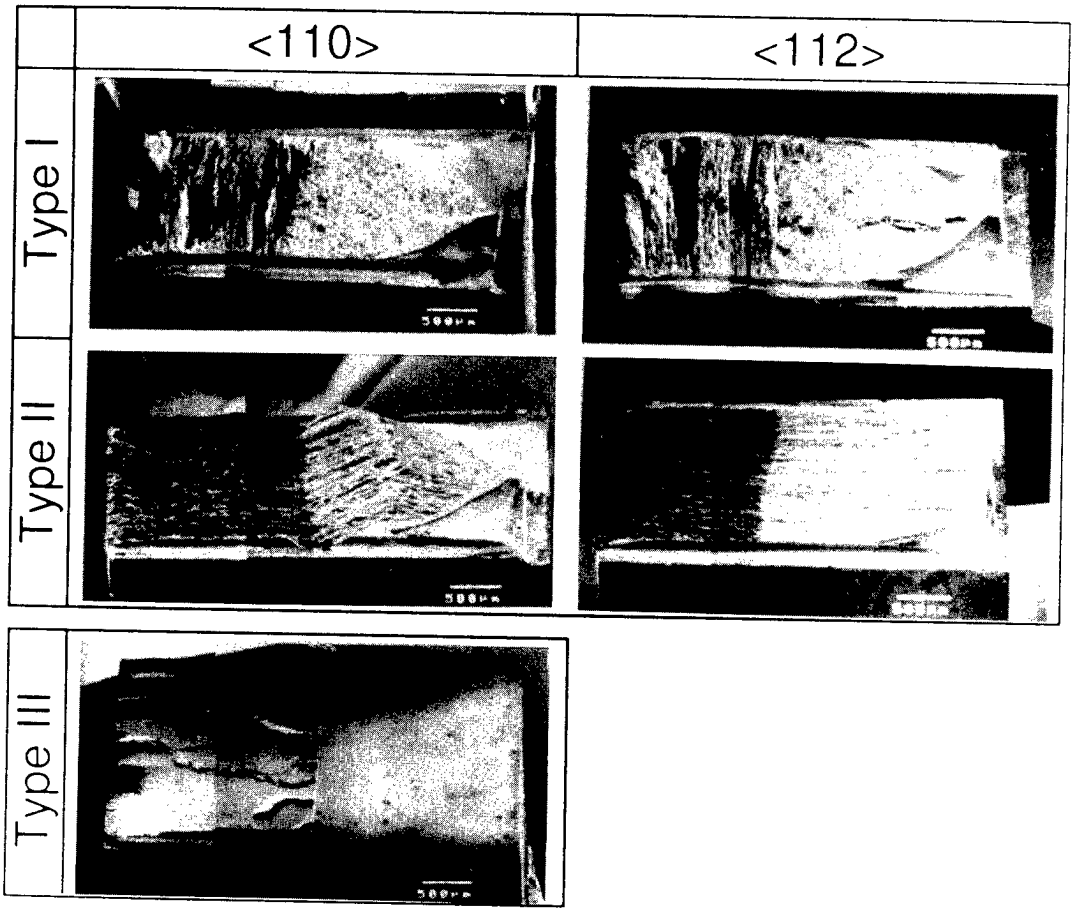


Figure 11: Fracture surfaces of PST specimens of Ti-49.3Al alloy tested at a displacement rate of 0.02mm/min in a vacuum of 1.33 x 10^{-3} Pa.

Figure 12 shows surfaces of broken ligament of specimens of types I and II tested (a) in air (b) in a vacuum of 1.33 x 10^{-2} Pa and (c) in a vacuum of 1.33 x 10^{-3} Pa at a higher magnification than Fig.11. In each specimen, the crack propagates from top to bottom. Although delamination with a narrow opening can not be observed at this magnification, the frequency of delamination is seen to increase in order of (a), (b) and (c).

In our previous paper, we examined microstructures of fracture surfaces of specimens of types I and II tested in air on a much finer scale[15]. The following is a summary of the results.

(1)The fundamental fracture process of γ lamellae in specimens of types I and II is cleavage-like failure on {111} habit planes intersecting the lamellar boundaries as has been reported in polycrystalline two-phase TiAl alloys[33-35].

(2)None of the possible fracture habit planes in specimens of types I and II are parallel to their notch plane, and thus their fracture surfaces have to be composed of a combination of different {111} planes in order for the average fracture surface to be parallel to the notch plane.

(3)Since two neighboring γ lamellae in PST crystals are very often twin-related, as has been confirmed by TEM examinations of the lamellar structure of PST crystals [12], fracture habit planes in two neighboring γ lamellae are often symmetrical with respect to the lamellar boundary between the two lamellae. The average fracture plane of such a twin-related pair of γ lamellae is parallel to {112}. Thus, fracture surfaces of specimens with the {112}-type notch plane are basically composed of such symmetric pairs of habit planes that often run throughout the ligament with some scattered facets.

(4)In the case of specimens with the {110}-type notch plane, their fracture surfaces consist of patches of {112}planes slant by about 30° with respect to the notch plane. If the crack tip in specimens with the {110}-type notch plane propagates along a set of zigzag {112} planes, the average plane of crack propagation can be {110}. Such {112} patches show the same microstructural characteristics as fracture surfaces of specimens with the {112}-type notch plane.

(5)Thus, specimens with the {110}-type notch plane exhibit much rougher surfaces than those with the {112}-type notch plane.

(6)In Ni-base superalloys, fracture often occurs along {111} planar slip bands under cyclic loading conditions. Once a crack with a coplanar slip band is initiated, it becomes difficult to activate secondary slip with a shear displacement inclined to the crack plane and thus localized, coplanar slip prevails [36]. The difficulty of activating non-coplanar secondary slip results in large normal stresses near the crack tip, and thus leads to easy crack propagation along coplanar slip bands and a fracture surface with a cleavage-like appearance [36]. The fracture morphology observed in PST crystals notched and fractured in bending in air may partly be interpreted in terms of the model of fracture along planar slip bands [15, 36].

In contrast to the fracture surface morphology for specimens tested in air, failure in vacuum does not occur on {111} habit planes, although failure still occurs in a brittle manner. Figure 13 shows a comparison of fracture surfaces between specimens of type II-<110> fractured in air and in a vacuum of 1.33 x 10^{-3} Pa. Two obvious differences exist between Fig.13(a) and (b); firstly, {111} fracture habit planes observed in air are no longer observed in vacuum; and secondly, delamination parallel to the lamellar boundaries occur much more frequently in vacuum than in air. This is in good agreement with observations presented in Fig.12. The implications of these two differences in the fracture surface morphology between in air and in vacuum will be discussed in the next section.

Delamination parallel to the lamellar boundaries

Recent observations and Auger analyses of fracture surfaces of PST crystals fractured in air, in hydrogen gas and in ultra-high vacuum have revealed that the mode of fracture of PST crystals of type III is always cleavage

through the α_2 phase [38, 39]. We drew the same conclusion from our recent fracture surface observations. Figure 14(a) and (b) show the fracture

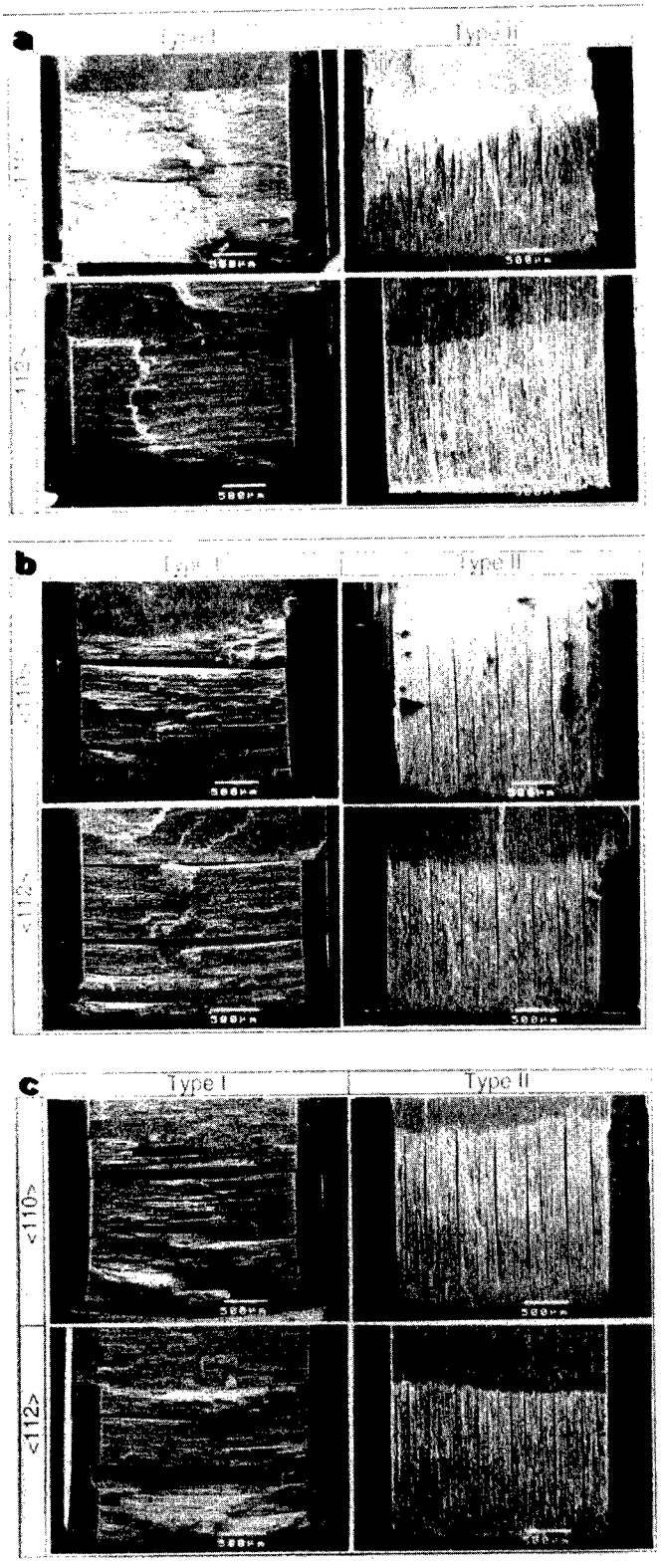


Figure 12: Fracture surfaces of PST specimens of Ti-49.3Al alloy of types I and II tested at a displacement rate of 0.02mm/min (a) in air, (b) in a vacuum of 1.33 x 10^{-2} Pa and (c) in a vacuum of 1.33 x 10^{-3} Pa.

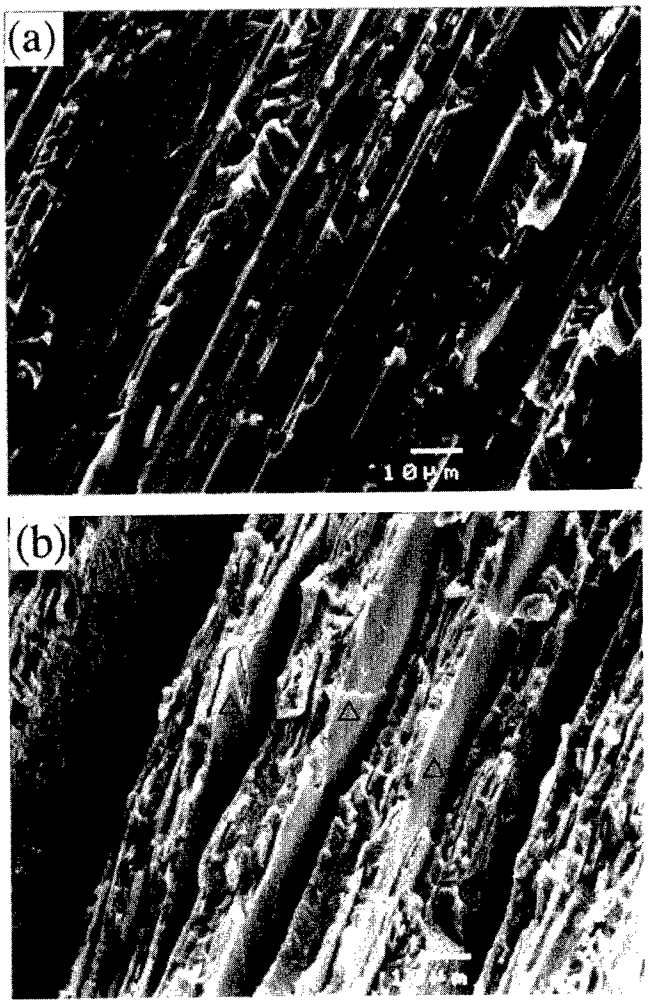


Figure 13: Fracture surfaces of PST specimens of Ti-49.3Al alloy of type II-<110> tested at a displacement rate of 0.02 mm/min (a) in air and (b) in a vacuum of 1.33 x 10^{-3} Pa.

surface of a PST specimen of type III fractured in a vacuum of 1.33 x 10^{-3} Pa. A wavy pattern observed on the fracture surface is characteristic of cleavage through the α_2 phase (Fig.14 (b)). Such a wavy pattern is often observed on surfaces of cracks created by delamination in specimens of types I and II, as indicated by circles in Fig.13(b). In addition, delamination cracks with smooth surfaces indicated by triangles are observed (Fig.13(b)). Cracks with such smooth surfaces are believed to be formed by delamination along γ / γ lamellar interfaces. Thus, delamination occurs both along lamellar boundaries and within α_2 lamellae when the main crack propagates perpendicularly to the lamellar boundaries. However, considering that all of the fracture surfaces exposed by bend testing of PST crystals of type III is α_2 [39], cleavage of the α_2 phase is found to be much easier than delamination along γ / γ lamellar interfaces. Dispersion of small particles such as silicides may be effective in increasing cleaveage resistance within the α_2 phase (Figs.9 and 10).

Toughening mechanisms in air

Type II-<112> Of the five notch orientations, type III gives the lowest fracture toughness which is determined by cleavage through the α_2 phase. Fracture toughness for the remaining four notch types of the crack arrester and crack divider orientations is associated with fracture of γ lamellae. Of these four notch orientations, type II- <112> gives the lowest fracture toughness. Failure for this notch orientation occurs by cleavage-like failure on {111} habit planes producing the average {112}-type fracture surface parallel to the notch plane. In addition, delamination parallel to the lamellar boundaries occurs because of triaxial stresses in front of the crack tip (Fig.12(a)). Recently we succeeded in observing in-situ delamination-type

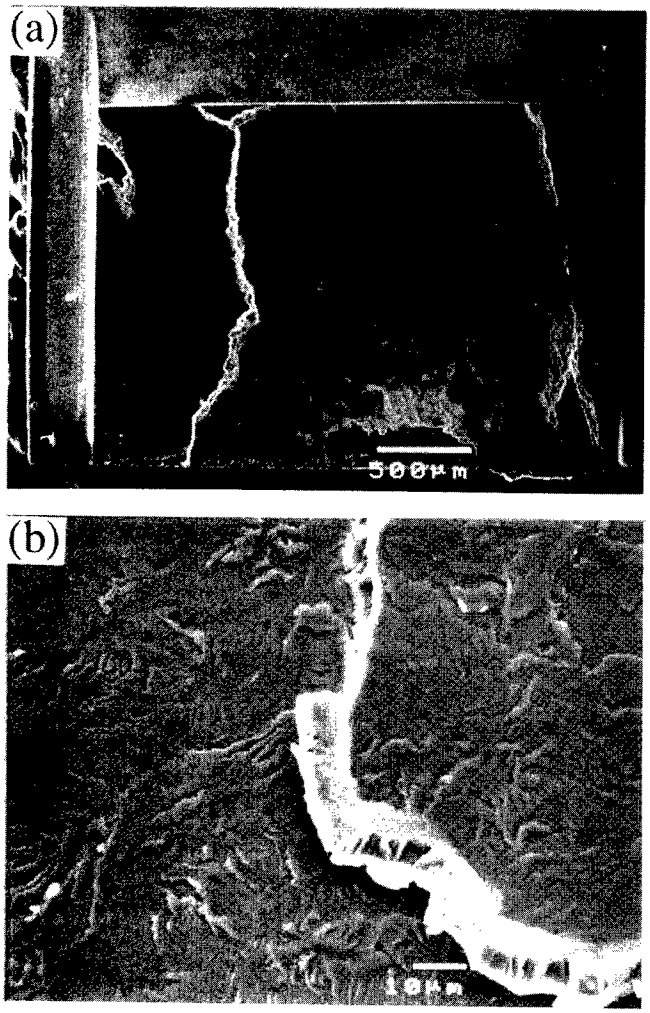


Figure 14: Fracture surface of PST specimens of Ti-49.3Al alloy of type III tested at a displacement rate of 0.02 mm/min in a vacuum of 1.33 x 10^{-3} Pa at (a) low and (b) high magnification.

separation in the close vicinity of the crack tip in a specimen loaded in SEM. Such delamination cracks formed in the specimens of type II does not cause the tip of main crack to branch. However, plane-stress conditions prevail at the crack tip because the delamination tends to reduce the ligament to a bundle of thin sheets. The plane-stress fracture toughness is higher than the plane-strain fracture toughness, and thereby delamination-type separation results in increasing the fracture toughness of the specimen. Such a toughening mechanism is called thin-sheet toughening and has been observed in aluminum alloys with highly anisotropic microstructures with a large volume fraction of dispersoids[40-42] or consisting of large pancake-shaped grains[43]. Thus, the fracture toughness for type II-<112>, maked by A in Fig.15, may be interpreted in terms of a sum of the basic fracture toughness associated with creating the average {112}-type fracture surface composed of {111} habit planes and a toughening contribution due to thin-sheet toughening. Fracture toughness for other three notch types of the crack arrester and crack divider orientations is higher than that for type II-<112>. This indicates that additional toughening mechanisms are operative for these notch orientations.

Type I-<112> Fracture surfaces of the types I-<112> and II-<112> are quite similar to each other and they are characterized by ridges composed by two $\{11\bar{1}\}$ planes and the delamination-type separations perpendicular to the fracture surface. Thus, the difference in fracture toughness between the types I-<112> and II-<112>, marked by B in Fig.15, is related to the difference in the direction of crack propagation with respect to the lamellar boundary. The delamination-type separation for type I-<112> results in not only the thin-sheet toughening but also in branching the tip of the main

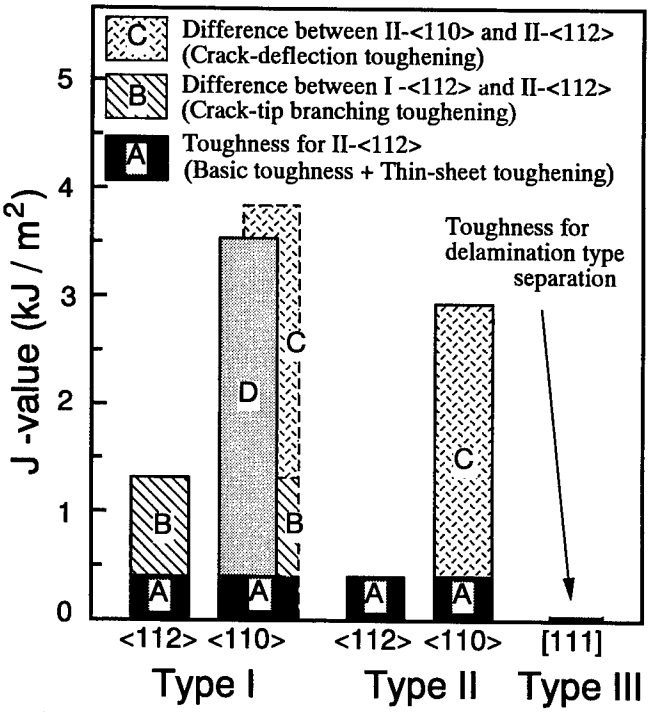


Figure 15: Toughening contributors to the toughness of PST crystals of Ti-49.3Al alloy with five different notch orientations. Bending tests were conducted at a displacement rate of 0.02 mm/min in air [15].

crack. Thus, the branching of the tip of main crack is a toughening contributor for the type I-<112> which causes the difference in toughness between types I-<112> and II-<112>.

Type II-<110> For types II-<110> and II-<112>, crack propagates in the same crack-divider manner. Thus the delamination-type separation equally contributes to the toughness of the two notch types. The difference in fracture toughness between these notch types, which is marked by C in Fig.15, must arise from the difference in the orientation of the notch plane. For type II-<110>, crack propagation occurs along a set of zigzag {112} planes. Such crack deflection provides an increase in fracture toughness [44]. We thus think that the difference in fracture toughness between these two notch types is mainly due to crack-deflection toughening. However, the difference in fracture toughness is considerable (Fig.15), and thus it is likely that there are some other toughening mechanisms including crack deflection, which are simultaneously responsible for the difference in toughness between types II-<110> and II-<112>.

Type I-<110> Type I-<110> is the toughest of all the notch types investigated. The difference in toughness between types I-<110> and II-<112> marked by D in Fig.15 is nearly equal to the sum of the difference between the types I-<112> and II-<112>, represented by B, and that between the types II-<110> and II-<112>, represented by C. This is reasonable since, in type I-<110>, the crack propagates perpendicular to the lamellar boundary on a {110} plane, and hence crack-tip branching and crack deflection mechanisms simultaneously contribute to the toughness of type I-<110>.

Toughening mechanisms in vacuum

Fracture toughness values of PST crystals tested in vacuum with the crack arrester and crack divider orientations are much higher than those tested in air. Thus, the fracture toughness of PST crystals is found to be sensitive to test environment, as is the tensile ductility (fig.8). The largest difference in fracture toughness between specimens tested in vacuum and in air is found for type II-<112>. Toughness values for type II-<112> in vacuum of 1.33 x 10^{-2} Pa and 1.33 x 10^{-3} Pa are ten and twenty times as large as the corresponding fracture toughness in air (Fig.7). When tested in vacuum, fracture surfaces of γ lamellae are no longer composed of {111} fracture habit planes and are rough in comparison to those in air (Fig.13). Such changes in fracture surface morphology are believed to give rise to an increase in fracture toughness in vacuum. Disappearance of fracture habit

planes in vacuum occurs not only in bending tests of notched specimens but also uniaxial tensile tests of unnotched specimens [26]. When the fracture stress of the γ phase increases in vacuum, the magnitude of triaxial stresses in front of the crack tip increases and thus the propensity of delamination along γ / γ interfaces is enhanced (Fig.13). This also results in increasing fracture toughness in vacuum. Such toughening mechanisms in vacuum are expected to be operative for all four notch types of the crack arrester and crack divider orientations. Thus, there must be some additional toughening contributors for types II-<110>, I-<112> and I-<110> giving higher fracture toughness values than II-<112>.

If the interpretation of the notch type dependence of fracture toughness in air holds good in vacuum, J(II-<112>) $\fallingdotseq$ J(II-<110>) and J(I-<110>) $\fallingdotseq$ J(I-<112>) since no significant difference in fracture surface morphology exists between specimens notched along {110} and {112}, where J is the fracture toughness for the corresponding notch orientation given in each parenthesis. Also J(I-<110>) - J(II-<110>) $\fallingdotseq$ J(I-<112>) - J(I-<112>) if the crack-tip branching toughening mechanism contributes equally to the toughness of specimens notched along {110} and {112}, which is the case when tested in air. However, these are obviously not the case in vacuum.

Also in vacuum, the crack arrester orientations give higher values of fracture toughness than the crack divider orientations and thus crack-tip branching due to delamination parallel to the lamellar boundaries is an important toughening contributor for the crack arrester orientations. However, J(I-<110>) - J(II-<110>) > J(I-<112>) - J(II-<112>). This suggests that the crack-tip branching toughening works more effectively for specimens notched along {110} than it does for those notched along {112}. In addition, J(I-<110>) > J(I-<112>), J(II-<110>) > J(II-<112>) and J(I-<110>) - J(I-<112>) > J(II-<110>) - J(II-<112>). This indicates that an additional toughening mechanism characteristic of specimens notched along {110} is still operative in vacuum. However, the mechanism does not seem to be directly associated with the appearance of fracture surface and the mechanism works more effectively for the crack arrester type than the crack divider type. However, a reasonable description of fracture toughness of PST crystals and its dependence on the notch type and notch orientation in vacuum has yet to be given.

Effects of displacement rate and alloy composition on the fracture toughness of PST crystals

Effects of displacement rate. When tested at a low displacement rate of 0.02 mm/min, fracture toughness of PST crystals in air is much lower than that in vacuum. However, when tested at a much higher displacement rate of 10mm/min, such environmental loss in fracture toughness drastically decreases and the fracture toughness level in air becomes as high as that at 0.02 mm/min in a vacuum of 1.33×10^{-3} Pa. In vacuum, fracture toughness does not show any strong dependence on strain rate. Measurements of fracture toughness of PST crystals were conducted only in air and vacuum. However, tension tests of unnotched PST crystals were made in four different atmospheres (air, dry air, hydrogen gas and vacuum) at strain rates in the range of 2.0×10^{-4} to $1.0 \times 10^{-1} s^{-1}$. The results for tensile tests along <110> parallel to the lamellar boundaries (Fig.8) can be summarized as follows: (1) the tensile elongation increases in order of hydrogen gas, air, vacuum and dry air and (2) the tensile elongation does not depend on strain rate in vacuum, but it increases with increasing strain rate in air and hydrogen gas. These results strongly suggests that the tensile elongation of PST crystals is sensitive to test environment and the environmental sensitivity can be interpreted in terms of embrittlement due to moisture-induced hydrogen [26, 45]. Thus, the difference in fracture toughness between in air and in vacuum may also be interpreted in terms of hydrogen embrittlement.

Effects of alloy composition We observed no significant effects of Cr addition on the fracture toughness of PST crystals. The addition of Cr has been found to be effective in reducing environmental embrittlement of PST crystals in uniaxial tension, and thereby enhancing tensile ductility [2]. However, such an alloying effect is less prominent for loading parallel to the lamellar boundaries than loading in a direction inclined at an angle in the range of 30° - 60° to the lamellar boundaries where PST crystals deform by shear in γ lamellae parallel to the lamellar boundaries. In the case of loading perpendicular to the lamellar boundaries, alloying additions exhibit no positive effects on the ductility of PST crystals. Stress and strain conditions in specimens loaded in bending in our fracture study are rather close to those for uniaxial loading parallel or perpendicular to the lamellar boundaries. This would be a reason for the result on the effect of Cr addition on the fracture toughness of PST crystals. In addition, the amount of Cr added (0.4at%) may not be high enough to affect the fracture behavior and fracture toughness of PST crystals.

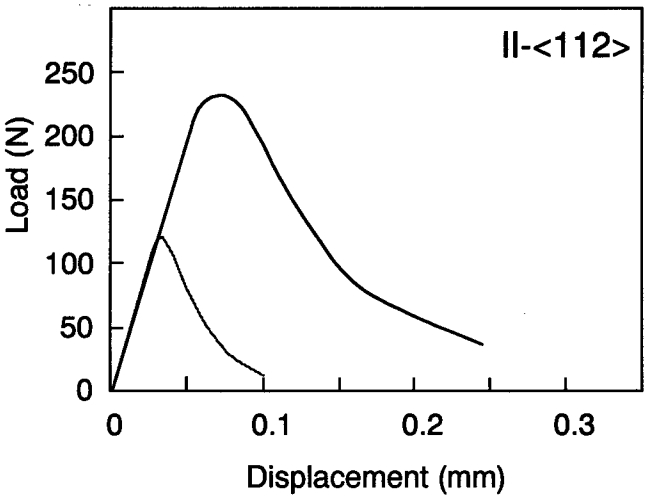


Figure 16: Load displacement curves for PST specimens of Ti-47.0Al (thick line) and Ti-49.3Al (thin line) alloys of type II-<112> tested at a displacement rate of 0.02 mm/min in air.

In sharp contrast to the addition of Cr, decreasing Al content from 49.3 to 47.0 at% gives rise to significant improvements in the fracture properties of PST crystals except for type III where the fracture toughness is always in the range of 3.0 - 4.0 MPa$\sqrt{m}$ regardless of test environment, displacement rate and alloy composition. Figure 16 shows a load-displacement curve for a Ti-47.0Al alloy specimen of type II-<112> tested at a displacement rate of 0.02 mm/min in air. In comparison to the corresponding load-displacement curve of Ti-49.3 alloy, the fracture toughness of type II-<112> of the Ti-47.0Al alloy is seen to be about ten times as large as that of the Ti-49.3Al alloy. Considering that type II-<112> gives the lowest fracture toughness of the crack arrester and crack divider types, other crack arrester and crack divider types of Ti-47.0Al alloy are expected to show even higher values of fracture toughness.

Figure 17 shows a result of our preliminary work to measure fracture toughness of PST crystals of a Ti-47.0Al alloy with crack arrester orientations in air and in vacuum. Both load and displacement values corresponding to the maximum in each curve are large, and thus the corresponding J value can be as high as 40 KJ/m^2. However, such a large J value may not be regarded as J_{IC} since the specimen size requirements for J = J_{IC} are not satisfied. Much larger specimens are needed to measure J_{IC} of PST crystals of Ti-47.0Al alloy with crack arrester orientations. Reasons for incresing toughness of PST crystals by decreasing Al content from 49.3 to 47.0 at% has yet to be clarified. However, we believe that the difference in the thickness and distribution of α_2 lamellae between the two alloys is closely associated with the difference in fracture toughness. The volume fraction of the α_2 phase in Ti-47.0Al alloy is about four times as high as that in Ti-49.3Al alloy. In addition, the thickness and spacing of α_2 lamellae is rather smaller in the former alloy than in the latter alloy. Thus, the propensity of delamination along α_2 lamellae in Ti-47.0Al alloy is expected to be much higher than that in Ti-49.3Al alloy. This may be a reason for the higher fracture toughness of PST crystals of Ti-47.0Al alloy. Figure 18 shows an example of fatigue-precrack stopped by a delamination type separation perpendicular to the precrack. During the fatigue-precracking of PST crystals of Ti-47.0Al alloy with crack arrester orientations, such crack deflection often occurred and hindered the further propagation of the precrack. Fracture toughness of PST crystals of Ti-49.3Al and Ti-47.0Al alloys measured at different displacement rates in air and in vacuum will be presented and discussed in detail elsewhere.

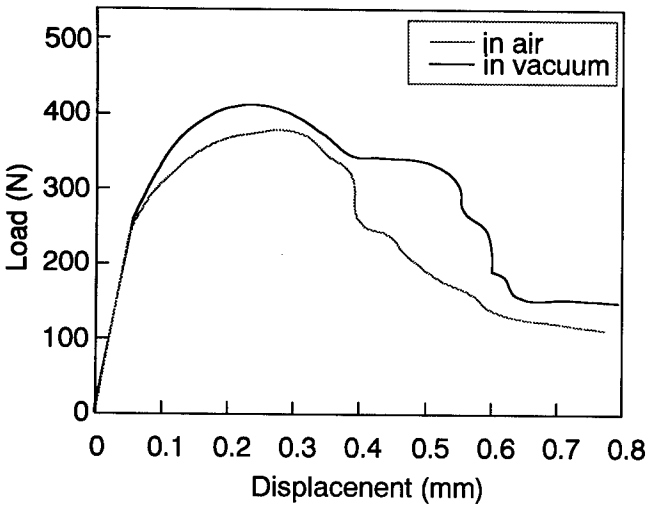


Figure 17: Load displacement curves for a PST specimen of Ti-47.0Al alloy of type I-<110> tested at a displacement rate of 0.02 mm/min in air and in vacuum.

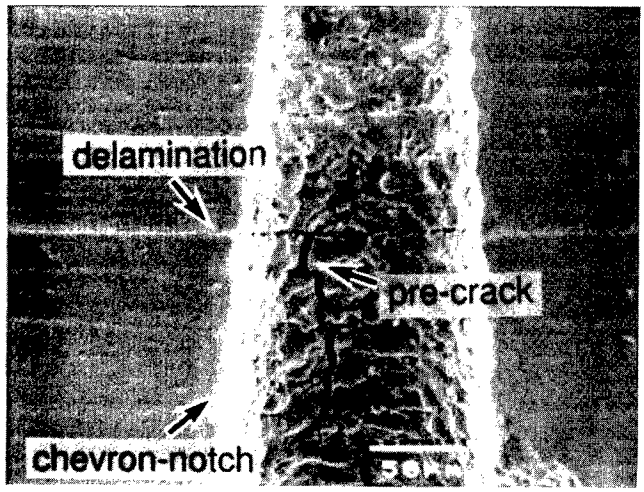


Figure 18: Crack deflection due to a delamination-type separation perpendicular to the crack. This was observed during fatigue-precracking of a PST specimen of Ti-47Al alloy of type I-<110>.

Conclusions

Fracture behavior and toughness of PST crystals of Ti-49.3Al, Ti-47.0Al and Ti-48.9Al-0.4Cr (at%) alloys and directionally solidified ingots of Ti-48Al and Ti-43Al-3Si (at%) alloys were investigated by three-point bend tests of notched specimens. Specimens of PST crystals were Chevron-notched, fatigue-precracked and then side-grooved. Bend tests were conducted in air and in vacuum at load-line displacement rates of 0.02 and 20 mm/min at room temperature. The results obtained are summarized as follows:

1. Fracture in PST specimens of type III (notched parallel to the lamellar boundaries) occurs by cleavage through the α_2 phase. Fracture toughness is in the range of 3.0 - 4.0 MPa$\sqrt{m}$, regardless of test environment, displacement rate and alloy composition.
2. When PST specimens of types I (crack arrester) and II (crack divider) are tested in air, {111} fracture habit planes, which intersect the lamellar boundaries, are observed on their fracture surfaces. When specimens are notched along the same crystallographic plane in γ lamellae, namely along {112} or {110}, fracture toughness for type I is higher than that for type II since the former orientation is conducive to toughness arising from the branching of the main crack tip due to a delamination-type separation parallel to the lamellar boundaries. For the same type of notch, fracture toughness of specimens notched along {110} is higher than that of specimens notched along {112} since the former group of specimens are more conducive to a crack deflection toughening mechanism. Thus, the five notch orientations give increasing fracture toughness values in the sequence of III, II-<112>, I-<112>, II-<110>, I-<110> when tested in air.
3. Fracture toughness of PST specimens of types I and II are sensitive to test environment and load-line displacement rate. {111}fracture habit planes are not observed on fracture surfaces of specimens fractured in vacuum but are observed for those fractured in air.
4. Fracture toughness of PST specimens tested at a displacement rate of 0.02 mm/min in a vacuum of 1.33×10^{-3} Pa is 4 - 20 times as large as that in air at the same displacement rate depending on notch orientation. Fracture toughness of PST specimens of types I and II tested at a displacement rate of 10 mm/min in air is comparable to that obtained at a displacement rate of 0.02 mm/min in a vacuum of 1.33×10^{-3} Pa.
5. In vacuum, the five notch orientations give increasing fracture toughness values in the sequence of III, II-<112>, II-<110>, I-<112>, I-<110>. The crack-tip branching toughening due to delamination parallel to the lamellar boundaries seems to work more effectively in vacuum than in air.
6. No significant difference in fracture behavior and fracture toughness between PST crystals of Ti-49.3Al and Ti-48.9Al-0.4Cr alloys was observed. Decreasing Al content from 49.3 to 47.0 at% gives rise to increasing fracture toughness of PST crystals. Difference in the thickness and distribution of α_2 lamellae between the two alloys is believed to be closely associated with the increase in fracture toughness in Ti-47.0Al alloy.
7. For type III, the silicon containing Ti-43Al-3Si alloy was considerably tougher than the binary alloy. Small silicide particles may direct the propagating crack away from the plane parallel to the lamellar boundaries increasing the energy needed for fracture.

Acknowledgments

This work was supported by "Research for the Future" Program (JSPS-RFTF 96R12301), The Japan Society for the Promotion of Science (JSPS). SY and KK would like to thank JSPS for their research fellowships.

References

1. Y-W. Kim and D. M. Dimiduk, JOM, 43(8)(1991), 40-47.
2. M. Yamaguchi and H. Inui, Structural Intermetallics, edited by R. Darolia, J. J. Lewandowski, C. T. Liu, P. L. Martin, D. B. Miracle and M. V. Nathal (TMS, Warrendale, Pa, 1993), 127-142.
3. Y-W. Kim, JOM, 46(7)(1994), 30-39.
4. C. M. Austin and T. J. Kelly, Gamma Titanium Aluminides, edited by Y-W. Kim, R. Wagner and M. Yamaguchi (TMS, Warrendale, Pa, 1995), 21-32.
5. R. Wagner, F. Appel, B. Dogan, P. J. Ennis, U. Lorenz, J. Mullauer, H. P. Nicolai, W. Quadakkers, L. Singheiser, W. Smarsly, W. Vaidya and K. Wurzwallner, Gamma Titanium Aluminides, edited by Y-W. Kim, R. Wagner and M. Yamaguchi (TMS, Warrendale, Pa, 1995), 387-404
6. K. S. Chan, JOM, 44(5)(1992), 30-38.
7. K. S. Chan and Y-W. Kim, Metall. Trans., 23A (1992), 1663-1677.
8. K. S. Chan and Y-W. Kim, Acta metall. mater., 43 (1995),439-451.
9. K. S. Chan, Gamma Titanium Aluminides, edited by Y-W. Kim, R. Wagner and M. Yamaguchi (TMS, Warrendale, Pa, 1995), 835-847.
10. C. T. Liu, P. J. Maziasz, D. R. Clemens, J. H. Schneibel, V. K. Sikka, T. G. Nieh, J. Wright and L. R. Walker, Gamma Titanium Aluminides, edited by Y-W. Kim, R. Wagner and M. Yamaguchi (TMS, Warrendale, Pa, 1995), 679-688.
11. C. T. Liu, J. H. Schneibel, P. J. Maziasz, J. L. Wright and D. S. Easton, Intermetallics, 4(6)(1996), 429-440.
12. H. Inui, M. H. Oh, A. Nakamura and M. Yamaguchi, Phil. Mag. A, 66(4)(1992), 539-555.
13. H. Inui, M. H. Oh, A. Nakamura and M. Yamaguchi, Acta metall. Mater. 40(11)(1992), 3095-3104.
14. H. Inui, K. Kishida, M. Misaki, M. Kobayashi, Y. Shirai and M. Yamaguchi, Phil. Mag. A, 72(6)(1995), 1609-1631.
15. S. Yokoshima and M. Yamaguchi, Acta mater., 44(3)(1996), 873-883.

16. K. Kishida, D. R. Johnson, Y. Shimada, H. Inui and M. Yamaguchi, Gamma Titanium Aluminides, edited by Y-W. Kim, R. Wagner and M. Yamaguchi (TMS, Warrendale, Pa, 1995), 219-229.
17. M. J. Blackburn, Technology and Application of Titanium, edited by R. T. Yaffee and N. E. Promisel (Oxford: Pergamon, 1970), 633.
18. W. L. Server, R. A. Wullaert and R. O. Ritche, J. Eng. Mater. Tech., 102 (1980), 192.
19. Y. Mutoh, I. Sakamoto, K. Nomura and K. Aya, Trans., Jpn. Soc. Mech. Eng., Ser. 468A (1985), 2008.
20. Y. Mutoh, I. Sakamoto and S. Takeda, Jpn. Soc. Mech. Eng., Ser. 503A (1988), 1434.
21. R. Gnanamoorthy, Y. Mutoh, N. Masahashi and Y. Mizuhara, Metall. Trans., 26A, (1995), 305.
22. R. W. Hertzberg, Deformation and Fracture Mechanics of Engineering Materials (John Wiley & Sons, 1989), 314.
23. H. E. Deve, A. G. Evans and D. S. Shin, Acta metall. mater., 40 (1992), 1259.
24. N. J. Rogers and P. Bowen, Structural Intermetallics, edited by R. Darolia, J. J. Lewandowski, C. T. Liu, P. L. Martin, D. B. Miracle and M. V. Nathal (TMS, Warrendale, Pa, 1993), 231-240.
25. B. Dogan, D. Schoneich, K. H. Schwalbe and R. Wagner, Intermetallics, 4(1)(1996), 61-70.
26. M. H. Oh, H. Inui, M. Misaki and M. Yamaguchi, Acta metall. Mater., 41(7)(1993), 1939-1949.
27. H. A. Lipsitt, D. Shechtman and R. E. Schafrik, Met.Trans., 6A (1975), 1991.
28. R. E. Schafrik, Met.Trans. 8A (1977), 1003.
29. C. L. Fu and M. H. Yoo, Phil. Mag. Lett. 62 (1990), 159.
30. T. Nakano, T. Kawanaka, H. Y. Yasuda and Y. Umakosi, Proc.3rd Japan International SAMPE Symposium, edited by T. Kishi, N. Takeda and Y. Kagawa, (The Japan Chapter of SAMPE, Tokyo, 1993), 1334.
31. D. R. Johnson, H. Inui and M. Yamaguchi, Acta mater., 44(6)(1996), 2523-2535.
32. D. R. Johnson, Y. Masuda, H. Inui and M. Yamaguchi, Acta mater., in press.
33. B. Kad, B. F. Oliver and P. M. Hazzledine, Microstructure Science vol.18, edited by T. A. Place, J. D. Braun, W. E. White and G. E. Vander Voort, (.ASM International, Materials Park, OH,1991), 201.
34. F. Appel, U. Christoph and R. Wagner, Phil. Mag. A, 72(2)(1995), 341-360.
35. M. H. Yoo and C. L. Fu, Mater. Sci. Eng. A153(1992), 470.
36. D. A. Koss and K. S. Chan, Acta metall.mater. 28 (1980), 1245.
37. K. S. Chan, Acta metall.mater. 35 (1987), 981.
38. Y. Umakoshi, T. Nakano and T. Yamane, Mater. Sci. Eng. A, A152(1992) 81-88.
39. L. Heatherly Jr., E. P. George, C. T. Liu and M. Yamaguchi, Intermetallics, 5(4)(1997).
40. K. S. Chan, Metall.Trans., 20A (1989),155.
41. K. S. Chan, Metall.Trans., 20A (1989), 2337.
42. K. T. Venkateswara Rao, W. Yu and R. O. Ritchie, Metall. Trans. 19A (1988), 549.
43. K. T. Venkateswara Rao, G. R. Odette and R. O. Ritchie, Structural Intermetallics, edited by R. Darolia, J. J. Lewandowski, C. T. Liu, P. L. Maracle and M. V. Nathal (TMS, Warrendale, Pa, 1993), 829-835.
44. S. Suresh, Metall. Trans. 16A(1985), 249.
45. T. Nakano and Y. Umakoshi, Intermetallics, 2(3)(1994), 185-192.

DEFORMATION AND FRACTURE BEHAVIOR IN TiAl ALLOYS UNDER MONOTONIC AND CYCLIC LOADING CONDITIONS

Young-Won Kim* and Dennis M. Dimiduk
Wright Laboratory, Materials Directorate
Wright-Patterson AFB, OH 45433

* UES, Inc., Dayton, OH 45432

ABSTRACT

Deformation and fracture behavior of two-phase TiAl alloys was investigated under monotonic as well as cyclic tension loading conditions for duplex and lamellar microstructural forms. The Hall-Perch relationship with an abnormally high constant in fully-lamellar material is explained as a combined function of grain-size and deformation-anisotropy characteristic of the lamellar structure. The effects of microstructure on the behavior are compared and analyzed for deformation temperatures below and above the brittle-ductile transition (BDT). The crack initiation toughness and associated strains near the crack tip are used to explain the inverse relationship between ductility and toughness observed at RT. The effect of temperature on the transition of cleavage-type transgranular fracture to intergranular and/or interlamellar fracture is discussed, along with the boundary weakening which is enhanced with increasing strain rate. The competition between the effects of grain size, lamellar spacing and plastic zone size on tensile and toughness properties is discussed.

1. INTRODUCTION

Compositions of emerging gamma TiAl alloys range in general within Ti-(45-48)Al-3(Cr, Mn, V)-(2-4)Nb-(0-1)(W, Ta, Mo) [1-4]. Their constituent phases include gamma as the matrix phase, alpha-2 as the major second phase, and, occasionally, beta phase as third phase. For the last ten years, numerous investigations have shown that the mechanical properties of gamma titanium aluminides are known to strongly depend on microstructure [2, 4-6]. The variations of microstructure that can be controlled in these alloys are numerous, but they exist in four broad groupings; that is near-gamma, duplex (DP), nearly-lamellar (NL), and fully-lamellar (FL) microstructures 6]. DP and FL microstructures are two typical microstructures and have been subjected to the most investigation. A number of mechanical property measurements have been made on these microstructures [5-9], but the studies of fundamental understanding in deformation and fracture behavior have been concentrated mainly on single-phase or DP microstructures [10-12] and on PST crystals [13, 14]. Only for the last few years, has attention been drawn to the deformation and fracture behavior of two-phase alloys of engineering importance, particularly in FL conditions [15-24]. In general, FL microstructures consist of large lamellar grains resulting in poor tensile properties but improved fracture resistance, and duplex microstructures consist of fine grains which yield low toughness and high-temperature (HT) strength. Our understanding of the behavior of these microstructures at RT is qualitatively quite advanced, although detailed observations and quantitative analyses remain to be made. Systematic investigations of the elevated temperature deformation and fracture processes have just begun.

In this paper, our recent experimental data [25] on tensile, fracture toughness, and fatigue properties at various temperatures are analyzed to correlate and combine them with previous results [5, 15, 17, 18, 20-23] in an effort to understand the whole deformation and failure process. Explanations and semi-quantitative analyses are made on the dependence of tensile deformation and ductility on microstructural features, the inverse relationship between ductility and toughness, and the effect of microstructure on toughness. Fatigue deformation and failure will also be analyzed and compared with those under monotonic loading conditions.

2. EXPERIMENTAL

Ingots of three alloys, with nominal compositions (in at%) of Ti-47Al-1Cr-1V-2.5Nb (alloy G1) Ti-47Al-1.5Cr-0.5V-2.3Nb (alloy G8), and Ti46.5Al-2Cr-3Nb-0.2W (alloy K5), were prepared by skull melting and casting, followed by HIP'ing at 1260°C for 3 hrs under an argon pressure of 173 MPa. Alloy billets cut from the HIP'ed ingots were hot-worked by a two-step isothermal forging procedure at 1150°C. DTA analyses combined with metallographic observations were used to determine the alpha transus ($T\alpha$) for each alloy on forged material. Two types of microstructures, duplex and lamellar, were produced from each alloy material through specific annealing treatments, followed by controlled cooling. The anneal treatment for a specific duplex microstructure for each alloy was conducted at a temperature 55°C below the $T\alpha$. Fully-lamellar (FL) microstructures were produced in alloys G1 and G8 by annealing at temperatures between $T\alpha$+1° and $T\alpha$+35°C to yield various grain sizes, while refined FL (RFL) structures were controlled in alloy K5 by annealing at $T\alpha$+35°C. Lamellar spacings for each lamellar material were varied by employing alloy/microstructure-specific cooling methods and rates developed recently [25-27]. All materials were then given a stabilization treatment at 900°C for 6 h. Tensile properties were measured in air on specimens with a gage diameter (GD)of 3.5 mm at temperatures between RT and 1000°C and at strain rates in the range from $1x10^{-5}s^{-1}$ to $1x10^{-1}s^{-1}$ [5, 23,25, 29]. Larger-size specimens with a GD of 7.5 mm were used to test the relative size effect (specimen-size vs. GS), as described later. Gage sections of the round-bar tensile specimens were mechanically polished to a 600-mesh surface-finish. The progress

George R. Irwin Symposium on Cleavage Fracture
Edited by Kwai S. Chan
The Minerals, Metals & Materials Society, 1997

Table I. Compositions, Post-Forging Heat-Treatments, and Microstructures for the Alloys Used in the Experiments

Alloys	Composition (at%)	Tα (°C)	Annealing Temperature (°C)	Microstructures (GS)
G1	Ti-47.0Al-1.0Cr-0.9V-2.6Nb+I	1355	1280	DP1 (30 μm)
			1357-1380	FL (250~2600 μm)
G8	Ti-47.0Al-1.5Cr-0.5V-2.3Nb+I	1362	Similar to above	same as above
K5	Ti-46.5Al-2.0Cr-3.0Nb-0.2W+I	1325	1270	DP2 (12 μm)
			1360	RFL (300 μm)

I: 800 (O+C+N+H) (in wt/ppm)

of the RT tensile deformation and crack-initiation process was directly observed on electropolished flat gage-section specimens.

Fracture toughness and resistance testing was conducted on precracked compact-tension (CT) specimens having the dimensions, 2.5x2.5x0.5 cm or 5 x5 x1.0 cm, at RT, 650°C and 800°C [5, 15, 17, 20]. Fracture toughness measurements were conducted at a loading rate of 1.5 MPa$\sqrt{m}$, and fracture resistance testing at various strain rates ranging from 4x10-1 to 4x10-5 mm/sec [15, 17, 28]. Fracture surfaces were investigated in detail in order to quantify specific fracture modes. Load controlled fatigue tests were performed in air at 600°C, 800 °C and 870°C on smooth hourglass-shaped high-cycle-fatigue (HCF) specimens, having electro-polished gage sections with a minimum diameter of 4.7 mm, at a frequency of 25 Hz and a sinusoidal variation of load with time in the tension mode (R=0.1) [25, 29].

Microstructures, deformation traces/features appearing on the specimen surface as well as underneath the fracture surface, crack initiation events, and fracture surfaces were observed/recorded using light microscopes, the back-scattered-electron (BSE) imaging technique, and the scanning electron microscope (SEM).

3. RESULTS

3.1 Alloys and Microstructures

The chemical analyses of the forged materials for three alloys (G1, G8, and K5) investigated are listed, along with interstitial levels, in Table 1. The annealing temperatures with respect to the alpha-transus (Tα) and resulting microstructures are also listed in Table 1. Figure 1 a shows the DP1 microstructure, produced in G1 and G8, consisting of small (-30 μm) gamma grains with small amounts (2-5 %) of α_2 plates/particles dispersed in the matrix. The DP2 microstructure, a finer duplex (-12 μm), obtained in alloy K5, contains the beta phase (B2) particles as an additional phase, Figure 1b. FL microstructures produced in alloys G1 and G8 consist of widely-ranging lamellar grain size (250-2600 μm), with small amounts of fine (5-15μm) γ-grains along lamellar grain boundaries (GB). Figure 1c shows a typical FL microstructure having a GS of 1100 μm, which is designated as 'FL(1100)'. The lamellar spacing for FL materials were relatively coarse, ranging from 1-5 μm, due to slow cooling rates employed during processing. RFL materials having various GS's (150-600μm) were produced in alloy K5. However, only the 'RFL(300)' material consisting of 300μm lamellar grains with fine (5-20 μm) GB γ/B2 grains, Figure 1d, were used in the investigation. The presence of beta phase made controlling grain size easy, which has been documented [35]. Because of relatively fast cooling rates that can be applied, the lamellar spacing for the RFL structure of alloy K5 ranged from 0.3 to 0.8 μm.

3.2 Tensile Behavior

Tensile properties of DP1 and FL(1100) materials measured at strain rates around $5x10^{-4}s^{-1}$ are plotted as a function of temperature for a temperature range from RT to 1000°C [5, 23, 30], Figure 2. Drastic differences exist in the temperature dependence of tensile properties between these microstructures. For the DP1 structure, the ultimate tensile strength (UTS) remains unchanged up

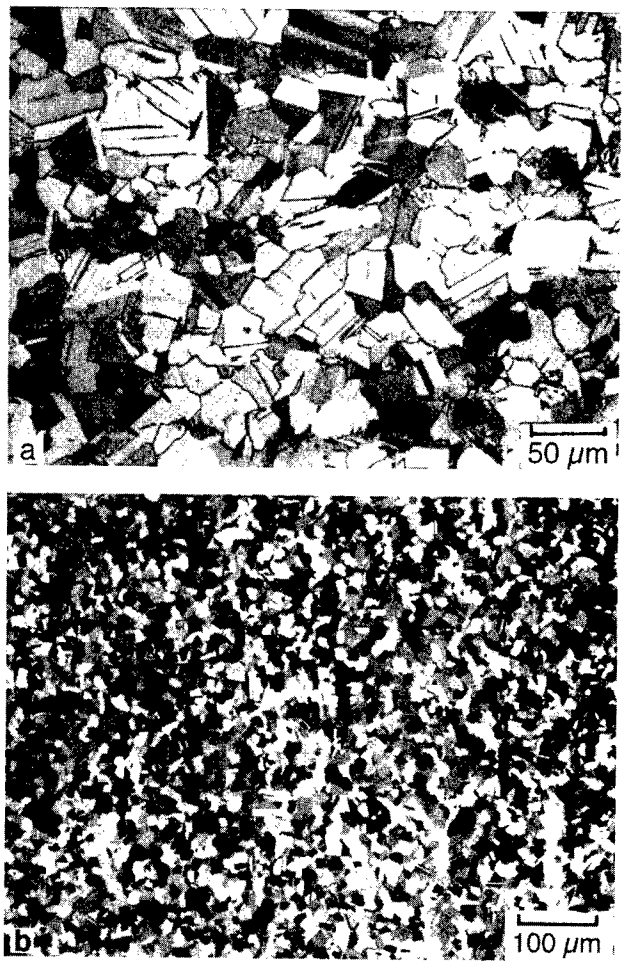
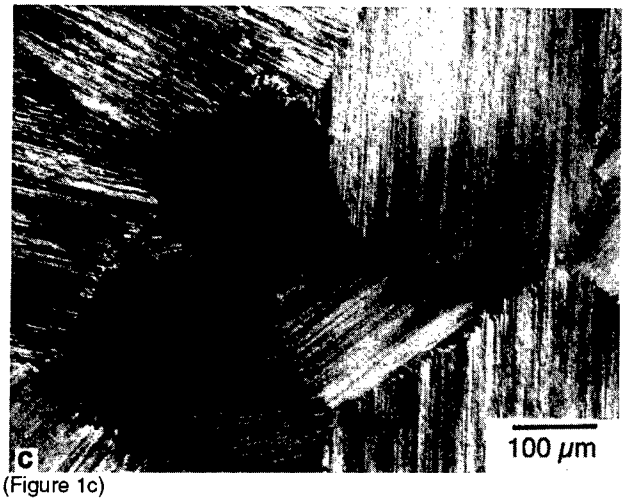
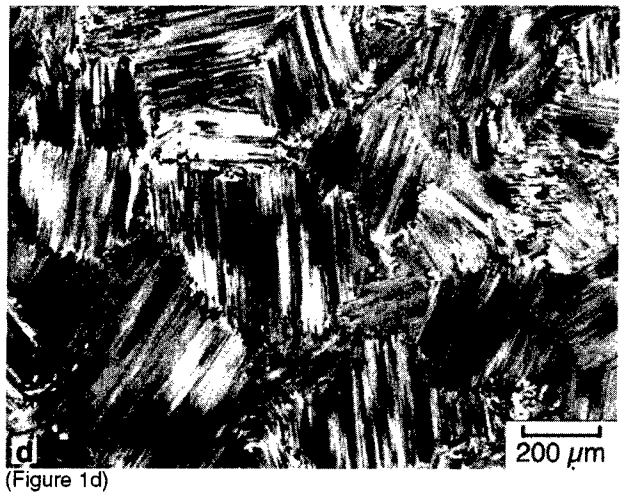


Figure 1. Optical micrographs of microstructures for: (a) DP1, (b) DP2, (c) FL (1100), and (d) RFL(300). Figures 1 c and d are in next page.



(Figure 1c)



(Figure 1d)

to 800°C while the yield strength (YS) decreases gradually over the same temperature range. Both strengths decrease rapidly at higher temperatures to maintain only about half of their RT levels at 950 °C. FL(1100) specimens exhibit fairly low strengths at RT, but superior strength retention at elevated temperatures, losing not more than 25% of the RT strength at 950°C. The brittle-ductile-transition (BDT) temperature is about 700°C for the DP1 material and about 810 °C for the FL(1100) material. RT tensile elongations are 2.7% at RT and 6.5% at 700°C for the DP1 material, and 0.8% at RT and 2.5 % at 800 °C for the FL(1100) material.

DP2 and RFL materials show comparable strength levels at RT in spite of a factor of 25 larger grain size in the RFL material; however, they also exhibit significant differences in tensile behavior with temperature, Figure 3. The RFL material provides much greater high-temperature strength retention. However, the degree of the strength retention is lower than for the FL(1100) microstructure. The DP2 material exhibits higher ductility than the RFL material throughout the temperature range examined. The BDTT lies around 680 °C for the DP2 material and about 780 °C for the RFL material. Tensile elongation is 2.5% at RT and 7.5% at 700 °C for DP2 material, and 0.8% at RT and 4.5% at 800 °C for the RFL material.

RT tensile properties are plotted in Figure 4 as a function of microstructure and GS. Both strength and ductility decrease as grain size increases, especially, within a class of microstructures.

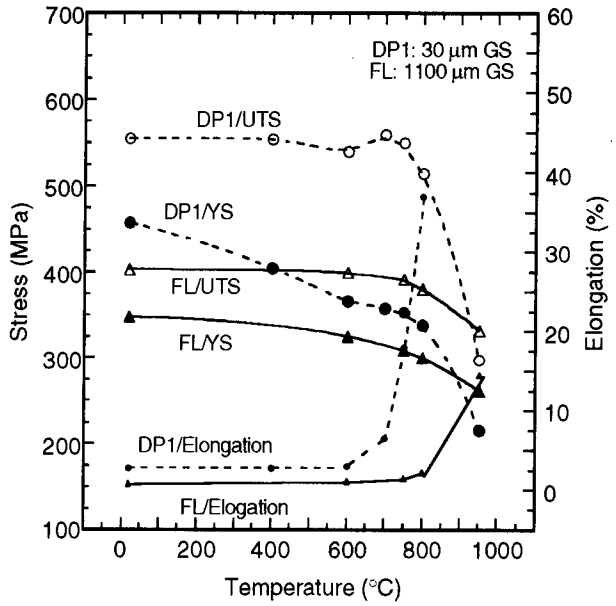


Figure 2. Tensile properties of alloys G1 and G8 in DP1 and FL(1100) microstructural forms as a function of temperature

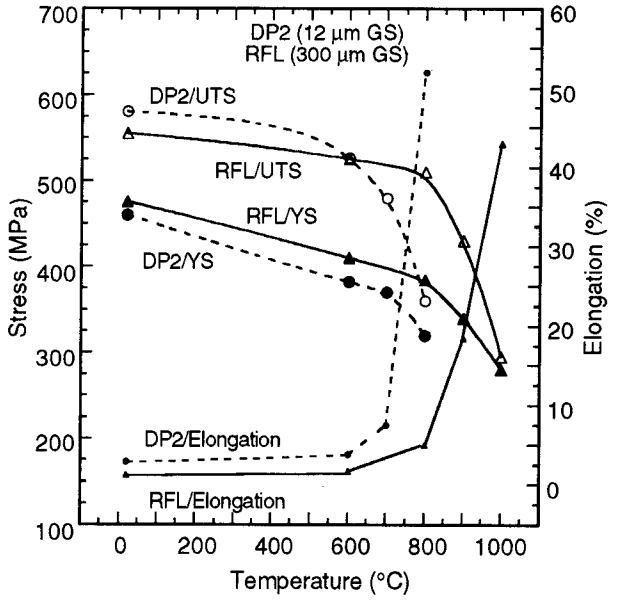


Figure 3. Tensile properties of alloy K5 in DP2 (12 μm) and RFL(300 μm) microstructural forms as a function of temperature

Note that the tensile strengths of lamellar materials having 250-300 μm grains are comparable to those of duplex materials. Typical RT stress-strain curves for the materials are shown in Figure 5. The DP2 flow curve shows yield point behavior that is followed by low-rate work-hardening; though not shown here, a similar behavior is shown for the DP1 microstructure. The RFL(300) material microyields at a stress level of about 0.70 YS ($YS=\sigma_{0.2\%}$) and exhibits relatively high-rate of work hardening. The FL(1100) material shows a similar flow behavior; however, with much lower levels of microyielding stress (σ_o=0.60 YS), flow stress, and strain-to-failure.

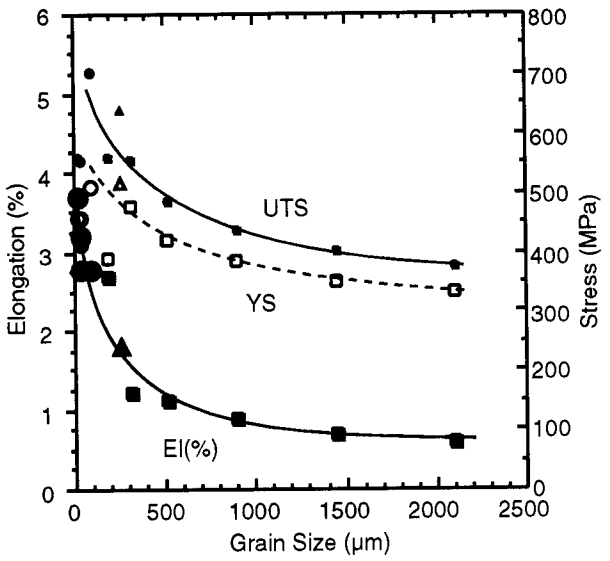


Figure 4. RT tensile properties as a function of microstructure and grain size

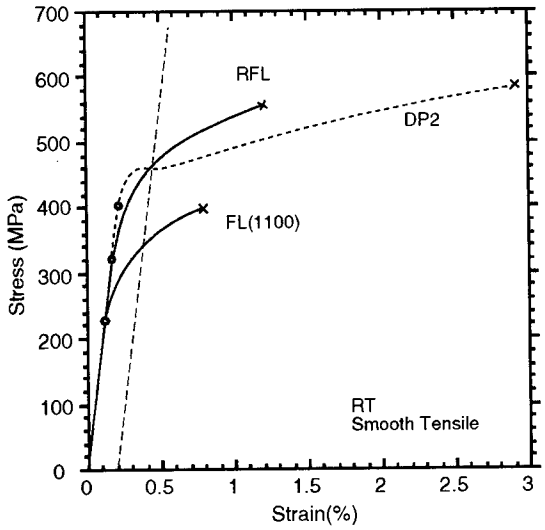


Figure 5. Typical RT tensile stress-strain curves of TiAl alloys in DP2, and RFL(300) and FL(1100) microstructural forms. Open circles indicate the microyielding stresses (σ_0) where flow begins to deviates from the elastic deformation.

In Figure 6, the relationship between GS (250-2600 μm) and YS ($\sigma_y=\sigma_{0.2\%}$) is plotted for FL materials having approximately 1 μm lamellar spacing (LS). The relationship, measured on 3.5 mm gage-diameter (GD) specimens, satisfies the Hall-Petch (HP) relationship, $\sigma_y=\sigma_0+k_y d^{-1/2}$, with k_y=4.5 MPa√m [30, 31]. This unusually large HP constant is compared to that (~1 MPa√m) for a duplex material [11, 32] in Figure 6. Having realized that large GD/GS ratios may influence the constant, a complimentary experiment was recently conducted for a FL material having a GS of 820 μm on tensile specimens with different GD's between 1.2 and 7.5 mm [25]. The experiment showed the existence of a critical GD/GS ratio of about 5, above which YS appears to remain constant but below which YS decreases with decreasing ratio.

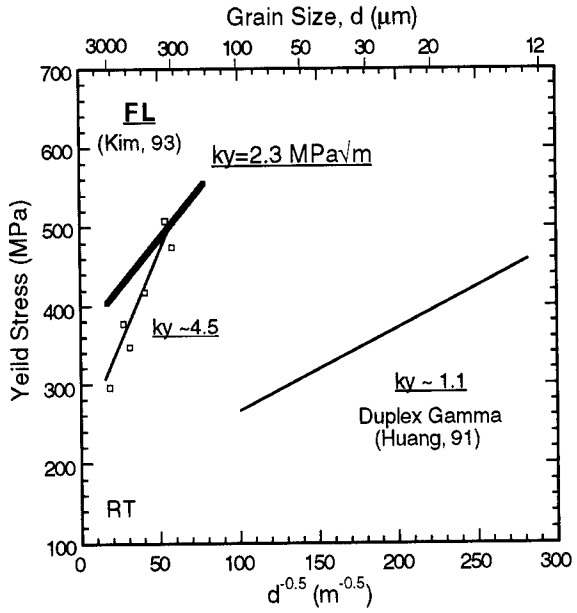


Figure 6. RT yield stress ($s_{0.2\%}$) as a function of grain size in lamellar materials (250-3000 μm GS and ~1μm lamellar spacing), showing the Hall-Petch relationship having two different constant values: ky=4.5 MPa√m from small-gage-section specimens and ky=2.3 Mpa√m corrected for large-gage-section specimens. Also shown for comparison are the GS-YS relationships on duplex materials (11, 32) and PST crystals in the hard orientation [14].

Using these results, a correction was made for a new value of k_y =2.3 Mpa√m also shown in Figure 6.

Plastic deformation at RT was planar within a grain for both DP and lamellar materials, as observed optically as well as in SEM [23, 25]. For lamellar materials, deformation starts in the grains in soft orientation (SO) well below the YS stress levels and then propagates into the adjacent grains, usually in a hard orientation (HO), through the buildup of stress concentration at grain boundaries (GB). This process is exemplified for the RFL material in Figure 7 where deformation bands/marks are visible on the electropolished flat specimens. Here, the specimen was observed during an interrupted tensile test and a predetermined surface area was periodically observed and recorded using an optical microscope. At a low stress level of $\sigma_{0.1\%}$, surface deformation lines are shown to take place in SO or parallel to the lamellar boundaries (Figure 7a), while at strains greater than the yield strain translamellar deformation begins to occur usually in the adjacent, HO grain interior near the stress concentration (Figure 7b). It is noteworthy that some of the HO grains remain undeformed even at loads near the fracture strain.

The RT fracture in DP materials is dominantly transgranular (TG] cleavage-like failure, often exhibiting river patterns (Figure 8a) in spite of the 2.5% ductility and considerable deformation activity in the material [18, 23]. This trend continues up to the BDT temperatures. At 600-700°C, the fracture of DP specimens is predominantly intergranular (IG) at/near the crack-initiation sites with a few cleavage events (Figure 8b), but almost entirely IG fracture in the fast-growth regions (Figure 8c). As temperature increases, more deformation is evident within the grains, however, the planarity of deformation remains [23]. At 800°C and under low strain rates (<$5\times10^{-4}s^{-1}$), specimens begin to neck with significant

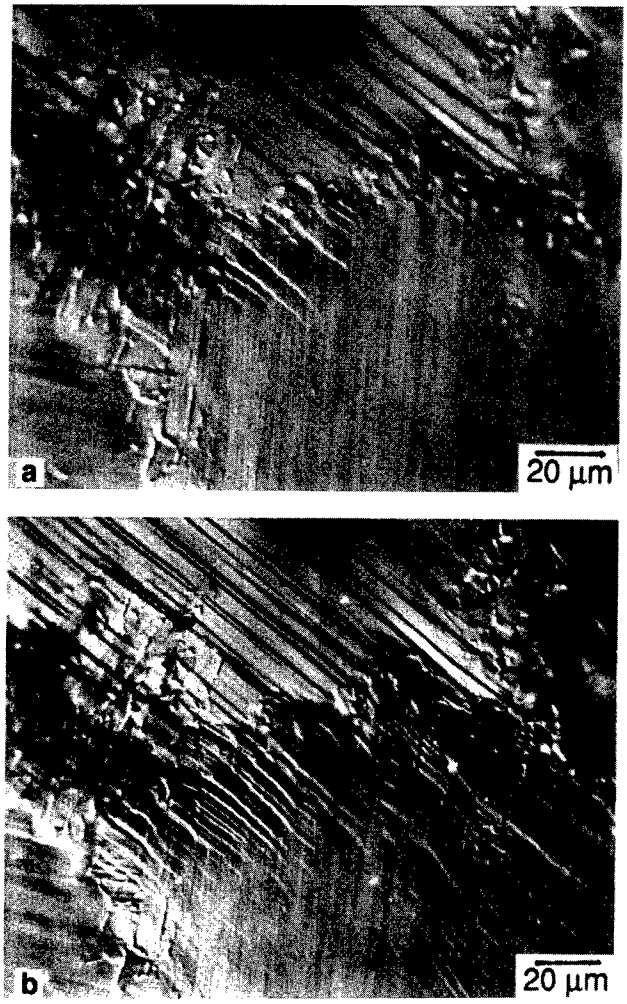
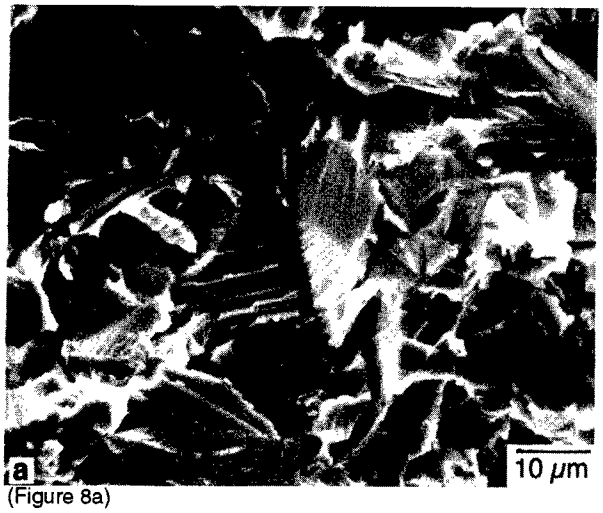


Figure 7. The progress of RT tensile deformation observed on the electropolished RFL specimens, after deforming to offset strains of: (a) 0.08% at $\sigma_{0.08\%}$=427 MPa and (b) 0.30% at $\sigma_{0.3\%}$=493 MPa. The fracture stress was $\sigma_f = \sigma_{0.92\%}$=525 MPa.



(Figure 8a)

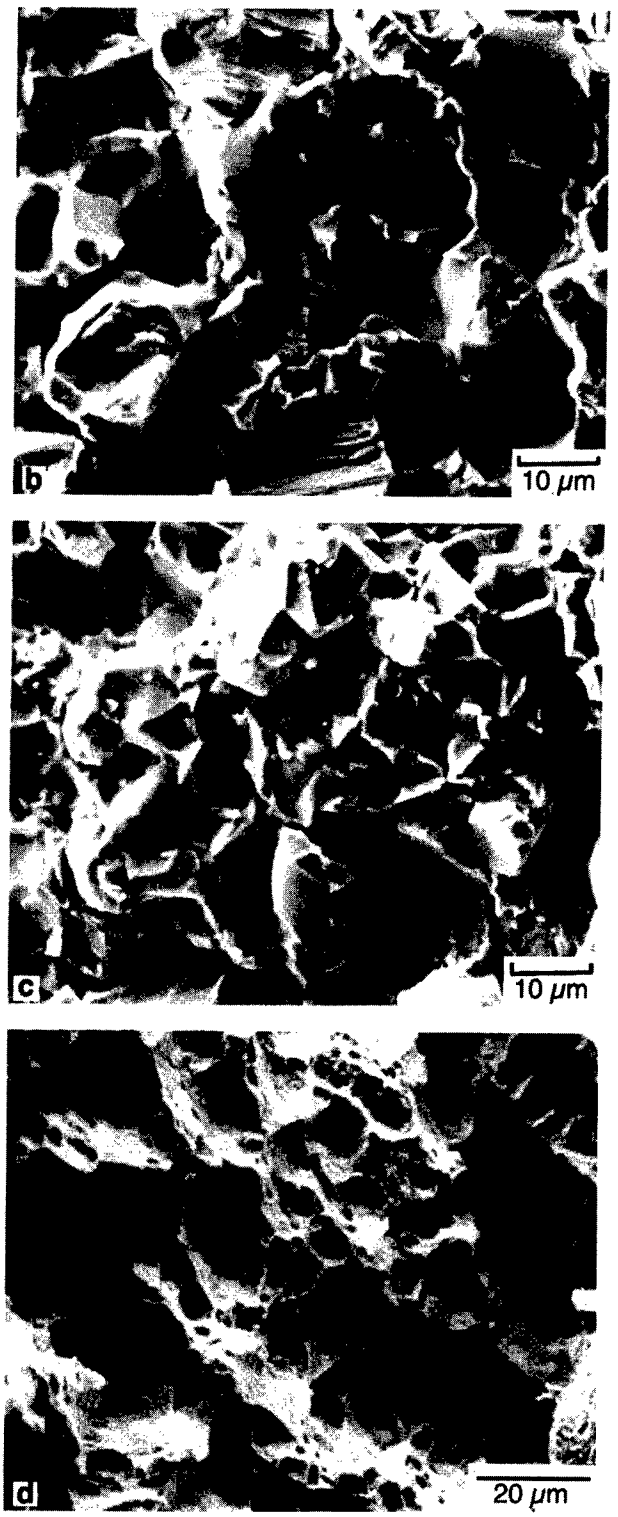


Figure 8. Tensile-fracture of duplex materials showing: (a) transgranular fracture at RT; (b) a mixture of translamellar and intergranular fractures near the crack-initiation sites at 600°C; (c) intergranular failure in the fast fracture (overloaded) regions at 600°C; and (d) dimpled rupture fracture at 800°C and $5X10^{-4}$ s^{-1}.

elongation, which involves tremendous amounts of deformation activity with multiple slip and twinning [23, 30]. This often results in dimpled rupture when elongation is greater than 40% [26], as shown in Fig. 8d. At 800°C and faster rates ($>10^{-3}s^{-1}$], IG fracture prevails with strains-to-failure smaller than 4% [25, 29]. At still higher temperatures, dynamic recrystallization takes place, leading to grain refinement and enhanced ductility [8]. The fracture at temperatures above 900°C involves the formation of voids often at GB's.

FL specimens exhibit three characteristic fracture features at RT: translamellar(TL) fracture, interlamellar (IL) fracture, and a mixture, depending on the lamellar orientation with respect to the crack path or stress axis, Figure 9a. TL fracture or cracking appears most frequently and often occurs in the crack arrester orientation (lamellar boundaries nearly perpendicular to the crack propagation direction), Figure 9b, or in a more complex manner, Figure 9c. Cleavage-type features with river patterns are often observed, and traces of planar deformation bands parallel to the lamellar boundaries are frequently observed on the fracture surfaces, Fig. 9b.

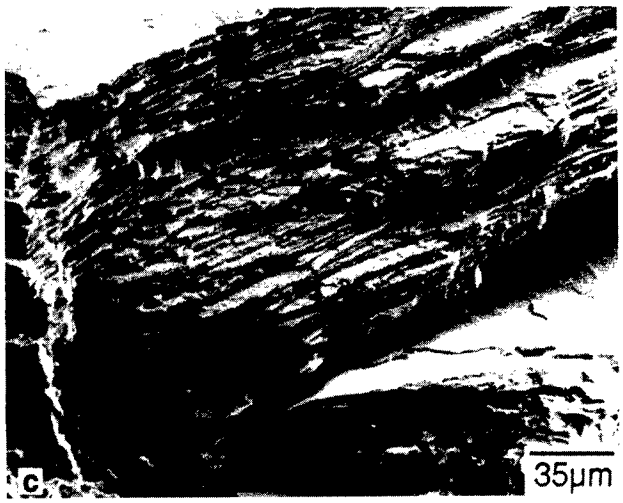
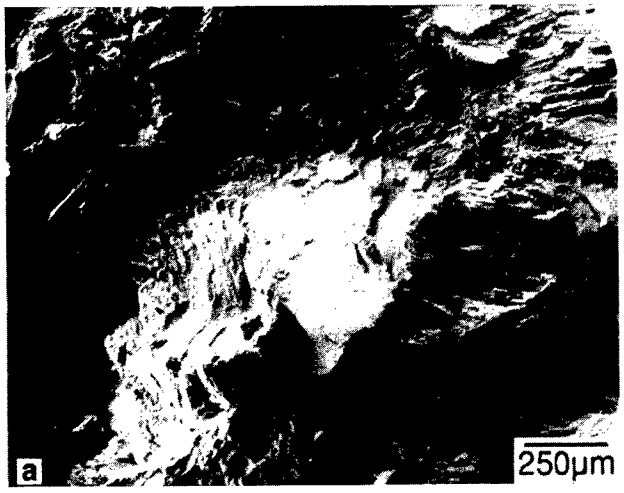
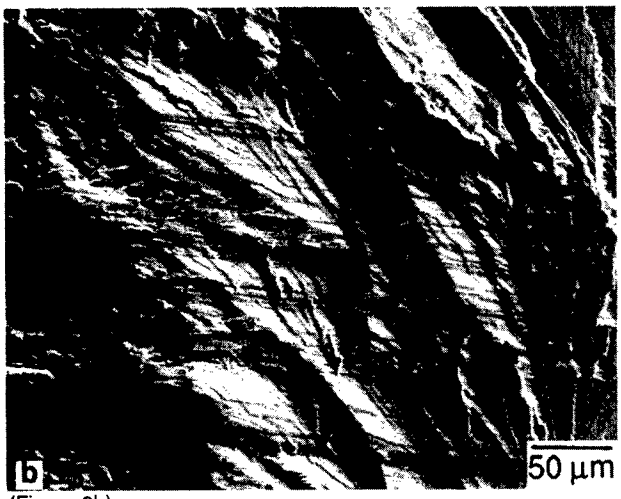


Figure 9. RT tensile fracture of lamellar materials showing: (a) the overall fracture surface with predominantly translamellar and occasional interlamellar failure; (b) translamellar fracture in the crack arrester orientation; and (c) complex translamellar failure.

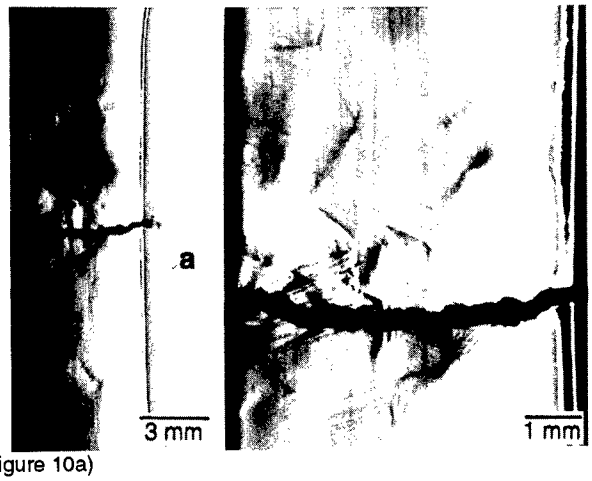




(Figure 9b)

The deformation bands in large-grained FL materials (with low strain-to-failure) are planar and in most cases parallel to the lamellar boundaries, often observed only in selective (soft) grains on the specimen surfaces (Figure 10a) as well as on the fracture surfaces (Figure 9b). In this large-grained FL material, TL deformation is observed only occasionally during deformation, but they occur more easily during fracture, within the plastic wake or process zone of the crack, Figure 10b.

The tensile fracture of FL(1100) specimens at 750°C is characterized by cleavage-type TL fracture, however, with increasing lamellar splitting and GB γ-grain boundary fracture, Figure 11a. The delamination spacing is roughly 15 μm, and the extent of splitting appears to increase with temperature, often leading to the IG fracture of grains. The occurrence of cleavage fracture in lamellar materials was reduced rather drastically above 800°C, especially for the RFL (300) material. At 800°C, boundary fracture involving both GB's and lamellar boundaries becomes important in RFL specimens, Figure 11b. The IL fracture appears



(Figure 10a)

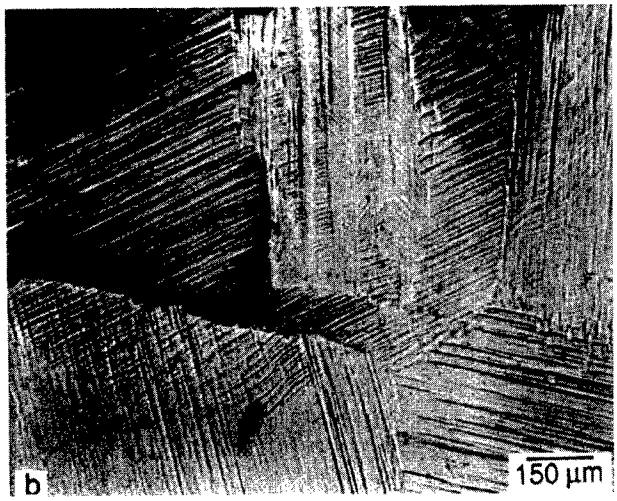


Figure 10. Tensile deformation traces on the electropolished, flat surfaces of large-grained FL specimens fractured at RT, showing: (a) deformation occurred only in soft grains and (b) planar deformation bands near the fracture surface. The plastic fracture strain was 0.15%

to be enhanced by the presence of GB γ-grains, Figure 11a. At 900°C, though not shown here, FL microstructures become unstable in the necked regions, and they begin to recrystallize into fine gamma grains at large strains, resulting in ductile rupture involving void formation beginning to prevail [8, 23]. Twins were observed on the 900°C fracture surface, indicating that twinning is still an important deformation mechanism at this temperature [8]. However, FL microstructures can be unstable even at 800°C when the tensile elongation becomes more than 8%, as was the case for tests conducted at a strain rate of $1x10^{-5}s^{-1}$ in vacuum [17].

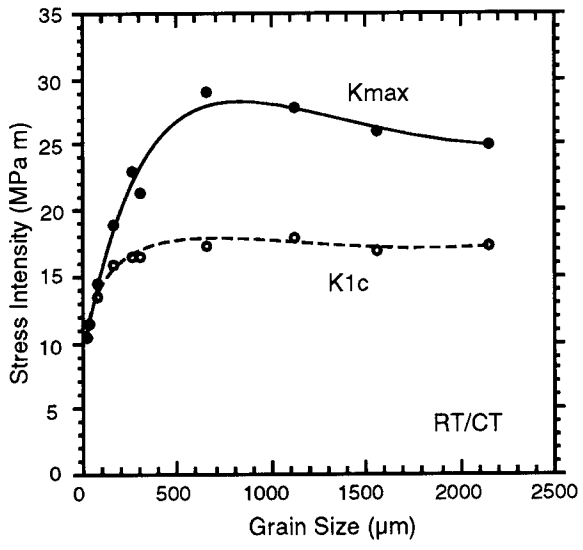


Figure 12. RT fracture toughness (K1c and Kmax) values for both duplex and lamellar materials are plotted against grain size.

3.2 Fracture Toughness/Resistance Tests

Fracture toughness (Kmax or) values measured at RT on 5 mm thick CT specimens for DP and FL including RFL(300) [5, 15, 25)

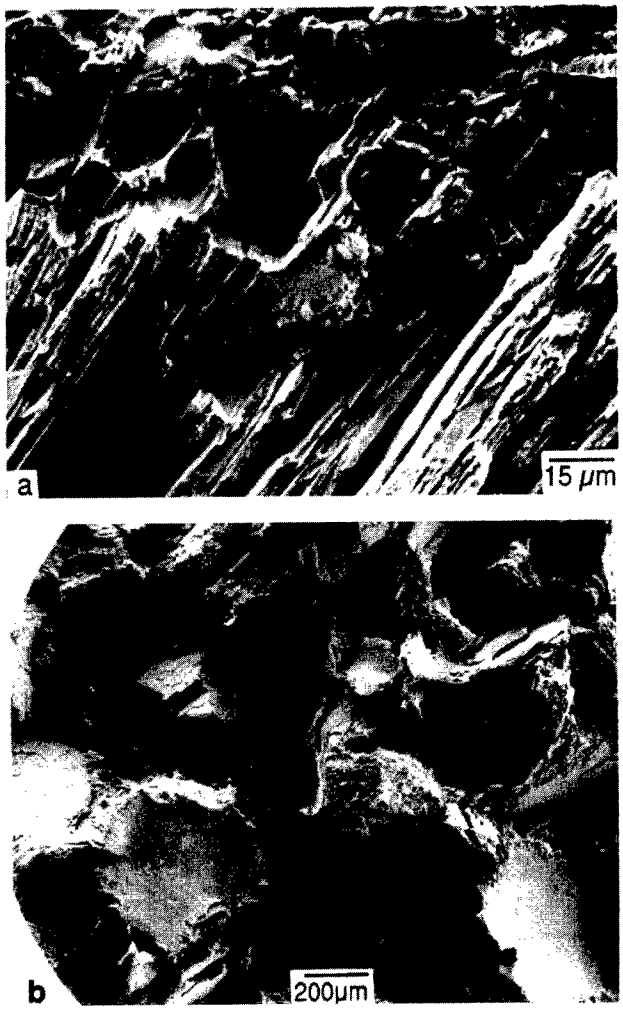


Figure 11. Elevated temperature fracture of lamellar materials, showing: (a) translamellar fracture with appreciable interlamellar splitting as well as intergranular fracture in FL (1100) material at 750 °C and (b) a mixture of translamellar, interlamellar and intergranular fracture in RFL(300) material at 800°C.

are plotted in Figure 12 as a function of GS (150-2600μm). Also included are the K1c values measured for selected specimens [15, 17, 20]. Clearly, increasing crack resistance is not present in DP materials while lamellar materials exhibit R-curve behavior, the degree of which (Kmax-K1c) appears to increase with grain size. The K1c varies between 15 and 20 MPa√m for the GS range investigated, and within this range the K1c apparently increases with GS. Kmax increases with GS from 16-20 MPa√m for GS=250 μm to about 30 MPa√m for GS=500μm, and then tends to decrease for larger GS's. The decreases in Kmax appear to take place when GS is larger than plastic-zone-size (PZS), as discussed later. The fracture resistance (Kmax-K1c] ceases to increase at the critical GS of about 500 μm. In Figure 13, fracture surfaces of FL CT specimens fractured at RT reveal that failure near the initiation region is characterized by cleavage-type TL fracture. At 800°C, fracture surfaces are more tortuous with a mixture of TL, IL and IG cracking.

Fracture resistance of FL(1600) material at 800°C decreases with loading, or strain rate over a range of $4x10^{-4}$ to $4x10^{-5}$ mm/sec [17,

28], while it appears to increase at RT with increasing loading rate over a range studied from $5x10^{-5}$ to 300 MPa$\sqrt{m}$/sec [19]. F or a given material and test temperature, increases in fracture resistance appear to be related, though yet to be quantified, to increased TL over IL fracture [28].

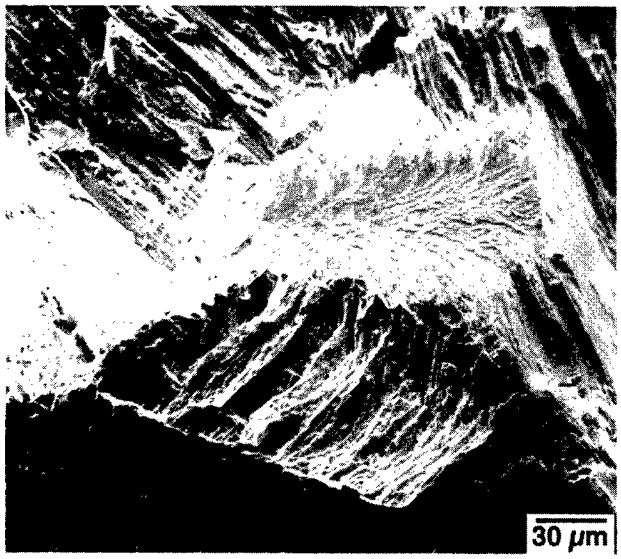


Figure 13. Fracture surfaces of fracture-toughness CT specimens of lamellar material, showing cleavage-type translamellar fracture at RT.

3.3 Fatigue Properties

The S-N curves obtained on standard hourglass type specimens are fairly flat [26, 29] at 600°C for both DP2 and RFL(300) microstructures, with the fatigue strength (FS) at 10^7 cycles

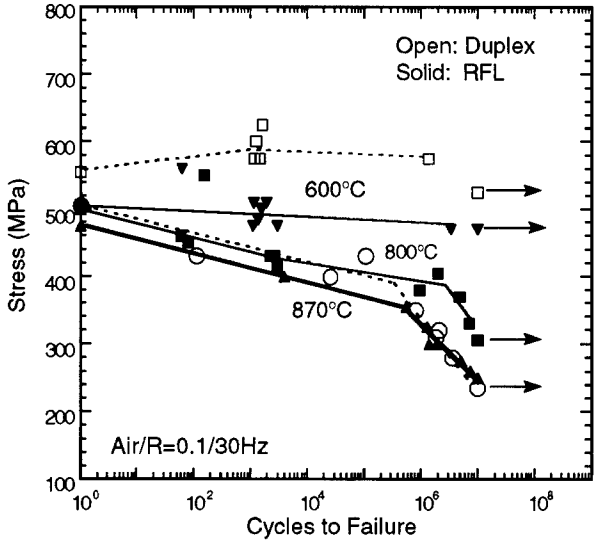


Figure 14. Fatigue stress-cycle (SN) curves of alloy K5 in DP2 and RFL(300) microstructural forms at 600, 800, and 870°C (RFL only). The maximum applied stresses (Smax) were normalized against yield stresses at respective temperatures.

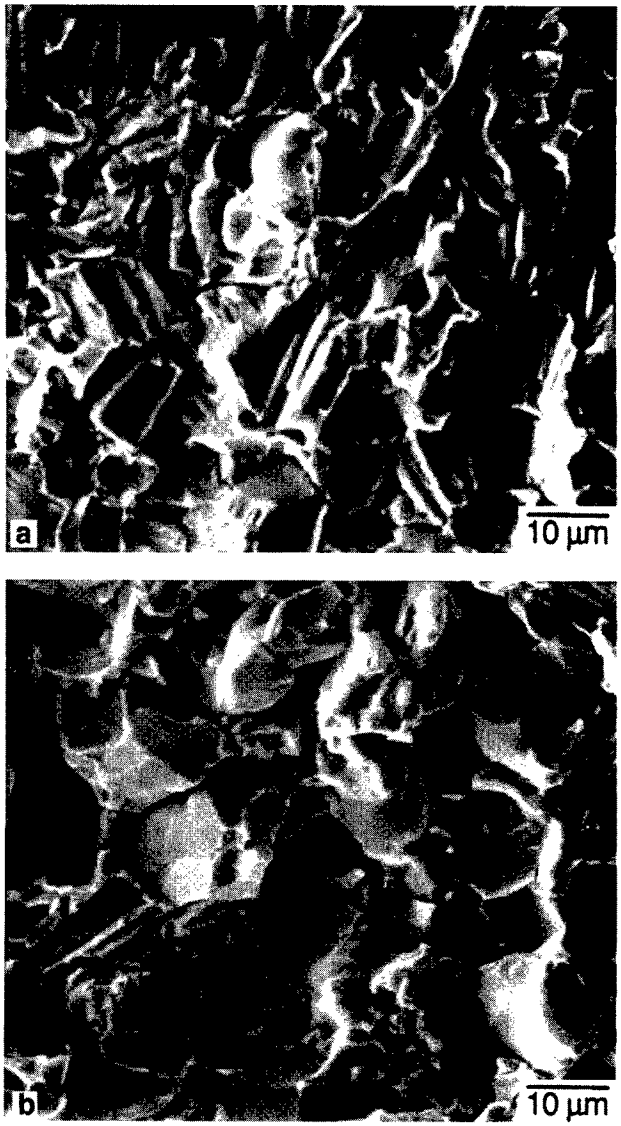
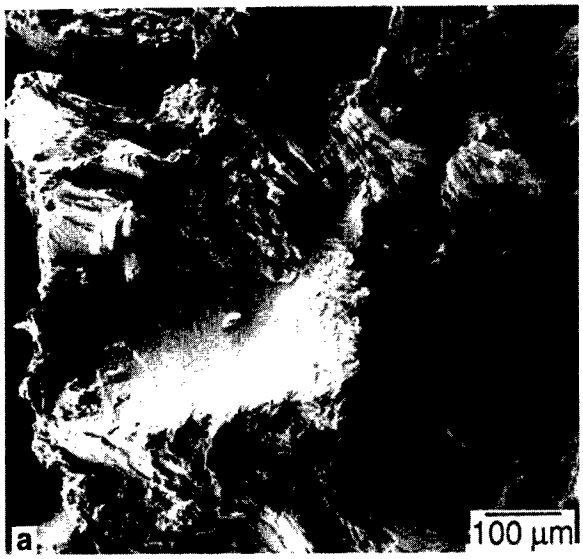


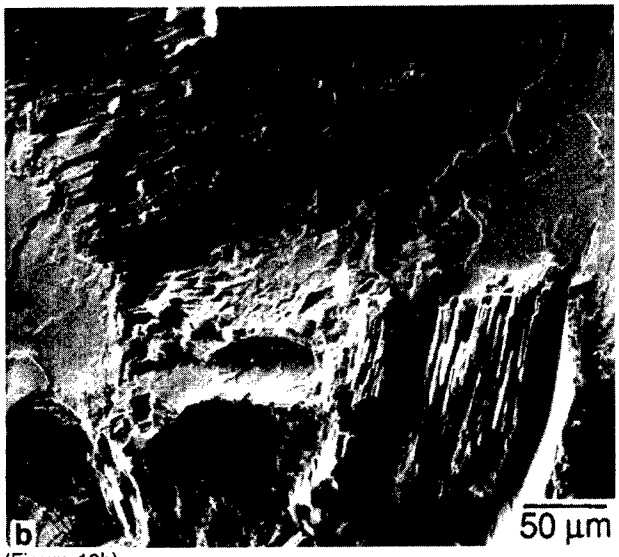
Figure 15. Fatigue-failed surfaces of DP2 specimens at 600°C, showing: (a) transgranular fracture near the crack initiation sites and (b) predominantly intergranular fracture in the fast-fracture regions.

approaching the ultimate tensile strength (UTS), Figure 14. At 800°C or higher, however, the fatigue resistance of RFL(300) material becomes higher than that of DP2 material in high cycle ($>10^5$) regimes, yielding a much higher FS, Figure 14. The above trends are consistent with the greater strength retention at high temperature in FL material shown in Figure 3.

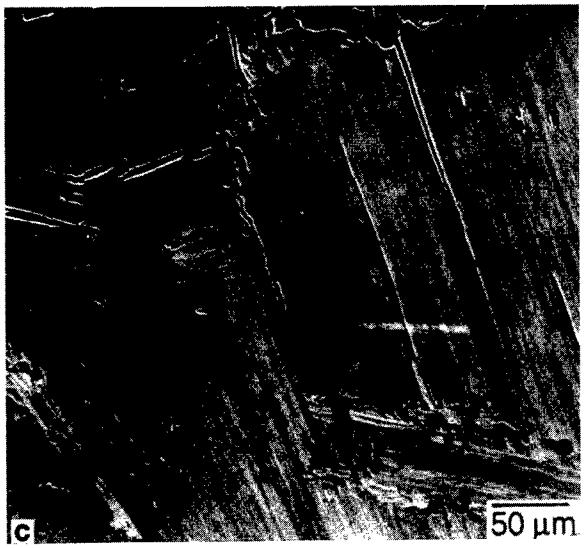
The structure in the DP2 material fatigued at 600°C as well as 800°C, shows tremendous deformation activity which is mostly planar as in tensile deformation [23, 29]. The fracture morphologies at both temperatures are observed to be similar for the material in high-stress-amplitude region. At 600°C, cleavage-type TG fracture is usually observed near the crack initiation sites (Figure 15a) while IG fracture appears to be predominantly present in the fast (overloaded) fracture regions (Figure 15b). In all cases, the crack initiation sites are located at the surface as is the case in the tensile tests.



(Figure 16a)



(Figure 16b)



(Figure 16c)

Figure 16. Fatigue-failed surfaces of RFL(300) specimens at 800°C, showing: (a) fracture after N=2310 cycles under a high Smax of 430 MPa, (b) fracture after N=7.2X10^6 cycles under a low Smax of 330 MPa; and (c) lamellar splitting, observed near the fracture surfaces, the frequency of which increases with decreasing maximum allpied stress (Smax).

For the RFL(300) material, fatigue crack initiation takes usually place in the interior, but near to the surface, of the specimen, followed by crack growth which is extended more with increasing temperature. The fracture surfaces exhibited predominantly cleavage-type TL failure at 600°C. At 800°C, a mixture of TL, IG and IL failure are typically observed, with IG failure becoming more appreciable at higher stress amplitudes (Figure 16a) than at low stress amplitudes (Figure 16b). The IG fracture regions usually are decorated with γ-grains and some second-phase particles which are also failed along the interfaces. In comparison to the tensile tests, the fatigue failure shows more IG failure and increased interlamellar splitting which becomes more extensive as the test temperature is raised, Figure 16c.

4. DISCUSSION

4.1 Tensile Deformation and Fracture

Room Temperature Yielding Behavior

There exist definite differences in the early stages of yielding between DP and lamellar material; that is, relatively low microyielding stresses ($\sigma_{0\%}$) and greater work-hardening rates in lamellar (FL and RFL) materials than in DP materials, Figure 5. The larger GS's and greater deformation anisotropy characteristic of lamellar materials are apparently responsible for the behavior. As shown in Figure 5, the normalized microyielding stress ($\sigma_0/\sigma_{0.2\%}$, with YS=$\sigma_{0.2\%}$) decreases with increasing GS. The relatively small microyielding stress and high-rate of work-hardening indicate that plastic deformation taking place in lamellar materials is highly anisotropic and nonuniform, as demonstrated in Figure 7a.

The Hall-Petch relationship between yield strength and grain size in FL microstructures exists with a large Hall-Petch constant of ky~2.3 MPa$\sqrt{m}$ for grain sizes from 250-2600 μm and yield strengths from 290-500 MPa, Figure 6. This corrected value is compared to those for fine duplex microstructures [11, 32] and that (0.5 MPa$\sqrt{m}$) for PST crystals in a hard orientation [14]. The occurrence of this unusually large H-P constant may be related to the strong anisotropic flow stress behavior [13, 14] of the lamellar structure. Taking the anisotropy into consideration, the HP relationship for FL material is proposed to be, $\sigma_y=\sigma_o+k_{d\lambda}d^{-1/2}$, where $\sigma_o=f(\lambda)$ and $k_{d\lambda}=f(d, \lambda)$ [33]. This empirical relation predicts: 1) σ_o increases with decreasing lamellar spacing; 2) the HP constant varies with both GS and lamellar spacing, approaching that for the DP material, for example, as spacing coarsens; and 3) YS can be unusually high for fine grains and fine lamellar spacing, Figure 17 (6). Recently, a more detailed analysis [34] confirmed that high yield-strength measured in relatively large-grained lamellar materials may be accredited to the deformation anisotropy of the lamellar structure and lamellar refinement.

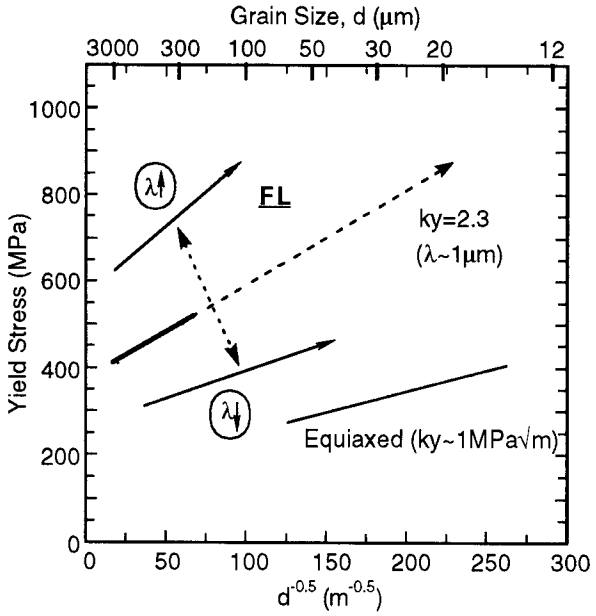


Figure 17. Generalized Hall-Petch relationship in lamellar materials as a function of grain size as well as lamellar spacing (l). The relationships for duplex materials and PST crystals are shown for comparison.

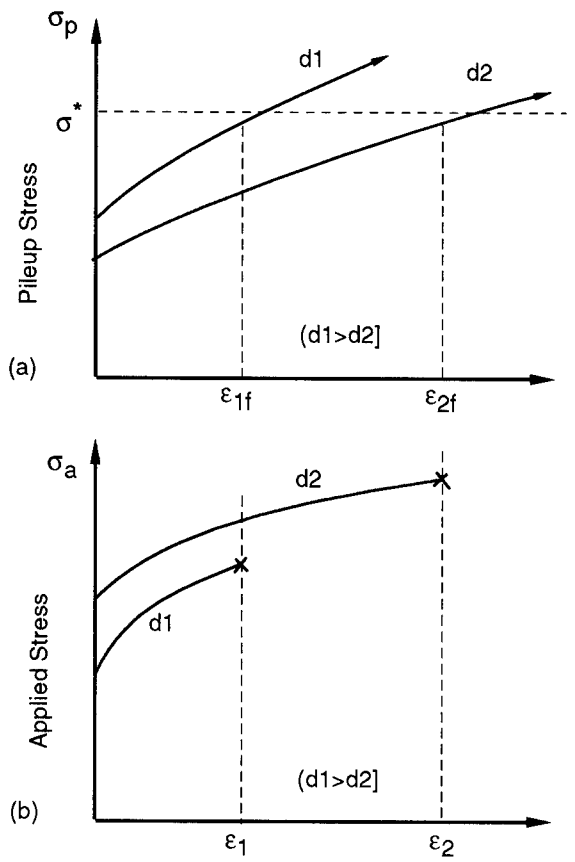


Figure 18. Grain size dependence of fracture strain and flow curves: (a) estimated RT Tensile flow behavior for two different grain sizes (d1>d2) near the dislocation-pileups, with respective fracture strains (ε_{if}) which are limited by the fracture stress (σ^*); and (b) bulk material's flow curves for the two grain sizes developed under applied stress, with the strains limited by the fracture strains (ε_{if}) and the fracture stresses controlled by the material's K1c.

RT Ductility

The ductility of gamma alloys decreases with increasing GS; for example, the ductility of FL microstructures decreases from 2.0 to 0.2% as the GS increases from 250 to 2600μm, Figure 4. This inverse relationship between ductility and grain size was recently analyzed by assuming the presence of a microcrack comparable to the average grain size and subsequently estimating the stress intensity of the crack and the resultant ductility due to crack propagation [15].

On the other hand, the decreases of tensile ductility with increases of grain size in lamellar materials can be explained using the characteristic anisotropy of tensile properties of lamellar structures [13, 14] and assuming that the fracture is controlled by the crack nucleation process [29] involving the pile-ups of dislocations under shear stress [30]. In this process, normal stress is built up ahead of a dislocation pileup, and is conveniently expressed as

$$\sigma_p = C(\varepsilon_p)^n d^{1/2} \quad \text{..... (A)}$$

where ε_p is plastic normal strain, 'n' the work-hardening coefficient, and 'd' GS. A microrack is formed when the pileup stress (σ_p) exceeds the critical stress, σ^*, needed to initiate a microcrack [35, 36, 37]. Fracture strains (ε_{f1} and ε_{f2}) for two different GS's ($d_1>d_2$) can then be obtained as shown in Figure 18a. Using the above relations and the plastic flow equation, $\sigma=A\varepsilon^n$, with A and n assumed to remain constant, the stress-strain curves for the two different lamellar grains are constructed as shown in Figure 18b.

It is apparent from_Figure 18 that ductility is primarily controlled by the amount of general yielding which will be greater for small grain sizes. In large-grained FL materials, cracking and subsequent fracture precedes general yielding resulting in nonuniform deformation and low strains-to-failure [21, 23, 31]. This is consistent with planar slip bands observed within soft lamellar grains, Figures 7 and 10, which lead to a dislocation pileup (Figure 7) nucleating a microcrack, often in an adjacent grain. Microcracking is usually preceded by either translamellar slip/twinning or additional interlamellar deformation, as evidenced in Figures 7b and 9a. The microcrack usually forms in the translamellar direction, although interlamellar cracking should be possible depending on the lamellar orientation. This plasticity-induced crack-nucleation has been recently tied to a tensile stress which is greater than yield stress [24]. Consequently, it can be concluded that uniaxial tensile ductility and failure are a stress-controlled crack nucleation event, where plasticity required. For smaller grain sizes, a finite propagation life may be required to reach the critical flow size for failure.

Brittle-Ductile Transition

Tensile ductility is characterized by the brittle-ductile transition temperature (BDTT) which varies from 680°C to 810°C depending on alloy composition and microstructure, as collectively plotted in Figure 19. The BDTT appears to increase with grain size or with decreasing RT ductility. It is also strain-rate sensitive, especially for fine microstructures, as was observed in a DP microstructure [26, 29]. The strain-rate sensitivity of BDT was also observed recently in

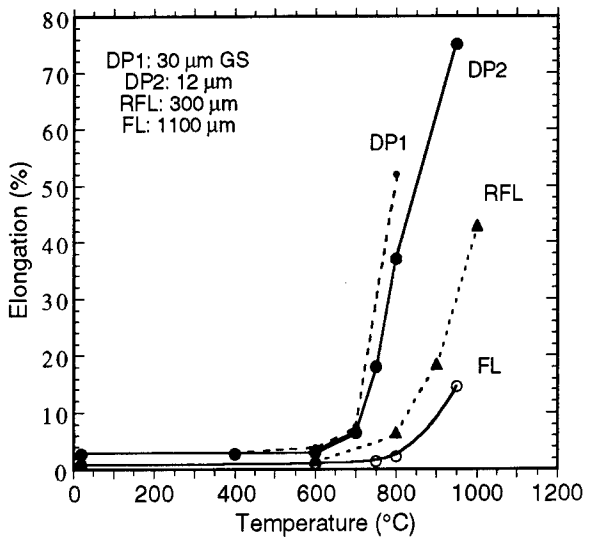


Figure 19. Plots of tensile ductility for duplex and lamellar materials against test temperature measured at a strain rate of 5x10-4s-1, showing the dependence of BDTT on microstructure and grain size.

Ti-55Al single crystals [38]. Since dynamic recrystallization was not observed at 800°C for strains at least up to 15 %, the enhanced ductility above the BDTT may be the direct result of increases in deformation activity, perhaps, including deformation systems. The apparent grain size dependence of BDT indicates that GB's may play a major role in initiating the drastic increases in deformation activity. This aspect needs to be elucidated with detailed measurements.

For a given grain size, tensile strengths at temperatures below BDTT's depend on cooling rate and methods [5, 18, 23] employed, with higher cooling rates yielding higher strength levels for both duplex as well as lamellar materials. With fast cooling rates, the α_2 phase in duplex material is present in fine particle (instead of plate) forms, resulting in increased strength and lowered ductility [5]. In lamellar materials, increasing cooling rates result in finer lamellar spacings which increase tensile strengths, as indicated in Figure 17. Decreases in lamellar spacing were predicted to enhance ductility in lamellar material 30], but this has not been quantified.

Fracture Process and Modes

Cleavage-type transgranular cracking is the dominant fracture mode at RT for both duplex and lamellar microstructures, although fine duplex materials often additionally show intergranular (IG) failure while lamellar materials occasionally show interlamellar (IL) fracture. This fracture behavior at RT is closely related to the low ductility observed in polycrystalline gamma TiAl alloys. In PST crystals. on the other hand, cleavage-like brittle IL fracture occurs even after more than 20% plastic strain [13, 39].

At temperatures near BDTT's, IG fracture begins to prevail for duplex microstructures (600-700°C) and delamination, IL and IG fracture become important for lamellar microstructures (>750°C) [23,29, 30]. In these temperature ranges, in spite of the increased deformation activity, however, transmission of slip and twining across GB's or lamellar interfaces appears to remain difficult [23]. The ductility still remains limited at the strain rates used for our investigation (>1x10^{-5}s^{-1}). At higher temperatures greater than BDTT+50°C, the change from TG crack initiation and ductile failure in the overload area at a low strain rate (<10^{-3}s^{-1}) to completely intergranular fracture at high strain rates demonstrates, that with increasing strain rate the cohesive strength of grain boundaries becomes lower than that of the grain interior. Nevertheless, the highest ductility appears to occur only when extensive recrystallization to fine grains is accomplished. The important aspects of apparent grain-boundary/interface weakening observed with increasing temperature, especially at high strain rates, requires more detailed investigation.

4.2 RT Ductility/Toughness Relationship

The inverse relation between ductility, initiation-toughness (K1c) and saturation-toughness (Kmax) are collectively plotted in Figure 20. The observations can be explained by analyzing the bulk tensile behavior and the crack-tip yielding behavior. As discussed, tensile ductilities of polycrystalline material are primarily controlled by the amount of general yielding which is greater at small grain sizes. In toughness testing large (>500μm) FL specimens, however, the crack tip plastic zone extends less than one grain diameter in front of the crack tip, thereby confining the deformation behavior to the characteristics of those few grains along the crack front. The K1c is then closely related to the intrinsic ductility of the lamellar structure and can be used to estimate the intrinsic tensile stress-strain curve of the material [30, 31]. The near-tip effective strains in the lamellar structure were measured to be over 20% at the onset of crack propagation [15] which is consistent with the direct ductility measurement on a TiAl PST crystal [13, 14]. In DP materials, on the other hand, the effective strains are the same as those (about 3%) for the tensile fracture strains [15].

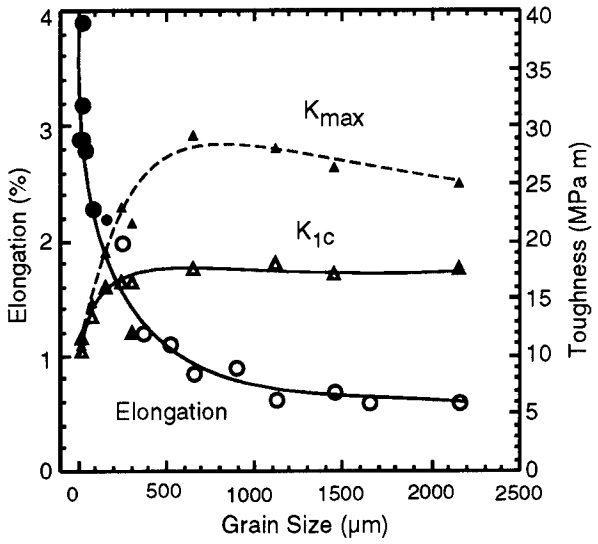


Figure 20. Plots of ductility and fracture toughness against grain size and microstructure, showing an apparent inverse relationship between ductility and fracture-toughness.

A comparison can been made between the measured general tensile curves (Figure 21a) and the stress-strain curves (Figure 21b) within the near-tip plastic zone for coarse (larger than plastic zone size) FL (1100) and fine DP2 materials [30, 31]. The stress strain curves in the plastic zone can be estimated using the following relationship [40] between K1c and the local near crack tip stress-strain response:

$$(K1c)^2 = C\, nE\sigma_y\varepsilon_{lf} \quad \text{..... (B)}$$

where C is a constant, n the local work hardening coefficient, E the elastic modulus, σ_y the material's yield stress, and ε_{lf} the local true fracture strain which corresponds to the maximum effective strain measured near the crack tip. The K_{1c} values used for this estimation were 10.5 and 17.5 MPa$\sqrt{m}$, respectively, for the FL and the duplex materials, Figure 20.

For FL materials, the PZS, r_p, at the onset of crack initiation is calculated to be 400-500 μm using the relation, $r_p=\alpha(K_{1c}/\sigma_y)^2$, and thus is contained within a grain in front of the crack tip. In this case, the local fracture strain is about 20% [15, 30], and the estimated flow curve is shown in Figure 21b. For duplex materials with fine GS's (< 50 μm), the material within the plastic zone (which is estimated to be in the range of 300 μm in size) is fairly isotropic and represents the bulk material with a fracture strain of about 3%, Figure 21 a & b. Thus the near-tip stress-strain curve is essentially identical to the tensile curve, indicating that if viewed from the perspective of local yielding, the toughness and ductility are directly, rather than inversely, correlated.

The above analysis shows that the 'so-called' inverse ductility/toughness relationship is caused simply by the difference in sampling between tensile testing and toughness testing. Within the plastic zone, the material obeys the classical relation between tensile properties and initiation toughness expressed by relation B.

When the grain size in lamellar material is smaller than the PZS, then the GB effects on the toughness may begin to prevail over the lamellar spacing effects [30]. The Stroh stress nucleating a crack at a dislocation pileup (usually against a GB) within the plastic zone may develop at a slightly higher applied stress level but with only a small increase in fracture strain. Systematic studies are needed to quantify the competition between grain size and lamellar spacing using large, thick specimens.

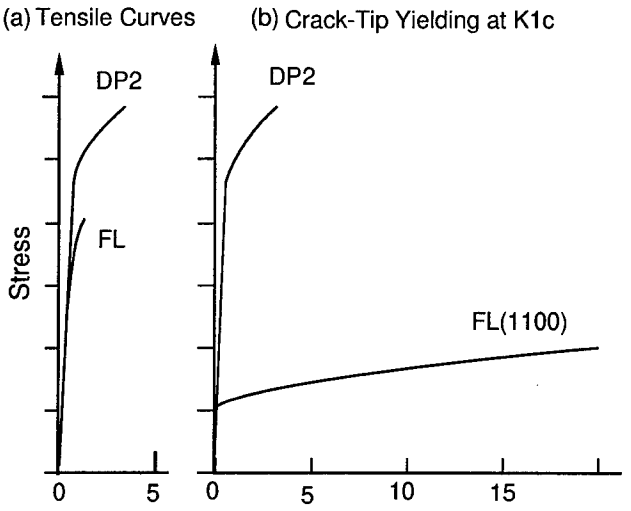


Figure 21. Comparison of general tensile yielding and crack-tip local yielding behavior between duplex material and lamellar material: (a) measured stress-strain curves typical of DP2 and FL (1100) materials (from Figure 4); and (b) estimated local (near crack-tip) flow behavior of DP2 and FL(1100) materials.

4.3 Fatigue Deformation and Failure

Fatigue deformation appears to exhibit trends which follow the tensile deformation behavior in that duplex materials show a higher fatigue stresses (FS) at temperatures below BDTT's but lower FS's than lamellar materials at higher temperatures (for the ranges of grain sizes and lamellar spacings studied). The fatigue deformation was found to be planar and interlamellar at temperatures at least up to 800°C, and the failure modes are predominantly transgranular at RT and increasingly intergranular as temperature increases with lamellar splitting becoming important [29, 33]. Crack initiation takes place at the specimen surfaces for DP material and primarily in the interior, especially at elevated temperatures, for FL materials. Unlike in DP material, the crack initiation in FL material is followed by an observable crack-growth stage. However, the relative significance of the crack-growth stage even in FL material with respect to fatigue lives was estimated to be insignificant [33]. Microstructural inhomogeneity often found in DP materials degrades the fatigue properties [25], as it does reduce tensile ductility [11].

The fracture morphology of the tensile specimen tested at a high strain rate and the fatigue specimen are essentially similar, but not exactly identical in some aspects. For example, the duplex microstructure showed intergranular crack initiation sites at high strain rate tensile testing, whereas under fatigue loading cracks always start transgranularly. This behavior is identical to tensile fracture at low strain rates. This indicates that during fatigue below and above the BDT temperature, and for low strain rate tensile tests above the BDT temperature, the cohesive strength of grain boundaries are higher than that of the grain interior of the duplex microstructure. This aspect needs to be studied in more detail.

CONCLUSIONS

RT and elevated temperature deformation and fracture behavior of gamma TiAl alloys was investigated for duplex (DP) and fully-lamellar (FL) microstructures under tensile, compact-tension and fatigue loading conditions. This paper reports and analyzes some observations made. FL structures are large in grain size in general and result in lower tensile ductility and strength, but greater strength retention at high temperatures, and higher brittle-ductile-transition temperatures than DP structures. These trends are reflected in the temperature dependence of fatigue-strength. An unusually strong relationship exists between yield stress and grain size for FL structures, however, resulting in the strength levels for finer FL microstructures exceeding those for DP structures. Ductility depends upon grain size and is limited by the formation of strain incompatibility induced microcracks which have a size comparable to the grain size. For both microstructures, both tensile and fatigue fracture is preceded by plastic deformation followed by cleavage-like failure. Fracture toughness is also a strong function of microstructure and temperature, with higher toughnesses achieved in FL structures and also at higher temperatures. The high fracture toughness for FL structures is explained in terms of the characteristic properties of the lamellar structure observed at the crack tip and in the crack wake; that is large plasticity and the ability for bridging ligaments to form. The inverse ductility-toughness relationship is explained by comparing the general tensile yielding behavior and the near-tip local plasticity measured at the onset of crack initiation. In all loading conditions, DP materials fail transgranularly at RT and intergranularly at high temperatures. Predominantly transgranular fracture is shown in FL materials over a range of temperatures as long as the microstructures are stable. Decreasing grain size, however, promotes intergranular fracture.

ACKNOWLEDGMENT

The authors acknowledge technical discussions with many researchers and the metallographic assistance of Ms. Sonya Boone, and YWK acknowledges support from the U.S. Air Force Wright Laboratory Materials Directorate, Wright-Patterson AFB, OH under Contract Nos. F33615-91-C-5663 and F33615-96-C-5258.

REFERENCES

1. Y-W. Kim, JOM, 41 (7) (1989), 24-30.

2. Y-W. Kim and D. M. Dimiduk, JOM, 43 (8) (1991), 40-47.

3. M. Yamaguchi and H. Inui, in Structural Intermetallics, eds., R. Darolia et al., TMS, PA , (1993), 127-142.

4. Y-W. Kim, JOM, 46(7) (1994), 30-39.

5. Y-W. Kim, Acta Metall. Mater., 40 (1992), 1121-1134.

6. Y-W. Kim and D. M. Dimiduk, in ISSI-2 Symposium Proc., eds., M. Nathal, et al., TMS, Warrendale, PA, 1997, in press.

7. D. S. Shih, S-C. Huang, et al., in Microstructure-Property Relationships in Titanium Aluminides and Alloys, eds. Y-W. Kim and R. R. Boyer, TMS, Warrendale, PA, (1991), 135-148.

8. S. Krishnamurthy and Y-W. Kim, in Ref. 7, pp. 149-163.

9. A. W. James and P. Bowen, Materials Sci. and Eng., A153 (1992), 486-492.

10. H. A. Lipsitt, D. Shechtman and R. Schafrik, Metall. Trans. A, 6A (1975), 1991-1997.

11. C. Koeppe, A. Bartels, et al., Met. Trans. A, 24A (1993), 1795- 1806.

12. S-C. Huang and E. L. Hall, Metall. Trans. A, 22A, (1991), 427-438.

13. H. Inui, M. H. Oh, A. Nakamura, and M. Yamaguchi, Acta Metall. Mater., 40 (1992), 3095-3104.

14. Y. Umakoshi, T. Nakano and T. Yamane, Mater. Sci. and Eng., A152 (1992), 81-88.

15. K. Chan and Y-W. Kim, Metall. Trans. A,, 23A (1992), 1663-1677.

16. H. E. Deve, A. G. Evans, and D. S. Shih, Acta Metall. Mater., 40 (1992),1259-1265.

17. K. Chan and Y-W. Kim, Metall. Trans. A, 24A (1993), 113-125.

18. Y-W. Kim and D. M. Dimiduk, MRS Symp. Proc, 288 (1993), 671-677.

19. M. G. Mendiratta, Y-W. Kim, and D. M. Dimiduk, MRS Symp. Proc., 288 (1995), 543-548.

20. K. Chan and Y-W. Kim, Acta Metall. Mater., 43 (1995,) 439-451.

21. G. Malakondaiah, Y-W. Kim and T. Nicholas, Scripta Metall., 30 (1994), 939-944.

22. K. Chan and Y-W. Kim, Metall. Trans. A, 25A, (1994), 1217-1228.

23. Y-W. Kim and D. M. Dimiduk, JIMIS-7 Proc. on High Temp. Deformation and Fracture, JIM, Sendai, Japan, 1993, pp. 373-382.

24. M. G. Mendiratta, R. L. Goetz, and D. M. Dimiduk, Metall. & Mater. Trans. A,, 27A (1996) 3903-3912.

25. Y-W. Kim and D. M. Dimiduk, Research in progress.

26. Y-W. Kim and D. M. Dimiduk, US Patent No. 5,226,985, July 13, 1993.

27. Y-W. Kim and D. M. Dimiduk, Filed for a US Patent, 22 April 1994.

28. K. V. Jata, N. U. Deshpande, and Y-W. Kim, Mater. Sci. & Eng., Submitted for publication (May, 1997).

29. J. Kumpfert, Y-W. Kim and D. M. Dimiduk, Mater. Sci. & Eng., A192/193 (1995), 465-473.

30. Y-W. Kim, Mater. Sci. & Eng., A192/193 (1995), 519-533.

31. Y-W. Kim, in Intermetallic Compounds, Proc. 3rd Japan International SAMPE Symp., Chiba, Japan, 1993, pp. 310-1317.

32. S-C. Huang and D. S. Shih, in Ref. 7, pp. 105-122.

33. Y-W. Kim, To be submitted to Metall. Mater. Trans A (1997).

34. D. M. Dimiduk, P. M. Hazzledine, T. A. Parthasarathy, S. Seshagari, and M Mendiratta, Metall. & Mater. Trans. A, (Submitted, March 1997).

35. A. N. Stroh, Phil. Mag., 46 (1955), 968-972.

36. A. N. Stroh, Proc. Royal Soc., A233 (1954), p. 404.

37. P. M. Hazzledine, B. K. Kad and M. G. Mendiratta, MRS Symp. Proc., 308 (1993), 725-730.

38. A. S. Booth and S. G. Roberts, Acta Mater., 45(3) (1997), 1045-1053.

39. M. H. Oh, H. Inui and M. Yamaguchi, Acta Metall. Mater., 41(7) (1993), 1939-1949.

40. J. Langford, et al., AFOSR Report, Southwest Research Institute, May 1989.

AN INVESTIGATION OF CLEAVAGE FRACTURE IN Mn-CONTAINING GAMMA-BASED TITANIUM ALUMINIDES

W. O. Soboyejo, C. Mercer and K. Lou

Department of Materials Science and Engineering, The Ohio State University, 2041 College Road, Columbus, OH 43210-1179.

Abstract

The results of a recent study of cleavage fracture are presented for ternary Mn-containing gamma-based titanium aluminides with duplex α_2 + γ microstructures. Yield and ultimate tensile strength and fracture toughness are shown to exhibit an inverse square root (Hall-Petch) dependence on the average grain size in these alloys. The Hall-Petch dependence is rationalized using an initiation-controlled fracture model. The high incidence of intergranular cleavage in Mn-containing alloys is shown to occur primarily as a result of the preferential segregation of Mn to grain boundaries.

I. Introduction

The fracture behavior of nearly/fully lamellar gamma-based titanium aluminides has been studied extensively in recent years by a number of investigators [1-11]. However, there have been fewer studies of fracture in duplex gamma alloys that are known to have higher ductilities but lower fracture toughness levels than their nearly/fully lamellar counterparts. Nevertheless, duplex gamma alloys have been studied in recent years because of the possible balance of properties that can be engineered in such alloys. These include room-temperature ductilities of 1-3% and fracture toughness levels between 15 and 25 MPa$\sqrt{m}$ [1,7,12].

The fracture behavior of duplex gamma alloys was first investigated by Lipsitt and co-workers [13]. In their studies, they showed that fracture in duplex binary alloys occurs predominantly by cleavage fracture mechanisms. They also observed a transition from cleavage to intergranular fracture at around 650 to 700°C. Subsequent work by Soboyejo et al. [6] showed that the transition from cleavage to intergranular failure was also associated with the segregation of sulphur to grain boundaries.

The effects of alloying on fracture mechanisms have also been studied by Mercer and Soboyejo in recent years [11,12]. These studies have shown that the room and elevated temperature failure modes in gamma alloys depend strongly on the alloying content (Cr, Mn, V, Nb) and microstructure. However, the basic causes of the changes in failure mode are not fully understood.

The current paper presents recent evidence of the fundamental causes of intergranular fracture in Mn-containing gamma alloys. Intergranular fracture is shown to occur predominantly as a result of the segregation of manganese to grain boundaries. The segregation of manganese is also shown to promote stable intergranular crack extension prior to catastrophic failure. Finally, room and elevated temperature yield/ultimate tensile strength and room temperature fracture toughness are shown to exhibit an inverse square root (Hall-Petch) dependence on the average grain/lamellar packet size. The observed Hall-Petch dependence is rationalized by considering dislocation/microstructure interactions associated with nucleation-controlled fracture.

The current paper is divided into six sections. The relevant theory is discussed briefly in Section II prior to a description of the materials, heat treatment schedules and microstructures in Section III. Experimental techniques are described in detail in Section IV. The experimental results and discussion of results are then presented in Section V. Finally, salient conclusions arising from the current study are summarized in Section VI.

II. Background Theory

The theory of cleavage fracture is presented in this section along with a summary of previous reports of Hall-Petch behavior [14-16]. Following the classical work of Orowan [17], cleavage fracture was generally believed to occur when bulk yield was preceded by atomic separation. However, subsequent work on notched or pre-cracked specimens showed that cleavage fracture could be preceded by localized crack-tip plasticity, i.e. dislocation motion. Since forward dislocation motion is often promoted by the applied stress fields, Stroh [18] postulated that nucleation-controlled cleavage fracture may occur as a result of dislocation pile-up against local microstructural features such as grain boundaries or precipitates. Such pile-up phenomena may give rise to slip or deformation-induced twinning in adjacent grains, or microcracking at the grain boundaries or in adjacent grains.

For the case of microcrack nucleation due to pile-up phenomena (Fig. 1), Stroh postulated that the microcrack nucleus will spread when the effective shear stress exceeds a critical value. Hence, for nucleation-controlled fracture, the effective stress required for the spread of a nucleus, τ_{eff}, is given by:-

$$\tau_{eff} = \tau_y - \tau_i \geq \frac{\pi\mu\gamma}{2(1-\nu)d} \qquad (1)$$

where τ_y is the applied shear stress, τ_i is the lattice frictional shear stress, μ is the shear modulus, γ is the shear strain, ν is Poisson's ratio and d is the average grain diameter. For nucleation-controlled fracture, Stroh also obtained the following expression for the cleavage fracture stress, σ_F, [18] :-

$$\sigma_F = \sigma_o + k_F d^{-1/2} \qquad (2)$$

George R. Irwin Symposium on Cleavage Fracture
Edited by Kwai S. Chan
The Minerals, Metals & Materials Society, 1997

where σ_o is a measure of the lattice frictional stress and k_F is a dislocation unpinning parameter. Equation 2 is similar in form to the Hall-Petch equation which was proposed earlier for the prediction of the grain size dependence on yield strength [14,15]. However, the constants in the Hall-Petch and Stroh equations have different numerical values.

Subsequent work by Cottrell [19] showed that fracture processes are not generally initiation-controlled. Instead, Cottrell argued that most fracture processes in ductile materials are propagation controlled. Cottrell thus obtained the following expression for the fracture stress, σ_F, as a function of grain size:-

$$\sigma_F \geq \frac{2\mu\gamma}{k_y^s} d^{-1/2} \qquad (3)$$

where k_y^s is a similar parameter to k_F in Equation (2), although it has a different numerical value. Note that the above equation also exhibits a dependence on $d^{-1/2}$. The work by Stroh [18] and Cottrell [19] also provided the basis for an alternative model for cleavage fracture in steels. This was proposed by Smith [20], who was the first to incorporate the effect of carbide particles. Using dislocation analysis, Smith showed that the cleavage fracture stress, σ_F, is related to grain size, d, and yield stress, τ_y, by the following expression:-

$$\left(\frac{c_o}{d}\right)^2 \sigma_F + \tau_y^2 \geq \frac{4E\gamma}{\pi(1-\nu^2)d} \qquad (4)$$

where c_o is the width of a carbide particle and E is the Young's modulus. Smith's model may be used to assess cleavage fracture in gamma titanium aluminides in which the effects of brittle α_2 precipitates are somewhat analogous to the effects of carbides in steels, i.e. the role of α_2 precipitates on the initiation of cleavage fracture in gamma titanium aluminides may be similar to the effect of carbide particles in steels. Further work on other materials have led numerous investigators to conclude that cleavage fracture generally nucleates from stress raisers (such as hard or brittle particles) in regions of high stress concentration in the vicinity of a notch or crack-tip. Such concepts have been developed by Ritchie, Knott and Rice in the R-K-R model [21]. The statistical aspects of cleavage fracture have also received further treatment in later work by Lin, Evans and Ritchie [22].

III. Material

The ingot material that was used in this study was procured from Duriron, Inc., Dayton, OH. Special precautions were made by Duriron to ensure that the 8.89 mm (~3.5 in.) diameter ingots had very low levels of interstitial oxygen and carbon after casting. These involved the use of "ultra clean" starting stock, and very high purity processing environments. The resulting ingot compositions, presented in Table I, are therefore significantly different from those in so-called "standard" gamma alloys. Note that the actual levels of Ti, Al, and Mn were very close to the intended nominal compositions. However, the levels of interstitial oxygen and carbon are below typical values of 0.6-0.8 and 0.2-0.3, respectively. The ingots were subsequently HIPed at 172 MPa for 4 hours at a temperature of 1260°C.

The ingots were extruded at The Wright Patterson Air-Force Base, Dayton, OH. The Ti-48Al-1.4Mn alloy (alloy A) was extruded with a reduction ratio of 14:1 at 1343°C. However, two processing conditions were used for the extrusion of the Ti-48Al-2Mn alloy. The first extrusion of this alloy was carried out at 1343°C with a reduction ratio of 14:1 to produce alloy B, while the second extrusion was carried out at 1343°C with a 10:1 reduction ratio to produce alloy C. The two extrusion conditions were used to explore the possible effects of stored work, which has been shown to strongly affect the fracture behavior of other gamma alloys [3].

The extruded alloys were subjected to two sets of heat treatments designed to change the volume fractions of lamellar and equiaxed grains, as well as the grain/packet sizes [3]. The first set of heat treatments involved recrystallization at different temperatures above the eutectoid temperature (1150 or 1250°C), prior to annealing for 4 or 100h at 982°C (below the eutectoid temperature). The second set of heat treatments involved only annealing sequences below the eutectoid. These included: annealing at 982°C for 4h or 100h, and an empirical three-stage heat treatment, HTC = 982°C/4h/AC + 704°C/8h/FC + 815°C/24h/AC (AC = Air Cool and FC = Furnace Cool), which has been shown to result in attractive combinations of room- and elevated-temperature properties in a wide range of gamma alloys [3]. It is important to note here that the elevated-temperature properties of the different alloys were not determined in the as-extruded conditions due to inherent microstructural instabilities of the alloys at the test temperature (815°C). A detailed analysis of the microstructural features of these as-extruded and heat treated gamma alloys is presented in Ref. 11.

Table I. Actual Compositions (Atomic %) of Cast Gamma Alloys

Alloy Composition	Constituent Elements							
	Ti	Al	C	O	N	H	Mn	S
Ti-48Al-1.4Mn	Bal	50.8	0.149	0.093	0.013	0.037	0.968	0.010
Ti-48Al-2Mn	Bal	48.2	0.041	0.099	0.086	0.075	1.983	0.010

Bal = Balance of composition

IV. Experimental Procedures

Following extrusion and heat treatment, the fracture properties of the alloys were investigated at room- and elevated-temperature. Tensile tests were performed on smooth "button-headed" cylindrical specimens with a gauge diameter of ~3 mm. The specimens were loaded monotonically to failure at a ramp rate of 5×10^{-4} s^{-1}. Fracture toughness tests were then performed in accordance with ASTM code E399 on single edge notched (SEN) bend specimens produced by electro-discharge machining (EDM), following pre-cracking under far-field compression [23]. The SEN specimens were loaded monotonically to failure under four-point (pure bend) loading using a ramp rate that corresponded to a stress intensity factor increase rate of 0.92 $MPa\sqrt{m}.s^{-1}$ at the crack-tip.

Fracture initiation mechanisms were studied using double edge notched (DEN) bend specimens containing identical notches which were also loaded to failure under four-point (pure) bend loading using the same stress intensity factor increase rate as was used for the SEN specimens. The separation of the notches (three times the notch depth of 2.5 mm) was chosen to ensure that the notches were independent and nominally identical during the initiation of stable crack growth. Stable crack growth was, therefore, expected to be similar in the two notches during the initial stages of damage. However, catastrophic failure was expected to occur from only one of the notches, thus leaving the other (unfractured) notch with useful information on the stable crack growth or crack initiation phenomena prior to final failure.

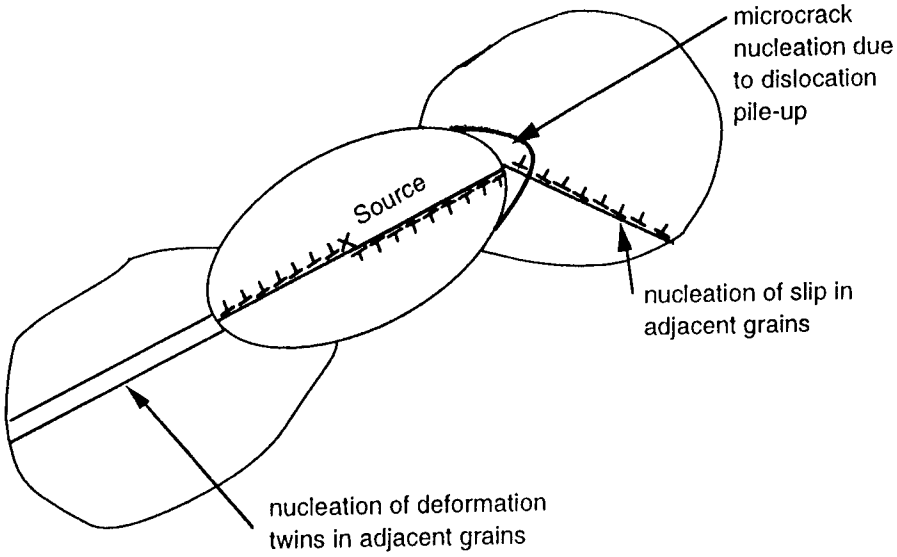


Figure 1. Schematic illustration showing microcrack nucleation due to dislocation pile-ups at grain boundaries.

In-situ Auger fracture experiments were conducted on impact specimens with square (1mm x 1mm) cross sections and a height of 9mm. The specimens, which were produced by electro-discharge machining, were fractured and analyzed in a Perkin-Elmer (PHI-600) scanning Auger microprobe (SAM). The vacuum pressure in the Auger chamber was approximately 1 x 10^{-8} Pa. A 10 kV electron beam, with a diameter of 0.3 μm, was used in the SAM analysis of intergranular and cleavage facets that were observed on the fracture surfaces of the impact specimens. Auger spectra were also obtained from α_2 precipitates that were observed on the grain boundary facets of all the specimens that were examined. These included specimens annealed solely below the eutectoid and those subjected to two-stage annealing above and below the eutectoid temperature. Secondary electron micrographs of the typical regions on the fracture surfaces were also obtained to illustrate the above features, and the fracture mechanisms were studied using techniques described in detail in Refs. 12 and 24.

V. Results and Discussion

(a) Tensile Properties and Fracture

The room and elevated temperature tensile properties for alloys A, B and C are given in Tables II-IV. Plots of room and elevated temperature yield stress and ultimate tensile stress versus $d^{-1/2}$, where d is the average grain/lamellar packet diameter, are presented in Figs. 2 and 3, respectively, in order to determine whether these alloys exhibited a Hall-Petch type strength dependence with grain size. The linear nature of the plots clearly show that yield stress and ultimate tensile stress exhibit a Hall-Petch dependence with grain/lamellar colony size. Therefore, as grain size increases as a consequence of higher temperature/duration annealing, a corresponding loss of strength will result. This is consistent with the experimental observations (Tables II-IV).

In addition to the effect of grain size discussed above, the reduction in yield/tensile strength that was observed with increasing thermal exposure, was also found to be associated with the occurrence of increased levels of intergranular fracture at room- and elevated-temperature, as shown by the fracture surfaces presented in Figs. 4 and 5. Such behavior is not typical of gamma alloys which tend to fail predominantly by cleavage or quasi-cleavage at room temperature [3,25,26]. It is important to note here that the fracture surfaces of the alloys subjected to two-stage annealing contained a high fraction of α_2 precipitates on the intergranular facets as shown in Fig. 4 (d). The α_2 precipitates will reduce the cohesion of the grain boundaries, and thus promote the occurrence of intergranular fracture.

Crucial evidence of the main cause of intergranular fracture at room temperature was provided by the in-situ Auger fracture studies. The Auger analysis of grain boundary facets and cleavage facets in the specimen annealed at 982°C for 100 h revealed that very high levels of Mn was present at the grain boundaries, in addition to Ti, Al, C, and O (Table V). However, very little Mn was detected on the cleavage facets which were observed to contain Ti, Al, C, and O (Table V). A typical fracture surface of an impact specimen that was fractured in-situ in the SAM is shown in Fig. 6. Stronger evidence of the role of Mn segregation was obtained from the specimen subjected to two-stage annealing at 1250°C/2h/AC + 982°C/4h/AC, as shown in Table V. However, S was not detected on the grain boundary facets of this specimen, presumably as a result of the relatively high level of Mn segregation which may have obscured the experimental evidence of S segregation. This is possible since the levels of S in the bulk are extremely small in comparison with those of the Mn, as shown in Table I.

The results, therefore, indicate that intergranular fracture is promoted by the segregation of Mn to grain boundaries during extrusion and annealing solely below the eutectoid. There is also

Table II. Effects of Heat Treatment on the Mechanical Properties of Alloy A

(a) 25°C

Heat Treatment/ Condition	Fracture Toughness (MPa√m)	Plastic Elongation to Failure (%)	Offset Yield Stress (MPa)	Ultimate Tensile Stress (MPa)	Young's Modulus (GPa)	Predicted Yield Stress (MPa)
1250°C/2h/AC+982°C/4h/AC	4.0	1.2	345	399	153	474
1250°C/2h/AC+982°C/100h/AC	7.7	0.8	320	359	197	436
1150°C/2h/AC+982°C/4h/AC	9.7	1.3	334	397	143	406
1150°C/2h/AC+982°C/100h/AC	7.8	1.0	310	354	148	345
982°C/4h/AC	10.8	1.4	418	475	142	312
982°C/100h/AC	7.0	0.6	321	342	142	342
HTC	11.5	1.6	409	475	157	328
As-Extruded*	24.7	1.6	482	599	152	474

(b) 815°C

Heat Treatment	Plastic Elongation to Failure (%)	Offset Yield Stress (MPa)	Ultimate Tensile Stress (MPa)
1250°C/2h/AC+982°C/4h/AC	2.6	279	382
1250°C/2h/AC+982°C/100h/AC	1.4	274	392
1150°C/2h/AC+982°C/4h/AC	3.4	275	361
1150°C/2h/AC+982°C/100h/AC	8.4	272	414
982°C/4h/AC	29.2	354	464
982°C/100h/AC	6.2	270	400
HTC	50.1	325	436

AC = Air Cool; FC = Furnace Cool * - Included for comparison
HTC=982°C/4h/AC+704°C/8h/FC+815°C/24h/AC

Table III. Effects of Heat Treatment on the Mechanical Properties of Alloy B at 25°C

Heat Treatment/ Condition	Plastic Elongation to Failure (%)	Proportionality Limit (MPa)	Offset Yield Stress (MPa)	Ultimate Tensile Stress (MPa)	Young's Modulus (GPa)	Predicted Yield Stress (MPa)
1250°C/2h/AC+982°C/4h/AC	0.2	324	348	352	151	-+
1250°C/2h/AC+982°C/100h/AC	0.6	320	335	355	216	359
1150°C/2h/AC+982°C/4h/AC	0.6	297	318	349	155	-+
1150°C/2h/AC+982°C/100h/AC	0.6	290	313	338	168	353
982°C/4h/AC	1.3	264	367	419	160	-+
982°C/100h/AC	0.6	303	317	340	162	350
HTC	1.2	350	357	397	146	-+
As-Extruded*	0.8	421	452	532	173	430

AC = Air Cool; FC = Furnace Cool * - Included for comparison
HTC=982°C/4h/AC+704°C/8h/FC+815°C/24h/AC + - Not predicted (insufficient data)

some evidence of the segregation of S to the grain boundaries. However, the detected levels of S are small in comparison with the detected levels of Mn at the grain boundaries. The reduction in yield/tensile strength and that was observed to occur upon heat treatment at high temperatures/durations may, therefore, be attributed partly to the Hall-Petch dependence of yield/tensile strength on grain size and partly to the reduction of grain boundary cohesion that occurs as a result of Mn and S segregation.

Table IV. Effects of Heat Treatment on the Mechanical Properties of Alloy C

(a) 25°C

Heat Treatment/ Condition	Fracture Toughness (MPa √m)	Proportionality Limit (MPa)	Plastic Elongation to Failure (%)	Offset Yield Stress (MPa)	Ultimate Tensile Stress (MPa)	Young's Modulus (μm)	Predicted Yield Stress (GPa)
1250°C/2h/AC+982°C/100h/AC	5.8	319	0.4	332	349	168	–+
1150°C/2h/AC+982°C/4h/AC	6.1	302	0.4	308	330	208	333
1150°C/2h/AC+982°C/100h/AC	7.0	299	0.6	290	332	177	313
982°C/4h/AC	6.3	368	1.1	359	396	190	–+
982°C/100h/AC	5.6	299	0.6	306	334	205	315
HTC	6.6	361	1.4	357	394	170	–+
As-Extruded*	8.9	385	1.7	392	487	174	377

(b) 815°C

Heat Treatment	Plastic Elongation to Failure (%)	Offset Yield Stress (MPa)	Ultimate Tensile Stress (MPa)
1250°C/2h/AC+982°C/4h/AC	0.8	286	303
1250°C/2h/AC+982°C/100h/AC	0.7	286	324
1150°C/2h/AC+982°C/4h/AC	0.9	272	324
1150°C/2h/AC+982°C/100h/AC	0.3	279	287
982°C/4h/AC	33.9	288	395
982°C/100h/AC	2.3	265	355
HTC	39.9	279	400

AC = Air Cool; FC = Furnace Cool * - Included for comparison
HTC=982°C/4h/AC+704°C/8h/FC+815°C/24h/AC + - Not predicted (insufficient data)

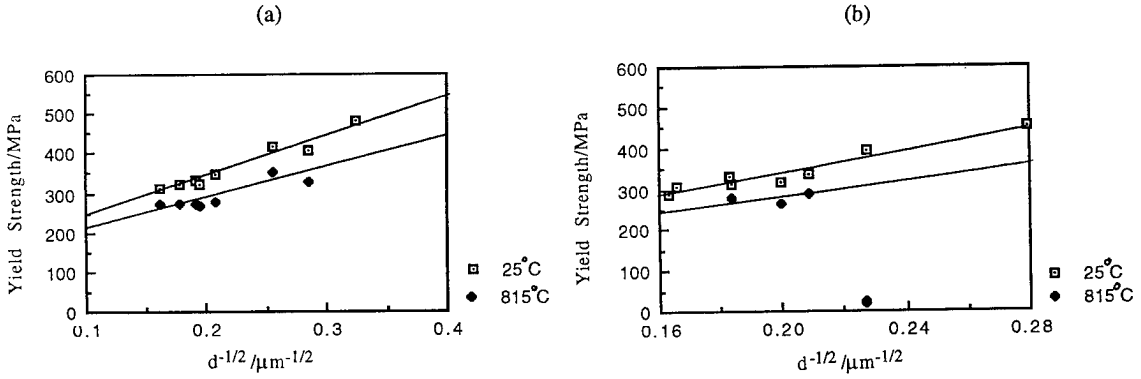


Figure 2. Plots of yield stress versus $d^{-1/2}$ showing Hall-Petch behavior for (a) alloy A and (b) alloy B.

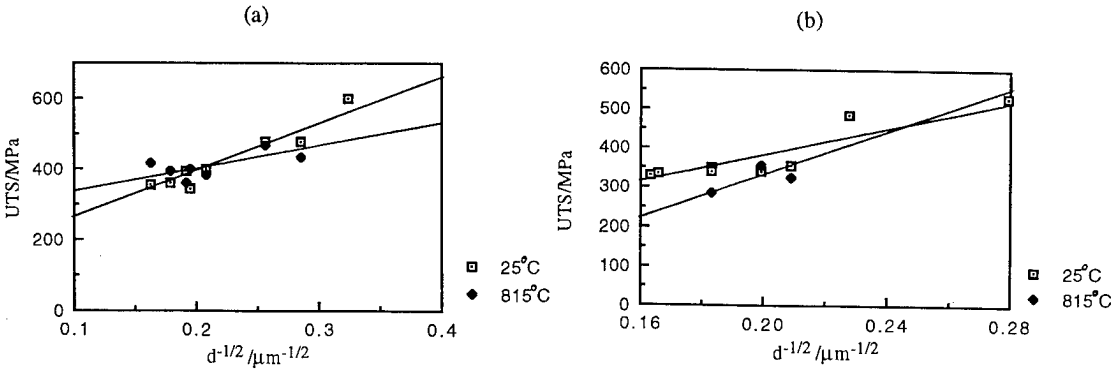


Figure 3. Plots of ultimate tensile stress versus $d^{-1/2}$ showing Hall-Petch type behavior for (a) alloy A and (b) alloy B.

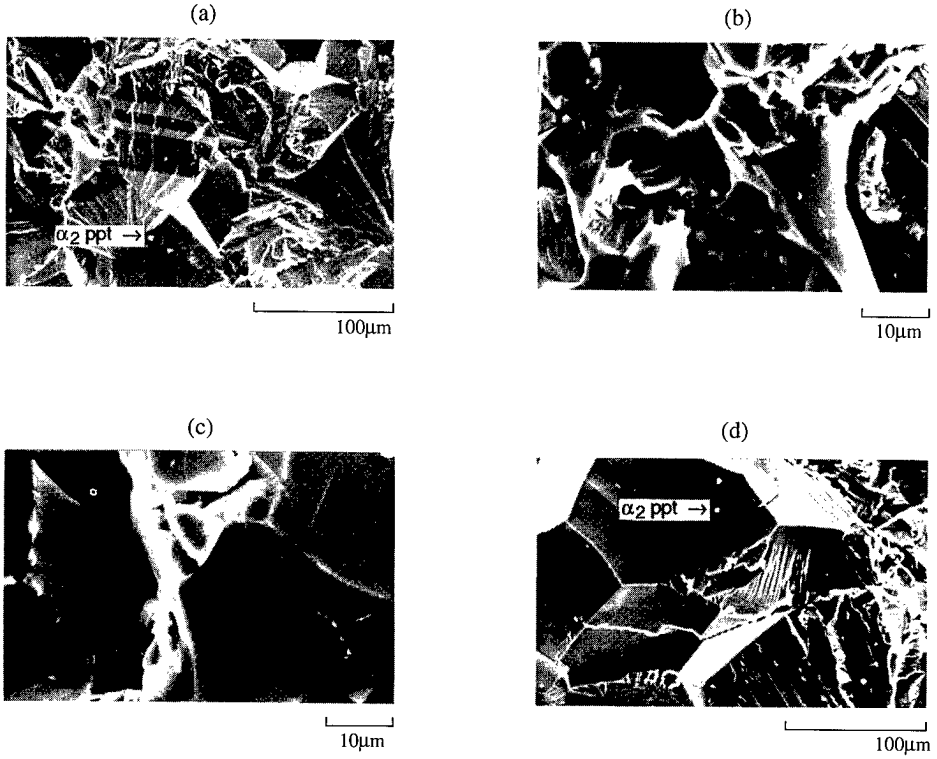


Figure 4. Fracture surfaces following tensile fracture at room temperature for (a) alloy B (1150°C/2h/AC + 982°C/4h/AC), (b) alloy B (1250°C/2h/AC + 982°C/4h/AC), (c) alloy C (1150°C/2h/AC + 982°C/4h/AC) and (d) alloy C (1250°C/2h/AC + 982°C/4h/AC).

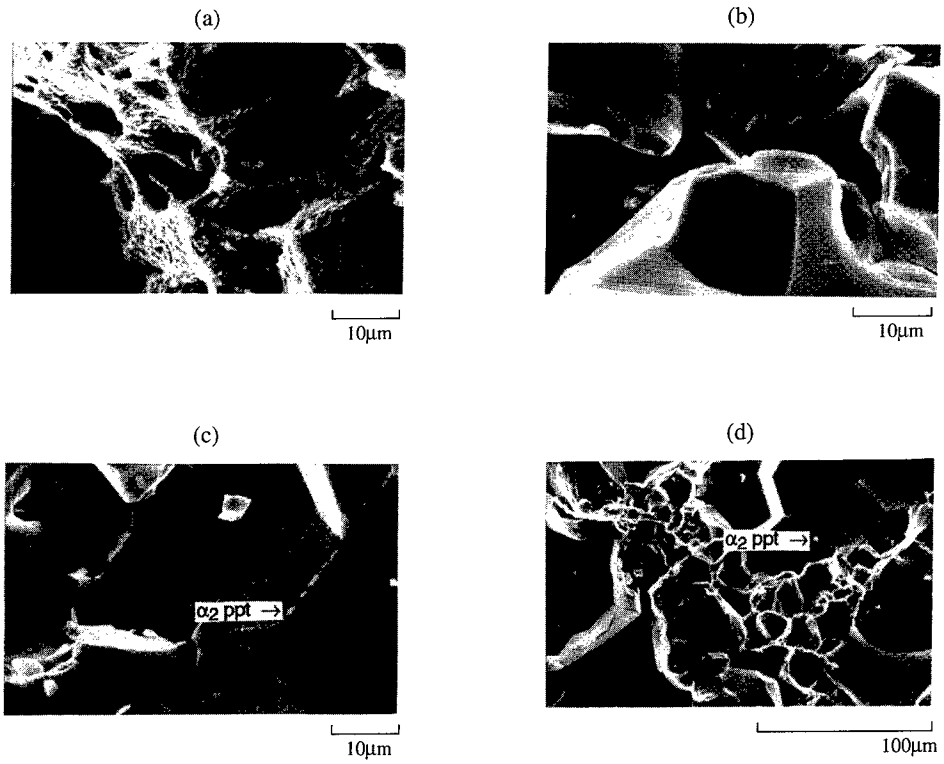


Figure 5. Fracture surfaces following tensile fracture at 815°C for (a) alloy A 982°C/4h/AC), (b) alloy A (982°C/100h/AC), (c) alloy B (1150°C/2h/AC + 982°C/100h/AC) and (d) alloy B (1250°C/2h/AC + 982°C/100h/AC).

(b) Fracture Toughness

With the exception of as-extruded Ti-48Al-1.4Mn, all the alloys had very low fracture toughness values (Tables II-IV), in comparison with other gamma alloys [1,2,3,5,7,12]. The low fracture toughness levels are attributed to the occurrence of intergranular fracture (Fig. 4) instead of the transgranular cleavage fracture mode that is typically observed at room temperature. Also, the fracture toughness levels generally decreased with increasing Mn content and annealing duration, as would be expected from alloys that are susceptible to Mn segregation. Sulphur segregation may also play an additional role, as was observed in the impact fracture specimens that were failed in-situ in the scanning Auger microprobe. The relatively low fracture toughness values obtained in this study are, therefore, attributed largely to the reduction of grain boundary cohesion by Mn and S segregation. The lower fracture toughness values of the alloys subjected to two-stage annealing are also attributed partly to the precipitation of grain boundary α_2 precipitates (Fig. 4) which can also reduce grain boundary cohesion.

Table V. Auger Estimates of Fracture Surface Compositions of Alloy B Annealed at 1250°C/2h/AC + 982°C/100h/AC.

Region on Fracture Surface	Composition (Atomic %) Al	Ti	O	C	Mn
Grain Boundary Facet (GBF)	35	54	1	2	8
Cleavage Facet	29	56	8	5	2
Alpha-2 Particle on GBF	27	55	6	5	7

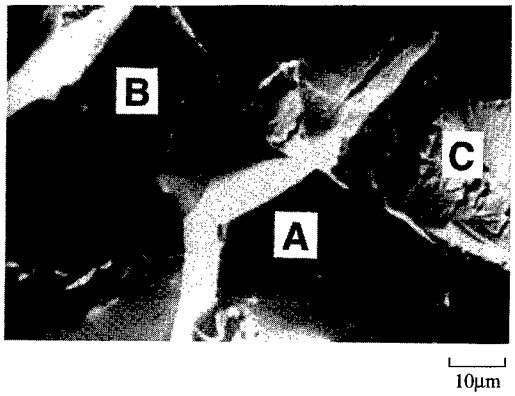


Figure 6. Typical fracture surface of impact specimen fractured in Auger chamber: A - grain boundary facet, B - cleavage facet and C - α_2 particle.

A possible cause of the reduction in fracture (initiation) toughness was revealed by the double-notched specimens which were used to study the crack initiation mechanisms. These showed clearly that crack initiation occurred predominantly at the grain boundaries located at the notch-tip or in the regions slightly ahead of the notch and that stable crack growth prior to catastrophic failure occurred by an intergranular mode, (Fig. 7).

Prior to grain boundary microcrack nucleation, it is presumed that dislocations pile up against the grain boundaries within the regions of high stress concentration at the notch-tip. In some cases, pile-up may result in the initiation of deformation-induced twinning or slip as discussed in a previous paper [11]. However, in the case of materials with reduced grain boundary cohesion, intergranular microcrack nucleation may occur, as shown from the unfractured halves of the double-notched specimens (Fig. 7).

Upon the nucleation of the initial microcracks, stable crack growth may occur. However, the extent of stable crack growth depends on the microstructure of the gamma alloys [7,8]. In the case of duplex alloys, such as those examined in this study, the resistance to stable crack growth is very limited [7,8]. We may therefore assume that fracture in duplex gamma alloys is initiation-controlled. The assumption of initiation-controlled fracture is well supported by the 'Stroh' plots of ultimate tensile stress versus $d^{-1/2}$ (Fig. 3).

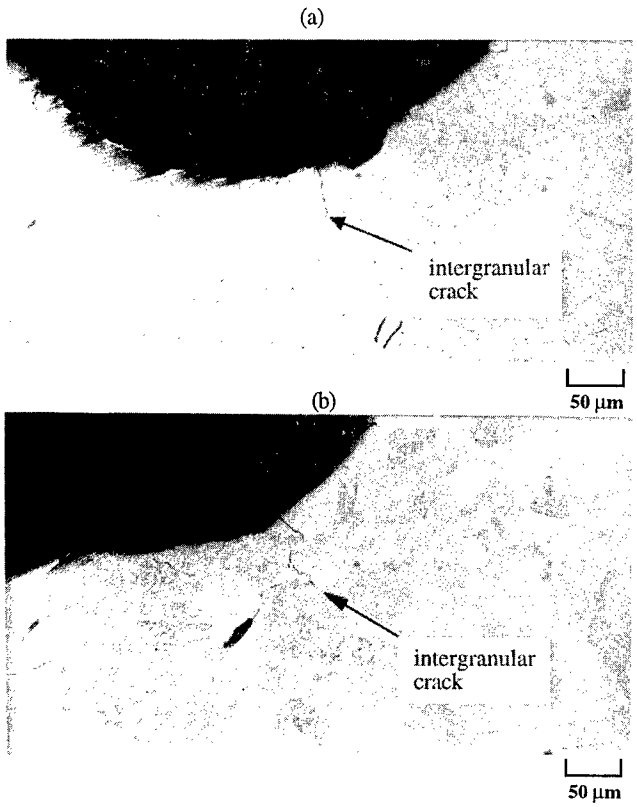


Figure 7. Initiation of intergranular fracture in DEN fracture toughness specimens of alloy B annealed at 1250°C/2h/AC + 982°C/100h/AC.

The assumption of initiation-controlled fracture is also supported by plots of room temperature fracture toughness, K_{Ic}, versus $d^{-1/2}$, that are presented in Fig. 8. These show clearly that, in addition to yield/tensile strength, a Hall-Petch type dependence on grain size also exists for fracture toughness. Armstrong [27] has proposed the following expression that relates fracture toughness, K_c, to grain size by a similar inverse square root dependence:-

$$K_c = CS^{1/2} [\sigma_o + k\, d^{-1/2}] \qquad (5)$$

where C is a constant of proportionality and S is the width of the plastic zone around the crack tip during fracture. The trends shown in Fig. 9 certainly support this theory which was proposed originally for conventional metallic materials such as steels and aluminum alloys.

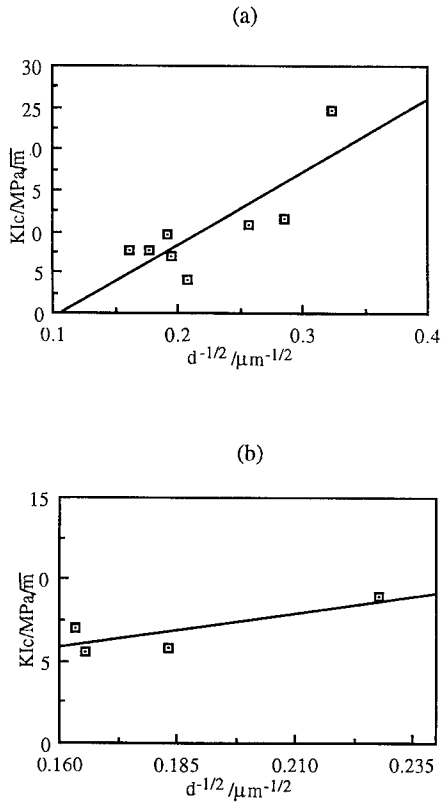


Figure 8. Plots of fracture toughness, K_{Ic} versus $d^{-1/2}$ showing Hall-Petch type behavior for (a) alloy A and (b) alloy B.

VI. Conclusions

1. Fracture in Mn-containing gamma alloys occurs predominantly as a result of intergranular fracture. Intergranular fracture in these alloys is associated with the segregation of Mn and S to grain boundaries during processing or heat treatment.

2. Fracture in duplex Mn-containing gamma alloys is initiation-controlled. The measured fracture strengths and fracture toughness levels exhibit an inverse square root dependence on $d^{-1/2}$ that is consistent with the 'Stroh' model for initiation-controlled cleavage fracture. A similar dependence of the yield strength on $d^{-1/2}$ is observed at room- and elevated temperature. However, the empirical constants are different.

3. The strong dependence of yield/ultimate strength and fracture toughness on $d^{-1/2}$ is consistent with the results obtained for conventional metallic materials [27]. The dislocation-based arguments proposed in this paper may, therefore, have general implications for other materials. However, further work is required to verify these possibilities.

Acknowledgments

The research has been supported by a grant from The Division of Materials Research of The National Science Foundation, with Dr. Bruce MacDonald as Program Monitor. The authors are also grateful to Professor Ron Armstrong for his useful discussions on the effects of grain size.

References

1. Y-W. Kim and D. M. Dimiduk: J. of Metals, 1991, Vol. 43, pp. 40-47.

2. W. O. Soboyejo: An Investigation of then Effects of Heat Treatment on Microstructure and Fracture Behavior of Extruded Ti-48Al-1.5Cr, Proceedings of the 7th World Conference on Titanium, San Diego, CA, June 28-July 2, 1992, The Minerals, Metals and Materials Society.

3. W. O. Soboyejo, D. S. Schwartz and S. M. L. Sastry: Metall. Trans. 1992, Vol. 23A, pp. 2039-2059.

4. K. S. Chan and Y-W. Kim: Metall. Trans. 1992, Vol. 23A, pp. 1663-1677.

5. Y-W. Kim: Acta Metall. Mater. 1992, Vol. 40, pp. 1121-1134.

6. W. O. Soboyejo, K. Lou and M. McConnell: Scripta Metall. Mater. 1994, Vol. 31, No. 1, pp. 63-68.

7. K. S. Chan: J. of Metals, 1992, Vol. 44, pp. 30-38.

8. K.S. Chan: Metall. Trans. 1993, Vol. 24A, pp. 569-583.

9. A. W. James and P. Bowen: Fracture and Fatigue of TiAl based Aluminides, Proceedings of the 7th World Conference on Titanium, San Diego, CA, June 28-July 2, 1992, The Minerals, Metals and Materials Society.

10. H. Dève and A. G. Evans: Acta Metall. Mater. 1991, Vol. 39, pp. 1171-1176.

11. W. O. Soboyejo, C. Mercer, K. Lou and S. Heath: Metall Trans. 1995, Vol. 26A, pp. 2275-2291.

12. W. O. Soboyejo and C. Mercer: The Effects of Alloying and Microstructure on the Fracture of Intermetallic Compounds Based on TiAl, Symposium on Fatigue and Fracture of Ordered Intermetallics, W. O. Soboyejo, T. S. Srivatsan and D. L. Davidson, Editors, TMS, Warrendale, PA, 1993.

13. H. A. Lipsitt, D. Shectman and R. E. Schafrik: Metall Trans. 1975, Vol. 6A, pp. 1991-1996.

14. E. O. Hall, Proc. Phys. Soc., 1951, 64B, p. 747.

15. N. J. Petch, Iron Steel Inst., 1953, 173, p. 25.

16. C. Mercer and W. O. Soboyejo: Scripta Metall. Mater. 1996, Vol. 35, No. 1, pp. 17-22.

17. E. Orowan: Trans. Inst. Engrs. Shipbuilders Scot., 1945, 89, p. 165.

18. A. N. Stroh, Proc. R. Soc. , 1954, A223, p. 404.

19. A. H. Cottrell: Trans. Am. Inst. Min. Metall. Petrol. Engrs., 1958, 212, p. 192.

20. Smith, E: Proceedings of the Conference on the Physical Basis of Yield and Fracture, 1966, Inst. Phys. Phys. Soc. Oxford, England, p. 36.

21. R. O. Ritchie, J. F. Knott and J. R. Rice: Journal of the Mechanics and Physics of Solids, 1973, Vol. 21, pp. 395-410.

22. T. Lin, A. G. Evans and R. O. Ritchie: Journal of the Mechanics and Physics of Solids, 1986, Vol. 34, pp. 477-497.

23. S. Suresh and J. R. Brockenbrough: Acta Metall. 1988, Vol. 36, pp. 1444-1470.

24. W. O. Soboyejo, K. T. Venkateswara-Rao, S. M. L. Sastry and R. O. Ritchie: Metall. Trans. 1992, Vol. 24A, pp. 585-600.

25. D. Shectman, M. J. Blackburn and H. A. Lipsitt: Metall. Trans. 1974, Vol. 5, pp. 1373-1381.

26. A. W. Thompson: Proceedings of the 7th World Conference on Titanium, TMS, Warrendale, PA, 1992, Vol. II, pp. 1155-1161.

27. R. W. Armstrong, Hall-Petch Analysis of Yield, Flow and Fracturing, Materials Research Society Proceedings, (in press).

BRITTLE FRACTURE IN B2 COMPOUNDS

P.R. Munroe# and I. Baker*

Materials Science and Engineering, University of New South Wales, Sydney, NSW 2052, Australia

* Thayer School of Engineering, Dartmouth College, Hanover, NH 03755

Abstract

The fracture behavior of ordered b.c.c. or B2 compounds is reviewed. Although only a small number of compounds with this crystal structure have been studied in detail, it is apparent that a large number of factors influence the fracture behavior of these materials. Polycrystalline NiAl is intrinsically brittle because it deforms by <001> slip, which provides insufficient slip systems for plastic flow. In contrast, single crystal NiAl is intrinsically quite tough and ductile, but poor ductility can result from factors such as impurities, heat treatment and sample orientation. Similarly, the fracture of FeAl is strongly affected by extrinsic factors such as heat-treatment and testing environment, but also suffers from intrinsically weak grain boundaries. It is apparent that an understanding of the extrinsic factors which may affect B2 compounds is required so that the intrinsic fracture behavior of the compound can be determined.

Introduction

Intermetallic compounds, in particular transition metal aluminides, have received considerable attention over the past twenty years. These materials offer the potential of high strength, high creep resistance, together with low density and good oxidation resistance. Unfortunately, many of the compounds exhibit both low ductility and low fracture toughness around room temperature. The problem of poor toughness cannot be attributed to a single cause but arises from a variety of phenomena [1]. One of the most common is the adoption of a large unit cell and/or low symmetry crystal structure, in which difficult dislocation nucleation and glide, and/or a lack of easy slip systems is common. It is not surprising, therefore, that ordered-b.c.c. or B2 structured compounds have been heavily investigated because they have high symmetry and a small unit cell, exhibiting the simplest crystal structure that can be adopted by a compound, see Figure 1. Nevertheless, many B2 compounds exhibit little ductility, being susceptible to embrittlement through a variety of phenomena. The factors which embrittle intermetallic compounds can be sub-divided into two groups: *intrinsic* and *extrinsic*. *Intrinsic* factors are those associated with the material itself, for example a material which exhibits "weak" grain boundaries or extremely planar slip, whereas *extrinsic* factors are those associated with external factors such as the testing environment.

George R. Irwin Symposium on Cleavage Fracture
Edited by Kwai S. Chan
The Minerals, Metals & Materials Society, 1997

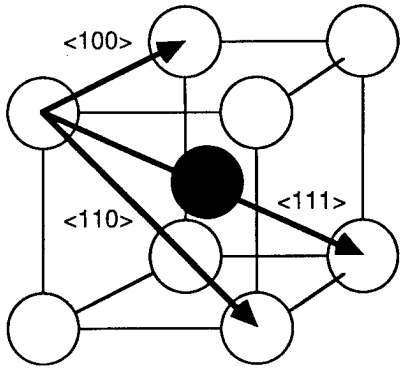


Figure 1.The B2 crystal structure, showing the possible slip vectors.

A large number of compounds adopt the B2 crystal structure but in only a small number of them, most notably NiAl, FeAl, FeCo and CuZn, has fracture been studied in any detail. In this paper the fracture of these and other B2 compounds will be discussed in terms of the underlying micromechanisms.

Defects in B2 Compounds

B2 compounds are normally based around an AB stoichiometry. However, few intermetallic compounds exist only at their precise stoichiometries. Many compounds, for example NiAl, exist over a wide range of compositions, which usually span both sides of the stoichiometric composition. In addition, some B2 compounds such as FeSi exist only at compositions far from stoichiometry (~10-24 at. % Si, depending on temperature). In a non-stoichiometric alloy there is a clear requirement that the excess atoms of one species must be accommodated in some way so that the crystal structure is maintained. This can occur either by the excess atoms substituting on the sublattice of the deficient species (antisite atoms) or by having vacancies present on the sublattice of the deficient species (constitutional vacancies). Both types of defect cause substantial hardening- with vacancy hardening greater than that from anti-site atoms - and, hence, can enhance brittle fracture. Deviation from stoichiometry produces constitutional disordering. On the other hand, some B2 compounds, for example CuZn, may exhibit thermal disordering, undergoing an order-disorder transformation when heated.

The site-specific location of atoms in an ordered lattice also necessitates greater complexity in processes such as slip and diffusion. For slip, the passage of a single a/2<111> dislocation, as occurs in b.c.c alloys, creates disorder and produces an anti-phase boundary (APB) along the slip plane in a B2 compound. This is energetically unfavorable. Thus, slip occurs in most compounds either by the motion of a superdislocation consisting of paired a/2<111> dislocations coupled by an APB, or by the motion of a perfect <100> dislocation. Both of these slip vectors are considerably longer than that in a b.c.c metal. In addition, <110> slip has been noted both in CuZn and NiAl single crystals following straining at high temperature [2]. Several models have been developed to rationalize which type of slip vector operates [3-7]. Unfortunately, none of the models appear to possess a general predictive capability for all B2 compounds. Thus, this is an area in great need of a theoretical breakthrough. The motion of paired a<111> superdislocations in B2 compounds is reminiscent of the motion of dislocations in f.c.c. metals, where the dislocation dissociates into a pair of Shockley partials. An important distinction is that in the B2 compound both partials in the superdislocation possess the same Burgers' vector, and hence the same cross-slip plane.

Diffusion is more difficult in B2 compounds than in b.c.c. metals because vacancy movement in B2 compounds is more complicated. During diffusion the jump of an atom on to a nearest-neighbor site will usually result in that atom occupying the wrong sublattice and will, therefore, create local disorder. Thus, in B2 compounds, diffusion of vacancies may occur through a six-jump cycle (Figure 2), since this does not leave a disordered lattice in its wake [8]. This more complex diffusion mechanism means that vacancies often migrate more slowly than in disordered materials and diffusion-assisted processes such as creep are slower. On the other hand, some B2 compounds, for example FeAl, have extremely high concentrations of thermal vacancies at elevated temperatures, which will accelerate creep.

Bearing these thoughts in mind, the behavior of individual B2 compounds will be examined.

NiAl

NiAl has been the most widely studied B2 compound. It has a high melting point (1911K), high Young's modulus (~190-240 GPa) [9], relatively low density (5.5-6.0 Kgm^{-3}) and good resistance to oxidation. It also exists over a wide range of composition, from about 42 at. % Al to 55 at. % Al at room temperature (unless otherwise stated all compositions are in atomic percent), and remains strongly ordered up to its melting point. Thus, NiAl-based alloys have found application as coatings in high temperature environments. NiAl has also been studied as a gas turbine blade material. Unfortunately, its low room-temperature ductility and toughness render it difficult to use in this application. As a consequence there has been considerable activity aimed at improving its plasticity.

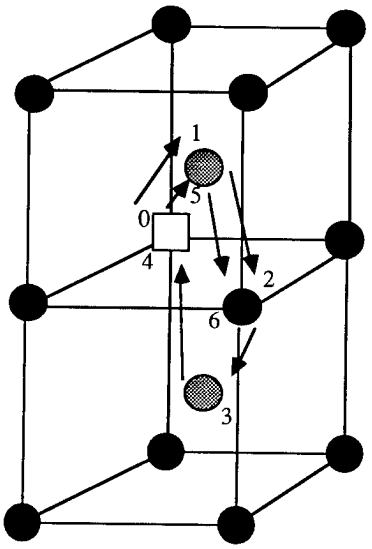


Figure 2. Six-jump cycle for diffusion in B2 compounds. The square represents a vacancy.

Slip in NiAl

NiAl exhibits <001> slip, usually on {110} planes [4]. However, in certain unusual situations, for example in appropriately-oriented single crystals, deformation by the motion of <111> superdislocations can occur [10-13], and evidence of <110>{110}slip has been found in NiAl bicrystals deformed at room temperature and at 933K [14]. An important feature of slip by <001> dislocations is that it provides only three independent slip modes, that is less than the five required by Von Mises criterion for extensive polycrystalline plasticity, thus precluding extensive ductility in polycrystals. However, the operation of <001> slip does not preclude extensive plasticity in single crystals.

In theory, <001> slip can occur on a spectrum of {hk0} planes, so screw dislocations can easily cross-slip, producing macroscopically non-crystallographic slip. In practice, cross-slip occurs readily in Ni-50Al [11,15-17], but becomes more difficult with increasing (Ni-rich) deviation from the stoichiometric composition [16-18]. Planar slip in Ni-rich NiAl is possibly a combination of two effects. First, NiAl is elastically anisotropic and the anisotropy increases with increasing Ni content. This may cause the mobility of dislocations to be reduced on some planes, thus limiting the planes onto which cross-slip can occur. Second, the dislocation core may become non-planar with the addition of Ni, again making cross-slip more difficult. Support for the second suggestion comes from high resolution transmission electron microscopy [19] where it was shown that the cores of <100> edge dislocations in stoichiometric NiAl are compact , whereas the cores of similar dislocations in off-stoichiometric NiAl are much more spread out [19].

Single Crystals

The mechanical behavior of single crystal NiAl is strongly dependent upon orientation, temperature and composition. When crystals are tested in a hard orientation at room temperature, that is with the <001> direction parallel to the compression axis such that the usual <001>{110} slip systems have no resolved shear stress on them, deformation occurs by <111> slip on {110} or {112} planes [10-12, 20]. The critical resolved shear stresses for this is very high (~700 MPa) [13]. These crystals are brittle in tension at room temperature and fail before yielding, but exhibit compressive ductility up to 16% [21,22]. However, such crystals exhibit a brittle-to-ductile transition at about 600K and can exhibit 50% elongation at 1000K [13,20,23]. At elevated temperatures deformation occurs by a combination of <110> and <001> slip augmented by thermally activated dislocation climb [13,20]

In contrast, if single crystals are tested in soft orientations <001>{110} slip systems are active, and significant tensile ductility can be achieved. A wide range of elongations have been reported, and it is now apparent that the plasticity of NiAl single crystals, in such orientations, is dependent upon a wide range of extrinsic factors including impurity content, specimen gripping conditions, heat treatment, pre-straining and orientation. Recently, Levit et al. obtained a tensile elongation of 28% in nominally stoichiometric NiAl at room temperature in crystals oriented with [213] parallel to the stress axis [24], i.e. far from a duplex slip orientation. These specimens were pre-strained at 1273K, which produced a microstructure containing subgrain boundaries comprised of <001> dislocations. It was suggested that the boundaries acted as a source of mobile dislocations during room temperature straining. Levit et al. also indicated that the extent of the tensile ductility is dependent upon the geometry of the sample. That is, higher ductilities are observed when the tensile axis is unconstrained and free to rotate [24].

Many intermetallics suffer from environmental embrittlement (see later). However, Lahrman et al. have shown that the test environment has no appreciable effect on the tensile ductility of stoichiometric NiAl single crystals [25].

Polycrystalline NiAl

Polycrystalline stoichiometric NiAl, tested in tension at room temperature, exhibits very limited tensile ductility [26-30], although Hahn and Vedula have reported elongations to failure up to about 4% [26]. As noted above NiAl deforms at room temperature by the movement of <001> dislocations, which cannot provide sufficient independent strain components to accommodate the plastic incompatibilities that occur at grain boundaries during deformation. This is consistent with the observation of intergranular fracture for this alloy. A number of workers have investigated additions such as Mn and Cr to NiAl as a mechanism to increase plasticity [31,32]. The idea being to promote <111> slip and, thus, increase the number of independent slip systems [32]. However, there is no evidence to suggest that these ternary additions produce any changes in slip behavior [33]. On the other hand, Patrick et al. showed that replacing 40 at. % Ni by Fe, in Ni-40Al was sufficient to change the room temperature slip vector from <001> to <111> [34].

The possibility that intergranular failure in this alloy might arise through impurities which have segregated to the grain boundaries has been ruled out using Auger electron spectroscopy which indicates that the boundaries are clean [29]. Another possibility is that the grain boundaries are intrinsically weak. Since both the chemistry and bonding at the grain boundaries affects their strength, there have been several studies both experimental and modeling to examine these. Atom probe studies by Camus and co-workers [35,36] showed that some grain boundaries in stoichiometric NiAl were enriched in nickel (and depleted in aluminum) in a zone which extends up to about 0.5 nm from the boundary plane. Consistent with this, Fonda and Luzzi [37,38] obtained a high resolution TEM image of a $\Sigma 5$ (310) grain boundary in NiAl (composition not specified) and found that the image could be simulated best using a model in which the nickel sites had 50% constitutional vacancies and the aluminum sites had 50% vacancies and 50% Ni anti-site atoms. This configuration, containing a very high density of nickel anti-site defects, would appear to be unlikely. Chen et al. [39] modeled grain boundaries using the embedded atom method and found both that excess Ni had only a minor strengthening effect on the grain boundaries and that deviation from the stoichiometric composition was accommodated by the creation of vacancies on the minority element sites at the grain boundary. Petton and Farkas [40] examined the effect of having excess Ni or Al atoms at a $\Sigma 5$ (210) boundary in NiAl via atomistic simulations. For the stoichiometric compound the energy of the boundary ranged from 746 to 1,713 mJ m^{-2} depending on the exact location of the boundary with respect to the Ni and Al atoms. Excess Ni atoms lowered the average boundary energy whereas excess Al atoms increased the average boundary energy due the appearance of large interstitial holes there. However, experimental evidence to support these predictions has not been obtained.

Although brittle intergranular fracture appears not to be associated with impurity segregation to the grain boundaries, segregation can improve their mechanical behavior. For example, it is well known that trace additions of boron to nickel-rich Ni_3Al suppress intergranular fracture and lead to dramatic increases in ductility. Similarly, additions of boron to NiAl which segregates to the grain boundaries promote transgranular fracture [29] although this boron does not enhance ductility, the fracture strength is raised (from ~229 MPa to 329 MPa), indicating that the boundaries are strengthened [29].

It has been suggested that texture can influence the tensile ductility of stoichiometric NiAl at room temperature [26,29]. A strong <111> texture is often observed in NiAl following extrusion and it has been suggested that NiAl with a strong crystallographic texture acts like a 'soft' single crystal material [41]. However, Baker and Schulson have shown that in materials, such as NiAl, which exhibit <001> slip, quasi-plane strain deformation cannot account for ductility where there are only three mutually-orthogonal slip vectors [42].

Baker et al. showed that off-stoichiometric alloys are brittle at room temperature: fracture occurs before yielding predominantly by transgranular fracture [43,44]. In NiAl anti-site defects form in nickel-rich alloys and constitutional vacancies form in aluminum-rich compositions. These defects interact strongly with glide dislocations and greatly increase yield strength

such that fracture occurs before plastic yielding, although the fracture stress of NiAl increases from 300 MPa at stoichiometry to 595 MPa for Ni-42Al [44]. It is tempting to conclude that the grain boundaries are stronger in the off-stoichiometric alloys. However, grain boundary failure appears to require prior plastic flow and all the off-stoichiometric alloys failed prior to yielding (Table 1).

Composition (at. %)	Failure Strain (%)	Failure Stress (MPa)	Yield Stress (MPa)
Fe-34Al	6	665	359
Fe-40Al	3	430	253
Fe-45Al	3	497	309
Fe-50Al	0	400	890
Ni-50Al	2	300	115
Ni-48Al	0	442	260
Ni-45Al	0	445	560
Ni-42Al	0	594	780

Table 1. Failure strains, yield strengths and fracture strengths in tension of polycrystalline FeAl and NiAl at room temperature strained at 1 x 10^{-4} s^{-1}. After Baker et al. [44].

Noebe et al. [45] demonstrated a correlation between the fracture behavior of polycrystalline NiAl-based alloys and their yield strength (Figure 3). As noted above, in low strength NiAl, for example at stoichiometry, brittle intergranular fracture (BIF III) occurs following some localized plastic flow. However, in higher strength NiAl alloys, for example in powder-processed materials, brittle intergranular fracture (BIF II) occurs at the yield point so that no appreciable ductility is observed. In this instance some localized yielding may occur, but at stresses the same as or higher than the stress required for crack propagation so fracture occurs immediately. In off-stoichiometric NiAl and in alloys doped with boron or carbon the yield strength is very high and fracture occurs without any plastic deformation by transgranular cleavage (cleavage I). Thus, where little plastic deformation occurs transgranular fracture occurs, but when slip is easy and there is some plasticity, the slip incompatibility at the grain boundaries leads to intergranular fracture. An exception to this behavior is when substantial quantities of iron replace both Ni and Al [46]. In this case, cleavage occurs (Figure 4) after 1-2% plastic elongation at very high stresses, e.g. 770 MPa for Ni-30Al-20Fe, and 850 MPa for Ni-40Al-30Fe.

Schulson suggested that plasticity could be increased by refining the grains to below the critical size where the stress to nucleate cracks is less than that required to propagate cracks [46]. Schulson and Barker subsequently showed that significant ductility could be achieved in Ni-49Al at 400°C at 1 x $10^{-4}s^{-1}$ by refining the grain size to about 20μm [48]. However, if this approach was to be successful in improving the ductility at room temperature the grain size would have to be the order of 3μm, which would likely affect creep resistance adversely.

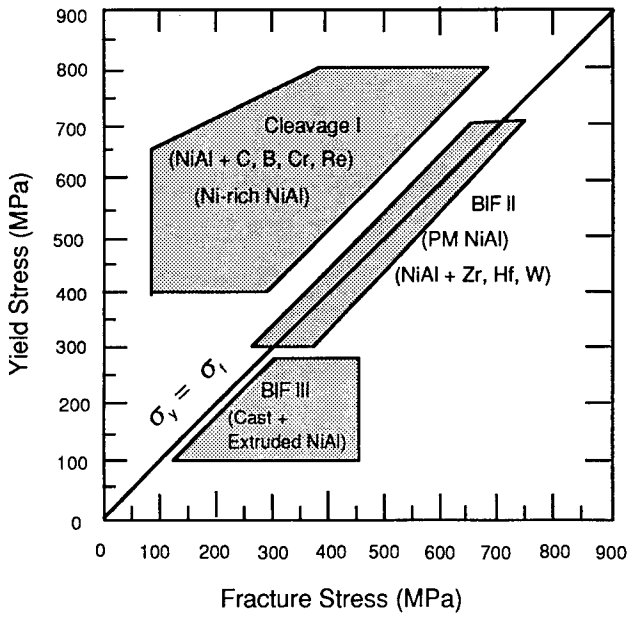


Figure 3. Relation between alloying additions, room temperature tensile properties and fracture initiation mechanisms in NiAl alloys, see text for details. (BIF = Brittle intergranular fracture.) After Noebe et al. [45].

There has been little published on the effect of heat-treatment on the ductility of polycrystalline NiAl. Bowman et al. [49] demonstrated that material air-cooled material exhibited lower tensile ductility than furnace-cooled material. Neither the testing environment nor the strain appear to affect the room temperature ductility of polycrystalline NiAl [44]. However, if a hydrostatic pressure (500 MPa) is imposed on polycrystalline stoichiometric NiAl during tensile testing, fracture strains in excess of 10 % can be obtained [50]. The pressurization appears to suppress damage accumulation and stable microcracks are observed along the gauge length of the specimen [50].



Figure 4. Room-temperature transgranular fracture surface of Ni-30Al-20Fe which fails at a fracture strength of ~ 750 MPa after 2% strain [46].

As for single crystal NiAl, polycrystalline NiAl exhibits a brittle-to-ductile transition temperature at around 500K at a strain rate of 1 x 10^{-4} s^{-1} [27], the temperature increasing with increasing strain rate and grain size [51,52]. A number of studies have associated the observed onset of climb and thermally-assisted cross-slip with the transition [4,49,51]. Another possibility is that additional slip systems become active at the transition temperature [14,53]. However, it is likely that the <110> and <111> dislocations observed in NiAl following hot deformation are junction dislocations formed by the interaction of non-equivalent <001> dislocations [42].

Fracture Toughness

A number of measurements have been made of the fracture toughness of both single crystals and polycrystals of NiAl-based alloys.

The fracture toughness of single crystal, stoichiometric NiAl depends upon the notch orientation. Higher K_{1C} values, of between 7 and 12 MPa.$m^{1/2}$, have been observed when the notch is cut normal to <001> oriented crystals, than when the notch is cut perpendicular to <011> oriented crystals (5 MPa.$m^{1/2}$) [54]. The fracture of stoichiometric NiAl single crystals occurs by cleavage primarily on {110}: a few facets having orientations between {115} and {117} have also been observed [54,55].

Hack et al. [55] have shown that heat treatment can affect the fracture toughness of stoichiometric NiAl. Samples air cooled after elevated temperature annealing exhibited a higher fracture toughness value for the {100} plane (~13 MPa.$m^{1/2}$) than samples which were furnace cooled (~4 MPa.$m^{1/2}$). Even higher values (17 MPa.$m^{1/2}$) can be obtained by giving specimens a 673K anneal followed by an air cool [55]. Annealing at 473K or slow cooling after a 673K anneal has a detrimental effect on the {100} fracture toughness with values as low as 2.8 MPa.$m^{1/2}$ being obtained after the 473K anneal [55]. This behavior has been ascribed to a strong strain-aging effect arising from interstitial solutes which lock dislocations and prevent plastic energy-dissipative processes. Pre-straining at 673K to introduce mobile dislocations had little effect on the fracture toughness of samples given air cools after the 673K anneal. By comparison, for the 473K heat treatment, the pre-strain at 673K appears to have introduced enough mobile dislocations to swamp the capacity of solute atoms to immobilize them and, hence, the fracture toughness was increased to ~11 MPa.$m^{1/2}$ [55].

Vehoff has presented data showing that four-point bend-tested <100>-oriented, NiAl crystals, which cleave along {100}, exhibit a fracture toughness of ~ 4 MPa $m^{1/2}$ at a loading rate of 0.2 μm s^{-1} but 6 MPa $m^{1/2}$ at a loading rate of 20 μm s^{-1} in air [56]. This behavior suggests there is probably a small environmental effect on the fracture toughness of single crystals. In contrast, data by Schneibel et al. showed no effect of loading rate on the fracture toughness of polycrystalline NiAl [57], with the corollary that the crack growth occurred in an unstable run-arrest fashion. Such behavior would probably make the fracture toughness insensitive to the imposed loading rate.

Values for the room temperature plane-strain fracture toughness (K_{1C}) of polycrystalline NiAl are typically ~5 MPa.$m^{1/2}$ [57-62]. The grain size has little effect on K_{1C} at least in the range 20-200 μm [62]. Values of 4.1 to 6.6 MPa.$m^{1/2}$ obtained for powder-processed Ni-45Al are comparable to values obtained by others in polycrystalline stoichiometric NiAl. Although in these studies large-grained samples showed only transgranular cleavage, a mixed mode (cleavage plus intergranular) fracture was obtained in the fine-grained specimens [62].

Increases in fracture toughness have been noted in very nickel-rich (<~40 at. % Al) polycrystals [60]. The microstructure for such compositions is strongly dependent on heat treatment and can be altered to produce either single phase B2 grains or a two-phase B2 + $L1_2$ microstructure. Higher toughness values (~9 MPa.$m^{1/2}$) observed for quenched single-phase Ni-38.5Al have been attributed martensitic transformation toughening [60]. Even higher K_{1C} values (~13 MPa.$m^{1/2}$) have been observed in alloys heat treated to form $L1_2$ regions around the B2 grains [60], the increases have been attributed to the effects of crack blunting in the two phase microstructure. Fracture studies performed on polycrystalline materials at higher temperatures indicate that toughness increases with increasing temperature. A brittle-to-ductile transition is observed between about 550K and 650K, and K_{1C} values of up to 50 MPa.$m^{1/2}$ have been observed [58].

Yoo and Fu [63] calculated, from first principles, the ideal cleavage energy for stoichiometric NiAl on {100} and{110} to be 5.5 J m^{-2} and 4.1 J m^{-2}, respectively, suggesting that cleavage should occur on {110}, as is observed [54]. These workers used their calculated cleavage energies to estimate the fracture toughness of stoichiometric NiAl on {100} and {110} to be 0.98-1.06 MPa.$m^{1/2}$ and 0.85-0.99 MPa.$m^{1/2}$, respectively at absolute zero (the range arises because they considered cleavage in different directions). Measured values [54] are typically four to five times higher than the calculated values, indicating that crack-tip plasticity plays an important role in the cleavage fracture of NiAl.

To summarize, the fracture behavior of single crystal NiAl is affected by many extrinsic factors such orientation and impurity content. Through the use of careful heat treatments, careful specimen gripping and pre-straining, the ductility and toughness of single crystal NiAl can be quite large (28% and 17 MPa.$m^{1/2}$ respectively). In contrast, polycrystalline NiAl exhibits low room temperature ductility and low room-temperature fracture toughness, since the operating slip vector (<001>) provides insufficient slip systems for plastic flow.

FeAl

Introduction

B2-structured FeAl exists at room temperature from around 35 at. % Al to 50 at. % Al, but at higher temperatures the compositional stability of FeAl widens slightly [64]. At room temperature FeAl deforms by <111> slip, but at higher temperatures deformation occurs through the motion of <001> dislocations [65]. The transition temperature at which <001> deformation becomes dominant varies with composition and decreases as the aluminum concentration increases [65-67]. Although <111> slip

provides sufficient slip systems to satisfy Von Mises criterion, polycrystalline FeAl is still largely brittle at room temperature. Stoichiometric FeAl fails in tension at around half the yield strength, although ductility increases as the iron content increases [44,66,68-70]. The fracture behavior of FeAl depends not only on composition, but also on a number of *extrinsic* effects such as the testing environment and heat treatment. For compositions with less than about ~40 at. % aluminum the mechanical behavior of FeAl is dominated by environmental embrittlement effects [71], whereas in compositions with higher aluminum contents vacancy-hardening effects, strongly affect the mechanical behavior [72].

Environmental Embrittlement

The mechanical behavior of iron-rich FeAl was first shown to be strongly dependent on testing environment by Liu et al. who showed that Fe-36.5Al when tested in air at room temperature exhibited an elongation to failure of 2% and transgranular fracture [71]. However, when the same alloy was tested under vacuum it exhibited an elongation of 5.5% and mixed mode failure, and when tested in dry oxygen 18% elongation and intergranular fracture. This suggests that it is the cleavage planes which are more susceptible to environmental embrittlement than the grain boundaries. Similarly, Gaydosh and Nathal noted that the elongation of Fe-40Al increased from ~1%, when tested in air, to ~5%, when the tested under vacuum [69], although intergranular failure was observed under both conditions. Further increases in ductility were noted in samples heat treated to remove excess thermal vacancies (see below) suggesting that these effects are additive [69]. Thus, environmental embrittlement leads to either intergranular fracture or transgranular cleavage in FeAl, depending on the composition.

Liu et al. suggested that the environmental effect was caused by local embrittlement from hydrogen at crack tips [71]. This hydrogen is liberated from water molecules, present in air, which react with aluminum atoms in the aluminide to yield alumina and atomic hydrogen. The hydrogen may then diffuse to crack tips and cause embrittlement. Nagpal and Baker subsequently demonstrated that if mechanical testing is performed at rapid strain rates, environmental factors are less important since there is insufficient time to allow the diffusion of hydrogen to occur [73]. They showed that the tensile elongation in air of Fe-45Al is independent of strain rate for rates up to 1 x 10^{-2} s^{-1}, but increases with increasing strain rate, up to a maximum (of 9%) at 1 s^{-1} (Figure 5). Both the yield stress and the intergranular fracture mode are independent of strain rate for this composition.

Environmental embrittlement which has been studied and reviewed in detail, has been shown to affect a large number of intermetallic compounds, principally aluminides and silicides [75-77]. Such environmental effects can mask the *intrinsic* behavior of a compound, requiring testing in either an inert atmosphere or at high strain rates for observation.

A number of detailed studies have been performed on the mechanisms of environmental embrittlement in FeAl [77-81]. These suggest that the rate-controlling process is the formation of hydrogen through the interaction of water molecules with aluminum atoms.

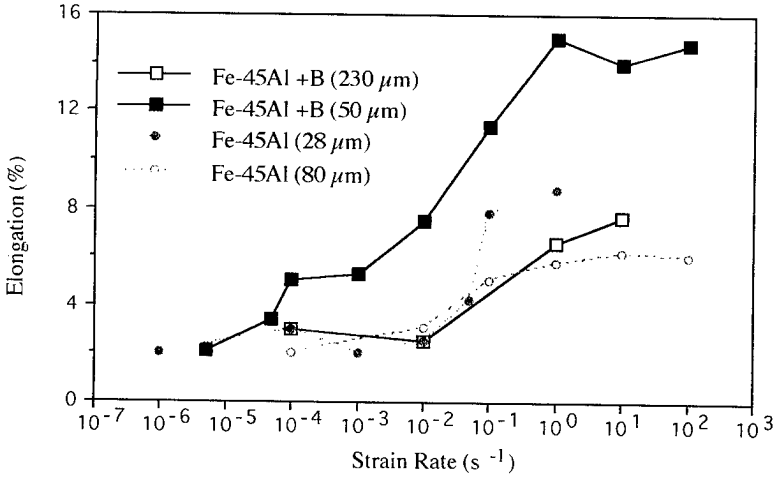


Figure 5. Graph of elongation versus strain rate for large-grained low-temperature-annealed, boron-doped and undoped Fe-45Al of different grain sizes tensile tested in air. After Baker et al. [74].

However, the role of hydrogen on both crack nucleation and crack propagation in FeAl remains unclear. One possibility is that hydrogen enhances crack nucleation by promoting the formation of sessile <001> dislocations, which Munroe and Baker, based on their TEM observations, suggested might nucleate cleavage cracks on {100} planes [82]. Studies by Kasul and Heldt indicate that hydrogen diffusion in FeAl is slow at room temperature [78], suggesting that crack nucleation may occur very near to the surface. Thus, hydrogen would only be required to diffuse small distances. It has also been suggested that the transport of hydrogen during deformation is assisted by the motion of glide dislocations [78,81].

There has been relatively little reported on the fracture behavior of single crystal FeAl. Gaydosh et al. studied the fracture of <001>-oriented Fe-40Al single crystals under tension at room temperature in air [83]. Failure occurred at very low elongations (<1%), but relatively large reductions in area at the neck, indicating highly localized plastic flow. Subsequent studies by Nathal and Liu on the same material, but tested in an oxygen environment, revealed elongations to failure in excess of 10% [84].

For some compounds, solutions which mitigate the effects of environmental embrittlement have been established. Boron additions to Ni_3Al increase plasticity by ameliorating environmental embrittlement [85]. Similarly, there is some evidence to suggest that additions of chromium to Fe_3Al reduce its susceptibility to environmental effects [86], although the origins of this beneficial effect are still not understood. In contrast, solutions to overcome environmental embrittlement in FeAl have not been established. Clearly, a better understanding of the role of hydrogen in the crack nucleation and crack propagation processes would more easily allow solutions to be sought.

Compositional Effects

As the aluminum content of FeAl increases, the room temperature fracture mode changes from transgranular to mixed mode fracture to intergranular fracture when tested in air [43,66,67,69,87] (Figure 6). (Interestingly, some intergranular fracture surfaces contain cleavage cracks.) However, the compositions at which these transitions occur depends upon factors such as the heat treatment and the impurities present. Auger electron spectroscopy of intergranular fracture surfaces indicate that even if grain boundaries are clean and free from impurities they still fracture. This suggests that the grain boundaries in FeAl are intrinsically brittle [88].

The intergranular fracture exhibited by iron-rich FeAl has prompted several workers to attempt to improve the ductility of this compound through boron additions [68,70,88]. The strain to failure of Fe-43Al increases from ~1% to ~13% through the addition of boron, together with a change in fracture mode from intergranular failure to transgranular cleavage[89]. The boron segregates to the grain boundaries and, this, presumably increases their strength [88,89]. Carleton et al. [90] recently investigated the effect of Fe:Al ratio on the room-temperature elongation in vacuum of FeAl doped with 300 ppm boron and found little change in the strain to failure (~10%) in the range 40 to 45 at. % Al, although the strain to failure for similarly-doped Fe-48Al was significantly less at 2%.

Other workers have shown that other alloying additions may alter the fracture behavior without necessarily improving ductility. For example, Gaydosh et al. showed that additions of carbon, hafnium or zirconium changed the fracture mode of Fe-40Al in air from a mixed mode failure to wholly intergranular, and decreased the ductility [70]. However, if boron is added to the carbon and zirconium-containing alloys ductility increases to a level equivalent to that of the binary alloy (4-5 % elongation). The boron additions changed the fracture mode to transgranular cleavage, as did the addition of Hf or Hf + B to Fe-40Al [70]. The boron resulted in the presence of borides in some of these alloys.

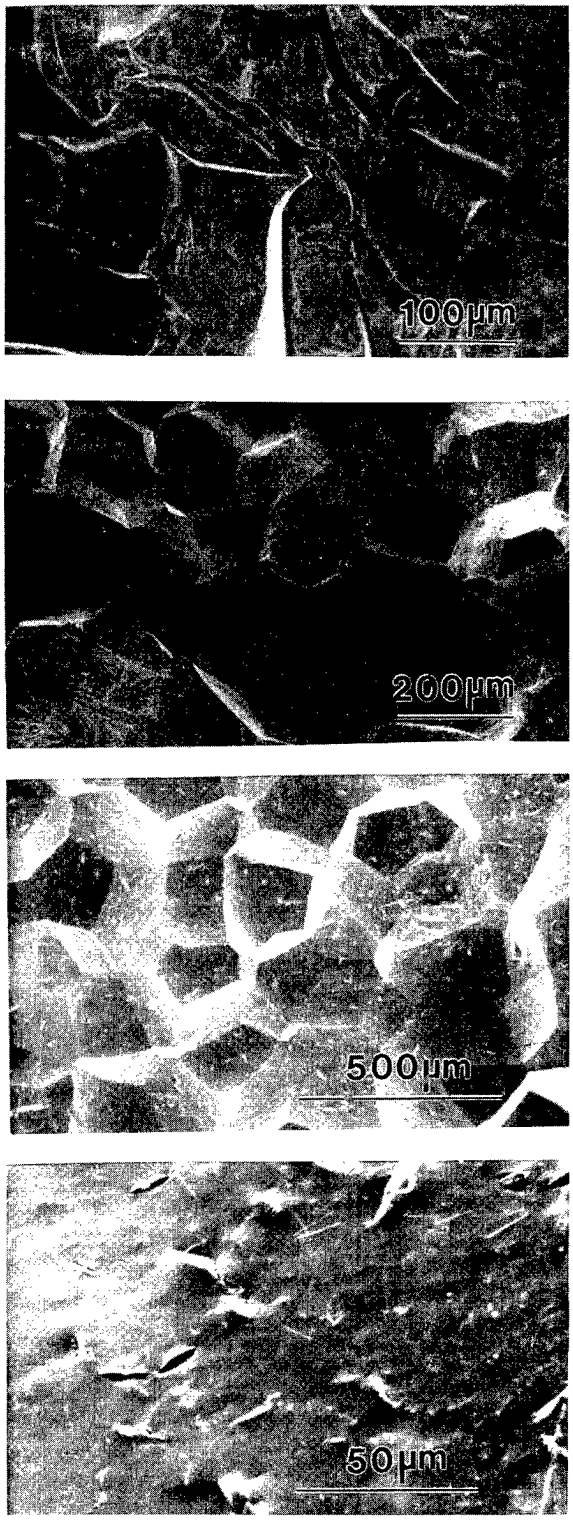


Figure 6. Fracture surfaces of FeAl containing (a) 40 at. % Al and (b) 43 at. % Al strained at room temperature; and (c) 48 at. % Al strained at 500 K, where particle-like features are present on the grain boundaries which at higher magnification (d) can clearly be observed to be cleavage cracks. Note that the fracture mode becomes increasingly intergranular as the stoichiometric composition is approached. After Baker et al [87].

Environmental effects can mask alloying effects. Baker et al. [74] tested fine-grained Fe-45Al at 1 x 10^{-4} s^{-1} in tension air at room temperature and found that adding 500 ppm boron did not appreciably affect ductility, which was ~2-3 %. However, at a higher strain rate of $1s^{-1}$ (where the environmental effect is negligible) the elongation increased from 6-9%, in undoped FeAl, to 15 % when 500 ppm boron was added (Figure 5).

Heat Treatment

The mechanical behavior of FeAl is also strongly affected by heat treatment. FeAl has a low energy of formation of thermal vacancies, which is composition-dependent, decreasing from around 0.94 eV to 0.77 eV as the aluminum content increases from 38.5 at. % Al to 47 at. % Al [91-94]. This means that large vacancy concentrations form during heat treatments at temperatures greater than ~973K. Conversely, the energy of migration for vacancies is high. It is also composition-dependent and as the aluminum content increases from 38.5 to 47% it increases from around 1.57 eV to 1.75 eV [94]. This means that these vacancies are relatively immobile and slow to diffuse out of the lattice. Thus, large supersaturations of thermal vacancies are retained after elevated temperature anneals. These excess vacancies can be removed through prolonged heat treatments at intermediate temperatures (673K-773K), which, are extremely effective in hardening the lattice and low ductilities are observed in samples heat treated to retain vacancies [73,95]. Compositions close to stoichiometry retain more vacancies following high temperature heat treatment and are therefore more susceptible to vacancy hardening effects [73]. Thus, it has been clearly shown that increasing vacancy concentration leads to a reduction in ductility [96] (Figure 7). However, the mode of fracture exhibited by binary FeAl is independent of the prior heat treatment conditions and, thus, vacancy concentration. In contrast, Alexander showed that the fracture behavior of Fe-35.8Al-0.05Zr-0.24B during impact testing can be affected by heat treatment [97]. Oil-quenched samples, where the retained vacancy concentration would be expected to be high, exhibited mixed mode fracture at room temperature whereas the furnace-cooled material exhibited transgranular fracture.

Grain Boundary Effects

Gaydosh and Crimp [98] determined the room-temperature ductility of melt-spun ribbons of FeAl of various compositions both before and after grain-growth anneals and found that the grain size had essentially no effect on the ductility of Fe-40Al and Fe-50Al tested in air where they obtained ~6% and 0% elongation, respectively. By comparison, Fe-45Al showed >6% elongation in air for annealed ~10 μm grains, as opposed to ~1.5% for as-solidified ~7 μm grains. This behavior probably reflects the effect of retained vacancies from melt-spinning on reducing the ductility of the fine-grained material rather than the effect of grain size *per se*. On the other hand, Gaydosh et al. [83] showed a steady increase in the room-temperature elongation of bulk furnace-cooled Fe-40Al in air from ~1% for 220 μm grains to ~3% for 15 μm grains. The largest room-temperature elongation for bulk binary FeAl tested in air was reported by Strothers and Vedula [99]. They obtained 7% elongation in annealed, slow-cooled Fe-40Al containing Y_2O_3 particles. The grain size was ~5 μm suggesting that slight ductility improvements are possible at room temperature by reducing the grain size, but a slip homogenizing effect from the particles may also have contributed to the improved elongation.

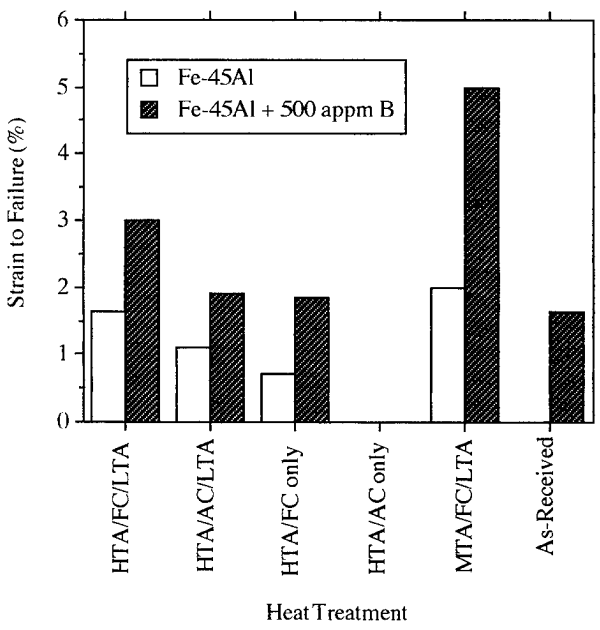


Figure 7. Strain to failure for Fe-45Al and Fe-45Al + B after various heat treatments: HTA - 10 h at 1223 K; MTA - 48 h at 933 K; LTA - 120 h at 673 K; FC - furnace cool at 60 K/h; AC - air cool. HTA grain size - 230 μm; no HTA grain size - 50 μm [96].

Grain boundary effects can also be obscured by environmental embrittlement. Baker et al. [74] tested Fe-45Al in air at a high strain rate of 1 s^{-1} where environmental effects are negligible (Figure 5). They obtained 9 % elongation in a 28 μm grain-sized specimen compared to 6 % elongation in a 80 μm grain-sized specimen. Similar material doped with 500 ppm boron also showed an increase in elongation from 8 % to 15 % as the grain size decreased from 200 μm
to 50μm.

Fracture Toughness

There have been a number of measurements of the fracture toughness of both single crystals and polycrystals of FeAl. Chang et al. showed that the fracture toughness of single crystal Fe-40Al was strongly dependent upon orientation [54]. Tests were performed on samples containing notches normal to the tensile axis and the highest toughness (56 $MPa.m^{1/2}$) was noted when the <011> axis was parallel to the stress axis. Lower fracture toughness values were noted for <111> (38-43 $MPa.m^{1/2}$) and <001> (33 $MPa.m^{1/2}$) crystals. Fracture occurred by cleavage on {001} planes. An even lower fracture toughness (12 $MPa.m^{1/2}$) was determined for directionally-solidified Fe-48Al, which suggests that fracture toughness decreases with increasing aluminum content [100].

Environmental embrittlement affects the fracture toughness. Measurements on Fe-45Al performed at high loading rates, where environmental effects are negligible, yielding fracture toughness values about 35% greater (at 56 MPa.m$^{1/2}$), than tests performed at slower loading rates [101]. Similar observations were recorded by Schneibel and Jenkins who measured the fracture toughness of Fe-40Al and Fe-45Al in air as a function of crack velocity [57,102].

Fracture Mechanisms

Baker and Horton [103] performed *in-situ* deformation experiments in the transmission electron microscope, and observed no obvious difference in the behavior of either dislocations or cracks as a function of Fe:Al ratio. Dislocation emission from cracks occurred readily as they propagated through grains, and it is almost surprising that FeAl is not extremely ductile. Liu and George [104] suggested that polycrystalline FeAl lacks ductility because the grain boundaries are intrinsically weak. The variation in fracture mode with composition suggests that the grain boundaries are weakest at the stoichiometric composition and increase in strength as the iron content increases. This suggestion is further reinforced by the failure of stoichiometric FeAl before yielding (at typically one-half to one-third of the yield strengths) and the observation that high quality channeling patterns can be obtained from intergranular fracture facets of this composition (Figure 8), indicating that little local plastic flow has occurred at the fracture surface during crack propagation, but not from Fe-45Al [43]. These observations suggest that dislocations play little part in the fracture of the stoichiometric composition and that grain boundaries in iron-rich FeAl fracture after plastic flow because the yield stress is below the intrinsic strength of the grain boundaries.

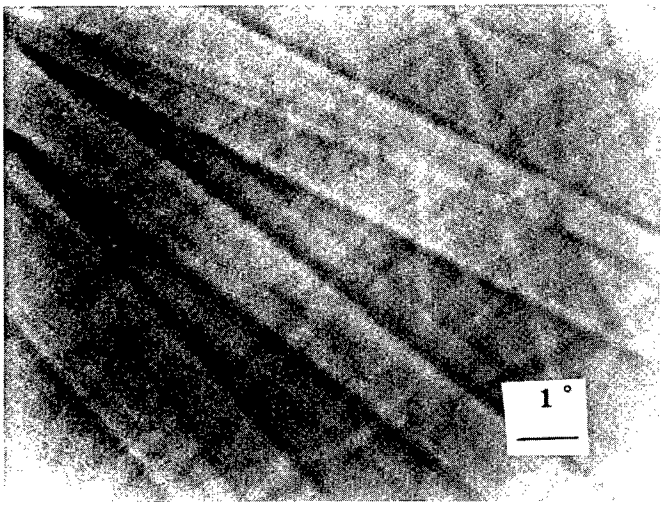


Figure 8. Selected area channeling pattern from intergranular facet of Fe-50Al. After Nagpal and Baker [43].

Fu and Yoo [105,106] calculated, from first principles, the elastic cleavage energy for FeAl. They obtained fracture toughness values for stoichiometric FeAl of 1.40 MPa.m$^{1/2}$ on {100} and 1.3-1.42 MPa.m$^{1/2}$ on {110} and for Fe-40Al of 0.93-1.08 MPa.m$^{1/2}$ for {100} and 0.88-1.15 MPa.m$^{1/2}$ for {110}. These are far less than the experimentally determined values noted above [54], suggesting that elastic fracture does not occur in FeAl. Fu and Yoo [106] also suggested that charge transfer from Al to Fe was the basic bonding mechanism in FeAl. Fu and Painter [107] extended the above work to consider the effect of hydrogen on FeAl in an attempt to explain the hydrogen embrittlement encountered by this compound. They suggested that hydrogen-induced embrittlement was due to a weakening of the d-bonding-charge localized on the Fe sites because of charge transfer from Fe to H atoms. They calculated that hydrogen could reduce the cleavage energy on {100} by up to 70% at high concentrations and suggested that the effect of hydrogen on the cleavage strength was more important than its effect on dislocation behavior. However, Schultz and Davenport [108] suggested that charge transfer is not important for the properties of B2 aluminides.

A possible crack nucleation mechanism, see Figure 9, for transgranular fracture in FeAl was proposed by Munroe and Baker [82] based on their observations of pairs of <100> dislocations, see Figure 10, which appear to have formed by the collision of gliding a/2<111> APB-coupled partial dislocations during room-temperature deformation; for example, by $a/2[111] + a/2[\bar{1}1\bar{1}] \Rightarrow a[010]$.



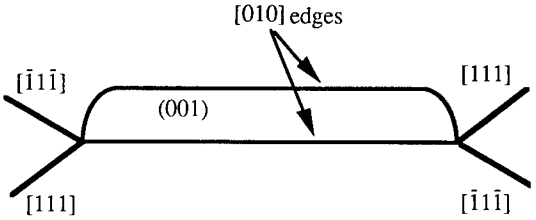


Figure 9. (a) Bright field transmission electron micrograph of [010] dislocations (arrowed) in Fe-34Al after 1% strain in compression at room temperature. Beam direction is close to [111]; (b) Schematic of the arrangement of a/2<111> and <100> dislocations in FeAl after collision of two pairs of a/2<111> gliding on {110}. After Munroe and Baker [82].

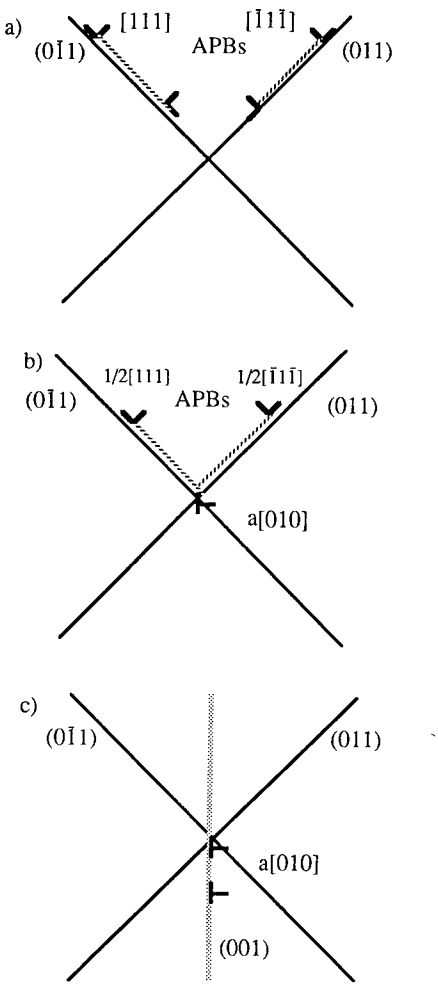


Figure 10. Schematic illustration of the formation of a<001> dislocations: (a) two <111> dislocations, each consisting of two a/2<111> dislocations; (b) after the two leading partials have interacted to form an a<001> dislocation, which is still connected to the trailing a/2<111> partials; and (c) the trailing a/2<111> partials interact to form a second a<001> dislocation, which repels the a<001> dislocation already present which curves away from the second a<001> dislocation, as shown in Figure 8. After Munroe and Baker [82].

They suggested that the <100> dislocations would lead to cleavage on {100}, the fracture plane later observed by Chang et al. [54], although this agreement does not prove that the mechanism is correct. The reaction is energetically favorable and becomes more so as the composition becomes less iron-rich, since the APB energy between the a/2<111> partials increases with increasing aluminum concentration. This is consistent with the qualitative observation of a greater density of <001> dislocations as the aluminum concentration increases [82]. Since Mandsziej showed that the formation of <100> dislocations in high chromium b.c.c. iron was promoted by the presence of hydrogen during plastic strain [109], it is possible that hydrogen, from water vapor, might enhance the formation of <100> dislocations in FeAl and, promote cleavage cracking at lower strains. The hydrogen could do this by segregating to the dislocation cores (both the a<100>'s and the a/2<111>'s), thus, changing their mobility [107]. The hydrogen might also be expected to segregate to the APB, coupling the a/2<111> partials, since the interstitial holes are larger there [108]. The driving force for the reaction to produce <100> dislocations (from isotropic elasticity theory) is at least twice the APB energy [82] and since the hydrogen atoms in the APB would raise the strain energy the effect of hydrogen effect on the APB would be to promote <100> dislocation formation. Li and Liu [110] suggested that hydrogen could also lower the elastic energy of a <100> dislocations and, hence, hydrogen would enhance their formation.

Fracture at Elevated Temperatures

A number of workers have shown that FeAl exhibits significant ductility at elevated temperatures. Baker and co-workers tested material which was large-grained and given a low temperature anneal prior to testing, to minimize the effects of thermal vacancies [87,96,111], and observed elongations to failure of up to ~150% at temperatures of 900K. They also showed that the ductility of FeAl was largely insensitive to composition at elevated temperatures with all off-stoichiometric alloys exhibiting large elongations. The fracture mode also changed with increasing temperature. Dimple-type ductile rupture (Figure 11a) is observed at temperatures greater than 650K, the onset of which coincided with a sharp ductility increase. Some recrystallization and grain boundary migration were noted at grain boundaries and near the fracture surface following testing at temperatures of 800K or greater (Figure 11b). However, it is probable that recrystallization occurred after testing since the fracture surface was not decorated with new small grains.

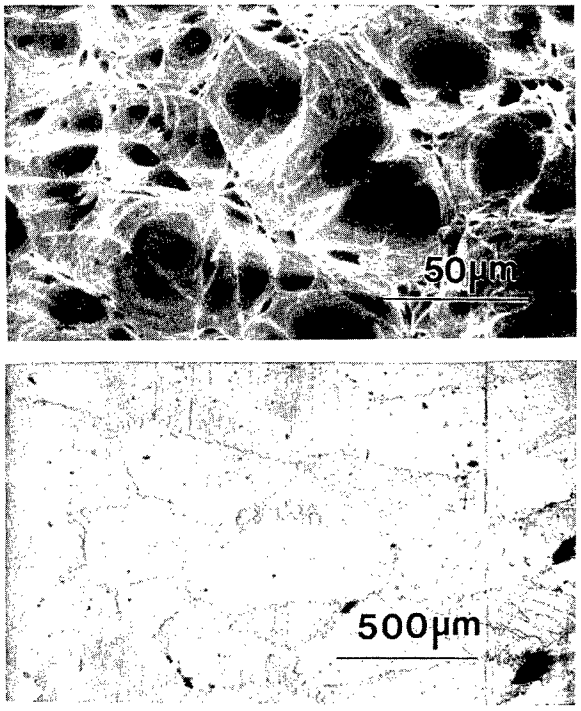


Figure 11. (a) Scanning electron micrograph of fracture surface of Fe-48Al and optical micrograph showing grain boundary migration in Fe-40Al, both deformed at 800K. After Baker et al. [87].

A number of other studies have been performed on FeAl which had not been given a low temperature anneal or which was not large-grained. Mendiratta et al. [112] were the first to report the temperature dependence of the ductility of off-stoichiometric FeAl. They found that fine-grained Fe-35Al exhibited a gradual rise in elongation to failure from ~6% at 293K to ~20% at 773K, after which the ductility dropped.

Similar behavior was noted in Fe-40Al by other workers [70]. Baker and Gaydosh measured the reduction in area of fine-grained Fe-37Al-2Ni from 300K to 1100K [66]. They found transgranular cleavage and a gradual increase in ductility up to 900K and then a sharp ductility drop at 1000K, after which it increased slightly again. Fracture was intergranular with considerable grain boundary plasticity and cavitation at the higher temperatures. Gaydosh et al. [70] noted a similar change in fracture mode in Fe-40Al with increasing temperature. Baker and Gaydosh [66] also studied fine-grained Fe-47Al and found no ductility until 600K, but 90% reduction in area at 700K. The fracture mode changed from mostly intergranular with a little transgranular cleavage below 800K to dimple-type rupture at 900K. Above 900K grain boundary fracture was accompanied by considerable plastic flow and cavitation at the boundaries. The lack of any ductility in Fe-47Al below 600K [63], even though it was fine grained, is probably related to the lack of a low-temperature vacancy-removing anneal in this material. Yoshimi et al. [113] demonstrated that retained vacancies decrease the fracture strains of polycrystals of both Fe-40 Al and Fe-46Al (in vacuum) even up to ~ 773K. They showed that a low-temperature anneal (150 hrs at 713K) tended to increase the proportion of transgranular cleavage as oppose to intergranular fracture up to 773K, above which ductile rupture occurred.

The effect of different strain rates on fracture at elevated temperature has been briefly studied: Baker and Gaydosh [66] found that for both Fe-37Al-2Ni and Fe-47Al, increasing the strain rate from 1×10^{-4} s^{-1} to 1 s^{-1} at elevated temperature produced a change from intergranular fracture to transgranular fracture with less grain boundary cavitation. However, there was little effect on the fracture strain at the different strain rates. Gaydosh et al. [70] noted similar fracture behavior in Fe-40Al.

Klein and Baker [114] studied the effects (in vacuum) of adding 500 ppm B to Fe-45Al. The fracture mode of unalloyed Fe-45Al changed from mostly intergranular at 300-400K to ductile, dimple-type rupture at 600K. By comparison, for the boron-doped alloy, the fracture was mixed-mode, transgranular cleavage plus intergranular fracture, below 700 K and ductile rupture at 700K. Interestingly, whilst unalloyed Fe-45Al showed a slight drop in elongation at 700-800K before recovering its ductility at 900K, the boron-doped alloy showed a much more dramatic drop and little increase in ductility with increasing temperature above 700K (Figure 12). Carleton et al. investigated the elongation in vacuum of FeAl (40 to 48 at. % Al) doped with 300 ppm B as a function of temperature [90]. Like unalloyed FeAl, these alloys showed slow increases in ductility from room temperature up to 500-600 K and then more rapid increases up to 700-800K. However, the boron-doped alloys showed catastrophic drops in elongation above 800K, whereas unalloyed FeAl alloys exhibit only slight drops in elongation around 700-800K before their elongations increase to >100 % at 900K [87]. For the worst case, boron-doped Fe-48Al, the elongation to failure dropped from >40% at 800 K to ~2% at 1100 K [89]. The elongation drop was associated with a change in fracture mode from ductile rupture to intergranular fracture with considerable grain boundary cavitation. Gaydosh et al. [66] observed similar behavior in both unalloyed Fe-40Al and Fe-40Al doped with C or Zr with or without B although the elongation drops were less dramatic.

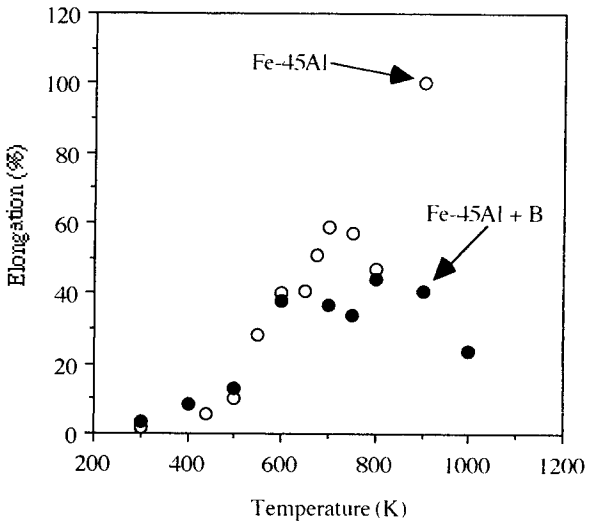


Figure 12. Elongation as a function of temperature for large-grained low-temperature-annealed Fe-45Al and Fe-45Al + 500 ppm B. After Klein and Baker [114].

Again, failure was accompanied by considerable grain boundary cavitation above 900K. Interestingly, Fe-40Al alloys doped with Hf or Hf and B did not show a ductility drop at high temperatures and the occurrence of grain boundary cavitation was much less than in the other alloys [66].

In summary, the fracture behavior of FeAl is strongly affected by *extrinsic* factors such as the testing environment and heat treatment; which can mask the *intrinsic* behavior of FeAl. When testing under conditions where these factors are negligible the stoichiometric alloy exhibits brittle intergranular fracture at room temperature, whereas iron-rich alloys show a few percent elongation, with the fracture mode becoming increasingly transgranular with increasing iron concentration. The ductility increases with increasing temperature and at higher temperatures the fracture mode changes to ductile, dimple-type rupture.

FeCo

FeCo is stable over an unusually wide range of composition from ~25 to ~75 at. % Co. It is also disorderable; the order-disorder transformation temperature varies with composition and exhibits a maximum of 1003K at the stoichiometric composition [64]. If FeCo is quenched from above the order-disorder transformation temperature disorder may be retained at room temperature, although complete disorder can only be retained in very thin sections [115].

Stoichiometric FeCo in the ordered state fractures before yielding [116-121]. However, different modes of fracture have been reported in the literature. Zhao and Baker observed predominantly intergranular fracture with a small amount of transgranular cleavage [116,117], whereas other workers have observed transgranular failure [118-121]. However, Auger electron spectroscopy by Zhao et al. indicated the presence of sulfur on the grain boundaries of their alloy which may have influenced the mode of fracture [117].

Some ductility (~4%) is exhibited by disordered stoichiometric FeCo, although disorder produces no significant change in the fracture mode [116,117]. $Fe_{70}Co_{30}$ exhibits very similar behavior to the stoichiometric alloy in both the ordered and disordered conditions, that is failure without yielding when ordered and limited ductility (~7%) when disordered [116,117]. In contrast, Zhao and Baker found that $Fe_{30}Co_{70}$ exhibits appreciable ductility and dimple-type fracture in both the ordered (~17% elongation) and disordered (~22% elongation) states.

Although ordered stoichiometric FeCo is very brittle the addition of a small amount (2 wt. %) of vanadium endows this material with some ductility [119]. FeCo-2V exhibits strains to failure of about 5% in the ordered state and about 15% when disordered; both materials fail transgranularly [119,122]. Under both conditions FeCo-2V exhibits {110}<111> slip [123], but the difference in plasticity can be related to a change in slip character which occurs when this material is disordered. In the ordered state, where deformation occurs through the motion of paired dislocations, slip is planar. Conversely, in the disordered state the dislocations are not paired and slip is wavy, since the propensity for cross-slip is higher. This reduces the likelihood of internal stresses leading to crack nucleation.

Interestingly, Kuruvilla and Stoloff demonstrated that FeCo-2V is susceptible to hydrogen embrittlement in both the disordered and ordered states [124]. In the ordered state brittle transgranular cleavage was observed during testing in both air and in hydrogen. However, in the disordered state, dimple-type fracture was noted in the specimens tested in air whilst transgranular cleavage was again observed in hydrogen.

Why ordered FeCo is brittle is unclear. It has sufficient slip systems for general plasticity, is not strongly-ordered and even when lacking impurities fractures transgranularly (at yielding at the stoichiometric composition). Possibly the sessile <001> dislocations nucleate cleavage cracks, as suggested for FeAl [82]. It is also unclear why deviation from stoichiometry on the Co-rich side leads to ductile rupture whilst with deviations away from stoichiometry on the iron-rich side the fracture mode remains brittle. It is clear that disorder which leads to wavy slip, as opposed to planar slip in the ordered state, improves ductility (Figure 13).

CuZn

CuZn, better known as β-brass, is a B2 compound which is also disorderable. At room temperature it exists from about 46 to 50 at. % Zn [64]. The order-disorder transition temperature is at ~740K and varies only slightly with composition. CuZn exhibits <111> slip at room temperature, but other slip vectors such as <001> and <110> have been noted following deformation at higher temperatures or in appropriately oriented single crystals. Shea and Stoloff obtained reductions in area of about 50% for Cu-48Zn when tested in argon at room temperature [125,126]. Slightly lower ductilities were noted as the zinc content decreased or if nickel or manganese was added at the expense of copper. Intergranular cracks formed in these alloys which propagated into the grain interiors and ultimately led to a dimpled transgranular failure. The extent of the intergranular cracking was attributed to the ease of cross-slip, for example, manganese additions restricted cross-slip and increased the susceptibility to intergranular cracking.

β-brass is susceptible to embrittlement in a variety of environments [126]. Stress corrosion cracking occurs in ammoniacal solutions and failure occurs through transgranular cracking. β-brass is also susceptible to liquid metal embrittlement. Gallium environments lead to large transgranular failure, whist indium and indium-mercury environments promote intergranular failure. Single crystals of β-brass exhibited transgranular failure on {001} planes in gallium environments, irrespective of composition or crystal orientation.

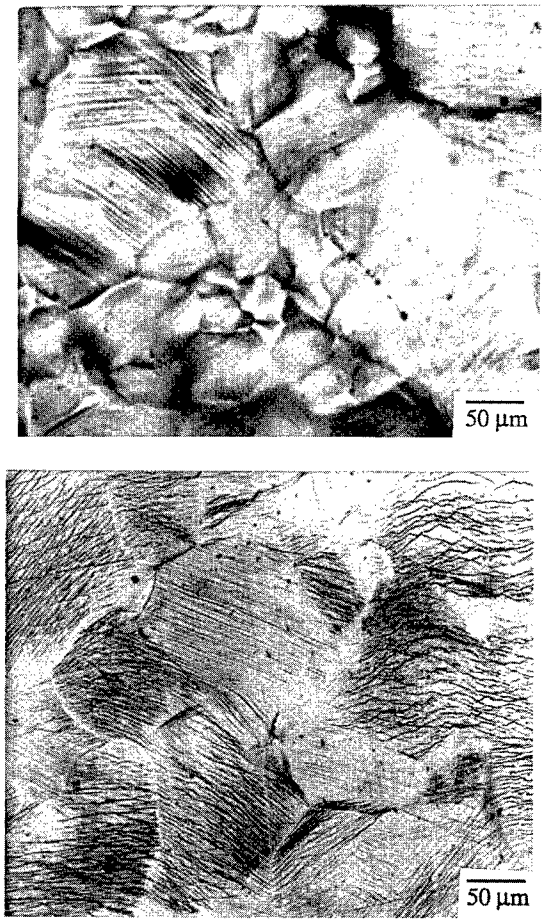


Figure 13. Optical micrographs of slip traces on the surface of Fe-30Co compressed at room temperature in (a) the ordered state (planar slip); and (b) the disordered state (wavy slip). After Zhao and Baker [116].

Other Compounds

A number of other B2 compounds have been studied, but in much less detail than the materials described above. Their fracture behavior is briefly described below.

CoAl

CoAl has a melting point of 1921K and is stable over a wide range of composition (~47-57 at. % Al) [64]. Like NiAl it exhibits <001> slip at both ambient and elevated temperatures [127], although Yaney et al. noted <111> dislocations in material extruded at 1505K [128]. Its fracture behavior is, in general, very similar to that of NiAl. Single crystal CoAl, tested at room temperature, exhibited no plastic elongation irrespective of composition [129]. Room temperature testing of polycrystalline CoAl has shown that stoichiometric CoAl exhibits a mixture of intergranular fracture and transgranular cleavage, whilst both Co-rich and Al-rich compositions exhibits transgranular cleavage [130] (Figure 14). High quality channeling patterns were obtained from both intergranular and transgranular fracture surfaces in stoichiometric CoAl and transgranular fracture surfaces of the off-stoichiometric alloys (Figure 14), indicating that fracture occurs after little dislocation activity and that failure most probably occurs elastically. Chang et al. studied the fracture of cobalt-rich CoAl single crystals. A K_{1C} value of ~3 $MPa.m^{1/2}$ was obtained for Co-49Al, indicating that it is somewhat less tough than NiAl [53] and the fracture plane was again noted to be {110}. As for NiAl, polycrystals won't show much ductility due to the lack of slip systems. It remains unclear whether CoAl single crystals could exhibit greater ductility, like NiAl, if tested under carefully-controlled conditions

RuAl

RuAl has attracted attention because of its excellent corrosion resistance and high temperature properties, although the cost of ruthenium clearly prohibits its widespread application. RuAl exists over a narrow range of compositions, and is stable at room temperature from about 47 to 50 at. % Ru [64].

Fleischer and co-workers examined the room temperature behavior of a number of RuAl-based compositions [131-134], and showed that the room temperature compressive ductility of RuAl is strongly dependent upon composition [133]. $Al_{53}Ru_{47}$ fractures before yielding, but both the stoichiometric alloy and $Al_{47}Ru_{53}$ exhibit compressive ductilities in excess of 10%, but there have been no reports of tensile ductility.

$Al_{47}Ru_{53}$ which is two phase, and contains a Ru solid solution as both an intergranular phase and as intragranular rods, exhibits transgranular cleavage, but Al-rich RuAl fails predominantly by intergranular fracture [133]. Auger electron spectroscopy showed that the grain boundaries in $Al_{53}Ru_{47}$ were aluminum-rich, and it was speculated that this might be associated with the presence of a layer of Al_2Ru at the boundaries [132]. Boron additions to Al-rich RuAl promote a fibrous, ductile fracture and improve both strength and compressive plasticity [132-134]. Burgers' vector analysis of Ru-rich RuAl revealed the presence of <111>, <110> and <001> dislocations [133]. Thus, Fleischer and co-workers attributed the compressive ductility of this compound to the large number of possible slip systems [133]. Although, if all the dislocation types were active during deformation significant tensile ductility might be expected in this material in the absence of other embrittling phenomena.

More recently Wolff and Sauthoff have studied the mechanical behavior of a number of (Ru, Ni)Al alloys, since the addition of Ni at the expense of Ru significantly lowers the material's cost. [135] These alloys again exhibited significant room temperature compressive ductility, but no tensile plasticity. The mode of fracture or active slip systems were not determined.

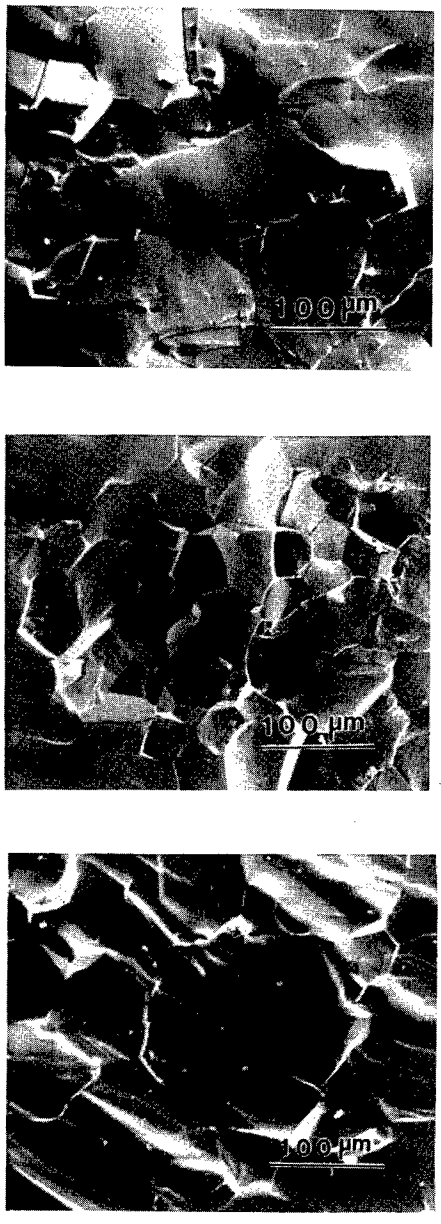


Figure 14. Scanning electron micrographs of room temperature fracture surfaces of a) Co-47Al, b) Co-50Al and c) Co-52Al. After Xiao and Baker [130].

AgMg

AgMg has been studied by a number of workers, usually as a model B2 system, and is stable at room temperature from 41 to 53 at. % Mg [64] At room temperature it deforms by <111> slip, usually on {112} planes [136,137], which provides sufficient slip systems for ductility in polycrystals.

Turning first to single crystals, Mitchell et al. observed strains to failure of about 6% during tensile testing of nominally stoichiometric AgMg at 237.5K; failure occurred by cracking on {001} planes [136]. These workers also found evidence of <001> slip in crystals oriented to decrease the resolved shear stress for <111> slip. However, Murakami et al. found evidence of <001> slip only after deformation at temperatures above 450K [137], although their studies were performed only in compression on silver-rich material. Kurfman found that nominally stoichiometric AgMg was notch sensitive at room temperature during bending tests and unpolished samples failed prematurely with cracking along {001} planes [138]. It is possible that these cracks might be associated with the interaction of <111> dislocations to form sessile <001> dislocations [82].

Terry and Smallman showed that the plasticity and fracture mode of polycrystalline AgMg is strongly dependent upon composition. Both stoichiometric and Mg-rich compositions fail intergranularly without yielding at room temperature [139], suggesting that the boundaries of these compositions are intrinsically weak. As the Mg content is decreased plasticity increases, with decreasing incidence of intergranular fracture. Ag-41.3Mg is quite ductile at room temperature, showing negligible intergranular failure [139]. Wood and Westbrook also observed intergranular fracture in magnesium-rich specimens, although they attributed this to local segregation [140].

NiBe

Beryllides have attracted some interest because of their very low densities, good high temperatures strength and superior oxidation resistance. Most beryllides exhibit complex crystal structures and fail before yielding. However, NiBe is a B2-structured compound which is stable over a wide range of compositions. Stoichiometric NiBe deforms by <001> slip at room temperature and Pharr et al. noted some tensile ductility (1.3%) at this temperature [141]. Failure occurred predominantly by intergranular fracture, although some transgranular cleavage was also noted, consistent with the lack of independent slip systems for plastic flow in polycrystals. Although NiBe possess similar specific properties to NiAl, toxicity problems associated with its handling provide a major drawback to its application.

PdIn/CsBr/AuZn

The compounds PdIn, CsBr and AuZn have been reported to exhibit <100> slip at room temperature. Limited ductility has been observed in polycrystalline, near-stoichiometric compositions of both PdIn [142] and CsBr [143] at room temperature, both materials exhibiting principally intergranular fracture. In contrast, polycrystalline AuZn [144] is ductile in tension at room temperature, both at stoichiometry, and when Au-rich and Zn-rich. It has been suggested that <111> slip contributes to deformation, in addition to <100> slip, thus providing sufficient slip systems for plastic flow, although no direct experimental evidence has been provided [144]. It has also been suggested that polycrystalline AuZn exhibits a stress-induced martensitic reaction, which may be responsible for its ductility [145].

NiTi

Some B2-structured materials, for example NiTi [146] and (Co,Ni)Zr [147,148] and (Co,Ni)Zr-based compounds, display considerable ductility at room temperature even though they exhibit <100> slip, when only limited ductility may be expected. For example, at room temperature an elongation to fracture of over 40% has been observed in $(Co_{40}Ni_{10})Zr_{50}$ [147,148]. This behavior is associated with the occurrence of a reversible stress-induced martensitic transformation.

Conclusion

The fracture behavior of a number of B2 compounds has been reviewed. The generally low room temperature toughness and ductility of these materials can be attributed to a number of causes. In some compounds, for example, single crystal NiAl or very iron-rich FeAl, *extrinsic* factors dominate behavior and significant ductility and toughness can be achieved during testing under circumstances where these factors are controlled. However, in other materials *intrinsic* factors dominate the fracture behavior. For example, in polycrystalline NiAl low ductility and toughness is associated with a lack of independent slip systems, whereas in FeAl the grain boundaries are intrinsically weak .

Acknowledgements

This work was supported by the Division of Materials Science, Office of Basic Energy Sciences, U.S. Department of Energy through Grant DE-FG02-87ER45311.

References

1. I. Baker and E.P. George, Metals and Materials, 8 (1992), 318-323.

2. I.Baker and P.R.Munroe, High Temperature Alumindes and Intermetallics, eds. S.H. Whang et al., (TMS, Warrandale, PA), (1990), 425-452.

3. W.A. Rachinger and A.H. Cottrell, Acta Metall., 4 (1956), 109-113.

4. A. Ball and R.E. Smallman, Acta Metall., 14 (1966), 1517-1526.

5. D.I. Potter, Mat. Sci. Eng., 5 (1969/70), 201-209.

6. E.P. Lautenschlager, T. Hughes and J.O. Brittain, Acta Metall., 15 (1967), 1347-1357.

7. M.G. Mendiratta and C.C. Law, J. Mat. Sci., 22 (1987), 607-611.

8. M. Koiwa, "Ordered Intermetallics - Physical and Mechanical Behaviour", eds. C.T. Liu et al., (Kluwer Academic Publishers, Dordrecht, Netherlands), (1992), 449-464.

9. N. Rusovic and H. Warlimont, Phys. Stat. Solidi, 44 (1977), 609-619.

10. M.H. Loretto and R.J. Wasilewski, Phil. Mag., 23 (1971), 1311-1328.

11. R.T. Pascoe and C.W.A. Newey, Phys. Stat. Sol., 29 (1968), 357-366.

12. P. Veyssiere and R. Noebe, Phil. Mag. A, 65 (1992), 1-13.

13. R.D. Field, D.F. Lahrman and R. Darolia, Acta Metall., Mater., 39 (1991) 2951-2959.

14. D.B. Miracle, Acta Metall. Mater., 39 (1991), 1457-1468.

15. J. Bevk, R.A. Dodd, and P.R. Strutt, Metall. Trans., 4 (1973), 159-166.

16. P. Nagpal and I. Baker, J. Mater. Sci. Lett., 11 (1992), 1209-1210.

17. P. Nagpal, I. Baker, and J.A. Horton, J. Intermetallics, 2 (1994), 23-29.

18. I. Baker, P. Nagpal, F. Liu, and P.R. Munroe, Acta Metall. Mater., 39 (1991), 1637-1644.

19. M.J. Mills and D.B. Miracle, Acta Metall. Mater., 41 (1993), 85-95.

20. J.T. Kim and R. Gibala, High Temperature Ordered Intermetallic Alloys, IV, eds. L.A. Johnson et al, Materials Research Society, Pittsburgh, 213 (1991), 261-266.

21. R.J.Wasilewski, S.R. Butler and J.E. Hanlon, Trans. AIME, 239 (1967), 1357-1364.

22. R.D.Noebe, J.T.Kim and R.Gibala, High Temperature Ordered Intermetallic Alloys, II, eds. N.A. Stoloff et al., Materials Research Society, Pittsburgh, 81 (1987), 473-480.

23. R.D. Noebe, A. Misra and R. Gibala, ISIJ Int., 31 (1991), 1172-1185.

24. V.I. Levit, I.A. Bul, J. Hu and M.J. Kaufman, Scripta Mater., 34 (1996), 1925-1930.

25. D.F. Lahrman, R.D. Field, and R. Darolia, Scripta Metall. Mater., 28, (1993), 709-714.

26. K.H. Hahn and K. Vedula, Scripta Metall., 23 (1989), 7-12.

27. R.D. Noebe, R.R. Bowman, C.L. Cullers and S.V. Raj, High Temperature Ordered Intermetallic Alloys, IV, eds. L.A. Johnson et al., Materials Research Society, Pittsburgh, 213 (1991), 589-596.

28. A.G. Rozner and R.J. Wasilewski, J. Inst. Metals, 94 (1966), 169-175.

29. E.P. George and C.T. Liu, J. Mater. Res., 5 (1990), 754-762.

30. P. Nagpal and I. Baker, Scripta Metall. Mater., 24 (1990), 2381-2384.

31. C.C. Law and M.J. Blackburn, Rapidly Solidified Lightweight Durable Disk Material, Pratt and Whitney Aircraft Co., West Palm Beach, Florida USA, Final Technical Report AFWAL-TR-87-4102 1987.

32. D.B. Miracle, S. Russell, and C.C. Law, High Temperature Ordered Intermetallic Alloys, III, eds. C.T. Liu et al., Materials Research Society, Pittsburgh, 213 (1991), 225-230.

33. J.D. Cotton, R.D. Noebe and M.J. Kaufman, J. Intermetallics, 1 (1993), 117-126.

34. D.K. Patrick, K-M. Chang, D.B. Miracle and H.A. Lipsitt, High Temperature Ordered Intermetallic Alloys IV, eds. L.A. Johnson et al., Materials Research Society, Pittsburgh, 213 (1991), 267-272.

35. P.P. Camus, I. Baker, J.A. Horton, and M.K. Miller, J. de Phys., 49 C6 (1988), 329-333.

36. M.K. Miller, R. Jayaram and P.P. Camus, Scripta Metall., 26 (1992), 679-684.

37. R.W. Fonda and D.E. Luzzi, High Temperature Ordered Intermetallic Alloys V, eds. I. Baker et al., Materials Research Society, Pittsburgh, 288 (1993), 361-366.

38. R.W. Fonda and D.E. Luzzi, Phil. Mag. A, 68 (1993), 1151-1164.

39. S.P. Chen, A.F. Voter, R.C. Albers, A.M. Boring and P.J. Hay, High Temperature Ordered Intermetallic Alloys III, eds. C.T. Liu et al., Materials Research Society, Pittsburgh, 213 (1989), 149-155.

40. G. Petton and D. Farkas, Scripta Metall. Mater., 25 (1991), 55-60.

41. P.S. Khadkikar, G.M. Michal and K. Vedula, Metall. Trans. A, 21A (1990), 279-288.

42. I. Baker and E.M. Schulson, Metall. Trans. A, 15A (1984), 1129-1136.

43. P. Nagpal and I. Baker, Mater. Charac., 27 (1991), 167-173.

44. I. Baker, P. Nagpal, O. Klein and F. Liu, "Processing and Properties of Materials", eds. M.H. Loretto and C.J. Beevers, MCE publications, vol. 2, (1992), 665-670.

45. R.D. Noebe, R.R. Bowman and M.V. Nathal, "Physical Metallurgy and Processing of Intermetallic Compounds", eds. N.S. Stoloff and V.K. Sikka, Chapman and Hall, New York, (1996), 212-296.

46. S. Guha, I. Baker, P.R. Munroe and J.R. Michael, Mater. Sci. Eng., A152 (1992) 258-263.

47. E.M. Schulson, Res. Mech. Lett., 1 (1981), 111-114.

48. E.M. Schulson and D.R. Barker, Scripta Metall., 17 (1983), 519-522.

49. R.R. Bowman, R.D. Noebe, S.V. Raj and I.E. Locci, Metall. Trans. A, 23A (1992), 1493-1508.

50. R.W. Margevicius and J.J. Lewandowski, Scripta Metall. Mater., 25 (1991), 2017-2022.

51. R.D. Noebe, C.L. Cullers and R.R. Bowman, J. Mater. Res., 7 (1992), 605-612.

52. E.M. Schulson, High Temperature Ordered Intermetallic Alloys, III, eds. C.C. Koch et al., Materials Research Society, Pittsburgh, 39 (1985), 193-204.

53. C.H. Lloyd and M.H. Loretto, Phys. Stat. Solidi, 39 (1970), 163-170.

54. K.M. Chang, R. Darolia, and H.A. Lipsitt, Acta Metall. Mater., 40 (1992), 2727-2737.

55. J.E. Hack, J.M. Brzeski, and R. Darolia, Scripta Metall. Mater., 27 (1992), 1259-1263.

56. H. Vehoff, High Temperature Ordered Intermetallic Alloys V, eds. I. Baker et al., Materials Research Society, Pittsburgh, 288 (1993), 71-82.

57. J. Schneibel, M.G. Jenkins, and P.J. Maziasz, High Temperature Ordered Intermetallic Alloys,V, eds. I. Baker et al., Materials Research Society, Pittsburgh, 288 (1993), 549-554.

58. S. Reuss and H. Vehoff, Scripta Metall. Mater., 24 (1990), 1021-1026.

59. J.J. Lewandowski, G.M. Michal, I.E. Locci and J.D. Rigney, Alloy Phase Stability and Design, eds. G.M. Stocks et al., Materials Research Society, Pittsburgh, 186, (1991), 341-347.

60. K.S.Kumar, S.K. Mannan and R.K. Viswanadham, Acta Metall. Mater., 40 (1992), 1201-1222.

61. W.A. Kaysser, R. Laag, J.C. Muuray and G.E. Petzow, Int. J. Powder Metallurgy, 27 (1991), 43-49.

62. J.D. Rigney and J.J. Lewandowski, Mat. Sci. Eng., A149 (1992), 143 -151.

63. M.H. Yoo and C.L. Fu, Mat. Sci. Eng., A153 (1992), 470-478.

64. T. Massalski, Binary Phase Diagrams, ASM, Metals Park Ohio, 1986.

65. M.G. Mendiratta, H.K. Kim and H.A. Lipsitt, Metall. Trans. A, 15A (1984), 395-399.

66. I. Baker and D.J. Gaydosh, Mater. Sci. Eng., 96 (1987), 147-158.

67. P.R. Munroe and I. Baker, J. Mater. Sci., 24 (1989), 4246-4252.

68. M.A. Crimp, K.M. Vedula and D.J. Gaydosh, High Temperature Ordered Intermetallic Alloys II, eds. N.A. Stoloff et al., Materials Research Society, Pittsburgh, 81 (1987), 499-504.

69. D.J. Gaydosh and M.V. Nathal, Scripta Metall. Mater., 24 (1990), 1281-1284.

70. D.J. Gaydosh, S.L. Draper and M.V. Nathal, Metall. Trans. A, 20A (1989), 1701-1714.

71. C.T. Liu, E.H. Lee and C.G. McKamey, Scripta Metall., 23 (1989), 875-890.

72. P. Nagpal and I. Baker, Metall. Trans. A, 21A (1990), 2281-2282.

73. P. Nagpal and I. Baker, Scripta Metall. et Mater., 25 (1991), 2577-2580.

74. I. Baker, O. Klein, C. Nelson, and E. P. George, Scripta Metall. Mater., 30 (1994), 863-868.

75. N.S. Stoloff and C.T. Liu, J. Intermetallics, 2 (1992), 75-88.

76. C.G. Mckamey, "Physical Metallurgy and Processing of Intermetallic Compounds", eds. N.S. Stoloff and V.K. Sikka, Chapman and Hall, New York, (1996), 351-391.

77. N.S. Stoloff, "Physical Metallurgy and Processing of Intermetallic Compounds", eds. N.S. Stoloff and V.K. Sikka, Chapman and Hall, New York, (1996), 479-516.

78. D.B. Kasul and L.A. Heldt, Metall. Trans. A, 25 (1994), 1285-1290.

79. J.C.M. Li and C.T. Liu, Scripta Metall. et Mater., 33 (1995), 661-668.

80. N.R. Gleason, C.A. Gerken and D.R. Strongin, Applied Surface Science, 72 (1993), 215-225.

81. G.M. Camus, N.S. Stoloff and D.J. Duquette, Acta Metall., 37 (1989), 1497-1501.

82. P.R. Munroe and I. Baker, Acta Metall., 39 (1991), 1011-1017.

83. D.J. Gaydosh, S.L. Draper, R.D. Noebe, and M.V. Nathal, Mater. Sci. Eng., A150 (1992), 7-20.

84. M.V. Nathal and C.T. Liu, J. Intermetallics, 3 (1995), 77-82.

85. E.P. George, C.T. Liu and D.P. Pope, Acta Mater., 44 (1996), 1757-1764.

86. C.G. McKamey, J.A. Horton and C.T. Liu, J. Mater. Res., 4 (1989), 1156-1163.

87. I. Baker, H. Xiao, O. Klein, C. Nelson and J. D. Whittenberger, Acta Metall. Mater., 43 (1995), 1723-1730.

88. C.T. Liu and E.P. George, Scripta Metall. et Mater., 24 (1990), 1285-1290.

89. C.T. Liu and E.P. George, High Temperature Ordered Intermetallic Alloys IV, eds.L.A. Johnson et al., Materials Research Society, Pittsburgh, 213 (1991), 527-532.

90. R. L. Carleton, E. P. George, and R. H. Zee, Intermetallics, 3 (1995), 433.

74. I. Baker, O. Klein, C. Nelson, and E. P. George, Scripta Metall. Mater., 30 (1994), 863-868.

91. J.P. Rivière and J. Grilhe, Scripta Metall., 9 (1975), 967-970.

92. R. Würschum, C. Grupp and H.-E. Schaefer, Physical Review Letters, 75 (1995), 97-100.

93. D. Paris and P. Lesbats, J. of Nuclear Materials, 69/70 (1978), 628-32.

94. J.P. Rivière and J. Grilhe, Acta Metall., 20 (1972), 1275-1280.

95. B. Schmidt, P. Nagpal, and I. Baker,High Temperature Ordered Intermetallic Alloys III, eds. C.T. Liu et al., Materials Research Society, Pittsburgh, 213 (1989), 755-760.

96. O. Klein and I. Baker, Scripta Metall. Mater., 30, (1994), 627-632.

97. D.J. Alexander, Processing, Properties and Applications of Iron Alumindies, eds. J.H. Schneibel and M.A. Crimp, TMS, Warrendale, (1994), 193-202.

98. M.A. Crimp, K.M. Vedula and D.J. Gaydosh, High Temperature Ordered Intermetallic Alloys II, eds. N.S. Stoloff et al., Materials Research Society, Pittsburgh, 81 (1987), 499-504.

99. S.D. Strothers and K. Vedula, Prog. Powd. Met., 43 (1987), 597-610.

100. K-M. Chang, Metall. Trans. A, 21A (1991), 3027-3028.

101. O. Klein, I. Baker and P. Nagpal, High Temperature Ordered Intermetallic Alloys V, eds. I. Baker et al., Materials Research Society, Pittsburgh, 288 (1993),935-940.

102. J.H. Schneibel and M.G.Jenkins, Scripta Metall. Mater., 28 (1993), 389-394.

103. I. Baker and J.A. Horton, Phil. Mag. A, 67 (1993), 479-489.

104. C.T. Liu and E.P. George, Scripta Metall. Mater., 24 (1990), 1285-1290.

105. C.L. Fu and M.H. Yoo, High Temperature Ordered Intermetallic Alloys IV, eds. L.A. Johnson et al., Materials Research Society, Pittsburgh, 213 (1991), 667-672.

106. C.L. Fu and M.H. Yoo, Acta Metall. Mater., 40 (1992), 703-711.

107. C.L. Fu and G.S. Painter, J. Mater. Res., 6 (1991), 719-723.

108. P.A. Schultz and J.W. Davenport, Scripta Metall. Mater., 27, 1992, 629-634.

109. S. Mandsziej, Scripta Metall. Mater., 25 (1991), 213-218.

110. J.C.M. Li and C.T. Liu, Scripta Metall. Mater., 27 (1992), 1701-1705.

111. H. Xiao and I. Baker, Scripta Metall. Mater., 28, (1993), 1411-1416.

112. M.G. Mendiratta, S.K. Ehlers, D.M. Dimiduk, W.R. Kerr, S. Mazdiyasni and H.A. Lipsitt, High Temperature Ordered Intermetallic Alloys II, eds. N.A. Stoloff et al., Materials Research Society, Pittsburgh, 81 (1987), 393-399.

113. K. Yoshimi, N. Matsumoto, S. Hanada and M.H. Yoo, Processing, Properties and Applications of Iron Alumindies, eds. J.H. Schneibel and M.A. Crimp, TMS, Warrendale, (1994), 205-216.

114. O. Klein and I. Baker, Scripta Metall. Mater., 30, (1994), 1413-1417.

115. D.W. Clegg and R.A. Buckley, J. Met. Sci., 7 (1983) 48-53.

116. L. Zhao and I. Baker, Acta Metall. Mater., 42 (1994), 1953-1958.

117. L. Zhao, I. Baker and E.P. George, High Temperature Ordered Intermetallic Alloys V, eds. I. Baker et al, Materials Research Society, Pittsburgh, 288 (1993), 501-506 .

118. A.M. Glezer and I.V. Maleyeva, Phy. Met. Metall., 68 (5) (1989), 65-72.

119. T.L. Johnston, R.G. Davies and N.S. Stoloff, Phil. Mag., 12 (1965), 305-317.

120. M.J. Marcinkowski and J. Larsen, Metall. Trans., 1 (1970), 1034-1036.

121. A.M. Glezer and I.V. Maleyeva, Phy. Met. Metall., 66 (1988), 174-176.

122. N.S. Stoloff and R.G. Davies, Acta Metall., 12 (1964), 473-485.

123. M. Yamaguchi, Y. Umakoshi and T. Yamane, Scripta Metall., 16 (1982), 607-609.

124. A.K. Kuruvilla and N.S. Stoloff, Scripta Metall., 16 (1982), 83-87.

125. M.M. Shea and N.S. Stoloff, Metall. Trans., 5 (1974), 755-762.

126. M.M. Shea and N.S. Stoloff, Mater. Sci and Eng., 12 (1973), 245-253.

127. M. Yamaguchi and Y. Umakoshi, Prog. Mat. Sci., 34 1-148, (1990).

128. D.L.Yaney, A.R. Pelton and W.D. Nix, J. Mater. Sci., 21 2082-2087, (1986).

129. R.L. Fleischer, J. Mater. Res., 8 (1993), 59-69.

130. H. Xiao and I. Baker, Mater. Charac., 33 (1994), 187-191.

131. R.L. Fleischer and R.J. Zabala, Metall. Trans. A, 21A (1990), 2709-2715.

132. R.L. Fleischer, C.L. Briant and R.D. Field, High Temperature Ordered Intermetallic Alloys IV, eds. L.A. Johnson et al., Materials Research Society, Pittsburgh, 213 (1991), 463-474.

133. R.L. Fleischer, R.D. Field and C.L. Briant, Metall. Trans. A, 22A (1991), 403-414.

134. R.L. Fleischer, Metall. Trans. A, 24A (1993), 227-230.

135. I.M. Wolff and G. Sautoff, Metall. Trans. A, 27A (1996),1395-1399.

136.J.B. Mitchell, O. Abo-el-Fotoh and J.E. Dorn, Metall. Trans. A, 2A (1971), 3265-3275.

137. K. Murkami, Y. Umakoshi and M. Yamaguchi, Phil.Mag. A, 37 (1978), 719-730.

138.V.B. Kurfman, Acta Metall., 13 (1965), 307-315.

139.J.C. Terry and R.E. Smallman, J. Inst. Metals., 92 (1963-64), 334-336.

140.D.L. Wood and J.H. Westbrook, Trans. AIME, 224 (1962), 1024-1037.

141. G.M. Pharr, S.V. Covington, J. Wadsworth and T.G. Nieh, J. Mater. Res., 6 (1991), 2653-2659.

142. P.R. Munroe, I. Baker and P. Nagpal, J. Mater. Sci., 26 (1991), 4303-4306.

143. L.D. Johnson and J.A. Pask, J.Am.Ceramic. Soc., 47 (1964), 437.

144. A.R. Causey and E. Teghtsoonian, Metall. Trans. A, 1A (1970), 1177.

145. E.M. Schulson, Private Communication, (1989).

146 A.G. Rozner and R.J. Wasilewski, J. Inst. Metals, 94 (1966), 169.

147. C. Lall, M.H. Loretto and I.R. Harris, Acta Metall., 26 (1978), 1631.

148. D. Hossain, I.R. Harris and, G. Barraclough, J.Less-Common Metals, 37 (1974), 35.

MIXED-MODE CLEAVAGE FRACTURE OF AN IRON ALUMINIDE UNDER MONOTONIC LOADING

F. Robert Frasier and J. P. Hirth
School of Mechanical and Materials Engineering
Washington State University
Pullman WA USA 99164-2920

Polycrystalline 3-point bend specimens of an Fe_3Al alloy were K tested in a desiccated Ar atmosphere. Specimens were taken from a warm-rolled plate of nominal 6mm thickness and were fabricated in the T-L orientation. The measured K_{1c} was found to be 31 MPa·√m. Fractographic examination of mode I specimens revealed that fracture had occurred by a complex mixture of mode I transgranular cleavage and mode III intergranular failure. No substantial evidence of ductile rupture was seen on the fracture surfaces. These results are unexpected for this alloy tested in a moisture-free atmosphere. A model for the state of stress responsible for these observations will be introduced, and the implications of these results will be discussed.

George R. Irwin Symposium on Cleavage Fracture
Edited by Kwai S. Chan
The Minerals, Metals & Materials Society, 1997

Introduction

Iron aluminides based upon modifications of stoichiometric Fe_3Al are ordered intermetallic alloys that offer the potential for good oxidation resistance, excellent sulfidation resistance, lower material costs than many Ni / Cr alloyed stainless steels and potentially greater specific mechanical properties than many stainless steels. Iron aluminides have been of interest to metallurgists since the 1930's, when their excellent oxidation resistance was first noted [1, 2]. However, limited ductility (<5%) at room temperature (RT), and a sharp drop in yield strength above 600 °C have limited their application as structural materials. Several excellent reviews of the early work on iron aluminides exist [3, 4]. More recent studies have shown that through careful control of composition and microstructure, engineering ductility can be increased to potentially useful levels (15-20%) [5, 6, 7, 8].

Phase relationships in the binary Fe-Al system are well known [9, 10, 11]. Near Fe_3Al, three equilibrium phases have been confirmed: a disordered solid solution (α), an Fe_3Al with an imperfectly ordered B2 structure, an ordered Fe_3Al with the DO_3 structure, and the requisite two-phase boundary regions, $\alpha+DO_3$ and $\alpha+B2$.

Both of the ordered structures, DO_3 and B2 are derived from the body-centered cubic structure. B2 is BCC with iron atoms at the corners of the cube, and an aluminum atom occupying the body center site. DO_3 consists of eight B2 unit cells, stacked to maximize the distance between Al atoms. In a sense, the DO_3 structure can be considered to be a "pseudo B2", in that for stoichiometric Fe_3Al, only half of the Al sites of a B2 structure are actually occupied by aluminum atoms. The other body center sites are occupied by iron in binary alloys, or by either iron or chromium with equal probability in ternary alloys. The transition temperature between B2 and DO_3 is 550 °C for stoichiometric Fe_3Al, and the transition is very sluggish [12]. For the B2 structure, room temperature slip occurs by movement of a pair of anti-phase boundary (APB) coupled dislocations, with the Burgers vector $^a/_2\langle 111\rangle$ [13, 14, 15, 16, 17, 18]. These can couple as $\langle 100\rangle$ dislocations that glide on {110} or {100} planes. Secondary $\langle 111\rangle$ dislocations are sometimes also observed. In the DO_3 structure, slip occurs by movement of a unit dislocation consisting of four $^a/_4\langle 111\rangle$ dislocations, coupled by two different APB's. Hence, both structures hypothetically meet the von Mises criterion for polycrystalline slip. The presence of five active, independent slip systems would indicate that Fe_3Al should be intrinsically ductile at room temperatures.

However, early work on the iron-aluminides found very poor room temperature ductility. The first significant success at increasing room temperature ductility occurred in the 1950's and 1960's [19, 20, 21, 22]. Through a combination of micro-alloying and hot-working to control grain structure, room temperature ductilities as high as 10% were reported. In general, alloys and processing schedules that resulted in finer grain sizes led to improved room temperature ductility [23]. The predominance of intergranular fracture under tensile loading, especially at aluminum levels greater than 20 atomic percent, led to the view that long range order was responsible for retarding cross-slip of screw dislocations with a concurrent reduction in the number of active slip systems [24]. More recent work has found that intergranular fracture is strongly affected by interstitial impurities, especially carbon.

More recently, there have been new approaches to improved alloys. Some work has focused on producing rapidly solidified powders as a means of achieving microstructural refinement [5, 25, 6]. Other work has concentrated upon alloying with the aim of producing wrought material for fossil energy applications [7,8, 26, 27, 28, 29]. The alloy used in the current research was developed in the latter program for elevated temperature use and given the designation FA-129. The nominal composition of this alloy is listed as [7]: Fe-28Al-5Cr-0.5Nb-0.2C (at.%). After thermo-mechanical processing, this alloy has been reported to exhibit greater than 15% RT ductility and a tensile yield strength of approximately 525 MPa [7]. Although the material used in the present tests was not examined for type or degree of ordering, the thermo-mechanical processing would result in a structure that is essentially 100% imperfectly ordered B2 [30].

Although the above referenced programs of alloying and thermo-mechanical processing met with a good deal of success in improving the RT mechanical properties of iron-aluminides, the underlying cause(s) of the brittle behavior of what would at first appear to be a ductile structure were not directly addressed. However, as early as 1985, environmental embrittlement had been suspected [31, 32]. Between 1985 and 1990, a number of studies have confirmed environmental water vapor as the culprit in the low RT ductility noted in many ordered alloys, including Fe_3Al, FeAl and NiAl [33, 34, 35, 36, 37, 38, 39, 40].

Experimental Methods

All fracture toughness testing in this work was carried out by means of three point bend specimens. This specimen geometry has several advantages when dealing with an intractable material. Principally, it is less complex to fabricate, and consumes less material.

The dimensions of the specimens used for mixed mode fracture toughness testing of FA129 are consistent with those for a reduced size 3 point bend specimen defined in ASTM E-399 and are shown in Figure 1.

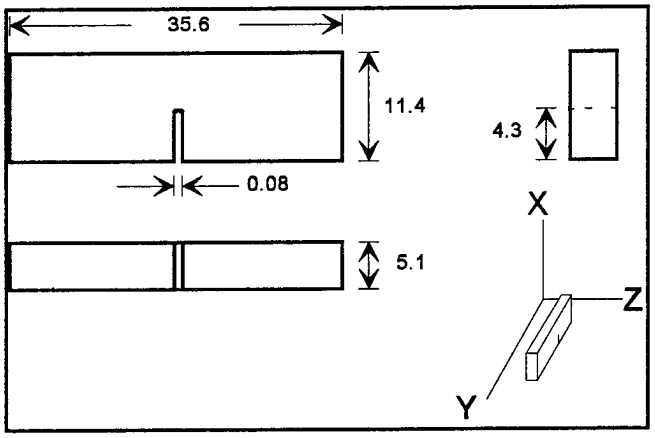
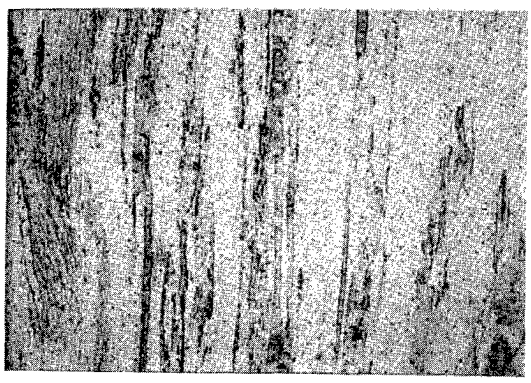


Figure 1. Reduced three point bend specimen geometry. All dimensions in mm.



50 um 200X 0.25 n.a.



200 um 50X 0.12 n.a.

Figure 2. Microstructure of FA129 as tested.

FA129 was received from the Oak Ridge National Engineering Laboratory in the form of a warm-rolled and heat treated bar approximately 100 mm wide by 6.5 mm thick, with a usable length of approximately 150 mm. Specimens were machined from heat treated stock, with both diamond and cemented carbide tooling. All machining work was performed under a mineral oil-based coolant, to prevent any potential environmental effects. Specimens were cut from stock in the T-L orientation, according to the orientation code from the standard. Starting notches were cut to within 1.3mm of final length with a diamond saw.

Attempts to fatigue pre-crack the starting notch as specified in ASTM E-399 were unsuccessful. Even with a chevron notch configuration, stable fatigue crack growth proved difficult to control. Therefore, final starting notches were machined into the specimens using an unbonded silicon carbide lapping technique. This method was able to produce starting notches with a consistent notch root radius of 0.038 mm.

Clearly, 0.038 mm is not the atomistically sharp notch of a fatigue precrack. Mode I fracture toughness specimens were prepared with starting notch root radii of 0.13mm down to 0.038 mm. The notch root radius for each specimen was quantified by optical microscopy, ensuring that the numbers used for calculation were as tested, not just as expected from the equipment setup. As a result of the earlier references to a potential environmental effect on the fracture behavior of this alloy, specimens were tested in a desiccated and cold trapped argon atmosphere. Testing was carried out under load controlled conditions, with the loading rate set to provide ΔK = 36.3 MPa•√m/min. Crack opening displacement was monitored with a clip-type extensometer. K_{1c} values for three specimens of each notch root radius were obtained. These tests indicated that a notch root radius of 0.038mm provided an accurate indication of K_{1c} in this alloy.

Metallographic preparation of FA129 was difficult compared to conventional metallic materials. The known sensitivity of iron aluminides to environmental water embrittlement made the use of non-aqueous polishing regimes seem prudent. However, material removal rates were extremely slow. A partial solution to the problem was to attack polish fine ground specimens on slow turning, felt covered polishing wheels charged with α alumina abrasive and an attack reagent consisting of 1 gram of anhydrous CrO_3 in 35 ml of distilled water. The wheel(s) were pre-charged with abrasive, and the reagent dispensed steadily from a gravity feed reservoir. The use of attack polishing made it possible to obtain damage free surfaces with no pullout or smearing.

Most metallographic work in the recent literature has used etchants based on picric or acetic acid. Neither of these etchants gave satisfactory results in our experience. However, a modified Keller's etchant, with increased HF, gave good results. This etchant provided good grain boundary definition, and minimal pitting or over-etching. Representative microstructures are shown in Figure 2. As a result of the thermomechanical treatment, this alloy exhibits a banded structure, with highly elongated grains in the T-L direction. The dark spots seen in figure 2 are small, primary α crystallites, as shown in Figure 3.

Due to the small amount of material on hand, it was not possible to perform yield strength tests on FA129. However, data published by ORNL indicates that the yield strength should be in the region of 500 MPa.

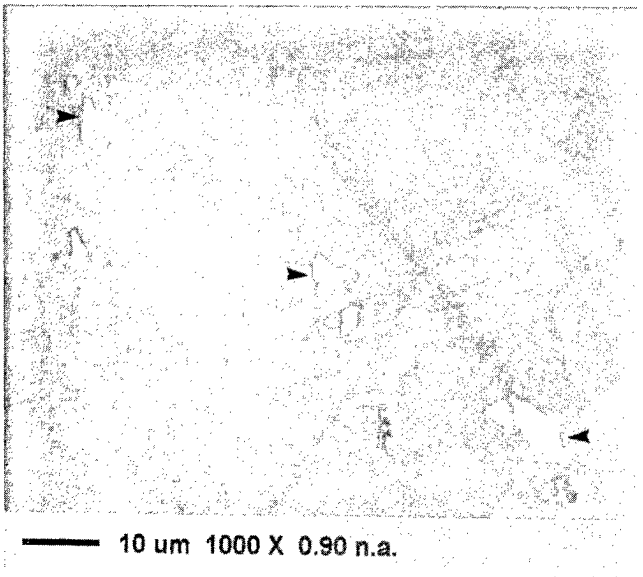


Figure 3. Primary alpha phase (arrows).

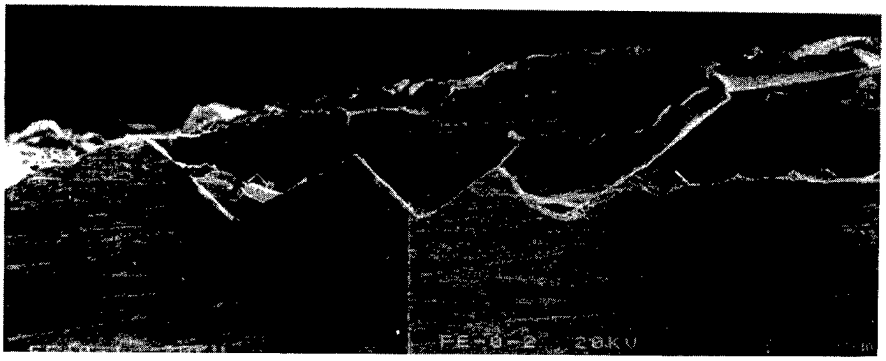


Figure 5. Vertical section of fracture surface showing mixed mode I/II nature of crack initiation. Propagation direction L-R.

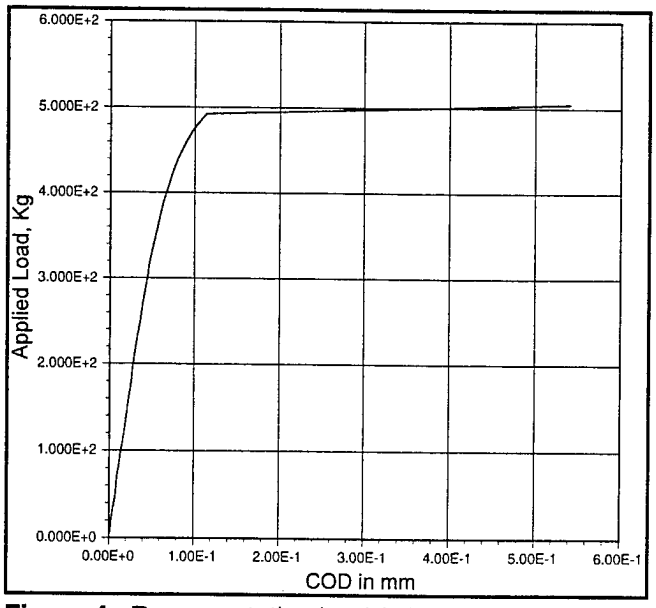


Figure 4. Representative load / displacement curve.

Results

The crack path in all fracture specimens was a mix of transgranular and intergranular. As the vertical section through the fracture surface (Figure 5) shows, the transgranular crack initiates in a mixed mode I/II fashion, with the mixed mode steps eventually damping out to pure mode I. These steps are almost perfectly oriented at 45 degrees to the mode I fracture plane. In Figure 6, the arrows point out areas where the crack plane deviates as it crosses grain boundaries, and the "river patterns" of cleavage fracture are quite visible. Evident also in this plate, is the dramatic intergranular cracking that occurred normal to the gross crack plane. This characteristic is common for all the specimens tested.

Three point bend testing of FA129 resulted in strictly valid K_{tc} data. There was no measurable stable crack growth, although the process of multi-plane, multi-orientation cracking exhibited by the specimen would be expected to dissipate more energy than a brittle flat crack. However, all of the load-extension data recorded was well within the E-399 parameters for what constitutes valid K_c testing. Figure 4 shows the results of a K test for FA129.

Discussion

In the current tests, FA129 fractured by a mix of transgranular and intergranular cleavage. The crack path(s) proceed in a complex, mode I/II mode I/III fashion. Interestingly, in spite of the ductility improvement of FA129 compared to binary Fe_3Al, fracture toughness values were average compared to other metals, approximately 31 MPa$\sqrt{m}$. Additionally, although this alloy should hypothetically meet the von Mises criterion near the crack tip, and the near tip region should exhibit ductile fracture, there is no fractographic evidence of dimpled rupture.

The intergranular cracking seen in figure 6 that lies in a plane parallel to the broad lateral surface (normal to the z axis) of the specimen and containing the direction of the applied load (i.e. in the y direction) occurred in mixed mode I/III, even for mode I specimens. That is, the mode III loading forms at the tip of these transverse cracks due to the direct σ_{yy} loading, and the mode I loading arises because of the transverse σ_{zz} stress associated with the plane strain condition. Absolute magnitudes for these grain boundary K_I and K_{III} are impossible to determine. But it is clear that at least a portion of the total energy that went into the fracture process was of this type of mixed mode.

An examination of the river patterns and extension characteristics of the mode I/II transverse cracks (see figure 6), indicates that the intergranular cracking occurred ahead of the transgranular lateral cracks. As pointed out in the figure, the river patterns indicate that transgranular cleavage runs towards the transverse fracture surfaces from positions inside the grain(s). The implication of this observation is that at least some portion of the z axis constraint could have been relieved by intergranular, mode I/III cracking, leading to a final fracture process that occurs under near plane stress conditions.

As noted earlier, the specimens contain a dispersion of very small (1.6 - 6.4 μm) primary α particles, often found on the grain boundaries. In figure 6, it can be seen that the river patterns often appear to originate at these second phase particles. One possible mechanism that could be operating in this alloy is cracking at the interface as a consequence of significant elastic incompatibility between the primary alpha phase and the matrix. These second phase particles would then act as crack initiation sites, both for the transgranular and intergranular fracture modes. Since all of the testing in this work was carried out in a controlled environment designed to exclude atmospheric water vapor specifically to prevent the influence of such intergranular failure, the regularity and persistence of these mixed mode intergranular cracks may indicate that grain boundaries in these alloys are directly vulnerable to mode I/III loading.



Figure 6. Fractograph showing cleavage step initiation (arrows).

Also of interest is the consistent initiation of transgranular cleavage in a mixed mode I/II orientation (figure 5). Transgranular cleavage in the individual grains initiated in a mode I/II manner and propagated in a sawtooth fashion. The amplitude of the sawteeth damped out within four or five cycles and the lateral crack transformed to pure mode I transgranular cleavage. There are two complementary models to explain this behavior. The maximum principle stress criterion, first put forth by Baker [41] and subsequently expanded by Erdogan and Sih [42], suggested that for brittle materials, if the local condition for fracture is the attainment of a critical tensile stress on some plane, then the maximum principle stress (σ_1^{max}) is the stress measure of importance. For quasi-static loading, the angle of maximum principle stress is at a crack extension angle of 53.3 degrees, corresponding to a mixed mode I/II crack. For higher velocities, the plane of maximum principle stress with respect to the mode I crack plane varies with the velocity of the crack and gives rise to a crack extension angle θ, that can vary from 0 degrees (mode I extension), to 90 degrees (pure mode II). At low speeds (V_{crack} less than approximately 0.2 C_t, where C_t is defined as the transverse velocity of sound for the material), this angular variation has a shallow maximum at θ between approximately 53 and

90 degrees. The gradual variation of the orientation of the plane of σ_1^{max} at low speeds would minimally constrain the crack plane orientation. As V_{crack} approaches C_t, two consequences occur. The absolute magnitude of the principal stress increases, and two sharp, local maxima appear at 0 and 90 degrees. This change in the stress distribution arises out of the foreshortening of the near-crack-tip stress field because of the relativistic source effects at the crack and in the limit, as V_{crack} approaches C_t, the stress field would become simply a line of infinite magnitude centered on the crack tip. With this change in the orientation of σ_1^{max}, the crack plane orientation will begin to be driven ever more strongly toward a mode I configuration.

Also relevant to the mode I/II initiation, Sih [43] developed the strain energy density criterion (SED). SED states that crack growth takes place in the direction of stationary strain energy density. For any given combination of mode mixities, the strain energy density can be expressed as a function of θ, S(θ). According to SED, fracture will take place in the direction of minimum S, at a crack extension angle θ_m. As shown in Figure 7, both the σ_1^{max} and SED criteria lead to a predicted crack extension angle of approximately 53.3 degrees in the quasi-static limit.

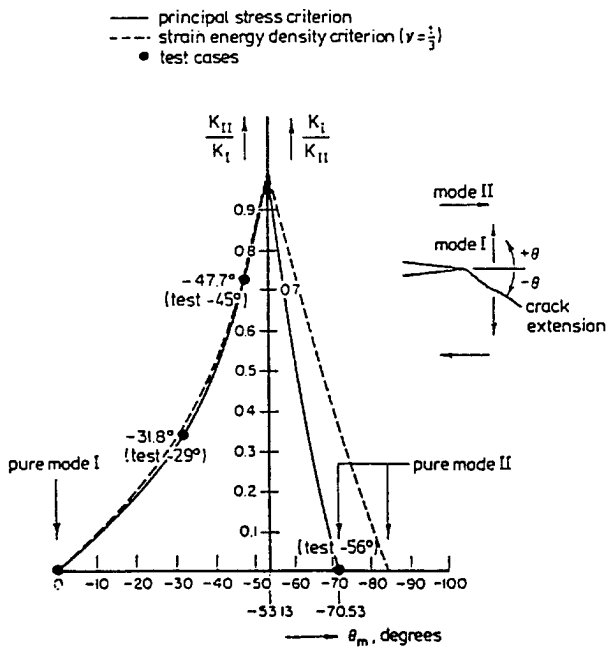


Figure 7. Comparison of maximum principle stress and SED criterion. After Sih, et. al.

Either or both of the above outlined models can account, at least qualitatively, for the transgranular sawtoothed fracture seen in all of the FA129 specimens tested. Some combination of minimum strain energy density and principle stress produced conditions that favored an initial θ of approximately 53 degrees. As crack velocity presumably increased with propagation, and crack tip momentum effects began to dominate, the crack would be forced from a mixed mode nature into a plain mode I as observed. The above models are based on the assumption of a linear elastic near-crack-tip region. However, plastic deformation is limited in the higher crack velocity limit, so the models appear to consistently explain the observed results.

Thus, as tested, FA129 is susceptible to both forms of mixed mode fracture behavior, I/III and I/II. Transverse grain boundaries experience localized mixed mode I/III fracture, and appear to fail in advance of the lateral transgranular cleavage, which shows a marked preference for mixed mode I/II fracture, until crack tip dynamic effects become dominant. On a macroscopic scale, K_{III} appears to introduce a redundant work component. However on the scale of the near-crack-tip plastic zone, which for this alloy is microscopic, both K_{III} and K_{II} have a significant influence on the fracture process.

Conclusions

1. The Fe_3Al-based alloy appears to be susceptible to intergranular, mixed mode I/III fracture. This susceptibility appears to remain even when measures are taken to prevent grain boundary hydrogen embrittlement as a result of the reduction of atmospheric water.

2. Fracture occurs by a dual process of mixed mode I/III intergranular cracking in a plane normal to the z axis of the specimen, followed by transgranular mixed mode I/II cracking which occurs on a plane closely related to the maximum principle normal stress. There is no evidence of ductile rupture in either fracture process.

3. The local mixed mode cracking results in a reduction of the macroscopic plane strain constraint designed into the fracture toughness specimen. The resultant transgranular cleavage initiates in a mixed mode I/II fashion, and propagates in this way until crack tip momentum effects begin to dominate and the cleavage plane transforms into a pure mode I orientation.

Acknowledgements

The authors are grateful for the support of this research by the National Science Foundation under Grant DMR 9420511. They are also grateful to

Dr. C.T.Liu of Oak Ridge National Laboratory, who graciously supplied the FA-129 alloy, and to Dr. H. A. Lipsitt of Wright State University, who recommended the modified Keller's etchant.

References

1. N. Zeigler, AIME Trans., **100**, 1932, 267
2. C. Sykes and J. Bampfylde, J. Iron and Steel Inst. **130**, 1934, 389
3. D. Harwick and G. Wallwork, Rev. High Temp. Mater. **4**, 1978, 47.
4. P. Tomaszewicz and G. R. Wallwork, Rev. High Temp. Mater. **4**,1978, 76
5. R. G. Bordeau, Development of Iron Aluminides, AFWAL-TR-87-4009 (Air Force Wright Aeronautical Laboratories, Wright-Patterson Air Force Base, OH, 1987).
6. G. Culbertson and C. S. Kortovicg, Development of Iron Aluminides, AFWAL-TR-85- 4155, (Air Force Wright Aeronautical Laboratories, Wright-Patterson Air Force Base, OH, 1986).
7. V. K. Sikka, C. G. McKamey, C. R. Howell and R. H. Baldwin, Fabrication and Mechanical Properties of Fe_3Al-Based Aluminides, ORNL/TM-11465 (Oak Ridge National Laboratory, Oak Ridge, TN, March 1990).
8. C. G. McKamey, in Proceedings of the Fourth Annual Conference on Fossil Energy Materials, ORNL/FMP-90/1 (U.S. Department of Energy, Oak Ridge, TN, August 1990), p. 197.
9. Binary Alloy Phase Diagrams, edited by T. B. Massalski (ASM, Metals Park, OH, 1986).
10. P. R. Swan, W. R. Duff, and R. M. Fisher, Trans. AIME **245**, 1969, 851.
11. H. Okamato and P. A. Beck, Metall. Trans. **2**,1971, 569.
12. R. N. Wright, J. R. Knibloe and C. L. Trybus, INEL-2-The Influence of Processing on Microstructure and Properties of Aluminides, ORNL/FMP--90/2 (Oak Ridge National Laboratory, Oak Ridge, TN, December, 1990).
13. T. Yamagata and H. Yoshida, Mat. Sci. Engrg, **12**, 1973, 95.
14. T. Yamagata, Trans. Jpn. Inst. Metals, **18**, 1977, 715.
15. Y. Umakoshi and M. Yamaguchi, Phill. Mag. A, **41**, 1980, 573.
16. M. G. Mendiratta, H. M. Kim, H. A. Lipsitt, Metall. Trans. A, **15A**, 1984, 395.
17. I. Baker and D. J. Gaydosh, Mater. Sci. Engrg., **96**, 1987, 147.
18. P. R. Munroe and I. Baker, Acta. Metall., **39**, 1991, 1011.
19. J. F. Nachman and W. J. Buehler, Application, Properties, and Fabrication of Thermenol Type Alloys, NAVORD Report 4237 (U.S. Naval Ordnance Laboratory, Silver Spring, MD, May 4, 1956).
20. J. F. Nachman and W. J. Buehler, The Fabrication and Properties of 16-Alfenol-A New Strategic Aluminum-Iron Alloy, NAVORD Report 2819 (U. S. Naval Ordnance Laboratory, Silver Spring, MD, April 9, 1953).
21. J. F. Nachman and W. J. Buehler, Applications and Properties of Iron (10-17%) Aluminum Alloy, NAVORD Report 4130, (Naval Ordnance Laboratory, Silver Spring, MD, December 5, 1955).
22. J. F. Nachman and W. J. Buehler, Thermenol, A Non-Strategic Aluminum-Iron Base Alloy for High Temperature Service, NAVORD Report 3700, (U. S. Naval Ordnance Laboratory, Silver Spring, MD, June, 1954).
23. W. J. Lepowski and J. W. Holladay, The Present State of Development of Iron-Aluminum-Base Alloys, Titanium Metallurgical Laboratory, Battelle Memorial Institute (Memorandum of November 18, 1957).
24. M. J. Marcinkowski, M. E. Taylor and F. X. Kayser, J. Mater. Sci., **10**, 1975, 406.
25. E. R. Slaughter and S. K. Das, in Rapid Solidification Processing: Principles and Technologies, II, edited by R. Mehabrian, B. H. Kear, and M. Cohen, (Claitor's Pub. Div., Baton Rouge, LA, 1980), p. 354.
26. C. G. McKamey, C. T. Liu, J. V. Cathcart, S. A. David and E. H. Lee, Evaluation of Mechanical and Metallurgical Properties of Fe_3Al-Based Aluminides, ORNL/TM-10125 (Oak Ridge National Laboratory, Oak Ridge, TN, September, 1986).
27. C. G. McKamey, C. T. Liu, S. A. David, J. A. Horton, D. H. Pierce, and J.J. Campbell, Development of Iron-Aluminides for Coal-Conversion Systems, ORNL/TM-10793, (Oak Ridge National Laboratory, Oak Ridge, TN, July, 1988).
28. C. G. McKamey, V. K. Sikka, T. Zacharia, S. A. David, and D. J. Alexander, in Fossil Energy Advanced Research and Technology Development Materials Program Semiannual Progress Report for the Period Ending September 30, 1990, ORNL/FMP-90/2 (U. S. Department of Energy, Oak Ridge, TN, December, 1990), p. 235.
29. R. R. Judkins and D. N. Braski, Proceedings of the Fourth Annual Conference on Fossil Energy Materials, ORNL/FMP-90/1, (U. S. Department of Energy, Oak Ridge, TN, August, 1990).

30. R. N. Wright, J. R. Knibloe and C. L. Trybus, INEL-2-The Influence of Processing on Microstructure and Properties of Aluminides, ORNL/FMP--90/2 (Oak Ridge National Laboratory, Oak Ridge, TN, December, 1990).
31. T. Takasugi and O. Izumi, Scr. Metall., **19**, 1985, 903-7.
32. K. Kuruvilla and N. S. Stoloff, in High Temperature Ordered Intermetallic Alloys I, p. 229-238, ed. C. C. Koch, C. T. Liu and N. S. Stoloff, MRS Symp. Proc. Vol. 39, Materials Research Society, 1985
33. T. Takasugi, N. Masahashi, and O. Izumi, Scr. Metall., **20**, 1986, 1317.
34. C. T. Liu, E. H. Lee and C. G. McKamey, Scr. Metall., **23**, 1989, 875.
35. C. T. Liu, C. G. McKamey and E. H. Lee, Scr. Metall.
36. T. Takasugi and O. Izumi, Acta Metall. **34**, 1986, 607.
37. N. Masahashi, T. Takasugi and O. Izumi, Metall. Trans. A, **19A**, 1988, 353.
38. O. Izumi and T. Takasugi, J. Mater. Res., **3**, 1988, 426.
39. N. Masahashi, T. Takasugi and O. Izumi, Acta Metall., **36**, 1988, 1823-36.
40. N. S. Stoloff, J. Metals, **40 (12)**, 1988, 23.
41. Baker, B. R., Journal of Applied Mechanics, **29**, 1962, 449-58.
42. Erdogan, F. and Sih, G. C., J. Basic Engrg., **85**, 1963, 519-27.
43. Sih, G. C., Int. J. Fracture, **10**, 1974, 305-322.

CLEAVAGE OF CERAMIC AND MINERAL SINGLE CRYSTALS

Richard C. Bradt
Department of Metallurgical and Materials Engineering
A 129 H Bevill Research Building
The University of Alabama
Tuscaloosa, AL 35487 - 0202 USA

Abstract

The cleavage of ceramic and mineral single crystals is reviewed from the perspectives of the phenomenon that illustrate its special character relative to the crystal structure of the material. A basic geometric mineralogical classification is employed throughout the review. Criteria for the cleavage process are examined in the historical structural sense as well as in a fracture mechanics sense. It is concluded that fracture toughness is the appropriate criterion for cleavage of these materials. Summarizing experimental cleavage fracture toughnesses reveals that most ceramic and mineral crystals cleave at K_{Ic} levels which are less than 2 MPa $m^{1/2}$,but are frequently less than 1 MPa $m^{1/2}$, with the exception of diamond.

The cleavage of $MgAl_2O_4$ spinel on different crystal planes, where the crack has been restricted to extend on a plane through specimen and crack configuration control illustrates the brittle, elastic nature of the cleavage toughness of that structure. When the fracture toughness of the $MgAl_2O_4$ spinel is measured for the {100} cleavage plane at increasing temperatures, it is observed that the cleavage toughness initially decreases with increasing temperature until the brittle-ductile transition occurs. Plastic flow causes a rapid toughness increase with further temperature increases above the brittle-ductile transition.

Finally, experimental cleavage toughnesses for sapphire are compared with theoretical calculations of the surface energies for the same crystalline planes. From this consideration it is further confirmed that the phenomenon of cleavage in these types of materials on their preferred cleavage planes occurs with very little, or perhaps no accompanying dislocation plastic flow. It also suggests that energies for cleavage on non-preferred cleavage planes may differ substantially from theoretical calculations of the surface energy.

Introduction

The cleavage, or fracture of minerals and ceramics on specific crystal planes and the fascinating repetitive geometrical shapes that result readily arouses the interest and the curosity of every form of technologist who observes the cleavage of large macroscopic crystals, or sees the remarkable geometric patterns of cleavage at high magnifications in a scanning electron microscope. The crisp, repetitive patterns are a characteristic of the cleavage phenomenon that are easily remembered, for they create a distintive and lasting impression unlike any other structural feature of crystal fracture, or crystal growth. Practically every textbook addressing ceramics, minerals, rocks or gemstones contains a section or chapter on cleavage, usually according it a prominence second only to the Mohs hardness scale in terms of mechanical property characterization of the different crystal structures. It is common to find that descriptions of crystal structures in various mineralogical references emphasize the cleavage plane of the crystal structure during its description. (1-9)

It is also common for metallurgical reviews and mechanical metallurgy texts to address the cleavage phenomenon, albeit not with the same level of significance and reverance expressed within the aforementioned non-metallic texts. The typical metallurgical perspective is controversial relative to the role of dislocation plastic flow, and there is only abbreviated discussion of the dominance or control of the cleavage phenomenon by the character of the crystal structure. Occasionally these texts attempt to justify the fracture, or cleavage on a preferred crystallographic plane through theoretically calculated fracture stresses of the particular metal on that crystal plane. In spite of these differences, most metallurgists generally associate cleavage with brittle fracture. (10-13)

The phenomenon of cleavage in its purest form is the fracture of a crystalline material that is dominated by its crystal structure. When a crystalline material cleaves, it preferentially fractures along a planar surface which is determined by the character of the crystal structure on that surface of the material. Cleavage occurs in the tensile, or opening mode, which, not surprisingly, is often also referred to as the cleavage mode. Cleavage can occur during the fracture of a large macroscopic single crystal or during the fracture of individual crystal grains within a polycrystalline aggregate. It is not unusual for the cleavage fracture to appear as a large, smooth, almost mirror-like planar surface that extends over a large areal portion of the fracture surface. However, when these large planar fracture surfaces are closely examined, they are invariably observed to consist of sharp, distinct staircase-like patterns that are geometrically characteristic of the multiplicity of the cleavage planes in the particular crystal structure of interest. Schultz, Jensen and Bradt have reviewed many of these aspects of cleavage in non-metallic materials. (14)

Figure 1 illustrates the appearance of a {100} cleavage surface of halite (NaCl) in the scanning electron microscope. The lower magnification micrograph illustrates the staircase-like pattern that results from the presence of a multiplicity of cleavage planes of the {100} type within the common rock salt NaCl structure. It is evident that the "stairs" or ledges are not all of the same width, nor of the same extent or length, as sections of various lengths are missing along many of them on an individual basis. However, it is almost universal that the many fracture surfaces are planes within the family of {100}

George R. Irwin Symposium on Cleavage Fracture
Edited by Kwai S. Chan
The Minerals, Metals & Materials Society, 1997

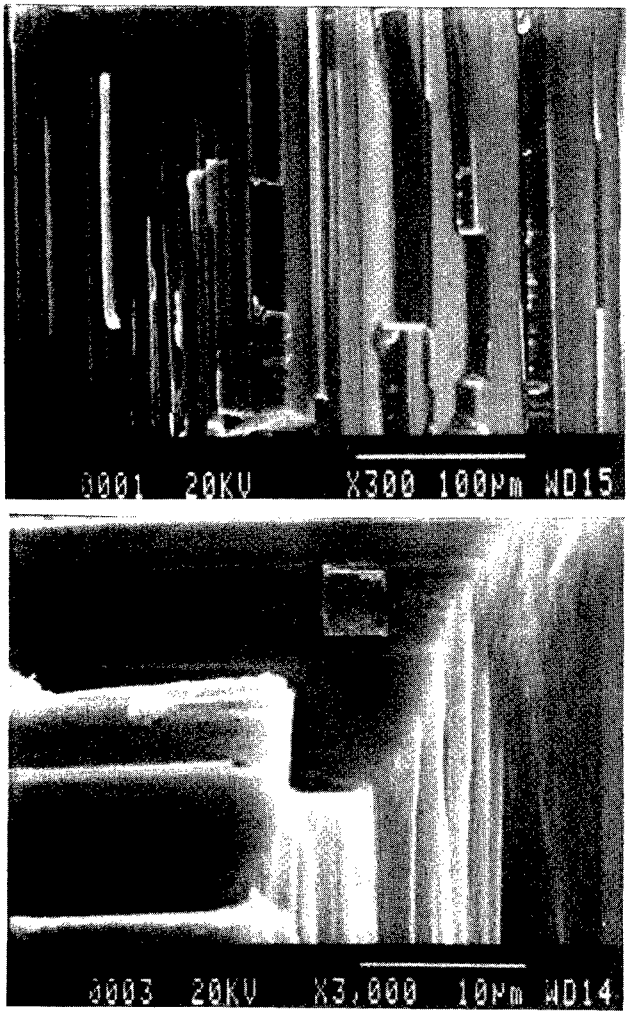


Figure 1: Scanning electron micrographs of the cleavage surfaces of single crystal halite (NaCl) at 300x and at 3,000x.

indices. As the angles between different members of the {100} family of planes are 90°, it is evident that during the cleavage of NaCl the main extending crack is making many abrupt right angle turns during the dynamic generation of this step-like fracture surface. It is further informative in the higher magnification micrograph of Figure 1 that the {100} character of the cleavage surface is maintained on an increasingly finer scale as one examines the cleavage surface more closely. The abrupt right angle changes are maintained at the finer ledges or "stairs" suggesting perhaps the presence of a fractal-like character to this basic cleavage pattern. In the higher magnification micrograph, a cm-on-edge cube of NaCl is superimposed just to illustrate the distinctive right angle features at all scales.

Although the above illustration of the fine scale repetitive cleavage pattern created by the multiplicity of the {100} cleavage planes in NaCl should suffice to establish the presence of these patterns for all crystalline minerals and ceramics, it is always more satisfying to also consider the process in another crystal system, a non-cubic one. Figure 2 illustrates the cleavage phenomenon on the "smooth" fractured surface of an optical quality calcite ($CaCO_3$) crystal, a larger one of which is again superimposed on the micrograph for comparison of the scale of the geometry. This magnification of the $CaCO_3$ rhombohedral cleavage is intermediate to those for the cubic cleavage for the NaCl previously illustrated, so not surprisingly also is the fine scale of the repetitive nature of the angular cleavage of this calcite. The character of the remarkable sawtooth-like pattern in calcite is interesting and generally confirms the variabilities of the spacings and sizes of the individual cleavage surfaces that were noted for the cubic cleavage in the NaCl structure.

Although the crystallographic nature of the cleavage process appears to be incredibly precise and quite well defined in the above rock salt and calcite scanning electron microstructures, in fact it can be quite variable. Even though individual members of an isostructural group of crystals usually cleave on the same family of planes; for example the NaCl structure exhibits cubic cleavage on the {100}, the ZnS sphalerite structure exhibits dodecahedral cleavage on the {110} and CaF_2 exhibits octahedral cleavage on the {111}, the quality of these individual cleavages can and do vary considerably within each of these groups of crystal structures.

Mineralogists frequently categorize cleavage in a very qualitative sense as perfect, good, distinct and indistinct. The terms parting and quasi-cleavage are also occasionally applied to fractures when particularly poor cleavage occurs, but the fracture still appears to be in a crystallographic sense, perhaps only of sorts. Cleavage manifests itself in many ways, not all of them completely understood.

In is necessary to mention that not all fractures in ceramic and mineral crystals is cleavage in character. Some mineral and ceramic structures simply do not exhibit preferred cleavage planes. One such structure which is common to most materials scientists is the garnet structure, a cubic crystal structure that finds scientific and technical application as an abrasive grain and as a magnetic material, as well as its common use as the deep red gemstone with which we are familiar. The garnet structure is reportedly hard and tough but does not exhibit a well defined cleavage plane, although some mineral texts do suggest that it is susceptible to parting on the {110}. As garnet is an island silicate structure, perhaps that particular form of silicate structure does not possess a distinct cleavage character. Conchoidal fracture is also one that is void of cleavage. It is associated with ceramics and minerals, particularly in the glassy state and for very fine grain size polycrystalline structures. It is also associated with crystalline quartz, a material which will be addressed later in this paper.

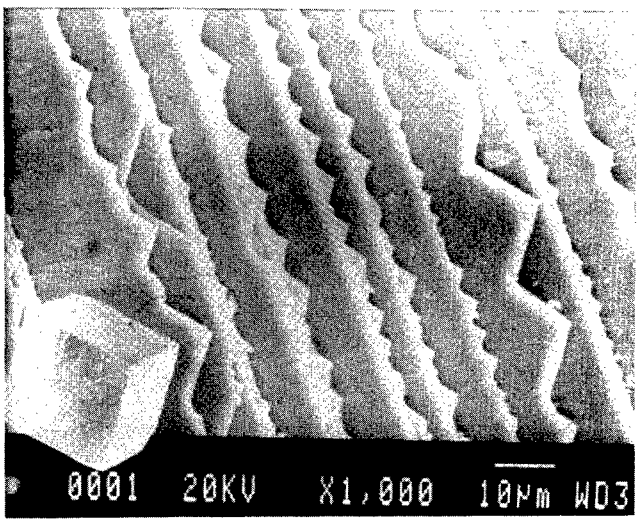


Figure 2. Scanning electron micrograph of the cleavage surface of calcite ($CaCO_3$) at 1,000x. Compare the pattern with that in Figure1.

Cleavage Criteria

As with all natural phenomena, it is the objective of those who study and observe that phenomenon to determine or propose a criterion for its occurrence. The cleavage phenomenon is no different, as it has drawn the attention of numerous scientists from different disciplines for decades, many of whom have naturally suggested that different criteria are responsible for the control of cleavage in mineral and ceramic crystals. As these criteria are usually related to the crystal structure, they are worthy of consideration even though they are frequently structure specific in their application, rather than global in a sense of the universal predictability of the cleavage phenomenon. (15,16) These criteria will be briefly reviewed from the perspectives of crystal structure, crystal properties and fracture toughness for the cleavage plane. More detailed discussions of these criteria have been presented by Schultz, Jensen and Bradt (14).

Crystal Structure Criteria

The distinctive geometry of the cleavage process and the external geometry of naturally occurring crystals leads to a natural association of those two features. However, those crystal planes which dominate during the natural growth of crystals are not consistently the same ones that prominently experience cleavage. This is because the physical and chemical processes that control crystal growth are not the ones that dominate the cleavage phenomenon. Nevertheless, there are examples of the correspondence of the cleavage planes and crystal growth planes that are well known to most mineralogists and crystallographers. The {100} planes for the halite (NaCl) structure and the {111} planes for the fluorite (CaF_2) structure are familiar examples. Halite cubes and fluorite octahedra are common to all mineral collectors. However, as tempting as this cleavage and growth plane association may seem, a critical examination of the growth and cleavage processes quickly reveals that the correspondence of cleavage planes and growth planes is a fortuitous one for those few instances where in fact the two types of planes are coincident.

Once convinced that the common growth planes of crystals are not consistently the cleavage planes of those crystals, then perhaps it is logical to consider the planes which bound the unit cell as a possibility, for they also frequently exhibit the distinctive geometry that is exhibited by cleavage planes. One has only to consider the case of the halite (NaCl) structure to find an example of the correspondence between the unit cell bounding planes and the cleavage planes; i.e. the {100}. However, applying the bounding planes of the unit cell as the criterion for cleavage fails miserably once a wider number of crystal structures are examined. Obviously, the fluorite (CaF_2) structure, which is cubic, but cleaves octahedrally on the {111}, provides a clear contradiction to the criterion of the unit cell bounding planes. That concept must also be rejected as the universally determinant criterion for cleavage.

Further examining the structural approach to cleavage, it is appropriate to consider the most closely packed crystal planes as a possibility. As the slip planes for dislocation motion are usually the closely packed planes and thus have clearly demonstrated their ability to experience the breaking of bonds during plastic flow, there is a natural tendency to suspect that they may also be susceptible to bond breakage during cleavage. Similar to the previous suggestions, the criterion of the most closely packed planes does not yield a universally applicable result for all crystal structures. The halite (NaCl) structure cubes and the classical cleavage rhombohedra of the calcite ($CaCO_3$) structure are among the numerous contradictions.

Other simple structural criteria which have been considered and which are familiar to all those who study crystallography can also be proposed and, in fact, may apply to cleavage for specific instances. However, continuing pursuit of a universal structural feature that defines the cleavage planes for all crystal structures leads to repeated discouragement. It finally leads one to the conclusion that it is the properties of the crystal structure which must be examined for a universal criterion, rather than the crystal structure itself. Of course the structure and the properties are directly related.

Crystal Property Criteria

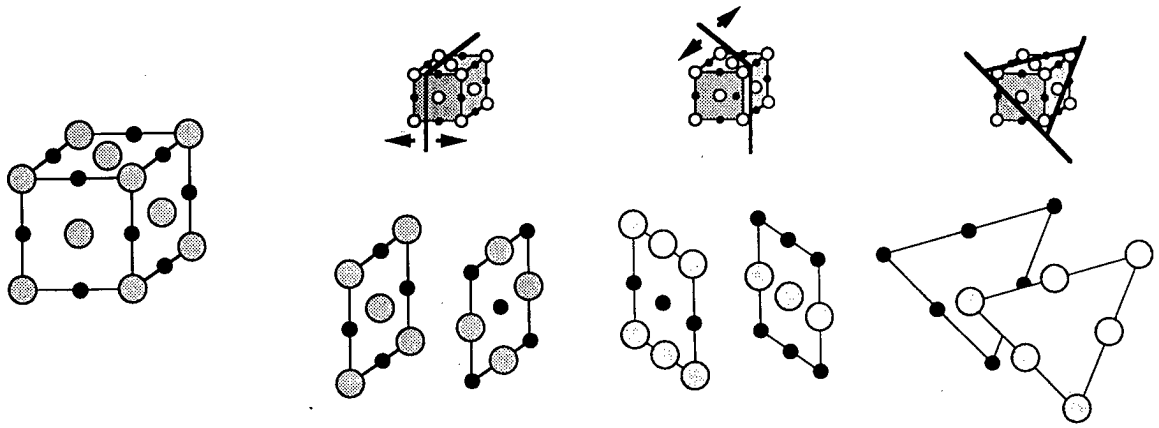
Once it is realized that consideration of the physical properties of crystals may be a more appropriate approach to understanding the cleavage criterion, then various crystal properties can be readily examined as possible criteria. As cleavage involves the breaking of bonds, it follows that any successful cleavage criterion must necessarily physically relate to the bonds and the ions, groups of ions, or the atoms which constitute those bonds. As simple as it may appear, it is essential to understand that cleavage constitutes the rupture or breaking of the bonds between atoms or ions, not splitting the atoms or ions themselves. When cleavage occurs, then the two resulting fracture surfaces will consist of matching pairs of ions or atoms across the newly created surfaces.

This paired matching of the fracture surface features is a basic factor which prevents certain crystal planes from experiencing cleavage in the simple ionic structures. Ionic crystals will not cleave on crystal planes which result in all positive charges on one fracture face and all negative charges on the other fracture face. From the charge perspective, those crystal planes are known as non-neutral planes. Examples of non-neutral planes in several common ionic structures are the {111} in the halite (NaCl) structure, both the {110} and {100} in the fluorite (CaF_2) structure, and the {100} and {111} in the sphalerite (ZnS) structure. The converse of this argument is that only those crystal planes which are neutral, in the sense of their ionic charge distribution, will be cleavage planes.

This crystal-plane neutrality condition is easily recognized on the {100} and {110} planes of the halite (NaCl) structure where the configuration of cations and anions is an alternating one, as shown in Figure 3. It is equally obvious that if those bonds which are perpendicular to the {111} in the halite (NaCl) structure were to cleave, then planes of all cations would separate from planes of all anions, yielding two oppositely charged cleavage surfaces. The ionic neutrality on crystal planes specifies that non-neutral planes will not experience cleavage in any highly ionic crystal structures.

Having considered on the bonds within a crystal structure, it is appropriate to address several of the various cleavage criteria that have been suggested on the basis of the bonds. These suffer from the rather imprecise nature of bonds, their varying strengths, a balance of ionicity versus covalency, and the anisotropy which they possess within the various crystal structures. Nonetheless, this approach does provide some structural insight and merits consideration.

The popular bond density concept simply proposes that the minimum number of bonds per unit area determines the cleavage plane in a crystal structure. Lower bond densities are associated with the more weakly bonded crystal planes, and it is those planes that are more readily cleaved. Differences in directional bonding strengths are quite obvious for graphite and for talc, where one set of bonds is van der Waals in character and the others are covalent. Few other crystal



The Halite (NaCl) Structure {100} Cleavage {110} Cleavage {111} Cleavage

Figure 3: Schematic of cleavage in the halite (NaCl) structure, illustrating the resulting ionic patterns on the fracture faces after cleavage on the {100}, the {110} and the {111} planes. Note that both the {100} and the {110} planes yield neutral surfaces, but cleavage on the {111} yields opposing fracture surfaces that consist only of one type of ion. The resulting {111} cleavage yields non-neutral opposing surfaces, a result which is not generally known to be susceptible to cleaveage.

structures are so distinct. The bond density approach is not very satisfactory, nor has it been very successful as a universal criterion, for it cannot easily incorporate the different bond strengths and the anisotropy of those bond strengths into the criterion.

Another bond character approach to cleavage plane prediction has been advanced by Whittaker [17]. In an attempt to circumvent the difficulties in specific bond strengths or a calculated bond density into the criterion for the cleavage of ionic crystals, Whittaker has incorporated the concepts of Madelung energy and Evjen cells to define geometric building blocks within a crystal structure. The common or shared faces of those blocks represent potential cleavage planes. This approach does have intuitive appeal, but it lacks in universal application to all crystals for as noted by Whittaker, an obvious exception to this approach is halite (NaCl).

The natural extension of the bond density concept is to consider that physical property which is directly related to the strength of the bonds, the elastic modulus. Stronger bonds between planes should result in a higher Young's modulus perpendicular to that crystal plane. In contrast, weaker bonds should be associated with lower elastic moduli and thus identify the cleavage planes as those with the minimum Young's modulus. As attractive as this approach appears, the elastic modulus criterion does not consistently apply even to the most simple structures. For example, sylvite (KCl) and galena (PbS), which both have the halite (NaCl) structure and exhibit {100} cleavage planes, also have their Young's moduli maxima in the <100>. The diamond cubic structure, which has the Young's modulus maximum in the <111>, also cleaves on the {111}. Cleavage in these crystals is not in agreement with that which is expected from the application of the minimum elastic modulus criterion. It is evident that the elastic modulus is not, by itself, consistently capable of predicting the cleavage planes of crystal structures.

The same type of summary statement can also be applied to a criterion based on the surface free energy of the crystal planes. It can be argued that an energy criterion, in which the cleavage plane is the plane of the minimum surface energy, should apply. However, similar to the previously discussed criteria, Gilman [15] applies the minimum surface energy concept and notes that it has exceptions, most notably the potassium halides. The minimum surface energy concept is not a sufficient one to consistently predict the preferred cleavage planes of crystals. It may be more applicable to crystal growth planes.

In an effort to arrive at a suitable criterion for cleavage, investigators have attempted to theoretically calculate the cleavage strength of various single crystals on low indice crystal planes [18, 19]. The approach invariably necessitates an estimate of the surface energies of those planes and reveals the need for the application of dynamic, rather than static, elastic moduli. In a related approach based on an equilibrium calculation of Coulomb and Born-Mayer repulsive-interaction potentials for spinel ($MgAl_2O_4$), Mishra and Thomas [20] suggest that the {111} planes of spinel should have the lowest surface energy and should be the cleavage plane, whereas the actually observed cleavage plane for spinel is the {100}. Often, values of the parameters which are utilized in the calculations based on potential functions are not known with adequate certainty, yet these types of theoretical approaches to cleavage do illustrate several important points. When dynamic conditions are incorporated into the calculations, the cleavage strengths are different than for static or quasi-static equilibrium conditions and usually greater strengths are predicted. Some success results from using the dynamic theories, similar to the previous criteria. At the present, however, theoretical approaches to cleavage plane prediction, although not without merit, cannot be considered to have been very successful. Their primary contribution appears to be that of heralding the importance of the dynamics of the cleavage phenomenon.

In summarizing the various cleavage criteria which are based on the structure of a crystal or its properties, it may be concluded that each one of the aforementioned characteristics will correctly predict some cleavage planes, but every one of those criteria fails when applied in a universal sense. In retrospect, this should not be surprising because cleavage is a dynamic fracture process, and most of the aforementioned structural attributes or physical properties are static, or quasi-static in nature. If any cleavage criterion is to be universally applicable, then the appropriate dynamic criterion must be applied.

A Fracture Toughness Criterion

As Schultz, Jensen and Bradt (14) have noted, because cleavage occurs rapidly and catastrophically, application of the critical crack growth resistance parameters for the opening mode, either the fracture toughness, K_{Ic}, or the strain energy release rate, G_{Ic}, [21, 22], is an appropriate criterion to consider for cleavage. As the focus of this paper is primarily on brittle single crystals and because the stress intensity concept is currently being used extensively in the design, evaluation, and testing of brittle materials, the fracture toughness K_{Ic} will be considered as the single crystal cleavage criterion.

The fracture toughness of a material K_{Ic} is a measure of the resistance of the material to crack growth [23]. To consider the fracture toughness (K_{Ic}) as a cleavage criterion, it is necessary to refer to several independent experimental studies where different researchers have actually made experimental measurements of the crack growth resistance on several crystallographic planes of different crystal structures. These fracture toughness measurements are made by some form of indentation pre-cracking, or by utilizing guide notches to force the crack to initiate on the crystallographic plane of interest (24). Of course, after extending only a short distance, every propagating crack in the single crystal will eventually be redirected by the crystal structure on to the preferred cleavage plane, as a number of the authors have illustrated in their publications.

In Table I, experimental cleavage toughnesses (K_{Ic} values) are listed for several common low indice crystal planes each for single crystals of griceite (LiF), gallium phosphide (GaP), silicon (Si), and spinel ($MgAl_2O_4$). For each of these four crystal structures, the well established cleavage plane has the lowest experimentally measured fracture toughness value. It must be concluded that the experimental K_{Ic} value, the fracture toughness, is the appropriate criterion for the cleavage of ionic and covalently bonded crystal structures.

Table I Experimental fracture toughnesses for single crystals

Crystal	Plane	K_{Ic}(MPa $m^{½}$)	Reference
LiF (griceite)	{100}*	0.50	25
	{110}	0.70	25
	{111}	1.50	25
GaP	{100}	0.73	26
	{110}*	0.65	26
	{111}	0.81	26
Si (silicon)	{100}	0.95	27
	{110}	0.90	27
	{111}*	0.82	27
$MgAl_2O_4$ (spinel)	{100}*	1.18	28
	{110}	1.54	28
	{111}	1.90	28

*Indicates the commonly observed cleavage plane.

Interestingly, for the primarily ionic halite structure of griceite (LiF), where charge effects are expected to be highly dominant, the cleavage toughness differences between the three low indice crystal planes are much more pronounced than for the primarily covalently bonded gallium phosphide (GaP) and silicon (Si) and the mixed character bonds of the spinel ($MgAl_2O_4$) structure. This point will be addressed during the consideration of other ceramic and mineral structures.

Cleavage of Ionic and Covalent Crystals

It is desirable to address the cleavage toughnesses of brittle ceramics and minerals in terms of some form of orderly structural classification. The cleavage of various brittle ionic and covalently bonded crystal structures can be systematically considered by applying the mineralogically based structural approach presented by Sorrell [1]. Sorrell's structural categories begin with the traditional mineralogical layer structures, including mica and graphite, two materials which are well known for their easy cleavage. It then proceeds with two-directional cleavage and finally considers the situation for cleavage planes which constitute three-dimensional geometries that are familiar to all crystallographers and materials scientists. However, not all brittle materials of interest, nor all of those for which fracture toughnesses have been measured, can be conveniently classified into these structural groups. Those with multiple cubic, rhombohedral, or octahedral cleavage planes are several examples. Consequently, several crystal structures must be discussed individually beyond the structural classification by Sorrell. It should be noted that other systematic approaches are also possible, including the crystal symmetry classification [29]. However, the Sorrell structural classification is more than adequate for cleavage classification and discussion within the scope of this paper.

Layer Structures

Cleavage in the layer structures, such as the different mica structures and graphite, may be expected to be similar for all other layer structures, such as the many clays and also molybdenite (MoS_2). Unfortunately, only a few of these materials have been the subject of actual single crystal cleavage measurements. Nevertheless, the experimental results for those few layer structures provide a reliable baseline for the discussion of all other single crystal cleavage toughness values. Layer structures also provide a convenient basis to understand just how easy the single crystal cleavage process may become under nearly ideal conditions of brittle fracture.

Table II summarizes the cleavage toughness values for several layer structures. The first toughness listed, that of graphite, is estimated from the theoretical surface energy and elastic modulus in Gilman's [15] review paper. It seems to be extraordinarily low. However, the following explanation can be offered which suggests that actual experimental results may be preferable to those types of theoretical estimates. For example, if the graphite toughness calculated from theory (K_{Ic} =0.035 MPa $m^{½}$) is compared with the experimental results which Sakai et al. [30] report a highly oriented pyrolytic carbon (K_{Ic} =0.53 MPa $m^{½}$), then it is evident that about an order of

Table II Cleavage toughnesses of several layer structures

Material	Plane	K_{Ic}(MPa $m^{½}$)	Reference
graphite	{0001}	0.03	15
pyrolytic carbon	{0001}	0.53	30
muscovite mica	{0001}	0.19	15
$YBa_2Cu_3O_x$	{001}	1.10	31
ice		0.11	32

magnitude difference exists. Theoretical approaches to the calculation of surface energies are based on static or quasi-static equilibrium models, in contrast to the actual fracture process which leads to the formation of cleavage surfaces and which is a highly dynamic, non-equilibrium process. It should not be surprising that differences are observed between theory and experiment. In retrospect, it would be remarkable if static equilibrium theory and an irreversible dynamic experiment yielded the same cleavage toughnesses. However, the most important message revealed by this summary of graphite cleavage toughnesses is that they are consistently less than 1 MPa $m^{½}$. The cleavage of layer structures is a relatively easy process as most materials scientists are well aware.

Also listed in Table II is the reported cleavage toughness for the ceramic superconductor, $YBa_2Cu_3O_x$ [31]. Similar to the other layer structures, its toughness is also low, although somewhat higher than the values for graphite and the mica. It might be argued that the measurement (1.10 MPa $m^{½}$) is perhaps too high. However, the cleavage toughness of this structure is not too different than the other layer structures and is still relatively low in comparison with the toughnesses of many other materials [22]. The $YBa_2Cu_3O_x$ results supports the conclusion that the cleavage toughnesses of most layer structures appear to be less than 1 MPa $m^{½}$.

Wan et al. [33] have studied the cleavage of muscovite mica and observed that moisture has a significant effect on the crack growth resistance, confirming the observation first noted by Obriemoff [34]. The difference is often as much as a factor of five. That finding and its relationship to charging effects on the mica fracture surfaces is highly significant from a fundamental perspective. However, even a factor of five times the reported fracture toughness for mica (0.19 MPa $m^{½}$) does not alter the conclusion that the cleavage toughnesses of nearly all layer structures are less than 1 MPa $m^{½}$. Layer structures are not very tough.

Chain Structures

The cleavage of single crystal chain structures is typically parallel to the structural chains in those crystals. In the literature it is often referred to as prismatic, after the prism-like geometric forms that result. Cleavage toughness values for single or double chain silicate structures as do not appear to have ever been measured, as none have been reported in the literature. Nevertheless, a number of details have been established regarding the cleavage of these interesting structures. The cleavage planes of chain structures are always parallel to the chain lengths as the chains constitute the strongest bonds in the structures. Crystals having the single chain structure are typified by the pyroxene group of rock forming minerals and yield intersecting cleavage surfaces that appear to be at right angles, although they actually cleave at angles of 87° and 93°. From these angles the minerals can be readily identified in the field by geologists.

Crystals having the double chain structure are typified by the amphibole group of silicate minerals and result in angles which are quite different from 90°. These double chain silicates cleave in a manner to yield surfaces which intersect at characteristic angles of nearly 60° and 120° (actually 56° and 124°).

Cleavages of other chain structures, such as the sulfides stibnite (Sb_2S_3) and bismuthenite (Bi_2S_3), are also of interest. These may also be expected to follow the same principles as for the cleavage of the silicate chain structures. These sulfide structures contain zigzag chains in the form of ribbons in which S and Sb or Bi alternate 'parallel' to the <001> of the orthorhombic crystals [35]. The chains are not broken during perfect cleavage on the {010}, planes which are parallel to the chain lengths. Cleavage toughnesses for these sulfide chain structures have not been measured either. Similarly, the toughnesses of borate chain structures whose cleavage is usually described as being perfect [36] have not been measured either. Both the sulfide and the borate chain structures may be expected to have cleavage toughnesses less than 1MPa $m^{½}$, too.

Cleavage of Cubic Structures

The simplest of the three-directional (dimensional) cleavages is the cubic variety as commonly observed for the halite (NaCl) structure, a cubic crystal structure which also exhibits a cubic cleavage geometry on the {100}. Figure 1 illustrates the virtually perfect 90° cubic cleavage of halite (NaCl). Figure 3 depicts the ionic arrangement on the cleavage surfaces. Structures other than the halite (NaCl) structure also exhibit cleavage that displays a cubic geometry. Table III lists a number of materials for which cubic cleavage is readily observed and for which the cleavage toughnesses have been measured and have been reported in the literature. Similar to the previous layer structure cleavages, these cleavage toughnesses are not very large either. In fact, with the exception of the spinel ($MgAl_2O_4$) all are less than 1MPa $m^{½}$.

The cleavage toughnesses in Table III clearly suggest the presence of an ionic size effect on the fracture. That effect is apparent when the toughnesses of griceite (LiF) and magnesia (MgO) are compared with those of potassium bromide (KBr) and galena (PbS). The former two crystals consist of higher elastic modulus structures with much smaller ions, whereas the latter two consist of larger, more highly polarizable ions. However, all four have the NaCl structure which facilitates direct comparison. The cleavage toughnesses of the former (LiF and MgO) are about three times greater than those of the latter (KBr and PbS). The more tightly bonded, higher elastic modulus ionic crystal structures exhibit substantially larger cleavage toughnesses.

Neither pyrite (FeS_2) nor spinel ($MgAl_2O_4$) have the simple halite (NaCl) structure, but both of these structures exhibit cubic cleavage on the {100} planes. It is of interest that these two crystal structures both exhibit much higher cleavage toughnesses, about 1 MPa $m^{½}$. Pyrite (FeS_2) is a metallic-like crystal, where in the case of the spinel ($MgAl_2O_4$) the increased toughness may arise from the stronger bonds

Table III Toughnesses for some cubic cleavages

Crystal	Plane	K_{Ic}(MPa $m^{½}$)	Reference
KBr	{100}	0.12	37
KCl (sylvite)	{100}	0.15	37
NaCl (halite)	{100}	0.17	37
LiF (griceite)	{100}	0.31	38
	{100}	0.50	25
MgO (magnesia)	{100}	0.81	15
PbS (galena)	{100}	0.18	39
	{100}	0.32	15
FeS_2 (pyrite)	{100}	0.96	39
$MgAl_2O_4$ (spinel)	{100}	1.18	28

involving the trivalent (Al^{3+}) cations. It is speculative, but the sequence of increasing toughness in the series LiF: MgO: $MgAl_2O_4$ may be related to the ionic charge contributions. These subtleties notwithstanding, the cleavage toughnesses for the cubic cleavage geometry, i.e. the {100} of cubic crystal structures, are similar in magnitude to those of the layer structures, although perhaps slightly higher. Some of the cubic cleavages appear to exhibit cleavage toughnesses of about 1 MPa $m^{½}$, but in general, those crystals which exhibit cubic cleavage and have been measured are not very tough.

Rhombohedral, Octahedral, and Dodecahedral Cleavage

Following the basic cubic cleavage geometry, Sorrell lists the rhombohedral and octahedral geometric cleavage forms. However, there are several published results of cleavage toughnesses for the sphalerite (ZnS) structure, a cubic crystal structure which cleaves on the {110}. This is a form of dodecahedral cleavage which is a three-dimensional type of cleavage with some of the axes between intersecting cleavage planes being orthogonal and some not. Several dodecahedral cleavage toughnesses are listed in Table IV. The cleavage toughnesses of the dodecahedral geometry which are summarized in Table IV are all less than 1 MPa $m^{½}$. This level of toughness is not very impressive, yet having previously summarized and considered other single crystal cleavage toughnesses, it is perhaps the magnitude of cleavage toughness which should be expected. From the values in Table IV, it is possible to suggest a Coulomb-like charge effect as GaP('3 x 5') slightly exceeds ZnS('2 x 6') and thus might be expected to be a little tougher (15/12). Of course, additional experimental measurements of related crystal structures are needed to substantiate this hypothesis. However, it follows the trend of the ionic charge contributions as previously suggested for cubic cleavage of the halite (NaCl) structure crystals.

Table IV Cleavage toughnesses for some dodecahedral cleavages

Crystal	Plane	K_{Ic}(MPa $m^{½}$)	Reference
GaP	{110}	0.65	26
ZnS (sphalerite)	{110}	0.23	15
InS	{110}	0.21	15

Rhombohedral cleavage as exhibited by the calcite ($CaCO_3$) structure on the $\{10\bar{1}1\}$ is Sorrell's next category. That geometry is depicted in Figure 2. It is quite familiar to every mineralogist and mineral collector as the large cleavage rhombohedra of optical quality calcite ($CaCO_3$) which are often displayed for their double refraction characteristics. The entire structural series from calcite ($CaCO_3$) to magnesite ($MgCO_3$), including rhodochrosite ($MnCO_3$), siderite ($FeCO_3$), and smithsonite ($ZnCO_3$), exhibit virtually perfect $\{10\bar{1}1\}$ rhombohedral cleavage, as does dolomite, the double carbonate of calcium and magnesium ($CaMg(CO_3)_2$). However, calcite ($CaCO_3$) is the only one of the series which has had its cleavage toughness actually measured and reported. Three different aughors report nearly identical experimental results for calcite, including Gilman [20] (0.18 MPa $m^{½}$), Santhanam and Gupta [40] (0.22 MPa $m^{½}$), and Atkinson and Avdis [39] (0.19 MPa $m^{½}$). Obviously, calcite ($CaCO_3$) has a low cleavage toughness as it cleaves very easily. No doubt that is why virtually perfect cleavage rhombohedra abound in nature and the crystallographic dominance of the cleavage persists to the submicron levels which are illustrated in Figure 2.

The octahedral cleavage displayed by fluorite (CaF_2) on its {111} is the last element of the structural classification for cleavage presented by Sorrell. Several other crystals which are known to cleave with that geometry have had their toughnesses measured and published. Table V summarizes those cleavage toughness results. The three alkaline earth fluorides have toughnesses of the magnitudes typical for cleavage, less than 1 MPa $m^{½}$. The toughness values decease from Ca through Ba as do the elastic moduli. It should be noted that the covalent bonding which is dominant in both silicon (Si) and diamond (C) yields significantly higher cleavage toughnesses. This effect is to be expected from some of the previous discussions on charge and bond effects. The diamond (C) cleavage toughnesses which are in the 3-5 MPa $m^{½}$ range are some of the highest reliable single crystal cleavage toughness values which have ever been reported. As the high hardness of diamond is well know, it is evident that coupling this high cleavage toughness value with the extraordinarily high hardness value makes diamond almost ideal for the industrial abrasive applications. It might be expected that Borazon, the synthetic cubic structure of BN, will exhibit a similar cleavage toughness to that of diamond, 3-5 MPa $m^{½}$, once large crystals are grown and the cleavage toughness is measured.

Table V Several octahedral cleavage toughnesses

Crystal	Plane	K_{Ic}(MPa $m^{½}$)	Reference
CaF_2 (fluorite)	{111}	0.45	15
	{111}	0.33	41
SrF_2	{111}	0.27	41
BaF_2 (frankdicksonite)	{111}	0.22	41
Si (silicon)	{111}	0.82	27
C (diamond)	{111}	3.60	42
	{111}	2.90	15
	{111}	4.10	42
	{111}	5	43

A related crystal structure which might also be expected to exhibit the octahedral cleavage geometry is that of stabilized cubic zirconia (ZrO_2), which has a defect fluorite structure. Guillou et al. [44] have measured calcia (CaO) stabilized cubic zirconia and Pajars et al. [45] have considered the yttria (Y_2O_3) stabilized form. The measured cleavage toughnesses of those single crystals varied from about 0.9 to 1.9 MPa $m^{½}$. In another study [46] the toughness was reported to be 1.5 MPa $m^{½}$. Interestingly, none of those crystals cleaved on the {111}, the well established cleavage plane for the fluorite structure. It may be that the introduction of the numerous anion vacancies into the stabilized defect fluorite structure of cubic zirconia has a profound effect on the role which that structure assumes in defining the cleavage plane. That effect is not understood, but for it to create a non-{111} cleavage tendency in the fluorite (CaF_2) structure, the effect must be substantial.

Other Crystal Structures

There are, of course, numerous other crystal structures which exhibit well defined cleavage that cannot be readily categorized within the aforementioned structural classification scheme. Large single crystals of quartz (SiO_2) occur naturally at many locations throughout the

world. It also is synthetically produced on a commercial scale by hydrothermal techniques for use in piezoelectric devices. The fracture of single-crystal quartz often assumes the macroscopic appearance of a totally conchoidal surface. However, Bloss and Gibbs [47] have suggested that those apparent conchoidal fractures are really a submicroscopic combination of cleavage planes similar to those which are depicted in Figure 1 for halite (NaCl) or Figure 2 for calcite ($CaCO_3$). Table VI summarizes some of the published cleavage toughness measurements for the fracture of quartz on specific planes at room temperature. Atkinson and Meredith [16] list another dozen toughness values for quartz, but some of those appear to have been measured by questionable techniques and therefore are not included in Table VI.

Table VI Measured cleavage toughnesses of quartz

Type	Plane	K_{Ic}(MPa $m^{1/2}$)	Reference
Brazilian Quartz	{0001}	1.15	48
	$\{01\bar{1}0\}$	0.97	48
	$\{01\bar{1}1\}$	0.86	48
	$\{11\bar{2}0\}$	0.85	48
	$\{11\bar{2}1\}$	0.94	48
Synthetic Quartz	{0001}	1.17	48
	$\{11\bar{2}0\}$	0.96	48
	{0001}	1.24	48
	$\{11\bar{2}0\}$	0.95	48
	$\{01\bar{1}1\}$	0.85	48
	$\{0\bar{1}11\}$	1.00	49
	$\{0\bar{1}11\}$	1.01	50

The summary of cleavage toughness values in Table VI is an excellent point from which to address the occurrence of macroscopic conchoidal fracture as compared with distinct planar cleavage on a microscale for single crystal quartz. From the cleavage perspective, Brace and Walsh [51], Bloss and Gibbs [47], and Martin and Durham [52] all observed and reported distinct rhombohedral cleavage on the $\{10\bar{1}1\}$. A zig-zag form of crack growth on these planes prior to macroscopic crack bifurcation has also been noted by Ball and Payne [53]. However, equally or more significant is the additional observation by Ball and Payne that for single crystals oriented to fracture on the $\{11\bar{2}0\}$, a completely smooth planar fracture surface results and no macroscopic crack bifurcation occurs. They have reported that the $\{11\bar{2}0\}$ fracture surfaces of single crystal quartz are very much like those of glass. For natural quartz, the results in Table VI support the $\{11\bar{2}0\}$ as the preferred cleavage plane, although the toughness differences between a number of different crystal planes of quartz are not very great. It must be concluded that it is the near equality of the cleavage fracture toughnesses of quartz on a number of different crystal planes that causes the conchoidal appearance of macroscopic fractures, but yet results in a distinct cleavage character for some specific conditions.

The Brittle Nature of Cleavage in Ceramics and Minerals

There has been considerable historical controversy over the extent of plastic flow during the fracture of materials, particularly in their brittle state. Some of this has persisted from the early experimental studies of dislocations in the alkali halides, others finds its origin in the fact that many ceramic and mineral studies have been completed by scientists originally trained as metallurgists during an era when dislocations were believed to be central to the answer to every technical materials problem. The author of this paper is one of the latter, one who had previously found it difficult to put aside some of the plastic deformation prejudices relating to flow and fracture. The cleavage of ceramics and minerals have not been an exception to this crack tip plasticity controversy. However, anyone, this author included, assessing the levels of cleavage cleavage for single crystal ceramics and minerals, as previously summarized, must indeed question the extent or magnitude of dislocation plastic flow about the crack tip during cleavage crack extension in these materials.

To further address this situation it is appropriate to initially contrast these cleavage toughness levels with well accepted brittle materials, such as WC-Co alloys and cast irons, two well known brittle materials with everyday industrial applications. WC-Co alloys range in fracture toughness from about 10 MPa $m^{1/2}$ for the 3 w/o Co compositions to nearly 20 MPa $m^{1/2}$ for the 15 w/o Co compositions (54). These hard brittle cutting tool materials are more than an order of magnitude tougher than cleavage for the ceramic and mineral single crystals which have been presented. Cast irons present a further substantiating contrast (55). Gray iron is the most brittle of the cast irons with fracture toughnesses generally in the 15 - 20 MPa $m^{1/2}$ range, while the ductile cast irons range from about 25 - 70 MPa $m^{1/2}$ and the malleable cast irons are reported to vary from 45 - 65 MPa $m^{1/2}$ in fracture toughness. Even cast irons are an order of magnitude tougher than the cleavage of single crystal ceramics and minerals and some cast irons are two orders of magnitude greater in fracture toughness. Comparisons like this quite strongly suggest that crack tip dislocation plastic flow must not be a major phenomenon during the cleavage of these brittle materials.

Additional experimental evidence confirming the brittle elastic nature of the single crystal cleavage process in ceramics and minerals exists from two types of experimental studies, those previously noted for the measurement of fracture resistance on several possible cleavage planes within the same crystal structure and also the effect of temperature on the cleavage toughness of a specific crystal structure. The results of those studies for single crystal $MgAl_2O_4$ spinel, which is well known to cleave on the {100} will be addressed separately.

Figure 4 illustrates the cleavage fracture toughnesses of single crystal $MgAl_2O_4$ spinel on three prominent low indice crystal planes, the {100}, the {110} and the {111} versus the elastic modulus normal to those crystal planes (56). As the magnesium aluminate spinel is quite elastically anisotropic, the E<111> is nearly twice the E<100>, it provides an excellent example to compare the toughnesses for restrained, or forced cleavage fracture on different crystal planes of the same crystal structure. A straight line connects the three sets of cleavage toughness / elastic modulus data. This clearly illustrates that the Young's modulus perpendicular to the cleavage plane is the dominant factor determining the cleavage plane for the crystal structure. It also suggests that the cleavage fracture is predominantly an elastic fracture process.

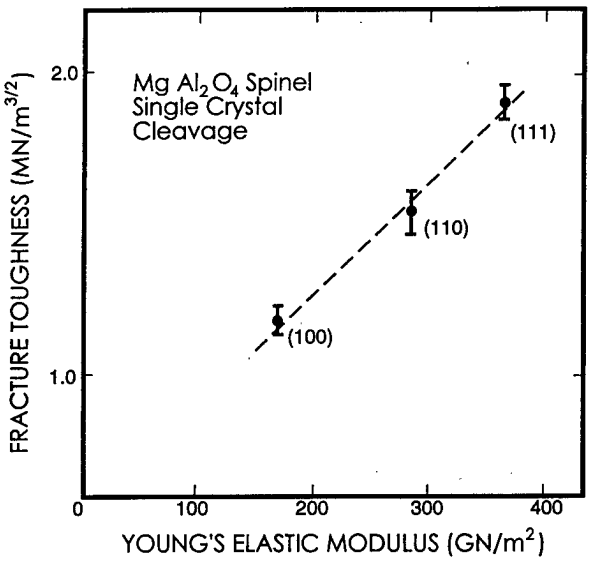


Figure 4: The cleavage toughness variation with the elastic modulus in single crystal $MgAl_2O_4$ spinel at room temperature.

The form of Figure 4 is readily predicted from the standard equation for the fracture toughness:

$$K_{Ic} = \sqrt{\frac{2\,E\,\gamma_f}{(1-\nu^2)}} \qquad (1)$$

where the quantities have their usual meanings; specifically E is the elastic modulus perpendicular to the fracture surface, γ_f is the fracture surface energy and ν is Poisson's Ratio. Replacing γ_f with Kelly's result for the surface energy of a solid (57):

$$\gamma_f = E\lambda^2 / a_o\pi^2 \qquad (2)$$

where a_o is the interatomic spacing for the crystal plane of interest, in this instance the cleavage plane, yields the result that:

$$K_{Ic} \propto E \qquad (3)$$

which is exactly the relationship depicted in Figure 4. Thus the experimental result that the cleavage toughness of $MgAl_2O_4$ on several low indice crystal planes is directly proportional to the elastic modulus normal to those planes suggests a elastic cleavage process which is free of significant dislocation plastic flow in the vicinity of the cleavage crack tip.

Stewart and Bradt (28) in their study of the fracture of single crystal $MgAl_2O_4$ spinel, measured the {100} cleavage toughness as a function of temperature to 1400°C at different strain rates to address the brittle to ductile transition. The brittle to ductile transition is discussed elsewhere (58), but the form of the cleavage toughness versus temperature is highly relevant to the understanding of the dominantly brittle nature of cleavage on the {100} of the single crystal $MgAl_2O_4$ spinel. Figure 5 illustrates the temperature dependence of the cleavage toughness on the {100}plane. Two regions of different toughness trends are evident, a low temperature region where the toughness decreases linearly with increasing temperature and a high temperature region where the toughness rapidly increases with increasing temperature. The decreasing toughness region extends from the room temperature measurements through about 900°C, while the rapid toughness increase occurs above that temperature. The fact that there is a rapidly increasing toughness region at elevated temperatures, where dislocation plastic flow at the crack tip is expected to become the dominant factor, suggests that one must investigate the elastic nature of the cleavage process as the cause for the decrease in toughness in the low temperature region. Replacing

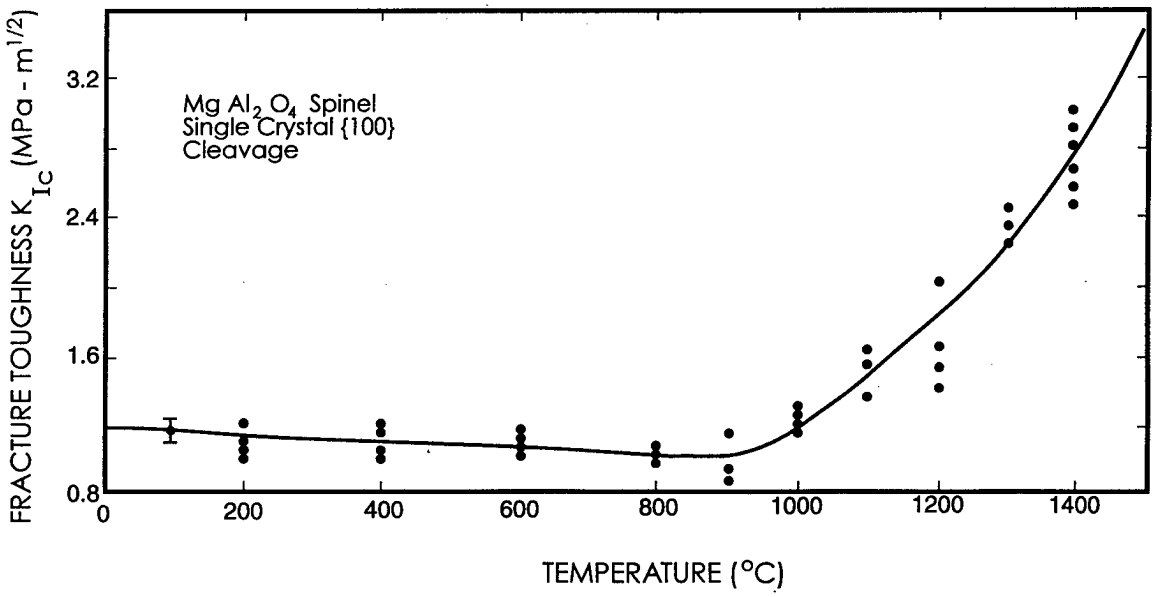


Figure 5: The fracture toughness variation with temperature for cleavage on the {100} plane of $MgAl_2O_4$ from room temperature through 1400°C. Note the presence of two regions, a low temperature region that exhibits a linear toughness decrease with increasing temperature and a high temperature region where the toughness increases rapidly with increasing temperature. This is a classical brittle to ductile transition, where the low temperature region decrease is a consequence of the decrease of elastic modulus with increasing temperature and the high temperature, rapid increase in the toughness is a result of the increase is dislocation plastic flow in the vicinity of the crack tip.

γ_f in Equation (1) with the form in Equation (2) yields:

$$K_{Ic} = \frac{\sqrt{2\,E\lambda}}{\pi\, a_o^{1/2}\,(1-\nu^2)^{1/2}} \qquad (4)$$

This form of the fracture toughness can then be differentiated with respect to temperature to yield:

$$\frac{dK_{Ic}}{dT} = \frac{\sqrt{2\,\lambda}}{\pi\, a_o^{1/2}(1-\nu^2)^{1/2}}\left\{\left(\frac{dE}{dT}\right) - \tfrac{1}{2}E\alpha + \frac{E\nu}{(1-\nu^2)}\left(\frac{d\nu}{dT}\right)\right\} \qquad (5)$$

where α is the linear coefficient of thermal expansion and the other terms have their usual meanings. All of the terms in Equation (5) can be evaluated from literature data. When the values are inserted and the temperature dependence of the cleavage toughness is calculated, it is dominated by the temperature dependence of the elastic modulus and yields a $(dK_{Ic}/dT) = -1.3 \times 10^{-4}$ MPa $m^{1/2}/°C$, which compares quite favorably with the experimental result for the {100} cleavage of -2.5×10^{-4} MPa $m^{1/2}/°C$ in the low temperature region. It must be concluded that the cleavage of the {100} of $MgAl_2O_4$ spinel below about 900°C occurs in a brittle elastic manner with very little or no crack tip dislocation plastic flow. By analogy with the cleavage of the other single crystal ceramics and minerals with similarly low values of the fracture toughness on the cleavage planes, it must also be concluded that the cleavage phenomenon in single crystal ceramics and minerals occurs with very little, or no dislocation crack tip plastic flowat low temperatures, which includes room temperature for most ceramics and minerals of interest.

The summaries of cleavage toughnesses for ceramic and mineral single crystals, the role of the of elastic modulus in determining the cleavage plane in spinel and the effects of temperature on the {100} cleavage of spinel all reinforce the fact that the cleavage process is indeed a rather brittle one in these types of materials at room temperature. Proceeding with another viewpoint for consideration of the cleavage of these materials, if they truly are brittle and without appreciable dislocation plastic flow at the crack tip during fracture, then there should exist some form of agreement of the experimental cleavage surface energies with theoretically calculated thermodynamic surface energies. Although it was previously noted with reference to the cleavage of graphite that one can be mislead by these theoretical approaches, this form of comparison nonetheless merits consideration. For sapphire, or single crystal alumina, which is well known to cleave on the rhombohedral, or the R-plane, there exist excellent fracture toughness measurements and also several independent theoretical estimates of the thermodynamic surface energies for the same crystal planes which have been experimentally measured for fracture toughness. Study of the brittle to ductile transition in sapphire has also been completed, thus enabling further comparison with the results for the cleavage of spinel.

Table VII summarizes properties and calculations for comparison of the experimental cleavage energies and the theoretical themodynamic surface energies of sapphire on the C, R and M-planes. The cleavage measurements are those of Iwasa and Bradt (58), whereas the three different theoretical calculations of the surface energies are those of Tasker (59), Mackrodt (60) and Hartman (61), designated as T, M and H, respectively in the summary. The toughnesses were measured on large single crystals, while the theoretical calculations appear to be of the unrelaxed variety. These unrelaxed calculations may be expected to translate to a more realistic comparison with cleavage measurements than the previous quasi-static surface energy discussed for graphite and which considerably underestimates its cleavage toughness. As a point of reference, unrelaxed surface energy calculations are about a factor of two higher than similar relaxed ones, although none of the latter appear to have been published for sapphire.

Table VII Sapphire cleavage and theoretical energies

Crystal Plane	E (GPa)	K_{Ic} (MPa $m^{1/2}$)	Cleavage (J/m^2)	Theoretical (J/m^2)		
				T	M	H
C{0001}	465	4.54	21.54	6.5	5.9	4.8
R{10$\bar{1}$1}	440	2.38	6.45	6.4	5.6	4.8
M{10$\bar{1}$0}	430	3.14	11.43	6.9	6.5	—

The theoretical surface energies from each of the three investigators are quite similar, varying from about 5 - 7 J/m^2. This general agreement of the three theoretical results gives one confidence in the calculations, as one can never be quite sure of the details of the computer simulations unless one actually writes the code. This result also suggests that the surface energy of sapphire, at least for these three low indice crystal planes is not very anisotropic. This result is in agreement with the elastic anisotropy, which is also summarized in Table VII for the same crystal planes and which in fact is not very anisotropic at all. (62) It is significant that the cleavage plane of sapphire, the R-plane, has excellent agreement between the experimentally measured cleavage surface energy and the three theoretical thermodynamic surface energies, as all are about 6 J/m^2. This suggests that the cleavage fracture of sapphire on its R-plane, the well known rhombohedral cleavage plane, is substantially brittle, at least the amount of crack tip dislocation activity is not very energy consuming beyond the thermodynamic surface energy. In contrast, both the basal (C) plane and the prism (M) plane exhibit experimental cleavage surface energies that are significantly larger than the theoretically calculated surface energies, perhaps suggesting that dislocation crack tip plasticity, or twinning is consuming additional energy during the forced fracture of these non-cleavage planes. Kim and Roberts (63) in their recent study of the brittle to ductile transition confirm that it is at elevated temperatures, ~1,000°C, in agreement with the above conclusion regarding the minimal role of dislocation plastic flow for fracture of sapphire on the rhobohedral cleavage plane at room temperature.

Summary and Conclusions

The single crystal cleavages of ceramics and minerals, groups of ionically / covalentally bonded materials that are often synonymous, have been reviewed and are summarized. It is concluded that the appropriate criterion for the crystal cleavage plane is the minimum fracture toughness. The magnitudes of cleavage toughnesses are generally 1 MPa $m^{1/2}$, or less, indicative of extremely brittle behavior and suggestive of little, or no significant dislocation crack tip plasticity during the cleavage fracture process. Several experimental and theoretical studies were also reviewed, further confirming the brittle, elastic nature of the cleavage phenomenon in these types of materials.

Acknowledgements

The author acknowledges the contributions of many individuals to his ceramic and mineral interests, including: C.C. Sorrell, R.C. DeVries, G. W. Brindley, R.A. Schultz, M.C. Jensen, M. Iwasa and R.L. Stewart. He apologizes to anyone he may have accidentally omitted.

References

(1) C.A. Sorrell, "Minerals of the World", Golden Press, New York, New York (1974).
(2) W.C. Roberts, G.R. Rapp, Jr., and J. Weber, "Encyclopedia of Minerals", Van Nostrand, New York, New York (1974).
(3) L.B. Berry and B. Mason, "Mineralogy", Freeman, San Francisco, California (1959).
(4) K. Frye, "Encyclopedia of Mineralogy", Hutchinson Ross, Stroudsburg, Pennsylvania (1981).
(5) W.D. Deer, R.A. Howie and J. Zussman, "Rock Forming Minerals, Vol 1", J. Wiley, New York, New York (1962).
(6) M. Fleischer and J.A. Mandarino, "Glossary of Mineral Species", Mineralogical Record, Tucson, Arizona (1991).
(7) C.D. Gribble, "Rutley's Elements of Mineralogy", Unwin Hyman, Boston, Massachusetts (1988).
(8) J. Sinkankas, "Gemstone and Mineral Data Book", Winchester Press, New York, New York (1972)
(9) C.S. Hurlburt, Jr. and R.C. Kammerling,"Gemology", J. Wiley, New York, New York (1991).
(10) G.E. Dieter, "Mechanical Metallurgy", McGraw-Hill Publishing, New York, New York (1986).
(11) I. Lemay, "Principles of Mechanical Metallurgy", Elsevier Publishing, New York, New York (1981).
(12) M.A. Meyers and K.K. Chawla, "Mechanical Metallurgy", Prentice-Hall Publishers, Englewood Cliffs, New Jersey (1984).
(13) T.N Courtney, "Mechanical Behavior of Materials", McGraw-Hill Publishing, New York, New York (1990).
(14) R.A. Schultz, M.C. Jensen and R.C. Bradt, Int. J. of Fracture, Vol. 65 (1994) 291.
(15) J.J. Gilman, 193 in "Fracture", J. Wiley, New York, New York (1959).
(16) B.K. Atkinson, "Fracture Mechanics of Rock", Academic Press, New York, New York (1987).
(17) E.J.W. Whittaker, Mineralogical Magazine, Vol. 46 (1982) 398.
(18) O. Vingsbo, Materials Science and Engineering, Vol. 8 (1971) 32.
(19) J.A. Schweitz and O. Vingsbo, Materials Science and Engineering, Vol, 8 (1971) 275.
(20) R.K. Mishra and G. Thomas, J. App. Phys., Vol. 48 (1977) 4576.
(21) B.R. Lawn and T.R. Wilshaw, "Fracture of Brittle Solids", Cambridge University Press, Cambridge, England (1975).
(22) R.W. Hertzberg, "Deformation and Fracture Mechanics of Engineering Materials", J. Wiley, New York, New York (1996).
(23) M.F. Kanninen and C.H. Popelar, "Advanced Fracture Mechanics", Oxford University Press, Oxford, England (1985).
(24) M. Sakai and R.C. Bradt, Int. Mat. Rev., Vol. 38 (1993) 53.
(25) K.Hayashi, M. Namura and T. Nishikawa, J. Mat. Sc. Jap., Vol. 35 (1986) 66.
(26) K.Hayashi, M.Ashizuka, R.C. Bradt and H. Hirano, Mat. Lttrs. Vol. 1 (1982) 116.
(27) C.P. Chen and M.H. Leipold, Bull. Amer. Cer. Soc., Vol. 59 (1980) 469.
(28) R.L. Stewart and R.C. Bradt, J. Mat. Sc., Vol. 15 (1980) 67.
(29) G.A. Wolff and J.D. Broder, Amer. Mineral., Vol. 45 (1960) 1230.
(30) M. Sakai, R.C. Bradt and D.B. Fischbach, J. Mat. Sc., Vol. 21 (1986) 1491.
(31) R.F. Cook, T.R. Dinger and D.R. Clarke, Appl. Phys. Lttrs., Vol. 51 (1987) 454.
(32) H.W. Liu and K.J. Miller, Journal of Glaciology, Vol. 22 (1979) 135.
(33) K.T. Wan, N. Aimard, S. Lathabai, R.G. Horn and B.R. Lawn, J. Mats. Res., Vol. 5 (1990) 172.
(34) J.W. Obriemoff, Proc. Roy. Soc. London, Vol. 127A (1930) 290.
(35) H. Li, M.C. Jensen and R.C. Bradt, J.Mat.Sc., Vol. 27 (1992) 1357.
(36) A.V. Milovsky and O.V. Knonov, "Mineralogy", Mir Publishers, Moscow, Russia (1985).
(37) S.W. Freiman, P.F. Becher and P.H. Klein, Phil. Mag. Vol. 31 (1975) 829.
(38) C.N. Ahlquist, Acta Met., Vol. 22 (1974) 1133.
(39) B.K. Atkinson and V. Avdis, Int. J Tock Mech. Min. Sc. and Geomech. Abstracts, Vol. 17 (1980) 383.
(40) A.T. Santhanam and Y.P. Gupta, Int. J. Rock Mech. Min. Sc., Vol. 5 (1968) 253.
(41) P.F. Becher and S.W. Freiman, J. App. Phys.,Vol. 49 (1978) 3779.
(42) J.E. Field and J.C. Freeman, Phil. Mag., Vol. 43 (1981) 595.
(43) N.V. Novikov and S.N. Dub, J. Hard Mat., Vol. 2 (1991) 3.
(44) M.O. Guillou, G.M. Carter, R.M. Hooper, J.L. Henschel, J. Hard Mat., Vol. 1 (1990) 65.
(45) A. Pajares, F. Guibearteau, A. Dominguez-Rodriguez and A.H. Heuer, J. Amer. Cer. Soc., Vol. 71 (1988) C332.
(46) R.P. Ingal, D.Lewis, B.A. Bender, and R.W. Rice, J.Amer.Cer. Soc., Vol. 65 (1982) C150.
(47) F.O. Bloss and G.V. Gibbs, Amer. Mineral., Vol. 48 (1963) 821.
(48) M. Iwasa and R.C. Bradt, Mat. Res. Bull., Vol. 22 (1987) 1241.
(49) B.K. Atkinson, Pure and Appl. Geophys., Vol. 117 (1979) 1011.
(50) P.G. Meredith and B.K. Stkinson, Earthquake Pred. Res., Vol. 1 (1982) 377.
(51) W.F. Brace and J.B. Walsh, Amer. Miner., Vol. 47 (1962) 1111.
(52) R.J. Martin, III and W.B. Durham, J.Geophy.Res., Vol. 80 (1975) 4837.
(53) A. Ball and A.W. Payne, J.Mat.Sc., Vol. 11 (1976) 731.
(54) R.C. Leuth, 791 in Fract. Mech. Cer., Vol. 2, Plenum Pub. Corp., New York, New York (1974).
(55) C.F. Walton and T.J. Opar, "Iron Castings Handbook", Iron Castings Society, New York, New York (1981).
(56) R.L. Stewart, M. Iwasa and R.C. Bradt, J. Amer. Cer. Soc., Vol. 64 (1981) C22
(57) A. Kelly, "Strong Solids", Clarendon Press, Oxford, England (1966).
(58) M. Iwasa and R.C. Bradt, Adv. in Ceramics, Vol. 10 (1983) 767.
(59) P.W. Tasker, Adv. in Ceramics, Vol. 10, (1983) 176.
(60) W.C. Mackrodt, J.Chem.Soc.Faraday Trans., Vol. 85, No.5, (1989) 541.
(61) P. Hartman, J. Crys. Growth, Vol. 96 (1989) 667.
(62) H.S. Kim and S. Roberts, J.Amer. Cer. Soc., Vol. 77 (1994) 3099.

Static and Cyclic Fatigue Failure at High Temperature in Ceramics Containing Grain Boundary Phase: Experiments

K. J. Hsia, N. Dey[1], and D. F. Socie[2]
Department of Theoretical and Applied Mechanics
Departments of Materials Science and Engineering[1] and Mechanical Engineering[2]
University of Illinois at Urbana-Champaign, Urbana, IL 61801, USA

Abstract

Fatigue behavior of a commercial grade alumina with 6 wt% of grain boundary viscous phase was investigated. Uniaxial tensile tests were conducted under both static and cyclic loading at 1000 C. The fatigue lifetime was measured as a function of the maximum applied stress. The failure mechanisms were studied using scanning electron microscopy. Under static loading, two different failure mechanisms were observed: at high applied stresses, fracture was dictated by the slow growth of a single dominant flaw along the grain boundaries; at low applied stresses, fracture occurred due to the nucleation, growth and linkage of multiple macrocracks. Under cyclic loading within the stress range in the present investigation, fracture was dominated by the slow growth of a single crack. In the slow crack growth regime where crack growth is driven by Irwin's stress intensity factor [1], the lifetime under cyclic loading was longer than that under static loading (for the same maximum stress) by approximately a factor of 30. Extensive crack surface bridging by viscous grain boundary phase behind the crack tip was observed. The viscous bridging was believed to be the most important factor for the observed cyclic strengthening behavior.

Introduction

It is now realized that ceramics have great potentials as structural materials in high temperature applications. The major restrictions, however, are the extreme brittleness and the lack of characterization of their mechanical properties at high temperatures. Recent research work on ceramics have been focused on identifying high temperature failure mechanisms under various loading conditions. These materials often contain a small volume fraction of intergranular glassy phase to aid the sintering process. This intergranular phase adversely affects the high temperature mechanical properties [2]. Thus understanding the behavior of intergranular glass phase at high temperature is a key step towards a more complete understanding of high temperature failure behavior of ceramic materials.

Failure of polycrystalline ceramics at high temperature may initiate from pre-existing flaws (microcracks and processing pores), or from flaws generated during service (voids and cavities) [2, 3]. The dominant failure mechanisms strongly depend on the material's microstructure (grain size, volume fraction and nature of the grain boundary phase, etc.), temperature, and the level and type (static or cyclic) of

George R. Irwin Symposium on Cleavage Fracture
Edited by Kwai S. Chan
The Minerals, Metals & Materials Society, 1997

the applied loading. In the present study, we focus on the role of intergranular viscous glassy phase on the failure behavior of ceramics under static and cyclic loading at high homologous temperatures. An experimental study of high temperature failure mechanisms under static and cyclic loading in a polycrystalline alumina containing a continuous grain boundary phase is presented.

Although many experiments have been conducted under static loading conditions [2-18], limited information exists for failure under cyclic loading conditions [19-27]. Lin and Socie [19] conducted static and cyclic fatigue experiments under different types of cyclic loading on a 99.8 wt% alumina at 1200 C. They reported increased time to failure under cyclic loading compared to that under static loading. To investigate the effect of grain boundary viscous phase on high temperature static and cyclic fatigue properties, in the current study, we use a polycrystalline alumina with 6 wt% grain boundary phase (significantly higher percentage of grain boundary phase than that used by Lin and Socie). We also investigate the effect of the level of applied stress on the high temperature failure mechanisms in this material.

Material and Experimental Procedure

Material and Test Specimen

Experiments were conducted on a commercial grade of vitreous bonded aluminum oxide, Coors AD-94*, reported to contain 94 wt% aluminum oxide. The grain boundary phase of this material contains about 4 wt% to 6 wt% SiO_2 and small amount of impurities, like MgO, CaO, Fe_2O_3, ZrO_2, BaO_2, TiO_2 and K_2O. The material consists principally of aluminum oxide grains bonded by a continuous intergranular glassy phase. The average grain size is about 7 to 9 μm with some grains as large as 30 μm. Irregularly shaped inherent processing pores of microscopic dimension (2 to 10 μm) are interspersed throughout the material.

As received materials were supplied in the form of cylindrical rods of 304.8 mm long and 12.7 mm in diameter. Uniform-gage tensile specimens were circumferentially ground to produce a gage length of 25 mm with a diameter of 6.3 mm using a 150-grit diamond grinding wheel. Details of the specimen preparation may be found in reference [19].

Test Procedure and Loading Path

Uniaxial tensile tests were conducted under both static and cyclic loading at high temperature. The gage section of specimen was heated to 1000 C in air. After reaching 1000 C, the specimens were maintained at this temperature for 30 minutes to achieve steady state temperature distribution before starting the experiment.

Specimens for static fatigue were tested to failure under constant tensile load. Cyclic fatigue tests were conducted under a square loading wave with a stress ratio R=0.1 and frequency of 2 Hz. Creep deformation during static and cyclic loading was continuously measured using a laser extensometer**.

Experimental Results

Lifetime under static and cyclic loading

Fig. 1 shows the test results of the cyclic fatigue lifetime (square symbols) and the static fatigue lifetime (circular symbols). The number of cycles to failure during cyclic loading, N_{cf}, was converted to the time to failure, t_{cf}, using the relation

$$t_{cf} = N_{cf} \times \left(\frac{1}{\nu}\right) \tag{1}$$

where ν is the frequency of loading wave. Time to failure under cyclic loading consists of both the loaded and the unloaded portions of the loading wave form. For static fatigue, the time to failure, t_{sf}, is plotted against the applied stress, σ_∞^{max}; and for cyclic fatigue, t_{cf} is plotted against the peak applied stress, σ_∞^{max}. Each point represents a single specimen tested to failure. The arrows indicate that the specimens did not fail when the test was terminated.

* Grade AD-94, Coors Ceramics Co., Golden, Co

** Model 1102 laser dimensional sensor and model 1100 multidimensional processor, Zygo Corporation, Middlefield, CT.

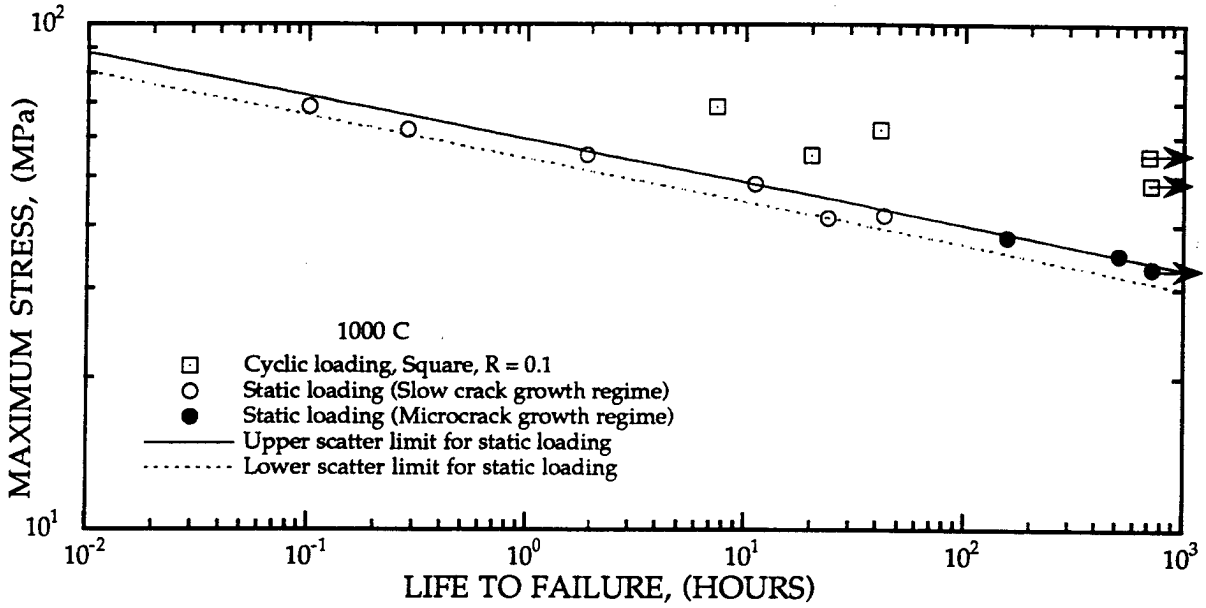


Fig. 1 Comparison of the static and cyclic fatigue lifetime

Linear regression analysis of the static fatigue lifetime data shows that static fatigue lifetime data in this stress-temperature regime can be fitted into a simple power law expression, as,

$$t_{sf} = A\,(\sigma_{\infty}^{max})^{-n} \qquad (2)$$

where t_{sf} is in hours, σ_{∞}^{max} is in MPa, n is equal to 11.7 and A is equal to 3.12×10^{20}. The correlation coefficient of this linear regression is 0.89. To estimate the scattering of the experimental data, the slope of this best fitting curve was used to draw two parallel lines such that all the static fatigue data of the specimens failed due to slow crack growth (open circles) fell between them. These two lines are termed lower and upper scatter limits of the static fatigue life. The scattering in the current study is apparently smaller than those by others [28-31], perhaps due to the uniaxial tensile specimens used here.

It should be noted that the specimens which failed under a static load higher than 40 MPa, represented by open circles in Fig. 1, showed evidence of different failure mechanism from the ones failed under a lower static load. Failure mechanisms will be discussed in detail in the next section.

Typical creep deformation curves under high and low stress static loading are shown in Fig. 2. Fig. 2 shows that under high stresses (e.g., 42 MPa), steady state creep was never achieved and fracture occurred at a very low strain (below 0.1%). But under low stresses (e.g., 35 MPa), the specimens failed after reaching the steady state creep and failure strain was above 0.3%. For comparison, the creep curve under cyclic loading with a maximum stress of 42 MPa is also shown in Fig. 2. It is seen that the creep rate during primary stage under cyclic loading of 42 MPa is approximately equal to that under static loading of 42 MPa. However, under static loading of 42 MPa, the specimen failed after 43 hours during the primary stage of creep. But under cyclic loading of 42 MPa, the specimen did not fail even after reaching steady state creep when the test was terminated after 550 hours.

One interesting result seen in Fig. 1 is that on average, for a given maximum stress, the lifetime under cyclic loading is approximately 30 times longer than that under static loading. Prolonged lifetime under cyclic loading has been observed in several ceramic systems [19-27]. Perhaps a more relevant question is why, and under what conditions, such a strengthening under cyclic loading will exist. To answer this, the failure mechanisms must be understood.

Failure Analysis

Scanning electron microscopy (SEM) was used for the post failure fractographic analysis. The fracture surface was examined for any visible evidence of the damage

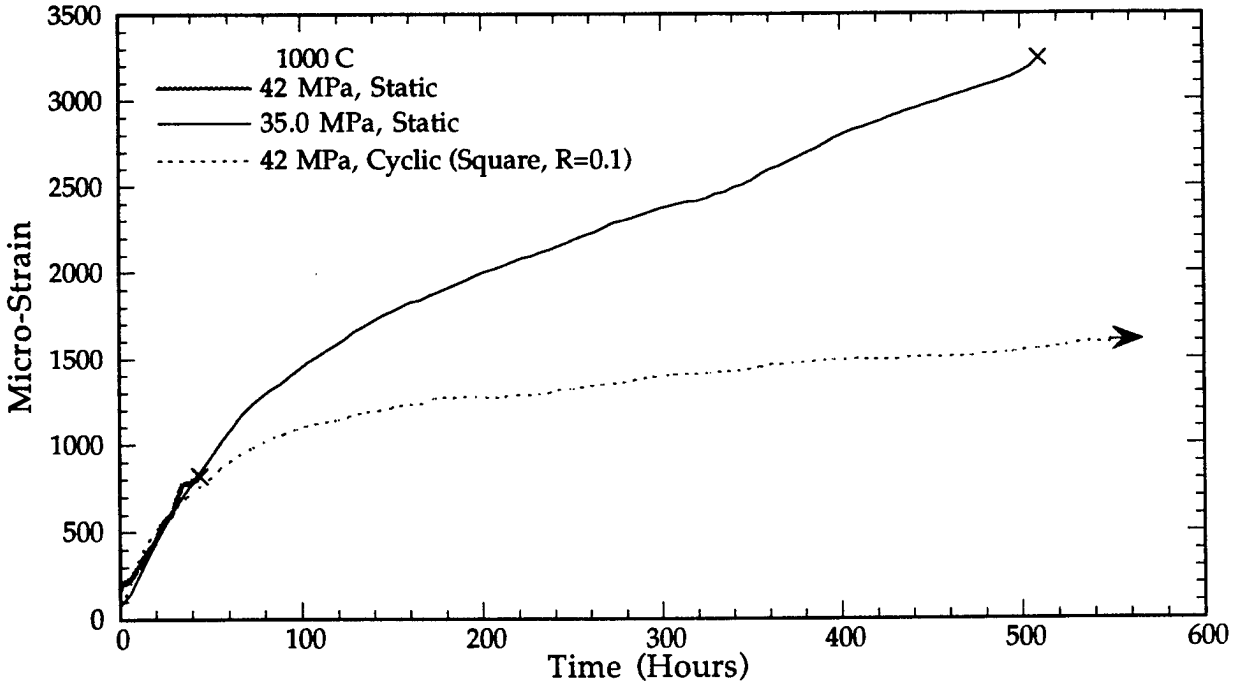


Fig. 2 Typical creep curves for AD94 alumina under static and cyclic loading (the arrow indicates that the specimen did not fail when the test was terminated)

mechanisms. The broken gage sections of all specimens were also axially sliced into four sections parallel to the loading direction and each internal section was mechanically polished and sputter coated with gold-palladium for SEM examination.

One particular feature common to specimens failed under both static and cyclic loading is that a grain boundary viscous phase is clearly seen on the fracture surface, as shown in Fig. 3. The viscous phase is mostly concentrated in the channels of triple grain junctions as in the region marked by "M" in Fig. 3. Furthermore, fracture surface analysis showed that all specimens failed intergranularly. These features are very important in determining the difference between the static fatigue and the cyclic fatigue behavior.



Fig. 3 Micrograph of a typical fracture surface showing viscous grain boundary phase (specimen failed under cyclic loading at 1000C)

Under static loading condition, two different failure processes were identified by examining the failure surfaces. Under high applied stress (>40 MPa), the fracture surface is rather flat. Apart from the main fracture plane, the axially sectioned internal surface does not show any secondary macrocracks or grain sized microcracks. This indicates that failure under high static stress was caused by the growth of a single dominant crack. On the other hand, fracture surface of the specimens failed at low stresses (i.e., $\sigma_{\infty}^{max} \leq 40$ MPa) shows regions of crest and trough, an evidence that non-coplanar secondary cracks were also growing on other adjacent planes. An axial slice from the gage section of a specimen failed under 38 MPa static load revealed the existence of many subcritical macrocracks. Figure 4 shows a high magnification micrograph of a typical subcritical macrocrack which follows an intergranular

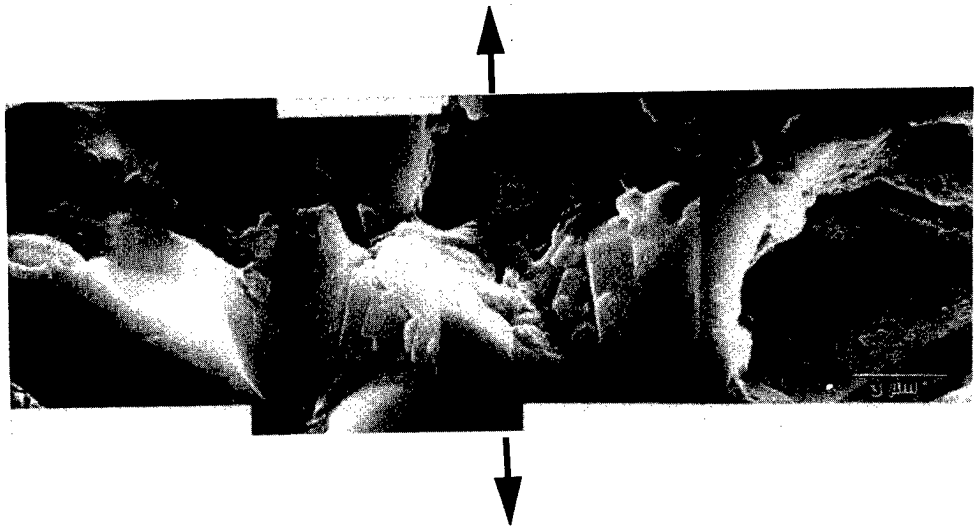


Fig. 4 SEM micrograph of the path of a subcritical macrocrack in an axially cut section of the specimen showing viscous bridges (static loading, σ_{∞}^{max}=38 MPa)

zig-zag path. It is also noted that along almost its entire length, the crack surfaces are bridged together by the viscous grain-boundary phase. This can be more clearly seen in Fig. 5, which shows that the two grains are bridged by the viscous phase and the viscous phase is drawn into sheet-like appearance with several cavities in it. This bridging behavior is expected to exist at both high and low stress levels under static loading. Bridging by the viscous grain boundary phase shields the crack tip by carrying some of the load and leads to R-curve behavior at elevated temperatures [32, 33].

It was also found that under static loading of 35 MPa, the outer surface of the gage section was heavily decorated with subcritical macrocracks, cracks which nearly reached the critical length for fast fracture. The macrocrack density under this load was far greater than even that under static loading of 38 MPa. Certain features of the growth of these subcritical macrocracks were observed. Fig. 6(a) shows a typical subcritical macrocrack originated from the specimen surface with a heavily damaged zone ahead of the crack tip. It is the linkage of the macrocrack with the microcracks in the damage zone which gives rise to the growth of the macrocrack. Sometimes the macrocrack may link with several microcracks such that crack branching results as shown in Fig. 6(b). Although such clear evidence of the crack growth mechanisms for specimens failed by a single dominant crack growth can not be visually observed, it is suspected that crack surface bridging and linkage of the main crack with grain boundary microcracks may also prevail under high static loading.

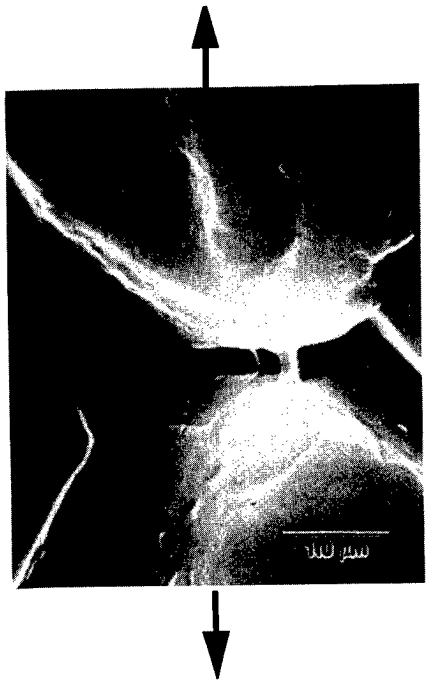


Fig. 5 High magnification micrograph of the viscous grain boundary phase bridging the crack surfaces (static loading, σ_{∞}^{max}=38 MPa)

It is concluded that under static loading, two different failure mechanisms are present: at high applied stress, failure is caused by slow growth of a single dominant crack; at low applied stress, failure is caused by growth and coalescence of multiple microcracks. In both processes,

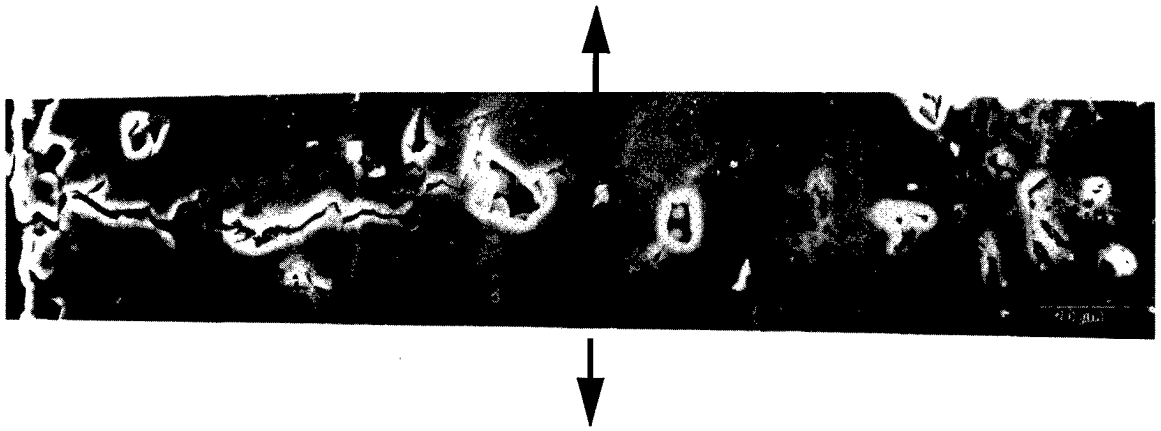


Fig. 6(a)

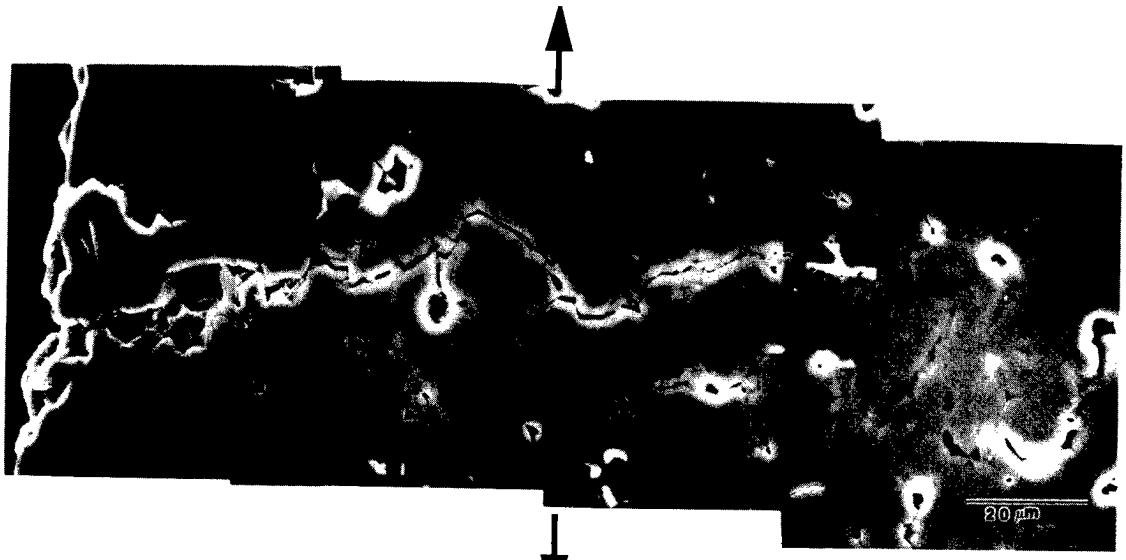


Fig. 6(b)

Fig. 6 Crack growth characteristics observed in an axially cut section of a specimen failed under low static loading (σ_{∞}^{max} = 35 MPa, 1000 C). (a) Showing the heavily damaged zone with facet-sized microcracks ahead of the subcritical macrocrack tip; (b) Showing the crack tip branching.

bridging of grain boundary viscous phase exists, although its effect is likely to be more profound in the slow crack growth process.

The features on the fracture surface of the specimens failed under cyclic loading with a maximum applied stress greater than 55 MPa were very similar to that on the specimen failed under static loading greater than 40 MPa (i.e., relatively flat fracture surface). SEM examination of the fracture surface revealed that intergranular cracking was the predominant fracture mode and the fracture surface was smeared with a viscous grain boundary phase. SEM examination of the axially sliced internal sections did not show macrocracks of any detectable size or any evidence of creep damage. Hence similar to the high stress static loading, it is concluded that fracture of all failed specimens under cyclic loading was dominated by growth of a single macrocrack to the critical size.

Specimens loaded under cyclic loading with a maximum applied stress less than 55 MPa did not fail and the tests were terminated after running for more than 700 hours. The axially sliced gage sections of these specimens were examined by SEM to detect any evidence of creep damage such as the formation of microcracks and stress-induced creep cavities. No

microcracks of a detectable size were observed on any of these axial sections nor did the density of cavities or pores showed any appreciable increase compared to the microstructures of the as received material. These observations are consistent with the creep deformation curve under cyclic loading of σ_{∞}^{max} = 42 MPa in Fig. 2, which shows that the creep strain (a measure of accumulated creep damage) was about 0.16% when the test was terminated after 550 hours.

Discussion

Slow crack growth regime

As described above, the failure of the specimens under high static loading (>40 MPa) and of all failed specimens under cyclic loading is the result of the slow growth of a single dominant crack to a critical size. In the slow crack growth regime our experiments show that fracture occurs at a very low creep strain (below 0.1%), indicating a highly localized deformation and failure process. Growth of a single crack by direct extension along the grain boundaries by viscous flow of the grain boundary phase, without considering creep deformation in the bulk, was analyzed by Tsai and Raj [2]. They approximated this problem with that of the separation of two parallel, rigid plates separated by a thin fluid film. The growth velocity, V_g, of the macrocrack under a mode I stress intensity factor can be given by

$$V_g = 3\times10^4 \left(\frac{\delta}{d}\right)^3 \left(\frac{k_1^2}{\eta E}\right) \qquad (3)$$

where k_1 is the local value of the stress intensity at the triple junction produced by grain boundary sliding, δ is the thickness of the fluid layer in two grain channels, E is the Young's modulus of the matrix, η is the viscosity of the grain boundary phase and d is the grain size.

The prediction of this simple model is indeed consistent with the comparison of our experimental results with that of Lin and Socie [19]. Lin and Socie conducted uniaxial tensile static and cyclic fatigue experiment on a 99.8wt% pure alumina (AD-998, COORS Ceramics Co., Golden, CO) at 1200 C. The microstructural parameter, δ/d, is much smaller in their material than that in ours. On the other hand, the viscosity of the grain boundary phase of their material (at 1200 C), η, is significantly lower than ours (at 1000 C). Despite the difference in volume fraction of the grain boundary phase, the average grain size and the composition of the grain boundary phaseof the material used by Lin and Socie are nearly the same as in our material. For comparison, the tensile static fatigue results of AD-998 at 1200 C and AD-94 at 1000 C are plotted in Fig. 7. It is seen that the dependence of static fatigue life to the

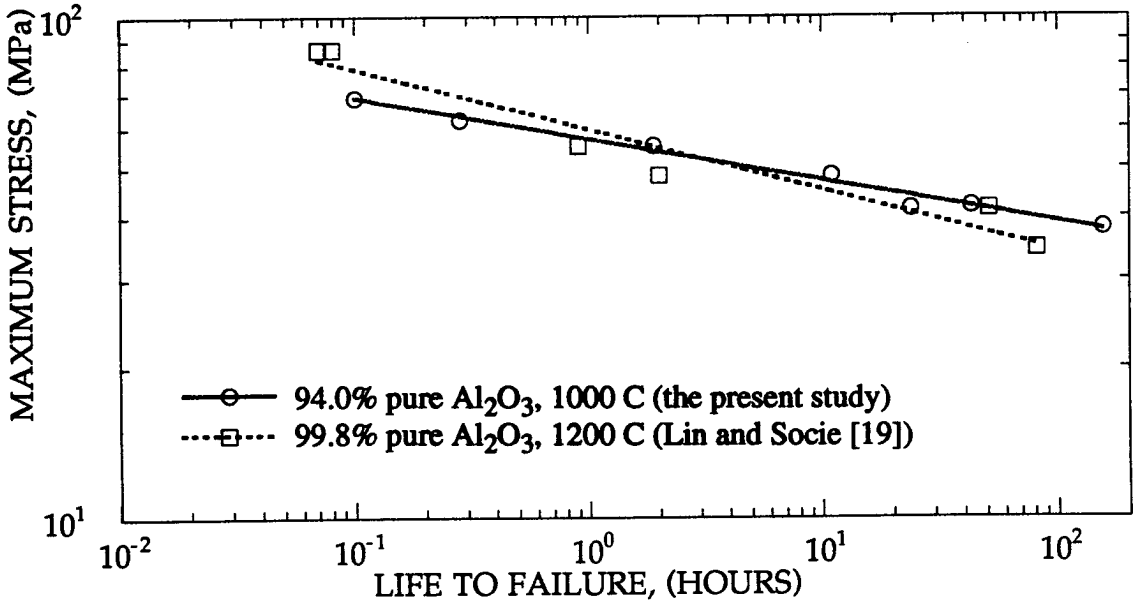


Fig. 7 Comparison of tensile static fatigue test results of AD-998 at 1200 C [19] and AD94 at 1000 C

far field applied stress for AD-94 at 1000 C is nearly identical to that of AD-998 at 1200 C.

According to Equation (3), if the two different materials have the same value of the parameter, $(\delta/d)^3/(\eta E)$, the crack growth velocity in them should be the same at the same crack tip stress intensity level. Therefore, the fatigue life of the two materials should have the same dependence on the applied stress. Although the microstructural parameter, δ/d, of the material tested by us is much larger than that tested by Lin and Socie [19], the value of viscosity at our testing temperature is also much higher than that at Lin and Socie's testing temperature. The overall effect of these parameters in the two materials may lead to a similar crack growth rate. Moreover, the similar slopes of the fatigue life vs. stress plot in Fig. 7 for these two materials seems to suggest that Tsai and Raj's model [2] and its associated mechanism may be acceptable for static fatigue failure in the slow crack growth regime. This simple model, however, does not take into account of the bridging of viscous phase behind the crack tip. The model will not explain the difference between static and cyclic loading, which will be discussed later.

Microcrack growth regime

Our experimental observations clearly indicate that, under static loading, the failure mechanism changes from slow crack growth to microcrack nucleation and coalescence when the applied stress level decreases. Microcracks are formed either by growth of processing pores, or by cavity nucleation and growth in the grain boundary phase.

However, Marion et al [7] showed that cavity nucleation requires that a negative hydrostatic pressure in the viscous phase must exceed a critical value. An estimate of this critical value shows that it is substantially higher than the applied far field stress (often 20-30 times the far field stress) [34]. To achieve such a high local stress, sources of high stress concentration must be available. Recently, we proposed that the source of such stress concentration is the heterogeneous distribution of grain size in ceramics [35]. A model invoking compatibility condition between large and small grains has been developed which showed that, under long term creep condition, the hydrostatic tensile stress concentration in the grain boundary phase near the large grains can indeed reach 15-30 times the far field applied stress.

Comparison of Lifetime under Static and Cyclic Loadings

Fig. 1 shows that the high temperature cyclic fatigue life is at least an order of magnitude longer than the corresponding static fatigue life. Since the failure mechanism of all specimens fractured under cyclic loading is slow crack growth, we consider possible strengthening effect during cyclic loading on slow crack growth. In ceramic materials, rate of slow crack growth is determined exclusively by the stress intensity factor, K_I, and it follows a phenomenological power law equation of type [36].

$$v = \frac{da}{dt} = AK_I^n = A\left(Y\sigma\sqrt{\pi a}\right)^n \tag{4}$$

where v is the crack growth velocity, a is the crack size, K_I is the mode I stress intensity factor, A and n are temperature and environment dependent material constants, Y is the geometric factor, and σ is the applied stress. Based on this equation, if assuming that cyclic fatigue damage is simply the accumulation of static fatigue damage, then the cyclic fatigue lifetime for a square wave form loading (R=0.1) should be equal to about twice the static fatigue lifetime, a significant underestimate of the real cyclic fatigue life.

However, the applied far field stress intensity is often used in Equation (4). Perhaps the most important mechanism for cyclic strengthening is the crack face bridging by viscous grain boundary phase. Figs. 4 and 5 show that the crack surface behind the crack tip is extensively bridged by viscous ligaments. The bridging forces reduce the crack tip stress intensity and thus retard the crack propagation velocity.

Since bridging ligaments are viscous at elevated temperature, their mechanical response (bridging force) depends upon the crack surface opening rate, as shown by the measurement of Jakus et al [37]. Under static loading, crack face opening rate is only caused by crack tip extension, which is extremely low. Therefore, the bridging force under static loading is small. On the other hand, under cyclic loading of a reasonable frequency, the continuous change of the relative displacements of crack faces gives rise to a high bridging force and high crack tip shielding. Moreover, viscous bridging ligaments also dissipate a

large amount of energy during cyclic loading which would effectively impede the slow crack growth process.

The above discussion indicates that many material and loading parameters are expected to affect the cyclic crack growth behavior, such as the volume fraction of the grain boundary viscous phase, viscosity of the viscous phase which depends on the testing temperature and the loading frequency. For given viscosity of the grain boundary phase, a higher loading frequency will produce larger bridging forces, thus result in increased crack tip shielding and longer fatigue life. Evidence of such phenomenon was reported by Suresh and co-workers [24, 25]. They measured the cyclic (sine wave form) crack growth rates for an alumina (0.13 Hz and 2 Hz at 1050 C) and a silicon carbide reinforced alumina matrix composite (0.1 Hz and 2 Hz at 1400 C), and found that higher frequency cyclic loading resulted in more crack growth retardation and lower growth rate than the lower frequency cyclic loading.

A mechanistic model based on this mechanism has been developed by us [38]. A critical parameter controlling whether the cyclic strengthening is present has been identified. The parameter is a function of material properties such as the Young's modulus of the ceramic and viscosity of the grain boundary phase, and of microstructural quantities such as grain size and grain boundary phase thickness. The model predicts that under proper loading conditions, the cyclic fatigue life can be two orders of magnitude longer than the corresponding static fatigue life.

Conclusions

Uniaxial tensile experiments, under static and cyclic loading, of an alumina with about 6 wt% grain boundary viscous phase at 1000 C have been conducted. The lifetime under cyclic loading is greater than under static loading by approximately a factor of 30. The micromechanisms of failure have been examined. Under static loading, two distinct failure regimes have been identified. (a) At high stresses, fracture occurs by the slow growth of a single dominant crack along grain boundaries. (b) At low stresses, fracture occurs due to nucleation, growth and linkage of multiple microcracks. Fracture of all specimens under cyclic loading was due to slow growth of a single dominant crack.

Extensive crack surface bridging by viscous grain boundary phase behind the crack tip is detected. This viscous bridging behind the crack tip is responsible for the improved lifetime under cyclic loading.

Acknowledgments: This work was supported by the U.S. Department of Energy under Contract No. DE-FG02-91ER-45439. The SEM studies were conducted at the Center for Microanalysis at the Materials Research Laboratory at the University of Illinois at Urbana-Champaign.

References

1. G. R. Irwin, in *Handbuch der Physik*, Springer-Verlag, Berlin, Vol. 6, 551 (1958).

2. R. L. Tsai and R. Raj, Acta metall. 30, 1043 (1982).

3. B. J. Dalgleish, S. M. Johnson and A. G. Evans, J. Am. Ceram. Soc. 67, 741 (1984).

4. A. G. Evans, J. Am. Ceram. Soc. 65, 127 (1982).

5. A. G. Evans and A. Rana, Acta metall. 28, 129 (1980).

6. D. S. Wilkinson and V. Vitek, Acta metall. 30, 1723 (1982).

7. J. E. Marion, A. G. Evans, M. D. Drory and D. R. Clarke, Acta metall. 31, 1445 (1983).

8. M. D. Thouless, C. H. Hsueh and A. G. Evans, Acta metall. 31, 1675 (1983).

9. W. Blumenthal and A. G. Evans, J. Am. Ceram. Soc. 67, 751 (1984).

10. S. M. Johnson, B. J. Dalgleish and A. G. Evans, J. Am. Ceram. Soc. 67, 759 (1984).

11. B. J. Dalgleish, E. B. Slamovich and A. G. Evans, J. Am. Ceram. Soc. 68, 575 (1985).

12. D. R. Clarke, J. Mater. Sci. 20, 1321 (1985).

13. K. Jakus, S. M. Wiederhorn and B. J. Hockey, J. Am. Ceram. Soc. 69, 725 (1986).

14. M. D. Thouless and A. G. Evans, Acta metall. 34, 23 (1986).

15. R. A. Page and K. S. Chan, Metall. Trans. A 18, 1843, (1987).

16. G. D. Quinn, J. Mater. Sci. 25, 4361 (1990).

17. A. G. Robertson, D. S. Wilkinson and C. H. Caceres, J. Am. Ceram. Soc. 74, 915 (1991).

18. D. S. Wilkinson, C. H. Caceres and A. G. Robertson, J. Am. Ceram. Soc. 74, 922 (1991).

19. C. -K. J. Lin and D. F. Socie, J. Am. Ceram. Soc. 74, 1511 (1991).

20. C. -K. J. Lin, D. F. Socie, Y. Xu and A. Zangvil, J. Am. Ceram. Soc. 75, 637 (1992).

21. N. Dey, D. F. Socie and K. J. Hsia, J. Am. Ceram. Soc. 79, 2353-63 (1996).

22. T. Fett, G. Himsolt and D. Munz, Adv. Ceram. Mater. 1, 179 (1986).

23. M. Masuda, T. Soma, M. Matsui and I. Oda, J. Ceram. Soc. Jpn. 97, 612 (1989).

24. S. Suresh, pp. 759-68 in Fatigue 90, Vol. 2, Edited by H. Kitagawa and T. Tanaka, Materials and Component Engineering Publications Ltd., Birmingham, U.K., 1990.

25. L. X. Han and S. Suresh, J. Am. Ceram. Soc. 72, 1233 (1989).

26. A. G. Evans, L. R. Russell and D. W. Richerson, Metall. Trans. A 6, 707 (1975).

27. M. Kawai, H. Fujita, Y. Kanki, H. Abe and J. Nakayama, pp. 269-78 in Proceedings of the First International Symposium on Ceramic Components for Engines, Edited by S. Somiya, E. Kanai and K. Ando, Elsevier Applied Science Publishers Ltd., London, U.K., 1983.

28. S. Lathabai, Y.-W. Mai, and B. R. Lawn, J. Am. Ceram. Soc. 72, 1760 (1989).

29. D. A. Krohn and D. P. H. Hasselman, J. Am. Ceram. Soc. 55, 208 (1972).

30. H. N. Ko, J. Mater. Sci. Lett. 5, 464 (1986).

31. H. N. Ko, J. Mater. Sci. Lett. 8, 1438 (1988).

32. A. Bornhauser, K. Kromp and R. F. Pabst, J. Mater. Sci. 20, 2596 (1985).

33. K. Kromp and R. F. Pabst, J. Am. Ceram. Soc. 66, 106 (1983).

34. K. S. Chan and R. A. Page, J. Am. Ceram. Soc. 76, 803 (1993).

35. N. Dey, K. J. Hsia and D. F. Socie, "The Effects of Grain Size Distribution on Cavity Nucleation and Creep Deformation in Ceramics Containing Viscous Grain Boundary Phase", Acta Materialia, in press.

36. A. G. Evans and E. R. Fuller, Metall. Trans. A 5, 28 (1974).

37. K. Jakus, J. E. Ritter and R. H. Schwillinski, J. Am. Ceram. Soc. 76, 33 (1993).

38. N. Dey, D. F. Socie and K. J. Hsia, Acta metall. mater. 43, 2163-75 (1995).

SUBJECT INDEX

A

Alloys,
- 20MnMoNi55 steels, 108, 187-189
- 22NiMoCrCr37, 42
- 300M QT steels, 178
- 708 steels, 53, 104, 195
- 733B steels, 53, 69-72, 97, 181
- α-Fe, 125, 130-131
- austenitic stainless steels, 247, 250-258
- CrMoV steels, 187-188
- Cu, 160
- Cu-Al-Co, 247, 255-256
- dual phase steels, 237-243
- Fe-Cr-Co-Mo, 247, 254-258
- HY80 steels, 73
- HY130 steels, 52
- low carbon steels, 195
- Mo, 140
- mild steels, 51
- Nb-Cr-Ti, 207-209, 214
- pressure vessel steel, 42
- TiAl, 207-208, 210, 293-302
- Ti_3Al, 207-208
- Ti-6Al-4V, 64, 75-78
- TiNi, 247, 258, 342

Alpha + Beta Alloys, 69, 75, 78, 207

Alumina, 207, 367-375

Aluminides (see Intermetallics also)
- CoAl, 341
- FeAl, 329, 333-338
- Fe_3Al, 347-352
- NiAl, 328-333
- PST TiAl crystals, 293-302
- RuAl, 341
- TiAl, 207-208, 305-316, 293-302, 319-327
- Ti_3Al, 207-208, 293

Atomistic Fracture, 147

B

B2 Compounds
- AgMg, 341
- AuZn, 341
- CoAl, 341
- CsBr, 341
- CuZn, 340
- FeAl, 329, 333-338
- Fe_3Al, 347-352
- FeCo, 339
- NiAl, 329-333
- NiBe, 341
- NiTi, 247, 258, 342
- PdIn, 341
- RuAl, 341

Bend Test, 54, 295, 347-349

Bridging Ligaments, 66, 81-89, 101, 233-234, 240-241

Bridgman Technique, 249

Brittle Fracture
- 3D model, 81-92
- atomistic model, 147-155
- carbide thickness effect, 53, 171, 172
- crack arrest, 95-106, 233-234
- critical distance, 171-181
- dislocation model, 59-65, 125-135, 137-145, 157-162
- ductile-to-brittle fracture transition, 51-55, 125-135, 137-145, 157-162, 183, 189-190, 247-262, 331, 333, 355
- energy rate method, 107-122
- extrinsic factors, 329 334-335
- fractography, 59-65, 69-78, 177, 180, 271-275, 297-300, 309-313, 332, 335, 338, 339, 351, 356
- grain size effect, 52, 57, 171, 209, 210, 239-240, 307-308, 314-316, 319-327
- HAZ, 263-269
- historic failure, 11, 19-20
- intrinsic factors, 329

maximum principal stress criterion, 351
notch specimens, 171, 172, 237
probabilistic fracture model, 90-101, 193, 196-201
process zone model, 173, 243
RKR model, 82, 171, 172, 194
shear-induced fracture, 207-220
single crystals, 247-262, 331, 355-365
steels, 51-55, 237-244
strain energy density criterion, 352
temperature, 51-55, 174, 239
thermal stress, 217-218
weak-link model, 185-190, 243
weld metals, 41, 54, 171-181
Weibull's theory, 15, 171, 172

C
Ceramic, 355-364, 367-375
Charpy Impact Properties, 51-52, 54
Cleavage (see Brittle Fracture also)
atomistic model, 147-155
brittle-to-ductile fracture transition, 51-55, 125-135, 137-145, 157-162, 183, 189-190, 247-262, 266, 331, 333, 355
criteria, 51-54, 172, 175, 183-187, 193-203, 216-217, 230, 237, 239, 242-244, 297, 307, 369, 373, 351, 352, 357-363
dislocation model, 59-65, 125-135, 137-145, 157-162
fracture stress, 51-54, 160, 183-187, 193-203, 216-217, 230, 237, 239, 242-244, 297, 307, 369, 373
fracture surface, 59-65, 69-78, 177, 180, 271-275, 297-300, 309-313, 332, 335, 338, 339, 351, 356
grain size effect, 52, 57, 171, 210, 215, 239-240, 307-308, 314-316, 319-327
HAZ, 263-269
historic failure, 11, 19-20
ligament tearing model, 81-89
mechanism, 54-55, 59-66, 69-78, 125-135, 137-145, 171-181, 207-218, 229-234, 240-243, 329-342
notch specimen, 171, 172, 237,
plane, 295, 297-301, 333-338, 355-364
plasticity-induced, 59-66, 81-92, 95, 125-134, 137-143, 208-215
process zone model, 171, 243
single crystals, 247-262, 331, 355-365
statistical model, 90-91, 193, 196-201, 171-181
weak-link model, 185-190, 243
Compositional Effects, 335-336
Constraint, 62, 114-115, 183-186
Coplanar Slip Cracking, 208-210, 298
Crack Bridging (see Bridging Ligaments)
Crack Extension Force, 16, 17
Crack Initiation (see Cleavage Mechanism)
Crack Instability, 111-114, 215
Crack Orientation Effects, 293-302
Crack-tip Blunting, 116, 137, 299-300
Crack-tip Fracture Processes, 59-66, 69-78, 125-135, 137-143, 185-187, 197, 207-218, 232-234, 241, 299-300, 367-372
Crack-tip Shielding, 137, 140-142
Creep, 367-375
Creep Crack Growth, 367-375
Crystal Structure, 357
CTOD, 175, 266
Cyclic Oxidation, 217-218

D
Decohesion of Slipband, 208-210, 298
Defects, 329-330
Deformation Behavior, 305-316
Deformation Mechanism, 247-248
Deformation Twinning, 248, 251, 253
Delayed Cleavage, 90-92
Dislocations, 60-65, 126-132, 138-139, 210-212, 248-261
embryo, 127-130
instability, 157
nucleation, 125-130, 158-159
mobility, 125, 131-132, 137-140, 158- 159
pileups, 56, 230, 210-212
free zone, 141

Ductility, 210, 215, 293-294, 307-308, 314-316, 339
Duplex Microstructure, 305-309, 312, 314-315, 319
Dynamic Fracture, 18, 19, 27, 28, 100, 232-234

E
Electron Back Scatter Diffraction, 271
Embedded Atom Method, 331
Energy Rate Model, 107
Environmental Embrittlement, 334-335

F
Fatigue Crack Growth Data, 76
Fatigue Life Data, 312
Fractography, 59-65, 69-78, 267, 271-275, 297, 300, 309-313, 332, 335, 338, 339, 351, 356, 324, 325
Fracture (see Brittle Fracture and Cleavage also)
  compressive, 215-218
  ductile, 69, 189, 53, 338
  ductile-to-brittle fracture transition, 51-55, 125-135, 137-145, 183, 189-190, 247-262, 266, 331, 333, 355
  grain size effect, 52, 171, 210, 215, 239-240, 307-308, 314-316
  HAZ, 263-269
  initiation, 95-96, 229
  intergranular, 309, 312, 326, 335, 347
  interlamellar, 309, 311
  mixed mode, 62-66, 208-213, 347-352
  shear-induced, 207-218
  tensile, 215, 307-310, 313-316, 334
  toughness, 56, 57, 98, 132, 139, 174, 189, 190, 239-240, 242, 266, 293, 296-297, 299, 311, 315, 359-364
  transgranular, 312, 329 347
  translamellar, 309-311
Fracture Mechanics
  analytical, 18
  BCS crack, 25
  crack extension force, 16
  crack opening displacement concept, 25
  creep and visco-elastic fracture, 28
  Dugdele-Barrenblatt crack, 24-25
  dynamic fracture, 18, 27-28, 100, 232-234
  elastic-plastic fracture mechanics, 26, 27
  fatigue, 23
  first application, 17
  Griffith's work, 8-10
  historic review, 3-30, 39-45
  HRR field, 26, 27
  in Eastern Europe, 20, 21
  in Germany, 19, 39-45
  Inglis' stress concentration, 8
  Irwin's plastic zone size correction, 23
  Irwin's work, 14-19
  Irwin-Orowan extension of Griffith criterion, 15
  J-integral, 26, 27
  K-concept, 17
  photomechanics, 16
  RKR model, 82, 171, 172, 194
  size effect, 4, 6, 7, 15
  small-scale yielding, 24, 25
  standardization, 21-22
  strain energy release rate, 16
  strip-yield model, 24, 25
  Westergaard stress function, 11
Fracture Mode, 62-66, 208-213, 347-352
Fracture Resistance Curve, 42, 108, 109, 230
Fully Lamellar Microstructure, 208, 294, 305-307

G
Gamma TiAl, 208, 293, 305
Glass, 41, 43, 44, 63
Grain Boundary Effects, 336
Grain Boundary Fracture, 309, 312, 326, 347, 335, 370-372
Grain Size Effect, 52, 210, 215, 239-240, 307-308, 314-316
Griffith Criterion, 7, 8, 138, 159, 172, 207, 242, 363

H
Hall-Petch Relation, 56, 57, 307-308, 314-316, 319-327
Heat Affected Zone, 263-269
Heat Treatment, 249, 305-306, 194, 195, 349
High Temperature Fracture, 367

I
Impact Properties (see Charpy Impact Properties)
Inclusion, 54, 55, 171-181
Indentation, 44
Interface Delamination, 298, 299, 310
Intergranular Fracture, 309, 312, 326, 335, 347
Interlamellar Fracture, 309, 311
Intermetallics (see Aluminides also)
AgMg, 342
AuZn, 342
CoAl, 341
CsBr, 342
CuZn, 340
FeAl, 329, 333-338
Fe_3Al, 347-352
FeCo, 339
NiAl, 329-333
NiBe, 342
NiTi, 342
PdIn, 342
PST Ti crystals, 293-302
RuAl, 341
TiAl, 207-208, 293-302, 305-316
Ti_3Al, 207-208, 293
Irwin-Orowan Extension of Griffith Criterion, 15
Irwin's Biography, 11-30
Irwin's Plastic Zone Size Correction, 23

J
J_{Ic}, 107, 188-190, 211, 296, 300
J-Q Theory, 183-187
J-resistance Curve, 42
J Testing, 295

K
K Concept, 13
K_{Ic} (see Fracture Toughness)
K Testing, 348, 349

L
Lamellar Microstructure (see Fully Lamellar Microstructure)
Ligaments (see Bridging Ligaments)
Ligament Tearing Model, 81-89
Ligament Tearing Work, 81-89
Line Tension, 61

M
Machining of Brittle Materials, 43, 44
Mechanical Properties (see Yield Strength, Tensile Properties, and Fracture Toughness also), 322, 323
Microcracks, 55, 83-87, 99, 208, 209, 212, 213, 215-218, 232, 234, 240, 241
Microstructural Mechanics, 51
Microstructure, 70-78, 238, 265, 266, 306, 307, 349, 350
Microstructure/Property Relation, 53, 56, 210, 215, 239, 240, 242, 267, 293, 308, 311, 314-316, 319-327
Minerals, 62, 355-364

N
Nitrides, 263-269
Nucleation
crack (see Cleavage Mechanism)
dislocation, 125-130

O
Oxidation, 217-218
Oxides, 218, 368

P
Planar Slip, 208-210, 298, 329
Plastic Deformation, 69, 137, 247-261, 305-316, 330, 332
Plasticity-Induced Fracture, 59-66, 81-92, 95, 125-134, 137-143, 208-215

Plastic Zone, 208, 209, 212, 213, 232, 234
Probability Distribution Function, 178, 179, 181
Process Zone, 137, 197, 208, 209, 211, 232, 234, 241, 243

R
River Pattern, 59-66
Rock Salt, 207, 217

S
Schmid Law, 248
Semiconductor
Ge, 139, 161
Si, 131-133, 160, 161
Shear Fracture, 55, 128-130, 347, 351-352
Shear-Induced Fracture, 207-218
Shear Ligament, 66, 82
Shockley Partial Dislocations, 248
Slipband Cracking, 207, 215, 297-302
Slipband Decohesion, 207-210
Slip System, 248-261, 329-338
Statistical Fracture, 15, 171, 172, 185-190, 243
Strain Energy Release Rate, 16, 17, 39
Strain Rate Dependence, 161, 297, 334
Strength (see Yield Strength and Tensile Strength)
Strength/Ductility Relation, 307, 308
Strength/Toughness Relation, 57, 174, 243
Stress-Strain Curve, 250, 252, 256, 258
Stroh Crack, 207-218, 319-321

T
TEM, 250, 253, 337
Temperature Dependence, 52, 54, 139, 142, 174, 189-190, 195, 197, 201, 218, 239, 253-255, 257, 259, 307, 315, 339
Tensile Fracture, 215, 307-310, 313-316, 334
Tensile Properties, 52-55, 195, 197, 201, 210, 239, 242, 243, 250, 252, 254-259, 293, 297, 307, 308, 314, 316, 332, 339
Thin Sheet Toughening, 299, 300
Tilting Crack, 64, 81
TiN Particles, 263-269
Toughness (see Fracture Toughness, K_{Ic}, J_{Ic})
Toughening Mechanism, 299, 300
Transgranular Fracture, 312, 329, 347
Translamellar Fracture, 309-311

W
Welds, 41, 54, 73-74, 171-181, 263-269
Wing Crack, 215-218

Y
Yield Strength, 52, 54, 57, 160, 174, 195, 197, 201, 230, 242, 254, 255, 257, 258, 307, 308, 314-316, 332

AUTHOR INDEX

A
Akiyama, N., 293
Argon, A.S., 125
Armstrong, R.W., 51, 69

B
Baker, I., 329
Beazley, D.M., 165
Bradt, R.C., 355

C
Cao, W.-D., 237
Chan, K.S., 207
Chumlyakov, Y.I., 247
Ciftan, M., 167

D
Davis, C.L., 263
Dey, N., 367
Dickson, J.I., 277
Dimiduk, D.M., 305
Donahue, E., 289

E
Edsinger, K.V., 221, 223

F
Farkas, D., 163
Foct, J., 277
Folk, R.H., II, 157
Frasier, F.R., 347

G
Gerberich, W.W., 285
Gibala, R., 287
Gonis, A., 167

H
Hirsch, P.B., 137
Hirth, J.P., 347
Holian, B.L., 165
Hsia, K.J., 367
Hull, D., 59

I
Inui, H., 293
Irwin, G.R., 51, 69

J
Johnson, D.R., 293

K
Kim, Y.-W., 305
Kioussis, N., 167
Kireeva, I.V., 247
Kirillov, V.I., 247
Kishida, K., 293
Knott, J.F., 171
Kolednik, O., 271
Kriese, M.D., 285

L
Labovitz, S.M., 157
Landes, J.D., 183
Li, D.M., 193
Litvinova, E.I., 247
Lomdahl, P.S., 165
Lou, K., 319
Lu, G., 167
Lucas, G.E., 221, 223, 289

M
Marder, M., 147
McClintock, F.A., 81
Mercer, C., 319
Messai, A.H., 277
Miranda, C.A.J., 183
Moody, N.R., 285
Munroe, P.R., 329

O
Odette, G.R., 221, 223, 289
Ortiz, M., 125

P
Paris, P.C., 47
Pippan, R., 271
Pope, D.P., 157
Preston, D., 165

R
Roberts, S.G., 137
Rosenfield, A.R., 229
Rossmanith, H.P., 3

S
Semprimoschnig, C.O.A., 271
Smith, E., 95
Soboyejo, W.O., 319
Socie, D.F., 367
Sommer, E., 39
Strangwood, M., 263
Surikova, N.S., 247

T
Thompson, A.W., 225
Tregoning, R.L., 69
Turner, C.E., 107

V
Vogt, J.-B., 277

X
Xu, G., 125

Y
Yamaguchi, M., 293
Yao, M., 193
Yokoshima, S., 293

Z
Zhang, L.P., 263
Zhang, X.J., 51, 69
Zhou, S.J., 165